

# Model-Based Systems Engineering of Flight Control for VTOL Transition Aircraft

Jorg Nicolai Angelov

Vollständiger Abdruck der von der TUM School of Engineering and Design der Technischen Universität München zur Erlangung eines  
Doktors der Ingenieurwissenschaften (Dr.-Ing.)  
genehmigten Dissertation.

Vorsitz: Prof. Dr. Sophie Armanini

Prüfer der Dissertation:

1. Prof. Dr.-Ing. Florian Holzapfel
2. Prof. Dr.-Ing. Manfred Hajek

Die Dissertation wurde am 01.09.2022 bei der Technischen Universität München eingereicht  
und durch die TUM School of Engineering and Design am 28.11.2022 angenommen.

All models are wrong, but some are  
useful.

---

George Edward Pelham Box

# Abstract

The new era of air mobility yields exciting trends and developments in the area of electric VTOL aircraft. Being a novel type of aerial vehicle, engineers are facing various challenges regarding the development of feasible concepts for operating and controlling these systems. Due to the lack of practical experience, the formulation of established requirements represents a difficult task that needs to be properly addressed.

To this end, the present thesis proposes a model-based systems engineering approach for developing operational concepts and flight control functions for VTOL transition aircraft. The application of systems-theoretic paradigms such as the concept of systems thinking as well as following a comprehensive process model for addressing problems and challenges support the proper development of high-quality solutions.

Furthermore, the integration and utilization of system models during the development yields the possibility to specify, simulate, and validate requirements on different abstraction levels. The applied model-based design (MBD) process helps creating new kinds of systems that have not been realizable before.

Following the systems engineering principle of a top-down development approach, the behavioral specification of a reference VTOL transition aircraft configuration is derived based on the operational and performance requirements that are proposed by certification bodies like the European Union Aviation Safety Agency (EASA) and the Federal Aviation Administration (FAA). The resulting Simplified Vehicle Operations (SVO) are aimed at enabling carefree handling of the aircraft by providing an intuitive and unified command concept throughout every flight phase as well as deeply integrating flight envelope protections. Thereby, the utilization of a novel control inceptor concept supports the handling and pilot's awareness of the current flight state.

By modeling the aircraft's behavior in terms of a system-architecture-agnostic executable specification model under consideration of kinetic constraints, the proposed SVO and command concept is validated early on in the development process without requiring knowledge about the specific functional topology or individual components of the VTOL transition aircraft. Thereby, the specification model is verified against existing handling quality requirements and evaluated in the context of pilot-in-the-loop simulations.

The functional decomposition into an executable control architecture model and the subsequent implementation of a code-generateable design model enable the consecutive specification and validation of the flight controller functions and algorithms by means of

model simulation. The systematic application of unit and integration tests, static code analysis, as well as statistical methods and optimization algorithms for finding rare failure events furthermore support comprehensive verification of the resulting flight controller and ensure its functional integrity in the presence of uncertainties and disturbances.

# Zusammenfassung

Die neue Ära des Luftverkehrs bringt spannende Trends und Entwicklungen im Bereich der elektrischen, senkrechtstartenden Flugzeuge mit sich. Bedingt durch die Neuheit dieser Art von Luftfahrzeugen sehen sich Ingenieure etlichen Herausforderungen gegenüber, geeignete Konzepte für die Operation und Regelung dieser Systeme zu entwickeln. Aufgrund fehlender praktischer Erfahrungen stellt die Formulierung etablierter Anforderungen eine schwierige Aufgabe dar, mit der es sich in angemessener Art und Weise auseinanderzusetzen gilt.

Zu diesem Zweck wird in der vorliegenden Arbeit ein modellbasierter, systemtechnischer Ansatz für die Entwicklung von Betriebskonzepten und Flugregelungsfunktionen für senkrechtstartende Transitionsflugzeuge vorgestellt. Sowohl die Anwendung systemtheoretischer Paradigmen wie das Konzept des Systemdenkens als auch das Befolgen eines ganzheitlichen Prozessmodells zur Auseinandersetzung mit Problemen und Herausforderungen unterstützen die sachgemäße Entwicklung hochqualitativer Lösungen.

Darüber hinaus bietet die Integration und Nutzung von Systemmodellen während der Entwicklung die Möglichkeit, Anforderungen unterschiedlichen Abstraktionsgrades zu spezifizieren, zu simulieren und zu validieren. Der angewandte modellbasierte Entwicklungsprozess ermöglicht es, neuartige Systeme zu realisieren, die zuvor nicht möglich gewesen wären.

Nach dem systemtechnischen Prinzip eines Top-down-Entwicklungsansatzes wird die Verhaltensspezifikation für eine Referenzkonfiguration eines senkrechtstartenden Transitionsflugzeuges auf Grundlage operationeller und leistungsbezogener Anforderungen hergeleitet, welche von Zertifizierungsstellen wie der European Union Aviation Safety Agency (EASA) und der Federal Aviation Administration (FAA) vorgegeben werden. Das daraus resultierende Simplified Vehicle Operations (SVO) Konzept zielt darauf ab, die unbeschwerte Bedienung des Flugzeuges durch ein intuitives und einheitliches Steuerkonzept in jeder Flugphase zu ermöglichen und dabei die Einhaltung der Flugbereichsgrenzen sicherzustellen. Dabei unterstützt der Einsatz eines neuartigen Steuerknüppelkonzepts das Flugverhalten und das Bewusstsein des Piloten über den aktuellen Flugzustand.

Durch die Modellierung des Flugzeugverhaltens in Form eines systemarchitekturunabhängigen, ausführbaren Spezifikationsmodells unter Berücksichtigung kinetischer Randbedingungen wird das hergeleitete SVO- und Steuerkonzept bereits in einem frühen Stadium des Entwicklungsprozesses validiert, ohne dass dabei Kenntnisse über die spezifische

Funktionstopologie oder individuelle Komponenten des Transitionsflugzeuges erforderlich sind. Dabei wird das Spezifikationsmodell gegenüber bestehender Anforderungen an das Flugverhalten verifiziert und im Rahmen von Pilot-in-the-Loop-Simulationen bewertet.

Die funktionale Zerlegung in ein ausführbares Reglerarchitekturmodell und die anschließende Implementierung eines codegenerierbaren Entwurfsmodells ermöglichen die schrittweise Spezifikation und Validierung der Flugregelungsfunktionen und -algorithmen mittels Modellsimulation. Die systematische Anwendung von Komponenten- und Integrationstests, statischer Codeanalyse sowie statistischer Methoden und Optimierungsalgorithmen zum Auffinden seltener Fehlerereignisse unterstützen darüber hinaus eine umfassende Verifikation des resultierenden Flugreglers und stellen dessen Funktionsfähigkeit in Anwesenheit von Unsicherheiten und Störungen sicher.

# Vorwort

Die vorliegende Dissertation ist während meiner Tätigkeit als wissenschaftlicher Angestellter am Lehrstuhl für Flugsystemdynamik an der Technischen Universität München in den Jahren 2017 bis 2022 entstanden. Einige Abschnitte dieser Arbeit wurden bereits vorab veröffentlicht in [1] und [2].

An dieser Stelle möchte ich mich zunächst bei Prof. Dr.-Ing. Florian Holzapfel bedanken, der den Lehrstuhl leitet und mir ermöglicht hat, praxisnah an der Entwicklung spannender Systeme von morgen zu arbeiten. Das mir entgegengebrachte Vertrauen, die fachlich anregenden Diskussionen sowie die unkomplizierte Abwicklung von Prozessen weiß ich sehr zu schätzen. Außerdem gilt mein Dank Prof. Dr.-Ing. Manfred Hajek für seinen Einsatz als Zweitgutachter der Dissertation. Als Leiter des Lehrstuhls für Hub-schraubertechnologie und aufgrund seiner langjährigen Industrieerfahrung ist sein Fachwissen von mir hoch angesehen.

Des Weiteren möchte ich mich bei meinen vielen Kollegen am Lehrstuhl für den fachlichen Austausch und die gute Zusammenarbeit trotz pandemiebedingter Einschränkungen bedanken. Insbesondere möchte ich mich bei Valentin Marvakov, Pranav Bhardwaj und Stefan Raab bedanken für die vielen fachlichen Diskussionen und kritischen Denkanstöße in den letzten Jahren.

Zu guter Letzt gilt mein größter Dank meinen Eltern, Violeta und Asen, die mich immer nach Kräften unterstützt haben und ohne die ich nicht in der Lage gewesen wäre, diesen Meilenstein zu erreichen, sowie meiner Freundin Eva, die mir zur Seite stand und meinen Enthusiasmus über die Welt der Wissenschaft und Ingenieurskunst geduldig ertragen hat und in Zukunft hoffentlich noch weiterhin ertragen wird.





# Table of Contents

- List of Figures VIII
  
- List of Tables IX
  
- Acronyms XI
  
- Symbols and Indices XV
  
- 1 Introduction 1**
  - 1.1 Motivation and Background . . . . . 1
  - 1.2 State of the Art . . . . . 3
  - 1.3 Mission Statement . . . . . 6
  - 1.4 Contributions . . . . . 8
  - 1.5 Outline . . . . . 10
  
- 2 Model-Based Systems Engineering 13**
  - 2.1 Principles of Systems Engineering . . . . . 13
    - 2.1.1 Systems Thinking . . . . . 13
    - 2.1.2 Process Model . . . . . 15
      - 2.1.2.1 From the General to the Specific . . . . . 16
      - 2.1.2.2 Variant Creation . . . . . 17
      - 2.1.2.3 Problem Solving Cycle . . . . . 18
      - 2.1.2.4 Phased Approach . . . . . 22
  - 2.2 The Role of Models in Systems Engineering . . . . . 27
    - 2.2.1 Models as Abstraction of Reality . . . . . 27
    - 2.2.2 Verification and Validation Through Model Simulation . . . . . 29
  
- 3 Mission Specification and Reference Configuration 35**
  - 3.1 Mission Specification . . . . . 35
    - 3.1.1 Operational Requirements . . . . . 35
    - 3.1.2 Performance Requirements . . . . . 36
      - 3.1.2.1 Take-off and Climbing . . . . . 37
      - 3.1.2.2 Landing . . . . . 40

3.2	Reference Configuration of the Aircraft . . . . .	41
3.2.1	Kinetic Configuration . . . . .	42
3.2.2	Control Inceptors . . . . .	45
<b>4</b>	<b>Behavioral Specification of the System</b>	<b>51</b>
4.1	Continuity-Based Input-Output Mapping . . . . .	52
4.2	Simplified Vehicle Operations for Onboard Piloted VTOL Transition Aircraft	57
4.2.1	Low Velocity Operation: Hover . . . . .	58
4.2.1.1	Left Longitudinal and Lateral Stick Channel During Hover Phase . . . . .	58
4.2.1.2	Right Longitudinal Stick Channel During Hover Phase . .	62
4.2.1.3	Right Lateral Stick Channel During Hover Phase . . . . .	63
4.2.2	Medium Velocity Operation: Transition . . . . .	64
4.2.2.1	Left Longitudinal Stick Channel During Transition Phase	65
4.2.2.2	Left Lateral Stick Channel During Transition Phase . . . .	67
4.2.2.3	Right Longitudinal Stick Channel During Transition Phase	68
4.2.2.4	Right Lateral Stick Channel During Transition Phase . . .	68
4.2.3	High Velocity Operation: Wingborne . . . . .	70
4.2.3.1	Left Longitudinal Stick Channel During Wingborne Phase	70
4.2.3.2	Left Lateral Stick Channel During Wingborne Phase . . .	73
4.2.3.3	Right Longitudinal Stick Channel During Wingborne Phase	73
4.2.3.4	Right Lateral Stick Channel During Wingborne Phase . .	75
4.3	Design Reference Model . . . . .	77
4.3.1	Outer Loop Control for Hover Phase . . . . .	80
4.3.1.1	Vertical Velocity Control . . . . .	81
4.3.1.2	Across-Heading Velocity Control . . . . .	82
4.3.1.3	Along-Heading Velocity Control Without Use of Traction System . . . . .	83
4.3.1.4	Along-Heading Velocity Control With Use of Traction Sys- tem . . . . .	84
4.3.1.5	Heading Rate Control . . . . .	86
4.3.2	Outer Loop Control for Transition Phase . . . . .	86
4.3.2.1	Roll Angle Control . . . . .	86
4.3.2.2	Angle of Attack and Lateral Velocity Control . . . . .	86
4.3.2.3	Vertical Velocity Control . . . . .	89
4.3.2.4	Airspeed Control . . . . .	89
4.3.3	Outer Loop Control for Wingborne Phase . . . . .	90
4.3.3.1	Vertical Velocity Control . . . . .	90
4.3.3.2	Lateral Specific Force Control . . . . .	93
4.3.4	Inner Loop Control . . . . .	94
4.3.5	Force and Moment Emulation . . . . .	96

4.3.5.1	Control Forces and Moments . . . . .	96
4.3.5.2	Gravitational and Aerodynamic Forces . . . . .	99
4.3.6	Rigid-Body Equations of Motion . . . . .	100
4.4	Verification and Validation of Behavioral Specification . . . . .	101
4.4.1	Hover Flight . . . . .	101
4.4.1.1	Translational Control . . . . .	101
4.4.1.2	Yaw Control . . . . .	105
4.4.2	Transition and Wingborne Flight . . . . .	107
4.4.3	Pilot-in-the-Loop Simulation . . . . .	108
<b>5</b>	<b>Control Architecture Specification</b>	<b>111</b>
5.1	Principles of Incremental Nonlinear Dynamic Inversion . . . . .	112
5.2	On Considering Control Effector Limitations . . . . .	116
5.2.1	Motivation . . . . .	116
5.2.2	Saturation Analysis in Time Domain . . . . .	118
5.2.3	Effective Inner-Loop Bandwidth . . . . .	119
5.2.4	Effective Outer-Loop Bandwidth . . . . .	121
5.2.5	Roll Stabilization Example With Two Motors . . . . .	125
5.3	Control Architecture Specification Model . . . . .	132
5.3.1	Voting and Monitoring . . . . .	136
5.3.2	Moding . . . . .	138
5.3.2.1	Execution Mode Layer . . . . .	139
5.3.2.2	Flight Mode Layer . . . . .	139
5.3.2.3	Powered Lift Mode Layer . . . . .	143
5.3.2.4	Degradation Mode Layer . . . . .	145
5.3.3	Command Scaling and Transformation . . . . .	147
5.3.3.1	Control-Margin-Awareness-Based Stick Mapping . . . . .	148
5.3.3.2	Airspeed Limits . . . . .	151
5.3.3.3	Forward and Lateral Channel Command . . . . .	153
5.3.3.4	Vertical Channel Command . . . . .	155
5.3.3.5	Turn Channel Command . . . . .	164
5.3.4	Outer Loop . . . . .	169
5.3.4.1	Hover and Powered Lift Control . . . . .	171
5.3.4.2	Highspeed Control . . . . .	193
5.3.5	Inner Loop . . . . .	208
5.3.5.1	Complementary Acceleration Filter . . . . .	210
5.3.5.2	Feedback Assembly . . . . .	214
5.3.5.3	Euler Angle Rate Control . . . . .	217
5.3.5.4	Rotational Acceleration Control . . . . .	220
5.3.5.5	Forward Specific Force Control . . . . .	224
5.3.5.6	Control Effector Estimation . . . . .	226

5.3.5.7	Control Allocation . . . . .	230
5.4	Verification and Validation of Control Architecture . . . . .	248
5.4.1	Bottom-Up Verification of Side-Step Maneuver . . . . .	252
5.4.1.1	Plant Description . . . . .	252
5.4.1.2	Simulation Results . . . . .	253
5.4.2	Validation by Full Flight Mission Simulation . . . . .	257
5.4.2.1	Take-Off and First Climb Segment . . . . .	258
5.4.2.2	Transition and Second Climb Segment . . . . .	259
5.4.2.3	Cruise Flight . . . . .	261
5.4.2.4	Approach . . . . .	262
5.4.2.5	Retransition and Final Approach . . . . .	263
5.4.2.6	Landing . . . . .	264
<b>6</b>	<b>Control Algorithm Design and Implementation</b>	<b>265</b>
6.1	Controller Discretization . . . . .	266
6.1.1	Derivation of the Z-Transformation . . . . .	267
6.1.2	Bilinear Transformation . . . . .	269
6.1.3	Frequency Prewarping . . . . .	271
6.1.4	Implementation of the Difference Equation . . . . .	272
6.2	Control Design Model . . . . .	275
6.2.1	Modeling Guidelines . . . . .	277
6.2.2	Implementation of Component Design Model for Complementary Filter . . . . .	279
6.2.3	Code Generation and Software-in-the-Loop Simulation of Comple- mentary Filter . . . . .	281
6.3	Verification and Validation of Control Algorithms and Source Code . . . . .	284
6.3.1	Static Code Analysis . . . . .	284
6.3.2	Unit and Integration Tests . . . . .	287
6.3.3	Subset Simulation and Counter Optimization for Finding Rare Fail- ure Events . . . . .	289
<b>7</b>	<b>Conclusion and Outlook</b>	<b>293</b>
7.1	Summary and Conclusion . . . . .	293
7.2	Outlook and Perspectives . . . . .	298

# List of Figures

1.1	Electric VTOL Aircraft. Top row: Joby S4, Kitty Hawk Cora, Lilium Jet. Bottom row: Voloconnect, Volocity, Aurora PAV (Sources: Company sites and evtol.news) . . . . .	1
1.2	‘V’-Model Development Process [3] . . . . .	3
2.1	Three Categories of Systems [4] . . . . .	14
2.2	From the General to the Specific (Adapted from [3]) . . . . .	16
2.3	Variant Creation in Increasing Detail (Adapted from [3]) . . . . .	17
2.4	Problem-Solving Cycle [3] . . . . .	19
2.5	Modeling Dimensions (adapted from [5]) . . . . .	28
2.6	Model-Based ‘V’-Model Development Process Using Requirement Specification Models (green) for Validation . . . . .	29
2.7	Model-Based Validation Loop . . . . .	31
3.1	Possible Take-off Paths [6] . . . . .	38
3.2	“Reference Volume Type 1” Vertical Take-off and Landing Procedure Parameters [6] . . . . .	39
3.3	Landing Path [6] . . . . .	40
3.4	Exemplary NASA Concept Vehicles: Quadrotor, Side-by-Side Helicopter, and Tilt-Wing Aircraft Concept [7] . . . . .	42
3.5	Exemplary Lift-Plus-Cruise Concept Vehicle [8] . . . . .	43
3.6	Existing Lift-Plus-Cruise Transition Aircraft. Top row: Autoflight V1500M, Aurora PAV. Bottom row: Voloconnect, Kitty Hawk Cora (Sources: Company sites) . . . . .	44
3.7	Boeing 737-300 Cockpit (left) and Airbus A320 Cockpit (right) (Source: flugzeug-lexikon.de) . . . . .	45
3.8	EZ Fly Control Inceptor Concepts [9] . . . . .	46
3.9	Control Inceptor Mapping in Patent from Joby Aviation [10] . . . . .	47
3.10	VTOL Simulator Mock-Up at the Institute of Flight System Dynamics (FSD) of the Technical University of Munich (TUM) [11] . . . . .	48
3.11	Schematic Representation of the Control Inceptors . . . . .	49

4.1	Mapping of Left Control Inceptor During Switch From Transition Mode (red) to Wingborne Mode (blue) for Three Different Cases . . . . .	56
4.2	SVO Table: Command and Target Variables During Hover, Transition, and Wingborne Flight . . . . .	58
4.3	Left Control Inceptor in Spring-Centered Position (a), in Throttle Lever Position (b), and Close-Up of the Detent Notch (c) . . . . .	59
4.4	Coordinate Frames . . . . .	60
4.5	Mapping of Left Control Inceptor to Translational Rate During Hover Flight	61
4.6	Cockpit Control Deflection/Force Versus Translational Rate According to ADS-33E-PRF [12] . . . . .	62
4.7	Mapping of Left Control Inceptor During Transition . . . . .	66
4.8	Overview of Left Control Inceptor Mapping for Transition Mode (red) and Wingborne Mode (blue) . . . . .	71
4.9	Rate of Climb for Different Airspeeds . . . . .	74
4.10	Design Reference Model (DRM) as Highest Abstraction Level of Closed-Loop System (figure adapted from [3]) . . . . .	77
4.11	Control Structure of DRM . . . . .	79
4.12	Angle of Attack During Transition Phase (No Wind) . . . . .	87
4.13	Angle of Sideslip . . . . .	93
4.14	Powered Lift Dynamics . . . . .	97
4.15	Hover Maneuver Vertical Channel . . . . .	102
4.16	Hover Maneuver Forward Channel . . . . .	103
4.17	Translational Rate Equivalent Risetime (ADS-33E-PRF [12]) . . . . .	104
4.18	Moderate-Amplitude Heading Changes (Attitude Quickness) . . . . .	105
4.19	Lateral Wind Gust During Hover Flight . . . . .	106
4.20	Complete Transition and Retransition Maneuver of DRM . . . . .	108
4.21	Pilot-in-the-Loop Simulation . . . . .	109
4.22	Mission Task Elements . . . . .	109
5.1	Roll Rate Response for Different Amplitudes . . . . .	119
5.5	2D Example Configuration . . . . .	126
5.9	Control Architecture Specification Model (CASM) on the Architecture Specification Level (figure adapted from [3]) . . . . .	132
5.10	High-Level Structure of the CASM . . . . .	135
5.11	Mid Value Selection Voting for Three Redundant Signals . . . . .	137
5.12	Control Law Moding Hierarchy . . . . .	138
5.13	Effect of Built-In Testing on Probability of Mission Failure [13] . . . . .	140
5.14	Command Scaling and Transformation Block . . . . .	148
5.15	Generalized Control-Margin-Awareness-Based Stick Mapping . . . . .	149
5.16	Airspeed Limits Block . . . . .	151
5.17	Forward and Lateral Channel Command Block . . . . .	153

5.18	Vertical Channel Command Block . . . . .	155
5.19	Absolute Maximum Climb Rate Block . . . . .	156
5.20	Absolute Maximum Sink Rate Block . . . . .	159
5.21	Stability Boundary of VRS Model [14] . . . . .	160
5.22	Linear Maximum and Minimum Height Rate Block . . . . .	163
5.23	Turn Channel Command Block . . . . .	164
5.24	Maximum Vertical Force Block . . . . .	165
5.25	Absolute Maximum Heading Rate Block . . . . .	167
5.26	Linear Maximum Heading Rate Block . . . . .	168
5.27	Outer Loop Block . . . . .	169
5.28	Hover and Powered Lift Control Block . . . . .	171
5.29	Powered Lift Based Height Rate Control Block . . . . .	172
5.30	Powered Lift Command Saturation . . . . .	176
5.31	Horizontal Kinematic Velocity Control block . . . . .	178
5.32	Forward Velocity Control block . . . . .	179
5.33	Equilibrium Pitch Angle During Traction-Based Forward Control . . . . .	185
5.34	Forward Velocity Control block . . . . .	187
5.35	Hover Attitude Protection block . . . . .	191
5.36	Attitude Limits in Different Heights . . . . .	192
5.37	Highspeed Control Block . . . . .	193
5.38	Wingborne Height Rate Control Block . . . . .	194
5.39	Pitch and Angle of Attack Control Block . . . . .	199
5.40	Excess Powered Lift for Different Total Lift Demands . . . . .	201
5.41	Lateral Control Block . . . . .	203
5.42	Highspeed Attitude Protection block . . . . .	206
5.43	Powered Lift Control Block . . . . .	207
5.44	Inner Loop Block . . . . .	209
5.45	First Order Complementary Filter Type I . . . . .	211
5.46	First Order Complementary Filter Type II . . . . .	213
5.47	Euler Angle Rate Control Block . . . . .	218
5.48	Rotational Acceleration Control Block . . . . .	221
5.49	Roll Rate Induced Local Angle of Attack Change . . . . .	223
5.50	Forward Specific Force Control Block . . . . .	225
5.51	Control Effector Estimation Block . . . . .	227
5.52	Comparison of Second-Order Dynamics and Equivalent First-Order Dy- namics for Different Relative Dampings . . . . .	229
5.53	Control Allocation Block . . . . .	232
5.54	Singular Value Decomposition (SVD) . . . . .	240
5.55	Closed-Loop Model with CASM and Plant . . . . .	249
5.56	Types of Verification for Requirements on Different Levels . . . . .	251

5.57	Core of Plant Simulation Model in Matlab Simulink . . . . .	252
5.58	Powered Lift Motor RPMs During Side-Step Maneuver . . . . .	253
5.59	Specific Control Roll Moment Rate . . . . .	254
5.60	Roll Acceleration Estimation . . . . .	255
5.61	Tracking Performance During Side-Step Maneuver . . . . .	256
5.62	Flight Mission Simulation . . . . .	257
5.63	Take-Off and First Climb Segment . . . . .	258
5.64	Transition to the Fixed-Wing Flight Regime . . . . .	259
5.65	Maximum Climb During Second Climb Segment . . . . .	260
5.66	Cruise Flight . . . . .	261
5.67	Approach . . . . .	262
5.68	Retransition and Final Approach . . . . .	263
5.69	Vertical Landing . . . . .	264
6.1	Discretizing a Signal With the Dirac Comb . . . . .	267
6.2	Approximating an Integral with Trapezoidal Integration . . . . .	269
6.3	Forward Euler Integration of Control Effector Step Response for Different Sample Times . . . . .	274
6.4	Control Design Model (CDM) on the Design Specification Level (figure adapted from [3]) . . . . .	275
6.5	Component Design Model of Complementary Filter . . . . .	279
6.6	Software- vs. Model-in-the-Loop Simulation of Complementary Filter . . .	282
6.7	Simulation Results of Software- vs. Model-in-the-Loop Simulation of Com- plementary Filter . . . . .	283
6.8	Types of Structural Coverage [15] . . . . .	286
6.9	Exemplary Hardware-in-the-Loop Setup for a Flight Control Computer [16]	288
6.10	Finding Rare Failure Events With Subset Simulation Using Markov Chain Monte Carlo Sampling . . . . .	291



# List of Tables

- 3.1 Definitions in the Context of SC VTOL . . . . . 37
- 4.1 Vertical Rate Requirements During Hover Flight [12] . . . . . 62
- 4.2 Heading Rate Requirements During Hover Flight [12] . . . . . 63
- 4.3 Maximum Values for Vertical Rate Response Parameters – Hover and Low Speed [12] . . . . . 102
- 5.1 Simulation Parameters of 2D Example . . . . . 130
- 5.2 Truth Table for Lower Airspeed Limit . . . . . 151
- 5.3 Truth Table for Upper Airspeed Limit . . . . . 152
- 5.4 Parameters of Second-Order and Equivalent First-Order System for Different Dampings . . . . . 230
- 6.1 Example of Modeling Guidelines [17] . . . . . 277
- 6.2 Design Assurance Levels and Applicable Process Objectives in DO-178C [18] 285



# Acronyms

<b>ADS</b>	Air Data System
<b>AMS</b>	Attainable Moment Set
<b>BIT</b>	Built-in Test
<b>BMS</b>	Battery Management System
<b>CASM</b>	Control Architecture Specification Model
<b>CDM</b>	Control Design Model
<b>CFP</b>	Critical Failure for Performance
<b>CMP</b>	Certified Minimum Performance
<b>CO</b>	Counter Optimization
<b>CPU</b>	Central Processing Unit
<b>CTO</b>	Continued Take-off
<b>ConvL</b>	Conventional Landing
<b>ConvTO</b>	Conventional Take-off
<b>DAL</b>	Design Assurance Level
<b>DFT</b>	Discrete Fourier Transform
<b>DRM</b>	Design Reference Model
<b>EConvTO</b>	Elevated Conventional Take-off
<b>ESC</b>	Electronic Speed Controller
<b>FAA</b>	Federal Aviation Administration
<b>FCC</b>	Flight Control Computer
<b>FFS</b>	Force Feel System
<b>FTO</b>	Final Take-off
<b>GPS</b>	Global Positioning System
<b>HIL</b>	Hardware-in-the-Loop
<b>HMI</b>	Human-Machine Interface
<b>HQRS</b>	Handling Quality Rating Scale
<b>HS</b>	Highspeed
<b>IMU</b>	Inertial Measurement Unit
<b>INCOSE</b>	International Council on Systems Engineering
<b>INDI</b>	Incremental Nonlinear Dynamic Inversion
<b>INO</b>	Incremental Nullspace Optimization

<b>ISA</b>	International Standard Atmosphere
<b>ITAE</b>	Integral Time Absolute Error
<b>LDP</b>	Landing Decision Point
<b>LDRV</b>	Landing Distance Required for VTOL
<b>LS</b>	Lowspeed
<b>MBD</b>	Model-Based Development
<b>MBSE</b>	Model-Based Systems Engineering
<b>MC/DC</b>	Modified Condition/Decision Coverage
<b>MCMC</b>	Markov Chain Monte Carlo
<b>MCS</b>	Monte Carlo Sampling
<b>MCT</b>	Maximum Continuous Thrust
<b>MHQRM</b>	Minimum Acceptable Handling Qualities Rating
<b>MISRA</b>	Motor Industry Software Reliability Association
<b>MPT</b>	Maximum Peak Thrust
<b>MTE</b>	Mission-Task Element
<b>MTO</b>	Maximum Take-off Thrust
<b>NDI</b>	Nonlinear Dynamic Inversion
<b>PFDD</b>	Primary Flight Display
<b>PID</b>	Proportional-Integrative-Derivative
<b>PSC</b>	Problem Solving Cycle
<b>PWM</b>	Pulse-Width Modulation
<b>RAM</b>	Requirement Assessment Model
<b>RL</b>	Reinforcement Learning
<b>RPI</b>	Redistributed Pseudo-Inverse
<b>RSM</b>	Requirement Specification Model
<b>RSPI</b>	Redistributed Scaled Pseudo-Inverse
<b>RTO</b>	Rejected Take-off
<b>SALM</b>	Specific Aerodynamic Lift Margin
<b>SCFM</b>	Specific Control Forces and Moments
<b>SEAL</b>	Specific Excess Aerodynamic Lift
<b>SEML</b>	Specific Excess Mixed Lift
<b>SET</b>	Specific Excess Thrust
<b>SIL</b>	Software-in-the-Loop
<b>SS</b>	Subset Simulation
<b>STD</b>	Specific Thrust Deficiency
<b>SVD</b>	Singular Value Decomposition
<b>TDP</b>	Take-off Decision Point
<b>TOGA</b>	Take-off/Go-Around
<b>TOSS</b>	Take-off Safety Speed
<b>UAM</b>	Urban Air Mobility

<b>VL</b>	Vertical Landing
<b>VRS</b>	Vortex Ring State
<b>VTO</b>	Vertical Take-off
<b>VTOL</b>	Vertical Take-off and Landing



# Symbols and Indices

## Symbols

Throughout this thesis, bold symbols denote either a vector or a matrix. Matrices are furthermore denoted with capital letters. If not mentioned otherwise, velocities, forces, and moments are always interpreted with respect to the center of gravity. For time derivatives of vector signals, the upper indices denote the coordinate frames with respect to which the derivatives are considered. The lower index denotes the coordinate system in which the vector is represented. Furthermore, kinematic velocities are interpreted with respect to a flat and non-rotating earth surface.

### Kinematics

$V$	Velocity
$d$	Stick deflection
$\alpha$	Angle of attack
$\beta$	Angle of sideslip
$\boldsymbol{\omega}$	Vector of rotational rates
$p$	Roll rate
$q$	Pitch rate
$r$	Yaw rate
$\boldsymbol{\epsilon}$	Vector of euler angles
$\phi$	Roll angle
$\theta$	Pitch angle
$\psi$	Heading angle
$\dot{\boldsymbol{\epsilon}}$	Vector of euler angle rates
$\dot{\phi}$	Roll angle rate
$\dot{\theta}$	Pitch angle rate
$\dot{\psi}$	Heading (angle) rate
$\mathbf{M}_{AB}$	Rotation matrix from B frame to A frame
$h$	Height above ellipsoid
$\omega$	Angular frequency or rotational rate

**Kinetics**

---

$g$	Reference gravitational acceleration
$f$	Specific force
$m$	Mass or specific moment
$F$	Force
$M$	Moment
$I$	Moment of inertia
<hr/>	
$\rho$	Reference air density
$S$	Reference wing surface area
$C$	Constant or coefficient
$L$	Lifting force
$D$	Drag force
$Q$	Side force
$T$	Thrust force
<hr/>	
$\delta$	Vector of aerodynamic control surface deflections
$\beta$	Vector of propeller pitch angles
$w$	Vector of rotational motor speeds
$u$	Vector of control inputs
$B$	Control effectiveness matrix
$\nu$	Vector of pseudo controls
<hr/>	

**Other**

---

$K$	Gain or constant
$E$	Energy
$t$	Time
$s$	Laplace variable
$z$	z-domain variable
$T$	Time interval
$P$	Probability distribution
<hr/>	



**Indices****Coordinate Frames**


---



---

<i>I</i>	Inertial frame
<i>B</i>	Body frame
<i>C</i>	Control frame
<i>O</i>	North-East-Down frame
<i>K</i>	Kinematic frame
<i>S</i>	Stick frame

---

<i>x</i>	Value in x-direction
<i>y</i>	Value in y-direction
<i>z</i>	Value in z-direction
<i>G</i>	Center of gravity

---

**Speeds**


---



---

CAS	Calibrated Air Speed
TOSS	Take-off Safety Speed
FTO	Final Take-off Speed
stall	Stall speed
stall,p	Safe speed
NO	Maximum speed for Normal Operations
NE	Never Exceed speed

---

US	Underspeed
OS	Overspeed
LS	Lowspeed
HS	Highspeed
HV or hvr	Hover
TS or trans	Transition
WB or wb	Wingborne

---

aer	Aerodynamic value
kin	Kinematic value
hor	Horizontal value
vert	Vertical value

---

**Control**


---



---

<i>d</i> or des	Desired value
<i>c</i> or cmd	Commanded value
<i>r</i> or ref	Reference value
<i>e</i> or err	Error value
<i>F</i> or filt	Filtered value

## SYMBOLS AND INDICES

---

ctrl or ctr	Control value
ec	Error control value
msr	Measured value
mdl	Modeled value
est	Estimated value
req	Required value
lead	Lead-filtered value
exc	Excess value
ff	Feedforward
fb	Feedback
<hr/>	
min	Minimum value
max	Maximum value
lo	Lower value
hi	Higher value
up	Upper value
lim	Limit value
abs	Absolute value
sat	Saturation value
<hr/>	
TS	Thrust Stick
CS	Climb Stick
PL	Powered Lift
TS	Traction System
AS	Aerodynamic Surface
OEI	One Engine Inoperative
<hr/>	

### Other

---

$i, j, k$	Current step or index
0	Initial or reference value
qdr	Quadratic related value
lin	Linear related value
eff	Effective value
opt	Optimal value
OP	Operational
AGL	Above Ground Level
LF	Low-frequency
HF	High-frequency

# 1

## Introduction

### 1.1 Motivation and Background <sup>1</sup>

Disruptive innovations in the area of electric propulsion, batteries, power electronics, and embedded computer systems are opening up a new era of air mobility [19] [20] and the use of *model-based development* (MBD) [21] [22] [23] [24] enables new kinds of systems that have not been possible before.

Specifically, rapid advances in the development of electric *vertical take-off and landing* (VTOL) aircraft are a key enabler for new types of missions and application scenarios, which are not feasible or not economical using existing vehicle concepts. Improving accessibility of remote areas, alleviating urban traffic congestion, or enabling faster and more economical transportation means for first responders represent some of the driving forces that have brought worldwide attention to electric VTOL aircraft (Figure 1.1) [25] [26] [27] [28] [29] [30].



**Figure 1.1:** *Electric VTOL Aircraft.* Top row: *Joby S4, Kitty Hawk Cora, Lilium Jet.* Bottom row: *Voloconnect, Volocity, Aurora PAV* (Sources: Company sites and evtol.news)

The capability of taking off and landing vertically enables more compact infrastructure and hence easier integration of these mobility concepts into urban environments. At the same time, the use of electric motors decreases the system complexity due to the lack of high-maintenance gearboxes, gas turbines, or piston engines and hence decreases the acquisition and operational cost of the vehicle and enables significantly lower noise profiles as compared to classical systems such as helicopters [26].

Additionally, extensive use of embedded computer systems and sensor technology enables a high degree of flight control automation and augmentation, which improves the handling of such new type of aircraft or makes it even possible in the first place. The concept of *Simplified Vehicle Operations* (SVO) leads to lower qualification requirements for the pilot and significantly reduces both the training time before as well as the workload during operation of the VTOL aircraft [9] [11].

The high degree of automation and the substantial use of software changes the human role in the interaction with the vehicle from being a pilot to being a high-level operator to ultimately being a supervisor only, which changes the way one should assess and enforce emerging properties of the system such as handling qualities or safety [31]. A systems-theoretic approach to the development of VTOL aircraft supports comprehensive consideration of their extensive functional aspects and yields a sound basis to cope with the inherent functional complexity of these systems [3] [32].

The lack of existing or established requirements for the development and operation of VTOL aircraft constitutes a challenge that is faced by the certification bodies like the European Union Aviation Safety Agency (EASA) and the Federal Aviation Administration (FAA) but also by the companies that are already developing electrical VTOL aircraft or plan to operate them in the near future [26] [27] [28] [29] [30].

The recently released Special Condition [33] by EASA yields a complete set of dedicated technical specifications for the type certification of onboard piloted VTOL aircraft and paves the road for future certification. The generality of the specifications on a high level leads to more freedom in the conceptual design and operation of this new type of aircraft.

However, it also introduces the challenge to come up with valid solutions and face unknown unknowns, as there are no existing guidelines for the development. Generating viable solutions for aircraft operation, design, and control constitutes a challenging task especially for VTOL transition aircraft, which represent a special case of the VTOL category and combine the capabilities of vertical take-off and landing with efficient fixed-wing flight [34] [35] [36].

The wide operational envelope, high degree of functional automation, and insufficient experience with this type of vehicle makes it difficult to establish requirements as to how the system should behave and if the behavior is desirable and feasible both from an operational point of view and from a design or control point of view.

---

<sup>1</sup>prepublished in [1]

Therefore, it is particularly important to approach the development of VTOL transition aircraft with systems-theoretic paradigms and to support it with the principles of model-based design. The successive analysis and simulation of models with increasing fidelity allows for stepwise validation of system aspects and requirements with increasing concretization (from behavioral and performance aspects to the architectural control design to the concrete implementation). This enables systematic creation, validation, and concretization of requirements in each phase throughout the system development and ensures the quality of the outcome.

## 1.2 State of the Art

Requirement-driven development has been widely adopted in the aerospace industry as a well-accepted means to accelerate development, reduce cost, and increase quality for complex avionics enabled functions in aircraft [23] [18]. As a generalized methodology for problem solving, the field of *Systems Engineering* incorporates the requirement-driven nature and provides powerful paradigms and guidelines for the systematic development of complex solutions and systems [3] [37] [21] [32].

Being one of the leading concepts in industry, the ‘V’-model based development process (Figure 1.2) allows for systematic specification, validation, design, implementation, and verification of a desired system or function and is a well-known method for addressing requirement-driven development [3] [38].

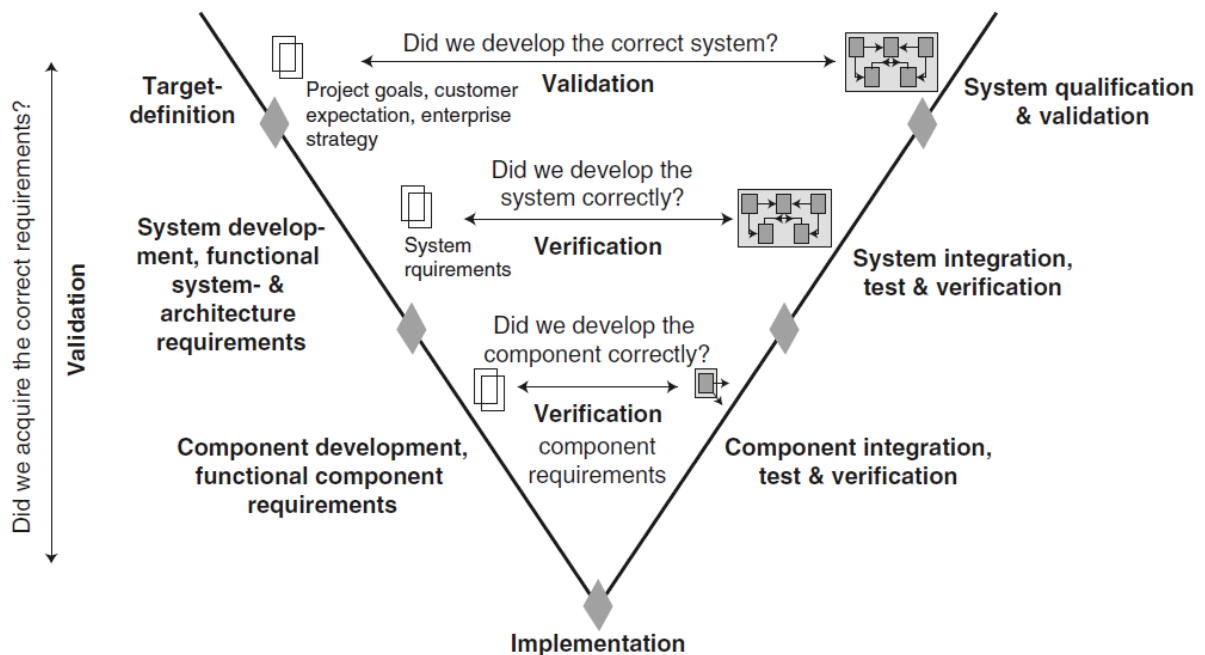


Figure 1.2: ‘V’-Model Development Process [3]

Furthermore, the use of model-based development (MBD) [21] [22] [23] [24] comprises developing and testing system models of increasing fidelity and hence allows for systematic verification and validation of both user requirements and derived system and subsystem requirements. Thus, the system concept and design is validated early on in the development process, which helps saving time and cost and increases quality of the output [23] [21] [38].

The basis for the applicable requirement standards for certifiable aircraft and rotorcraft is provided by the European Union Aviation Safety Agency (EASA) and the Federal Aviation Administration (FAA). Throughout the past decades experience has been gathered from operation of airborne systems and has been summarized in terms of general, qualitative requirements for airworthiness (EASA Certification Standards, respectively chapter 14 of the United States Code of Federal Regulations), for whose implementation EASA refers to American Military Standards such as MIL-STD-1797B, MIL-F-8785C, MIL-F-83300, or SAE AS 94900A [39] [40].

Latter are aimed at providing quantitative requirements regarding handling qualities, performance, and stability- and robustness requirements for both conventionally controlled and fly-by-wire aircraft as well as accurateness requirements for autopilots, in order to ensure safe and robust operation of airborne vehicles. Thereby, flying and handling qualities of an aircraft are defined as “those properties which describe the ease and effectiveness with which it responds and the pilot is able to perform the tasks required in support of an aircraft role” (G.E. Cooper and R.P. Harper, 1969).

Furthermore, the requirements for the flying qualities of an aircraft depend on the type of aircraft, the flight mission as well as the flight phase. Therefore, MIL-F-8785C is subdivided concerning classes, flight phases, and levels, i.e. concerning the particular function. Similarly, the Aeronautical Design Standard ADS-33E-PRF [12] defines handling quality requirements and performance specifications for military rotorcraft and provides typical operational mission scenarios in form of Mission-Task-Elements (MTEs), which aim to yield the entire spectrum of intended operations for rotorcraft and are used to support verification of its handling qualities.

However, existing requirement standards do not properly account for novel aircraft configurations like vertical take-off and landing transition aircraft, as present standards are mainly focused on classical design, function, and control principles. Generalizing the certification requirements allows for more design freedom and functional freedom within the development of future aircraft configurations.

This trend can also be observed in the recent publication of the new amendment of EASA’s Certification Specification (CS 23, Amendment 5), which has reduced its content from 131 pages in July 2015 (Amendment 4) to 33 pages in March 2017. Additionally, EASA has published a complete set of dedicated technical specifications in the form of a Special Condition [33], which “has been established to prescribe the technical specifications for the type certification of a person-carrying vertical take-off and landing (VTOL)

heavier-than-air aircraft in the small category, with lift/thrust units used to generate powered lift and control” [33, p. 4].

As part of the Special Condition, EASA has also released the Proposed Means of Compliance [41], which presents a (modified) method of *Minimum Acceptable Handling Qualities Rating* (MHQRM) for VTOL aircraft and paves the road for future certification of this new type of vehicle.

The “rapid progress in automation technology such as sensors and embedded computer systems represents a key enabler for the successful development of highly augmented flight control functionality of VTOL aircraft” [1, p. 11].

Implementation of complex avionic functions such as automated tracking of control variables requires the use of feedback control within the aerial system. The military specification SAE AS 94900A published by SAE International establishes general development, design, performance, test, and quality assurance requirements for the flight control systems of military piloted aircraft. Stability and robustness requirements are provided e.g. in terms of gain and phase margins of the linearized closed-loop system.

For classical proportional–integral–derivative (PID) feedback controller, both the command input response and the stability characteristics of the closed-loop system are structurally coupled by design. By using a gain-scheduled linear control loop, the gains are tuned such as to satisfy the gain and phase margin requirements for the closed-loop system. These are usually verified by linear frequency analysis of a mathematical representation of the system.

Nevertheless, the use of modern control strategies such as *Incremental Nonlinear Dynamic Inversion* (INDI) [42] [43] [44] [45] [46] provides several advantages over classic linear PID control. Dynamic Inversion controllers use and invert a mathematical representation of the system’s dynamics and provide the necessary control action to generate a desired closed-loop behavior [47] [44].

The inverting nature of dynamic inversion controllers is especially useful in the context of Simplified Vehicle Operations, where the desired behavior of the system is described on a high level of abstraction in order to yield highly intuitive handling. The relationship between the high-level control variables and the control actions of the system is furthermore inverted in order to yield the desired control law.

To this end, INDI implements the desired dynamic closed-loop response in the time-domain using a nonlinear reference model. This enables independent and thorough design of the system’s dynamic behavior in response to pilot inputs for different flight phases and considerably simplifies controller design for novel configurations such as transition aircraft, where the desired dynamic behavior of the system might be hard or impossible to describe in the frequency domain. It additionally allows for straightforward consideration of flight envelope protections and system limits within the controller.

The reference model can be developed such that the generated reference response of the closed-loop system meets applicable handling quality requirements. Analyzing it through

real-time simulation with a pilot in the loop enables early validation of the desired aircraft response. This represents a big advantage especially for new aircraft configurations, where there is no real-world experience available to validate the behavior of the system.

Within the context of INDI, the reference model generates reference accelerations and state trajectories as a response to pilot inputs that are used as feedforward and reference signals to calculate the desired corrective response of the system based on the currently measured and estimated system acceleration and states. As a consequence, INDI allows for separation of the command input response design specified by the reference model (feedforward path) and the design of tracking and stability characteristics (feedback path) of the closed-loop system.

Using acceleration feedback signals, INDI enables high-bandwidth disturbance rejection. Disturbances and uncertainties in model parameters are compensated by high-bandwidth sensor feedback, yielding similar characteristics as adaptive controllers and reducing the dependency on system models.

However, instead of updating the internal parametrization of e.g. model quantities, neural networks, or feedback gains based on available measurements, INDI acts as a memory-less type of adaptive controller. The robustness against model uncertainties represents a big advantage in the context of controlling transition vehicles, as the wide flight envelope in which this type of aircraft will operate and the lack of experience about the dominating physical effects harbors a lot of uncertainty.

### 1.3 Mission Statement

Due to the novelty and disruptive nature of electrical VTOL aircraft, it is of uttermost importance to support their development with model-based principles, as they allow for early evaluation of concepts and designs by gathering virtual experience. The outdated approach of aerospace pioneers to collect experience by trial and error is neither practically feasible nor desirable in the modern aerospace engineering context.

The main mission of this thesis is to provide a systems-theoretic and model-based methodology for the development of flight control functionality for onboard piloted VTOL transition aircraft. The goal is to yield a sound concept for the functional aspects of aircraft operation and control considering possible missions, application scenarios, and VTOL design aspects. At the same time inherent challenges in flight control of this new type of aircraft are addressed, such as providing an unified and intuitive control concept throughout the whole operational flight envelope or considering the effects of high-inertia propellers on attitude stabilization in the hover phase.

Furthermore, the use of model-based analysis and simulation is aimed at providing means for successive validation of system requirements, such as to maximize quality and minimize development iterations and hence development time and cost. Following the systems-engineering principle to proceed *from the general to the detailed* [3], the proposed



models in this thesis consecutively increase in fidelity and concreteness, thereby enabling systematic specification and validation of requirements at increasing level of detail.

On the highest abstraction level, the *Design Reference Model* (DRM) represents a physically motivated specification of the aircraft behavior as a response to pilot inputs. Using rigid-body simulation and considering kinetic characteristics and constraints of the system (such as mass and inertia, propulsion and lift characteristics, and aerodynamic properties), the DRM enables simulation and analysis of the behavioral aspects of the VTOL transition aircraft.

Due to the system-architecture-agnostic nature of the model, it does not rely on a detailed control architecture and can thus be used quite early in the design process in order to “validate the aircraft’s behavior and kinetic design with respect to the given application scenarios and proposed concept of operations. Early validation is crucial when developing new systems due to the high amount of uncertainty regarding novel concepts and technologies. Being a disruptive technology, electric VTOL transition aircraft yield new operational scenarios, incorporate new behavioral aspects, and will hence require new methods and requirements for flying quality assessment” [1, p. 11].

After successful evaluation using the DRM, the next step of concretization consists in the functional decomposition of the underlying behavioral aspects into a feasible control architecture. The resulting *Control Architecture Specification Model* (CASM) specifies the target behavior of the major control components and their internal interfaces and interactions. By additionally taking into account the functional interfaces to external systems and components the controller is interacting with (such as sensors and control effectors), the CASM enables validation of the overall functional topology of the system while still being implementation-agnostic, i.e. independent of the specific realization of certain systems or components.

Testing at this level consists of closed-loop simulation of the CASM together with a plant model that provides the necessary functional topology and interfaces. This allows for verification and validation of the control architecture, sensor topology, and control effector topology against the VTOL aircraft’s behavioral specification and concept of operations.

The final level of concretization is subsequently reflected in the *Control Design Model* (CDM), which represents the decomposition and implementation of the control architecture down on the lowest design level and serves as the requirement specification for the flight control source code generation. As the final control algorithm design, the CDM has to account for implementation-specific constraints such as interfaces, data types, computing platform, processing power, hardware and software environment, and toolchains.

Simulation of the CDM allows for verification of the control algorithms with respect to the underlying control architecture specification. Furthermore, the CDM can be used for automatic source-code generation and deployment on the target hardware. Performing hardware-in-the-loop (HIL) simulation tests enables the final verification and validation of the flight controller.

## 1.4 Contributions

Following the outline of the mission statement in section 1.3, the contributions of the thesis are given as follows:

**C. 1 Unified Command Concept for Simplified Vehicle Operations of On-board Piloted VTOL Transition Aircraft:** A unified behavioral concept for VTOL transition aircraft as a response to pilot inputs is proposed. Pilot command variables are chosen such as to provide intuitive and consistent response of the aircraft throughout the whole flight envelope from the hover phase through the transition phase into the wingborne phase while considering control margins and flight envelope protections. The resulting Simplified Vehicle Operations (SVO) strategy is validated against concept of operations and handling qualities through (pilot-in-the-loop) model-based simulation. Validation activities include e.g. flying Mission Task Elements (MTE, according to ADS-33E-PRF [12] or novel type of missions) in the simulator or verifying against quantitative handling quality requirements.

**C. 1.1 Polar Stick Mapping for Direction Preserving Velocity Control:** A polar stick mapping is introduced that considers the inceptor-relative direction of deflection and the stick force to translational rate requirements from ADS-33E-PRF [12].

**C. 1.2 Different Strategies for Forward Translational Rate Control of VTOL Aircraft and Assessment in Relation to Handling Qualities.** Different strategies are proposed for forward translational rate control of systems with lift-plus-cruise configuration and handling qualities are subsequently assessed based on ADS-33E-PRF [12].

**C. 2 Methodology to Implement and Validate Desired System Behavior by Executable Specification Model:** An executable behavioral specification model (Design Reference Model) for aerial systems is designed based on the kinetic capabilities of the vehicle and its rigid-body dynamics, which takes into account the characteristics of force and moment producers such as bandwidth, rate limits, and maximum propulsion. Additionally, the model takes into account kinetic characteristics of the overall aircraft such as mass, inertia, and aerodynamics. Thereby, it enables validation of system behavior and kinetic design with respect to given application scenarios and proposed concept of operations by simulation and analysis of the specification model. It furthermore enables verification of the proposed behavioral concept against handling quality requirements and gives first insights about the behavior of the system without considering a detailed control or system architecture.

- C. 3 Incremental Strategy for Consecutive Executable Requirements Capture and Validation to Facilitate Process Frontloading:** The systems engineering process is applied to model-based development of the behavioral specification, control architecture, and control algorithm for an onboard piloted VTOL transition aircraft. A systematic model-based approach is presented for deriving, modeling, and validating the target closed-loop behavior of the aircraft considering its kinetic constraints. An INDI-based control architecture is subsequently derived considering the functional system topology in terms of sensory constraints and available control effectors using functional requirement decomposition of the target closed-loop behavior. The control architecture is derived and implemented as an executable specification model (Control Architecture Specification Model), which is used to validate the control law in closed-loop simulation. The final controller is designed by decomposing and concretizing the control architecture specification and considering hardware and software constraints as part of the Design Solution Definition. The individual control components are implemented and integrated into an executable Control Design Model, which is used to generate code and validate the controller implementation in simulation.
- C. 4 Continuity-Based Input-Output Mapping:** A novel multi-modal control law blending approach is presented that “enables transition-free control authority transfer between different modes of operation while maintaining maximum authority and continuity of each mode” [1, p. 8]. The approach considers maximum and minimum input-to-output gradients in order to avoid over or under sensitive mappings. It can furthermore be used in the context of multi-crew operation during priority switching or single pilot operation during distinct mode switches.
- C. 5 Design Guidelines for Controllers to Accommodate Control Effector Limitations:** A time-domain based analysis of the effective inner-loop bandwidth for rate saturated control effectors is presented based on the equivalent first order step response. Design guidelines for gain and saturation parameters are derived that yield maximum outer-loop bandwidth response behavior. The derived guidelines are validated by simulation of a simplified multicopter model with current-limited motors and high-inertia propellers.

Summarized, the contributions in this thesis aim to facilitate the development of novel aerial system configurations such as VTOL transition aircraft by providing a systematic model-based strategy that supports the successive specification, verification, and validation of system aspects and requirements in increasing detail. Furthermore, the developed concepts and solutions are generally applicable to a wide variety of systems and support certifiable development of future aircraft.

## 1.5 Outline

As pointed out in the previous subsections, the goal of this thesis is to yield flight control functionality for onboard piloted VTOL transition aircraft and perform stepwise validation of the requirements on each level. To this end, the thesis is structured as follows:

Section 2 introduces the concept of systems engineering as a generalized methodology for problem solving and illustrates the synergies with model-based development enabling virtual concept and design evaluation in the early phases of system development. The concept of requirement specification models and requirement assessment models is introduced and it is shown how they can serve to specify, verify, and validate aircraft and system requirements on different levels.

In section 3 the overall scope of the flight control development as well as the reference configuration of the VTOL transition aircraft are defined. Exemplary missions and general application scenarios are discussed and the proposed human-machine interface (HMI) concept in terms of the used control inceptors is shown.

Following the systems-theoretic driven development approach, the first part of section 4 derives the behavioral specification of the VTOL transition aircraft. With the focus on Simplified Vehicle Operations (SVO), a unified command concept is introduced that is compatible with the novel control inceptor design introduced in section 3 and that is realized by highly augmented flight control throughout the whole flight envelope. The target behavior of the aircraft is described in the three flight phases hover, transition, and wingborne as a response to control inceptor deflections.

Furthermore, a novel continuity-based input-output mapping is introduced, which was originally developed by the author to solve the problem of discontinuous command outputs during pilot priority switching of a tandem-seat fly-by-wire aircraft [2]. In the context of SVO for VTOL transition aircraft, this concept is used for the airspeed command mapping.

The second part of section 4 is concerned with developing the Design Reference Model (DRM), yielding the requirement specification model for the closed-loop system behavior as a response to pilot inputs. The DRM is based on a control-theoretic approach in order to yield the desired behavior according to the SVO and represents the functional baseline for the development of the control architecture in section 5. Two different behavioral strategies of forward translational rate control at low velocities are presented for lift and cruise configurations.

In the end of section 4 follows the verification and validation of the proposed behavioral specification by quantitative assessment with respect to existing performance specifications and handling quality requirements according to the Aeronautical Design Standard ADS-33E-PRF [12]. Additionally, piloted real-time simulations are presented as an effective way of performing concept validation.

After successful specification and validation of the behavioral aspects of the transition aircraft, section 5 is concerned with the development of the necessary control architecture

that will realize the specified behavior. Taking into account the functional topology of the system, a control strategy based on Incremental Nonlinear Dynamic Inversion is derived in compliance with the general design guidelines for good system architectures according to [3] such as modularity, independence, piecemeal engineering, and decentralization. The control architecture is represented in terms of the Control Architecture Specification Model (CASM), which specifies the target behavior of control components, their interfaces, and their interactions. It represents a concretization of the DRM down on a lower functional level, following the concept of functional requirement decomposition [32].

Furthermore, design guidelines for controller gain and saturation parameters are derived based on time-domain analysis of effective inner-loop bandwidth, in order to accommodate control effector rate saturations due to current-limited motor dynamics in the presence of high-inertia propellers. The proposed approach allows to choose parameter values for the outer loop, such as to obtain optimum bandwidth and preserve the desired damping characteristics.

Section 6 discusses the final concretization and implementation of the control architecture specification into the Control Design Model (CDM). The CDM represents the model-based specification of the control algorithm design and hence yields the concretization of the controller down on the lowest design level. Implementation-specific aspects such as controller discretization and code compliant modeling are addressed. Verification and validation strategies on this level include unit tests of control components, Markov Chain Monte Carlo (MCMC) methods, and hardware-in-the-loop simulation of the auto-generated controller source code that has been deployed on a target hardware.

The conclusion and outlook in section 7 give some remarks and insights into the developed methodology and provides a perspective on future development and operation of VTOL aircraft.



# 2

## Model-Based Systems Engineering

### 2.1 Principles of Systems Engineering

The following section introduces the principles of *Systems Engineering* as they are proposed in [3] and [32] and that are supported by concepts discussed in [4], [24], [31], and [48]. As a universal methodology for problem solving, systems engineering represents the basis for development of modern systems. It provides a general framework of paradigms and methods that helps analyzing and understanding complex relationships of elements in a structured manner and that facilitates the systematic creation of solution principles and complex systems.

#### 2.1.1 Systems Thinking

Systems thinking [48] represents the underlying thought basis of Systems Engineering and can be understood as a “way of thinking that enables better understanding and designing of complex phenomena (= systems)” [3, p. 3]. The central concept in systems thinking is the system itself, which the International Council on Systems Engineering (INCOSE) defines as “an arrangement of parts or elements that together exhibit behaviour or meaning that the individual constituents do not” [49]. This definition underlines the important and often quoted property of systems that “the whole is more than the sum of its parts”.

As Nancy Leveson points out in her book *Engineering a Safer World: Systems Thinking Applied to Safety* [31], coping with complexity using the traditional approach of *divide and conquer*, formally known as *analytic reduction*, is not feasible when systems become more and more complex and interconnected.

This is because analytic reduction presupposes an underlying linearity in the way a system can be decomposed in its parts and assumes that each element of a system can be considered outside of its context while the overall system behavior can be represented as the sum of its components’ behaviors. A lot of systems in nature as well as (simpler) technical systems do indeed exhibit these characteristics and fall under the category of *organized simplicity* according to figure 2.1 [31].

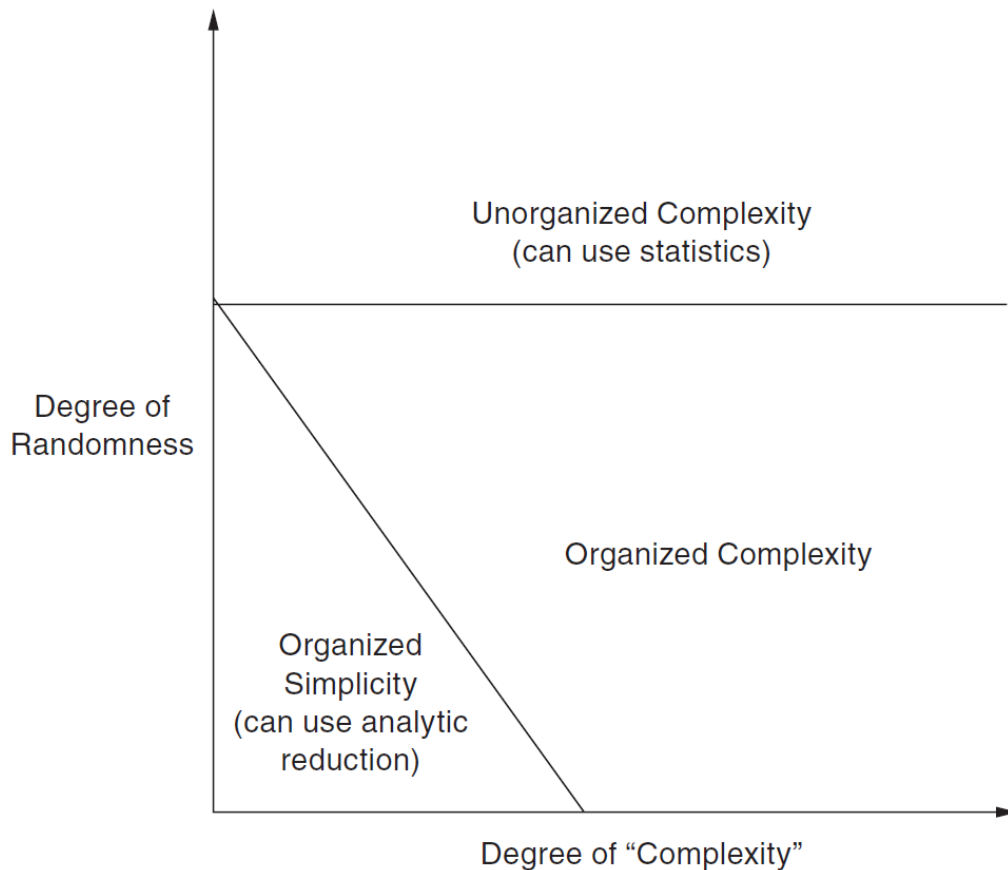


**Figure 2.1:** *Three Categories of Systems [4]*

However, nonlinear interactions as well as feedback loops between the elements of a system make linear decomposition unfeasible as a means of doing holistic analysis. These kind of systems fall under the category of *organized complexity* in figure 2.1 and yield characteristics that are too complex for analytic reduction while at the same time being too deterministic for statistical analysis, which can be applied to stochastic systems that exhibit *unorganized complexity* [31] [4].

The ever increasing presence of software in today's systems enables a variety of functionality and a level of complexity that puts most modern systems into the category of organized complexity [31] and hence makes the use of systems thinking indispensable.

In general, every system is delimited by a *boundary*, which in turn defines the scope of the system. The system boundary can be a virtual or physically motivated separation of the system from its environment. All elements within the boundary are assumed to be part of the system and together act as an entity in order to fulfill a specific purpose. In doing so, the system might have interactions with its surroundings, also referred to as the system environment.

It is important to have a clear understanding of how and by what means the interaction between the system and its environment takes place. The interactions can take various



forms such as information flow, energy flow, or material flow [3]. Depending on the level of concretization applied to the current system view, it might be useful to abstract the interactions in terms of functional interfaces and to concretize them into the physical representations throughout the system analysis or development.

The internal nature of a system is governed by its *structure*, which can be understood as the governing principles of how its elements and relations are ordered. The hierarchical structure thereby provides a very useful way of representing a system, as it allows to vary the degree of abstraction applied to the internal view of its elements. Each element of a system can furthermore be considered as a (sub)system itself, which enables the successive application of the proposed paradigms on each level of abstraction in a recursive manner.

Furthermore, the theory of hierarchy is tightly related to the concept of emergence. Emergent properties of a system are only visible on the highest abstraction level and have no meaning on the lower abstraction levels of the system [31]. Examples of emerging properties are the handling qualities and safety aspects of a VTOL transition aircraft. These properties are the result of the interaction of all elements that make up the aircraft, however can not be attributed to any of the elements alone when taken out of the system's context. In this regard the concept of emergence underlines the very definition of a system, which is "more than the sum of its parts".

Additionally, emergence is the fundamental mechanism of hierarchy that allows consecutive decomposition of a system into more and more detailed representations of its elements. On each hierarchy level the elements are represented in terms of their emerging properties, which in turn are the result of the underlying structure and interactions of its sub-elements. This concept is one of the fundamental principles of the systems engineering process model that is explained in the next subsection.

### 2.1.2 Process Model

The systems engineering process model provides general recommendations and methodologies that support the development and improvement of systems. It can be used as a comprehensive toolbox for coping with complex problems and yields a sound foundation for structuring the development process.

Building on the foundation of systems thinking, the basic principles of the systems engineering process model are presented, following the contents in [3] and which can also be found in [32]. Additionally, the important concepts of *validation* and *verification* are introduced and their importance in the practical development of systems is highlighted.

Addressing the development of complex systems in a structured manner is essential for the success of the underlying project. Not only can the results of a badly structured or unorganized development be expensive, the impacts might even include life threatening conditions, accidents, or substantial damage to the environment [31].

With the increasing scope and scale of modern systems, the damage potential is increasing as well. Therefore it is an inevitable part of the systems engineer's responsibility

to organize the system development and analysis in a structured manner.

According to [3], the systems engineering process model builds upon the following basic principles:

- Proceeding from the general to the specific
- Thinking in variants
- Problem-solving cycle
- Phased Approach.

These principles, which are introduced in the following, represent a meaningful whole and support the development of systems and the solution of general problems in a comprehensive manner.

### 2.1.2.1 From the General to the Specific

The principle to go *from the general to the specific* accommodates the emerging characteristics of systems. The basic idea behind this paradigm is to start looking at the problem at hand from the most general or abstract perspective and to avoid getting lost in details from the very beginning.

Only after getting the whole picture and gaining holistic insights such as to comprehend the effects and relationships at the highest abstraction level, the problem domain should be refined and the view on the system should be gradually concretized. Figure 2.2 conceptualizes this idea.

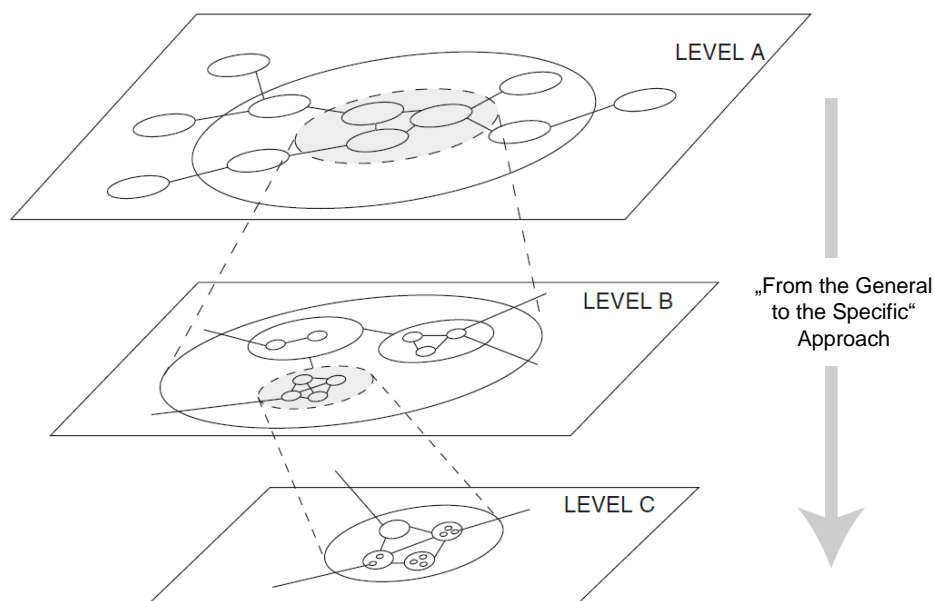


**Figure 2.2:** *From the General to the Specific (Adapted from [3])*

Especially for problems that are complex in nature and difficult to conceive, starting the process from a general perspective supports a holistic approach and provides a goal-oriented way of solving problems from scratch.

Going from the general to the specific tries to answer the overall question of *what* first, before it proceeds to deal with the more detailed question of *how*. This concept is particularly effective when systems become more entangled and intertwined [31] [3], as it becomes considerably more difficult to predict the effects of elements at the lower levels on emerging properties at the higher levels.

The alternative of the proposed top-down methodology is a bottom-up approach. Starting at the lowest abstraction level might be appropriate in special circumstances such as improving an existing system or a working solution [3]. In this case it might be useful to start dealing with the “devil that is in the detail” from the very beginning. Hence, the improving efforts can directly be targeted at the highest level of concretization, since their effects upstream are well understood and the overall principles and dominant interactions have already been analyzed beforehand.

### 2.1.2.2 Variant Creation

Thinking in variants aims to promote diversity among the developed solution principles. The general idea is to avoid sticking to the first solution that comes into mind but to explore possible alternatives for solving a given problem and applying this method successively at increasing levels of concretization.

The overall concept is illustrated below in figure 2.3.

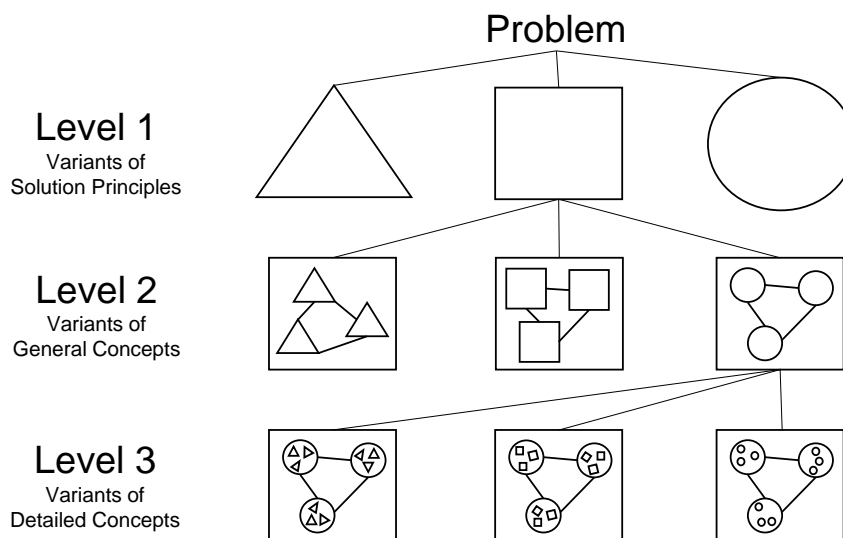


**Figure 2.3:** *Variant Creation in Increasing Detail (Adapted from [3])*

For almost every practical problem, there exist a variety of different ways one could develop a feasible solution. Furthermore, each possible concept for solving the problem comes along with distinctive characteristics that allow for both qualitative and quantitative assessment of the solution with respect to some given objectives, thereby providing a means of comparing and evaluating the different variants. The *Problem Solving Cycle* (PSC) builds up on that idea and is introduced in subsection 2.1.2.3.

The principle of using variant diversity to reach some state of optimality represents a fundamental mechanics in biological evolution and is even adopted in practice in the field of computational intelligence and machine learning [50]. The successive creation of variants, their evaluation based on objectives, and prioritization of the most feasible ones for further decomposition (i.e. *survival of the fittest*), represents a straightforward approach to arrive at good results and is quite general in its application.

Different variants in the initial phase correspond to distinct solution principles for a given problem, which vary in the basic mechanisms that will produce the desired results. In the context of developing a new type of transition aircraft, the initial variants might represent different ways of lift and thrust generation (e.g. separate lift and cruise system, thrust vectoring, tilt-wing, or tilt-rotor concepts) or different types of energy storage (electric batteries, fuel, hybrid concepts).

On the lower levels of concretization the variant creation might be concerned with generating various concepts for a given solution principle in the form of different system architectures or in the form of detailed component designs for a given architecture.

Sometimes it is necessary to concretize an initial solution variant into the lower design levels before one can completely assess the impact of a decision made at the higher conceptual levels, which yields the iterative nature of the process.

Although the principle of variant creation offers a great way to explore different solutions, it is often “violated in practice due to a lack of time” [3, p. 34] and other resources. However, it is important to recognize that especially decisions in the early phases of the system or solution development have a high influence on the overall success of the project and that conceptual changes in the later phases of the process will raise the costs in a disproportionate manner [51] [52] [32].

### 2.1.2.3 Problem Solving Cycle

The *problem-solving cycle* (PSC) represents a general workflow that can be used as a micro-logic to address any type of problem [3] and is originally based on the Dewey problem-solving logic [37]. It can be used within each of the individual phases of a project, which are summarized in subsection 2.1.2.4 and represent the macro-logic for the overall system development. The individual steps of the PSC are shown in figure 2.4.

The benefits of using a predetermined algorithm to approach any kind of problem is that it provides a step-by-step procedure with instructions to follow, which help to come up with the best possible solution. The deterministic nature of this approach furthermore

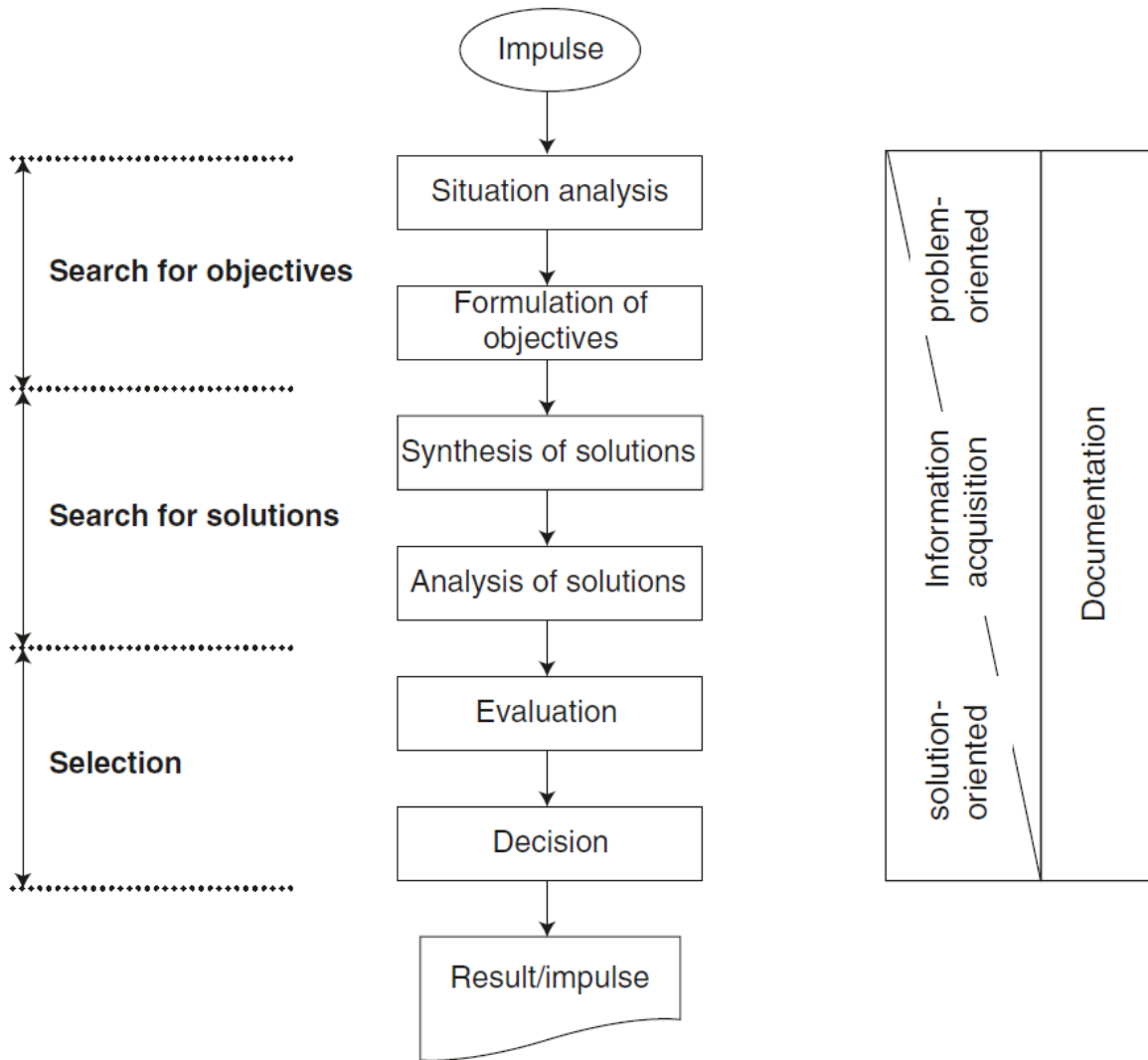


**Figure 2.4:** *Problem-Solving Cycle* [3]

guarantees that the individual steps towards the desired outcome are standardized and the quality of the process is ensured. The individual steps of the problem-solving cycle are adopted from [3] and introduced in the following.

**Impulse** The impulse triggers the start of the problem solving logic. Usually one is confronted with either an undesired state that is to be avoided or an opportunity that can be exploited. During the impulse, the problem or opportunity is concretized and delimited.

**Situation Analysis** After the initial impulse in the beginning of the problem-solving cycle, the situation analysis helps gain a better understanding of the problem area. This phase is used to do the proper research in order to gain insights into the important mechanisms that are related to the problem at hand. In the context of a task at the lower

abstraction levels within the system development, the emphasis lies on focusing on the initial situation on that level. Furthermore, the situation analysis lays down the basis for formulating concrete objectives in the next step.

In [3] different types of views are mentioned that can be used separately or concurrently:

- The system oriented view, which facilitates structuring the situation using the concept of systems thinking and puts emphasis on the functional aspects.
- The cause-oriented or diagnostic view, which is concerned with the underlying causes that are directly or indirectly responsible for the symptoms characterizing the situation.
- The solution-oriented or therapeutic view, which focuses on general solution principles or helps envisioning the target state. However, care must be taken to not restrict the solution space too much such as to maintain a certain degree of freedom during the solution synthesis.
- The future- or time-oriented view, which is concerned with the temporal development of the problem and solution field. It tries to answer the questions of how the situation would develop if no actions were taken and which important developments should be considered in the solution field.

**Formulation of Objectives** The step of formulating objectives is essential for finding the best possible way to solve a given problem or task, as it sets up the criteria against which to assess possible solutions. During this phase, concrete goals and requirements are worked out, which possible solution candidates should satisfy. Each objective should be quantifiable and at least verifiable.

However, the formulation of valid requirements is not always straightforward. This is often the case when neither the problem field or the solution field are particularly well known [3] or if the proposed objectives are indirectly derived or decomposed from a high-level task. The systematic and successive decomposition of requirements into more and more detailed aspects is furthermore addressed in subsection 2.1.2.4, where the ‘V’-model based development process is used to demonstrate a phase-driven development plan.

In general, the worked-out objectives shall be as solution-neutral as possible and agnostic to the exact realization in order to maximize the degree of creative freedom during the solution synthesis.

**Solution Synthesis** The solution synthesis represents the constructive and creative phase of the problem-solving cycle [37] [3]. During this phase, possible solution variants are worked out, which are aimed at meeting the objectives formulated in the previous step.

Using creativity techniques [53] can support the synthesis and allows for a balanced and unbiased approach to developing feasible solutions. Furthermore, it is important to avoid premature judgment of the generated solutions, as the systematic assessment and evaluation takes place in the next phases of the problem-solving cycle.

**Solution Analysis** The solution analysis represents the destructive and analytic phase of the problem-solving cycle [37] [3]. Each solution is assessed individually and is critically analyzed and verified against the existing objectives.

During this phase, a pre-selection of the available solution candidates is performed and it is ensured that no mandatory requirements are violated. These requirements might be related to the realizability or integrability of the solution as well as economical, functional, political, or safety-related aspects.

The overall assessment is of qualitative nature rather than quantitative. It ensures that only those solution variants that do not clearly meet exclusion criteria are considered for further evaluation.

**Evaluation** The evaluation phase consists of quantitative assessment and comparison of the remaining solution candidates with respect to the existing objectives and other applicable requirements.

Possible evaluation strategies include value-benefit analysis, plus-and-minus balance sheet, or cost-effectiveness analysis [54]. These allow for rational evaluation and quantitative rating of the solution candidates and provide a solid basis for the final decision process.

**Decision** The decision is the final step in the problem-solving cycle whose purpose it is to converge on a final solution. Depending on the overall scale of the problem, the decision process might include multiple teams from different domains. A systematic and unbiased consideration of the evaluation results helps to make a rational decision.

**Result** The solution decided upon represents the final result. This can either be the desired outcome itself or be the impulse that starts a new problem-solving cycle. Latter is the case when a solution is successively concretized by going from the general to the detailed and shows the close relationship of the problem-solving cycle to the previously discussed principles.

The problem-solving cycle represents a useful tool that guides through the solution-finding process and provides a general workflow to approach challenges of any kind. Applying this micro-logic successively in the context of a large-scale problem like the development of a complex system leads to the concept of a macro-logic that is embodied in a phased development approach.

### 2.1.2.4 Phased Approach

The general idea behind a phased development approach is to structure the process of creating a system into logically and temporally distinct stages. The individual project phases are concerned with increasingly detailed system aspects and can be seen as a concretization of the previously mentioned concept *from the general to the particular* [3].

Separating the system development into individual and delimited phases facilitates the general workflow by decomposing it in manageable pieces. Furthermore, each stage has its explicit focus, which supports a consistent mindset during each phase of the development.

In the following the ‘V’-model based development process is used as an example to lay out a phase-driven development plan that is widely adopted in the industry as a methodological approach to the development of modern systems. The proposed methodology is mainly based on classical systems engineering literature [23] [32] [22] [3], however shares similarities with classical aerospace standards such as ARP4754A [55]. The idea behind this approach is to divide the overall development into a top-down branch, which is concerned with successive specification and decomposition of requirements and the subsequent design and implementation of the system components, and a bottom-up branch, which is concerned with the integration, testing, and operation of the system.

The resulting ‘V’-shaped process flow is name-giving for this development methodology, which is illustrated in figure 1.2 and figure 2.6. The concepts of requirements, verification, and validation thereby play a crucial role and are addressed throughout the following summary of the ‘V’-model phases.

**Needs and Goals** Similarly to the problem-solving cycle, the ‘V’-model based process starts with defining the needs and goals that the system under development should meet. In case of developing a VTOL transition aircraft, these can be represented in terms of specific use case scenarios in the form of possible missions that are envisioned for this new type of aircraft.

The central concept that is used to represent the desired characteristics of the final system is called *requirement* [56]. On the highest abstraction level requirements are used to express and communicate the needs of a stakeholder. Thereby, possible stakeholders include but are not limited to the customer, government, or the end user [32].

Furthermore, requirements can be related to various aspects of the system such as its handling qualities, performance, ecological impact, and safety. Throughout the course of the development all requirements are successively decomposed and refined into more concrete requirements, which are derived in the descending left branch of the ‘V’-model.

According to [57], the two essential criteria that a good requirement should meet are:

- The need of the stakeholder is expressed *correctly* and hence the requirement is *valid*.
- The requirement is *testable* and hence *verifiable*.



To this end, the two important concepts of *verification* and *validation* are introduced.

**Verification** describes the process of ensuring that a certain characteristic of the system meets its requirements and thereby showing that it is *correctly* implemented or realized. Verification activities usually include testing the real system, an individual component, or using a simulation model to virtually check if the system or component meets its underlying requirements. Verification therefore tries to answer the following questions: ‘Is this (aspect of the) system or component correctly implemented or realized? Does it meet its underlying requirements?’ [58].

Requirements exist on different abstraction levels. On the highest level the verification process is concerned with testing the high-level or emerging characteristics of the system such as the overall performance, safety, or handling qualities. During the subsequent phases of the development process, requirements are more detailed and are related to more specific aspects of the system such as the bandwidth of a control loop, the accuracy of state estimation, the weight and dimensions of a component, the power consumption of a subsystem, or the force-gradient of a control inceptor.

Requirements on the lower levels typically result from decomposing higher level requirements with the goal of finding a more concrete representation of the parent requirement. The underlying assumption behind this decomposition is that by meeting the low-level requirements, the high-level requirements are fulfilled as well. The creative and challenging step thereby consists of finding a *valid* decomposition into requirements that will indeed result in the overall objectives being met and that is compatible with the needs and goals of the stakeholders, as judged by validation.

**Validation** describes the process of gaining confidence that a requirement or set of requirements does correctly represent the overall needs and goals of the stakeholder or of the parent requirement it is derived from. Validation is therefore concerned with answering the following questions: ‘Is this requirement or set of requirements a *correct* manifestation of the needs, goals, and objectives that drove its creation? Did we define the correct requirements that will yield the desired outcome?’ [58]. Requirements can thereby also be understood in terms of the overall system, architecture, or design specification, in which case the validation process makes sure that the *correct* system, architecture, or design is developed and that it meets the intended purpose.

The scope of validation hence always includes the overall purpose and goals of the system and is directed towards the big picture of the development. Even if the system meets all the requirements that have been derived during the development (i.e. the system is built or implemented correctly), it will not meet the expectations and objectives that drove the development of the system if the requirements were not valid in the first place (i.e. what has been built or implemented was not the right system). Requirements can be invalid, if they do not correctly, completely, consistently, and clearly communicate the stakeholder’s interests [58].

Early validation is therefore crucial for the success of a project and can be achieved through careful inspection of the requirements, gathering experience by trial and error, or virtual simulation of a system model. Model-based verification and validation is furthermore discussed in section 2.2.

**System Specification** The system specification represents the definition of the system and its requirements on the highest abstraction level. In the given context this refers to the overall system, i.e. for a transition aircraft the specification is conducted on aircraft level.

The focus mainly lies on emergent properties and functionalities, such as overall system behavior, performance, and safety. Additionally, the environmental impact can be an essential criteria as well, as it is for example for power plants or automobiles.

In general, the system requirements are derived such as to meet the needs, goals, and objectives of all stakeholders involved. In case of a VTOL transition aircraft, the system requirements could be derived from a specific use case scenario or flight mission.

Additionally, already existing requirements have to be taken into account, which in the case of rotorcraft and fixed-wing aircraft are for instance related to the dynamic behavior as a response to control inceptor inputs or specific performance characteristics of the system. These requirements have to be met in order to achieve satisfactory handling qualities and to ensure safe operation of the vehicle at all times and are imposed by the government through applicable certification standards.

Furthermore, these requirements usually originate from many years of flight experience and practicing trial and error with these traditional aircraft, which is how they were validated over time. However, care must be taken for novel configurations such as VTOL transition aircraft, as existing requirements, which apply to traditional systems, do not necessarily apply to novel configurations as well.

It is therefore important to carefully examine the applicability of existing rotorcraft and fixed-wing aircraft requirements on novel VTOL transition configurations. Furthermore, as will be discussed in section 2.2 and as is demonstrated in section 4.3, the use of models can help to perform virtual validation of the requirements on system level by using simulation and enables to gain confidence in the proposed system specification.

**Architecture Specification** After successful collection of system-level requirements, the architecture specification is concerned with deriving the functional system topology that is aimed at realizing the system specification while not violating any of the stakeholder's objectives and constraints. During this phase, the high-level objectives are decomposed into functional requirements, which are allocated to subsystems.

Hence, the term *architecture* “denotes (...) the allocation of functions to the elements of a structure” [3, p. 157] and can be interpreted as “a kind of solution principle” [3, p. 157].

Furthermore, subsystems are represented in terms of their emergent properties, which in turn yields their specification. Hence, the architecture defines the specification of all subsystems as well as their functional interfaces to and interactions with each other. Depending on the scope of the development, the architecture can be related to different aspects. For instance, if the development is concerned with the overall transition aircraft, the architecture comprises subsystems like energy storage, propulsion and powered lift system, wings, control surfaces, cockpit and control inceptors, and the landing gear.

On the other hand, if the scope of the development is merely concerned with the flight control functionality of the transition aircraft, the architecture is made up of all the necessary control subsystems that yield the desired behavior on the system-level. Section 5.3 demonstrates the development of a model that represents the control architecture specification and can be used to validate the control laws, which are used to yield the desired behavior of the VTOL transition aircraft.

**Component Design Specification** Once the architecture has been specified, the next phase is concerned with the concretization of the individual subsystems into a detailed design solution for the underlying components. The goal is to realize the functionality of all subsystems that are represented by the architecture specification resulting from the previous project phase.

Thereby, the design shall be specific enough such that the subsequent implementation of all components can be realized. Important aspects to consider are possible design constraints, governmental regulations, and the final interfaces.

Examples may include the exact geometry and composition of a wing in terms of a technical drawing or the electric circuit for a motor speed controller of a VTOL aircraft. In the context of model-based development of flight-control software, the design specification can be the model that represents the flight control code on the lowest abstraction level and from which the final source code can be generated in an automated manner.

**Implementation** The implementation phase deals with creating the individual components as specified by the detailed design specification. This phase represents the lowest point in the ‘V’-shaped process flow and is hence concerned with the physical creation of the system on the lowest level.

If the development process is concerned with creating the flight control software for a transition aircraft in the context of model-based development, the implementation phase can be automated in terms of automatic source code generation from the design model that is created in the preceding project phase.

Chapter 6 gives an overview about the creation of a flight control design model and the subsequent automatic source code generation. Additionally, section 2.2 discusses the general role of models in the systems engineering landscape.

**Component Testing** Once the components have been created or implemented, the development proceeds with the component testing phase. During this phase, the components are verified against their design specification, which preceded the implementation.

To this end, unit tests are conducted, which ensure that the built components satisfy all their underlying requirements. The component testing phase is aimed at answering the following questions: ‘Is the component built correctly? Does it perform as specified?’.

**Component Integration and Subsystem Testing** During this phase, the individual components are integrated into subsystems in order to create the building blocks of the overall system architecture. Testing at this level is focused on the interaction of the components with each other. Additionally, interfaces between components are brought into closer focus.

The goal is to verify if the functionality, which is expressed in terms of the architecture specification, is realized by the collective effort of the components within a subsystem. The questions answered during this phase are: ‘Is the subsystem built correctly? Do the components within the subsystem together yield the required functionality that is represented by the architecture specification?’.

**Subsystem Integration and System Testing** Once all subsystems are created, they are integrated into the overall system. Thereby, interfaces between individual subsystems represent an important aspect.

The focus during this phase lies on performing holistic testing and verifying (parts of) the system against the requirements on system level. The following questions are answered: ‘Is the system built correctly? Do the subsystems together yield the required functionality that is represented by the system specification?’

**System Operation and Validation** The final step of the development process is concerned with the operation and validation of the system. This phase is characterized by use cases and actual operation of the system in its intended environment by the customer or end user.

Once the system is actually used, it can be assessed if what has been developed is indeed the right system that fulfills all the needs, goals, and objectives of all stakeholders involved. The answer to the question ‘Has the right system been built?’ is a critical one, as it determines the overall success of the project. Even if the final product behaves according to its specification and meets all the system requirements, it is not guaranteed that it satisfies the needs of the stakeholder, as was mentioned in the paragraph about *validation*.

The next section discusses how the use of models in the systems engineering context enables early concept validation on system, architecture, and design level through virtual assessment within a simulation.

## 2.2 The Role of Models in Systems Engineering

With increasing complexity and scale of systems today, the importance of their high-level abstraction and description is becoming more recognized [24]. Thereby, models represent a very useful concept to provide a comprehensive representation of a system.

As mentioned throughout earlier sections of this thesis, models enable a holistic view on systems and thereby facilitate important processes such as efficient communication and validation of the system and its requirements that are represented by the model.

Furthermore, the International Council on Systems Engineering (INCOSE) defines model-based systems engineering (MBSE) as “the formalized application of modeling to support system requirements, design, analysis, verification and validation activities beginning in the conceptual design phase and continuing throughout development and later life cycle phases.”

In the following, the concept of models is defined in general and it is shown, how models are deployed throughout the remainder of this thesis to support the flight control development of a VTOL transition aircraft by means of virtual verification and validation activities.

### 2.2.1 Models as Abstraction of Reality

According to [59], “a model is a simplified representation of a real or imagined system that brings out the essential nature of this system with respect to one or more explicit purposes.”

In that sense, models are an essential and inevitable part of every development process, regardless of whether or not it is explicitly referred to as a model-based process. Both the design and analysis activities during the system development are necessarily tight to some sort of abstract representation of the yet-to-be-built system.

Therefore, “the definitions of system design and system analysis imply that models, modeling, and the manipulation and exercise of models are important preoccupations of systems engineers. In a sense, the work involved in the processes of system design and system analysis can be completely characterized as the creation and manipulation of models” [21, p. 19].

Models can take various forms such as physical models, mathematical models, behavioral models, process models, or architecture models [5] [3]. All of them have in common that they either do not represent the entirety of the original system’s characteristics, or that they represent them in a simplified and abstracted manner, or both.

Therefore, a model never is a true and complete representation of the system – in fact, only the system itself is. To put it in the words of the British statistician George Edward Pelham Box:

*“All models are wrong, but some are useful.”*

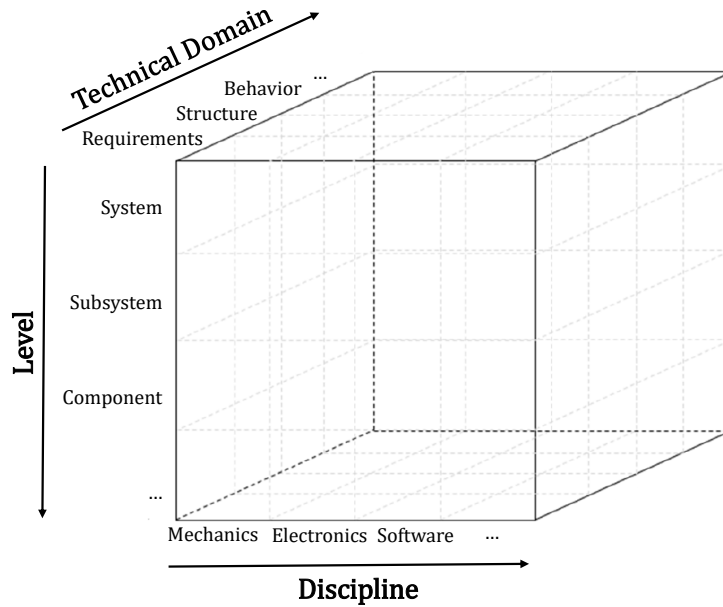


**Figure 2.5:** *Modeling Dimensions (adapted from [5])*

Nevertheless, centering the development process around models and deploying them throughout the overall system design and analysis phases provides considerable advantages especially for large and complex systems. Thereby, models of different fidelity level, technical domain, and discipline can be consulted, which are represented by the modeling dimensions in figure 2.5.

Furthermore, in [5] it is distinguished between system models and specific models, which are motivated by the concepts of system models and analytic models discussed in [60]. The difference between both types of models lies in their scope and fidelity.

While specific models provide the view of a single discipline on a single technical domain in a great amount of detail (e.g. a wiring harness model of a vehicle), system models target a more holistic view that accounts for at least two technical domains or disciplines [5]. Hence, system models are usually located in the upper half of the modeling cube from figure 2.5 and extend rather horizontally than vertically.

Since system models incorporate the information and views from several technical domains and disciplines, they support the concept of a *single source of truth* [5], which facilitates the communication of system aspects across development teams. Furthermore, the holistic representation of the system enables validation of the design and requirements of different disciplines by means of model analysis or simulation.

Within this thesis the flight control functionality of a VTOL transition aircraft shall be developed. Therefore, it is important to precisely characterize the scope of the development in order to assess what lies in its focus and what lies outside of it. This distinction also influences which aspects of the system are consecutively concretized in order to increase model fidelity as the development progresses.

To this end, it is specified that the end product of the development at hand is the flight control functionality in form of plain text source code. Thereby, flight control includes all the functionality that interfaces with available motors, actuators, sensors, and human-machine interface components in order to achieve a specific behavior of the overall aircraft as a response to pilot inputs.

In the following section it is shown, how models of different fidelity are used within the ‘V’-model development process in order to support the verification and validation activities for the flight control functionality of a VTOL transition aircraft.

## 2.2.2 Verification and Validation Through Model Simulation

The development of flight control functions in this thesis proceeds from the general to the particular as pointed out in subsection 2.1.2.1 and follows the phased ‘V’-model based development process described in subsection 2.1.2.4. It is demonstrated in the following how models are used to validate requirements during the individual stages of the flight control development by means of simulative verification and validation activities.

For every stage of the left, descending branch within the ‘V’-shaped process, a corresponding model is developed and used to validate the requirements on that particular level, as can be seen in figure 2.6. The model on each level is a representation of the requirements for that particular level of concretization and is referred to as *Requirement Specification Model (RSM)*.

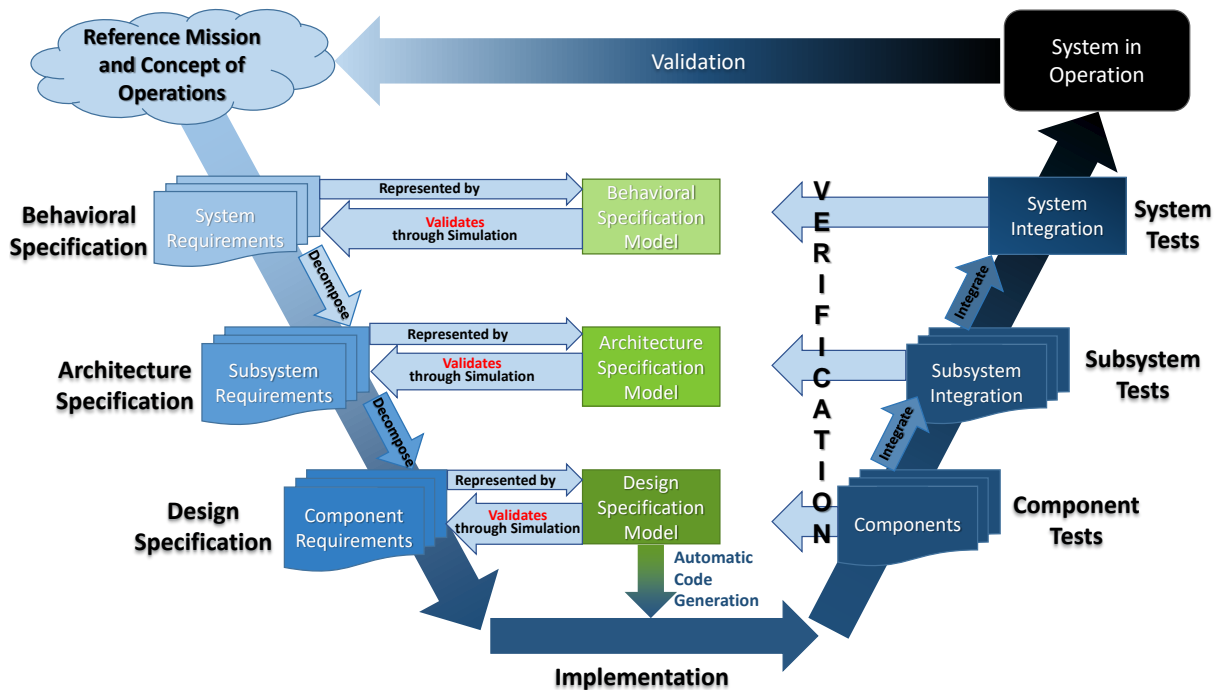


**Figure 2.6:** Model-Based ‘V’-Model Development Process Using Requirement Specification Models (green) for Validation

On system level the RSM is concerned with the overall behavior of the aircraft, thereby representing the system level requirements in terms of a *Behavioral Specification Model*. Behavior in the context of this thesis refers to the general motion response of the transition aircraft to pilot inputs in every particular situation. At this concretization level it is not yet considered in detail how and by which means the behavior is realized. In section 4.3 the *Design Reference Model* (DRM) is introduced, which represents the Behavioral Specification Model for the flight control development of a VTOL transition aircraft.

The subsystem requirements are concerned with the functional topology that realizes the behavior on system level. They are represented in terms of the system *architecture*, which “denotes (...) the allocation of functions to the elements of a structure” [3, p. 157].

Therefore, the RSM at this level represents the subsystem requirements in terms of an *Architecture Specification Model*. This model implements and integrates the functional specifications of all the subsystems agnostic to their final implementation or realization. In section 5.3 the *Control Architecture Specification Model* (CASM) is introduced, which specifies the functional topology of the proposed flight control algorithm in this thesis.

The lowest concretization level considers the final system design and is hence concerned with detailed component requirements, which are represented by the *Design Specification Model*. The design specification of the components is targeted at realizing the subsystem functionalities, which are governed by the desired architecture specification and which collectively realize the behavioral specification on system level.

The Design Specification Model shall be sufficiently specific such that a subsequent implementation of the individual components can be realized. In the context of the flight control development in this thesis, the implementation is assumed to be automated in terms of automatic code generation from the *Control Design Model* (CDM), which is introduced in chapter 6. To this end, additional requirements are imposed on component level that ensure the functional integrity of the generated source code.

In order to validate the requirements, which are represented by the Requirement Specification Models at each particular level, simulation and analysis are used. The model embedding this analysis process is referred to as *Requirement Assessment Model* (RAM). It is focused on assessing the RSM with respect to the underlying needs, goals, and objectives by means of virtual testing and verification with respect to those requirements that drove the creation of the RSM and against additional requirements that might be imposed from different sources.

The resulting verification and validation processes are depicted as a model-based validation loop in figure 2.7. Furthermore, during analysis the verification activities can be used in two different ways, horizontally and vertically:

First, it can be verified if each individual RSM correctly embodies the requirements it is supposed to represent (horizontal verification). Thereby, the correct implementation of the model and its functional integrity are ensured.



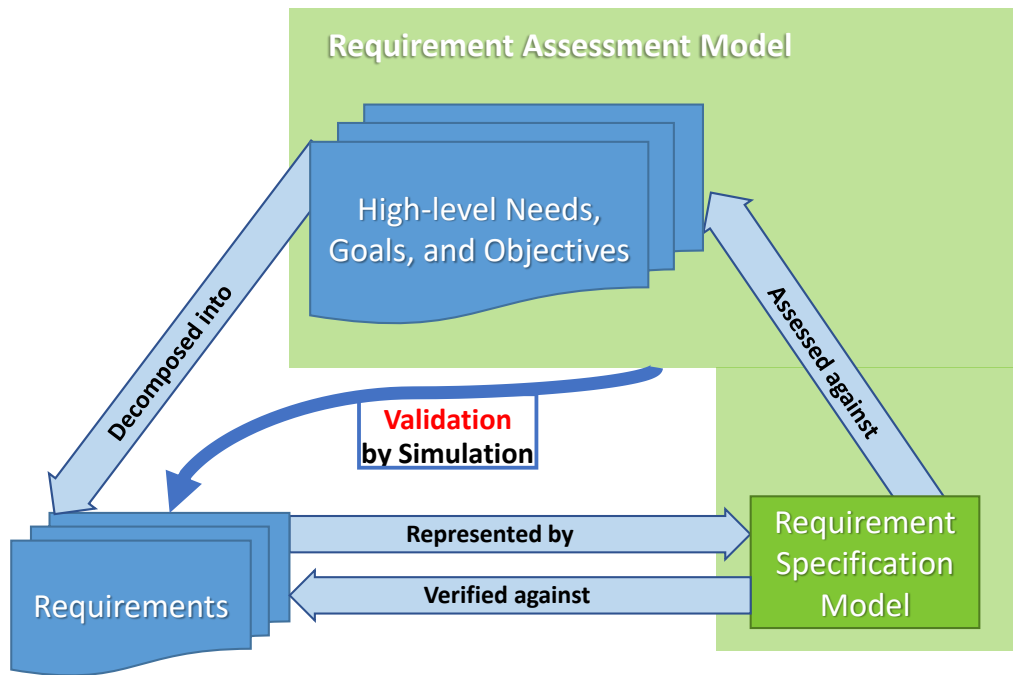


**Figure 2.7:** *Model-Based Validation Loop*

The main questions that are addressed during horizontal verification are:

- Does the Behavioral Specification Model correctly reproduce the specified behavior on system level? (e.g. by verifying that the vertical velocity builds up within the specified time, by verifying that the maximum airspeed is not exceeded, or by verifying that the roll angle response complies with the underlying specification)
- Does the Architecture Specification Model correctly represent the subsystem requirements? (e.g. by verifying if the modeled powered lift builds up with the specified dynamics, by verifying if the modeled control surfaces have the specified bandwidth and effectiveness, or by verifying if the modeled complementary filter within the control architecture yields the specified frequency characteristics)
- Does the Design Specification Model correctly represent the component requirements? (e.g. by verifying if the modeled electric current within the control surface actuator is within its specified limits or by verifying if the discrete implementation of the complementary filter uses the correct gain and data types)

The second way that verification can be used is to test the Requirement Specification Model against those high-level objectives that drove the RSM's creation and its decomposition into the underlying requirement specification (vertical verification). This assessment can be seen as part of the quantitative validation activity, since it is concerned with analysing the emerging properties of the RSM.

The main questions that are addressed during vertical verification are:

- Does the Behavioral Specification Model comply with overall mission, performance, safety, and handling quality requirements? (e.g. by verifying if the vertical rate response complies with existing handling quality requirements, by verifying if there is sufficient wing clearance to the ground during roll maneuvers, or by verifying if a certain mission can be completed in a specified time)
- Does the Architecture Specification Model fulfill the system level requirements that drove the creation of the architecture? (e.g. by verifying if the risetime for the vertical velocity is as specified, verifying if the maximum specified airspeed is exceeded, or verifying if the roll angle response complies with the specification)
- Does the Design Specification Model yield the functionality that is represented by the architecture specification on subsystem level? (e.g. by verifying if the electrically modeled control surface actuator provides the specified bandwidth or by verifying if the discretized complementary filter yields the desired frequency characteristics)

Note that while horizontal verification tests the RSM against its own specification, vertical verification tests against the parent requirements that the underlying requirement specification is derived from and that the parent RSM is verified against in a horizontal matter. In this sense, vertical verification can also be considered a local ('looking up one level') and quantitative (objectively testable) validation.

However, the overall validation process is also characterized by its application-oriented and holistic nature. The focus of this testing phase is put on specific use case scenarios. While one part of the validation work consists of doing vertical verification against given high-level objectives, another part consists of qualitative assessment by virtual operation of the system by a stakeholder or user.

Validation testing is aimed at replicating the actual use cases and performing virtual missions in terms of e.g. pilot-in-the-loop simulations. Thereby, the RSMs are used to validate the requirements on each level with respect to the overall needs, goals, and objectives.

The Behavioral Specification Model enables to operate an abstracted representation of the system which is agnostic to a concrete architecture or detailed design decisions. It hence enables validation of the behavioral requirements on system level and ensures that the proposed system behavior is desirable and compatible with the envisioned operational concept.

The Architectural Specification Model represents the system in terms of its functional topology. Testing on this level validates the functional decomposition and interactions on subsystem level and gives first insights about the feasibility of the proposed functional architecture.

Finally, the design of the system components on the lowest level is validated through assessing the Design Specification Model. These tests can include some form of software-, or hardware-in-the-loop simulation or even include several components of the real system (iron-bird testing).

Depending on which component or subsystem is validated, the overall system model can also have varying fidelity among its components. In chapter 6 the Control Design Model (CDM) is introduced, which represents the design specification for the flight control code on the lowest abstraction level. In order to validate the design specification, the CDM can be integrated into a system model, which represents the overall aircraft with all its components. However, not all components have to be modeled with the same fidelity as the CDM.

As long as the virtual environment provides the correct interfaces for interacting with the CDM, the remaining subsystems might as well be modeled in terms of their functional specification instead of being represented by their final design. In general, however, the confidence in the validation process is increased when the model provides the highest amount of detail.



# 3

## Mission Specification and Reference Configuration

This chapter aims to introduce an exemplary mission specification presented in section 3.1, which shall be realized using a reference configuration for a VTOL transition aircraft introduced in section 3.2. The requirements presented in this chapter are then used as a development basis and further decomposed in chapters 4 to 6 into a final control concept.

### 3.1 Mission Specification

The mission specification in this section is split up into two parts. In subsection 3.1.1 operational requirements are introduced, which support intended use case scenarios for an exemplary VTOL transition aircraft. In subsection 3.1.2 performance requirements are stated, which are proposed by EASA in their second publication of proposed means of compliance with the special condition VTOL [6].

#### 3.1.1 Operational Requirements

The operational requirements for the VTOL transition aircraft follow from an exemplary use case scenario of a transportation mission in or between urban environments. To this end, the mission is decomposed into the following flight related phases:

- **Vertical take-off:** The pilot shall be able to initiate a vertical take-off.
- **Translational control close to ground:** The pilot shall be capable of manipulating relative horizontal position, height, and heading of the aircraft with respect to stationary objects on the ground, thereby complying with the Mission Task Elements (MTE) presented in [12].
- **Transition into wingborne flight:** The pilot shall be able to initiate a transition into wingborne flight. During the transition phase, the pilot shall be able to control

the flight path in the horizontal and vertical plane and shall be able to abort the transition at any time.

- **Wingborne cruise flight:** During cruise flight, operation of the aircraft shall be similar to typical control regimes of fixed-wing aircraft. The pilot shall be capable of controlling the vertical flight path, flying turns, and controlling the airspeed of the aircraft.
- **Retransition and approach:** The pilot shall be able to initiate a retransition from pure wingborne flight into powered lift flight and control the airspeed, horizontal, and vertical flight path while approaching the desired landing area.
- **Vertical landing:** The pilot shall be able to land the aircraft vertically.

In general, the operation of the VTOL transition aircraft shall not require special piloting skills and is aimed to produce minimum workload. To this end, the operational concept shall provide intuitive control of the aircraft and shall take into account automatic flight envelope protections, which prevent the pilot from accidentally entering dangerous flight states. Additionally, a high degree of automation is desired in order to reduce the workload even further.

Intuitive control is thereby assessed with respect to the desired mission concept and the available human-machine interface, which is presented in section 3.2. As will be discussed in more detail in section 4.2, the command concept is aimed at providing control of high-level behavioral parameters of the aircraft through decoupling of command channels, automatic coordination, and compensation.

Given the wide operational envelope of VTOL transition aircraft, the control concept shall be specifically targeted at avoiding mode confusion of the pilot and integrate any necessary aircraft reconfiguration seamlessly into the overall mission procedure as part of a unified control strategy.

### 3.1.2 Performance Requirements

In this subsection quantitative performance requirements are discussed, which are presented by EASA in their second publication of proposed means of compliance with the special condition VTOL [6]. This document summarizes safety and design objectives for novel VTOL aircraft and addresses their unique characteristics. To this end, the special condition VTOL “prescribes airworthiness standards for the issuance of a type certificate, and changes to this type certificate, for a person-carrying VTOL aircraft in the small category” [6, p. 1].

The creation of the proposed means of compliance addresses the request of the industry for a standardized type certification of VTOL aircraft. It was furthermore publicly consolidated before it was issued by EASA in July 2019 [6].

In the following, the performance related contents are summarized, which are presented in [6] under MOC - Subpart B in MOC VTOL.2115, MOC VTOL.2120, and MOC VTOL.2130.

**Table 3.1:** *Definitions in the Context of SC VTOL*

Abbreviation	Definition <sup>1</sup>
CFP	A Critical Failure for Performance (CFP) is a failure or combination of failures that results in the maximum degradation for a given flight phase and performance parameter.
CMP	The Certified Minimum Performance (CMP) is the set of performance data obtained by considering the effect of single failures and combinations of failures that are not extremely improbable on the nominal performance parameters.
TDP	The Take-off Decision Point (TDP) is the first point defined by a combination of speed and height from which a Continued Take-off (CTO) is demonstrated meeting the Certified Minimum Performance (CMP), and is the last point in the take-off path from which a Rejected Take-off (RTO) is assured.
LDP	The characteristic point along the landing flight path is the Landing Decision Point (LDP), which is defined as the last point from which a bailed landing can be performed.
$V_{\text{TOSS}}$	Only primary controls should be used while attaining the Take-off Safety Speed ( $V_{\text{TOSS}}$ ) and while establishing the required climb gradient of at least 4.5% at the power rate setting declared by the applicant for the first take-off segment.
$V_{\text{FTO}}$	Any control can be used while attaining the Final Take-off Speed ( $V_{\text{FTO}}$ ) and while establishing the required climb gradient of at least 2.5% at maximum continuous power and a maneuvering capability of not less than 3°/s of turn rate while not descending.
$V_{\text{REF}}$	The landing reference speed ( $V_{\text{REF}}$ ) is the speed determined at the maximum flight glide path angle for which certification is sought and with all lift/thrust systems operative that is the initial speed that should be used to determine the area required to land and come to a stop.

<sup>1</sup> directly adapted from [41] and [6]

### 3.1.2.1 Take-off and Climbing

Section MOC VTOL.2115 and MOC VTOL.2120 in [6] are concerned with take-off and climbing performance requirements. Three different take-off trajectories are thereby considered by EASA and referred to as Conventional Take-off (ConvTO), Elevated Conven-

tional Take-off (EConvTO), and Vertical Take-off (VTO), which are depicted in figure 3.1. The former two are directly adopted from CS-27 category A rotorcraft requirements, while the latter is proposed “with the objective of providing an adapted take-off path for VTOL urban environment operations from vertiports” [6, p. 6].

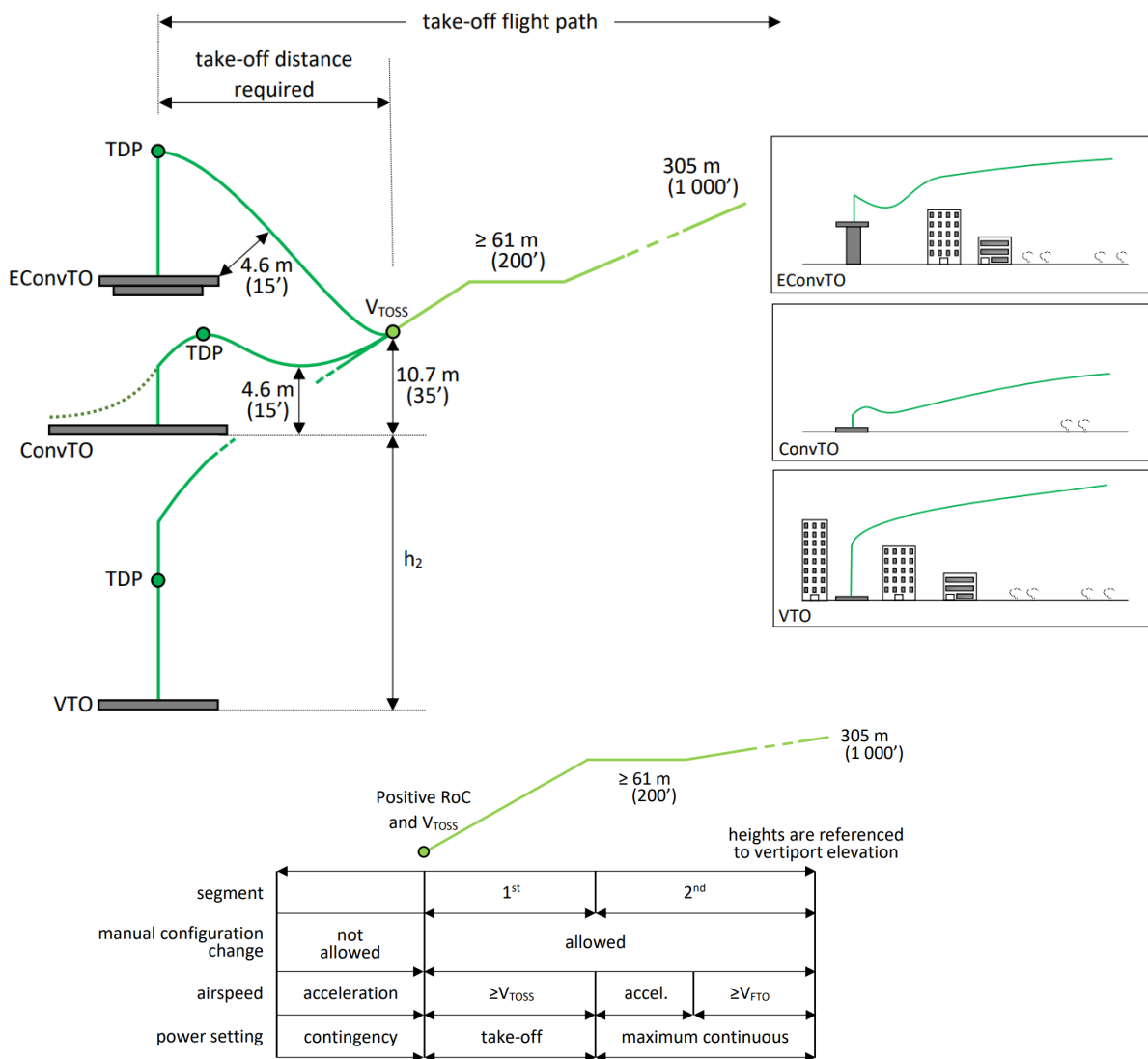


Figure 3.1: Possible Take-off Paths [6]

To this end, EASA specifies the take-off path for VTO operation on the basis of the following requirements (list adopted from [6]):

- (1) Obstacle clearance shall be established with respect to a “virtual elevated vertiport”, which is set at the top of the vertical climb.
- (2) The protection surfaces are established at the height of the virtual elevated vertiport, since the minimum gradients should be determined and demonstrated after reaching  $V_{TOSS}$ .



- (3) During the vertical segment, it should be possible to perform a Rejected Take-off (RTO) before reaching the Take-off Decision Point (TDP). Visual or synthetic cues can be used.
- (4) After the TDP it should be possible to perform a Continued Take-off (CTO). The applicant may choose to have a pure vertical or a backup (rearward) take-off trajectory. The maximum deviations from the nominal trajectories should be determined.
- (5) The TDP in the vertical segment can be placed at any point. Some applicants might elect to have a TDP lower than the top of the vertical segment, if the RTO cannot be performed safely from a given height upwards while meeting the Certified Minimum Performance (CMP) following a Critical Failure for Performance (CFP). Others may set the TDP at the bottom of the vertical segment because the RTO is not a foreseen option.

All three take-off paths ConvTO, EConvTO, and VTO only differ in the initial segment of the trajectory up to the point when the Take-off Safety Speed ( $V_{TOSS}$ ) is reached. This initial phase during take-off must not require any manual configurations by the crew.

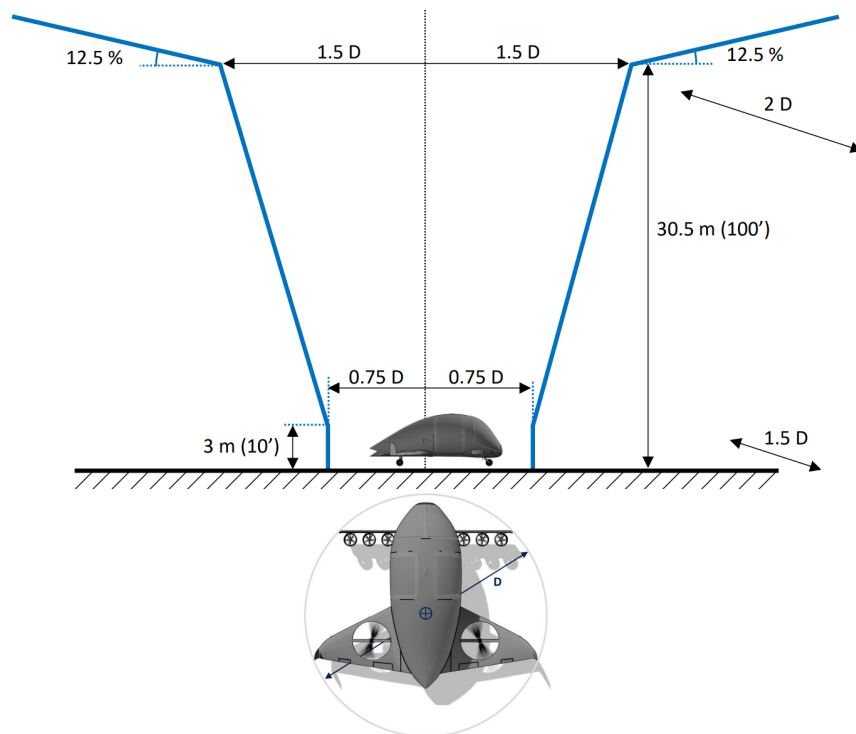


**Figure 3.2:** “Reference Volume Type 1” Vertical Take-off and Landing Procedure Parameters [6]

Figure 3.2 shows an exemplary reference volume suggested by EASA for departure and landing in the context of the vertical take-off and landing procedure. The volume is standardized by normalized dimensions expressed in terms of the smallest enclosing circle

diameter  $D$  of the VTOL aircraft and is specifically adapted to vertiports in obstacle-rich urban environments [6].

When reaching the Take-off Safety Speed ( $V_{\text{TOSS}}$ , see table 3.1), the first segment of the take-off path is initiated, in which manual configuration changes by the crew are allowed and during which the velocity shall be kept as close as practically possible to (but not less than)  $V_{\text{TOSS}}$ . Furthermore, a minimum rate of climb of 4.5% shall be maintained until a height of 61 m (200 ft) above the take-off elevation (or above the virtual elevated vertiport in the case of the VTO) is reached [6].

Upon arriving at the height of 61 m (200 ft) above the take-off elevation, the second segment of the take-off path begins, in which the VTOL shall accelerate to the Final Take-off Speed ( $V_{\text{FTO}}$ , see table 3.1). The minimum climb gradient during the second segment corresponds to 2.5%, unless  $V_{\text{FTO}}$  is reached while changing directional trajectory, in which case the VTOL aircraft shall be capable of at least maintaining level flight. Furthermore, after reaching the Final Take-off Speed, the aircraft shall be capable of horizontal directional changes of the trajectory of at least  $3^\circ/\text{s}$ , which corresponds to a standard turn rate.

The minimum climb gradient requirements in segment 1 and 2 are directly derived from the existing certification standards CS-27 and CS-29. For more detailed information regarding the take-off procedures including abnormal cases such as Rejected Take-off (RTO), the reader may refer to the official special condition document MOC-2 SC-VTOL [6].

### 3.1.2.2 Landing

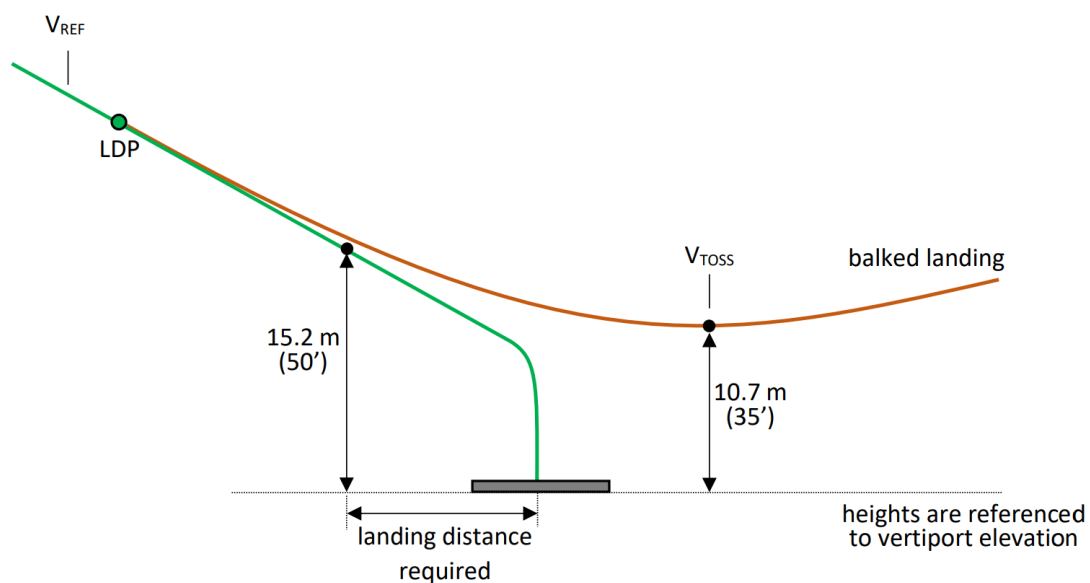


**Figure 3.3:** *Landing Path* [6]

In MOC VTOL.2130 [6], EASA distinguishes between two main types of landing: a Conventional Landing (ConvL) and a Vertical Landing (VL).

The trajectory for ConvL extends from the Landing Decision Point (LDP, see table 3.1 and figure 3.3) to the point at which the VTOL aircraft comes to a complete stop. The glide path during ConvL corresponds to whatever proves to be most appropriate as judged by the applicant [6].

The landing path for VL is specifically adapted to landing on vertiports in an Urban Air Mobility (UAM) environment for which strict requirements regarding sufficient obstacle separation apply. To this end, “the applicant may choose to have, from a point along the approach after the LDP, a pure vertical trajectory” [6, p. 16].

Figure 3.3 illustrates a nominal landing approach (green) and a bailed landing (brown). The landing distance required for VTOL aircraft (LDRV, [6]) corresponds to the horizontal distance between the point at which the aircraft is 15 m (50 ft) above the landing surface and the point at which it comes to a complete stop. Furthermore, the applicant shall report the landing distance required following a CFP that is recognized at the LDP to EASA [6].

According to table 3.1, the pilot must be able to initiate a bailed landing up until he reaches the LDP. After that a bailed landing is not assured [6]. Until reaching  $V_{REF}$  (see table 3.1), the bailed landing procedure must be performed without requiring any manual configuration changes by the crew, even in the event of a CFP.

Analogously to the take-off procedure, manual configuration changes are permitted once the aircraft regains the Take-off Safety Speed ( $V_{TOSS}$ ). From this point on the minimum climb gradients of the first and second segment, which were mentioned in subsection 3.1.2.1, have to be ensured. Furthermore, EASA requires the applicant to provide a “representative time to perform a go-around from LDP back to LDP (...) for determination of the energy reserve” [6, p. 17].

## 3.2 Reference Configuration of the Aircraft

As will be pointed out in chapter 4, an idealized development approach would yield the physical configuration and design of the VTOL aircraft as the result of a top-down requirement decomposition. Latter would start from the high-level operational and performance requirements given in section 3.1, proceed with a detailed behavioral specification of the VTOL, and would subsequently derive the physical design of the aircraft.

However, in the context of this thesis the behavioral specification of the VTOL aircraft and the subsequent flight control development are derived based on a given configuration concept, which is decided upon beforehand. In order not to pose unnecessary restrictions, the reference configuration is generalized to a maximum degree and only includes those characteristics that have a direct influence on possible behavioral and operational outcomes in the further development.

To this end, subsection 3.2.1 summarizes those aspects of the overall aircraft configuration, which influence the kinetic capabilities of the VTOL in terms of available force and moment producers such as propulsion units, control effectors, and other aerodynamic surfaces.

Furthermore, subsection 3.2.2 discusses the available control inceptors, which represent the main human-machine interface that the pilot uses to control the aircraft.

The kinetic configuration and the available control inceptors lay the foundation for the development of the behavioral specification in chapter 4.

### 3.2.1 Kinetic Configuration

This subsection introduces the kinetic configuration of the VTOL aircraft, which refers to the main kinetic characteristics that influence the aircraft's capability to generate forces and moments. Hence, the kinetic configuration of the aircraft comprises those aspects that underlie all possible behaviors of the VTOL in terms of its overall motion, performance, and operation.

Over the past decade, various configuration concepts for VTOL aircraft have been developed and analyzed [61] [7] [62] [8]. These concepts mainly differ in the type of propulsion (electric, turbo-electric, turbo-shaft, fuel cell, diesel, hybrid [62]) and the propulsion topology (pure multirotor, side-by-side helicopter, tilt-wing, tilt-rotor, vectored thrust, lift-plus-cruise [61] [7]).

As an exemplary illustration, figure 3.4 shows three concept vehicles developed by NASA, which represent a quadrotor with electric propulsion, a side-by-side helicopter with hybrid propulsion, and a tilt-wing aircraft with turbo-electric propulsion [7].



**Figure 3.4:** *Exemplary NASA Concept Vehicles: Quadrotor, Side-by-Side Helicopter, and Tilt-Wing Aircraft Concept [7]*

In general, the various configuration concepts yield different characteristics and therefore come with different advantages and disadvantages. As is mentioned in [61], the optimal aircraft configuration highly depends on the considered mission.

While pure multirotor configurations perform more efficiently in terms of the required energy during hover scenarios, vectored thrust jets and tilt-wing or tilt-rotor aircraft offer

a higher range, yield higher efficiency in cruise flight, and enable fixed-wing operation in the first place [61].

Lift-plus-cruise configurations thereby represent a compromise in terms of efficiency. Nevertheless, [8] points out that “the question of which aircraft type is optimally suited to performing economically viable Urban Air Mobility missions has been and will continue to be the subject of much debate” [8, p. 3].

Being a particularly new type of aircraft, the lift-plus-cruise configuration is chosen as the primary concept for the remainder of this thesis. As an illustrative example, figure 3.5 shows the turbo-electric lift-plus-cruise concept aircraft that was designed at NASA Ames Research Center and presented in [8]. Furthermore, figure 3.6 shows examples of electric lift-plus-cruise transition aircraft that are currently developed by commercial companies.

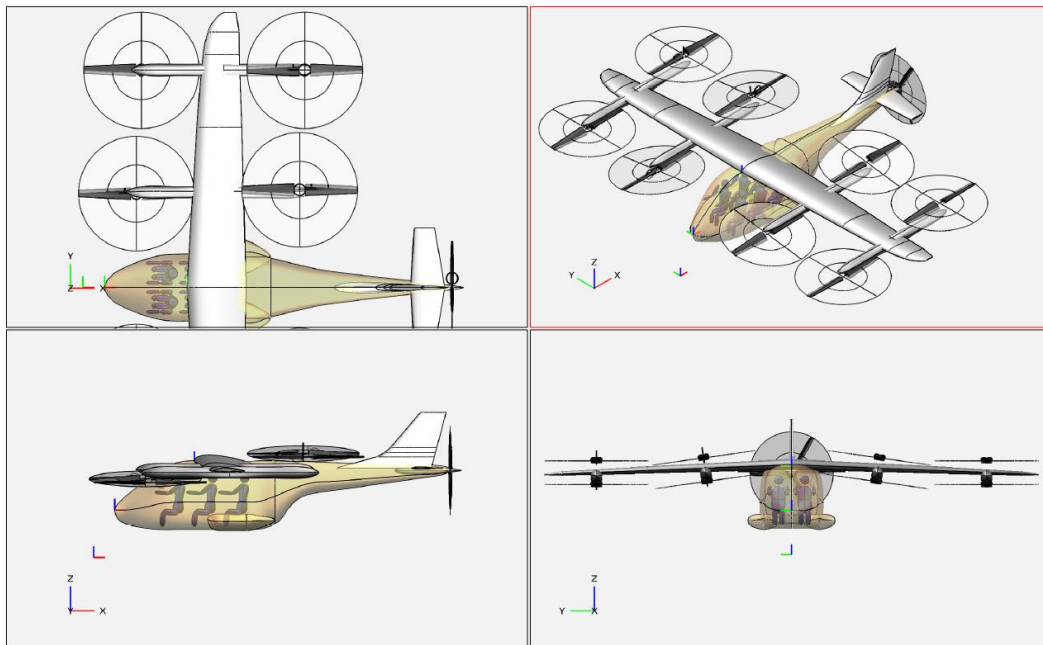


**Figure 3.5:** *Exemplary Lift-Plus-Cruise Concept Vehicle [8]*

According to [8], several potential advantages can be listed for lift-plus-cruise type aircraft:

- (1) Multiple lifting rotors, which are typically mounted on motor support booms, provide a high amount of redundancy in the powered lift production and hence enable compliance with respective safety requirements.
- (2) Lifting motors and propellers can share identical design, which simplifies manufacturing and maintenance aspects.
- (3) Rotational speed control of the lifting propellers is facilitated by their small size. In contrast to blade-pitch controlled rotors, which are usually used in traditional



**Figure 3.6:** *Existing Lift-Plus-Cruise Transition Aircraft.* Top row: *Autoflight V1500M, Aurora PAV.* Bottom row: *Voloconnect, Kitty Hawk Cora* (Sources: Company sites)

helicopters, RPM-controlled propellers provide easier and more robust lift control, since no complex mechanical parts are needed like a swashplate for collective and cyclic actuation.

- (4) Cruise optimized small wings can be used for higher efficiency, since the low-speed flight is supported by the powered lift system.
- (5) Since lift-plus-cruise type aircraft are essentially based on conventional aircraft with added powered lift capability, certification activities targeting the fixed-wing phase of the flight can be facilitated.
- (6) Higher disk loading due to the small total area of the lifting propellers is tolerable without excessive increase of battery size, since the required hover time is short in typical VTOL missions.
- (7) The high number of rotors reduces the necessary tip speed of each individual lifting propeller, which significantly decreases the noise profile.

In chapters 4 to 6, no specific configuration is considered for the development of the flight control functionality. However, the general configuration type of a lift-to-cruise aircraft is presupposed as a basis for the behavioral and control architecture specification.

Even though the developed behavioral concept in chapter 4 is to a large extent applicable across most transition aircraft configurations, some of the behavioral aspects are

specific to lift-to-cruise configurations. The resulting functional decomposition in chapter 5 is furthermore specific to the functional topology of lift-to-cruise aircraft, however can be adapted to different configurations without loss of generality.

### 3.2.2 Control Inceptors

Control inceptors represent the central element of the human-machine interface with which the pilot interacts in order to control the vehicle. To this end, helicopters are usually equipped with a cyclic stick for horizontal control, a collective stick and throttle for vertical control, and pedals for yaw control.

Furthermore, most conventional fixed-wing aircraft either use a yoke or a sidestick to control the pitch and roll axis respectively, pedals to control the yaw axis of the airplane, and a thrust lever to control the throttle. The most prominent representatives of either of the two fixed-wing control inceptors – yoke or sidestick – are Boeing and Airbus respectively, which established different technological philosophies in the production of their airplanes [63].

Although Boeing has only started to implement fly-by-wire technology with the start of their 777 model, they remained loyal to the pilot-centered design in which the final authority is attributed to the pilot [64]. Airbus, however, has been following an automation- and augmentation-centered control philosophy and has implemented fly-by-wire control from their A320 model onwards using passive sidesticks instead of yokes [65]. Two representative cockpits of the Boeing 737-700 and the Airbus A320 are shown in figure 3.7.



**Figure 3.7:** *Boeing 737-300 Cockpit (left) and Airbus A320 Cockpit (right) (Source: flugzeug-lexikon.de)*

The choice of control inceptors thereby has a significant impact on the overall handling and operation of the aircraft. Furthermore, the unique characteristics of control inceptors

can even impact the safety of occupants in certain circumstances and lead to deadly accidents, as was the case for the prominent disaster of Air France Flight 447 on June 1, 2009, which cost the lives of 228 passengers and crew of an Airbus A330 [66].

Due to an airspeed indication failure caused by ice crystals blocking the pitot tubes, the autopilot disengaged followed by a switch of the control system “from *normal* to *alternate* law, disabling the protections that automatically prevent excursion from the safe flight envelope” [66, p. 735]. Shortly thereafter, the pilot in control unintentionally maneuvered the aircraft into an aerodynamic stall without the other pilot realizing it. Particularly, [66] further elaborates:

Bonin’s actions were invisible to Robert because on Airbus aircraft each pilot has a sidestick to manually control the plane, located on opposite sides of the aircraft. The sidestick inputs of one pilot are therefore not apparent to the other. If pilots make conflicting sidestick inputs these are averaged by the system, a warning message is displayed and a synthetic voice calls out “dual input.” [66, p. 736]

It is a subject of much discussion, if the use of active instead of passive sidesticks [67] could have prevented the Air France accident by providing haptic feedback and coupling both pilot’s stick inputs in order to increase awareness, as is the case for the yokes of Boeing airplanes. The Bureau of Enquiry and Analysis for Civil Aviation Safety (BEA), which is an agency of the French government that investigates aviation accidents, furthermore states in their final report of the Air France Flight 447 accident that “[i]t is worth noting that the inputs applied to a sidestick by one pilot cannot be observed easily by the other one and that the conditions of a night flight in IMC make it more difficult to monitor aeroplane attitudes (pitch attitude in particular)” [68, p. 175].

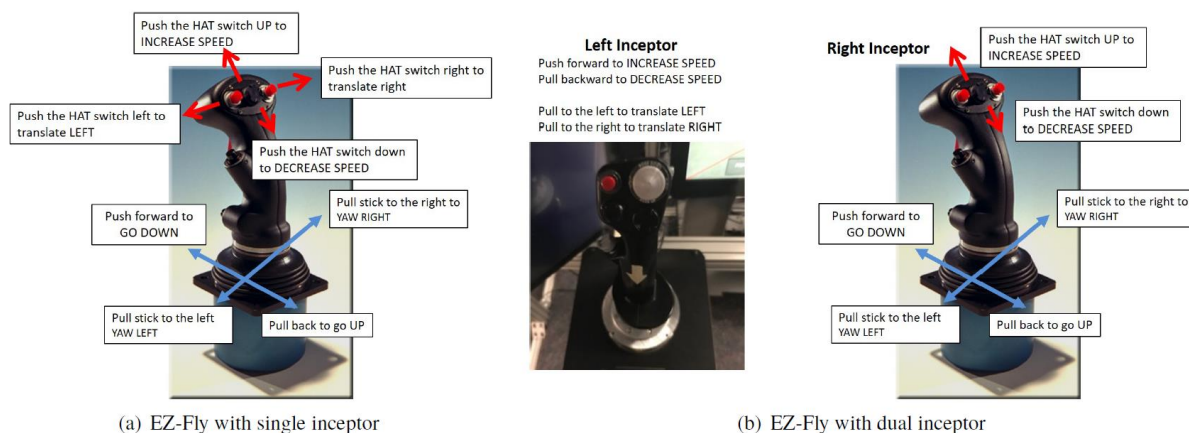


**Figure 3.8:** *EZ Fly Control Inceptor Concepts [9]*



Nevertheless, the recent development in the area of VTOL aircraft has shown that the use of one or two sidesticks per pilot [69] [10] [9] [11] [1] is being established as the most common approach to control such a vehicle.

In figure 3.8 two exemplary control inceptor configurations are presented – using single or dual conventional passive sidesticks – as the basis for the EZ-Fly [9] Simplified Vehicle Operations (SVO) strategy. Latter thereby represents one possible unified command concept for VTOL transition aircraft and is explained in further detail in [9].

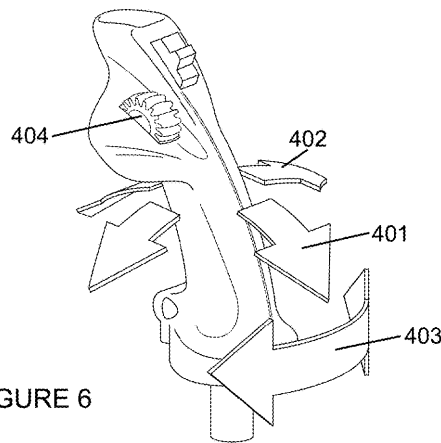


FIGURE 6

310

Flight Regime	Single Inceptor axis mapping and response types - Lon. Unified	Single Inceptor axis mapping and response types - Lon. + Lat. Unified
Hover:	X - vertical rate Y - lateral translational rate / acceleration Z - heading rate (yaw) A - longitudinal translational rate & acceleration (B - deck angle)	X - vertical rate Y - heading rate (yaw) Z - lateral translational rate / acceleration A - longitudinal translational rate & acceleration
Forward flight:	X - pitch rate/flightpath Y - roll rate/flightpath Z - sideslip A - airspeed rate  FMS could configures aircraft to allow delta-flightpath (or equivalent) control for conventional landings.	X - pitch rate/flightpath Y - roll rate/flightpath/heading rate Z - sideslip A - airspeed rate  FMS likely configures aircraft to allow delta-flightpath (or equivalent) control for conventional landings.
Ground operations:	Brake model uses forward stick X motion to command braking effort. (Button - Brake hold)  Z - steering*  A - Prop thrust, wheel motors	Brake model uses forward X motion to command braking effort. Button - Brake hold  Y - steering  A - wheel motors/prop taxi thrust

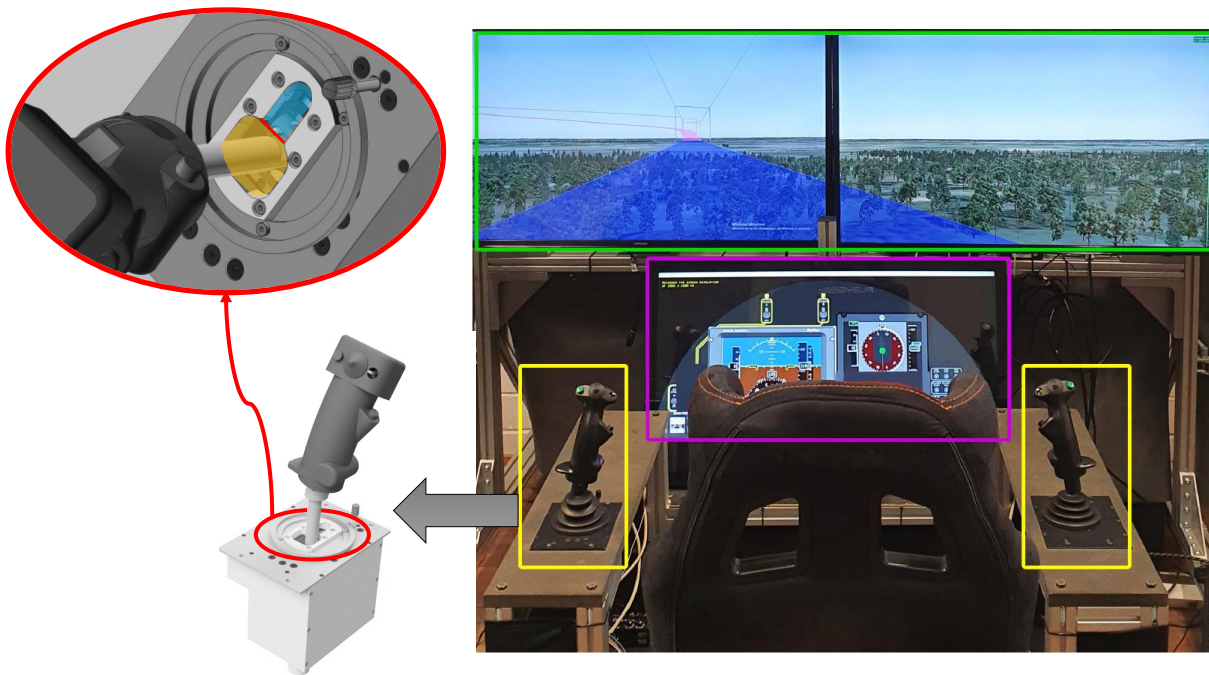
FIGURE 7

Figure 3.9: Control Inceptor Mapping in Patent from Joby Aviation [10]

Section 4.2 furthermore introduces the novel command concept for Simplified Vehicle Operations that was prepublished in [1] by the author and that represents one of the contributions of this thesis. It is tailored to a novel control inceptor design first published in [11], which is described in further detail at the end of this section.

Another control concept is illustrated in figure 3.9, which shows the patented control inceptor mapping from Joby Aviation [10]. It distinguishes between two different flight regimes of longitudinal unified control and longitudinal plus lateral unified control. The illustration in figure 3.9 shows a single sidestick, which is equipped with a thumb wheel for longitudinal translational rate and acceleration control. Furthermore, in [10] it is additionally specified that “the input mechanism can include one or more inceptors, a display, and any suitable interface components” [10, p. 5].

Finally, figure 3.10 illustrates the control inceptor configuration, which is used in the remainder of this thesis and shows the VTOL simulator mock-up at the institute of Flight System Dynamics (FSD) of the Technical University of Munich (TUM). It is comprised of several monitors (green), a primary flight display in the center (magenta), and two control inceptors (yellow).



**Figure 3.10:** *VTOL Simulator Mock-Up at the Institute of Flight System Dynamics (FSD) of the Technical University of Munich (TUM) [11]*

The control inceptor on the right is a sidestick, which is spring-centered and provides a digital output proportional to the deflection distance or angle of the stick. This is in contrast to the sidestick concept of some military aircraft like the F-16 or F-18 for which the digital output of the control inceptor and hence the interpreted command through the fly-by-wire system is proportional to the applied stick force rather than being proportional to the stick deflection [70] [71] [72].

The implemented artificial Force Feel System (FFS) for these highly agile aircraft thereby prohibits any stick movement except for slight deflections in each axis, which avoids cross-coupling of the pitch and roll channel and provides an intuitive way to create control margin awareness during e.g. high-g maneuvers [70] [71]. Furthermore, the limited stick deflections provide additional benefits against the adverse effects of limb-sidestick dynamic interactions during agile maneuvers [73].

However, since the presented mission profiles for VTOL transition aircraft do not foresee highly agile maneuvers, the application of conventional deflection-proportional control concepts is justified. Furthermore, the presented control inceptors for VTOL operation are passive sidesticks, similarly to Airbus sidesticks. Therefore, they do not provide tactile feedback to adapt the stick force characteristics dependent on the flight condition (or dependent on the co-pilot's inputs), as would be possible with active sidesticks [67]. Instead, the force characteristics are constant and only depend on the passive spring and damping elements of the stick.

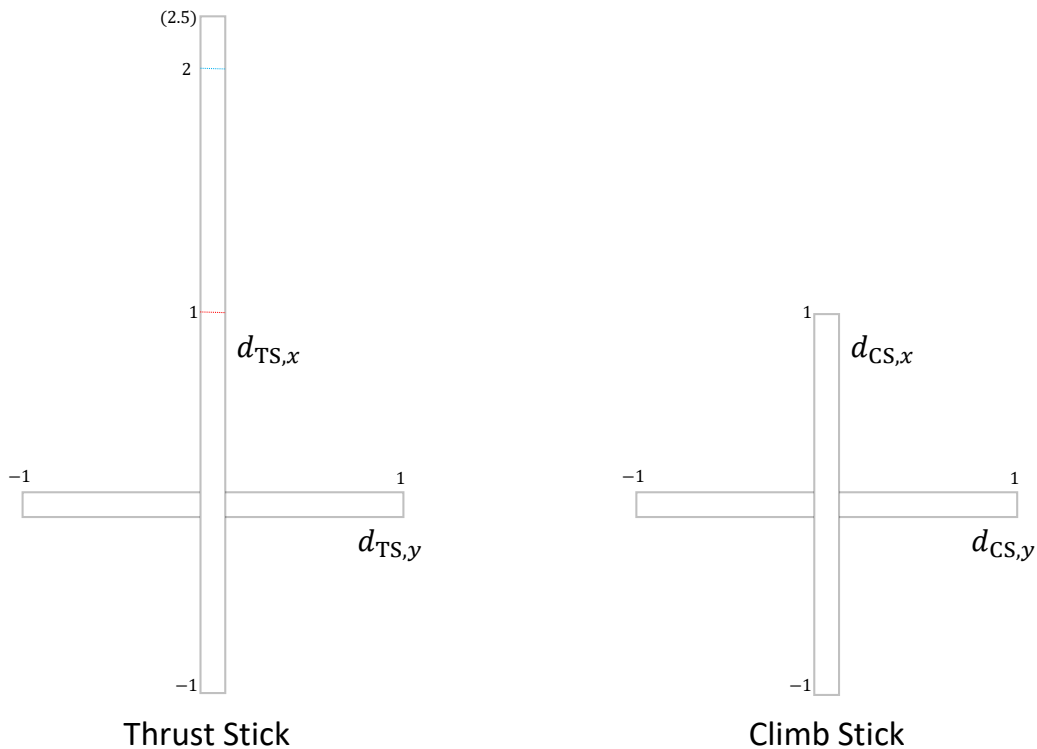


**Figure 3.11:** *Schematic Representation of the Control Inceptors*

The control inceptor on the left side is a custom-built solution, which was developed at FSD and was first published in [11]. It is based on the same conventional passive sidestick that is used on the right side in figure 3.10 (corresponding to the conventional Airbus sidestick) and is additionally modified in the longitudinal axis to account for the extended flight envelope of VTOL transition aircraft.

The red circle in figure 3.10 thereby shows a close-up of the underlying modification: Within the orange area, the stick behaves identical to the right control inceptor and provides a spring-centered force characteristic while permitting stick movement in all directions. The blue area indicates the force-free region of the control inceptor in which the stick maintains its current deflection upon releasing it. Additionally, the control inceptor's lateral degree of freedom is prohibited in this region of the stick.

The control inceptor characteristics within the blue region are aimed at mimicking a conventional thrust lever and hence provide a familiar interface for the pilot during the fixed-wing flight phase. Additional notches mark characteristic stick positions such as for Maximum Continuous Thrust (MCT) or Maximum Peak Thrust (MPT), which is indicated at  $d_{TS,x} = 2$  with a blue line in figure 3.11. The stick position  $d_{TS,x} = 2.5$  thereby corresponds to Maximum Take-off Thrust (MTO) or take-off/go-around thrust (TOGA) for aircraft performing Conventional Take-Off and Landing (CTOL).

The spring-centered region (orange area) and the force-free thrust-lever region (blue area) are separated by a detent notch (red line) in figure 3.10 and 3.11. In order to push or pull the stick through the detent notch, the stick force has to increase progressively upon approaching the detent.

It might additionally be desired to trigger the transition from one stick area to the other via a button press. This way, accidental transitions between both control inceptor regions are prevented, which supports safe aircraft operation in case of substantial configuration changes upon switching flight modes (such as the activation or deactivation of the powered lift system for lift-plus-cruise configurations).

The additional use of pedals for yaw control is omitted in the presented control inceptor concept. As will be discussed in section 4.2, the goal is to provide an intuitive control strategy for the pilot that is based on a high degree of automation and that enables SVO. Although the use of additional elements such as pedals is not completely excluded, the presented control approach in the following sections renders their use unnecessary due to the high degree of augmentation.

# 4

## Behavioral Specification of the System

The behavioral specification represents the first step in the systems-theoretic driven development approach, after having converged on the desired mission statement, needs, and goals. From a control perspective, the behavior of the system represents the highest abstraction level. In an idealized approach, the specification for how the system should behave could be developed independently of any assumptions about how the system will be designed in the end, as long as the behavior is physically feasible and fulfills all the needs and goals. The system architecture and design would subsequently be derived from the specification by stepwise decomposition, following the fundamental approach of systems engineering [3].

In practice however, a lot of high-level design decisions are made very early in the development process and have a great influence on the set of possible system behaviors. Usually these design decisions are the result of preceding concept phases or adapted from already existing systems and scaled or modified in order to fit the needs and requirements of the new project.

Only later in the development process it can be assessed, if the existing design decisions support the underlying behavioral specification and are feasible to satisfy all the requirements, yielding an highly iterative process. The creative challenge lies in creating a specification that among all possible variants of behavior both satisfies the existing objectives and is compatible with the given architecture and design constraints.

A behavioral specification for onboard piloted VTOL transition aircraft is proposed in the following, which is in line with the author's publications in [1] and [2]. The resulting Simplified Vehicle Operations (SVO) are described in section 4.2 and are motivated by the concepts presented in [45] and [9]. Modifications and adaptations are introduced to account for a novel control inceptor design (see [11]) and improve the handling, judged by virtual flight tests conducted in [74] and [1].

The goal is a behavioral concept that is compatible with the configuration from chapter 3 and that reduces the requirements on the skill level of the aircraft operator to a

minimum through highly automated closed-loop control of the transition vehicle throughout the whole flight envelope. The operational concept is aimed at enabling safe and efficient completion of typical missions described in section 3.1 and [12] (in the form of Mission Task Elements) and provide intuitive response of the transition aircraft to control inputs. [1]

Following a model-based development approach, section 4.3 introduces the *Design Reference Model* (DRM, inspired by NASA’s Design Reference Mission, also see [32]), which represents an executable specification model of the final system behavior based on rigid-body simulation considering the kinetic capabilities of the system. The Design Reference Model enables early validation of the proposed behavioral concept by considering virtual missions and model-based handling quality assessment. Furthermore, it supports the specification and validation of those system aspects that determine the kinetic capabilities of the system, such as mass, inertia, motors, actuators, and aerodynamic properties.

Early validation is crucial especially when developing new types of systems due to the high amount of uncertainty regarding novel concepts and technologies. The amount and duration of process iterations within the development is considerably reduced, thereby minimizing risk and cost and improving the quality of the final system. Additionally, modelling of the behavioral specification serves as a good basis for the development of the control architecture in chapter 5 through application of functional decomposition.

## 4.1 Continuity-Based Input-Output Mapping

In this section a novel bilinear input-output mapping concept is introduced, which was originally pre-published by the author in [2] and represents **contribution C.4** of this thesis. It is aimed at providing continuous outputs in the presence of discrete mode switches that alter the input value, input limits, and output limits of the underlying mapping in a discontinuous manner.

The introduction of fly-by-wire technology around the time of World War II has enabled the rise of digital control laws. The analog readout of control inceptors, the interpretation of the signals through software, and the subsequent command of control effectors and other aircraft subsystems have introduced a variety of possibilities and challenges in aviation.

Handling qualities and the overall aircraft response are highly dependent on the underlying command mapping and control laws. In particular, the presence of discrete mode switches, which change the command mapping characteristics or the command input source, might lead to unexpected aircraft behavior if not properly accounted for. Applicable examples include but are not limited to priority switching of command channels for multi-pilot operation or any control mode switch that alters the underlying output limits of the command mapping due to e.g. flight envelope considerations.

Discontinuous changes in the pilot’s command variables upon discrete mode switches

might lead to unexpected aircraft behavior. Hence, the continuity-based mapping concept can considerably improve the handling qualities for the operator by enforcing the continuity of the output during the mode switch and thereby avoiding discontinuous jumps in the commanded variable.

The proposed strategy was originally developed by the author in the context of pilot priority switching of a tandem-seat fly-by-wire aircraft, where an unexpected aircraft reaction upon command takeover is highly undesirable. In general, the concept can be applied in any bilinear input-output mapping context, which requires continuity of the output in the presence of discrete changes of the input, input limits, and output limits. Bilinear in this context means that changes in the input map linearly to the output while the slope of the mapping can be dependent on the direction of the input change.

Although the presented mapping is very general in its application, it is presented here in the specific context of speed control for a VTOL transition aircraft.

In the scope of the Simplified Vehicle Operations concept introduced in section 4.2, the longitudinal axis of the left control inceptor (thrust stick) from figure 3.11 is used to command a desired aircraft velocity. However, different modes and phases during operation of the transition aircraft require different limits in the allowed authority over commanded variables such as the airspeed. A more detailed introduction into the justification of adjusting the airspeed command (and protection) limits of the system based on the current flight phase is given in section 4.2.

In order to introduce and derive the novel command mapping, the mode switch from highspeed powered lift flight (denoted as *transition mode*) into the (pure) wingborne phase (denoted as *wingborne mode*) is considered in the following. The control inceptor area of interest is the thrust-lever region, which is marked off by a red dotted line in figure 3.11 and figure 4.3 and corresponds to the stick values  $1 \leq d_{TS,x} \leq 2$  in figure 3.11. Upon switching from the transition phase to the wingborne phase, the upper airspeed command limit changes discontinuously from  $1.x V_{\text{stall,p}}$  to the higher value  $V_{\text{NO}}$ , both of which are described in section 4.2.

In order to avoid any unintended aircraft reaction and maintain good handling qualities during and after a mode switch, the following requirements are proposed for the input-output command mapping of a given control inceptor channel:

1. The output must not change upon mode switching.
2. The output must not change when the input is held at a constant value.
3. Minimum and maximum inputs shall always yield minimum and maximum outputs respectively.
4. Input-to-output gradients shall be within appropriate limits.
5. The input-to-output gradient shall remain constant or shall not change rapidly in the direction in which the input is changing.

The novel stick mapping is based on an incremental approach, which yields the current command output based on the current stick input, previous stick input, and the previous command output. For each incremental step, the left-sided and right-sided gradients are adjusted based on the stick and command limits of that time step.

Applying this concept on the velocity mapping of the left control inceptor, it follows for the target airspeed

$$V_{CAS,d} = V_i = \begin{cases} V_{\min}, & \text{for } d_i \leq d_{\min} + \epsilon \\ V_{\max}, & \text{for } d_i \geq d_{\max} - \epsilon \\ V_{i-1} + \Delta V, & \text{for } d_{\min} + \epsilon < d_i < d_{\max} - \epsilon \end{cases} \quad (4.1)$$

where  $d_i$  and  $V_i$  are the current stick input and command output,  $V_{i-1}$  is the previous command output,  $d_{\min}$  and  $d_{\max}$  are the minimum and maximum stick input values,  $V_{\min}$  and  $V_{\max}$  are the minimum and maximum command output values,  $\epsilon > 0$  is a small positive number that avoids singularity of the gradient, and  $\Delta V$  is the output increment.

Note that (4.1) by definition satisfies requirement 3 for minimum and maximum stick inputs. For all other stick inputs, the output increment  $\Delta V$  is calculated according to

$$\Delta V = m_i (d_i - d_{i-1}) + \Delta V_{\text{up}} + \Delta V_{\text{lo}}, \quad (4.2)$$

with  $d_{i-1}$  representing the previous stick input,  $m_i$  representing the current gradient in the direction of the stick movement, and  $\Delta V_{\text{up}}$  and  $\Delta V_{\text{lo}}$  representing additional increments that provide gradient protection and are explained later on.

Furthermore, the left-sided and right-sided gradient  $m_i$  in (4.2) is calculated at each time step according to

$$m_i = \begin{cases} \min \left( m_{\max}, \max \left( m_{\min}, \frac{V_{\min} - V_{i-1}}{d_{\min} - d_{i-1}} \right) \right), & \text{for } d_i - d_{i-1} \leq 0 \\ \min \left( m_{\max}, \max \left( m_{\min}, \frac{V_{\max} - V_{i-1}}{d_{\max} - d_{i-1}} \right) \right), & \text{for } d_i - d_{i-1} > 0 \end{cases}, \quad (4.3)$$

such that the minimum and maximum command outputs  $V_{\min}$  and  $V_{\max}$  are approached linearly within the remaining stick distance to the minimum and maximum stick input values  $d_{\min}$  and  $d_{\max}$  respectively.

In order to comply with requirement 4, the calculation of the gradient is protected by the upper gradient limit  $m_{\max}$  and the lower gradient limit  $m_{\min}$  such as to ensure that the resulting mapping does not lead to an over-sensitive or under-sensitive aircraft reaction as a response to stick inputs.

For both the transition and wingborne phase, the stick limits for the velocity mapping in the thrust lever region are constant and are given by  $d_{\min} = d_{\text{TS},x,\text{notch}} = 1$  and  $d_{\max} = 2$  (see figure 3.11 for a definition of the coordinates). The minimum airspeed command is also the same in both modes and corresponds to  $V_{\min} = V_{\text{stall,p}}$ . However, the maximum airspeed command limit changes from  $V_{\max} = 1.x V_{\text{stall,p}}$  in the transition phase to the higher value  $V_{\max} = V_{\text{NO}}$  in the wingborne phase. For a more detailed description of the airspeed values, the reader may refer to section 4.2.



The sudden increase of the airspeed command's upper limit  $V_{\max}$  during stick inputs close to the upper stick limit  $d_{\max}$  would lead to a significant right-sided gradient according to (4.3) and hence to an over-sensitive mapping, if no gradient protection was provided.

However, due to the saturation of the gradient, the remaining stick distance to the upper stick limit would not be sufficient to reach the maximum command output. This represents a conflict in the requirements 3 and 4 and is resolved by introducing the previously mentioned additional increments  $\Delta V_{\text{up}}$  and  $\Delta V_{\text{lo}}$ , which compensate for the missing output increment such as to reach the maximum (or minimum) command output within the remaining stick distance subject to the maximum (or minimum) allowed gradient.

The gradient protecting increments  $\Delta V_{\text{up}}$  and  $\Delta V_{\text{lo}}$  are hence given by

$$\Delta V_{\text{up}} = \begin{cases} 0, & \text{for } m_{\min} \leq \frac{V_{\max} - V_{i-1}}{d_{\max} - d_{i-1}} \leq m_{\max} \\ (V_{\max} - V_{i-1}) - (d_{\max} - d_{i-1}) m_{\max}, & \text{for } \frac{V_{\max} - V_{i-1}}{d_{\max} - d_{i-1}} > m_{\max} \\ (V_{\max} - V_{i-1}) - (d_{\max} - d_{i-1}) m_{\min}, & \text{for } \frac{V_{\max} - V_{i-1}}{d_{\max} - d_{i-1}} < m_{\min} \end{cases} \quad (4.4)$$

and

$$\Delta V_{\text{lo}} = \begin{cases} 0, & \text{for } m_{\min} \leq \frac{V_{\min} - V_{i-1}}{d_{\min} - d_{i-1}} \leq m_{\max} \\ (V_{\min} - V_{i-1} - \Delta V_{\text{up}}) - (d_{\min} - d_{i-1}) m_{\max}, & \text{for } \frac{V_{\min} - V_{i-1}}{d_{\min} - d_{i-1}} > m_{\max} \\ (V_{\min} - V_{i-1} - \Delta V_{\text{up}}) - (d_{\min} - d_{i-1}) m_{\min}, & \text{for } \frac{V_{\min} - V_{i-1}}{d_{\min} - d_{i-1}} < m_{\min} \end{cases} \quad (4.5)$$

and are only added, if the right-sided and left-sided gradient are not within the respective gradient limits.

In order to illustrate the stick mapping, figure 4.1 shows three different scenarios, where the switch from transition mode to wingborne mode happens at three different stick positions: right behind the notch (1a), in the middle of the thrust lever region (1b), and close to the upper end of the thrust lever region (1c). Note that since pushing the stick behind the notch is only a necessary but not sufficient condition for the mode switch, the transition into the wingborne mode can be initiated at any stick position behind the notch.

In all three cases of figure 4.1 the operator starts during transition mode at stick position 0 right behind the notch. Next, the switch into the wingborne mode is initiated at stick position 1a, 1b, and 1c respectively. Hence, between stick position 0 and 1 the aircraft operates in transition mode, which is indicated by the red solid lines in all three cases (in the first case the transition phase collapses to a single point).

The stick is then further moved through position 2 to 5 during the wingborne mode, indicated by the blue solid lines. The dotted lines in figure 4.1 represent the virtual extension of the mapping, which indicates the input-output relationship if the stick was moved in the respective direction. Note that at any time the command limits of the respective mode are continuously reachable by minimum or maximum stick deflections.

If the right-sided gradient (towards the maximum) and the left-sided gradient (towards the minimum) are within the feasible limits shown in (4.4) and (4.5), the correcting

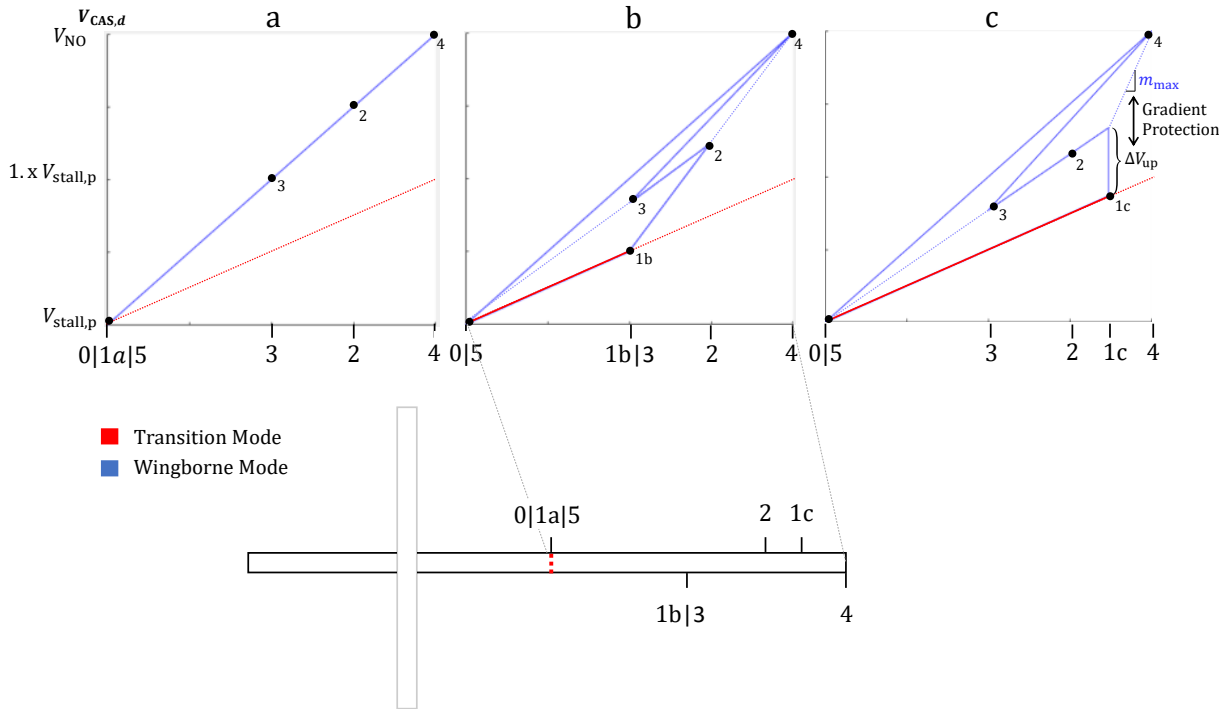


**Figure 4.1:** Mapping of Left Control Inceptor During Switch From Transition Mode (red) to Wingborne Mode (blue) for Three Different Cases

increments  $\Delta V_{up}$  and  $\Delta V_{lo}$  remain zero and a transition-free switch in the mapping can be achieved, as can be seen in the cases a) and b) of figure 4.1.

However, if the resulting gradients are not within the limits, the non-zero gradient protection increments lead to a discrete change in the command output during the mode switch, as can be seen in case c) of figure 4.1. Even though this jump in the output violates requirement 1, it resolves the conflict between requirements 1, 3, and 4 for mode switching at close-to-extreme stick inputs with a minimum jump in the command output value.

Case a) in figure 4.1 represents a special case for which the control inceptor is located right behind the notch in the moment of the mode switch. Since the lower command output limit  $V_{min}$  is identical for both transition and wingborne mode, the mapping reduces to a straight line and no gradient protection is necessary.

A more detailed description of the total airspeed mapping including the case of switching from the wingborne mode back to the transition mode is discussed in subsection 4.2.3.1.

In addition to the presented application scenario, a discrete change of the stick input, which occurs during command priority switching in multi-pilot operation, can be dealt with in an analogous manner with the presented stick mapping approach. The continuity of the command output is preserved by evaluating  $d_{i-1}$  of the first pilot as the previous stick input value of the second pilot's priority receiving stick in the moment of the switch.

## 4.2 Simplified Vehicle Operations for Onboard Piloted VTOL Transition Aircraft

In this section the command concept for onboard piloted transition vehicle is described in detail. It represents **contribution C.1** of this thesis and was pre-published by the author in [1].

The resulting Simplified Vehicle Operations are motivated by existing concepts like 'Unified' [75] (developed by UK's Royal Aircraft Establishment in the 1970's and 80's) and 'E-Z-Fly' [76] (developed at NASA Langley in the 1990's), which are also mentioned and described in [9]. A similar approach for remotely controlled VTOL drones is described in [45]. The concept at hand is specifically tailored to the novel control inceptor design [11] introduced in section 3.2 and is adapted to onboard operation of VTOL transition aircraft.

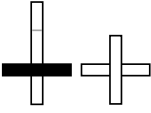
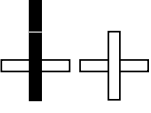
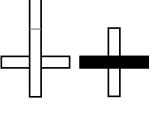
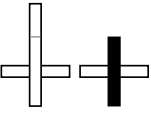
The focus of the proposed Simplified Vehicle Operations lies in providing an easy and intuitive control concept, which minimizes the pilot's required training before and workload during operation of such a novel configuration. It is specifically targeted at yielding excellent handling qualities for onboard operation and providing an unified control experience while flying the transition vehicle.

The proposed behavior shall be realized by highly automated closed-loop control of the VTOL aircraft throughout the whole flight envelope: from low speed hovering through the medium speed transition phase into the high speed wingborne phase.

The operational concept is based on two control inceptors: a passive side stick on the right and a passive sidestick on the left, which extends forward into a non-spring-centered region, mimicking a thrust lever. Figure 4.3 shows the novel control inceptor design, which was first mentioned in [11] and has been used in virtual flight test studies in [11] and [74]. The mapping from inceptor deflection to command as well as the choice of internally tracked target variables are chosen such as to provide good handling qualities in every flight condition and to account for flight envelope protections such that the commands do not exceed the physical capabilities of the vehicle in any given flight situation.

The behavioral specification of the transition vehicle is divided into three phases, which are distinguished by vehicle velocity (and dynamic pressure) and motivated by different kinematic and kinetic characteristics of low, medium, and high velocity operation of the VTOL aircraft and the different operational phases during typical missions.

The internally tracked variables as well as allocation of forces and moments are adapted to the current flight phase, however, the response of the transition aircraft to control inceptor inputs remains consistent throughout the entire flight envelope. An overview of the Simplified Vehicle Operation concept can be found in figure 4.2.

	$V_{Cy,d}$ $\rightarrow V_{Cy,c}$	$\beta_{kin,d}$ $\rightarrow V_{By,c} = \sin(\beta_{kin,d})V_{kin}$	$f_{By,d}$ $\rightarrow f_{By,c}$
	$V_{Cx,d}$ $\rightarrow V_{Cx,c}$	$V_{CAS,d} + \alpha_{kin,d}$ $\rightarrow V_{CAS,c} + \alpha_{kin,c}$	$V_{CAS,d}$ $\rightarrow V_{CAS,c}$
	$\psi_d$ $\rightarrow \psi_c$	$\psi_d$ $\rightarrow \phi_c = \sin^{-1}\left(\frac{\tan(\theta)\psi_d V_{Bz}}{\sqrt{g^2 + \psi_d^2 V_{Bx}^2}}\right) - x$ $x = \sin^{-1}\left(\frac{-\psi_d V_{Bx}}{\sqrt{g^2 + \psi_d^2 V_{Bx}^2}}\right)$	$\psi_d$ $\rightarrow \phi_c = \sin^{-1}\left(\frac{\tan(\theta)\psi_d V_{Bz}}{\sqrt{g^2 + \psi_d^2 V_{Bx}^2}}\right) - x$ $x = \sin^{-1}\left(\frac{-\psi_d V_{Bx}}{\sqrt{g^2 + \psi_d^2 V_{Bx}^2}}\right)$
	$\dot{h}_d$ $\rightarrow \dot{h}_c$ (Powered Lift)	$\dot{h}_d$ $\rightarrow \dot{h}_c$ (Powered Lift)	$\dot{h}_d$ $\rightarrow \begin{cases} \dot{h}_c & \text{Small Amplitudes} \\ V_{CAS,c} & \text{High Amplitudes at Maximum Thrust} \end{cases}$ (Aerodynamic Lift)
<b>Hover</b> $V_{hover}$		<b>Transition</b> $V_{stall}$	<b>Wingborne</b> $V$

**Figure 4.2:** SVO Table: Command and Target Variables During Hover, Transition, and Wingborne Flight

## 4.2.1 Low Velocity Operation: Hover

The control concept for low velocity operation of the transition aircraft is driven by the requirements of relative translational control with respect to earth-fixed objects. The Aeronautical Design Standard ADS-33E-PRF [12] defines performance specifications and handling quality requirements for military rotorcraft as well as typical operational missions in form of Mission-Task-Elements (MTEs) that represent the entire spectrum of intended operational usage and serve as behavioral basis for the control concept that is described in the following.

Note that the applicability of conventional rotorcraft requirements on VTOL transition configurations has to be considered on an individual basis and will ultimately be validated in terms of model-based simulation. Exemplary verification and validation activities are conducted in section 4.4.

### 4.2.1.1 Left Longitudinal and Lateral Stick Channel During Hover Phase

Using the left control inceptor the operator commands a horizontal translational rate with respect to ground. The target translational rate is defined as velocity vector in the control

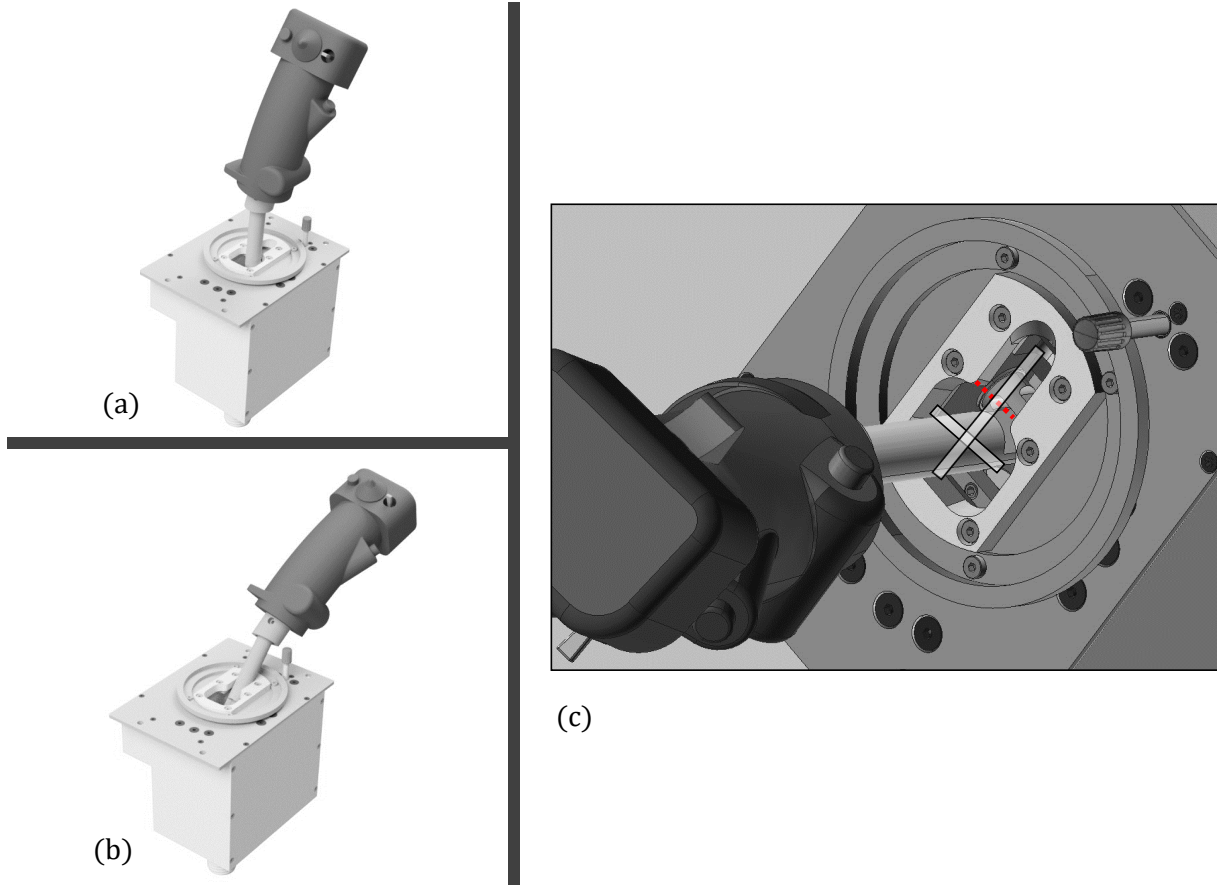


**Figure 4.3:** *Left Control Inceptor in Spring-Centered Position (a), in Throttle Lever Position (b), and Close-Up of the Detent Notch (c)*

frame, which is shown in figure 4.4. The control frame is horizontal to the earth surface and aligned with the heading of the VTOL aircraft, i.e. the north-east-down frame rotated by the heading angle of the vehicle.

In order to achieve good handling qualities, ADS-33E-PRF specifies the boundaries for the relationship between applied cockpit control force and the resulting target translational rate, which is shown in figure 4.6.

Motivated by one of the central control guidelines mentioned in [75], the movement of the transition vehicle should generally follow the control inceptor deflection. Hence, the deflection of the thrust stick determines the direction of the target translational rate by mapping the stick direction in inceptor-fixed coordinates (subscript  $S$ ) into the control frame (subscript  $C$ ) as can be seen in figure 4.5. Longitudinal and lateral stick deflections therefore correspond to along-heading and across-heading movement of the aircraft.

In order to achieve direction-preserving properties for the mapping of stick deflection  $(\mathbf{d}_{TS})_S = [d_{TS,x} \ d_{TS,y}]_S^T$  to target velocity  $(\mathbf{V}_{hor,c})_C = [V_{Cx,c} \ V_{Cy,c}]_C^T$ , the following relationship has to be satisfied:

$$\tan(\beta_C) = \frac{V_{Cy,c}}{V_{Cx,c}} = \frac{d_{TS,y}}{d_{TS,x}} = \tan(\beta_S) , \quad (4.6)$$

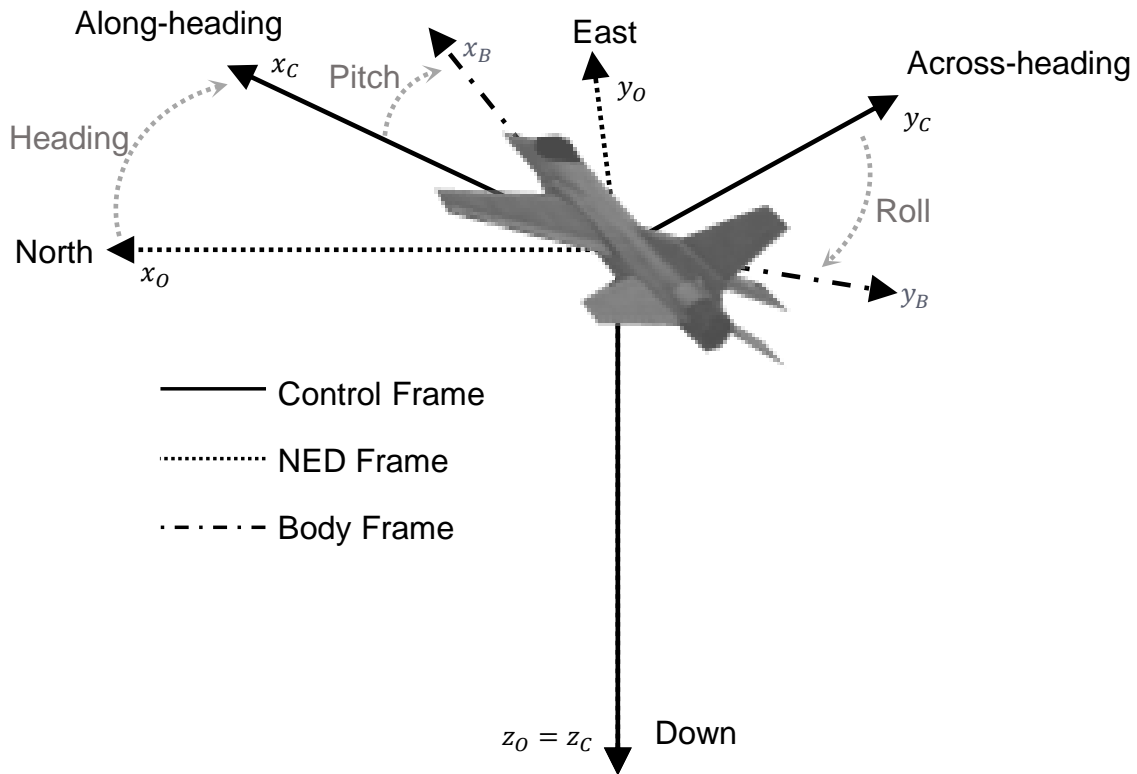


**Figure 4.4:** *Coordinate Frames*

with  $\beta_C$  and  $\beta_S$  being defined in figure 4.5.

Note that dependent on the force characteristics of the stick, it might be necessary to introduce a nonlinear mapping from stick deflection to translational rate, such that the stick force to translational rate requirements from figure 4.6 are met.

Furthermore, in order to satisfy the direction constraint (4.6), the target velocity is expressed in terms of polar coordinates

$$V_{Cx} = \cos(\beta_C)V_{\text{HOR,abs}} \quad V_{Cy} = \sin(\beta_C)V_{\text{HOR,abs}}, \quad (4.7)$$

with the translational direction  $\beta_C$  and translational rate  $V_{\text{HOR,abs}}$  being expressed in terms of the stick deflection according to

$$\beta_C = \beta_S = \text{atan2}(d_{\text{TS},y}, d_{\text{TS},x}) \quad V_{\text{HOR,abs}} = f(d_{\text{TS},x}, d_{\text{TS},y}). \quad (4.8)$$

The function  $f$  in (4.8) determines the relationship between absolute stick deflection and target translational rate. In case of a constant and omnidirectional stick spring constant  $C_{\text{spring}} = \frac{F_{\text{stick,lb}}}{\sqrt{d_{\text{TS},x}^2 + d_{\text{TS},y}^2}}$ , which denotes the stick force in pounds for a unit deflection in stick

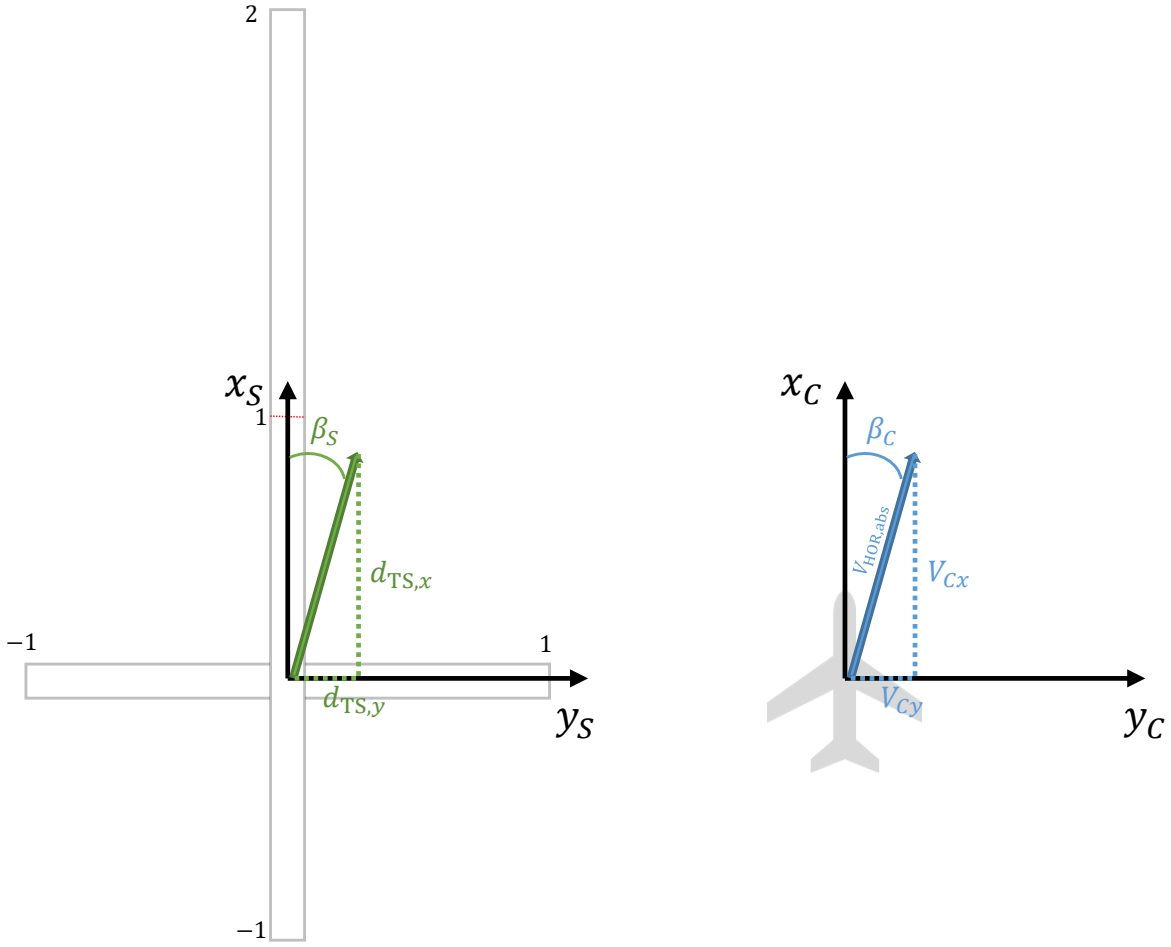


**Figure 4.5:** Mapping of Left Control Inceptor to Translational Rate During Hover Flight

coordinates  $(\mathbf{d})_S$ , the quadratic function

$$f(d_{TS,x}, d_{TS,y}) = aC_{\text{spring}}^2 (d_{TS,x}^2 + d_{TS,y}^2) + bC_{\text{spring}} \sqrt{d_{TS,x}^2 + d_{TS,y}^2}, \quad (4.9)$$

$$a \approx 0.83 \frac{ft/s}{lb^2}, \quad (4.10)$$

$$b \approx 5.83 \frac{ft/s}{lb}, \quad (4.11)$$

is located between the boundaries in figure 4.6c and therefore yields Level 1 handling qualities. Furthermore, the maximum forward velocity in hover is denoted as  $V_{\text{hover}} = V_{\text{TOSS}}$  (see subsection 3.1.2) and represents the border between hover operation and the transition phase.

Upon releasing the left control inceptor the system controls the translational rate to zero and holds the horizontal position with respect to ground, thereby compensating position drift, e.g. due to wind gusts.

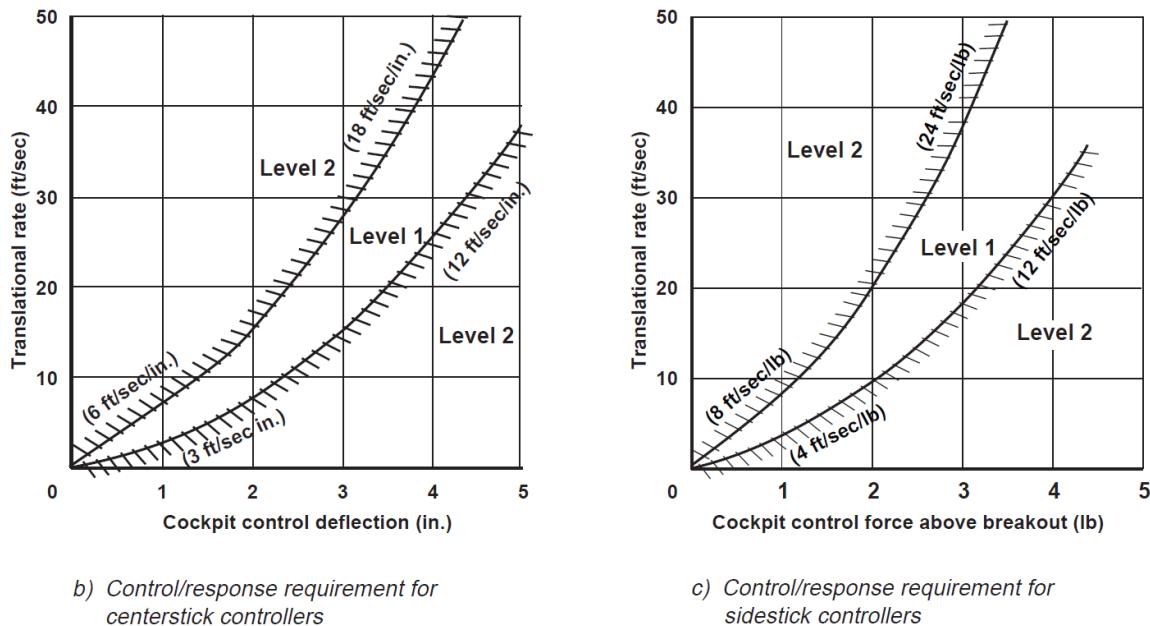


**Figure 4.6:** Cockpit Control Deflection/Force Versus Translational Rate According to ADS-33E-PRF [12]

#### 4.2.1.2 Right Longitudinal Stick Channel During Hover Phase

Deflections along the longitudinal direction of the right control inceptor are interpreted as a target vertical velocity  $\dot{h}_d = -V_{Cz,c}$ . Pulling or pushing the stick initiates a climb or descent rate respectively. Upon releasing the right stick, the VTOL aircraft stops the vertical motion and starts to hold the current altitude. Flight simulator tests conducted in [11] suggest that, if the longitudinal breakout force of the right stick during lateral deflections is not significant enough, a dead-zone in the longitudinal channel is necessary in order to account for undesired height changes during lateral deflections.

According to [12], the minimum climb and sink rate characteristics during hover have to satisfy the requirements in table 4.1.

**Table 4.1:** Vertical Rate Requirements During Hover Flight [12]

Handling Quality Level	Minimum Vertical Rate <sup>1</sup>
Level 1	160 ft/min
Level 2	55 ft/min
Level 3	40 ft/min

<sup>1</sup> achievable vertical rate 1.5 seconds after initiation of a rapid displacement

When operating close to the ground, the sink rate is limited based on the height above



ground level  $h_{AGL}$  according to

$$\dot{h}_{\min} = -V_{Cz,\max} = \frac{1}{T_h} (h_{TH} - h_{AGL}) , \quad (4.12)$$

in order to avoid unintentional flight into ground. Hence, the height above ground converges on the target height  $h_{TH} < 0$  with a time constant of  $T_h$ . A negative target height is chosen, such as to maintain a minimum sink rate capability of  $\frac{h_{TH}}{T_h}$  when touching the ground.

#### 4.2.1.3 Right Lateral Stick Channel During Hover Phase

The lateral axis of the right control inceptor is interpreted as a desired heading rate  $\dot{\psi}_d$ . Deflecting the stick to the left or right will result in a negative or positive heading rate respectively. Depending on the agility category, table 4.2 shows the required performance limits to achieve Level 1 or Level 2 and 3 handling qualities.

**Table 4.2:** *Heading Rate Requirements During Hover Flight [12]*

Agility Category	Achievable Heading Rate	
	Level 1	Level 2 and 3
Limited Agility	$\pm 9.5^\circ/\text{s}$	$\pm 5^\circ/\text{s}$
Moderate Agility	$\pm 22^\circ/\text{s}$	$\pm 9.5^\circ/\text{s}$
Aggressive Agility	$\pm 60^\circ/\text{s}$	$\pm 22^\circ/\text{s}$

Upon releasing the right stick, the VTOL aircraft shall hold the current heading. However, it might be necessary to give up the heading hold functionality in the presence of strong steady state wind due to the limited yaw authority of typical VTOL configurations compared to tail rotor configurations. Additionally, the presence of a tail rudder used for lateral control during wingborne flight increases the sensitivity to lateral gusts during hover flight. Further investigation of the yaw channel are conducted in section 4.4, where a lateral wind gust scenario is simulated and discussed in the context of verification and validation activities of the Design Reference Model introduced in section 4.3.

Since the left control inceptor defines the target velocity vector in the heading-dependent control frame, a demand in heading rate requires curvature of the kinematic velocity, and acceleration in the horizontal plane has to be provided by the system. Due to the lack of lateral force capability, this maneuver requires a change in vehicle attitude in order to tilt the lift vector into the horizontal plane. This behavior is a consequence of the underlying kinetic constraint of unidirectional force capability and hence has to be considered in the derivation of the Design Reference Model. As a consequence, an input in the right lateral stick channel during forward flight leads to a kinematically coordinated bank-to-turn maneuver. However, the coordination happens with respect to the across-heading velocity rather than the body lateral velocity.

In this context it also has to be considered, up to which velocity  $V_{Cx}$  the target heading rate  $\dot{\psi}_d$  can be supported by the system's lift performance and hence its capability of horizontally curving the velocity vector while maintaining sufficient vertical acceleration authority  $\ddot{h}_{\text{req}}$ . The equations of motion in  $z_C$  and  $y_C$  direction during a steady turn with velocity  $V_{Cx} = \text{const}$  are given respectively by

$$\dot{V}_{Cz} = -\ddot{h} = \cos(\phi) \cos(\theta) f_{Bz} + g \quad (4.13)$$

and

$$\dot{V}_{Cy} = 0 = -\sin(\phi) f_{Bz} - \dot{\psi} V_{Cx}, \quad (4.14)$$

with  $f_{Bz}$  denoting the specific force in body-vertical direction,  $\phi$  and  $\theta$  denoting the roll and pitch angle respectively, and  $g$  denoting the gravitational acceleration. The influence of the traction system on the vertical channel is neglected due to small pitch angles.

Hence, given the maximum specific lift force  $f_{\text{max}} = -f_{zB,\text{min}} > 0$  that the system can produce and assuming small pitch angles  $\theta$ , the maximum absolute target heading rate  $\dot{\psi}_{\text{abs,max}}$  at a given velocity  $V_{Cx}$  yields

$$\dot{\psi}_{\text{abs,max}} = \frac{1}{V_{Cx}} \sqrt{f_{\text{max}}^2 - (\ddot{h}_{\text{req}} + g)^2}, \quad (4.15)$$

while considering a required minimum authority in vertical acceleration  $\ddot{h}_{\text{req}}$ .

Note that the roll response during a change in heading indirectly occurs as a consequence of controlling and stabilizing the across-heading velocity component and is therefore coupled to the heading channel. This represents a different paradigm than for medium and high velocity operation, where the yaw response is governed by the lateral components of the velocity vector (or resulting lateral load factor due to aerodynamic forces) and hence is a consequence of the directly controlled roll angle.

### 4.2.2 Medium Velocity Operation: Transition

The transition phase starts after the VTOL aircraft reaches a kinematic velocity of  $V_{Cx} = V_{\text{hover}}$  and the left stick is located behind the detent notch in the throttle lever area, denoted by the red dotted line in figure 4.3. Furthermore, in order to switch back to the hover phase, the velocity has to drop below  $V_{Cx} = V_{\text{hover}} - \Delta V$  and the stick has to be located before the notch. The threshold  $\Delta V$  results from a hysteresis to avoid limit cycles at the border of both modes. The moding logic is adapted from [36]. In order to avoid mode confusion of the operator, the mapping of control inceptor channels to control variables during the transition phase is chosen such as to provide similar behavior of the VTOL aircraft as for the hover phase. However, the choice of internally tracked variables is adapted to the characteristics of medium to high velocity operation.

#### 4.2.2.1 Left Longitudinal Stick Channel During Transition Phase

The proposed mapping of the left control inceptor is driven by the following requirements during the transition phase:

1. The aircraft response to control inceptor deflections during transition shall be similar to hover and wingborne flight.
2. Transition into the wingborne phase shall happen at a defined angle of attack and airspeed during horizontal and straight flight.
3. There shall be sufficient margin towards stall when switching to the wingborne phase.
4. Acceleration shall be provided by the forward propulsion system rather than pitching down.
5. Deceleration of the aircraft shall be supported by respective pitch up movement at low dynamic pressures.
6. The authority to actively command changes in angle of attack shall be reduced at high dynamic pressures in order to avoid coupling with the powered lift system in the vertical channel and mitigate excessive loads.
7. The maximum airspeed shall be limited during transition in order to avoid excessive loads on the high power lift system.

Similarly to the hover phase, the longitudinal channel of the left stick corresponds to a velocity command during the transition phase. However, instead of the kinematic velocity with respect to earth, the indicated airspeed  $V_{CAS,d}$  is controlled through automatic command of forward thrust at a predefined kinematic angle of attack  $\alpha_{kin,d}$ . Both the airspeed and the angle of attack are determined based on the position of the left control inceptor and the current airspeed as is qualitatively shown in figure 4.7.

Right behind the detent notch the commanded airspeed is given by  $V_{CAS,d} = V_{stall,p}$ , which represents the target speed for the transition into the wingborne phase and is defined as

$$V_{stall,p} = (1 + p) V_{stall}, \quad (4.16)$$

where  $p$  is the margin towards stall speed and is chosen around  $p \approx 0.2$ . Note that the stall speed during the transition phase might be higher than in the wingborne phase due to adverse aerodynamic effects of the (idling) high power lift system.

The corresponding angle of attack

$$\alpha_{stall,p} = \frac{\alpha_{stall}}{(1 + p)^2} \quad (4.17)$$

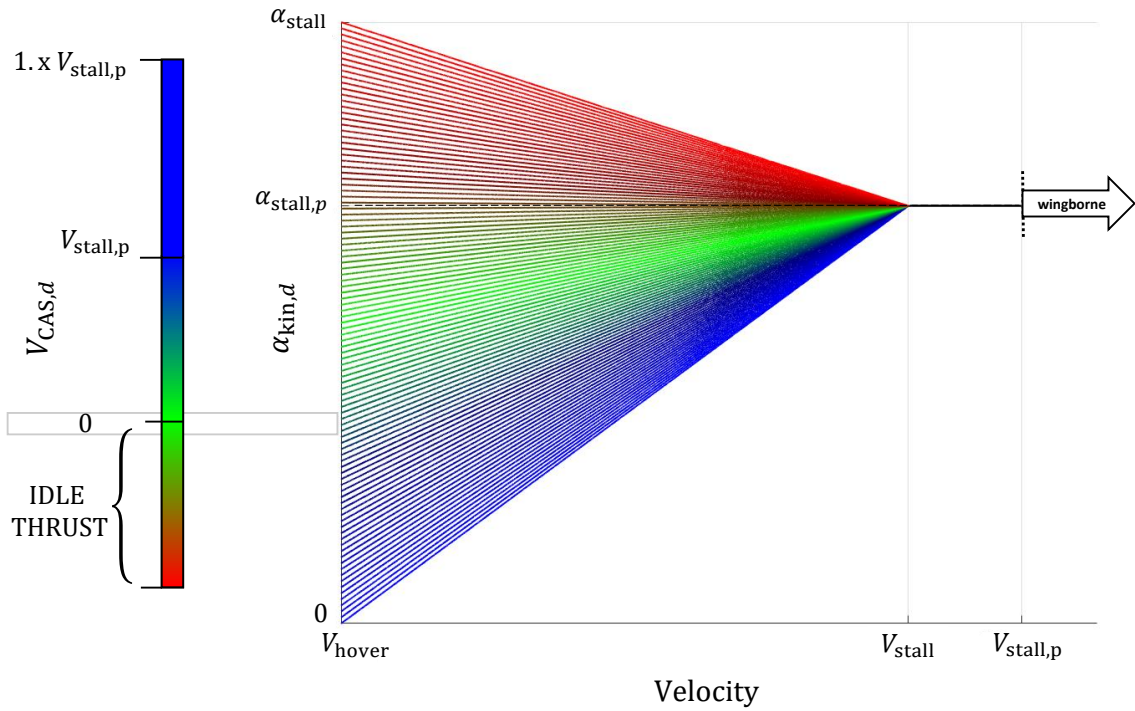


**Figure 4.7:** Mapping of Left Control Inceptor During Transition

builds up gradually over the speed and yields sufficient lift for horizontal and straight flight at a predetermined air density and velocity of  $V_{\text{stall},p}$  with the high power lift system not providing additional lift.

Below the centered stick position the forward thrust is set to idle and above it the commanded airspeed linearly scales from  $V_{\text{CAS},d} = 0$  to  $V_{\text{CAS},d} = V_{\text{stall},p}$  until right behind the detent notch. Since the stick travel while pushing the stick over the detent notch is small but non-zero, the target airspeed below the notch at the upper end of the spring centered stick range corresponds to a value  $V_{\text{CAS},d} < V_{\text{stall},p}$ , which represents the maximum speed for which the transition phase can be sustained.

In addition to setting the target airspeed  $V_{\text{CAS},d}$ , the left stick also sets the target angle of attack  $\alpha_{\text{kin},d}$ . In line with the requirements stated in the beginning of this section, the target kinematic angle of attack  $\alpha_{\text{kin},d}$  linearly scales over the stick range  $d_{\text{TS},x}$  and velocity  $V$  according to

$$\alpha_{\text{kin},d} = \begin{cases} a_{\alpha}V + b_{\alpha}, & \text{for } V \leq V_{\text{stall}} \\ \alpha_{\text{stall},p}, & \text{for } V > V_{\text{stall}} \end{cases}, \quad (4.18)$$

with the parameters  $a_{\alpha}$  and  $b_{\alpha}$  defined according to

$$a_{\alpha} = \frac{\alpha_{\text{stall},p} - \alpha_{\text{hover}}}{V_{\text{stall}} - V_{\text{hover}}} \quad b_{\alpha} = \alpha_{\text{stall},p} - a_{\alpha}V_{\text{stall}} \quad (4.19)$$

and the kinematic angle of attack at the lower speed boundary of the transition phase

given by

$$\alpha_{\text{hover}} = \frac{1 - \min(1, d_{\text{TS},x})}{2} \alpha_{\text{stall}}. \quad (4.20)$$

The stick deflection  $d_{\text{TS},x}$  is defined according to figure 3.11, where  $d_{\text{TS},x} = -1$  corresponds to a complete pull of the stick,  $d_{\text{TS},x} = 1$  corresponds to the upper end of the spring centered area right before the notch, and  $d_{\text{TS},x} = 2$  represents a complete push of the stick. Figure 4.7 shows the two-dimensional relationship in terms of a color-coded mapping.

Upon entering the transition phase and keeping the left control inceptor right behind the notch, the aircraft will level out with respect to the kinematic airflow ( $\alpha_{\text{kin},d} = 0$ ) and start accelerating using the forward propulsion system. While approaching the stall speed  $V_{\text{stall}}$ , the target angle of attack converges to the margin stalling angle of attack  $\alpha_{\text{kin},d} = \alpha_{\text{stall},p}$  and the high power lift system is close to idle. While flying below the stall speed, pulling the left stick into the spring centered area will - in addition to setting the target airspeed to  $V_{\text{CAS},d} = 0$  - increase the angle of attack and support deceleration.

After exceeding the stall speed  $V_{\text{stall}}$ , the target angle of attack is fixed at the value of  $\alpha_{\text{kin},d} = \alpha_{\text{stall},p}$ . Hence, moving the left stick while flying above the stall speed will merely change the target airspeed and hence the commanded thrust but not lead to a change in angle of attack. This strategy supports defined aerodynamic lift conditions before entering the wingborne phase at an airspeed of  $V_{\text{stall},p}$  and avoids generation of excessive loads while the high power lift system is active.

Another measure to avoid excessive aerodynamic loads on the high power lift system is to limit the maximum airspeed during the transition phase. At its maximum forward position the left stick sets the target airspeed to  $V_{\text{CAS},d} = 1.x V_{\text{stall},p}$ , where  $x$  accounts for a desired airspeed margin to get wingborne in the presence of uncertainties. Upon entering the wingborne state full airspeed authority is regained.

Note that a discrete change of the maximum airspeed authority shall not lead to a sudden change in the command  $V_{\text{CAS},d}$ . Hence, the transition-free strategy to account for discrete changes in command authority from section 4.1 is proposed in the wingborne subsection for the left longitudinal control inceptor.

#### 4.2.2.2 Left Lateral Stick Channel During Transition Phase

The left lateral stick channel is mechanically locked above the detent notch. Hence, a constant target value of zero for the lateral body-fixed velocity  $V_{By}$  or specific force  $f_{By}$  is set during the transition and wingborne phase respectively. However, for the sake of completeness, a possible command mapping is introduced nonetheless, as another control inceptor concept might introduce the possibility to command this channel. Note, however, that due to the vertical take-off and landing capability, the need to introduce lateral sideslip conditions is very limited.

The requirement to stabilize the lateral body-fixed velocity during transition is aimed

at avoiding cross stream conditions while the high power lift system is active. If a (kinematic) sideslip angle  $\beta_{\text{kin}} \neq 0$  during transition is desired nonetheless, the target value for the lateral velocity is set to

$$V_{By,c} = \sin(\beta_{\text{kin},d})V_{\text{kin}}, \quad (4.21)$$

with  $V_{\text{kin}}$  being the kinematic absolute velocity.

#### 4.2.2.3 Right Longitudinal Stick Channel During Transition Phase

The right longitudinal stick channel behaves identically to the hover phase and is interpreted as a desired height rate  $\dot{h}_d$ . Possible limits in the flight envelope of the vertical channel like translational rates, accelerations, and jerks have to be considered due to higher dynamic pressures. However, the detailed derivation of how the behavior is ultimately realized is part of the Design Reference Model in section 4.3.

Note that active control of the kinematic angle of attack based on the left control inceptor position and airspeed leads to an induced pitch response upon commands in the vertical rate channel. Hence, deceleration of the VTOL aircraft can be supported through an additional climb demand, which leads to additional pitch up motion.

#### 4.2.2.4 Right Lateral Stick Channel During Transition Phase

Deflections in the right lateral stick channel during transition flight are interpreted as a desired heading rate  $\dot{\psi}_d$ . However, instead of being directly controlled like in hover mode, the heading rate is the result of a coordinated turn with a target roll angle  $\phi_c$ . In contrast to the hover phase, the coordination during the transition phase happens with respect to the body lateral velocity component  $V_{By}$  due to the requirement of avoiding lateral cross stream while the high power lift system is active.

Although the aircraft's reaction upon lateral deflections of the right control inceptor is very similar to the hover phase, the description of the underlying control mechanism is important in order to fully understand the behavior, also in the presence of disturbances. Compensating lateral velocity deviations by means of yawing rather than a change of lift direction (by rolling) represents a different control paradigm that exploits the fact that with increasing velocity the sensitivity of body-relative accelerations with respect to a change in orientation is increasing. Overall, this behavior is aimed at preserving the velocity direction with respect to earth (or with respect to the air) by rotating the aircraft into the airflow rather than aligning the velocity with the heading of the aircraft.

The derivation of the required target roll angle  $\phi_c$  for a desired heading rate  $\dot{\psi}_d$  follows from the constraint of zero lateral body-relative acceleration

$$\dot{V}_{By} = f_{By} + \sin(\phi) \cos(\theta)g - rV_{Bx} + pV_{Bz} \stackrel{!}{=} 0, \quad (4.22)$$

where  $f_{By}$  denotes the lateral specific force and  $V_{Bx}$  and  $V_{Bz}$  denote the forward and vertical velocity components in the body frame. The yaw rate  $r$  and roll rate  $p$  are

further expressed in terms of euler angle rates according to

$$r = -\sin(\phi)\dot{\theta} + \cos(\phi)\cos(\theta)\dot{\psi} \quad p = \dot{\phi} - \sin(\theta)\dot{\psi}. \quad (4.23)$$

During the stationary turn maneuver, the roll and pitch angle remain constant, i.e.  $\dot{\phi} = \dot{\theta} = 0$ , and the lateral specific force  $f_{By}$  is assumed to be zero due to turn coordination and the absence of lateral force capability of the system. In case of wind at higher dynamic pressures, the stabilization smoothly shifts from lateral velocity to a lateral loadfactor stabilization, which is described in more detail in section 4.3. The lateral body acceleration can furthermore be expressed as

$$\dot{V}_{By} = \sin(\phi)\cos(\theta)g - \cos(\phi)\cos(\theta)\dot{\psi}V_{Bx} - \sin(\theta)\dot{\psi}V_{Bz} = 0. \quad (4.24)$$

Using the trigonometric identity  $a\sin(\phi) + b\cos(\phi) = A\sin(\phi + x)$  with  $A = \sqrt{a^2 + b^2}$  and  $x = \sin^{-1}\left(\frac{b}{A}\right)$ , it follows

$$A\sin(\phi + x) = \sin(\theta)\dot{\psi}V_{Bz}, \quad (4.25)$$

with  $A = \cos(\theta)\sqrt{g^2 + \dot{\psi}^2 V_{Bx}^2}$  and  $x = \sin^{-1}\left(\frac{-\dot{\psi}V_{Bx}}{\sqrt{g^2 + \dot{\psi}^2 V_{Bx}^2}}\right)$ .

Therefore, the required roll angle  $\phi_c$  that leads to a desired heading rate  $\dot{\psi}_d$  under the given assumptions yields

$$\phi_c = \sin^{-1}\left(\frac{\tan(\theta)\dot{\psi}_d V_{Bz}}{\sqrt{g^2 + \dot{\psi}_d^2 V_{Bx}^2}}\right) - \sin^{-1}\left(\frac{-\dot{\psi}_d V_{Bx}}{\sqrt{g^2 + \dot{\psi}_d^2 V_{Bx}^2}}\right). \quad (4.26)$$

Note that due to the choice of formulating the constraint in terms of the body-fixed lateral direction, the required roll angle follows from a quasi-kinematic relationship and hence only considers the necessary rotation to compensate for the gravity-induced lateral acceleration.

The maximum feasible heading rate  $\dot{\psi}_d$  under the constraint (4.24) is derived by considering the minimum required vertical acceleration performance  $\ddot{h}_{\text{req}}$  and the available maximum specific lift force  $f_{\text{max}} = -f_{zB,\text{min}} > 0$ . For small pitch angles, it follows from vertical force equilibrium (4.13) that

$$\cos(\phi) = \frac{(g + \ddot{h}_{\text{req}})}{f_{\text{max}}}, \quad (4.27)$$

which yields the maximum roll angle during a turn, for which the minimum required vertical acceleration  $\ddot{h}_{\text{req}}$  is reached at maximum lift force.

Inserting (4.27) into (4.24) yields the maximum feasible heading rate

$$\dot{\psi}_{\text{abs,max}} = \frac{g}{g + \ddot{h}_{\text{req}}} \frac{1}{V_{Bx}} \sqrt{f_{\text{max}}^2 - (\ddot{h}_{\text{req}} + g)^2}, \quad (4.28)$$

which is different than the maximum feasible heading rate from (4.15) for  $\ddot{h}_{\text{req}} \neq 0$ . Therefore, the stick mapping for the desired heading rate and consequently for the target roll angle has to account for the change in envelope limits when switching to the transition phase. This can either be achieved by choosing the minimum upper bound from (4.15) and (4.28) for both phases or using the approach introduced in the following wingborne section which enables transition free discrete changes in command authority.

### 4.2.3 High Velocity Operation: Wingborne

The transition into the wingborne phase is coupled to various conditions that will be discussed in detail in chapter 5. In general, the switch into the wingborne phase is initiated when sufficient aerodynamic lift can be provided and the left control inceptor is located behind the detent notch. The powered lift system is subsequently deactivated. Similarly, the re-transition is initiated when the left control inceptor is pulled below the detent notch and the airspeed is sufficiently low.

The command concept for the wingborne mode is targeted at extending the transition phase into high velocity operation. The role of airspeed changes from merely being an independent target variable to becoming a crucial resource for the generation of necessary aerodynamic moments and forces. Therefore, the role of envelope protections becomes particularly important and influences the overall behavioral concept during the wingborne phase.

A thorough description of the control inceptor deflection to aircraft response is given in the following.

#### 4.2.3.1 Left Longitudinal Stick Channel During Wingborne Phase

Identically to the transition phase, deflections of the left control inceptor during the wingborne phase are interpreted as target indicated airspeed  $V_{\text{CAS},d}$ . Figure 4.8 gives an overview of the target airspeed values over the stick range. Just as in the transition phase, the target command at the lower end of the thrust lever region corresponds to the margin stall speed  $V_{\text{CAS},d} = V_{\text{stall,p}}$ . Below the notch the target airspeed decreases to the stall speed  $V_{\text{CAS},d} = V_{\text{stall}}$ .

As already mentioned in subsection 4.2.2, switching to the wingborne mode comes along with a change in maximum command authority for the airspeed, which is limited during the transition phase due to structural integrity of the aircraft and the activated powered lift system. Maximum airspeed authority is completely available upon the mode switch and a full stick deflection corresponds to the maximum airspeed command  $V_{\text{CAS},d} = V_{\text{NO}}$  in the wingborne mode. During substantial climb maneuvers, airspeed is traded in for rate of climb, which is discussed in detail within the subsection for the right longitudinal stick channel.

If not properly accounted for, the airspeed command might be subject to a discon-



tinuous change in the moment of engaging the wingborne mode dependent on the stick position. Similar problems arise due to the change in the lower airspeed limit upon switching from wingborne mode back to the transition mode or for any other discrete change in command variables and their limits, as was mentioned for the lateral stick channel of the right stick in the transition phase.

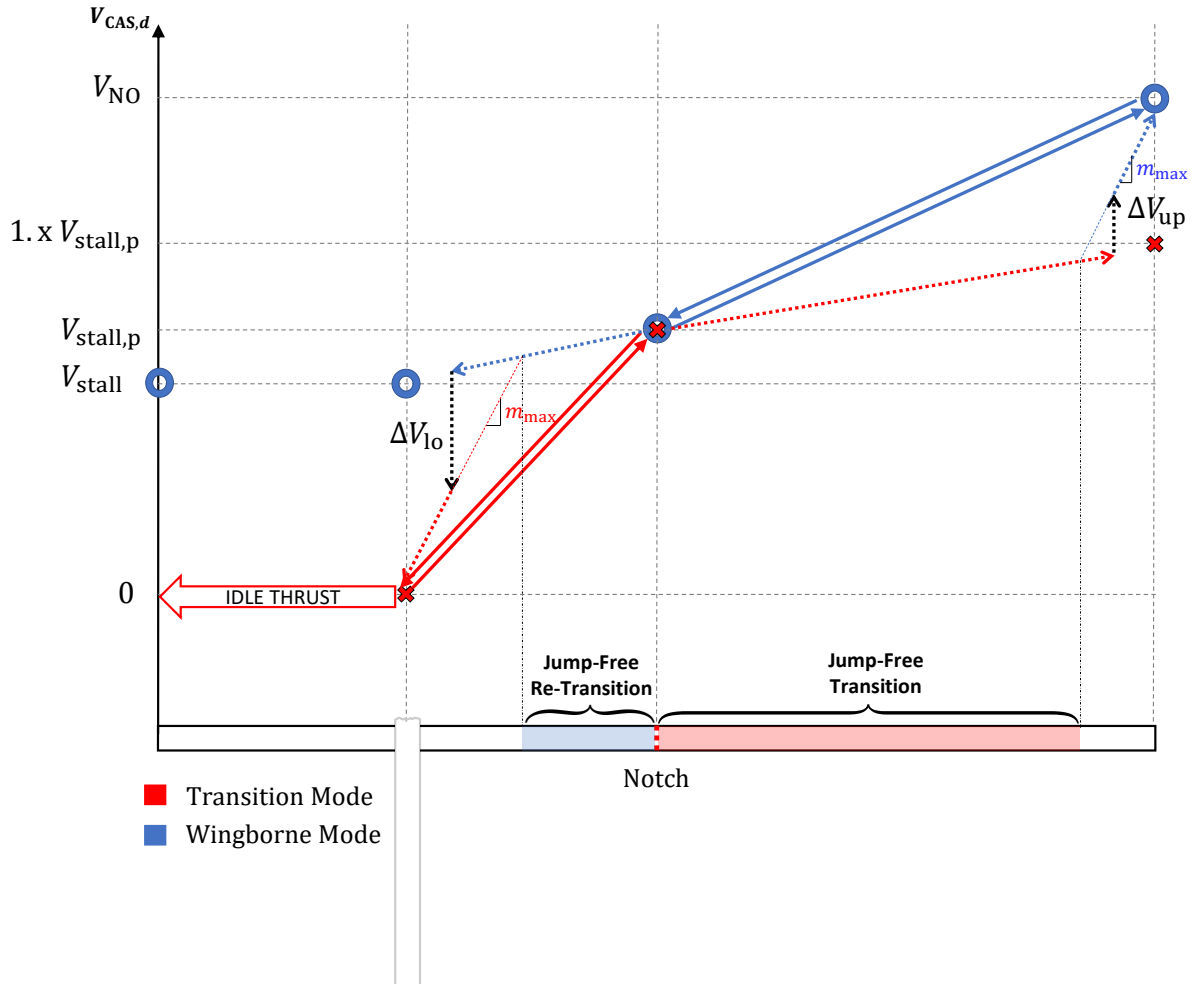


**Figure 4.8:** Overview of Left Control Inceptor Mapping for Transition Mode (red) and Wingborne Mode (blue)

Section 4.1 introduced the continuity-based stick mapping and applied it to the mode switch from the transition mode to the wingborne mode. The novel input-output mapping ensures that the command output (e.g. the airspeed command) is not subject to a discontinuous jump upon changing the command output limits during the discrete mode switch.

For the re-transition from the wingborne mode back to the transition mode, the stick has to be located before the notch and an analogous mapping strategy can be applied as in section 4.1. Furthermore, the stick limits are adapted to the upper part of the spring-centered region of the stick and yield  $d_{min} = d_{TS,x, \text{spring-center}} = 0$  and  $d_{max} = d_{TS,x, \text{notch}} = 1$ .

Note that if the stick is located at the spring center or below, the forward thrust system will be commanded to idle thrust upon switching back to the transition mode.

Figure 4.8 shows an overview of the left control inceptor mapping for both the transition and the wingborne phase. The red crosses represent the target airspeed values for the transition phase, as is also shown in figure 4.7. The blue circles represent the target airspeed values during the wingborne phase. Note that below the notch the commanded airspeed during the wingborne mode drops to the stall speed  $V_{CAS,d} = V_{stall}$  in order to initiate the re-transition.

The solid arrows on the right and left side of the notch level in figure 4.8 represent an exemplary stick path, where the transition and re-transition happen right behind and before the notch respectively, which represents the special case for which the left-sided and right-sided gradients remain constant throughout the stick movement and the mapping reduces to a straight line in both directions, just as in case a) of figure 4.1.

The dotted line on the right side of the notch represents the stick path from figure 4.1 case c), where the switch into the wingborne mode happens outside the stick range, for which a jump-free transition can be achieved. The stick range for a jump-free transition is shaded in red in figure 4.8 and results from simple geometric construction by projecting the point onto the stick axis from which the maximum command of the wingborne mode  $V_{NO}$  would be reached in the transition mode with the maximum gradient  $m_{max}$ .

The dotted line on the left side of the notch represents a switch from the wingborne mode into the transition mode outside the stick range for a jump-free re-transition. Since pulling the stick below the notch is only a necessary but not sufficient condition for the re-transition, the switch from the wingborne mode into the transition mode can be initiated at any stick position below the notch. The gradient protecting increment  $\Delta V_{io}$  is added, such as to preserve the maximum allowed gradient  $m_{max}$  towards the new minimum airspeed limit  $V_{min} = 0$  in the transition phase. Analogously to the switch into the wingborne mode, the stick range enabling jump-free re-transition is shaded in blue and results from projecting the point onto the stick axis from which the minimum command of the transition mode  $V_{min} = 0$  would be reached in the wingborne mode with the maximum gradient  $m_{max}$ .

Note that in the given context a violation of the lower stick gradient  $m_{min}$  cannot occur due to the conditioning of the mode switches on the relative notch position and the separation of the mapping below and above the notch. However, for the sake of completeness, it is still included in the proposed mapping strategy.

The proposed stick mapping provides intuitive control of the VTOL aircraft in the given flight modes by taking into account envelope protections and enables a smooth transition to and re-transition from the wingborne phase at any given situation.

The main disadvantage of the mapping is that a given stick position does not correspond to a fixed target velocity command, which might be desirable during the wingborne phase. An alternative strategy could combine the jump-free characteristics for the first

half of the throttle area with a fixed stick to velocity mapping in the upper part of the stick area. This approach would considerably reduce the stick area for which a jump-free transition can be achieved, however, it would provide a constant stick mapping in the upper throttle stick area (which could potentially be marked-off by a second notch), such that the operator can command a fixed airspeed by placing the stick within the designated upper stick area.

#### 4.2.3.2 Left Lateral Stick Channel During Wingborne Phase

During wingborne flight, the lateral body-fixed specific force  $f_{By}$  is controlled, which is motivated by lateral aerodynamic forces encountered during sideslip conditions. As was already mentioned in subsection 4.2.2, the left lateral stick channel is mechanically locked above the detent notch. However, for the sake of completeness, a possible command mapping is introduced nonetheless. Deflections in this channel are interpreted as a desired lateral body-fixed load factor  $n_{By,d}$  or aerodynamic sideslip angle  $\beta_{aer,d}$  and are controlled by setting the target specific force to

$$f_{By,c} = n_{By,d}g = C_{fy,\beta}V_{CAS}^2\beta_{aer,d}, \quad (4.29)$$

with  $V_{CAS}$  denoting the calibrated airspeed and  $C_{fy,\beta}$  summarizing the effects of mass, aerodynamic coefficients, and reference surface area for the lateral channel.

Note that in the case of a constant zero-command in this channel, aerodynamic turn coordination results at all times.

#### 4.2.3.3 Right Longitudinal Stick Channel During Wingborne Phase

Pulling or pushing the right stick commands a climb or sink rate  $\dot{h}_d$  respectively, just as for the transition and wingborne phase. The limits for the climb rate are governed by the available excess power of the transition aircraft at the given airspeed and altitude. It is of crucial importance to take into account the aircraft's propulsion power limit, since the command and control of excessive climb rates would lead to a rapid decrease of airspeed and hence to a possible stall condition or unanticipated re-transition and activation of the high-power lift system.

Both the airspeed and climb capability are ultimately governed by the available thrust and power characteristics of the system and hence cannot be controlled independently towards the border of the flight envelope. Figure 4.9 shows the qualitative relationship between airspeed and achievable maximum climb rate for propeller-driven aircraft. The underlying available propulsion power of the aircraft is assumed to be approximately constant over the airspeed.

For very low and high airspeeds, climb performance deteriorates due to the dominating presence of induced and parasitic drag respectively. The overall maximum climb rate  $\dot{h}_{max}$  is achieved at an airspeed of  $V_y$ , at which maximum excess power is available.

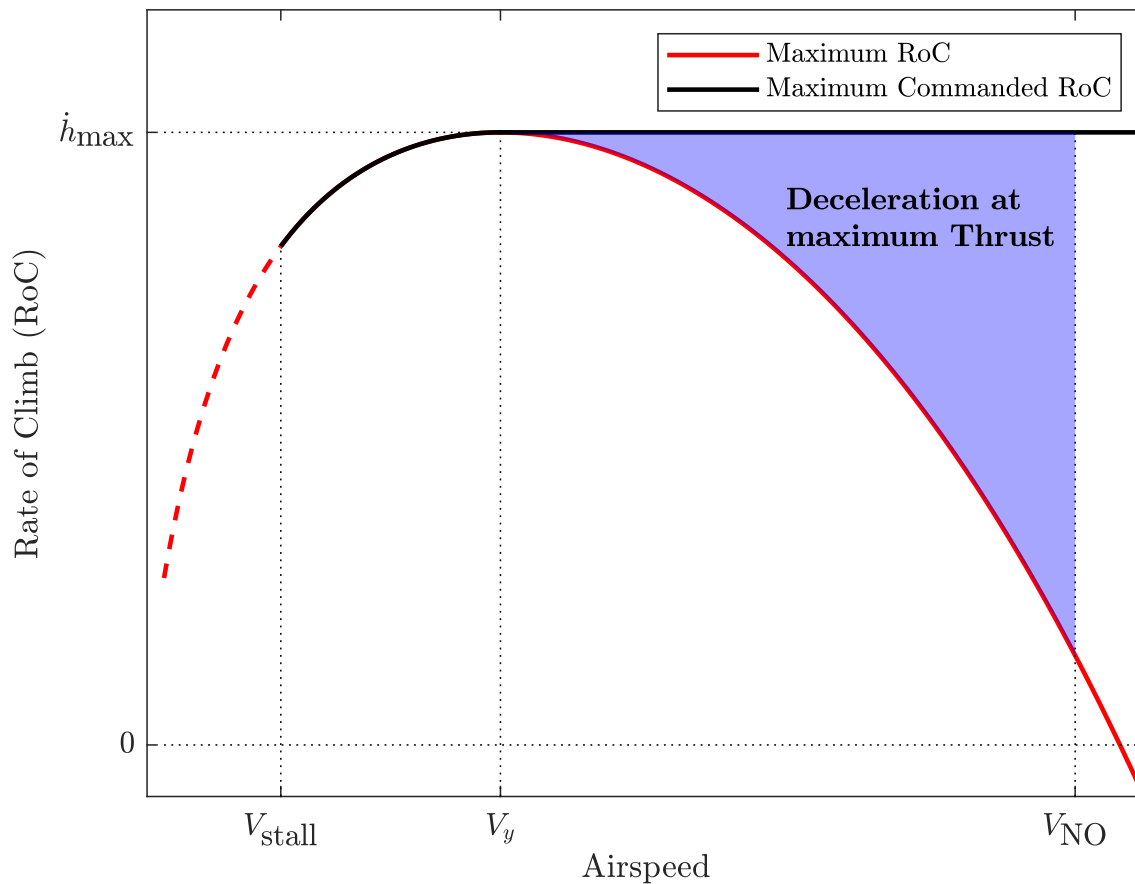


**Figure 4.9:** *Rate of Climb for Different Airspeeds*

For airspeeds lower than  $V_y$ , pulling the right control inceptor commands climb rates up to the maximum achievable climb rate at the current airspeed, as is indicated by the black line in 4.9, which shows the commanded rate of climb for a maximum pull of the right stick. The target airspeed is held through auto thrust during the climb maneuver.

After exceeding the optimal climb speed  $V_y$ , the maximum climb rate that can be commanded by a complete pull of the right stick is fixed at  $\dot{h}_{\max}$  and therefore exceeds the maximum vertical rate at which the aircraft can climb while keeping the airspeed constant.

Consequently, during a complete pull of the right control inceptor at an airspeed above  $V_y$ , the aircraft will initially start climbing while holding the airspeed constant up until the climb rate crosses the red curve in figure 4.9. At that point auto thrust will yield the maximum propulsion in order to track the target airspeed. The aircraft will then continue climbing with maximum thrust while decelerating until it reaches the optimal climb speed  $V_y$  and corresponding climb rate  $\dot{h}_{\max}$ . In this manner the transition aircraft always yields the absolute maximum climb rate  $\dot{h}_{\max}$  when fully pulling the right stick at airspeeds greater or equal to  $V_y$ .

The demand in climb rate is actively protected by considering the deceleration margin towards the airspeed given by  $V_{\text{prot}} = \min(V_{\text{CAS},d}, V_y)$  at maximum thrust condition. Given the total Energy of the system  $E = \frac{1}{2}mV^2 + mgh$ , the energy rate at full thrust yields

$$\dot{E} = mV\dot{V} + mgh\dot{h} = (\cos(\alpha)T_{\text{max}} - D)V, \quad (4.30)$$

with the aircraft's mass  $m$ , angle of attack  $\alpha$ , maximum thrust force  $T_{\text{max}}$ , and the drag  $D$ .

Considering (4.30), the commanded climb rate in wingborne flight is protected at any time by

$$\dot{h}_d \leq \frac{V}{g} \left( \underbrace{\frac{\cos(\alpha)T_{\text{max}} - D}{m}}_{\text{Specific Excess Thrust in Velocity Direction}} - \dot{V}_{\text{prot}} \right), \quad (4.31)$$

where

$$\dot{V}_{\text{prot}} = K_V (V_{\text{prot}} - V) \quad (4.32)$$

denotes the deceleration margin towards the protected airspeed in terms of a first order relationship with the time constant  $\frac{1}{K_V}$ .

Since the drag force in (4.31) cannot be measured directly, the estimation of the specific excess thrust in the velocity direction is later on estimated using inertial measurements and the remaining thrust capability of the system.

In order to command a sink rate, the right control inceptor is pushed forward. The maximum sink rate is only limited by avoiding over-speed conditions, which can occur if the system continues to gain speed while the thrust is already at an idle value.

During all flight phases from hover throughout the transition until the wingborne mode, the vertical channel is decoupled from the lateral channel through automatic attitude compensation during bank-to-turn maneuvers. Upon releasing the right stick, the current altitude is actively held by means of height hold functionality.

#### 4.2.3.4 Right Lateral Stick Channel During Wingborne Phase

The response to lateral deflections of the right control inceptor is identical to the transition phase and yields a desired heading rate  $\dot{\psi}_d$ , which results from a coordinated turn with the target roll angle  $\phi_c$  from (4.26). As was already mentioned in subsection 4.2.2, the limit of the achievable heading rate during a coordinated turn under the constraint of zero lateral body-relative acceleration  $\dot{V}_{By} = 0$  was given in (4.28) and depends on the required vertical acceleration capability  $\ddot{h}_{\text{req}}$  and maximum available specific lift force  $f_{\text{max}} = -f_{zB,\text{min}} > 0$  of the system.

During low speed operation, the available lift capability of the VTOL aircraft is approximately constant, as the required force is produced with the high-power lift system and is mostly independent of the current velocity. However, the maximum specific lift

force capability during the wingborne phase is directly dependent on the current airspeed  $V$  and air density  $\rho$  and is given by

$$f_{\max}(V) = \frac{1}{2m} \rho V^2 S C_{L,\max}, \quad (4.33)$$

with the aircraft's mass  $m$ , reference wing area  $S$ , and its maximum lift coefficient  $C_{L,\max}$ . Note that by definition the maximum lift force for  $V = V_{\text{stall}}$  is equal to the aircraft's weight and therefore

$$f_{\max}(V_{\text{stall}}) = g. \quad (4.34)$$

Hence, according to (4.28) the aircraft's lift capability upon entering the wingborne phase does not allow for any turn maneuver with  $\ddot{h} \geq 0$ . In order to still enable lateral controllability, the required vertical acceleration margin  $\ddot{h}_{\text{req}}$  is therefore traded in for a minimum heading rate capability  $\dot{\psi}_{\text{abs,min}}$ . As a consequence, a full lateral deflection of the right control inceptor during horizontal flight at airspeeds close to the stall speed will initiate a turn maneuver that leads to a desired heading rate of  $\dot{\psi}_d = \dot{\psi}_{\text{abs,min}}$  while yielding a (initial) sinking acceleration of

$$\ddot{h} = f_{\max} \cos(\phi_c) - g, \quad (4.35)$$

with  $\phi_c(\dot{\psi}_d)$  from (4.26).

This behavior prioritizes the lateral controllability over the vertical authority of holding the current altitude and hence allows for lateral flight path changes during low speed wingborne operation in order to avoid obstacles. As the aircraft's lift capability is increasing with growing airspeed  $V_{\text{CAS}}$ , lateral authority is adapted according to

$$\dot{\psi}_{\text{abs,max}} = \begin{cases} \dot{\psi}_{\text{abs,min}}, & \text{for } V_{\text{CAS}} < V_{\text{stall}} \sqrt{\frac{\ddot{h}_{\text{req}} + g}{g}}, \\ \max(\dot{\psi}_{\text{abs,min}}, \dot{\psi}_{\text{abs,max,raw}}), & \text{for } V_{\text{CAS}} \geq V_{\text{stall}} \sqrt{\frac{\ddot{h}_{\text{req}} + g}{g}}, \end{cases} \quad (4.36)$$

with the unprotected heading rate limit

$$\dot{\psi}_{\text{abs,max,raw}} = \frac{g}{g + \ddot{h}_{\text{req}}} \frac{1}{V_{Bx}} \sqrt{g^2 \frac{V_{\text{CAS}}^4}{V_{\text{stall}}^4} - (\ddot{h}_{\text{req}} + g)^2}, \quad (4.37)$$

which follows from (4.28) with  $f_{\max} = g \frac{V_{\text{CAS}}^2}{V_{\text{stall}}^2}$ .

Essentially, (4.36) sets the absolute command limit for the desired heading rate  $\dot{\psi}_d$  to the minimum heading rate  $\dot{\psi}_{\text{abs,min}}$  until the aircraft reaches enough airspeed such as to support the minimum heading rate  $\dot{\psi}_{\text{abs,min}}$  while yielding the minimum vertical acceleration capability  $\ddot{h}_{\text{req}} > 0$ . From that airspeed on, the absolute maximum heading rate  $\dot{\psi}_{\text{abs,max}}$  is governed by (4.37) and is approximately increasing linearly with growing airspeed.

In order to account for the discontinuous change in the target heading rate limit during the mode switch from transition flight into the wingborne phase, the same concept of jump-free command mapping can be applied as was introduced for the airspeed mapping in the wingborne section.

### 4.3 Design Reference Model

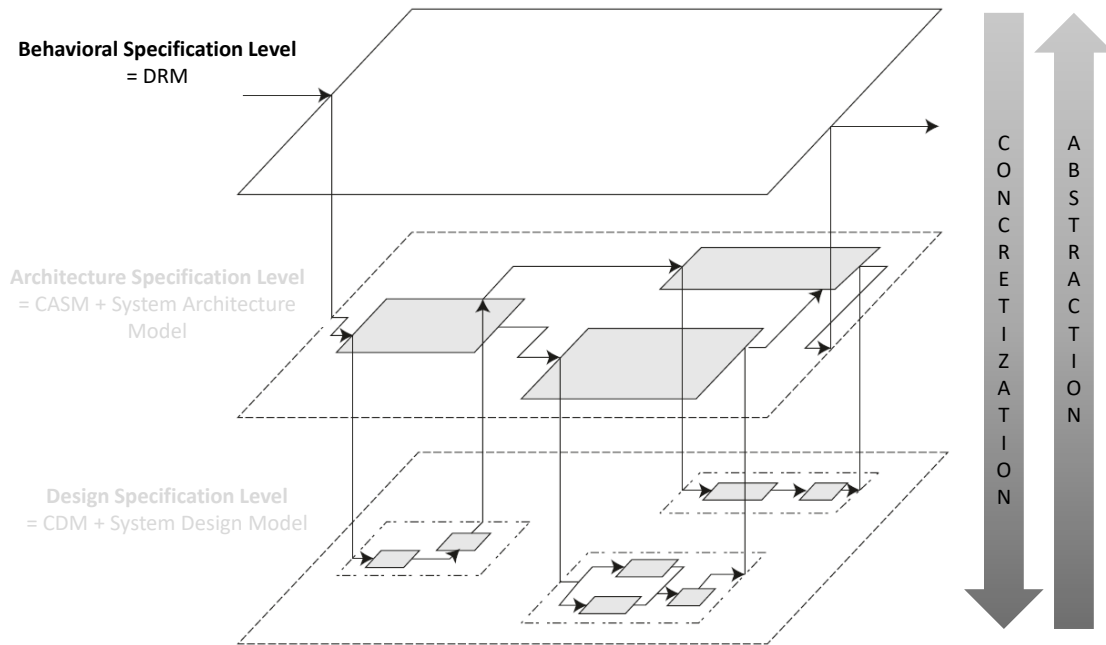


**Figure 4.10:** *Design Reference Model (DRM) as Highest Abstraction Level of Closed-Loop System (figure adapted from [3])*

The *Design Reference Model* (DRM) is a physically motivated specification of the closed-loop system behavior as a response to pilot inputs and disturbances. It thereby represents the aircraft behavior in terms of a system-architecture-agnostic rigid-body simulation model, which considers the kinetic characteristics and constraints of the system, such as propulsion and lift characteristics, aerodynamic properties, mass, and Inertia.

The DRM enables simulation of the system’s motion very early in the development process and hence facilitates validation of the vehicle response to pilot inputs and disturbances as well as validation of the overall kinetic capabilities of the system through pilot-in-the-loop simulation of virtual missions. It furthermore enables verification of the target behavior against existing handling quality requirements like stated in [12], [39], and [40] or other applicable requirements and represents **contribution C.2** of this thesis.

Note, however, that existing requirements regarding the behavior and handling of rotorcraft and fixed-wing aircraft are not necessarily applicable to VTOL transition aircraft one-to-one. An example has been mentioned in section 4.2 regarding the heading rate requirements during lateral gusts in hover flight, which are stated in [12] assuming typical rotorcraft configurations with a tail rotor. For transition aircraft, which typically have rudder surfaces or similar structures for lateral control during wingborne flight, the same requirements might be harder if not impossible to meet due to the increased sensitivity to wind and gusts.

In general, a new type of aircraft will yield new types of behavior and will hence require new methods and requirements for flying quality assessment. The European Union Aviation Safety Agency (EASA) has recently released the Proposed Means of Compliance with the Special Condition VTOL [41] [33]. Therein the (modified) method of Minimum Acceptable Handling Qualities Rating (MHQRM) is presented, which serves as an accepted means of compliance and uses the already introduced concept of Mission Task Elements (MTE) [12] as a validation basis. As mentioned in [33], possible validation activities include testing of the flight control functions in offline/piloted simulation.

The Design Reference Model represents the aircraft's behavior on the highest abstraction level and yields the final flight control functionality in a system-architecture-agnostic manner. It therefore serves as very effective tool for early validation of a proposed VTOL concept.

In order for the DRM to yield physically feasible behavior in the context of the proposed Simplified Vehicle Operations, the emphasis lies in simulating the aircraft's motion based on its underlying kinetic constraints and existing physical laws.

Consequently, the Design Reference Model is based on rigid-body simulation resulting in the translational and rotational dynamics of the system as a response to acting forces and moments.

Even though the detailed architecture of the control law is derived and specified later on in chapter 5, the DRM is based on a control-theoretic approach in order to yield the desired behavior according to the SVO that was specified in detail in section 4.2. The main differences with respect to the Control Architecture Specification Model (CASM), which is part of the next lower concretization level, are:

- Within the DRM the generation of forces and moments resulting from the system's control effectors (e.g. motors of the powered lift system, traction system, control surfaces, or other force and moment producers) are abstracted in terms of nonlinear transfer functions, which account for the bandwidth, rate limits, and absolute limits with which forces and moments can be produced by the aircraft. Within the later introduced control architecture this corresponds to the control allocation function, which distributes the force and moment demand among the available control effectors. The resulting forces and moments then result as a consequence of the modeled behavior of the control effectors in the overall context of the plant, in contrast to the DRM, where the plant is an inherent part of the model itself and hence represents the overall system in a more integrated and abstract way.
- All signals regarding the system's states are known and all of them can be used within the DRM in order to generate the aircraft motion. Since the Design Reference Model is mainly targeted at validating the aircraft's kinetic capabilities and the resulting behavior, consideration of which signals can actually be known in the context of a control architecture is not necessary. Note that within the later introduced Control Architecture Specification Model (CASM) care must be taken to not



yield a control architecture that requires inherently unknowable signals based on the assumed availability of sensors. The detailed description of the CASM and its distinction to the lowest concretization level - the Control Design Model (CDM) - follows in chapter 5.

- The DRM does not have to include any filters in the feedback path of its control structure. In contrast to the CASM, which has to account for and represent the characteristics of feedback signals, the DRM yields a simplified cascaded structure, which can use direct state feedback of the underlying system motion. Hence, modeling the behavior of notch filters or complementary filters in the feedback path is not necessary.

In order to generate the proposed behavior described in section 4.2, the necessary control signals in the hover, transition, and wingborne phase are derived in the following. The derivation is based on a cascaded nonlinear dynamic inversion approach and serves as the basis for the INDI control structure in chapter 5.

An overview of the DRM control structure is given in figure 4.11. The DRM is subsequently used in section 4.4 for verification and validation activities through simulation of the executable model.

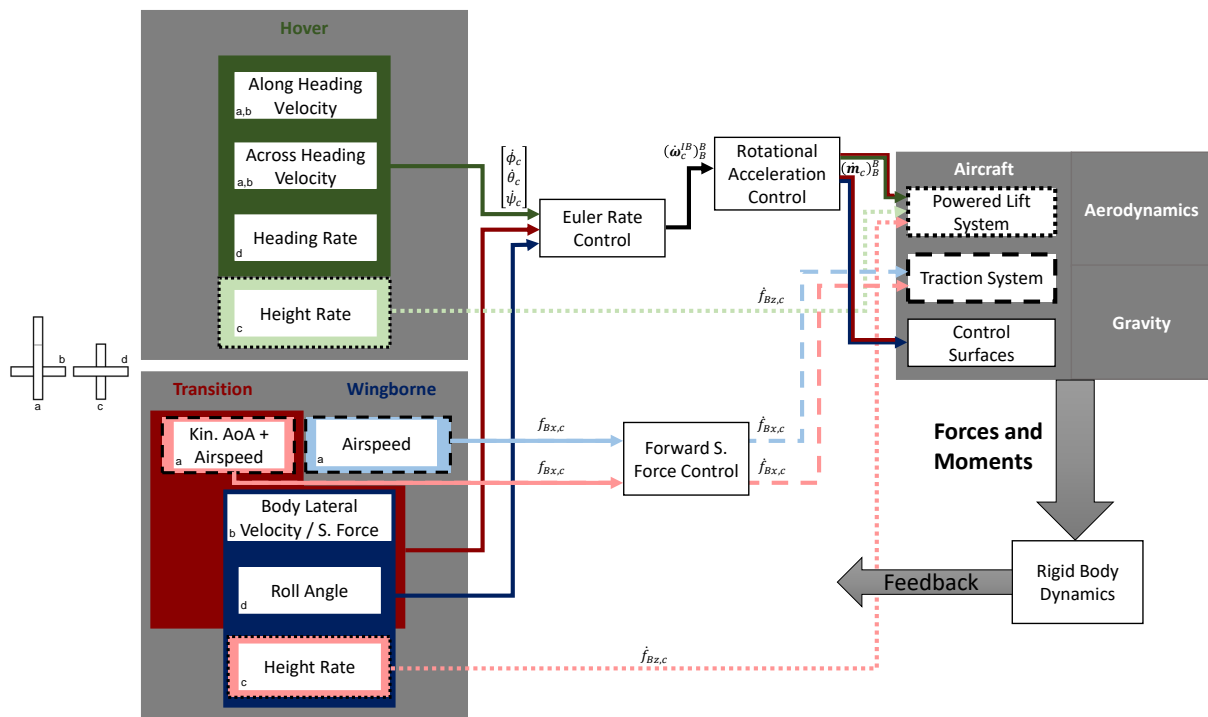


Figure 4.11: Control Structure of DRM

### 4.3.1 Outer Loop Control for Hover Phase

The target control variables of the outer loop during the hover phase are the kinematic velocity of the VTOL aircraft's center of gravity with respect to the earth surface denoted in the control frame (figure 4.4)  $(\mathbf{V})_C = [V_{Cx} \ V_{Cy} \ V_{Cz}]_C^T$  and the heading rate  $\dot{\psi}$ . The output (pseudo) control commands for the outer loop are given by the commanded euler angle rates  $\dot{\epsilon}_c = [\dot{\phi}_c \ \dot{\theta}_c \ \dot{\psi}_c]^T$  and the commanded body-vertical specific force rate  $\dot{f}_{Bz,c}$ .

The outer loop is aimed at yielding the desired second order velocity dynamics

$$(\ddot{\mathbf{V}})_C^{CC} = \mathbf{K}_{\dot{\mathbf{V}}} \left( (\dot{\mathbf{V}}_c)_C^C - (\dot{\mathbf{V}})_C^C \right), \quad (4.38)$$

with

$$(\dot{\mathbf{V}}_c)_C^C = \mathbf{K}_V \left( (\mathbf{V}_c)_C - (\mathbf{V})_C \right), \quad (4.39)$$

where  $(\mathbf{V}_c)_C$  is the commanded velocity in the control frame and  $\mathbf{K}_{\dot{\mathbf{V}}} = \text{diag}(2\omega_x d_x, 2\omega_y d_y, 2\omega_z d_z)$  and  $\mathbf{K}_V = \text{diag}\left(\frac{\omega_x}{2d_x}, \frac{\omega_y}{2d_y}, \frac{\omega_z}{2d_z}\right)$  denote the desired gains to yield a natural frequency  $\omega$  and relative damping  $d$  for each channel.

The translational acceleration  $(\ddot{\mathbf{V}})_C^C$  and jerk  $(\dot{\ddot{\mathbf{V}}})_C^{CC}$  in (4.38) are both derived with respect to the control frame and yield

$$(\dot{\mathbf{V}})_C^C = \left( \frac{d\mathbf{V}}{dt} \right)_C^C = (\mathbf{f})_C + (\mathbf{g})_C - \begin{bmatrix} 0 \\ 0 \\ \dot{\psi} \end{bmatrix}_C \times (\mathbf{V})_C \quad (4.40)$$

and

$$(\dot{\ddot{\mathbf{V}}})_C^{CC} = \left( \frac{d^2\mathbf{V}}{dt^2} \right)_C^{CC} = (\dot{\mathbf{f}})_C^C - \begin{bmatrix} 0 \\ 0 \\ \ddot{\psi} \end{bmatrix}_C \times (\mathbf{V})_C - \begin{bmatrix} 0 \\ 0 \\ \dot{\psi} \end{bmatrix}_C \times (\dot{\mathbf{V}})_C^C, \quad (4.41)$$

with the gravitational acceleration  $(\mathbf{g})_C$ , specific force  $(\mathbf{f})_C$ , and specific force rate  $(\dot{\mathbf{f}})_C^C$  denoted in the control frame.

Two variants for the forward control of the VTOL aircraft are presented here, distinguished by the use of the traction system in the hover phase. In the first variant the traction system is not used during hover and the VTOL aircraft only uses the powered lift system for maneuvering. Hence, the specific force of the system denoted in the control frame is given by

$$(\mathbf{f})_C = \mathbf{M}_{CB} \begin{bmatrix} 0 \\ 0 \\ f_{Bz} \end{bmatrix}_B = \begin{bmatrix} \cos(\phi) \sin(\theta) f_{Bz} \\ -\sin(\phi) f_{Bz} \\ \cos(\phi) \cos(\theta) f_{Bz} \end{bmatrix}_C, \quad (4.42)$$

with the specific force in body z direction  $f_{Bz}$  resulting from the powered lift system while neglecting other aerodynamic forces.

The corresponding rotation matrix  $\mathbf{M}_{CB}$ , which transforms a vector from the body frame into the control frame, is given by

$$\mathbf{M}_{CB} = \begin{bmatrix} \cos(\theta) & \sin(\phi) \sin(\theta) & \cos(\phi) \sin(\theta) \\ 0 & \cos(\phi) & -\sin(\phi) \\ -\sin(\theta) & \sin(\phi) \cos(\theta) & \cos(\phi) \cos(\theta) \end{bmatrix}, \quad (4.43)$$

with the roll angle  $\phi$  and pitch angle  $\theta$  of the system.

Furthermore, taking the time derivative of (4.42) yields the specific force rate denoted in the control frame

$$(\dot{\mathbf{f}})_C^C = \begin{bmatrix} -\sin(\phi) \sin(\theta) f_{Bz} & \cos(\phi) \cos(\theta) f_{Bz} & \cos(\phi) \sin(\theta) \\ -\cos(\phi) f_{Bz} & 0 & -\sin(\phi) \\ -\sin(\phi) \cos(\theta) f_{Bz} & -\cos(\phi) \sin(\theta) f_{Bz} & \cos(\phi) \cos(\theta) \end{bmatrix} \begin{bmatrix} \dot{\phi} \\ \dot{\theta} \\ \dot{f}_{Bz} \end{bmatrix}, \quad (4.44)$$

which is a function of the roll angle rate  $\dot{\phi}$ , pitch angle rate  $\dot{\theta}$ , and the body-vertical specific force rate  $\dot{f}_{Bz}$ .

Note that  $\dot{f}_{Bz}$  yields a much higher bandwidth than the euler angle rates  $\dot{\phi}$  and  $\dot{\theta}$ , since it is directly influenced by the high power lift system instead of being the result of the angular rotation of the whole aircraft. Hence, instead of inverting (4.44) to yield the desired pseudo control vector, the vertical velocity channel is chosen to be controlled separately and independently from the horizontal velocity channel, which is motivated by time-scale separation of the powered lift system dynamics and the aircraft's rigid body dynamics.

#### 4.3.1.1 Vertical Velocity Control

The desired body-vertical specific force rate  $\dot{f}_{Bz,d}$  follows from considering the z direction of (4.44), (4.41), (4.38), (4.39), and (4.40) and yields

$$\dot{f}_{Bz,d} = \underbrace{\tan(\phi) f_{Bz} \dot{\phi} + \tan(\theta) f_{Bz} \dot{\theta}}_{\substack{\text{Dynamic Inversion} \\ = \text{Attitude Rate Compensation}}} + \frac{2\omega_z d_z}{\cos(\phi) \cos(\theta)} (\dot{V}_{Cz,c} - \dot{V}_{Cz}), \quad (4.45)$$

with

$$\dot{V}_{Cz,c} = \frac{\omega_z}{2d_z} (V_{Cz,c} - V_{Cz}), \quad (4.46)$$

where  $V_{Cz,c} = -\dot{h}_c$  and  $V_{Cz} = -\dot{h}$  denote the commanded and fed back vertical rate,  $\dot{V}_{Cz} = f_{Cz} - g$  is the vertical acceleration,  $g$  is the gravitational acceleration, and  $\omega_z$  and  $d_z$  are the desired frequency and relative damping of the vertical rate dynamics.

In order to account for the rate and absolute limits of the powered lift system's force characteristics, (4.46) and (4.45) are saturated appropriately. Consideration of control effector limitations on the gain and saturation parameters of the control loop are discussed in section 5.2. In general, the overall body-vertical specific force rate command yields

$$\dot{f}_{Bz,c} = \max \left( \dot{f}_{Bz,\min}, \min \left( \dot{f}_{Bz,\max}, \dot{f}_{Bz,d} \right) \right), \quad (4.47)$$

where

$$\dot{f}_{Bz,\min} = \max\left(\dot{f}_{Bz,\min,\text{total}}, K_{f,\text{prot}}(f_{Bz,\min} - f_{Bz})\right) \quad (4.48)$$

and

$$\dot{f}_{Bz,\max} = \min\left(\dot{f}_{Bz,\max,\text{total}}, K_{f,\text{prot}}(f_{Bz,\max} - f_{Bz})\right) \quad (4.49)$$

define the specific force rate limits. The protections  $\dot{f}_{Bz,\min,\text{total}}$  and  $\dot{f}_{Bz,\max,\text{total}}$  in (4.48) and (4.49) represent the total specific force rate limits of the powered lift system, which mainly result from current limitations of the electric motors, as is also mentioned in section 5.2. Furthermore, the gain  $K_{f,\text{prot}}$  defines the convergence rate of the specific force towards the lower and upper limit  $f_{Bz,\min}$  and  $f_{Bz,\max}$  respectively.

### 4.3.1.2 Across-Heading Velocity Control

The lateral (across-heading) velocity is controlled with a desired roll angle rate, which follows from inversion of the lateral velocity dynamics in (4.44), (4.41), (4.38), (4.39), and (4.40) and yields

$$\dot{\phi}_d = \underbrace{-\frac{\tan(\phi)}{f_{Bz}} \dot{f}_{Bz,c} - \frac{\ddot{\psi}_{\text{lead}} V_{Cx} + \dot{\psi} \dot{V}_{Cx}}{\cos(\phi) f_{Bz}}}_{\substack{\text{Dynamic Inversion} \\ = \text{Climb and Turn Compensation}}} - \frac{2\omega_y d_y}{\cos(\phi) f_{Bz}} (\dot{V}_{Cy,c} - \dot{V}_{Cy}), \quad (4.50)$$

with

$$\dot{V}_{Cy,c} = \frac{\omega_y}{2d_y} (V_{Cy,c} - V_{Cy}), \quad (4.51)$$

where  $V_{Cy,c}$  and  $V_{Cy}$  denote the commanded and fed back lateral (across-heading) velocity,  $\dot{V}_{Cy} = \dot{f}_{Cy} - \dot{\psi} V_{Cx}$  represents the control-frame-relative lateral acceleration from (4.40), and  $\omega_y$  and  $d_y$  are the desired frequency and relative damping of the lateral dynamics. Furthermore,  $\dot{f}_{Bz,c}$  is the specific force rate command from (4.47) and  $\ddot{\psi}_{\text{lead}}$  represents the lead-filtered heading acceleration command, which compensates for the roll angle rate dynamics. Approximating the roll dynamics by the equivalent first order relationship

$$\ddot{\phi} = K_{\text{roll}} (\dot{\phi}_c - \dot{\phi}) \quad (4.52)$$

and enforcing  $\dot{\phi} = \dot{\psi}$  yields the desired heading acceleration command

$$\ddot{\psi}_{\text{lead}} = K_{\text{roll}}^{-1} \ddot{\psi} + \ddot{\psi}, \quad (4.53)$$

where  $K_{\text{roll}}^{-1}$  represents the equivalent first order time constant of the roll angle rate dynamics.

Note that for non-saturated heading acceleration demands and an equivalent first order heading rate time constant equal to the roll angle rate time constant  $K_{\text{yaw}} = K_{\text{roll}}$ , the heading acceleration command in (4.53) simplifies to  $\ddot{\psi}_{\text{lead}} = \ddot{\psi}_c$ , where  $\ddot{\psi}_c$  denotes the heading acceleration command from the later discussed inner loop. For the CASM and

CDM, the reference signals  $\ddot{\psi}_r$  and  $\dot{\psi}_r$  are used in (4.53), as the heading acceleration and jerk signals are usually prone to noise.

When operating at significant roll angles  $\phi$ , the vertical dynamics also have to account for the limited authority and bandwidth of the roll angle rate loop due to the coupling term  $-\frac{\tan(\phi)}{f_{Bz}} \dot{f}_{Bz,c}$  in (4.50). Hence, the later introduced control architecture in chapter 5 contains a reference model, which shapes the vertical rate dynamics dependent on the current roll angle, in order to account for the slower attitude dynamics. However, this reference model is left out in the DRM for the sake of simplicity.

The final roll angle rate command  $\dot{\phi}_c$  follows from the desired roll angle rate demand  $\dot{\phi}_d$  by considering the limitations according to

$$\dot{\phi}_c = \max \left( \dot{\phi}_{\min}, \min \left( \dot{\phi}_{\max}, \dot{\phi}_d \right) \right), \quad (4.54)$$

where

$$\dot{\phi}_{\min} = \max \left( \dot{\phi}_{\min,\text{total}}, K_{\phi,\text{prot}} (\phi_{\min} - \phi) \right) \quad (4.55)$$

and

$$\dot{\phi}_{\max} = \min \left( \dot{\phi}_{\max,\text{total}}, K_{\phi,\text{prot}} (\phi_{\max} - \phi) \right) \quad (4.56)$$

define the roll angle rate limits. These are given by the more restrictive value of both the absolute roll angle rate limits  $\dot{\phi}_{\min,\text{total}}$  or  $\dot{\phi}_{\max,\text{total}}$  and the rate defined by the convergence to the lower or upper roll angle limit  $\phi_{\min}$  and  $\phi_{\max}$  respectively with the time constant  $K_{\phi,\text{prot}}^{-1}$ .

#### 4.3.1.3 Along-Heading Velocity Control Without Use of Traction System

The forward (along-heading) velocity is controlled with a desired pitch angle rate  $\dot{\theta}_d$ , which follows from inversion of the first channel of (4.44), (4.41), (4.38), (4.39), and (4.40) and yields

$$\dot{\theta}_d = \underbrace{-\frac{\tan(\theta)}{f_{Bz}} \dot{f}_{Bz,c} + \tan(\phi) \tan(\theta) \dot{\phi}_c - \frac{\ddot{\psi}_{\text{lead}} V_{Cy} + \dot{\psi} \dot{V}_{Cy}}{\cos(\phi) \cos(\theta) f_{Bz}}}_{\substack{\text{Dynamic Inversion} \\ = \text{Climb and Turn Compensation}}} + \frac{2\omega_y d_y}{\cos(\phi) \cos(\theta) f_{Bz}} \left( \dot{V}_{Cx,c} - \dot{V}_{Cx} \right), \quad (4.57)$$

with

$$\dot{V}_{Cx,c} = \frac{\omega_x}{2d_x} (V_{Cx,c} - V_{Cx}), \quad (4.58)$$

where  $V_{Cx,c}$  and  $V_{Cx}$  denote the commanded and fed back longitudinal (along-heading) velocity,  $\dot{V}_{Cx} = \dot{f}_{Cx} + \dot{\psi} V_{Cy}$  represents the control-frame-relative longitudinal acceleration, and  $\omega_x$  and  $d_x$  are the desired frequency and relative damping of the longitudinal dynamics.

Analogously to the lateral channel, the coupling terms during climbing and turning are considered in the longitudinal channel as well, however due to less significant pitch angles and lateral velocity dynamics, they play a less important role as for the lateral

dynamics. The coupling term also includes the roll angle rate command  $\dot{\phi}_c$  from (4.54), where equivalent dynamics for the roll and pitch channel are assumed. Alternatively and analogously to (4.53), the roll rate command can be replaced with the lead command  $\dot{\phi}_{\text{lead}} = K_{\text{pitch}}^{-1} \ddot{\phi} + \dot{\phi}$ , where  $K_{\text{pitch}}^{-1}$  denotes the time constant of the first-order approximation of the pitch angle rate loop.

The final pitch angle rate command  $\dot{\theta}_c$  follows from the desired pitch angle rate demand  $\dot{\theta}_d$  from (4.57) by considering the limitations according to

$$\dot{\theta}_c = \max \left( \dot{\theta}_{\min}, \min \left( \dot{\theta}_{\max}, \dot{\theta}_d \right) \right), \quad (4.59)$$

where

$$\dot{\theta}_{\min} = \max \left( \dot{\theta}_{\min, \text{total}}, K_{\theta, \text{prot}} (\theta_{\min} - \theta) \right) \quad (4.60)$$

and

$$\dot{\theta}_{\max} = \min \left( \dot{\theta}_{\max, \text{total}}, K_{\theta, \text{prot}} (\theta_{\max} - \theta) \right) \quad (4.61)$$

define the pitch angle rate limits. These are given by the more restrictive value of both the absolute pitch angle rate limits  $\dot{\theta}_{\min, \text{total}}$  or  $\dot{\theta}_{\max, \text{total}}$  and the rate defined by the convergence to the lower or upper pitch angle limit  $\theta_{\min}$  and  $\theta_{\max}$  respectively with the time constant  $K_{\theta, \text{prot}}^{-1}$ .

#### 4.3.1.4 Along-Heading Velocity Control With Use of Traction System

For the second variant of forward velocity control, the traction system is used to generate a forward specific force  $f_{Bx}$ , while the pitch angle of the aircraft shall remain at a constant value  $\theta_{\text{hvr}}$ . However, for fixed-pitch propellers and non-reversible rotation speed of the traction system, deceleration of the system is supported by pitching up and tilting the powered lift contribution  $f_{Bz}$  backwards.

To this end, recall the control-frame relative acceleration denoted in the control frame from (4.40) in forward direction

$$\dot{V}_{Cx} = f_{Cx} + \dot{\psi} V_{Cy}, \quad (4.62)$$

where for the specific force in the x-direction of the control frame  $f_{Cx}$  both the contribution of the powered lift in  $f_{Bz}$  and of the forward thrust in  $f_{Bx}$  are considered

$$f_{Cx} = \cos(\phi) \sin(\theta) f_{Bz} + \cos(\theta) f_{Bx}. \quad (4.63)$$

Using (4.62) and assuming that the dynamics of the traction system is much faster than the pitch angle dynamics, (4.63) is simply inverted to yield the desired specific force in body-forward direction

$$f_{Bx, d} = \underbrace{-\cos(\phi) \tan(\theta) f_{Bz}}_{\text{Dynamic Inversion}} - \frac{\dot{\psi} V_{Cy}}{\cos(\theta)} + \underbrace{\frac{\dot{V}_{Cx, c}}{\cos(\theta)}}_{\text{Error Control}}, \quad (4.64)$$

with the forward acceleration command  $\dot{V}_{C_{x,c}}$  from (4.58).

The resulting specific force command  $f_{B_{x,c}}$  for the inner loop follows from saturating (4.64) according to the lower and upper specific force limits  $f_{B_{x,c},\min}$  and  $f_{B_{x,c},\max}$  respectively imposed by the limitations of the traction system and yields

$$f_{B_{x,c}} = \max(f_{B_{x,c},\min}, \min(f_{B_{x,c},\max}, f_{B_{x,d}})) . \quad (4.65)$$

Furthermore, the desired pitch angle rate dynamics

$$\dot{\theta}_d = K_\theta (\theta_{\text{hvr}} - \theta) = K_\theta \Delta\theta_c \quad (4.66)$$

are chosen such as to approach a fixed pitch angle  $\theta_{\text{hvr}} \geq 0$  during hover. However, the allowed (minimum) increment in pitch angle  $\Delta\theta_c$  is limited based on the lower limit of the traction system and its ability to generate sufficient deceleration in negative  $f_{B_x}$  direction.

To this end, consider an incremental deviation of (4.63) around some given  $\theta$  and  $f_{B_{x,d}}$  given by the linear approximation

$$\Delta f_{C_x} = (\cos(\phi) \cos(\theta) f_{B_z} - \sin(\theta) f_{B_x}) \Delta\theta + \cos(\theta) \Delta f_{B_x} . \quad (4.67)$$

Furthermore, let the increment

$$\Delta f_{B_{x,\min}} = f_{B_{x,\min}} - f_{B_{x,d}} \quad (4.68)$$

define the remaining deceleration margin for which the traction system approaches its lower limit. The minimum pitch angle increment  $\Delta\theta_{\min} = \theta_{\min} - \theta$  follows directly from enforcing (4.67) to be zero (i.e. no deviation in the desired along-heading specific force) while considering (4.68), and yields

$$\Delta\theta_{\min} = \frac{\cos(\theta) (f_{B_{x,d}} - f_{B_{x,\min}})}{\cos(\phi) \cos(\theta) f_{B_z} - \sin(\theta) f_{B_x}} . \quad (4.69)$$

The increment in (4.69) represents the minimum pitch angle increment (maximum amount of pitching down) for which the demand in forward specific force by the traction system  $f_{B_{x,d}}$  would reach the lower limit  $f_{B_{x,d}} = f_{B_{x,\min}}$ . Furthermore, (4.69) ensures that in the case of deceleration demands  $f_{B_{x,d}} < f_{B_{x,\min}}$  that exceed the lower limit of the traction system, the resulting pitch angle increment limit leads to a pitching-up motion and hence deceleration through the powered lifting force being tilted backwards.

The final pitch angle rate command  $\dot{\theta}_c$  follows from the desired pitch angle rate demand  $\dot{\theta}_d$  from (4.66) by considering the limitations according to

$$\dot{\theta}_c = \max(\dot{\theta}_{\min}, \min(\dot{\theta}_{\max}, \dot{\theta}_d)) , \quad (4.70)$$

where

$$\dot{\theta}_{\min} = \max(\dot{\theta}_{\min,\text{total}}, K_{\theta,\text{prot}} \Delta\theta_{\min}) \quad (4.71)$$

and

$$\dot{\theta}_{\max} = \min(\dot{\theta}_{\max,\text{total}}, K_{\theta,\text{prot}} (\theta_{\max} - \theta)) \quad (4.72)$$

define the pitch angle rate limits with  $\Delta\theta_{\min}$  from (4.69).

### 4.3.1.5 Heading Rate Control

Since the heading rate represents one of the pseudo control variables of the outer loop, the target command for the heading rate simply corresponds to the desired heading rate demand  $\dot{\psi}_c = \dot{\psi}_d$  from subsection 4.2.1.3, which is protected by (4.15).

## 4.3.2 Outer Loop Control for Transition Phase

The target control variables during the transition phase are the calibrated airspeed  $V_{CAS,c}$  and kinematic angle of attack  $\alpha_{kin,c}$ , the vertical velocity  $V_{Cz,c} = -\dot{h}_c$ , the body-lateral velocity  $V_{By,c}$ , and the roll angle  $\phi_c$  that leads to a desired heading rate  $\dot{\psi}_d$ .

Analogously to the hover phase, the pseudo control commands during the transition phase are given by the euler angle rates  $\dot{\epsilon}_c$  (used for controlling the roll angle, angle of attack, and lateral velocity), the body-vertical specific force rate  $\dot{f}_{Bz,c}$  (used for controlling the vertical velocity), and the body-longitudinal specific force  $f_{Bx,c}$  as part of the auto thrust system that controls the airspeed. The control laws are derived in the following.

### 4.3.2.1 Roll Angle Control

The desired roll angle dynamics yield

$$\dot{\phi}_d = K_\phi (\phi_c - \phi) , \quad (4.73)$$

with the roll angle  $\phi$ , the roll angle command  $\phi_c$  from (4.26) and the desired bandwidth of the roll angle loop  $K_\phi$ .

The final roll angle rate command  $\dot{\phi}_c$  follows from saturation of (4.73) analogously to (4.54). Note that the protection of the roll angle indirectly results from the limitation of the desired heading rate according to (4.28). However, due to additional requirements on the maximum roll angle (e.g. wing clearance above ground), the roll angle is additionally protected according to (4.55) and (4.56).

### 4.3.2.2 Angle of Attack and Lateral Velocity Control

Given the commanded angle of attack  $\alpha_{kin,c} = \alpha_{kin,d}$  from (4.18), the desired dynamics for the angle of attack yields

$$\dot{\alpha}_{kin,d} = K_\alpha (\alpha_{kin,c} - \alpha_{kin}) , \quad (4.74)$$

with the kinematic angle of attack  $\alpha_{kin}$  and the desired time constant of the angle of attack loop  $K_\alpha^{-1}$ .

According to figure 4.12, the kinematic angle of attack can be represented as a function of the velocities denoted in the body frame

$$\alpha_{kin} = \tan^{-1} \left( \frac{V_{Bz}}{V_{Bx}} \right) . \quad (4.75)$$



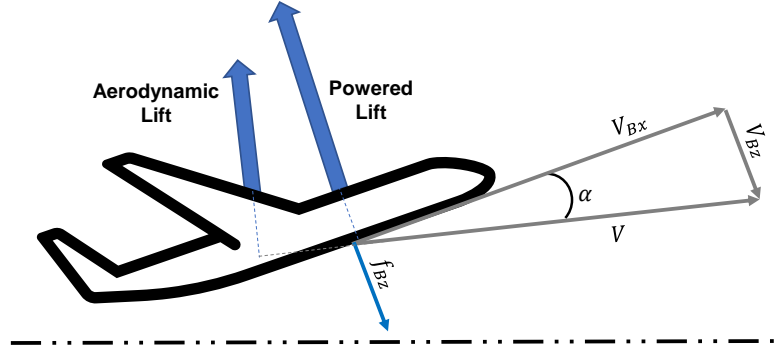


**Figure 4.12:** *Angle of Attack During Transition Phase (No Wind)*

The derivative of (4.75) furthermore yields

$$\dot{\alpha}_{\text{kin}} = q + \frac{V_{Bx} \left( \frac{dV}{dt} \right)_{Bz}^I - V_{Bz} \left( \frac{dV}{dt} \right)_{Bx}^I}{V_{Bx}^2 + V_{Bz}^2}, \quad (4.76)$$

which follows from using the chain rule on (4.75) considering the body-relative acceleration

$$\left( \frac{d\mathbf{V}}{dt} \right)_B = \begin{bmatrix} \dot{V}_{Bx} \\ \dot{V}_{By} \\ \dot{V}_{Bz} \end{bmatrix}_B = \left( \frac{d\mathbf{V}}{dt} \right)_B^I - (\boldsymbol{\omega}^{IB})_B \times (\mathbf{V})_B. \quad (4.77)$$

Here,  $(\boldsymbol{\omega}^{IB})_B = [p \ q \ r]_B^T$  denotes the body rate vector and the inertial acceleration denoted in the body frame is given by

$$\left( \frac{d\mathbf{V}}{dt} \right)_B^I = (\mathbf{f})_B + (\mathbf{g})_B = \begin{bmatrix} f_{Bx} - \sin(\theta)g \\ f_{By} + \sin(\phi) \cos(\theta)g \\ f_{Bz} + \cos(\phi) \cos(\theta)g \end{bmatrix}_B. \quad (4.78)$$

Furthermore, it is assumed that the body-lateral velocity  $V_{By}$  is much smaller than the body-longitudinal velocity  $V_{Bx}$  and hence changes in angle of attack mainly are influenced by pitch motion. Solving (4.76) for the pitch rate yields

$$q_d = \dot{\alpha}_{\text{kin},d} - \frac{V_{Bx} (f_{Bz} + \cos(\phi) \cos(\theta)g) - V_{Bz} (f_{Bx} - \sin(\theta)g)}{V_{Bx}^2 + V_{Bz}^2}, \quad (4.79)$$

where  $\dot{\alpha}_{\text{kin},d}$  denotes the desired angle of attack rate from (4.74).

Next, the body-lateral velocity  $V_{By}$  shall follow the command  $V_{By,c}$  from (4.21) by enforcing the desired dynamics

$$\dot{V}_{By,d} = K_{V_{By}} (V_{By,c} - V_{By}), \quad (4.80)$$

with the first order time constant  $K_{V_{By}}^{-1}$ .

Recalling the body-relative derivative (4.22) and using the euler angle differential equation to substitute the roll rate with  $p = \dot{\phi} - \sin(\phi) \tan(\theta)q - \cos(\phi) \tan(\theta)r$  yields

$$\dot{V}_{By} = f_{By} + \sin(\phi) \cos(\theta)g - rV_{Bx} + \left( \dot{\phi} - \sin(\phi) \tan(\theta)q - \cos(\phi) \tan(\theta)r \right) V_{Bz}. \quad (4.81)$$

Solving (4.81) for the yaw rate yields the desired pseudo control command

$$r_d = \frac{f_{By} + \sin(\phi) \cos(\theta)g + \dot{\phi}_c V_{Bz} - \sin(\phi) \tan(\theta) V_{Bz} q_d - \dot{V}_{By,d}}{V_{Bx} + \cos(\phi) \tan(\theta) V_{Bz}}, \quad (4.82)$$

where  $\dot{\phi}_c$  is the roll angle rate command resulting from the saturated demand from (4.73),  $q_d$  is the pitch rate demand from (4.79), and  $\dot{V}_{By,d}$  denotes the desired lateral dynamics from (4.80).

Furthermore, the main contribution in (4.82) results from the gravity-induced term  $r_g = \sin(\phi) \cos(\theta)g$ , which leads to body-lateral accelerations in the presence of roll angles  $\phi$ . In order to improve the performance of the turn coordination, the delayed yaw response of the system to the commanded gravity term  $r_{gc}$  can be anticipated in terms of the linear first-order approximation

$$\dot{r}_g = K_{yaw} (r_{gc} - r_g), \quad (4.83)$$

where  $K_{yaw}^{-1}$  denotes the surrogate first-order time constant of the yaw response, which will be derived in the paragraph for the inner-loop control.

The relationship in (4.83) is further used to yield the lead-command for the gravity compensation

$$r_{gc} = \sin(\phi) \cos(\theta)g + \underbrace{K_{yaw}^{-1} \left( \cos(\phi) \cos(\theta)g\dot{\phi} - \sin(\phi) \sin(\theta)g\dot{\theta} \right)}_{\text{Lead Portion}}, \quad (4.84)$$

which is used to replace the gravity term  $\sin(\phi) \cos(\theta)g$  in (4.82).

In a similar manner, the term  $\dot{\phi}_c V_{Bz}$  that compensates the roll induced build-up of body-lateral velocity in the presence of non significant angles of attack (and hence  $V_{Bz}$ ) can be replaced by the more general formulation  $\left( K_{yaw}^{-1} \ddot{\phi} + \dot{\phi} \right) V_{Bz}$ , which accounts for potentially different dynamics of the roll and yaw channel and for saturation in the roll acceleration.

In order to yield the overall desired euler angle rate demand, the pitch and yaw rate demands from (4.79) and (4.82) are expressed as desired pitch angle rate and heading rate according to

$$\begin{bmatrix} \dot{\theta}_d \\ \dot{\psi}_d \end{bmatrix} = \begin{bmatrix} \cos(\phi) & -\sin(\phi) \\ \frac{\sin(\phi)}{\cos(\theta)} & \frac{\cos(\phi)}{\cos(\theta)} \end{bmatrix} \begin{bmatrix} q_d \\ r_d \end{bmatrix}. \quad (4.85)$$

The final pitch angle rate command  $\dot{\theta}_c$  follows from saturating (4.85) according to (4.59). The limits are chosen analogously to (4.60) and (4.61). The protection of the pitch angle is especially important for significant vertical rate commands at low air speeds, as the angle of attack control loop would drive the system into inadvertent pitch attitudes.

The commanded heading rate  $\dot{\psi}_c$  follows from saturating (4.85) analogously to (4.59) considering the limit for the commanded heading rate  $\dot{\psi}_{abs,max}$ .

### 4.3.2.3 Vertical Velocity Control

The vertical velocity control loop for the transition phase is identical to the hover phase. Hence, the resulting demand in powered lift follows from the desired body-vertical specific force rate  $\dot{f}_{Bz,d}$  from (4.45).

However, in contrast to the hover phase, the airspeed during the transition phase can rise to significant levels, such that the effects of aerodynamic lift can not be neglected. In order to avoid undesired climbing due to the fixed angle of attack regime at increasing airspeeds, the angle of attack rate from (4.74) is dynamically limited through

$$\dot{\alpha}_{\text{kin},c} = \min(\dot{\alpha}_{\text{kin},d}, \dot{\alpha}_{\text{prot}}) , \quad (4.86)$$

where

$$\dot{\alpha}_{\text{prot}} = -\frac{2C_L\dot{V}}{C_{L\alpha}V} - \frac{\dot{f}_{Bz,d} - K_{f,\text{prot}}(f_{Bz,\text{PL,max}} - f_{Bz,\text{PL}})}{\frac{1}{m}\frac{1}{2}\rho V^2 S C_{L\alpha}} \quad (4.87)$$

denotes the limit angle of attack rate for which the powered lift would approach the lower threshold  $f_{Bz,\text{PL,max}} \leq 0$  under the demand of  $\dot{f}_{Bz,d}$  with a time constant of  $K_{f,\text{prot}}^{-1}$  due to the aerodynamic specific force rate derived in (4.102) within the paragraph for the vertical control during the wingborne phase.

By protecting the powered lift through (4.86) and (4.87), the angle of attack control loop will deviate from the fixed regime (4.18) whenever the demand in vertical specific force rate  $\dot{f}_{Bz,d}$  exceeds the limit first order dynamics  $\dot{f}_{Bz,\text{lim}} = K_{f,\text{prot}}(f_{Bz,\text{PL,max}} - f_{Bz,\text{PL}})$ . More particularly, when the powered lift decreases to its minimum value at higher airspeeds, the protection (4.87) will allocate any additional specific force rate demand in the down direction into the corresponding decrease of the angle of attack.

### 4.3.2.4 Airspeed Control

The target command for the calibrated airspeed  $V_{\text{CAS},c}$  follows from the derivation in subsection 4.2.3.1. Furthermore, the desired airspeed dynamics is given by

$$\dot{V}_{\text{CAS},d} = K_V (V_{\text{CAS},c} - V_{\text{CAS}}) , \quad (4.88)$$

with the time constant of the airspeed control loop  $K_V^{-1}$ .

The commanded acceleration follows from saturating (4.88) according to

$$\dot{V}_{\text{CAS},c} = \max(\dot{V}_{\text{min}}, \min(\dot{V}_{\text{max}}, \dot{V}_{\text{CAS},d})) , \quad (4.89)$$

where  $\dot{V}_{\text{min}}$  and  $\dot{V}_{\text{max}}$  denote the minimum and maximum allowed acceleration respectively.

For the derivation of the real airspeed dynamics, the force equilibrium in flight direction is considered for small sideslip angles:

$$\dot{V}_{\text{CAS}} = g_{Kx} + \cos(\alpha)f_{Bx} + \sin(\alpha)f_{Bz} , \quad (4.90)$$

where  $f_{Bx}$  and  $f_{Bz}$  denote the specific forces in forward and vertical body direction respectively and  $g_{Kx}$  represents the proportion of gravity in the kinematic direction of flight given by the x component of

$$(\mathbf{g})_K = \mathbf{M}_{KB} \mathbf{M}_{CB}^T (\mathbf{g})_C, \quad (4.91)$$

with the gravity vector in the control frame  $(\mathbf{g})_C = [0 \ 0 \ g]^T$ , the rotation matrix  $\mathbf{M}_{CB}$  from (4.43), and the rotation matrix

$$\mathbf{M}_{KB} = \begin{bmatrix} \cos(\beta) \cos(\alpha) & \sin(\beta) & \cos(\beta) \sin(\alpha) \\ -\sin(\beta) \cos(\alpha) & \cos(\beta) & -\sin(\beta) \sin(\alpha) \\ -\sin(\alpha) & 0 & \cos(\alpha) \end{bmatrix}, \quad (4.92)$$

which defines the transformation from the body frame to the kinematic frame.

The pseudo control variable for the airspeed control loop is the commanded body-longitudinal specific force  $f_{Bx,c}$ , which follows from (4.90) and (4.88) and yields

$$f_{Bx,c} = \frac{\dot{V}_{CAS,c}}{\cos(\alpha)} - \tan(\alpha) f_{Bz} + (\sin(\theta) - \tan(\alpha) \cos(\phi) \cos(\theta)) g, \quad (4.93)$$

with  $\dot{V}_{CAS,c}$  from (4.89).

### 4.3.3 Outer Loop Control for Wingborne Phase

The outer-loop control strategy during the wingborne phase is structurally very similar to the transition phase. The roll angle and airspeed loop are identical to the transition phase. The main differences lie in the generation of lift for controlling the vertical channel and the lateral control regime, which is blended from body-lateral velocity control to a body-lateral specific force control. Furthermore, time constants and limit parameters are adjusted to the moment and force characteristics of the system in the wingborne state.

#### 4.3.3.1 Vertical Velocity Control

After switching to the wingborne mode, the powered lift system is gradually shut down according to

$$\dot{f}_{Bz,\text{prop}} = \min \left( \dot{f}_{Bz,\text{max}}, -K_f f_{Bz,\text{prop}} \right), \quad (4.94)$$

where  $\dot{f}_{Bz,\text{max}}$  denotes the maximum rate with which the specific lifting force shall decrease and  $K_f^{-1}$  denotes the time constant for the convergence of the powered lift to zero. Note that when the switch into the wingborne mode happens, the powered lift system might already be idling, since one of the necessary but not sufficient conditions for the mode switch is that the powered lift contribution is below a certain threshold  $f_{Bz,\text{prop,thr}}$ .

Instead of the feedforward angle of attack regime (4.74) from the transition phase, the angle of attack is used for closed-loop control of the aerodynamic lift during the wingborne phase, in order to control the vertical velocity.

According to (4.41) and (4.44), the body-vertical specific force rate can be expressed as

$$\dot{f}_{Bz} = \tan(\phi)f_{Bz}\dot{\phi} + \tan(\theta)f_{Bz}\dot{\theta} - \frac{\ddot{h}}{\cos(\phi)\cos(\theta)}, \quad (4.95)$$

where  $\ddot{h}$  denotes the earth-vertical jerk and the effects of the specific net force and force rate in body-longitudinal direction are neglected due to small pitch angles.

Furthermore, in the wingborne phase the tilt of lift direction due to changes in the pitch angle  $\tan(\theta)f_{Bz}\dot{\theta}$  is assumed to be much smaller than due to changes in the roll angle  $\tan(\phi)f_{Bz}\dot{\phi}$  and is hence also neglected. The desired body-vertical specific force rate can thus be written as

$$\dot{f}_{Bz,d} = -\dot{f}_{Bz,\text{prop}} + \tan(\phi)f_{Bz}\dot{\phi} - \frac{\ddot{h}_d}{\cos(\phi)\cos(\theta)}, \quad (4.96)$$

where  $\dot{f}_{Bz,\text{prop}}$  only contributes while the powered lift system is shutting down and  $\ddot{h}_d$  denotes the desired earth-vertical jerk

$$\ddot{h}_d = 2\omega_h d_h (\ddot{h}_c - \ddot{h}), \quad (4.97)$$

with the commanded earth-vertical acceleration

$$\ddot{h}_c = \max\left(\ddot{h}_{\min}, \min\left(\ddot{h}_{\max}, \frac{\omega_h}{2d_h}(\dot{h}_c - \dot{h})\right)\right), \quad (4.98)$$

where  $\dot{h}_c$  and  $\dot{h}$  denote the commanded and fed back height rate,  $\ddot{h} = -f_{Cz} + g$  denotes the vertical acceleration,  $g$  is the gravitational acceleration, and  $\omega_h$  and  $d_h$  are the desired frequency and relative damping of the height rate dynamics in the wingborne phase. Furthermore,  $\ddot{h}_{\min}$  and  $\ddot{h}_{\max}$  denote the maximum sink and climb accelerations.

The specific force in body-vertical direction during the wingborne phase is the result of aerodynamic lift, which by definition acts perpendicular to the incoming airflow, and yields

$$f_{Bz} = -\frac{\cos(\alpha)L}{m} \approx -\frac{L}{m}, \quad (4.99)$$

where the angle of attack  $\alpha$  is assumed to be small, see also figure 4.12.

The aerodynamic lifting force  $L$  is further expressed according to the well-known relationship

$$L = \frac{1}{2}\rho V^2 S C_L, \quad (4.100)$$

with the air density  $\rho$ , true airspeed  $V$ , reference wing surface area  $S$ , and the lift coefficient  $C_L$ . Furthermore, the lift coefficient is approximated by

$$C_L = C_{L0} + C_{L\alpha}\alpha, \quad (4.101)$$

where  $C_{L0}$  denotes the zero angle of attack lift coefficient,  $C_{L\alpha}$  denotes the lift coefficient slope, and  $\alpha$  is the angle of attack.

Taking the derivative of (4.99) and considering (4.100) and (4.101) yields the aerodynamic specific force rate in the body-vertical direction

$$\dot{f}_{Bz} = -\frac{1}{m} \frac{1}{2} \rho S C_L 2V\dot{V} - \frac{1}{m} \frac{1}{2} \rho V^2 S C_{L\alpha} \dot{\alpha}, \quad (4.102)$$

where  $\dot{V}$  denotes the acceleration in the direction of the airflow and can be calculated according to (4.90).

The turn compensation term  $y_{TC} = \tan(\phi) f_{Bz} \dot{\phi}$  in (4.96) can furthermore be replaced by the lead-filtered command  $y_{TC,c}$  that takes into account the delayed response of the desired angle of attack rate  $\dot{\alpha}_d$ , which builds up according to the pitch dynamics of the inner loop. To this end, consider the turn compensation term  $y_{TC} = \tan(\phi) f_{Bz} \dot{\phi} = \frac{\sin(\phi)}{\cos^2(\phi)} \cos(\phi) f_{Bz} \dot{\phi}$ , where  $\cos(\phi) f_{Bz} = \text{const}$  is assumed, i.e. the lift contribution in the earth-vertical direction remains constant. The turn compensation term  $y_{TC}$  builds up according to

$$\dot{y}_{TC} = K_{\text{pitch}} (y_{TC,c} - y_{TC}) = \tan(\phi) f_{Bz} \ddot{\phi} + (1 + 2 \tan^2(\phi)) f_{Bz} \dot{\phi}^2. \quad (4.103)$$

Solving for the lead-filtered turn compensation command yields

$$y_{TC,c} = \tan(\phi) f_{Bz} \left( \frac{1}{K_{\text{pitch}}} \ddot{\phi} + \dot{\phi} \right) + \frac{1}{K_{\text{pitch}}} (1 + 2 \tan^2(\phi)) f_{Bz} \dot{\phi}^2, \quad (4.104)$$

where  $\frac{1}{K_{\text{pitch}}} \ddot{\phi} + \dot{\phi} = \dot{\phi}_c$  holds for non-saturated roll angle accelerations when  $K_{\text{pitch}} = K_{\text{roll}}$ . For the CASM and CDM, the reference signals  $\ddot{\phi}_r$  and  $\dot{\phi}_r$  for the roll angle are used, since the roll angle acceleration usually is prone to noise.

The overall angle of attack rate demand is hence given by

$$\dot{\alpha}_d = -\frac{2C_L \dot{V}}{C_{L\alpha} V} - \frac{-\dot{f}_{Bz,\text{prop}} + \tan(\phi) f_{Bz} \left( \frac{1}{K_{\text{pitch}}} \ddot{\phi} + \dot{\phi} \right) + \frac{1}{K_{\text{pitch}}} (1 + 2 \tan^2(\phi)) f_{Bz} \dot{\phi}^2 - \frac{\ddot{h}_d}{\cos(\phi) \cos(\theta)}}{\frac{1}{m} \frac{1}{2} \rho V^2 S C_{L\alpha}}, \quad (4.105)$$

with the desired earth-vertical jerk  $\ddot{h}_d$  from (4.97) and the acceleration in the direction of the airflow (no wind) given by

$$\dot{V} = \cos(\alpha) f_{Bx} + \sin(\alpha) f_{Bz} + (\sin(\alpha) \cos(\phi) \cos(\theta) - \cos(\alpha) \sin(\theta)) g. \quad (4.106)$$

The resulting angle of attack rate command follows from saturating (4.105) according to

$$\dot{\alpha}_c = \max(\dot{\alpha}_{\min}, \min(\dot{\alpha}_{\max}, \dot{\alpha}_d)), \quad (4.107)$$

where

$$\dot{\alpha}_{\min} = K_{\alpha,\text{prot}} (\alpha_{\min} - \alpha) \quad (4.108)$$

and

$$\dot{\alpha}_{\max} = K_{\alpha,\text{prot}} (\alpha_{\max} - \alpha) \quad (4.109)$$

define the angle of attack rate limits defined by the convergence to the lower or upper angle of attack limit  $\alpha_{\min}$  and  $\alpha_{\max}$  respectively with the time constant  $K_{\alpha,\text{prot}}^{-1}$ .

Furthermore, the resulting pitch rate command follows from (4.79) and substituting the angle of attack rate from (4.107).

### 4.3.3.2 Lateral Specific Force Control

Control of the lateral specific force is achieved by using the desired body-lateral acceleration  $\dot{V}_{By,d}$  as a pseudo control and deriving the desired yaw rate analogously to (4.82). To this end, the desired dynamics for the body-lateral specific force  $f_{By}$  is given by

$$\dot{f}_{By,d} = K_{f_{By}} (f_{By,c} - f_{By}) , \quad (4.110)$$

with the desired time constant  $K_{f_{By}}^{-1}$  of the lateral specific force dynamics and the target command  $f_{By,c}$  from (4.29), which by default is always 0 and hence leads to automatic turn coordination.

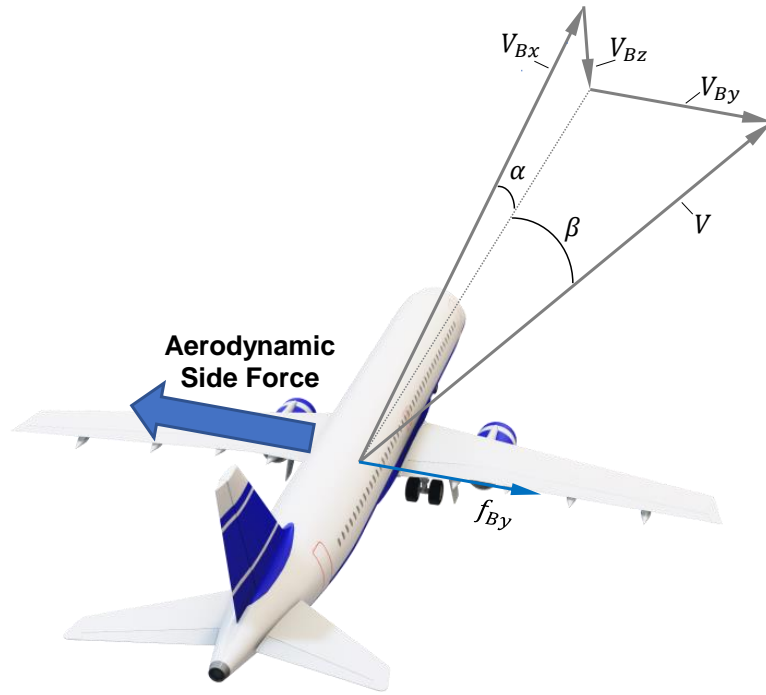


**Figure 4.13:** *Angle of Sideslip*

Due to small aerodynamic side slip angles  $\beta$ , the body lateral specific force is approximated by the relationship

$$f_{By} = \frac{1}{m} \frac{1}{2} \rho V^2 S C_{Q\beta} \beta , \quad (4.111)$$

with the aircraft's mass  $m$ , air density  $\rho$ , airspeed  $V$ , reference surface area  $S$ , the gradient of the lateral force coefficient  $C_{Q\beta}$ , and the sideslip angle  $\beta$ .

Furthermore, according to figure 4.13, the sideslip angle  $\beta$  can be expressed in terms of the velocity denoted in the body frame

$$\beta = \sin^{-1} \left( \frac{V_{By}}{V} \right) \quad (4.112)$$

and its derivative follows from the chain rule

$$\dot{\beta} = \frac{1}{\sqrt{1 - \frac{V_{By}^2}{V^2}}} \frac{\dot{V}_{By}}{V} \approx \frac{\dot{V}_{By}}{V} , \quad (4.113)$$

where it is assumed that  $V \gg V_{By}$  and the airspeed stays approximately constant, i.e.  $\dot{V} = 0$ .

The derivative of the body-lateral specific force follows from (4.111) and (4.113) and yields

$$\dot{f}_{By} = \underbrace{\frac{1}{m} \frac{1}{2} \rho S C_{Q\beta} \beta^2 V \dot{V}}_{\approx 0} + \frac{1}{m} \frac{1}{2} \rho V^2 S C_{Q\beta} \dot{\beta} = \frac{1}{m} \frac{1}{2} \rho V S C_{Q\beta} \dot{V}_{By}, \quad (4.114)$$

where the proportion that follows from acceleration  $\dot{V}$  in the presence of a sideslip angle  $\beta \neq 0$  is neglected due to small sideslip angles.

From (4.114) follows the desired body-lateral acceleration demand

$$\dot{V}_{By,d} = \frac{2m}{\rho V S C_{Q\beta}} \dot{f}_{By,d}, \quad (4.115)$$

with  $\dot{f}_{By,d}$  from (4.110).

The resulting yaw rate command directly follows from (4.82) by substituting  $\dot{V}_{By,d}$  from (4.115) and including the pitch rate command from the vertical velocity loop. Instead of performing a hard switch of the source for the desired body-lateral acceleration  $\dot{V}_{By,d}$ , the blending regime

$$\dot{V}_{By,d} = (1 - \lambda) \dot{V}_{By,d,transition} + \lambda \dot{V}_{By,d,wingborne}, \quad (4.116)$$

with

$$\lambda = \max(0, \min(1, c_1 V + c_2)) \quad (4.117)$$

will linearly blend the body-lateral acceleration demand over the current airspeed between  $\dot{V}_{By,d,transition}$  from (4.80) and  $\dot{V}_{By,d,wingborne}$  from (4.115) as characterized by the constants  $c_1$  and  $c_2$ .

### 4.3.4 Inner Loop Control

The inner loop control law of the DRM is structurally identical across all three flight phases and controls the euler angle rates, the rotational accelerations, and the forward specific force. Potential changes in gains and parameters between or within flight phases might have to be considered due to changing force and moment characteristics of the system with increasing airspeed (or height). The output commands of the inner loop are the specific force rate in the forward direction  $\dot{f}_{Bx,c}$  and the specific moment rates around the center of gravity  $(\dot{\mathbf{m}}_c)_B^B = (\mathbf{I}^G)_{BB}^{-1} (\dot{\mathbf{M}}^G)_B^B$ , where  $(\mathbf{I}^G)_{BB}^{-1}$  denotes the system's inertia around the center of gravity.

Given the euler angle rate command from the outer loop  $\dot{\epsilon}_c$ , the desired dynamics yield

$$\ddot{\epsilon}_d = \mathbf{K}_\epsilon (\dot{\epsilon}_c - \dot{\epsilon}), \quad (4.118)$$



where  $\mathbf{K}_\epsilon^{-1}$  is a diagonal matrix and denotes the desired time constants for the euler angle rate loop.

The inverse strapdown equation relates the euler angle rates to body-fixed rotational rates

$$\underbrace{\begin{bmatrix} p \\ q \\ r \end{bmatrix}}_{(\boldsymbol{\omega}^{IB})_B} = \underbrace{\begin{bmatrix} 1 & 0 & -\sin(\theta) \\ 0 & \cos(\phi) & \sin(\phi)\cos(\theta) \\ 0 & -\sin(\phi) & \cos(\phi)\cos(\theta) \end{bmatrix}}_{\mathbf{S}^{-1}} \underbrace{\begin{bmatrix} \dot{\phi} \\ \dot{\theta} \\ \dot{\psi} \end{bmatrix}}_{\dot{\boldsymbol{\epsilon}}} \quad (4.119)$$

and its time derivative yields

$$(\dot{\boldsymbol{\omega}}^{IB})_B^B = \dot{\mathbf{S}}^{-1}\dot{\boldsymbol{\epsilon}} + \mathbf{S}^{-1}\ddot{\boldsymbol{\epsilon}}, \quad (4.120)$$

with

$$\dot{\mathbf{S}}^{-1} = \begin{bmatrix} 0 & 0 & -\cos(\theta)\dot{\theta} \\ 0 & -\sin(\phi)\dot{\phi} & \cos(\phi)\cos(\theta)\dot{\phi} - \sin(\phi)\sin(\theta)\dot{\theta} \\ 0 & -\cos(\phi)\dot{\phi} & -\sin(\phi)\cos(\theta)\dot{\phi} - \cos(\phi)\sin(\theta)\dot{\theta} \end{bmatrix}. \quad (4.121)$$

The rotational acceleration command  $(\dot{\boldsymbol{\omega}}_c^{IB})_B^B$  follows from (4.120) and yields

$$(\dot{\boldsymbol{\omega}}_c^{IB})_B^B = \min\left(\dot{\boldsymbol{\omega}}_{\max}, \max\left(\dot{\boldsymbol{\omega}}_{\min}, \dot{\mathbf{S}}^{-1}\dot{\boldsymbol{\epsilon}} + \mathbf{S}^{-1}\ddot{\boldsymbol{\epsilon}}_d\right)\right), \quad (4.122)$$

with  $\ddot{\boldsymbol{\epsilon}}_d$  from (4.118) and the minimum and maximum rotational acceleration command  $\dot{\boldsymbol{\omega}}_{\min}$  and  $\dot{\boldsymbol{\omega}}_{\max}$  respectively.

Furthermore, the rotational acceleration  $(\dot{\boldsymbol{\omega}}^{IB})_B^B$  of the system follows from Euler's rotational equations of motion denoted in the body frame

$$(\dot{\boldsymbol{\omega}}^{IB})_B^B = (\mathbf{I}^G)_{BB}^{-1}(\mathbf{M}^G)_B - (\mathbf{I}^G)_{BB}^{-1}\left((\boldsymbol{\omega}^{IB})_B \times (\mathbf{I}^G)_{BB}(\boldsymbol{\omega}^{IB})_B\right), \quad (4.123)$$

with the total moment around the center of gravity  $(\mathbf{M}^G)_B$  and the inertia of the system around the center of gravity  $(\mathbf{I}^G)_{BB}$ .

Taking the time derivative of (4.123) yields

$$(\ddot{\boldsymbol{\omega}}^{IB})_B^{BB} = \underbrace{(\mathbf{I}^G)_{BB}^{-1}(\dot{\mathbf{M}}^G)_B}_{(\dot{\mathbf{m}}_c)_B^B} - (\mathbf{I}^G)_{BB}^{-1}\left((\boldsymbol{\omega}^{IB})_B \times (\mathbf{I}^G)_{BB}(\dot{\boldsymbol{\omega}}^{IB})_B^B + (\dot{\boldsymbol{\omega}}^{IB})_B^B \times (\mathbf{I}^G)_{BB}(\boldsymbol{\omega}^{IB})_B\right), \quad (4.124)$$

where  $(\dot{\mathbf{m}}_c)_B^B$  denotes the specific moment rate, which is used to yield the desired dynamics of the rotational jerk

$$(\ddot{\boldsymbol{\omega}}_d^{IB})_B^{BB} = \mathbf{K}_\omega \left( (\dot{\boldsymbol{\omega}}_c^{IB})_B^B - (\dot{\boldsymbol{\omega}}^{IB})_B^B \right), \quad (4.125)$$

with  $(\dot{\boldsymbol{\omega}}_c^{IB})_B^B$  from (4.122) and where  $\mathbf{K}_\omega^{-1}$  is a diagonal matrix and denotes the desired time constants for the rotational acceleration loop.

The resulting demand for the specific moment rate hence yields

$$(\dot{\mathbf{m}}_c)_B^B = \underbrace{(\ddot{\boldsymbol{\omega}}_d^{IB})_B^{BB}}_{\text{Error Control}} + \underbrace{(\mathbf{I}^G)_{BB}^{-1}\left((\boldsymbol{\omega}^{IB})_B \times (\mathbf{I}^G)_{BB}(\dot{\boldsymbol{\omega}}^{IB})_B^B + (\dot{\boldsymbol{\omega}}^{IB})_B^B \times (\mathbf{I}^G)_{BB}(\boldsymbol{\omega}^{IB})_B\right)}_{\text{Dynamic Inversion}}, \quad (4.126)$$

with  $(\dot{\omega}_d^{IB})_B^{BB}$  from (4.125).

Besides the rotational control, the inner loop also controls the commanded longitudinal specific force  $f_{Bx,c}$ , which is used in the airspeed control loop. To this end, the target rate of the specific force in forward direction is given by

$$\dot{f}_{Bx,c} = K_{f_x} (f_{Bx,c} - f_{Bx}), \quad (4.127)$$

with  $f_{Bx,c}$  from (4.93) and the desired time constant  $K_{f_x}^{-1}$  for the forward specific force loop.

Together with the commanded body-vertical specific force rate  $\dot{f}_{Bz,c}$  from (4.47), the resulting moment and force rates are emulated, which is described in the next paragraph. For the later introduced control architecture of the CASM, the force and moment rates are the required input signals for the control allocation, which yields the required commands to the motors and actuators of the aircraft.

### 4.3.5 Force and Moment Emulation

The forces and moments, which represent the inputs to the rigid body dynamics of the DRM, are given by the following contributions:

- gravitational force  $\mathbf{F}_{\text{grav}}$
- aerodynamic forces  $\mathbf{F}_{\text{aer}}$  and moments  $\mathbf{M}_{\text{aer}}^G$  around the center of gravity due to the airflow resulting from the velocity of the rigid body and wind
- control forces  $\mathbf{F}_{\text{ctrl}}$  and moments  $\mathbf{M}_{\text{ctrl}}^G$  around the center of gravity which are produced by the powered lift system, traction system, and the control surfaces.

Note that even though the control forces and moments are actually based on and therefore part of the aerodynamics, they are decoupled and abstracted in the context of the DRM, in order to achieve a system-architecture-agnostic representation of the system. Instead of modeling the interaction of available control effectors with the airflow and the airframe, the generation of forces and moments is modeled independently in terms of first order rate-saturated dynamics that take into account the force and moment characteristics of the electric motors and actuators. An example for the powered lift generation can be seen in figure 4.14.

#### 4.3.5.1 Control Forces and Moments

As mentioned in section 5.2, assuming approximately constant limits for the achievable control effector induced accelerations and jerks (refer to e.g. figure 5.7) leads to satisfactory performance when assuming current limited electric motors subject to aerodynamic drag moments.

Furthermore, statements about if the generated forces and moments (and force and moment rates) are in fact achievable by a given configuration of motors and actuators can be made by subsequent static trim analysis of a given simulation run of the DRM, where the required electric current and power for the generated control forces and moments can be calculated.

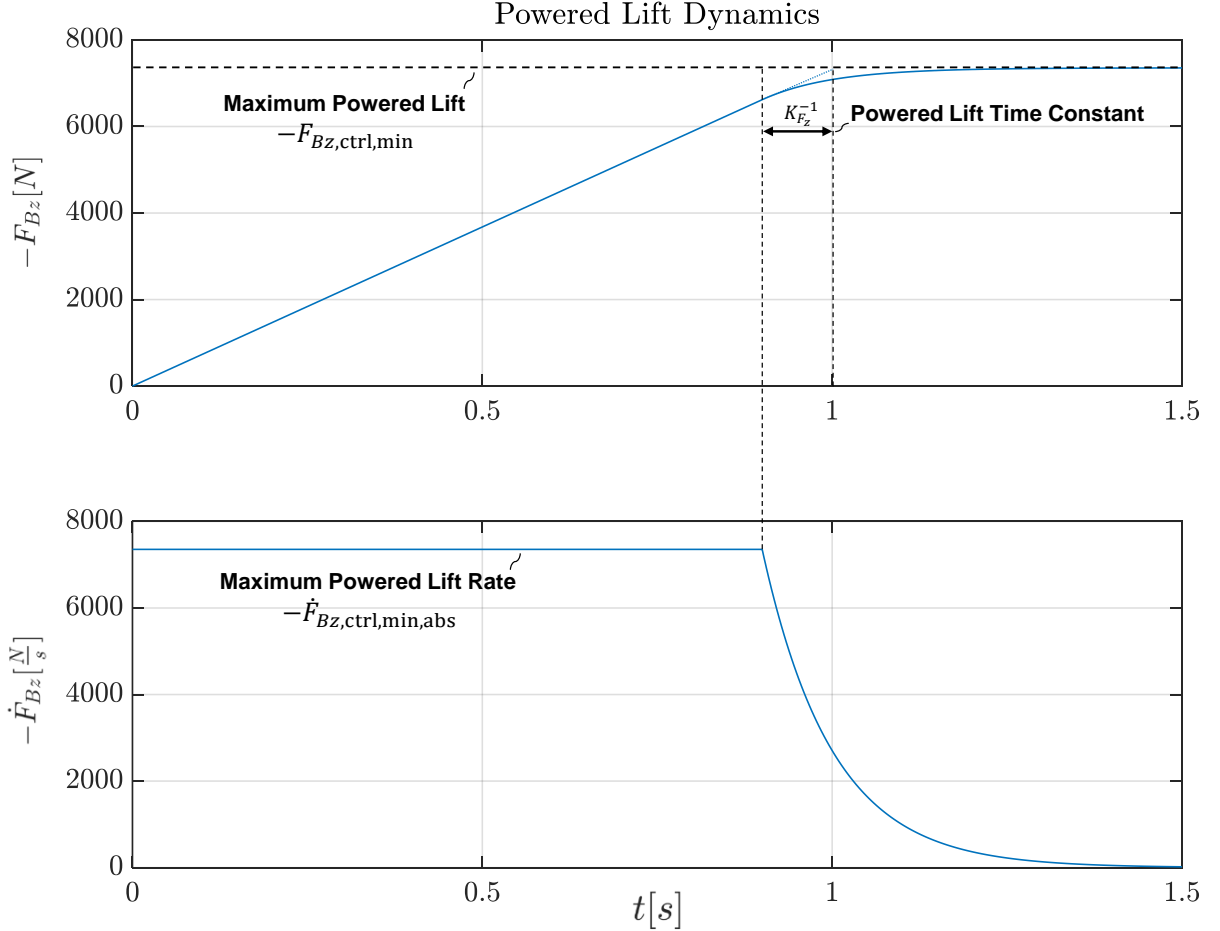


**Figure 4.14:** *Powered Lift Dynamics*

As mentioned in the beginning of section 4.2, it is assumed that no (significant) body-lateral forces are produced by the available motors and actuators. The powered lift system is assumed to produce the lifting force in the body-vertical direction and the traction system produces thrust in body-forward direction. The control force dynamics are modeled according to

$$(\dot{\mathbf{F}}_{\text{ctrl}})_B^B = \begin{bmatrix} \min \left( \dot{F}_{Bx,\text{ctrl,max}}, \max \left( \dot{F}_{Bx,\text{ctrl,min}}, m \dot{f}_{Bx,c} \right) \right) \\ 0 \\ \min \left( \dot{F}_{Bz,\text{ctrl,max}}, \max \left( \dot{F}_{Bz,\text{ctrl,min}}, m \dot{f}_{Bz,c} \right) \right) \end{bmatrix}_B, \quad (4.128)$$

with  $\dot{f}_{Bx,c}$  and  $\dot{f}_{Bz,c}$  from (4.127) and (4.47) respectively, the VTOL aircraft's mass  $m$ ,

and the control force limits defined according to

$$\dot{F}_{Bx,ctrl,max} = \min \left( \dot{F}_{Bx,ctrl,max,abs}, K_{F_x} (F_{Bx,ctrl,max} - F_{Bx,ctrl}) \right), \quad (4.129)$$

$$\dot{F}_{Bx,ctrl,min} = \min \left( \dot{F}_{Bx,ctrl,min,abs}, K_{F_x} (F_{Bx,ctrl,min} - F_{Bx,ctrl}) \right), \quad (4.130)$$

and

$$\dot{F}_{Bz,ctrl,max} = \min \left( \dot{F}_{Bz,ctrl,max,abs}, K_{F_z} (F_{Bz,ctrl,max} - F_{Bz,ctrl}) \right), \quad (4.131)$$

$$\dot{F}_{Bz,ctrl,min} = \min \left( \dot{F}_{Bz,ctrl,min,abs}, K_{F_z} (F_{Bz,ctrl,min} - F_{Bz,ctrl}) \right), \quad (4.132)$$

where  $\dot{F}_{Bi,ctrl,max,abs}$  and  $F_{Bi,ctrl,max}$  denote the maximum force rate and force limit and  $\dot{F}_{Bi,ctrl,min,abs}$  and  $F_{Bi,ctrl,min}$  denote the minimum force rate and force limit of the system. Furthermore, the time constant with which the  $i$ -th channel converges to its maximum or minimum limit is given by  $K_{F_i}^{-1}$ .

Figure 4.14 shows an exemplary simulation of the powered lift being commanded at its limit. Note that for fixed pitch propellers and unidirectional rotational speed of the powered lift motors and the traction motors it follows that  $F_{Bx,ctrl,min} \approx F_{Bz,ctrl,max} \approx 0$  N, i.e. no negative lifting force and thrust can be produced.

The generation of control moments follows analogously to the control forces. To this end, the moment dynamics are given by

$$(\dot{\mathbf{M}}_{ctrl}^G)_B = \min \left( (\dot{\mathbf{M}}_{ctrl,max}^G)_B, \max \left( (\dot{\mathbf{M}}_{ctrl,min}^G)_B, (\mathbf{I}^G)_{BB} (\dot{\mathbf{m}}_c)_B^B \right) \right), \quad (4.133)$$

with the aircraft's inertia  $(\mathbf{I}^G)_{BB}$ , the desired specific moment rate  $(\dot{\mathbf{m}}_c)_B^B$  from (4.126), and the control moment limits defined according to

$$(\dot{\mathbf{M}}_{ctrl,max}^G)_B = \min \left( (\dot{\mathbf{M}}_{ctrl,max,abs}^G)_B, \mathbf{K}_M \left( (\mathbf{M}_{ctrl,max}^G)_B - (\mathbf{M}_{ctrl}^G)_B \right) \right) \quad (4.134)$$

and

$$(\dot{\mathbf{M}}_{ctrl,min}^G)_B = \min \left( (\dot{\mathbf{M}}_{ctrl,min,abs}^G)_B, \mathbf{K}_M \left( (\mathbf{M}_{ctrl,min}^G)_B - (\mathbf{M}_{ctrl}^G)_B \right) \right), \quad (4.135)$$

with the maximum moment rate and moment limit  $(\dot{\mathbf{M}}_{ctrl,max,abs}^G)_B$  and  $(\mathbf{M}_{ctrl,max}^G)_B$ , and the minimum moment rate and moment limit  $(\dot{\mathbf{M}}_{ctrl,min,abs}^G)_B$  and  $(\mathbf{M}_{ctrl,min}^G)_B$  respectively. Furthermore, the matrix  $\mathbf{K}_M$  determines the time constants for the moment dynamics.

Note that in the context of generating the control forces and moments, the effects of aerodynamic forces and moments are considered as disturbances. Only within the vertical and lateral control regime during the wingborne phase the aerodynamic forces are modeled explicitly, as they represent the (pseudo) control variables for the respective loop.

For the channels in which generation of control forces and moments are considered, the aerodynamic effects such as damping forces and moments as well as external disturbances like wind gusts, are compensated by the closed loop control of the translational

and rotational accelerations. This strategy is representative of the incremental nonlinear dynamic inversion approach, which serves as the theoretical basis for the later introduced control architecture.

In contrast to the DRM, where the required specific force and moment rates are integrated directly to obtain the final control forces and moments, the control allocation within the CASM yields the required control effector rates (or increments) that are expected to produce the desired specific force and moment rates.

#### 4.3.5.2 Gravitational and Aerodynamic Forces

The modeling of the gravitational and aerodynamic forces are not the focus of this thesis, however for the sake of completeness are mentioned here. In general, the control concept used in the DRM and the overall control architecture that is later introduced in the CASM and CDM is quite independent of the exact modeling of the gravitational and aerodynamic forces, because the incremental inversion approach enables closed-loop control of the required translational and rotational accelerations (and hence forces and moments).

Merely knowledge about the aerodynamic lift and side force characteristics are required within the control regime of the wingborne phase, as these forces cannot directly be generated by control effectors but are the result of the rigid body interacting with the airflow.

In the scope of this thesis the gravitational force follows a simple 1D model and is given by

$$(\mathbf{F}_{\text{grav}})_O = m \begin{bmatrix} 0 \\ 0 \\ g \end{bmatrix}_O, \quad (4.136)$$

with  $g = 9.80665 \frac{m}{s^2}$  and the index O denoting the North-East-Down frame.

The aerodynamic forces are modeled according to

$$(\mathbf{F}_{\text{aer}})_A = \frac{1}{2} \rho V_A^2 S \begin{bmatrix} -C_D \\ C_Q \\ -C_L \end{bmatrix}_A, \quad (4.137)$$

with the total airspeed  $V_A$ , air density  $\rho$ , and reference wing area  $S$  and where  $C_D$ ,  $C_Q$ , and  $C_L$  denote the aerodynamic drag, side force, and lift coefficients respectively.

The aerodynamic moments around the center of gravity are modeled according to

$$(\mathbf{M}_{\text{aer}}^G)_A = \frac{1}{2} \rho V_A^2 S \begin{bmatrix} bC_l \\ \bar{c}C_m \\ bC_n \end{bmatrix}_A, \quad (4.138)$$

where  $C_l$ ,  $C_m$ , and  $C_n$  denote the aerodynamic moment coefficients around the roll, pitch, and yaw axis respectively,  $b$  is the wing span and  $\bar{c}$  denotes the mean aerodynamic chord (MAC) [77].

In general, all the dimensionless aerodynamic coefficients can be represented in terms of lookup tables of the form

$$C_i = f_i(\alpha, \beta), \quad (4.139)$$

where  $\alpha$  and  $\beta$  denote the aerodynamic angle of attack and angle of sideslip. In order to obtain the required aerodynamic derivatives for the control regime used in e.g. (4.105) and (4.115), the corresponding aerodynamic coefficients are fitted according to the linear approximations

$$C_L = f_L(\alpha, \beta) \approx C_{L0} + C_{L\alpha}\alpha \quad (4.140)$$

and

$$C_Q = f_Q(\alpha, \beta) \approx C_{Q\beta}\beta, \quad (4.141)$$

where for the fit of the lift coefficient  $C_L$  zero sideslip conditions are assumed and for the side force coefficient  $C_Q$  a representative trim angle of attack is assumed.

### 4.3.6 Rigid-Body Equations of Motion

At the core of the DRM are the rigid-body equations of motion, which describe the system in terms of its center of gravity velocity with respect to the earth surface  $\mathbf{V}_G$ , position with respect to some earth-fixed point  $\mathbf{r}_{OG}$ , rotational rate  $\boldsymbol{\omega}^{IB}$ , and orientation in terms of euler angles  $\boldsymbol{\epsilon} = [\phi \ \theta \ \psi]^T$ . In the scope of this thesis a flat and non-rotating earth is assumed.

The translational dynamics directly follows from Newton's second law of motion and yields

$$(\dot{\mathbf{V}}_G)^I = m^{-1} (\mathbf{F}_{\text{ctrl}} + \mathbf{F}_{\text{grav}} + \mathbf{F}_{\text{aer}}), \quad (4.142)$$

with the system's mass  $m$  and the control forces  $\mathbf{F}_{\text{ctrl}}$ , gravitational force  $\mathbf{F}_{\text{grav}}$ , and aerodynamic forces  $\mathbf{F}_{\text{aer}}$  that follow from (4.128), (4.136), and (4.137) respectively.

Furthermore, the position of the center of gravity is derived from

$$(\dot{\mathbf{r}}_{OG})^I = \mathbf{V}_G, \quad (4.143)$$

with the velocity of the center of gravity with respect to the earth surface  $\mathbf{V}_G$ .

The rotational dynamics follows from Euler's equation of motion and yields

$$(\dot{\boldsymbol{\omega}}^{IB})^B = (\mathbf{I}^G)^{-1} (\mathbf{M}_{\text{aer}}^G + \mathbf{M}_{\text{ctrl}}^G) - (\mathbf{I}^G)^{-1} (\boldsymbol{\omega}^{IB} \times \mathbf{I}^G \boldsymbol{\omega}^{IB}), \quad (4.144)$$

where  $\mathbf{I}^G$  denotes the system's inertia around the center of gravity,  $\boldsymbol{\omega}^{IB}$  is the body rotational rate with respect to earth (which denotes an inertial system in this context),  $\mathbf{M}_{\text{aer}}^G$  denote the aerodynamic moments around the center of gravity from (4.138), and  $\mathbf{M}_{\text{ctrl}}^G$  denote the control moments around the center of gravity that follow from (4.133).

The euler angles  $\epsilon = [\phi \ \theta \ \psi]^T$  are derived from the strapdown equation

$$\dot{\epsilon} = \begin{bmatrix} \dot{\phi} \\ \dot{\theta} \\ \dot{\psi} \end{bmatrix} = \underbrace{\begin{bmatrix} 1 & \sin(\phi) \tan(\theta) & \cos(\phi) \tan(\theta) \\ 0 & \cos(\phi) & -\sin(\phi) \\ 0 & \frac{\sin(\phi)}{\cos(\theta)} & \frac{\cos(\phi)}{\cos(\theta)} \end{bmatrix}}_S \underbrace{\begin{bmatrix} p \\ q \\ r \end{bmatrix}}_{\omega_B^{IB}}, \quad (4.145)$$

where  $\omega_B^{IB}$  denotes the body rotational rate.

## 4.4 Verification and Validation of Behavioral Specification

After having derived the necessary control approach for the Design Reference Model that yields to implement the desired behavior in terms of Simplified Vehicle Operations, this section is concerned with exemplary verification and validation activities of the proposed concept. The focus mainly lies on the qualitative evaluation of the system response behavior. However, quantitative assessment with respect to existing performance specifications and handling quality requirements is addressed as well, in order to support the overall verification and validation of the design reference dynamics. Additionally, piloted real-time simulation tests facilitate comprehensive validation of the behavioral concept.

The simulation results in the following are the result of the DRM being implemented in Matlab Simulink [78] according to section 4.3 with a fixed sample time of 1ms.

### 4.4.1 Hover Flight

#### 4.4.1.1 Translational Control

The first test case for the hover phase represents a simple climb maneuver followed by a forward flight maneuver and is shown in figure 4.15 and 4.16. It is distinguished between the two variants for the forward control in hover introduced in subsection 4.3.1, which differ in using the traction system for forward acceleration instead of pitching down.

Section 3.3 of the Aeronautical Design Standard ADS-33E-PRF [12] states hover and low speed requirements that can be used to verify the DRM response. For example, subsection 3.3.10 in [12] defines desired vertical rate response characteristics by introducing an equivalent first-order transfer function

$$\frac{\dot{h}}{\delta_c} = \frac{K \exp(-\tau_h s)}{T_h s + 1}, \quad (4.146)$$

where  $\delta_c$  denotes the collective input in [12], which corresponds to the longitudinal direction of the right stick in the scope of this thesis. Furthermore,  $T_h$  and  $\tau_h$  denote the time

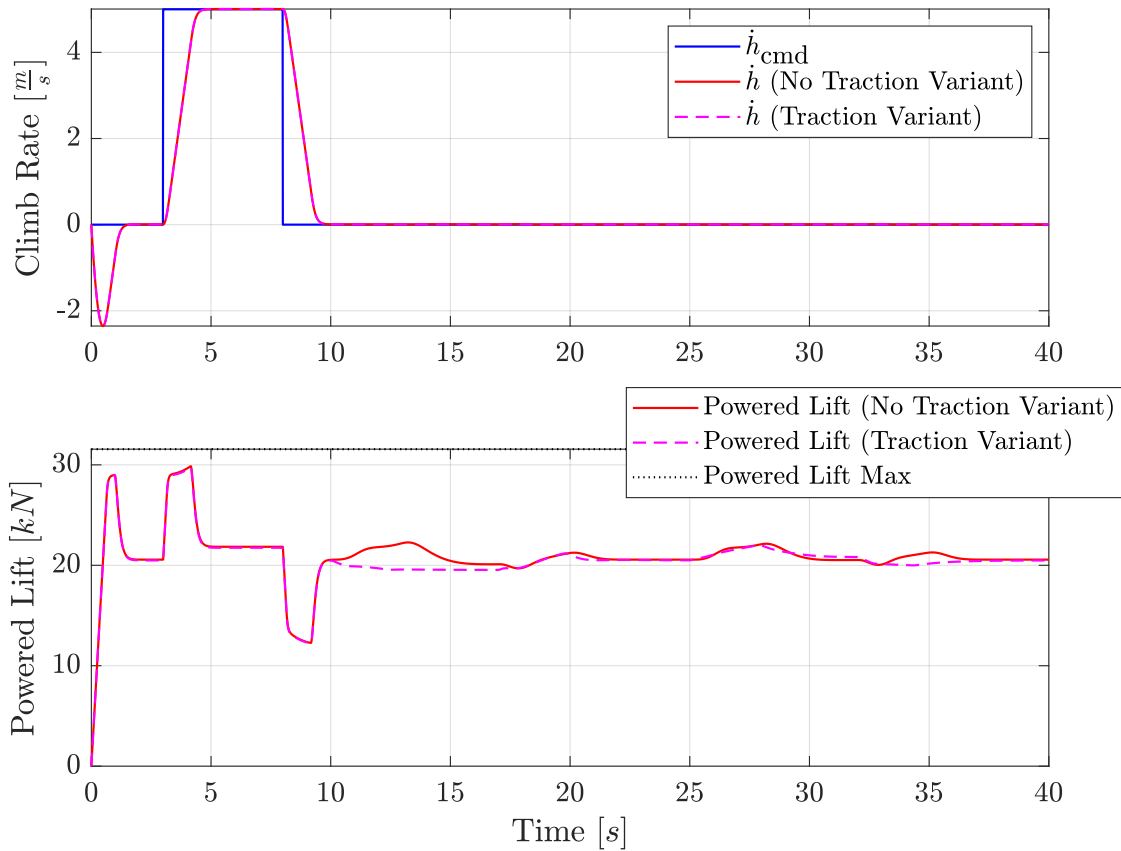


**Figure 4.15:** *Hover Maneuver Vertical Channel*

constant and time delay respectively and  $K$  is the constant that matches the stationary climb rate to the stick deflection.

The required maximum values for the vertical rate response parameters during hover and low speed flight can be obtained from table 4.3 and are adapted from [12].

**Table 4.3:** *Maximum Values for Vertical Rate Response Parameters – Hover and Low Speed [12]*

Handling Quality Level	Time Constant $T_{\dot{h}}[s]$	Time Delay $\tau_{\dot{h}}[s]$
Level 1	5.0	0.20
Level 2	$\infty$	0.30

The equivalent time constant  $T_{\dot{h}}$ , time delay  $\tau_{\dot{h}}$ , and scaling factor  $K$  of the vertical rate response are obtained by a nonlinear least-squares fit between the time domain representation of (4.146) excited by a unit step input

$$\dot{h}(t) = K \left( 1 - \exp \left( -\frac{t - \tau_{\dot{h}}}{T_{\dot{h}}} \right) \right) \quad (4.147)$$



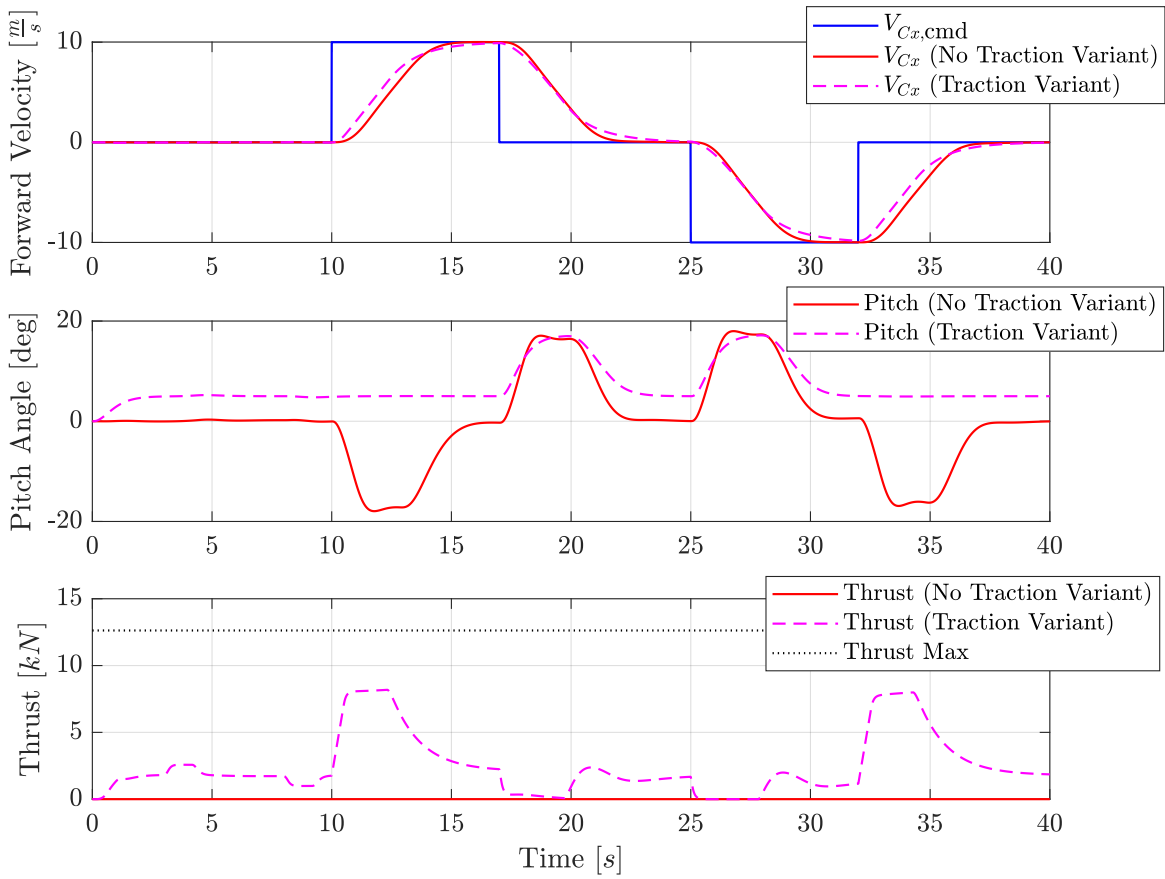


**Figure 4.16:** *Hover Maneuver Forward Channel*

and the DRM response in figure 4.15 (which contains both a positive and a negative step in the height rate). The fit is calculated for each step individually and the time variable  $t$  in (4.147) is offset by the time at which the corresponding step is commanded in the vertical channel. Note that the initial height drop in figure 4.15 is attributed to the initialization of the powered lift force at  $0\text{ N}$  and the lack of simulated ground reaction forces.

The forward maneuver can be seen in figure 4.16 and shows a forward-stop-backward-stop command for both variants of forward control. Note that for the traction variant the nominal pitch angle mentioned in subsection 4.3.1 is chosen to be  $\theta_{\text{hvr}} = 5\text{ deg}$ , such as to provide a faster deceleration response in case that no negative thrust can be produced.

While the pitch variant introduces significant pitch motion for both forward and backwards direction, the traction variant mostly maintains pitch attitude in the forward direction and only pitches up to fly backwards. Note that in contrast to conventional rotorcraft configurations, the VTOL transition aircraft is assumed to have fixed-pitch vertical lift propellers and hence a change in lift direction requires a change of the whole attitude of the aircraft. As a consequence, the achievable bandwidth in translational control - especially for small amplitudes - is considerably lower as compared to conventional rotorcraft,

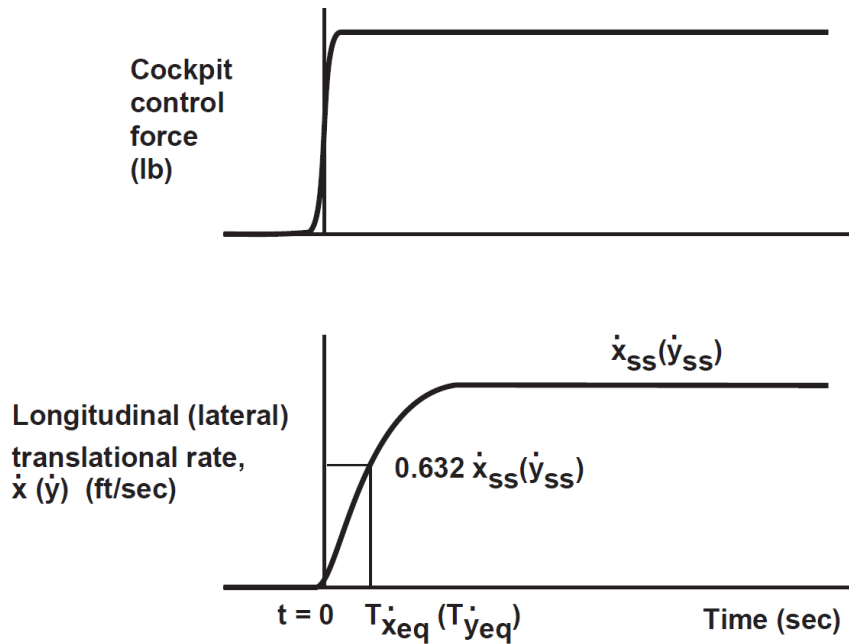


**Figure 4.17:** *Translational Rate Equivalent Risetime (ADS-33E-PRF [12])*

which tilt the rotor plane by cyclic pitch inputs to the main rotor in order to control the translational rate.

However, as can be seen in figure 4.16, the traction variant provides a faster response in the forward direction due to engagement of the forward thrust, but also provides a faster response in the backwards direction, because the powered lift is tilted backwards by default due to the nominal pitch angle of  $\theta_{hvr} = 5$  deg.

According to subsection 3.3.12 in ADS-33E-PRF [12], translational rate response types shall have a first order appearance with an equivalent rise time  $2.5 s \leq T_{\dot{x}_{eq}} (T_{\dot{y}_{eq}}) \leq 5 s$ . Figure 4.17 shows the definition of the equivalent rise time according to [12]. Note that the equivalent rise time is defined as the time for which the translational rate reaches  $63.2\% = 1 - e^{-1}$  of its stationary value.

Since the acceleration of the system might be limited due to restrictions on the maximum allowed attitude, the translational rate response might show nonlinear characteristics for high-amplitude commands and hence yield a varying equivalent rise time dependent on the input amplitude in the command channel.

A discussion on how saturations influence the equivalent bandwidth (and hence equivalent rise time) is made in subsection 5.2.2 and the insights can be used analogously to determine feasible values for the translational acceleration limits for  $\dot{V}_{C_{x,c}}$  and  $\dot{V}_{C_{y,c}}$  in (4.58) and (4.51) and for the corresponding gains of the velocity loop  $\frac{\omega_x}{2d_x}$  and  $\frac{\omega_y}{2d_y}$  respectively, such as to comply with the equivalent rise time requirements from [12].

#### 4.4.1.2 Yaw Control

For the yaw control during hover, two exemplary test cases are considered. Subsection 3.3.6 in ADS-33E-PRF [12] defines requirements for moderate-amplitude heading changes. The corresponding maneuver consists of rapidly changing the heading from one steady state to another and determining the handling qualities based on the ratio of peak yaw rate to change in heading [12].

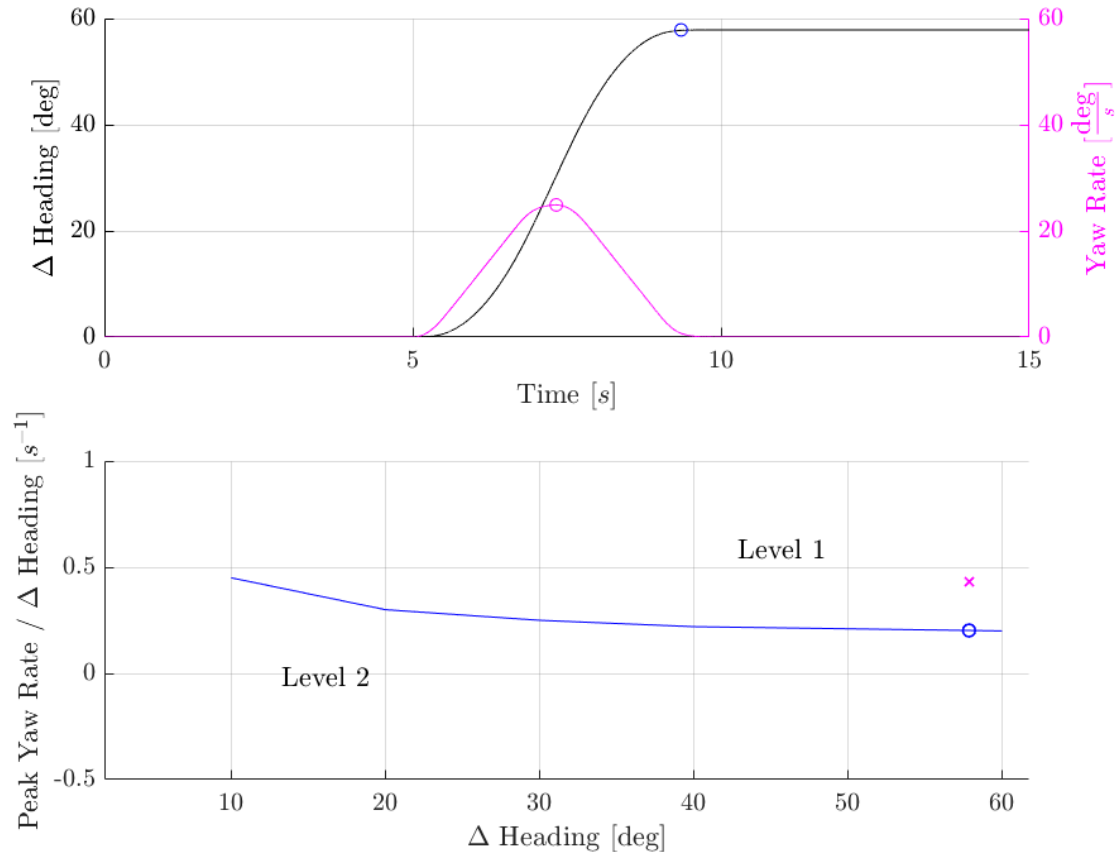


**Figure 4.18:** *Moderate-Amplitude Heading Changes (Attitude Quickness)*

Figure 4.18 shows the evaluation for the exemplary DRM maneuver and the handling quality level the response is classified as. Due to the limited yaw authority of typical VTOL configurations compared to conventional rotorcraft, insights on the extent to which yaw requirements can be satisfied with a proposed kinetic set up are useful for specification of the required powered lift system and its integration into the airframe (regarding lever arms or required tilt angles of the individual lifting motors to increase yaw authority).

Especially the requirements for lateral gust stability during hover flight represent a challenge for VTOL aircraft due to the increased sensitivity to wind that results from the aerodynamic surfaces needed for wingborne flight. ADS-33E-PRF [12] defines in subsection 3.3.7.1 the required yaw rate response to lateral gusts of up to 25 knots (12.86 meters per second) from the most critical direction and states that the peak yaw rate

within the first three seconds following the lateral gust shall not exceed  $0.30 \frac{\text{deg}}{\text{s}}$  ( $1.00 \frac{\text{deg}}{\text{s}}$  for Level 2) for every  $1 \frac{\text{ft}}{\text{s}} \approx 0.305 \frac{\text{m}}{\text{s}}$  of gust velocity. This requirement shall hold “in the presence of steady wind of up to 25 knots from the most critical direction” [12, p. 12].

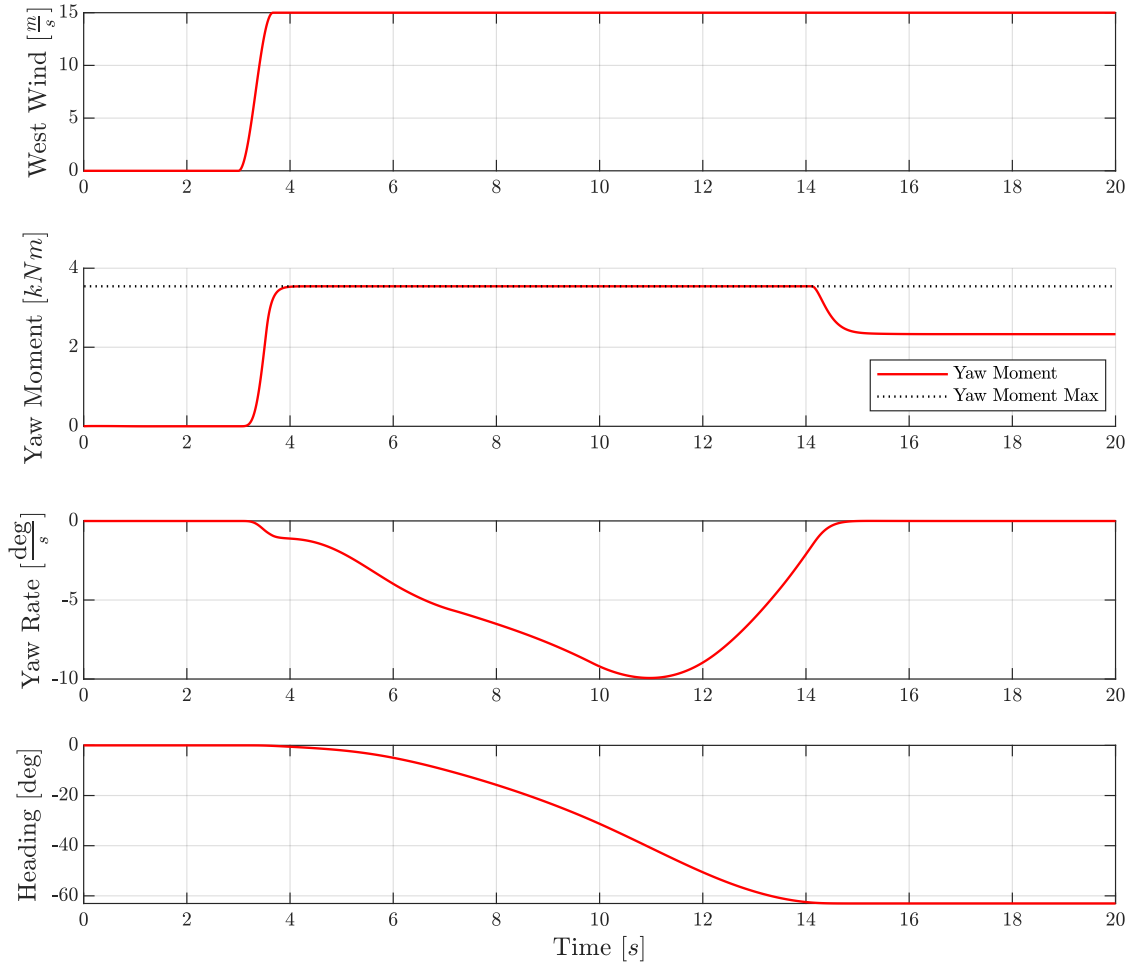


**Figure 4.19:** *Lateral Wind Gust During Hover Flight*

Figure 4.19 shows a DRM simulation for a lateral and continuous wind gust of  $15 \frac{m}{s}$  coming from west while the VTOL is hovering in place. The exemplary choice of limited yaw authority coupled with a significant aerodynamic yaw moment yields a saturated response in the yaw channel. After the gust arrives at  $t = 3$  s from the left side, the system counters the negative aerodynamic moment produced by the rudder with a positive control yaw moment. Note that although the rudder is not modeled explicitly within the DRM, its effect on the overall kinetic characteristics can be considered according to (4.138) and (4.139).

After the available control moment in the yaw channel is exhausted, the VTOL rotates counterclockwise (as seen from above) into the wind, following its natural weathercock stability. As soon as it reaches a heading of around -60 degrees, the wind is sufficiently aligned with the aircraft, such that the aerodynamic yaw moment can be compensated

by the available control authority.

For this particular case, the VTOL would not be able to hold its heading in the presence of significant steady state lateral winds. In general, the requirement to hold the heading during wind conditions has to be validated in the context of the overall mission profile of the VTOL aircraft.

#### 4.4.2 Transition and Wingborne Flight

In this subsection a complete mission is simulated with the DRM in order to validate the overall behavioral concept and the proposed control approach. Figure 4.20 shows the exemplary mission, which starts with a hover phase followed by acceleration into the transition phase and further into the wingborne phase and finally deceleration back into the transition phase and hover phase.

The first plot shows the indicated airspeed in red and the commands of the transition and wingborne mode in blue. Note that although the airspeed command is also indicated during the hover phase, kinematic translational rate control is active instead as discussed in the previous subsection. The horizontal blue dotted line indicates the indicated margin stall airspeed  $V_{\text{stall,p}}$  from (4.16) and represents the target airspeed for transition and retransition.

The second plot shows the height rate in red and the height rate command in blue. Note that the climb is performed with a constant maximum vertical acceleration during the wingborne phase according to (4.98) and that the stick command did not correspond to a maximum pull of the right stick for which the airspeed would be traded in for climb rate as discussed in subsection 4.2.3.3.

The third plot shows the angle of attack in red and the stall angle of attack as black dotted line. While horizontally accelerating in the hover phase, the angle of attack converges to  $\alpha = \theta_{\text{hvr}} = 5$  deg, since the traction variant discussed in subsection 4.3.1 is chosen for this maneuver. After entering the transition phase at a forward velocity of  $V_{\text{hover}} = 10 \frac{m}{s}$ , the angle of attack follows the regime from figure 4.7 along the blue line, corresponding to a full push of the left stick. During the (re)transition phase after the wingborne phase, the angle of attack follows the red line in figure 4.7 corresponding to a full pull of the left stick until  $t = 100$  s. For  $t > 100$  s, the left stick is released into the spring-centered neutral position ( $d_{Sx} = 0$ ) and hence the angle of attack is governed by the green line in figure 4.7. The corresponding commanded airspeed is  $V_{\text{CAS,d}} = 0$  according to figure 4.7.

The fourth plot shows the heading rate in red and the heading rate command in blue. Furthermore, the roll angle is also indicated as dotted magenta line, since demands in heading rate during the transition and wingborne phase are transformed into the corresponding roll angle demands according to (4.26).

The last two plots of figure 4.20 show the used powered lift and thrust force during the mission. During the transition phase that follows the hover phase, the powered lift

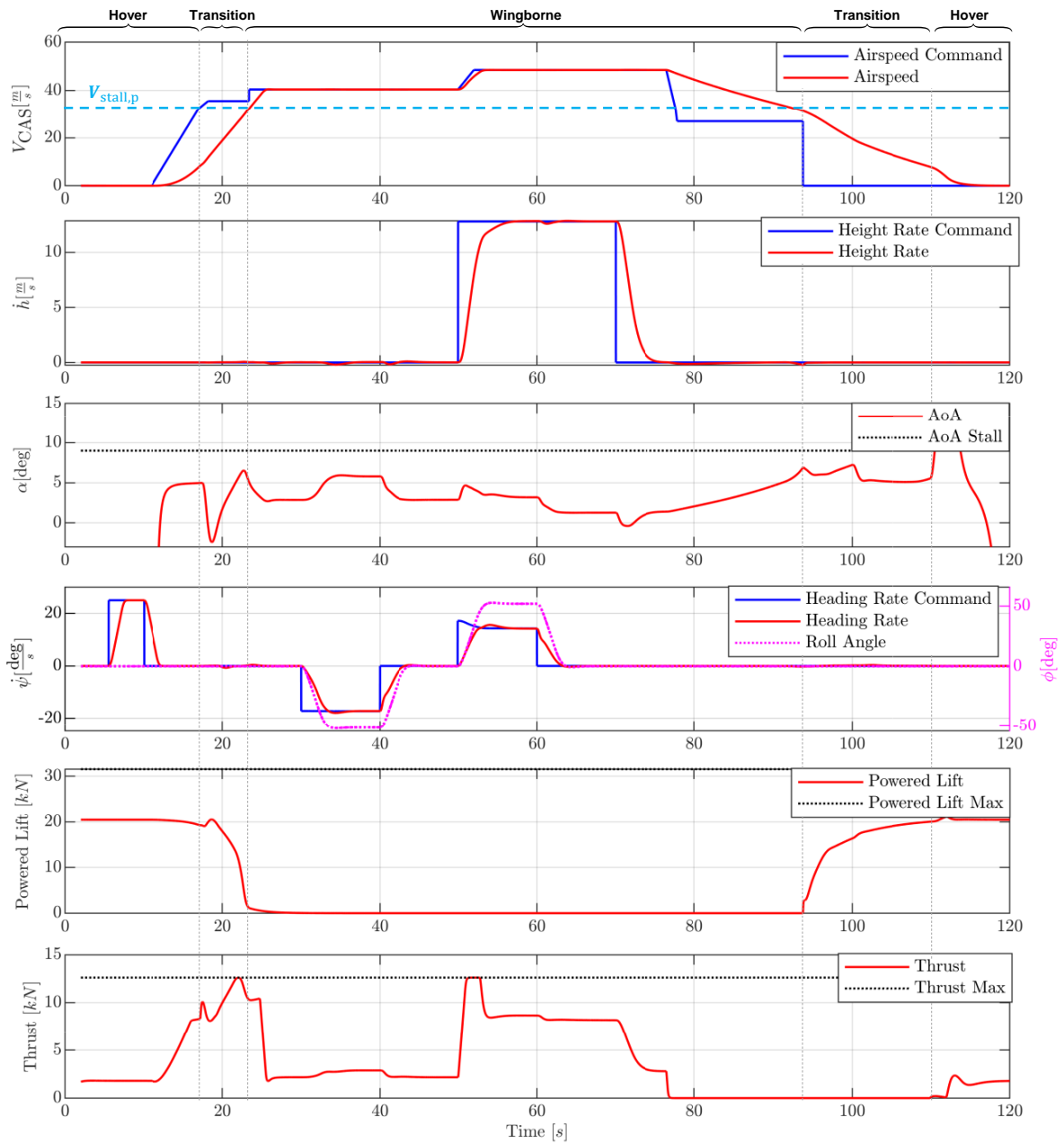


**Figure 4.20:** Complete Transition and Retransition Maneuver of DRM

demand is decreasing as the airspeed and angle of attack are gradually increasing. After entering the wingborne phase, the powered lift is gradually reduced according to (4.94) and stays at its minimum level throughout the wingborne phase.

#### 4.4.3 Pilot-in-the-Loop Simulation <sup>1</sup>

As already mentioned in the beginning of this chapter, EASA has recently published the Proposed Means of Compliance with the Special Condition VTOL [33], in which they

state that applicable validation activities for the flight control functions include piloted real-time simulation.

Testing the proposed behavior and control concept directly in terms of use case simulations represents a very effective way of validation, since it enables direct statements about the handling and general operation of the VTOL aircraft and does not rely on inferred statements based on existing requirements or metrics that might not be suitable or complete for VTOL operation.

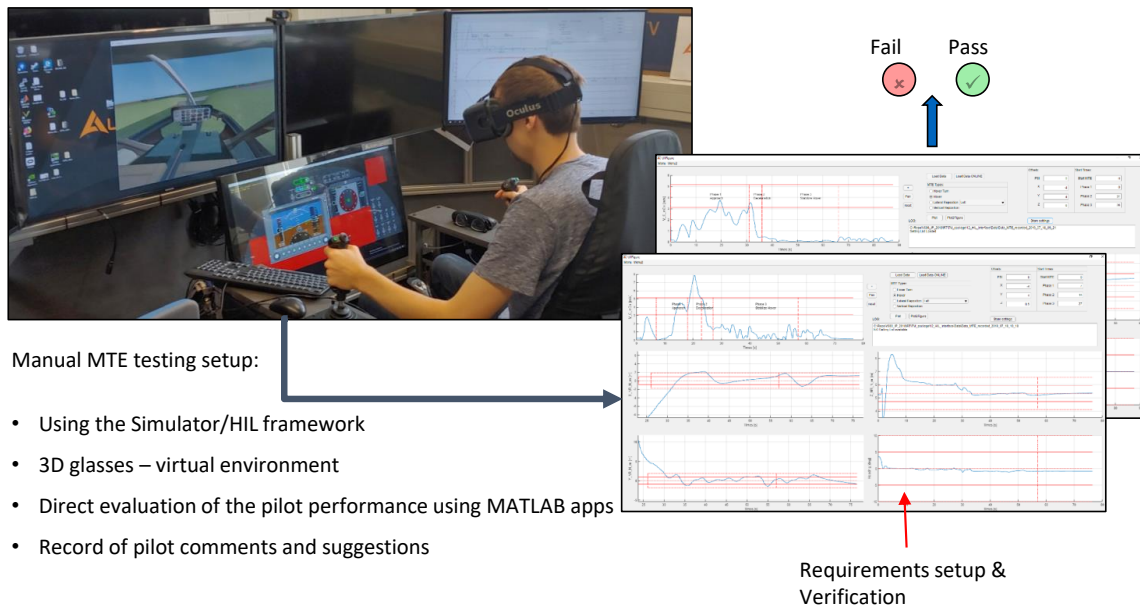


**Figure 4.21:** *Pilot-in-the-Loop Simulation*



**Figure 4.22:** *Mission Task Elements*

Figure 4.21 shows the test setup with the DRM running in real-time on a desktop PC. The two control inceptors are read out via Matlab Simulink [78] and the corresponding

response of the DRM is visualized in a virtual environment. Additionally, the integration of a virtual-reality headset supports immersion and improves the perceived experience during testing.

Possible test scenarios include performing exemplary missions or conducting Mission Task Elements (MTEs), which are defined in [12]. Figure 4.22 shows the virtual set up of the mission tasks described in 3.11.1 and 3.11.8 in ADS-33E-PRF [12], where the former is used to “check [the] ability to transition from translating flight to a stabilized hover with precision and a reasonable amount of aggressiveness” [12, p. 27] and the latter one is used to “check roll axis and heave axis handling qualities during moderately aggressive maneuvering” [12, p. 34].

After completion of the mission tasks, pilots or operators use a Cooper-Harper rating scale to evaluate the handling qualities based on a set of criteria.

---

<sup>1</sup>prepublished in [1]



# 5

## Control Architecture Specification

The second step in the system-theoretic driven development approach deals with the control architecture design for the VTOL transition aircraft. After having derived, modeled, and validated the behavioral specification in chapter 4, the goal of this chapter is to derive the necessary control architecture that will realize the specified behavior in the functional context of the overall system.

According to [3, p. 157], “the term *architecture* denotes (...) the allocation of functions to the elements of a structure. Thus the architecture of a system can be seen as a kind of solution principle.”

In the scope of the systems engineering landscape, the control architecture can be interpreted as the requirement specification of the control components’ target behavior and their interactions. Thereby, the control system and subsystem boundaries are chosen such that the resulting information flow reflects the functional interfaces of the final controller with respect to other functional components. In the context of this thesis, the controller boundaries include the functional chain from the incoming sensor and pilot interface signals on the input side to the command signals of available force and moment producers and indication signals for the human-machine interface on the output side.

As a consequence, the design of the control architecture must account for the functional topology of the VTOL aircraft and the subsystems it is interacting with. More particularly, the choice of available sensors, control inceptors, and control effectors as well as their functional interfaces have a direct influence on the control architecture design.

In addition to realizing the behavioral specification, the design of the control architecture should account for the general design principles that are mentioned in [3], such as modularity, independence, piecemeal engineering, and decentralization. Furthermore, additional emerging properties like safety and robustness have to be accounted for as well.

In section 5.1 the underlying control theory for Incremental Nonlinear Dynamic Inversion [42] [43] [44] [45] [46] is briefly introduced and put into the context of this thesis in order to derive the control strategy for the most inner control loop. The outer control loops follow from a cascaded nonlinear dynamic inversion approach and have for the most part been derived in section 4.3.

The reason for the cascaded control approach directly follows from the requirements of modularity, independence, and decentralization for the control architecture, since a complete inversion of the dynamics from the high-level control variables to the control effectors would yield a highly complex and interdependent structure, which increases the difficulty of developing and testing the control law later on.

Section 5.2 discusses the challenges of current limits and high-inertia propellers in the context of RPM-controlled electrical motors. To this end, design guidelines for gain and saturation parameters of an exemplary attitude stabilization loop are presented, which are aimed at providing the maximum outer-loop bandwidth response and which are derived based on the equivalent first order step response of the rate-saturated inner loop.

In section 5.3 the *Control Architecture Specification Model* (CASM) is introduced, which represents an executable model of the control architecture's functional specification. Note that in contrast to the Design Reference Model from section 4.3, the CASM only is a representation of the control architecture and does not represent an abstraction of the complete system. Instead, it emerges from the DRM through concretizing and decomposing the control structure of the DRM (left side of figure 4.11) and decoupling it from the overall aircraft and environment model (right side of figure 4.11).

Subsequent testing activities are then presented in section 5.4, which deals with simulation of the CASM in the loop with an aircraft model that provides the necessary functional interfaces in terms of sensors and control effectors and enables verification and validation of the proposed control architecture.

## 5.1 Principles of Incremental Nonlinear Dynamic Inversion

This section aims to derive the basic principles of Incremental Nonlinear Dynamic Inversion (INDI) by means of a systems engineering point of view using the example of rotational acceleration control. For a thorough theoretical discussion of INDI, the reader may refer to [42] [43] [44].

The overall objective of an inversion control law is to yield desired dynamics for some system's state by explicitly canceling and replacing the system's inherent (usually non-linear) dynamic relationships by means of a numerical model of the system [42] [43] [44]. The standard Nonlinear Dynamic Inversion (NDI) approach assumes absolute control (instead of rate or incremental control) of the available force and moments producers and hence requires detailed knowledge about the underlying kinetic characteristics of the aircraft, which might include complicated aerodynamic relationships. As a consequence, NDI control is known to be very sensitive to model uncertainties [44].

One possible way to deal with uncertainties is the use of Incremental Nonlinear Dynamic Inversion (INDI), which can be seen as an extension of NDI in which the inputs to the control effectors result from an incremental allocation approach by means of lin-

earizing the relationships on the force and moment level. As a consequence, the resulting control regime becomes substantially less dependent on extensive knowledge about the model and hence more robust. At the same time, high-bandwidth feedback of the system's accelerations becomes necessary, which creates additional requirements for filter design and aggravates the influence of sensor delays [43].

An alternative derivation of the 'incremental' concept of INDI can be found in [46], which is also used in the scope of this thesis. Therein, an extended INDI approach is introduced, which renders the discrete nature of the original incremental expression into a time-continuous one.

A complete inversion of the high-level control variables discussed in section 4.2 is theoretically possible, however the resulting strategy would yield a high-order, non-modular, and very complicated control law, which would tremendously increase the effort of developing and testing the proposed strategy later on. Instead, a modular, independent, and decentralized design of the control law is chosen in terms of a cascaded structure, as was introduced in section 4.3 and as adheres to the design principles for good system architectures in [3].

For the control of the rotational accelerations, longitudinal specific force, and height rate the INDI strategy will be used and is briefly derived in the following using the rotational acceleration tracking task as an example. The complete control architecture is however discussed in detail in section 5.3.

The derivation in the following is motivated by stating the objectives of the control loop first and working backwards towards the final control law, thereby adopting the central paradigms of systems engineering. In the context of the overall control strategy, the outer loop commands a rotational acceleration  $(\dot{\omega}_c^{IB})_B^B$  as in e.g. (4.122). Subscripts and superscripts denoting coordinate frames are left out in the following for better readability.

Based on the rotational acceleration command  $\dot{\omega}_c$  a specification for the desired rotational acceleration dynamics can be formulated in terms of a so called reference model, which represents the desired reference dynamics  $\dot{\omega}_r$  of the system. Introduction of a reference model not only enables explicit modeling of the specified behavior, which acts as the tracking target for the error controller and which could also be used in the context of functional monitoring, but also enables the generation of feedforward control signals. In general, this approach allows to separate the command input response and the stability characteristics of the closed-loop controlled system and hence provides a greater flexibility in fulfilling handling quality and stability requirements.

Depending on the scope of the reference model, the dynamics can be represented in a nonlinear and integrated manner as in [79] [80]. However, in the context of describing the rotational acceleration dynamics, a simpler saturated first-order model is used:

$$\ddot{\omega}_r = \min \left( \ddot{\omega}_{r,\max}, \max \left( \ddot{\omega}_{r,\min}, \mathbf{K}_{\dot{\omega}_r} (\dot{\omega}_c - \dot{\omega}_r) \right) \right), \quad (5.1)$$

where  $\ddot{\omega}_{r,\max}$  and  $\ddot{\omega}_{r,\min}$  denote the upper and lower reference rotational jerk limit respectively and  $\mathbf{K}_{\dot{\omega}_r}$  is the bandwidth matrix of the reference rotational acceleration dynamics.

The overall objective for the derivation of the INDI control law is to yield stable dynamics for the tracking error

$$\mathbf{e} = \dot{\boldsymbol{\omega}}_r - \dot{\boldsymbol{\omega}}, \quad (5.2)$$

which is defined as the difference between the reference rotational acceleration  $\dot{\boldsymbol{\omega}}_r$  and the real (or estimated) rotational acceleration  $\dot{\boldsymbol{\omega}}$ .

The target error dynamics is furthermore given by

$$\dot{\mathbf{e}} = -\mathbf{K}_e \mathbf{e} = -\mathbf{K}_e (\dot{\boldsymbol{\omega}}_r - \dot{\boldsymbol{\omega}}), \quad (5.3)$$

where  $\mathbf{K}_e$  denotes the error gain matrix and yields the desired tracking error bandwidth for each channel.

Note that due to separation of reference bandwidth  $\mathbf{K}_{\dot{\boldsymbol{\omega}}_r}$  and error bandwidth  $\mathbf{K}_e$ , the control design has an additional degree of freedom to increase performance and stability of the closed-loop system.

The rotational acceleration of the system follows from Euler's rotational equations of motion (4.144) and yields

$$\dot{\boldsymbol{\omega}} = \mathbf{I}^{-1} \mathbf{M}^G - \mathbf{I}^{-1} (\boldsymbol{\omega} \times \mathbf{I} \boldsymbol{\omega}), \quad (5.4)$$

where the indices denoting coordinate frames have been dropped for better readability.

The moments around the center of gravity  $\mathbf{M}^G$  are the result of external aerodynamic moments and the control moments that are generated by the control effectors. In the scope of this derivation only the powered lift system is considered, but the derivation for the control surfaces follows analogously.

It is furthermore assumed that the moments can be expressed in a control input-affine structure

$$\mathbf{M}^G = \mathbf{f}(\mathbf{x}) + \mathbf{G}(\mathbf{x})\mathbf{u}, \quad (5.5)$$

where  $\mathbf{x}$  is representative of the system's state and  $\mathbf{u}$  is the control input vector.

In the context of propeller generated forces, the control input vector can be expressed as  $\mathbf{u} = [w_1^2 \ w_2^2 \ \dots \ w_m^2]^T$ , where  $w_i$  denotes the rotational rate of the  $i$ 'th out of  $m$  propellers [81] [82]. This representation enables the input-affine structure in (5.5), since the control forces generated by the propellers are approximately proportional to the squared rotor speeds and hence the resulting dynamic pressure at the rotor blade [83] [84].

Before a control strategy can be derived, the functional interface to the control effectors has to be clarified. It is assumed that the motors of the powered lift system are controlled with an electronic speed controller (ESC), which controls the rotational speed of the propeller  $w_i$  given some target rotational speed  $w_{c,i}$ . In the context of the extended INDI approach [46], the control effector dynamics can be approximated by a first-order relationship

$$\dot{w}_i = \min(\dot{w}_{\max,i}, \max(\dot{w}_{\min,i}, K_w (w_{c,i} - w_i))) , \quad (5.6)$$

where  $\dot{w}_{\max,i}$  and  $\dot{w}_{\min,i}$  denote the maximum and minimum control effector rate and  $K_w$  is the bandwidth of the closed-loop controlled control effector. For an exemplary derivation of the motor dynamics, refer to subsection 5.2.5.

Inserting (5.4) into the target error dynamics (5.3) and using (4.124) yields

$$\ddot{\omega} = \mathbf{I}^{-1} \frac{d}{dt} (\mathbf{M}^G) - \mathbf{I}^{-1} (\boldsymbol{\omega} \times \mathbf{I} \dot{\boldsymbol{\omega}} + \dot{\boldsymbol{\omega}} \times \mathbf{I} \boldsymbol{\omega}) \stackrel{!}{=} \ddot{\omega}_r + \mathbf{K}_e (\dot{\omega}_r - \dot{\boldsymbol{\omega}}), \quad (5.7)$$

with  $\ddot{\omega}_r$  from (5.1).

Furthermore, solving for the specific moment rate  $\mathbf{I}^{-1} \frac{d}{dt} (\mathbf{M}^G) = \dot{\mathbf{m}}^G$  yields a similar relationship as in (4.126):

$$\dot{\mathbf{m}}^G \stackrel{!}{=} \ddot{\omega}_r + \mathbf{K}_e (\dot{\omega}_r - \dot{\boldsymbol{\omega}}) + \mathbf{I}^{-1} (\boldsymbol{\omega} \times \mathbf{I} \dot{\boldsymbol{\omega}} + \dot{\boldsymbol{\omega}} \times \mathbf{I} \boldsymbol{\omega}). \quad (5.8)$$

In (5.8) the pure feedback control part from (4.126) is replaced with the feedforward and feedback structure  $\ddot{\omega}_r + \mathbf{K}_e (\dot{\omega}_r - \dot{\boldsymbol{\omega}})$  using the reference dynamics.

In contrast to section 4.3, which yielded a system-architecture-agnostic representation of the aircraft, the functional output of the INDI control structure is on the level of the control effector commands  $w_{c,i}$ . Hence, the relationship (5.5) is used to yield the dynamics of the specific moment rate

$$\dot{\mathbf{m}}^G = \mathbf{I}^{-1} \frac{\partial \mathbf{f}}{\partial \mathbf{x}} \dot{\mathbf{x}} + \mathbf{I}^{-1} \dot{\mathbf{G}}(\mathbf{x}) \mathbf{u} + \underbrace{\mathbf{I}^{-1} \mathbf{G}(\mathbf{x})}_{\mathbf{B}_m} \dot{\mathbf{u}}, \quad (5.9)$$

where  $\dot{\mathbf{u}} = [2w_1\dot{w}_1 \quad 2w_2\dot{w}_2 \quad \dots \quad 2w_m\dot{w}_m]^T$  contains the control effector rates and  $\mathbf{B}_m$  denotes the control effectiveness matrix with respect to the specific moment rate.

From (5.9) and (5.8) follows

$$\mathbf{B}_m \dot{\mathbf{u}} = \ddot{\omega}_r + \mathbf{K}_e (\dot{\omega}_r - \dot{\boldsymbol{\omega}}) + \underbrace{\mathbf{I}^{-1} (\boldsymbol{\omega} \times \mathbf{I} \dot{\boldsymbol{\omega}} + \dot{\boldsymbol{\omega}} \times \mathbf{I} \boldsymbol{\omega}) - \mathbf{I}^{-1} \frac{\partial \mathbf{f}}{\partial \mathbf{x}} \dot{\mathbf{x}} - \mathbf{I}^{-1} \dot{\mathbf{G}}(\mathbf{x}) \mathbf{u}}_{\mathbf{a}(\dot{\mathbf{x}})}. \quad (5.10)$$

Note that the underlying assumption for INDI states that the state dynamics  $\dot{\mathbf{x}}$  are much slower than the control effector dynamics  $\dot{\mathbf{u}}$  [43] [85] [86] [87] [46] and hence the term  $\mathbf{a}(\dot{\mathbf{x}})$  in (5.10) is usually neglected, which is why incremental control yields a rather model-independent control strategy. However, if reasonable assumptions can be made about (some of) the terms in  $\mathbf{a}(\dot{\mathbf{x}})$ , the performance of the control-loop can be even increased [86]. For instance, neglecting the term  $\mathbf{I}^{-1} \frac{\partial \mathbf{f}}{\partial \mathbf{x}} \dot{\mathbf{x}}$  will decrease the effective bandwidth of the inner loop, as it contains the natural aerodynamic damping terms of the aircraft.

Although in the context of a complete inner loop control law the specific force tracking has to be derived as well, it is not further considered in the scope of this derivation. Additionally, it is assumed that the control effectiveness matrix  $\mathbf{B}_m$  can be uniquely inverted to  $\mathbf{B}_m^{-1}$ . In section 5.3 a more general discussion of the inner loop and control allocation strategy with redundant actuation is presented.

From (5.10) follows the desired rate of the squared motor speeds

$$\dot{\mathbf{u}}_d = \mathbf{B}_m^{-1} (\ddot{\mathbf{w}}_r + \mathbf{K}_e (\dot{\mathbf{w}}_r - \dot{\mathbf{w}})) , \quad (5.11)$$

where  $\mathbf{a}(\dot{\mathbf{x}})$  is neglected as stated above.

It follows from  $\dot{u}_i = 2w_i\dot{w}_i$  that

$$\dot{\mathbf{u}}_d = 2 \underbrace{\text{diag}(w_1, w_2, \dots, w_m)}_{\mathbf{W}} \dot{\mathbf{w}}_d \quad (5.12)$$

and hence the commanded control effector rate vector  $\dot{\mathbf{w}}_c = [\dot{w}_{c,1} \ \dot{w}_{c,2} \ \dots \ \dot{w}_{c,m}]^T$  follows from solving (5.12) for  $\dot{\mathbf{w}}_d$  and saturating it according to  $\dot{\mathbf{w}}_{\max} = [\dot{w}_{1,\max} \ \dot{w}_{2,\max} \ \dots \ \dot{w}_{m,\max}]^T$  and  $\dot{\mathbf{w}}_{\min} = [\dot{w}_{1,\min} \ \dot{w}_{2,\min} \ \dots \ \dot{w}_{m,\min}]^T$ :

$$\dot{\mathbf{w}}_c = \min \left( \dot{\mathbf{w}}_{\max}, \max \left( \dot{\mathbf{w}}_{\min}, \frac{1}{2} \mathbf{W}^{-1} \dot{\mathbf{u}}_d \right) \right) . \quad (5.13)$$

In (5.13) the rotational speed  $w_i$  of each motor is saturated from below such that  $\mathbf{W}$  remains non-singular. The singularity for  $w_i = 0$  results from the quadratic relationship between the motor speed and the resulting thrust force [83] [84] and leads to vanishing gradients for zero motor speeds.

Inverting the control effector dynamics (5.6) and using (5.13) yields the final incremental control law

$$\mathbf{w}_c = \mathbf{w} + K_w^{-1} \dot{\mathbf{w}}_c , \quad (5.14)$$

where  $\mathbf{w}_c$  denotes the motor speed command vector and  $\mathbf{w}$  is the vector of the current motor speeds.

Note that when the reference dynamic parameters and error gains are chosen appropriately – such that the demands to the motors do not exceed the saturation limits – the command from (5.14) yields the specified error dynamics from (5.3) under the previously mentioned assumptions.

In the following section 5.2 the effect of motor limits is discussed and a heuristic for choosing the inner-loop parameters is chosen (**contribution C.5**). The general control architecture around the INDI philosophy is then derived and discussed in section 5.3.

## 5.2 On Considering Control Effector Limitations

### 5.2.1 Motivation

Closed-loop control of an aerial system's rigid-body dynamics inevitably involves the use of force and moment producers such as aerodynamic control effectors or propellers driven by brushless electric motors. When it comes to stability and performance of these closed-loop controlled systems, control effector limitations play a crucial role. Typically, those limitations are the consequence of physical and technical constraints on the control

effector design or on the system they are integrated in. A typical example is the electric current through a brushless motor that is purposely limited, in order to avoid extensive heat build-up and hence avoid damage of the underlying components [88] [89].

With increasing size and mass of electrical VTOLs, the thrust demand for these systems increases as well, ultimately leading to requirements for larger propellers. When geometrically scaling up a system by a factor of  $s$ , the mass and inertia of that system approximately scale according to  $m \propto s^3$  and  $I \propto s^5$  respectively [90].

In order to achieve comparable performance, it might be desired to maintain the achievable translational and rotational acceleration capabilities of the scaled system. The therefor required thrust force  $T_p$  as well as aerodynamic drag produced by a propeller is – for constant tip speeds – proportional to its squared diameter [84], i.e.:  $T_p \propto D_p^2$ . Furthermore, the inertia  $I_p$  of a propeller scales with its diameter according to  $I_p \propto D_p^{n_p}$ , where  $n_p \approx 4$  accounts for allometric scaling of the propeller [91] [92] [93]. When opting for a constant thrust-to-weight ratio, it follows that

$$m \propto T_p \propto D_p^2 \propto I_p^{\frac{2}{n_p}} \quad (5.15)$$

and hence that the inertia  $I_p$  of the propeller approximately scales with the overall mass  $m$  of the system according to

$$I_p \propto m^{\frac{n_p}{2}} \approx m^2. \quad (5.16)$$

Furthermore, the demand for equal rotational acceleration capability for the scaled system requires even higher thrust forces, in order to keep the ratio of produced moment  $l \times T_p$  and overall system inertia  $I$  constant. Thereby,  $l$  represents a characteristic measure of the lever arm, which scales with the system accordingly. Hence, given the proportionalities  $I \propto s^5$ ,  $m \propto s^3$ , and  $l \propto s$ , it follows for a constant moment-to-inertia ratio

$$I \propto l \times T_p \rightarrow \frac{I}{l} \propto m^{\frac{4}{3}} \propto T_p \propto D_p^2 \propto I_p^{\frac{2}{n_p}}. \quad (5.17)$$

Analogously, it follows for the propeller inertia of the scaled system with equal rotational acceleration capabilities:

$$I_p \propto m^{\frac{2n_p}{3}} \approx m^{\frac{8}{3}}. \quad (5.18)$$

Hence, propeller inertia scales at least quadratically with the overall vehicle mass, leading to an over-proportional increase of the required electric current for generating the necessary motor torque to accelerate the propellers of a larger system. As a consequence, the electric current limitation of the motor will eventually lead to a saturation of the motor acceleration, especially for large and heavy vehicles. This saturation effect, however, represents a hard nonlinearity within the controlled system, since the obtained bandwidth of the motor becomes highly dependent on the amplitude of the demanded rotational rate of the propeller. When not properly accounted for, these nonlinearities can lead to instability or limit cycle oscillations of the system.

### 5.2.2 Saturation Analysis in Time Domain

In the following, a heuristic approach for deriving a control structure and for obtaining the control loop parameters in the presence of acceleration-limited motors is derived and represents **contribution C.5** of this thesis. This approach shall enable the control designer to intuitively assess the effects of saturated motor acceleration and provides a method for adapting the structure and gains of the loops around the motor. For simplicity, the stabilization of the roll dynamics of a generalized aerial system is considered.

Let the rotational jerk  $\ddot{p}$  of the overall system as response to a rotational acceleration demand  $\dot{p}_c$  be described as

$$\ddot{p} = \min \left( \ddot{p}_{\max}, \max \left( \ddot{p}_{\min}, K_{\dot{p}} (\dot{p}_c - \dot{p}) \right) \right), \quad (5.19)$$

where  $\ddot{p}_{\max}$  and  $\ddot{p}_{\min}$  represent the maximum and minimum rotational jerk that the system can produce (due to motor acceleration limits). As will be shown later, the assumption for constant roll jerk capability is only an approximation but nevertheless provides feasible results. Note that for small-amplitude rotational acceleration demands, (5.19) simplifies to the linear first order system

$$\ddot{p} = K_{\dot{p}} (\dot{p}_c - \dot{p}), \quad (5.20)$$

with  $K_{\dot{p}}$  denoting the gain of the roll acceleration loop, which is equivalent to its bandwidth, i.e exciting the inner loop with (small amplitudes)  $\dot{p}_c$  at (angular) frequency  $K_{\dot{p}}$  leads to an approximately 3dB attenuated response ( $\frac{\sqrt{2}}{2}$ ) in  $\dot{p}$ .

The roll acceleration loop can either be actively controlled in a closed-loop manner (like for INDI) or result from the open-loop command to the motors (like for NDI). In either case, given the motor (squared) rotational speed  $u$ , it can be seen that the roll jerk of the system

$$\ddot{p} = \frac{d}{dt} \dot{p} = \frac{d}{dt} f(u, p) = B\dot{u} + A\dot{p} \quad (5.21)$$

is limited by the maximum and minimum motor acceleration capability  $\dot{u}$ .

Next, consider the task of stabilizing the roll rate  $p$  of the system. If roll jerk limitations were neglected, one could choose the rotational acceleration demand

$$\dot{p}_c = -K_p p, \quad (5.22)$$

which according to (5.20) would lead to the second order dynamics

$$\ddot{p} = K_{\dot{p}} (\dot{p}_c - \dot{p}) = -K_{\dot{p}} \dot{p} - K_{\dot{p}} K_p p. \quad (5.23)$$

For a given (inner-loop) roll acceleration gain  $K_{\dot{p}}$ , the resulting natural frequency  $\omega_0$  and relative damping  $d$  of the roll rate dynamics are a function of the (outer-loop) roll rate gain  $K_p$  and yield

$$\omega_0 = \sqrt{K_{\dot{p}} K_p} \quad d = \frac{1}{2} \sqrt{\frac{K_{\dot{p}}}{K_p}}. \quad (5.24)$$



Furthermore, if the outer-loop gain is chosen as  $K_p = \frac{1}{2}K_{\dot{p}}$ , the resulting natural frequency and relative damping of the unsaturated system (5.20) yield  $\omega_0 = \frac{1}{\sqrt{2}}K_{\dot{p}}$  and  $d = \frac{1}{\sqrt{2}}$  respectively, which minimizes the ITAE (Integral Time Absolute Error) criterion [94].

However, applying this control law to the jerk limited dynamics from (5.19) results in the roll rate responses in figure 5.1, whose damping characteristics deteriorate with increasing initial roll rate  $p(t=0)$ . For small amplitudes in the roll rate, the resulting roll acceleration demand (5.22) does not lead to a saturated jerk and hence the roll acceleration loop maintains its bandwidth  $K_{\dot{p}}$ . In contrast, large amplitudes in  $\dot{p}_c$  lead to a saturated roll jerk (due to motor limitations) and therefore decrease the effective bandwidth of the inner loop.

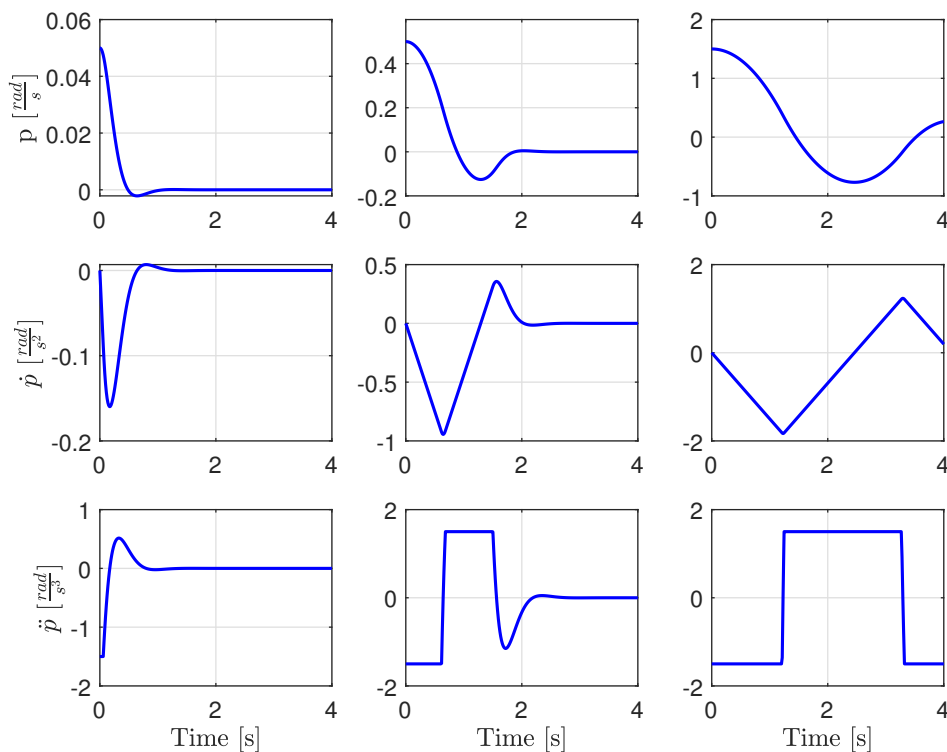


**Figure 5.1:** *Roll Rate Response for Different Amplitudes*

### 5.2.3 Effective Inner-Loop Bandwidth

For the sake of addressing the nonlinearity introduced by saturated jerk dynamics, let the effective bandwidth of the inner loop be defined in terms of its rise time as

$$K_{\dot{p},\text{eff}} = \frac{3}{T_{95}}, \quad (5.25)$$

where  $T_{95}$  denotes the time after which the roll acceleration  $\dot{p}$  reaches  $(1 - e^{-3}) \approx 95\%$  of the constant demand  $\dot{p}_c$  (starting at zero).

Note that for the unsaturated linear dynamics (5.20) (i.e. for small demands  $\dot{p}_c$ ), the time response of the roll acceleration to a constant demand  $\dot{p}(t) = (1 - e^{-K\dot{p}t})\dot{p}_c$  yields an effective inner-loop bandwidth of

$$K_{\dot{p},\text{eff,unsat}} = K_{\dot{p}}. \quad (5.26)$$

In order to approximate the effective bandwidth for large demands, the roll jerk is assumed to be at its limit during the overall step time, which yields the approximate surrogate dynamics

$$\ddot{p} = \text{sign}(\dot{p}_c - \dot{p})\ddot{p}_{\text{sat}}, \quad (5.27)$$

with  $\ddot{p}_{\text{sat}} = \min(|\ddot{p}_{\text{max}}|, |\ddot{p}_{\text{min}}|)$  being a conservative choice for the maximum roll jerk. The roll acceleration then reaches  $(1 - e^{-3}) \approx 95\%$  of its demand after  $T_{95,\text{sat}} = \frac{(1-e^{-3})\dot{p}_c}{\ddot{p}_{\text{sat}}}$ . Hence, for large input amplitudes the approximated effective inner-loop bandwidth is given by:

$$K_{\dot{p},\text{eff,sat}} = \frac{3}{T_{95,\text{sat}}} = \frac{3}{(1 - e^{-3})} \frac{\ddot{p}_{\text{sat}}}{\dot{p}_c}. \quad (5.28)$$

Note that the effective inner-loop bandwidth (5.28) is dependent on the input amplitude of the roll acceleration demand  $\dot{p}_c$ , which is a known characteristic of nonlinear systems [95] [96] [97] and is the result of saturated motor acceleration (e.g. due to electric current limitation).

Being able to express the effective inner-loop bandwidth as a function of input amplitude provides a way to guarantee a minimum inner-loop bandwidth when limiting the input. To this end, let the admissible roll acceleration demand be actively limited by  $|\dot{p}_c| \leq \dot{p}_{\text{sat}}$ , resulting in the limited form of (5.22):

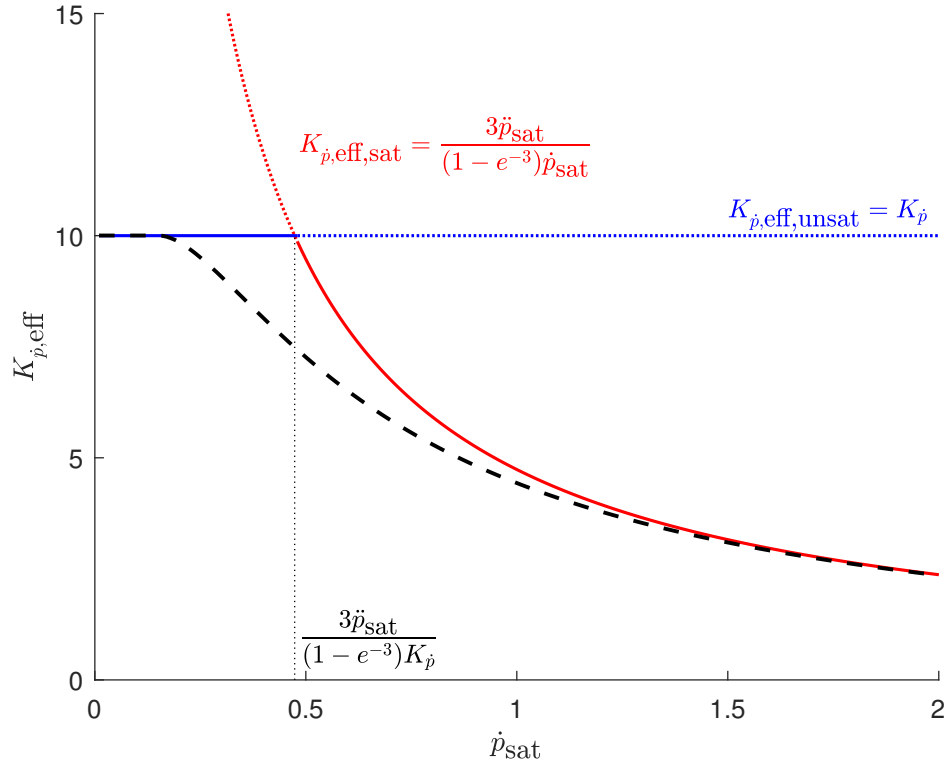
$$\dot{p}_c = \min(\dot{p}_{\text{sat}}, \max(-\dot{p}_{\text{sat}}, -K_p p)). \quad (5.29)$$

Figure 5.2 shows the effective inner-loop bandwidth  $K_{\dot{p},\text{eff}}$  for saturated roll acceleration demands (5.29) as a function of the admissible limit  $\dot{p}_{\text{sat}}$ . The dashed black line represents the numerically calculated effective bandwidth based on (5.25) and determining  $T_{95}$  from the simulated step response of (5.19) with  $\dot{p}_c = \dot{p}_{\text{sat}}$ . The blue and red line represent the approximation of the effective inner-loop bandwidth for small amplitudes (5.26) and large amplitudes (5.28) respectively, with their intersection at

$$\dot{p}_{\text{sat}}^* = \frac{3\ddot{p}_{\text{sat}}}{(1 - e^{-3})K_{\dot{p}}}. \quad (5.30)$$

Hence, the effective inner-loop bandwidth for saturated roll acceleration demands is approximated by the solid portions of the blue and red line and is given by:

$$K_{\dot{p},\text{eff}} = \begin{cases} K_{\dot{p}}, & \text{for } \dot{p}_{\text{sat}} \leq \dot{p}_{\text{sat}}^* \\ \frac{3\ddot{p}_{\text{sat}}}{(1-e^{-3})\dot{p}_{\text{sat}}}, & \text{for } \dot{p}_{\text{sat}} > \dot{p}_{\text{sat}}^* \end{cases}. \quad (5.31)$$



**Figure 5.2:** *Effective Inner-Loop Bandwidth for Saturated Input as a Function of Admissible Roll Acceleration ( $\ddot{p}_{\text{sat}} = 1.5$ ,  $K_{\dot{p}} = 10$ )*

### 5.2.4 Effective Outer-Loop Bandwidth

In a similar fashion, the effective outer-loop bandwidth can be defined based on the time it takes to reach a certain percentage of a stationary roll rate command (or equivalently: the time it takes for an initial roll rate (error) to subside below a certain percentage). To this end, the inner-loop dynamics are approximated by (5.20), where the (guaranteed) effective inner-loop bandwidth  $K_{\dot{p}} = K_{\dot{p},\text{eff}}$  according to (5.31) is assumed in order to account for the saturation effect on jerk level.

Furthermore, consider the limited roll acceleration demand

$$\dot{p}_c = \min(\dot{p}_{\text{sat}}, \max(-\dot{p}_{\text{sat}}, K_p(p_c - p))) \quad (5.32)$$

with  $K_p = \frac{1}{2}K_{\dot{p},\text{eff}}$  according to the ITAE criterion [94]. For commands that do not exceed the admissible roll acceleration limit  $\dot{p}_{\text{sat}}$ , the step response  $p(t)$  to a stationary roll rate command  $p_c$  approximately yields

$$p(t) \approx p_c \left( 1 - e^{-K_p t} \sqrt{2} \sin\left(K_p t + \frac{\pi}{4}\right) \right), \quad (5.33)$$

which reaches  $\left(1 - e^{-2} \sqrt{2} \sin\left(2 + \frac{\pi}{4}\right)\right) \approx 93\%$  of the stationary value after a time of  $T_{93} = \frac{2}{K_p}$ .

Motivated by the analytical second-order step response (5.33), hence, it follows for the definition of the effective outer-loop bandwidth:

$$K_{p,\text{eff}} = \frac{2}{T_{93}}. \quad (5.34)$$

For the case of unsaturated roll acceleration demands, the effective outer-loop bandwidth therefore yields

$$K_{p,\text{eff,unsat}} = \frac{1}{2}K_{\dot{p},\text{eff}}, \quad (5.35)$$

with  $K_{\dot{p},\text{eff}}$  from (5.31).

Note, however, that in the case of saturated roll acceleration demands, the roll dynamics can be approximated by the surrogate dynamics

$$\dot{p} = \text{sign}(p_c - p)\dot{p}_{\text{sat}} \quad (5.36)$$

and yield a rise time for the roll rate of  $T_{93,\text{sat}} = \frac{(1 - e^{-2}\sqrt{2}\sin(2 + \frac{\pi}{4}))p_c}{\dot{p}_{\text{sat}}}$ .

Hence, the effective outer-loop bandwidth for saturated roll acceleration demands is approximated by

$$K_{p,\text{eff,sat}} = \frac{2}{T_{93,\text{sat}}} = \frac{2}{\left(1 - e^{-2}\sqrt{2}\sin\left(2 + \frac{\pi}{4}\right)\right)} \frac{\dot{p}_{\text{sat}}}{p_c}, \quad (5.37)$$

which represents a line whose slope is proportional to  $\frac{1}{p_c}$ .

Figure 5.3 shows the effective outer-loop bandwidth  $K_{p,\text{eff}}$  for three different roll rate commands  $p_c$  in increasing order as a function of the admissible roll acceleration limit  $\dot{p}_{\text{sat}}$ . The dashed black line represents the numerically calculated effective bandwidth based on (5.34) and determining  $T_{93}$  from the simulated step response of (5.19) with  $\dot{p}_c$  according to (5.32). The magenta line represents the approximation of the outer-loop bandwidth for saturated roll acceleration demands according to (5.37) and the blue and red line approximate the outer-loop bandwidth for the case of unsaturated roll acceleration demands as in (5.35).

Note that for increasing roll rate commands  $p_c$ , the slope of the magenta line decreases and its intersection with the blue and red line shifts to the right, eventually in the direction of decreasing outer-loop bandwidth. In fact, for roll rate commands that satisfy

$$|p_c| \leq \frac{12}{\left(1 - e^{-2}\sqrt{2}\sin\left(2 + \frac{\pi}{4}\right)\right)(1 - e^{-3})} \frac{\ddot{p}_{\text{sat}}}{K_{\dot{p}}^2} \quad (5.38)$$

the intersection always happens on the horizontal blue line (which corresponds to  $K_{p,\text{eff}} = \frac{1}{2}K_{\dot{p}}$ ), yielding the range of roll rate commands for which a constant effective outer-loop bandwidth can be achieved. Hence, for roll rate (errors) or roll rate commands that satisfy (5.38), the optimum value for the roll acceleration limit  $\dot{p}_{\text{sat}}$  – that maximizes the effective outer-loop bandwidth – and the corresponding ITAE-optimal outer-loop gain  $K_p$  are given by

$$\dot{p}_{\text{sat,opt}} = \dot{p}_{\text{sat}}^* = \frac{3\ddot{p}_{\text{sat}}}{(1 - e^{-3})K_{\dot{p}}} \quad K_{p,\text{opt}} = \frac{1}{2}K_{\dot{p}}, \quad (5.39)$$

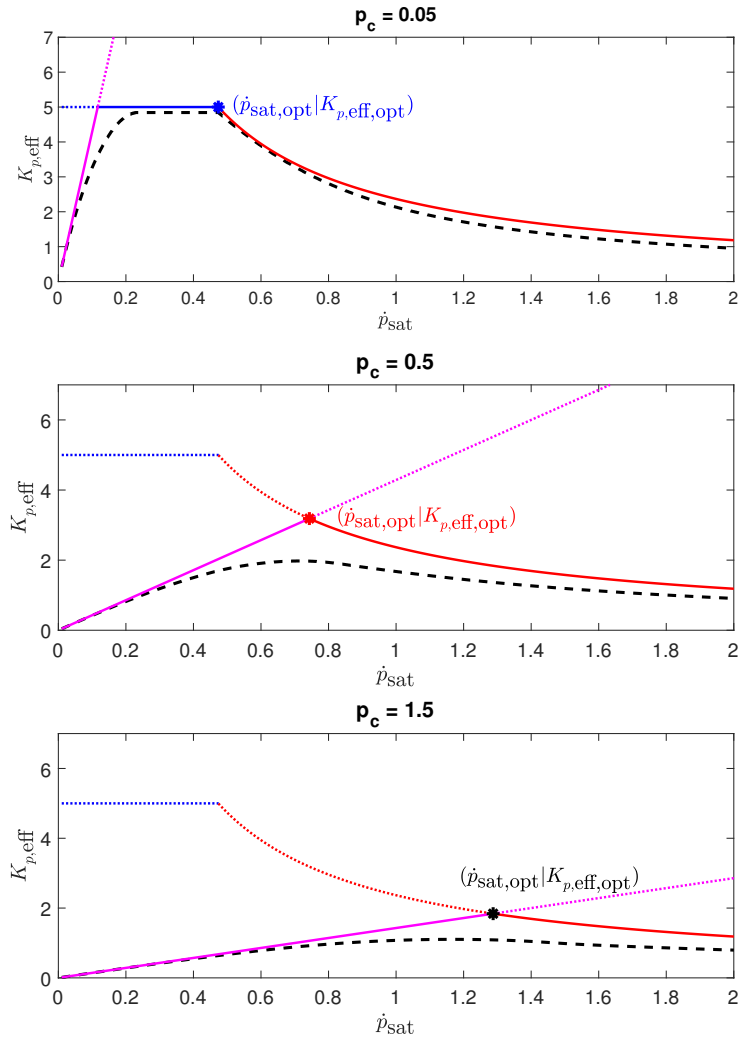


**Figure 5.3:** Effective Outer-Loop Bandwidth as a Function of Admissible Roll Acceleration for Different Command Amplitudes ( $\ddot{p}_{sat} = 1.5$ ,  $K_{\dot{p}} = 10$ )

with  $\dot{p}_{sat}^*$  from (5.30), and correspond to the blue star in the first plot of figure 5.3.

Note that the intersection of the magenta line in the first plot, which corresponds to a roll rate of  $p_c = 0.05$ , yields the same effective outer-loop bandwidth, but a lower admissible roll acceleration  $\dot{p}_{sat}$ . Hence, in order not to sacrifice effective bandwidth for higher roll rates, the optimum value for roll rates satisfying (5.38) is given by the intersection of the magenta line that would correspond to a roll rate of  $p_c = \frac{12}{(1-e^{-2}\sqrt{2}\sin(2+\frac{\pi}{4}))(1-e^{-3})} \frac{\ddot{p}_{sat}}{K_{\dot{p}}^2} \approx 0.203$  (and would pass through the blue star).

For large roll rate amplitudes

$$|p_c| > \frac{12}{(1-e^{-2}\sqrt{2}\sin(2+\frac{\pi}{4}))(1-e^{-3})} \frac{\ddot{p}_{sat}}{K_{\dot{p}}^2}, \quad (5.40)$$

the intersection of the magenta line happens on the descending portion of (5.35), which

corresponds to the second case in (5.31). For these roll rate amplitudes, the optimum values for  $\dot{p}_{\text{sat}}$  and  $K_p$  are given right at the intersection point (since the magenta line is strictly increasing and the red line is strictly decreasing):

$$\begin{aligned} \dot{p}_{\text{sat,opt}} &= \sqrt{\frac{3 \left(1 - e^{-2} \sqrt{2} \sin\left(2 + \frac{\pi}{4}\right)\right)}{4(1 - e^{-3})}} \ddot{p}_{\text{sat}} p_c, \\ K_{p,\text{opt}} &= \sqrt{\frac{3}{\left(1 - e^{-2} \sqrt{2} \sin\left(2 + \frac{\pi}{4}\right)\right) (1 - e^{-3})}} \frac{\ddot{p}_{\text{sat}}}{p_c}. \end{aligned} \quad (5.41)$$

Examples for (5.40) can be seen in the second and third plot of figure 5.3, corresponding to roll rates of  $p_c = 0.5$  and  $p_c = 1.5$  respectively. The optimum values at the intersection are marked with a red and black star.

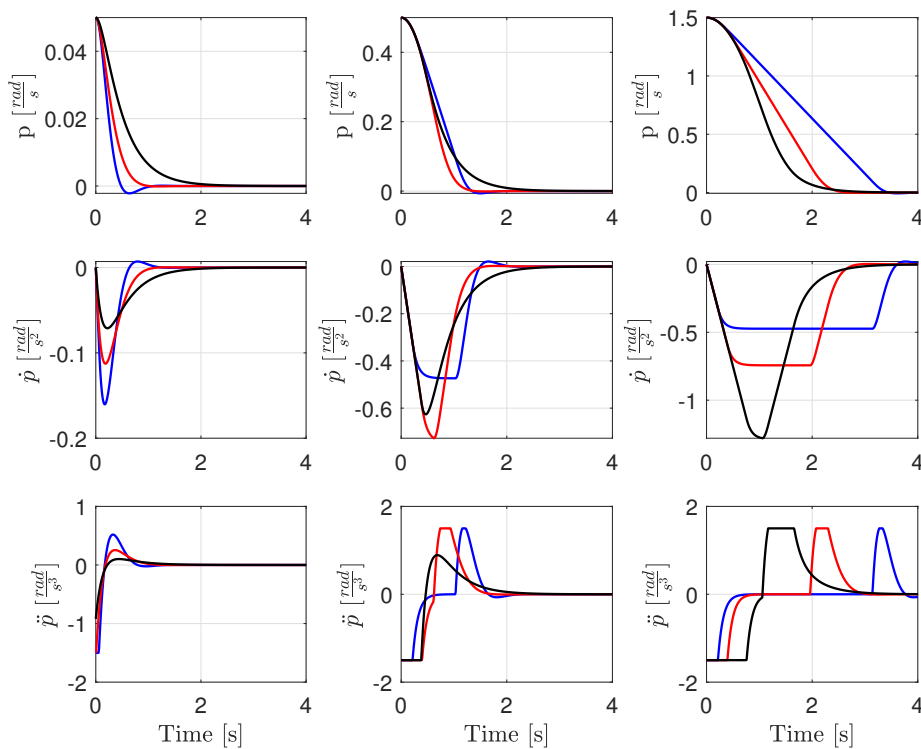


**Figure 5.4:** *Roll Rate Response for Different Amplitudes and Different Control Parameters (blue optimized for  $p = 0.05$ , red optimized for  $p = 0.5$ , black optimized for  $p = 1.5$ )*

In order to understand the time characteristics of all three cases in figure 5.3, consider the roll rate responses in figure 5.4. Each column from left to right corresponds to an initial roll rate of  $p_0 = 0.05$ ,  $p_0 = 0.5$ , and  $p_0 = 1.5$  respectively. The color of each roll response indicates for which of the three possible roll rate amplitudes in figure 5.3 it has been optimized. Each color provides maximum bandwidth for its corresponding roll rate in the respective column.

For instance, the blue line is optimized for small roll rates of  $p_c = 0.05$  (in fact, for roll rates up to  $p_c \approx 0.203$ , as pointed out above) and provides the fastest converging response

at an initial roll rate  $p_0 = 0.05$  in the first column. However, for higher amplitudes the roll acceleration saturates due to the low admissible limit  $\dot{p}_{\text{sat}}$  and hence leads to decreasing bandwidth in the second and third column.

In contrast, the black line is optimized for large roll rate amplitudes of  $p_c = 1.5$  and shows the fastest convergence in the third column, as the admissible roll acceleration limit  $\dot{p}_{\text{sat}}$  is highest for this case. But as a consequence of large admissible roll accelerations, the effective saturated inner-loop bandwidth is decreased according to (5.2) and therefore the admissible outer-loop gain  $K_p$  has to decrease accordingly, in order to maintain the damping characteristics. This consequently leads to slower convergence of the black line for lower amplitudes in the first two columns.

The red line achieves optimum bandwidth in the second column for an initial roll rate of  $p_0 = 0.5$ . However, for smaller amplitudes it converges slower than the blue line and for larger amplitudes it converges slower than the black line.

Note that all three colors share similar (optimum) damping characteristics throughout all initial roll rates (in contrast to the initial example in figure 5.1), since the outer-loop gain is chosen according to (5.35) and takes into account the decreasing saturated (and therefore worst-case) inner-loop bandwidth for increasing admissible roll accelerations according to (5.31).

In general, optimizing for low roll rate amplitudes yields higher outer-loop gains, but lower limits on the admissible roll acceleration. As a consequence, the bandwidth for low amplitudes is maximized, but rapidly drops for increasing amplitudes. Optimizing for high roll rates leads to faster response to large amplitudes and a more consistent effective outer-loop bandwidth for varying input amplitudes, but yields sub-optimal bandwidths for low amplitudes.

A possible way to choose the right roll rate amplitude for which to optimize the bandwidth for is either driven by design decisions or by the requirements of control loops that lie around the roll rate loop. In an iterative manner, the roll rate loop then becomes the new inner loop and its effective bandwidth for saturated roll rate commands can be represented as a function of its admissible input amplitude  $p_{\text{sat}}$  according to (5.39) and (5.41), with  $p_c = p_{\text{sat}}$ . The presented approach can also be used for reference model tracking controller, in order to tune the reference model parameters.

### 5.2.5 Roll Stabilization Example With Two Motors

In this section a 2D example of roll rate stabilization is provided assuming the configuration in figure 5.5 with two current-limited motors. In order to apply the results from the previous chapter, the motor dynamics and their control loop are considered as well as the control law for the rotational rate and acceleration loop of the system. It is assumed that the motor control loop is decoupled from the rigid-body control loop, i.e. the motor is interfaced with a rotational motor speed command  $\omega_c$  and its control loop sets the driving motor voltage such as to track the demanded rotational motor speed.

The dynamics of each motor's rotational speed  $\omega$  is given by Newton's second law for rotation

$$\dot{\omega} = \frac{1}{I_p} t = \frac{1}{I_p} (k_t i - k_D \omega^2) , \quad (5.42)$$

with propeller inertia  $I_p$  and the total motor torque  $t$  consisting of the driving torque (given by the product of electrical current  $i$  and the motor constant  $k_t$ ) and of the aerodynamic torque (given by the squared motor speed  $\omega^2$  and the drag coefficient  $k_D$ ). For simplicity, centrifugal moments of inertia are disregarded due to symmetry.

The dynamics of the electrical current are sufficiently fast such that a static relationship with respect to the input voltage is assumed:

$$i = \min \left( i_{\max}, \max \left( i_{\min}, \frac{1}{R} (V_c - V_{\text{emf}}) \right) \right) , \quad (5.43)$$

with the total (inner) resistance of the motor  $R$ , the driving voltage  $V_c$ , and the voltage due to back EMF  $V_{\text{emf}} = k_t \omega$ . The electrical current is limited by  $i_{\min}$  and  $i_{\max}$ .

Furthermore, the driving voltage is given by the motor controller according to

$$V_c = k_t \omega + \frac{R}{k_t} \left( I_p K_w (w_c - \omega) + k_D \omega^2 \right) , \quad (5.44)$$

which for simplicity is assumed to be an ideal dynamic inversion controller that – for non saturating currents – yields a first order response to a motor rate command  $w_c$ :

$$\dot{\omega} = K_w (w_c - \omega) , \quad (5.45)$$

with the motor bandwidth (for low amplitudes)  $K_w$ .

The roll acceleration  $\dot{p}$  and the total thrust force  $T$  of the system are modeled as a function of the left and right motor speed and yield:

$$\dot{p} = \frac{l}{I} (T_{p,L} - T_{p,R}) = \frac{l}{I} (c_T \omega_L^2 - c_T \omega_R^2) , \quad (5.46)$$

$$T = T_{p,L} + T_{p,R} = c_T \omega_L^2 + c_T \omega_R^2 , \quad (5.47)$$

with the inertia of the system  $I$  and the two motor thrust forces  $T_{p,L} = c_T \omega_L^2$  and  $T_{p,R} = c_T \omega_R^2$  with their lever arm  $l$  and thrust coefficient  $c_T$ .

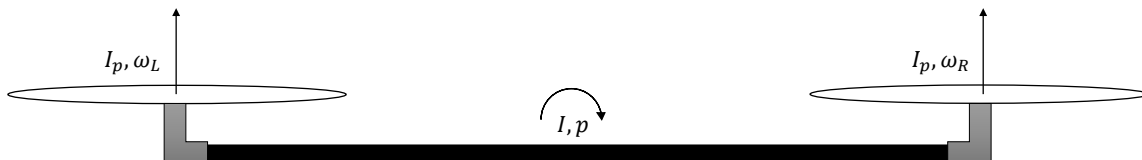


**Figure 5.5:** 2D Example Configuration



Furthermore, the roll jerk and the total thrust rate of the system can be stated as

$$\ddot{p} = \frac{l}{I} (\dot{T}_{p,L} - \dot{T}_{p,R}), \quad (5.48)$$

and

$$\dot{T} = \dot{T}_{p,L} + \dot{T}_{p,R}, \quad (5.49)$$

with  $\dot{T}_{p,L} = 2c_T\omega_L\dot{\omega}_L$  and  $\dot{T}_{p,R} = 2c_T\omega_R\dot{\omega}_R$  denoting the thrust rates of the left and right motor respectively. Taking into account the rotational acceleration of a motor (5.42) and considering the current limits (5.43), the maximum and minimum thrust rates of each motor over the rotational speed are given in figure 5.6.

Since no active motor breaking is assumed, the motor current is always greater than 0 (i.e.  $i_{\min} = 0$ ) and the lower thrust rate limit (blue line) is caused by pure aerodynamic deceleration of the propeller. The asymmetric characteristics of upper and lower thrust rate limit lead to restrictions in the attainable pure roll jerk (i.e. constrained by  $\dot{T}_P = 0$ ).

This is illustrated by the dotted lines in figure 5.7, which represent the pure roll jerk capability of the system plotted against the roll acceleration for a trim constraint of half the maximum total motor force. In contrast to that are the solid lines, which represent the total roll jerk capability of the system while disregarding the change in total thrust.

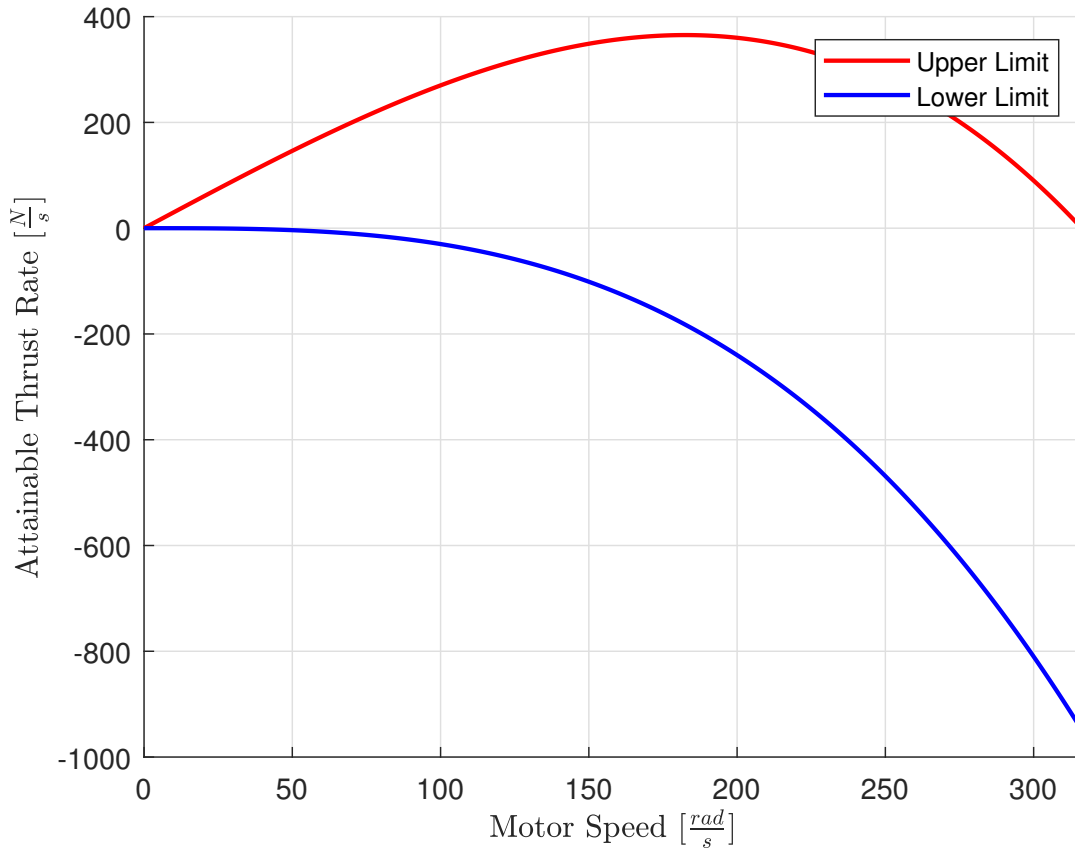


**Figure 5.6:** *Attainable Thrust Rates without Active Breaking*

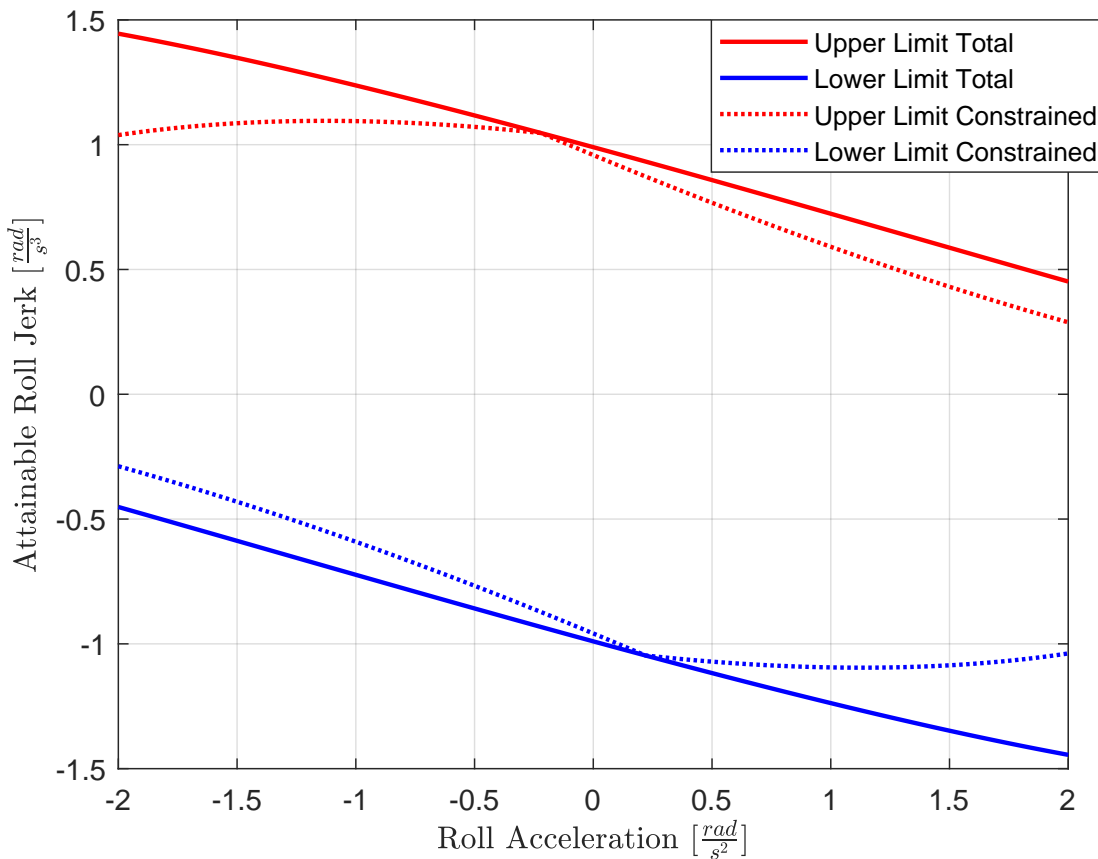


**Figure 5.7:** *Attainable Roll Jerk versus Roll Acceleration without Active Breaking*

In the context of incremental rigid-body inner-loop control, let the desired rotational jerk according to (5.20) and desired overall thrust rate be denoted as

$$\ddot{p}_c = K_{\dot{p}}(\dot{p}_c - \dot{p}) \quad \dot{T}_c = K_T(T_c - \hat{T}), \quad (5.50)$$

with  $K_{\dot{p}}$  and  $K_T$  denoting the inner-loop gains for the rotational acceleration and thrust loop.

While the rotational acceleration feedback  $\dot{p}$  is assumed to be the result of a low-pass filtered or complementary-filtered measured roll rate signal, the feedback signal for the thrust loop is generated according to internal estimation of motor rates, i.e.  $\hat{T} = c_T(\hat{\omega}_L^2 + \hat{\omega}_R^2)$ . The trim command for the thrust is given by the constant value  $T_c = c_T(\omega_{L,\text{trim}}^2 + \omega_{R,\text{trim}}^2)$ . Note, however, that in case of unattainable roll jerk demands the control allocation might disregard tracking the total force in order to prioritize the roll channel. Furthermore, the roll acceleration command  $\dot{p}_c$  is given by the outer loop according to (5.32).

Alternatively, when considering a non-incremental controller, both the roll acceleration loop and the thrust loop are replaced with corresponding feedforward commands by inverting equations (5.46) and (5.47) for a given  $\dot{p}_c$  and  $T_c$  respectively and obtaining the desired motor speeds  $\omega_{L,c}$  and  $\omega_{R,c}$ .

For the incremental strategy, the desired motor speed rates  $\dot{\omega}_{L,c}$  and  $\dot{\omega}_{R,c}$  are derived from (5.50) using (5.48), (5.49) and yield

$$\dot{\omega}_{L,c} = \frac{I\ddot{p}_c + \dot{T}_c}{4c_T\omega_L}, \quad \dot{\omega}_{R,c} = \frac{-I\ddot{p}_c + \dot{T}_c}{4c_T\omega_R}, \quad (5.51)$$

with  $\omega_L$  and  $\omega_R$  representing either measured or estimated motor rotational rates, which have a lower saturation greater than 0 in order to avoid the singularity in thrust rate sensitivity at zero motor rate. The singularity results from the quadratic relationship of the motor rate with respect to its generated thrust force, as was discussed in section 5.1.

In order to ensure stability of the inner loop, the gain  $K_p$  of the rotational acceleration loop in (5.50) is limited from above due to existing time delays, phase delays from filtering the roll acceleration signal, and finite controller sampling rate. However, since none of these effects are considered here and for the sake of comparability with subsection 5.2.2, the inner-loop gain for the roll acceleration is chosen to be  $K_p = 10$ .

The gain  $K_T$  for the thrust loop is merely limited by the controller sampling rate, as the feedback signal  $\hat{T} = c_T(\hat{\omega}_L^2 + \hat{\omega}_R^2)$  is not affected by time or phase delays but is calculated within the control law itself by using a motor model of the form (5.42) or (5.45) or a saturated version of (5.45). Without loss of generality, it is chosen to be equal to the rotational acceleration gain, i.e.  $K_T = 10$ .

Furthermore, given the desired motor speed rate (i.e. motor acceleration) commands in (5.51), the desired motor speed commands are obtained by inverting (5.45) and yield the incremental expressions

$$\omega_{L,c} = \omega_L + K_w^{-1}\dot{\omega}_{L,c}, \quad \omega_{R,c} = \omega_R + K_w^{-1}\dot{\omega}_{R,c}, \quad (5.52)$$

with  $\omega_L$  and  $\omega_R$  representing either measured or estimated motor speeds.

After having derived the inner-loop control law in (5.52), (5.51), and (5.50), let the outer-loop control law, which stabilizes the roll rate  $p$  around  $p_c$ , be given according to

$$\dot{p}_c = \min(\dot{p}_{\text{sat}}, \max(-\dot{p}_{\text{sat}}, K_p(p_c - p))) , \quad (5.53)$$

with  $\dot{p}_{\text{sat}}$  and  $K_p$  denoting the limit for the demand in roll acceleration and the outer-loop gain respectively.

In contrast to the simplified assumption in the previous chapter, the maximum roll jerk capability here is dependent on the roll acceleration being applied to the system according to the phase plane characteristics shown in figure 5.7. Note that the roll jerk capability primarily decreases in the same direction as it is applied, i.e. for increasing roll accelerations the rate with which the roll acceleration can increase further is decreasing.

However, roll jerk capability in the opposite direction is approximately maintained over a wide range (or even increased when disregarding the change in thrust). Hence, according to figure 5.7, the maximum roll jerk capability  $\ddot{p}_{\text{sat}}$  for the example at hand is chosen to be approximately constant and equal to the limit in the opposing direction of applied roll acceleration, i.e.  $|\ddot{p}_{\text{sat}}| \approx 1$ .

Figure 5.8 shows the simulation results for the stabilization of an initial roll rate of  $p_0 = 1.5$  for two different controller settings. Both controller settings operate on the same system parameters shown in table 5.1.

**Table 5.1:** *Simulation Parameters of 2D Example*

Identifier	Description	Value
$I_p$	Propeller inertia	$0.5 \text{ kg m}^2$
$k_t$	Motor torque constant	$1.0 \text{ Nm/A}$
$k_D$	Motor drag constant	$3.0 \times 10^{-4} \frac{\text{Nm}}{(\text{rad/s})^2}$
$i_{\max}$	Maximum motor current	$30.0 \text{ A}$
$i_{\min}$	Minimum motor current	$0.0 \text{ A}$
$R$	Motor resistance	$1.0 \Omega$
$K_w$	Motor bandwidth	$10.0 \text{ rad/s}$
$l$	Motor lever arm	$1.5 \text{ m}$
$c_T$	Thrust coefficient	$2.5 \times 10^{-2} \frac{\text{N}}{(\text{rad/s})^2}$
$I$	System inertia	$1.0 \times 10^3 \text{ kg m}^2$

The unoptimized setting on the left side of figure 5.8 does not take into account the limitations of the system and yields an outer-loop gain of  $K_p = 0.5K_p^* = 5$  according to the ITAE criterion and does not take into account a saturation of roll acceleration demand.

The black solid line on the right side of figure 5.8 represents the optimal control parameters with an outer-loop gain of  $K_p = \sqrt{\frac{3}{(1-e^{-2}\sqrt{2}\sin(2+\frac{\pi}{4}))}(1-e^{-3})}} \frac{\ddot{p}_{\text{sat}}}{p_0} \approx 1.5$  and admissible roll acceleration limit of  $\dot{p}_{\text{sat}} = \sqrt{\frac{3(1-e^{-2}\sqrt{2}\sin(2+\frac{\pi}{4}))}{4(1-e^{-3})}} \ddot{p}_{\text{sat}} p_0 \approx 1.05$  that minimize the step time of the outer loop for amplitudes equal to the initial roll rate  $p_0 = p(t=0)$  according to (5.41). For comparison, the dotted and dashed black line represent the trajectories for optimization of the control parameters with respect to one fifth respectively five times the initial roll rate amplitude.

As already clarified in subsection 5.2.2, the limited roll jerk capability leads to a decreased bandwidth of the inner loop for higher input amplitudes and hence to a reduction of relative damping and stability margins, if not properly accounted for like in the left column of figure 5.8. The example at hand shows the successful application of the proposed heuristic to choose the saturation and gain values for the outer loop, such as to obtain optimum bandwidth and preserve the desired damping characteristics.

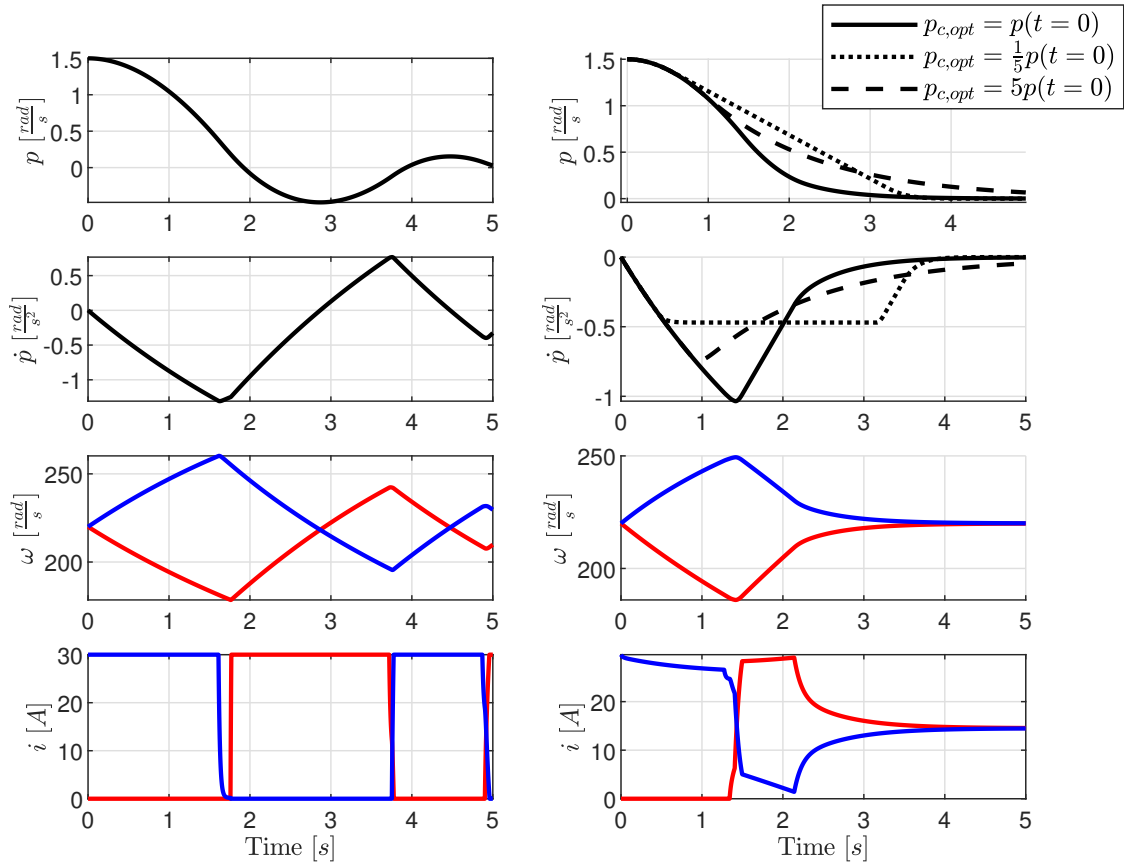


**Figure 5.8:** Simulation of Unoptimized and Optimized Controller. Red and Blue Lines Correspond to the Left and Right Motor Respectively.

## 5.3 Control Architecture Specification Model

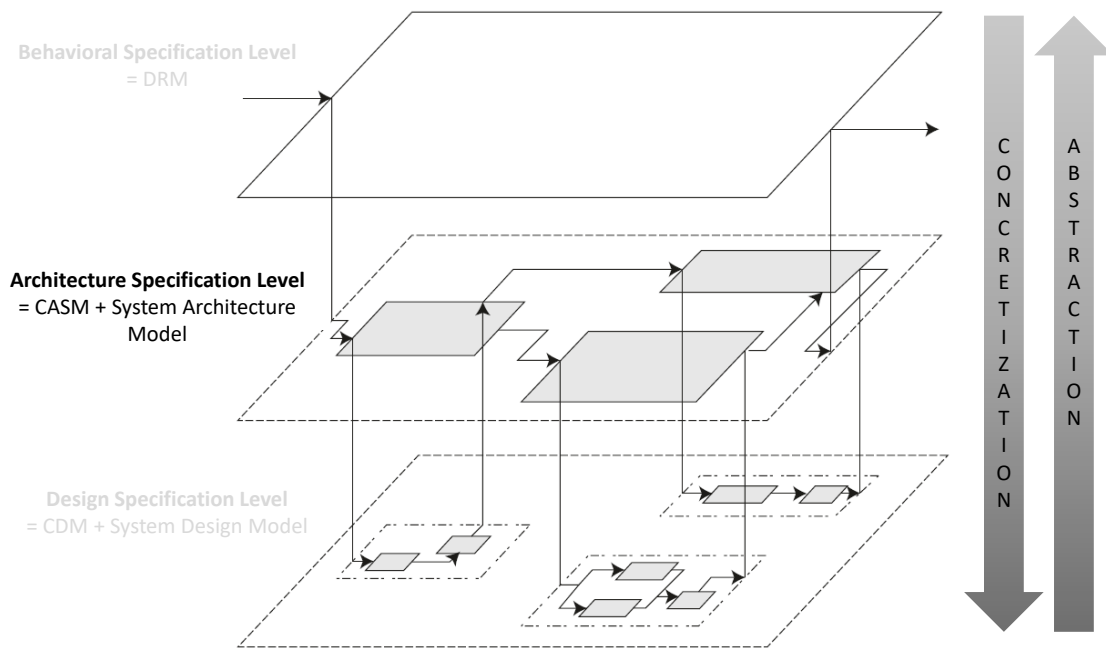


**Figure 5.9:** *Control Architecture Specification Model (CASM) on the Architecture Specification Level (figure adapted from [3])*

The *Control Architecture Specification Model* (CASM) specifies the target behavior of control components and their interfaces and interactions. It represents an extensive concretization of the Design Reference Dynamics – which are embodied in the Design Reference Model (DRM) – down on a functional level with higher granularity, following the concept of functional requirement decomposition [32].

In contrast to the Design Reference Model, which represents the system behavior in a holistic manner, the CASM only represents the control related part of the system, which includes the functional chain from incoming sensor and pilot signals to outgoing command signals. Hence, statements about emerging properties – such as the overall behavior of the integrated system – follow from closed-loop simulation of the CASM together with a plant model, which represents the VTOL aircraft in terms of its functional components.

In general, the design of the CASM is driven by the design principles for good architectures as they are presented in [3]: modularity, independence, integrability, scalability, decentralization, piecemeal engineering, and minimal prejudice. It must account for sensing and acting related constraints like the types of sensors, limited control algorithm sampling rate, delays, and types and number of motors and actuators.

The CASM specifies the desired control algorithm topology in terms of functional representations of all control components. To this end, it embodies the behavior and interactions of feedforward and feedback structures, pilot command scaling, complementary

filters, reference models, dynamic inversions, control allocation, moding, and other control components, which together yield the specified design reference dynamics embedded in the functional context of the system.

Since the CASM is implementation-agnostic, it is independent of the specific realization of individual systems and components and hence independent of implementation-related aspects such as computing platforms and interfaces to physical components in terms of data types, units, and sampling rates. Therefore, all interactions with components are abstracted in terms of their functional representations and interfaces.

Embedded in a closed-loop simulation with a system architecture and environment model, the CASM enables verification and validation of the control architecture with respect to the high-level requirements imposed by the behavioral specification and the SVO concept. It furthermore allows for (horizontal) verification of those functions that are realized by (the interaction of) control components and hence facilitates early evaluation of the control concept as it was pointed out in subsection 2.2.2.

The functional context in which the CASM is embedded represents an essential prerequisite for defining the system boundaries and developing a feasible control architecture that realizes the underlying behavioral specification. Hence, the functional interfaces between the CASM and the functional components of the plant model are the driving factor for the control architecture and the level of concretization and functional decomposition that is needed.

In the context of this thesis, the following assumptions are made in terms of available input signals on a functional level:

- Stick readouts  $(\mathbf{d}_{TS})_S$  and  $(\mathbf{d}_{CS})_S$  that represent the stick deflections of the left stick (throttle stick  $TS$ ) and the right stick (climb stick  $CS$ ) denoted in the stick frame  $S$  according to figure 3.11. These are used to interpret the pilot's intent and provide the target control variables as summarized in section 4.2.
- Inertial measurements of rotational rate  $(\boldsymbol{\omega}^{IB})_B$  and specific forces  $(\mathbf{f})_B$  at the center of gravity. If the inertial measurement unit (IMU) is at a significant distance from the center of gravity, corresponding considerations of the lever arms have to be taken into account. The inertial measurements are used in the inner loop of the controller and represent commonly used signals in flight control applications [98].
- Estimation of euler angles  $\boldsymbol{\epsilon}$ . If not available, corresponding data fusion functionality would have to be included into the CASM. Euler angles are mainly used for coordinate frame transformations, dynamic inversions, and attitude protections.
- Estimation or measurement of kinematic velocity of center of gravity with respect to earth denoted in north-east-down direction  $(\mathbf{V})_O$ . This signal is used in the context of the kinematic velocity control in the hover phase. The use of GPS-aided navigation in the context of flight control is widely adopted in the context of UAV control [99] [81].

- Airspeed measurement in terms of calibrated airspeed  $V_{CAS}$ , which is used for the airspeed tracking and auto-throttle functionality as well as airspeed protections and aerodynamic force related functionality. Thereby, the use of pitot tubes is among the most common approaches for measuring the airspeed [100].

For safety critical or comfort functions, the following sensor signals are additionally used:

- Measurement of the aerodynamic angle of attack  $\alpha$  using e.g. vanes [101]. This is used for stall protection and control margin awareness functionality.
- Feedback about failures of batteries, motors, and actuators as well as the power-on state of the powered lift system. This is used for failure mitigation and safe transition and retransition operation.
- Height above ground level  $h_{AGL}$  using e.g. a radar altimeter [102], which can be used for ground collision avoidance and lift-off detection. Latter can also be realized using weight-on-wheel sensors as in [103].
- Position measurement with e.g. GPS for position hold functionality.
- Height measurement using e.g. a barometric altimeter [104] for altitude hold functionality during fixed-wing flight.

Note that due to foresight in terms of the later control architecture, the high-level control structure of the DRM from section 4.3 is mainly based on the same input signals as mentioned above, despite the fact that on the behavioral concretization level every information about the system and its environment is accessible and can be used in order to generate the aircraft motion.

However, as was already pointed out in section 4.3, the development of the CASM requires caution as to avoiding the use of inherently unknowable signals given the context of available sensors. Furthermore, the CASM has to account for additional functional characteristics of the input signals such as noise, vibrations, delays, and measurement errors, which require the deployment of dedicated control functions such as voting and monitoring algorithms and complementary filters.

In contrast to the DRM for which the generation of forces and moments is abstracted in terms of nonlinear transfer functions, the CASM interfaces the available force and moment producers of the plant model. To this end, a lift-plus-cruise configuration is assumed, which was introduced in section 3.2.

The following functional interfaces to the available control effectors and motors thereby represent the outputs of the CASM:

- Rotational speed command  $\mathbf{w}_{PL,c}$  to the powered lift system. The assumption of RPM-controlled electrical motors is common in the context of multicopter control [82] [81] [85] [105] [106].



- Rotational speed command  $w_{TS,c}$  and blade pitch command  $\beta_{TS,c}$  to the traction system. Since the traction system operates in a wide range of airspeeds, a variable blade pitch system is assumed to account for the varying inflow conditions of the propeller.
- Deflection commands to the aerodynamic control surfaces  $\delta_c$ , which is a common approach for fly-by-wire control of fixed-wing aircraft [65] [107] [86] [43].

Since the DRM represents an executable specification of the system behavior and therefore includes the high-level control strategy, the derived concepts of the DRM can be reused, adapted, extended, and concretized for the CASM.

In the scope of the next sections the focus is therefore put on functional decomposition of the DRM control parts down on a concretization level which – together with the derived control concepts in section 4.3 – results in a complete functional specification of the controller. Figure 5.10 thereby shows the high-level structure of the CASM consisting of the three main functional blocks: voting and monitoring, moding, and the control law functionality.

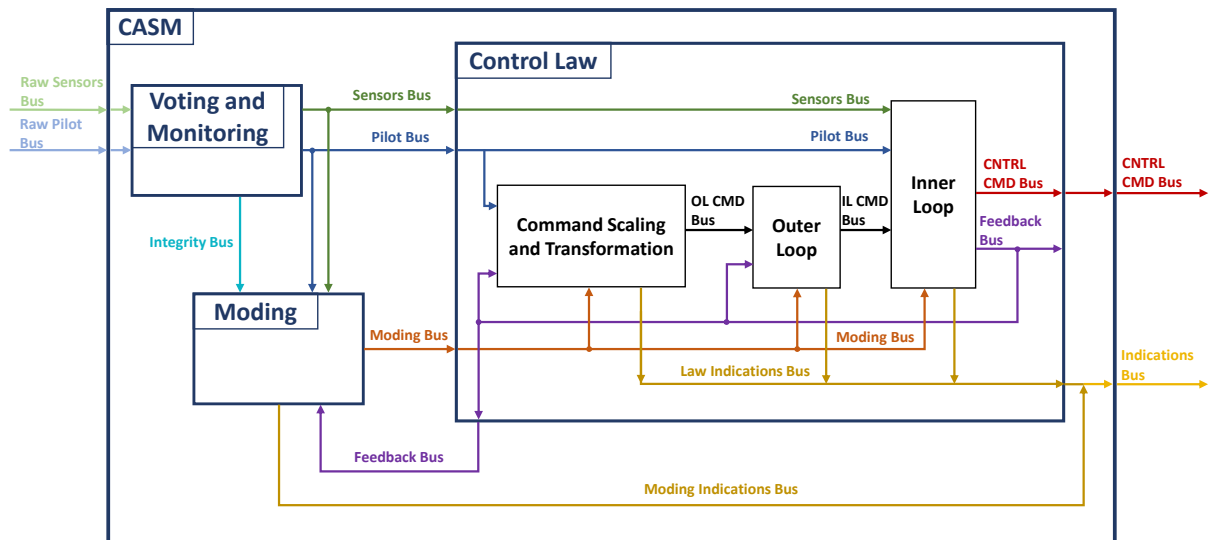


**Figure 5.10:** *High-Level Structure of the CASM*

The voting and monitoring block represents the functions that are concerned with the integrity checks of all incoming signals. Its actual implementation is highly dependent on the specific architecture and component implementation of the overall system. In the scope of the CASM, the voting and monitoring functionality allows for investigation of different degradation strategies of the controller with respect to corrupted or lost input signals.

The moding block represents the high-level automation and moding functionality of the controller, which determines the respective control law modes such as for the hover, transition, and wingborne phase. Additionally, the moding is responsible for any kind of configuration changes, the activation, and the deactivation of the powered lift system. It furthermore includes the arming and disarming procedures of the overall controller on ground as well as the built-in test (BIT) and degradation modes.

Finally, the control law block represents the actual control algorithm that shall yield the desired aircraft dynamics derived in 4 in the functional context of the system by providing the necessary control commands to the available motors and control effectors.

The main scope in the upcoming sections lies in the structure of the control law, while the voting and monitoring as well as the moding functionalities are merely introduced briefly for completeness.

### 5.3.1 Voting and Monitoring

The topic of signal integrity in the scope of electronic flight control systems has been gaining significant importance in the world of aviation since the introduction of fly-by-wire technology [13]. The increased use of complex control functions has improved the overall performance and survivability of aircraft and weapon systems. At the same time, “highly-reliable flight control system operation has become critically important to mission planning and execution” [13, p. 5].

In the context of the overall control architecture for the VTOL transition aircraft developed in this thesis, the voting and monitoring functionality is concerned with the availability and integrity of the incoming signals. The availability and integrity of the outgoing signals is not discussed in the scope of this thesis, however can in principle be achieved through redundant flight controller instances and functional monitoring of the overall system.

As can be seen in figure 5.10, the voting and monitoring block is located at the very beginning of the control flow and distributes the necessary signals to the moding and control law in the correct format, data type, unit, and coordinate frame. It checks the availability of signals by evaluating existing status information such as failure flags or heartbeat messages, in case the signal source provides them.

Additionally, the integrity of incoming signals is verified by either evaluating status information sent by the signal source or through monitoring of the inherent characteristics of the signal itself. To this end, the monitoring analyses if the incoming signals adhere to their specified range, rate of change, or frequency characteristics. Other faults such as frozen input values can also be detected.

An additional method for monitoring is the signal voting approach [108] [109] [13], which requires the respective signal to be available from redundant sources. Depending on the degree of redundancy, signal voting enables the realization of fail-passive, fail-operative, or double fault correction systems [13].

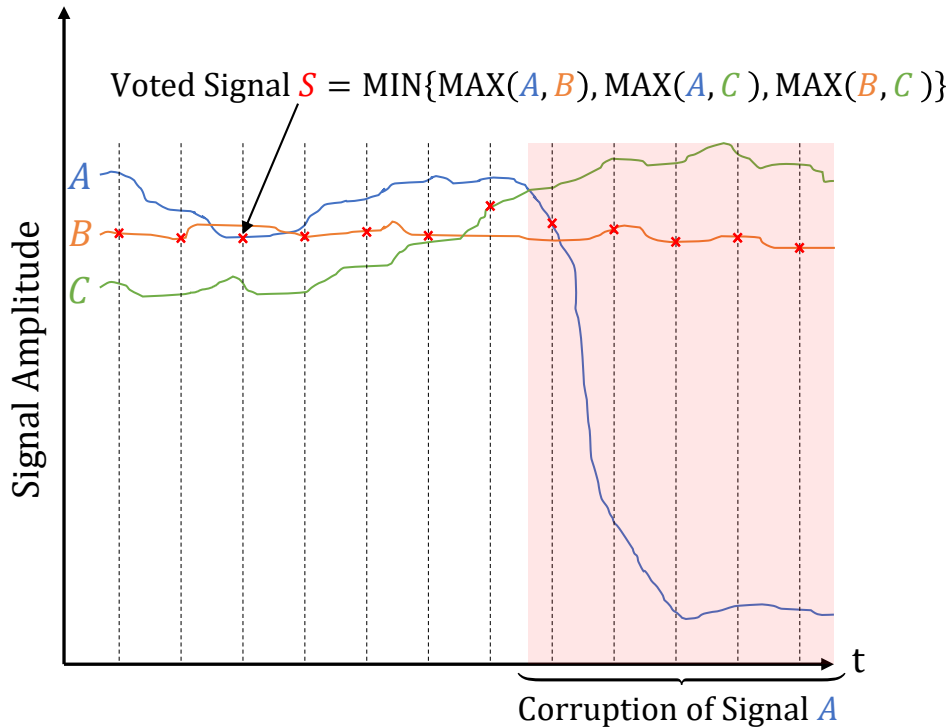


**Figure 5.11:** *Mid Value Selection Voting for Three Redundant Signals*

Figure 5.11 shows a simple mid value selection voter [13] [108], which takes the median value out of three available signals. Note that even though the algorithm is fairly simple, it effectively rejects any adverse effects of the corrupted signal A. In contrast to merely averaging the values and outputting the mean of the three redundant signals, the median or mid value selector provides a highly effective way to deal with outliers and hence renders the voting process fail-operative.

In fact, the median operation provides the highest possible finite sample breakdown point of 50%. Thereby, “the finite sample breakdown point of an estimator refers to the smallest proportion of observations that when altered can cause the value of the statistic to be arbitrarily large or small. The finite sample breakdown point of an estimator is a measure of its resistance to contamination” [110, p. 62].

The mean operation has a finite sample breakdown point of 0%, which means that even a single sample can compromise the final result. Hence, averaging redundant signals as a method of ensuring signal integrity is very sensitive to outliers.

The presented voting algorithm in figure 5.11 does not actively detect and isolate the faulty signal. There are, however, more sophisticated approaches [108], which isolate the faulty signal through pairwise comparison of the signals and subsequently exclude them from the further voting procedure. Such algorithms are especially useful in the case of quad-redundant signal sources, which are commonly used for double fault correction systems that “must continue to operate normally [after any first failure] and reject any second failure without transient disturbances or performance degradation” [13, p. 31].

### 5.3.2 Moding

The moding block is responsible for automating the controller and managing the entry into and transition between the different modes of the control law. Each mode thereby represents a characteristic set of functional requirements that is active at a time and enforced by the control law.

Figure 5.12 below shows an overview of the moding hierarchy used in the scope of this thesis.

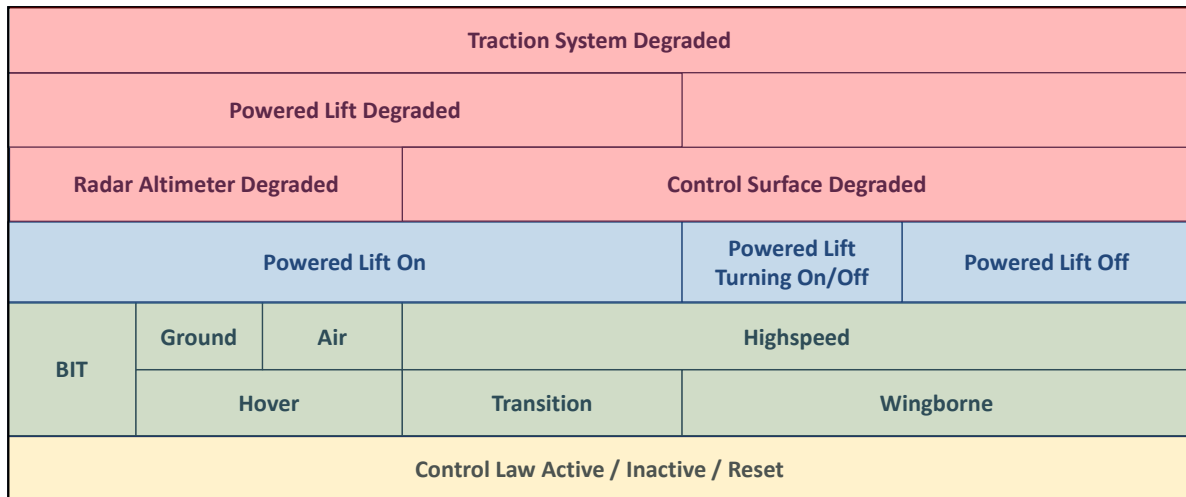


**Figure 5.12:** *Control Law Moding Hierarchy*

The modes are structured in four different layers. The bottom level in yellow represents the global execution mode layer in which the overall controller is activated, deactivated, or reset.

The green layer includes the flight modes that are active during the different flight phases of a mission: on ground before take off, after take off, in the transition phase, and in the fixed-wing flight phase.

The powered lift mode layer in blue summarizes the state of the powered lift system, which is necessary for safe transition into and from the wingborne phase as well as avoiding overspeed or underspeed conditions when the powered lift motors are engaged or disengaged respectively.

The degradation mode layer in red includes the considered failure modes and allows for graceful degradation [111] of the VTOL aircraft. In the scope of this thesis, graceful degradation is considered only for single failures of either a traction motor, powered lift motor, control surface, or radar altimeter.

In the following sections the different modes of each layer are discussed in more detail and the conditions for transitioning between modes are presented. An exhaustive discussion of the automation strategy for an onboard piloted VTOL transition aircraft can be found in [112].

### 5.3.2.1 Execution Mode Layer

The execution mode layer controls the global execution state of the control law. The following modes are thereby considered:

**Inactive** During this mode, all controller subsystems are deactivated and rendered memory-less (i.e. integration is turned off). Furthermore, the output of the controller is either set to zero or is entirely suppressed. This mode is used as the initial mode of the control law.

**Active** This mode is used to enable the overall functionality of the control law. The controller is sending commands to the motors and effectors of the system.

**Reset** This mode resets all controller components that have internal states such as integrators and memory blocks. All states are set to a predefined initial set of values and are held at this value while the reset mode persists. Hence, all components with memory that propagate their internal states are rendered static during the reset mode and output their initial set of values.

### 5.3.2.2 Flight Mode Layer

The flight mode layer contains the flight phase related modes, which enforce the set of functional requirements that are relevant for each particular flight state. Thereby, the following modes are considered in the order of occurrence during a typical mission:

**Built-In Test** During *Built-in Testing* (BIT) mode, the controller performs a variety of tests for the purpose of self-diagnosis. To this end, different components of the system are checked for correct functionality, which helps to prevent mission failure caused by undetected faults.

According to [13, p. 32], figure 5.13 “shows [the] probability of a one hour mission success when the in-flight failure monitoring capability is only 90 percent and various degrees of pre-flight Built-in Test (BIT) thoroughness are employed”. Thereby, it is clearly visible that the probability of mission failure for a given time of operation is considerably decreased as the extent of Built-in Testing is increased.

The following components are tested during the Built-in Testing mode for the VTOL transition aircraft:

- The functionality of the powered lift system is evaluated by successively commanding each lifting motor with a predefined and close-to-idle RPM value. The rotational rate of the lifting motors is then measured and fed back to the controller.

In doing so, both the functionality of the motors and the measurements as well as the feedback path of the RPM measurements are verified. The Built-in Test is

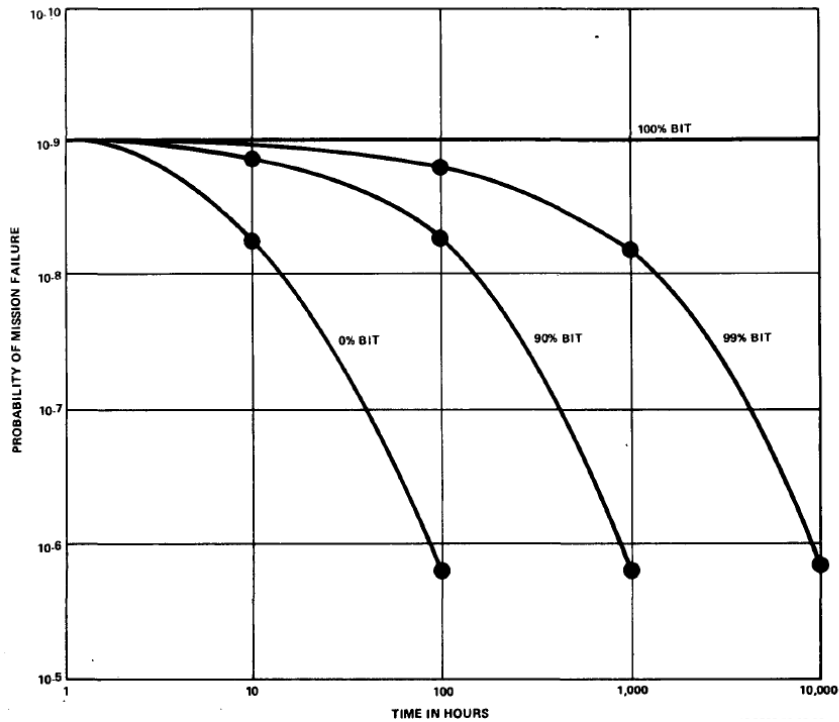


**Figure 5.13:** *Effect of Built-In Testing on Probability of Mission Failure [13]*

considered successful if each individual lifting motor can be successfully commanded and its RPM response can be correctly measured.

- The functionality of the traction system is evaluated by commanding each of the traction motors with a predefined and close-to-idle RPM value as well as altering the blade-pitch of each propeller. The rotational rate of the traction motors as well as the pitch angle of the propellers are then measured and fed back to the controller. Hence, the functionality of the traction motors, the propeller governors, as well as the measurements and feedback path of the RPM and blade pitch values are verified. The Built-in Test is considered successful if each individual traction motor and propeller can be successfully commanded and their response can be correctly measured.
- The aerodynamic control effectors are evaluated by commanding each individual control surface to a full deflection in each direction. The measured deflection angles are subsequently fed back to the controller. This verifies the functionality of each actuator as well as the measurement and feedback of each control surface's deflection angle.
- In order to test the correct read-out of the control inceptors, the operator deflects each control effector fully in each direction and checks the visual cues on the primary flight display (PFD).

**Hover (Ground)** The *Hover (Ground)* mode is one of the two modes that make up the hover mode of the control law. This mode is active after the BIT has finished successfully and the operator moves the climb stick (right stick in figure 3.10) to the maximum sink rate position, which corresponds to pushing the right stick forward according to section 4.2.

Being a submode of the hover phase, the *Hover (Ground)* mode is active when the VTOL is either about to take off or has landed while being in *Hover (Air)* mode. Thereby, the aircraft generally behaves according to subsection 4.2.1, however, special attention is required to account for the inherent effects of ground reaction forces and moments on the VTOL aircraft.

Due to the integrative behavior of the control demand in the context of Incremental Control, even the presence of small tracking errors on ground can lead to the well-known effect of integrator windup [113]. This happens as a consequence of the ground reaction forces that create an external disturbance moment, which the inner loop of the Incremental Nonlinear Dynamic Inversion controller counters by steadily adjusting the RPM values of the lifting motors. In subsection 5.3.5 it is shown how the integrator windup is prohibited during ground mode by bypassing the acceleration feedback with a model-based estimation.

Dependent on specific design decisions regarding the VTOL aircraft's landing gear height, its wingspan, and the location of its lifting and traction motors, it might be additionally necessary to restrict the admissible attitude close to ground in order to avoid accidental impact of the wings or propellers with the ground. Additionally, the use of the traction system might have to be prohibited on ground in order to avoid dangerous conditions including injuries and fatalities due to propeller impact [114].

**Hover (Air)** After taking off from ground the VTOL is in *Hover (Air)* mode, which is part of the hover phase. The purpose of having an explicit mode for the hover state is to provide a flight mode that is specifically targeted at performing mission tasks and satisfying requirements that occur during hover flight. The general behavior during this phase is described in subsection 4.2.1 including attitude and speed limitations.

Only during this mode the height above ground level is explicitly used in order to gradually adjust the limits of permissible attitude, sink rate, and the equilibrium pitch angle during longitudinal control of the aircraft using the traction system according to subsection 4.3.1.4.

The following conditions have to be satisfied for the transition from *Hover (Air)* mode to *Transition* mode:

- The pilot has to indicate his intention to initiate the transition by pushing the thrust stick over the detent notch (refer to subsection 3.2.2 and figure 3.11).
- The horizontal kinematic velocity in the direction of the heading  $V_{Cx}$  (figure 4.4) has to be close to or greater than  $V_{\text{hover}}$  (see subsection 4.2.1), which is defined to be equal to  $V_{\text{TOSS}}$  (see subsection 3.1.2).

**Transition** The *Transition* mode is used to bring the VTOL aircraft from the hover phase into the wingborne phase while adhering to the operational and performance requirements discussed in section 3.1. The general behavior during this mode is described in detail in subsection 4.2.2.

Similarly to the hover phase, the vertical channel in the transition phase is controlled with the powered lift system, while the pitch behavior of the aircraft is determined based on figure 4.7. Since the powered lift system is always completely engaged in *Transition* mode (see subsection 5.3.2.3), the airspeed is protected and never exceeds  $V_{CAS,d} = 1.x V_{stall,p}$ , as was discussed in subsection 4.2.2.

The following conditions have to be satisfied for the transition from *Transition* mode to *Hover (Air)* mode:

- The pilot has to indicate his intention to initiate the hover phase by pulling the thrust stick behind the detent notch (refer to subsection 3.2.2 and figure 3.11).
- The horizontal kinematic velocity in the direction of the heading  $V_{Cx}$  (figure 4.4) has to be less than  $V_{hover}$  (see subsection 4.2.1), which is defined to be equal to  $V_{TOSS}$  (see subsection 3.1.2).

The following conditions have to be satisfied for the transition from *Transition* mode to *Wingborne* mode:

- The pilot has to indicate his intention to initiate the fixed-wing flight by pushing the thrust stick over the detent notch (refer to subsection 3.2.2 and figure 3.11).
- The calibrated airspeed  $V_{CAS}$  has to be close to or greater than  $V_{stall,p}$  from (4.16).
- The powered lift motors have to be close to idle while the measured vertical specific force in the body frame  $f_{G,Bz}$  is close to  $-1g$ , which indicates the presence of sufficient aerodynamic lift.

**Wingborne** During fixed-wing flight, the control law is in *Wingborne* mode in which the powered lift motors are completely shut down. Since the generation of aerodynamic lift is vital during this phase, additional flight envelope protections become active, which prevent dangerous underspeed conditions and aerodynamic stall of the aircraft. The general behavior is described in detail in subsection 4.2.3.

Special emphasis is put on the climb and turn command channel, which enable the pilot to maneuver the aircraft along the borders of the safe flight envelope. Thereby, the maximum allowed climb and turn rate demands lead to maneuvers at the optimal climb angle speed and at the maximum feasible angle of attack.

More details are given in subsection 4.2.3.3 and subsection 4.2.3.4 respectively. Furthermore, the detailed functional specification of the command scaling and transformation is given in subsection 5.3.3.



The following conditions have to be satisfied for the transition from *Wingborne* mode back to *Transition* mode:

- The pilot has to indicate his intention to initiate the retransition by pulling the thrust stick back over the detent notch (refer to subsection 3.2.2 and figure 3.10).
- The calibrated airspeed  $V_{CAS}$  has to be close to  $V_{stall,p}$  from (4.16) but not greater than  $1.x V_{stall,p}$  (see subsection 4.2.2).
- All powered lift motors are turned on and operate close to their idle RPM. This is verified by using the RPM measurements of the powered lift system.

### 5.3.2.3 Powered Lift Mode Layer

The powered lift mode layer contains the possible modes that are related to the operation of the powered lift system. The operational state of the powered lift motors is an important factor that is considered for several flight envelope protections as well as the mode transitions to and from the *Wingborne* mode.

In particular, the following powered lift modes are considered:

**Powered Lift On** During *Powered Lift On* mode, the lifting motors are fully engaged and ready to reliably provide the specified lifting force. Thereby, the operation status of the powered lift system is actively verified by means of RPM feedback of each individual lifting motor prior to transitioning to *Powered Lift On* mode from *Powered Lift Turning On* mode.

Both the *Hover* mode and the *Transition* mode are thereby directly coupled to the *Powered Lift On* mode, which enforces the availability of the lifting motors in those flight phases. Additionally, the lower airspeed protection is disengaged, since the generation of powered lift is ensured and substitutes the aerodynamic lift.

Since the lifting motors are not fully disengaged, the upper airspeed protection prevents overspeed conditions while the lifting motors are running and ensures that the VTOL aircraft flies below  $1.x V_{stall,p}$  (see subsection 4.2.2).

The following conditions have to be satisfied for the transition from *Powered Lift On* mode to *Powered Lift Turning Off* mode:

- The pilot has to indicate his intention to turn off the powered lift system by pushing the thrust stick over the detent notch (refer to subsection 3.2.2 and figure 3.10).
- The calibrated airspeed  $V_{CAS}$  has to be close to or greater than  $V_{stall,p}$  from (4.16).
- The powered lift motors have to be close to idle while the measured vertical specific force in the body frame  $f_{G,Bz}$  is close to  $-1g$ , which indicates the presence of sufficient aerodynamic lift.

**Powered Lift Turning Off** The *Powered Lift Turning Off* mode is aimed at disengaging the powered lift system upon entering *Wingborne* mode and shutting each lifting motor off.

During *Powered Lift Turning Off* mode, the powered lift system is not engaged anymore and hence the control law operates in *Wingborne* mode and uses the angle of attack to control the vertical channel according to (4.105). As a consequence, the lower airspeed protection is engaged and ensures that the aircraft does not decelerate below the safe speed  $V_{\text{stall,p}}$  from (4.16). Additionally, the stall protection is engaged and prevents the aircraft from dangerous stall conditions.

Since the powered lift system is not yet considered to be fully disengaged either during *Powered Lift Turning Off* mode, the upper airspeed protection is engaged and prevents the aircraft from exceeding the maximum allowed airspeed  $1.x V_{\text{stall,p}}$  for running lifting motors (see subsection 4.2.2).

The following conditions have to be satisfied for the transition from *Powered Lift Turning Off* mode to *Powered Lift Off* mode:

- The RPM of each individual lifting motor is measured and it is verified that all motors are indeed turned off.
- If the measurement of at least one lifting motor fails or if at least one lifting motor's measured RPM value is above a threshold RPM after a predefined time interval, the pilot has to manually confirm the deactivation of the powered lift system.

**Powered Lift Off** During *Powered Lift Off* mode, the lifting motors are fully disengaged and are prohibited from being accidentally turned on. This is to prevent severe structural damage to the airframe upon activation of the lifting motors at high dynamic pressures. Since the lifting motors are not completely engaged, the control law operates in *Wingborne* mode and both the underspeed and stall protection are engaged.

Furthermore, the upper airspeed limit in *Powered Lift Off* mode is set to the maximum cruising speed for normal operations in the fixed-wing phase  $V_{\text{NO}}$  (see figure 4.8) and is not anymore restricted by the powered lift system.

The following conditions have to be satisfied for the transition from *Powered Lift Off* mode to *Powered Lift Turning On* mode:

- The pilot has to indicate his intention to activate the powered lift system by pulling the thrust stick back over the detent notch (refer to subsection 3.2.2 and figure 3.10).
- The calibrated airspeed  $V_{\text{CAS}}$  has to be close to  $V_{\text{stall,p}}$  from (4.16) but not greater than  $1.x V_{\text{stall,p}}$  (see subsection 4.2.2).

**Powered Lift Turning On** The *Powered Lift Turning On* mode is aimed at engaging the powered lift system before starting the retransition from *Wingborne* mode to *Transition* mode. The control law commands each lifting motor with its idle RPM during this mode.

Similarly to the *Powered Lift Turning Off* mode, the powered lift system is neither completely disengaged, nor is it completely engaged yet during *Powered Lift Turning On* mode. Hence, the control law operates in *Wingborne* mode and uses the angle of attack to control the vertical channel according to (4.105). Additionally, protections against stall, underspeed, and overspeed conditions are engaged analogously to the *Powered Lift Turning Off* mode.

The following conditions have to be satisfied for the transition from *Powered Lift Turning On* mode to *Powered Lift On* mode:

- The RPM of each individual lifting motor is measured and it is verified that all motors are indeed turned on and rotate at their idle RPM.
- If the measurement of at least one lifting motor fails or if at least one lifting motor's measured RPM value is below its idle RPM after a predefined time interval, the pilot has to manually confirm the activation of the powered lift system.

### 5.3.2.4 Degradation Mode Layer

The degradation mode layer includes the considered degradation modes of the control law. In the scope of this thesis, degradation modes are only considered for single failures of one lifting motor, all traction motors on one side, one control surface, or one out of two radar altimeters. The degradation modes are described in the following:

**Radar Altimeter Degraded** The *Radar Altimeter Degraded* mode is active if all radar altimeters have failed or if the integrity of the height above ground cannot be ensured anymore. Latter is the case for a single failure of one out of two radar altimeters or a mismatch of both radar altimeters.

Since the height above ground is not used during the highspeed phase, this mode has no effect in *Transition* mode and *Wingborne* mode. However, during *Hover* mode the loss of height above ground information leads to the following degradation strategies:

- For the roll angle protection limits  $\phi_{\min}$  in (4.55) and  $\phi_{\max}$  in (4.56), proximity to ground is assumed and the maximum admissible roll angles are restricted.
- For the pitch angle protection limits  $\theta_{\min}$  in (4.60) and (4.71) as well as  $\theta_{\max}$  in (4.61) and (4.72), proximity to ground is assumed and the maximum admissible pitch angles are restricted.
- For the equilibrium pitch angle  $\theta_{\text{hvr}}$  in (4.66), proximity to ground is assumed and it is set to 0.

Additionally, the maximum admissible sink rate  $\dot{h}_{\min}$  in (4.12) is not restricted in *Radar Altimeter Degraded* mode. This is because a restriction of the sink rate based on the assumption of ground proximity can be catastrophic, if the VTOL aircraft happens to be at high altitudes and low battery power in the moment of the radar altimeter failure.

**Powered Lift Degraded and Control Surface Degraded** The *Powered Lift Degraded* mode and *Control Surface Degraded* mode are engaged if at least one powered lift motor or aerodynamic control surface fail respectively. Thereby, it is assumed that the available lifting motors and control effectors provide sufficient redundancy to compensate any single failure.

To this end, the following failures are considered for both lifting motors and control surfaces:

- Complete power loss of a single unit: The unit does not respond to commands anymore. For a powered lift motor: no motor torque is applied and the propeller may be in a state of windmilling. For a control surface: no actuator torque is applied and the control surface may be free-floating. Passive damping elements may be necessary to avoid dangerous states of aerodynamic flutter [115].
- Hard-over of a single unit: The unit uncontrollably operates at its maximum capacity without being actively commanded. An affected lifting motor ramps up its RPM to the maximum value, while an affected control surface will deflect to the maximum or minimum deflection.
- Command freeze of a single unit: The unit remains at its last operating point indefinitely. An affected lifting motor will keep operating at the RPM value commanded in the instance of failure, whereas an affected control surface will be stuck at the deflection in the instance of failure.

The above mentioned failure cases are processed in the control allocation, which is described in more detail in subsection 5.3.5.7. It is assumed that the information about failures is provided to the controller as an additional input. Hence, the detailed monitoring strategy that identifies and isolates the failures is not in the scope of this thesis.

Other types of (soft) failures like the loss of control effectiveness are not considered in this thesis, however can in principle be dealt with analogously to [81] [82]. Additionally, since only single failures of a powered lift motor and an aerodynamic control surface are considered, any further failure after the first one is ignored. This strategy provides protection against false-positive failure detections, in case the system can only handle single failures.

**Traction System Degraded** During *Traction System Degraded* mode, the controller accounts for failures of the traction system and the subsequent loss of maximum thrust capability of the aircraft. Additionally, for asymmetric traction motor failures the resulting yaw moment has to be accounted for as well.

Only complete failures of one or more traction motors are considered and it is assumed that there are enough traction motors left to provide sufficient thrust in order to perform a full transition into fixed-wing flight. Hard-over or frozen RPM failures of the traction motors are not considered in the scope of this thesis.

Depending on when the failure occurs, the *Traction System Degraded* mode leads to the following reconfigurations within the control law:

- Within *Hover* mode the engagement of *Traction System Degraded* mode leads to a switch of the longitudinal translation control strategy from the traction variant introduced in subsection 4.3.1.4 to the pitch variant introduced in subsection 4.3.1.3. Thereby, latter does not use the traction system in the hover phase but controls the longitudinal motion using changes in the pitch angle only.
- Within *Transition* mode and *Wingborne* mode (i.e. during the highspeed phase) the engagement of *Traction System Degraded* mode
  - increases the commanded safe airspeed at the detent notch from  $V_{\text{stall,p}}$  to  $V_{\text{stall,p,OEI}}$ , which accounts for the increased demand in aerodynamic authority in the yaw channel due to the asymmetric thrust force,
  - additionally changes the lower airspeed protection limit to  $V_{\text{stall,p,OEI}}$ ,
  - and reconfigures the incremental allocation of the traction motors, such as to account for the rank deficiency in the thrust and yaw channel and additionally compensates for the adverse yawing moments using the remaining control effectors.

### 5.3.3 Command Scaling and Transformation

The command scaling and transformation represents the first part of the functional chain within the control law depicted in figure 5.10. It is used to transform the pilot stick inputs into high-level commands and tracking targets for the outer loop.

Thereby, the command scaling incorporates protection functions that are related to the limits of the system's available power, lift, and thrust capabilities such as to prevent the aircraft from entering critical flight states. In section 4.2 some of the scaling concepts have been derived qualitatively, however, the realization in terms of concrete functional algorithms is discussed in the following.

Figure 5.14 shows a high-level overview of the command scaling and transformation in terms of a functional block diagram.

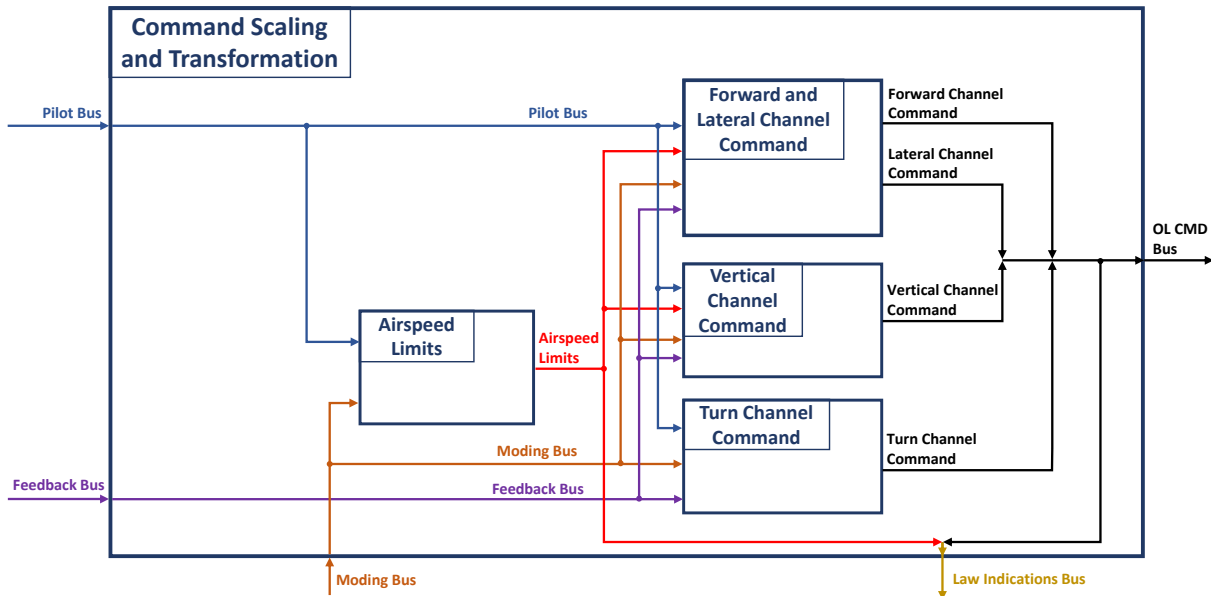


Figure 5.14: *Command Scaling and Transformation Block*

### 5.3.3.1 Control-Margin-Awareness-Based Stick Mapping

The general idea behind the command scaling is that the pilot commands fixed values of some high-level behavioral parameter within a predefined stick range, while large stick deflections (in particular full deflections) lead to the maximum command in the behavioral parameter that brings the aircraft to some performance or operational limit. In doing so, the stick mapping provides a very natural way of supporting the pilot’s awareness about the current control margins, which is referred to as Control Margin Awareness (CMA) in the following. Similar strategies have been published by the Institute of Flight System Dynamics of the Technical University of Munich in [116].

The presented scaling approach is applicable to those command channels that are typically limited by physical constraints or aircraft parameters related to the maximum thrust capabilities, structural limits, or stall characteristics. Awareness about the proximity to the current limits of the system is crucial, since “[f]lying near the edge of the safe operating envelope is an inherently unsafe proposition” [117, p. 1] and hence “approaches to pilot cueing based on predicting loss-of-control safety margins as the aircraft gets closer to the edge of the safe operating envelope” [117, p. 1] are worth considering.

The presented stick mapping thereby inherently implements a form of tactile cueing, since the pilot can feel (the proximity to) a full stick deflection and hence the available control margins in terms of the applied stick force. Additionally, the use of active stick technology can support the tactile cueing in terms of shaping the stick force characteristics when approaching the limit of the flight envelope. Similar concepts are found in [118], where neural networks are used to gather an adaptive online estimation of the maneuvering steady-state condition, which is then used to restrict the allowable control travel.

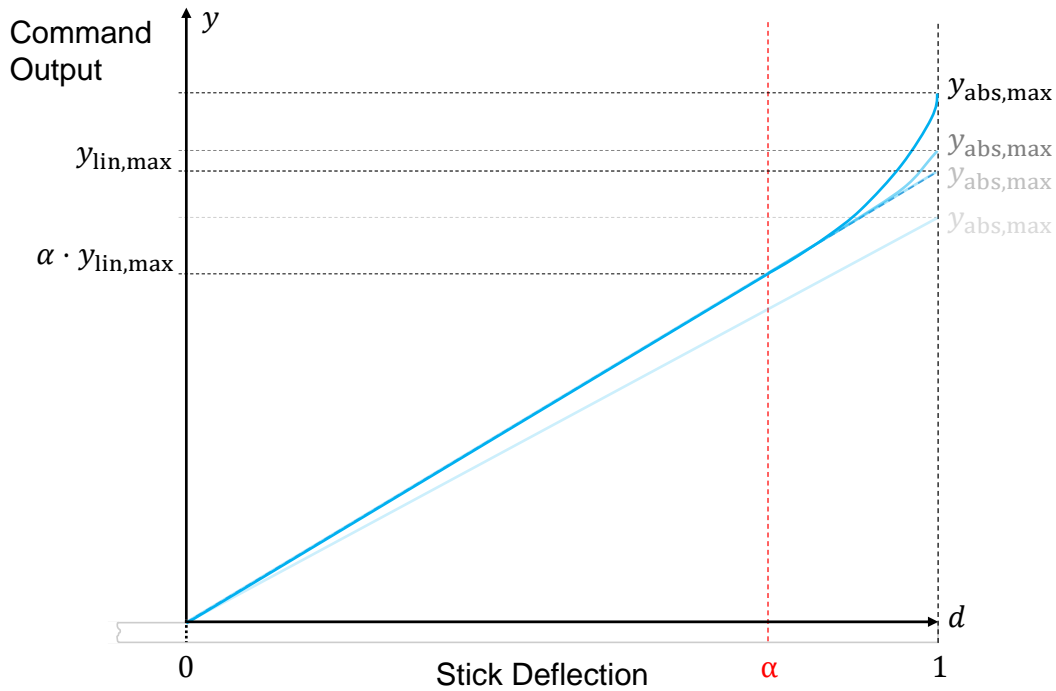


**Figure 5.15:** *Generalized Control-Margin-Awareness-Based Stick Mapping*

Figure 5.15 illustrates the generalized Control-Margin-Awareness-based stick mapping. Thereby, the following requirements are presupposed:

1. Within a predefined stick range the commanded variable  $y$  of a particular control channel shall have a constant relationship with respect to the stick deflection. This ensures a predictable aircraft reaction for moderate stick deflections, which supports compliance with operational requirements in the context of the flight mission.
2. For extreme or full stick deflections, the commanded variable  $y$  shall yield a maneuver at the limit of the safe flight envelope, operational flight envelope, or the aircraft's performance capabilities.
3. No control reversal shall occur, i.e. in case the maximum achievable control output is significantly limited due to external factors like disturbances, failures, or uncertainties, the overall stick mapping has to account for this by reducing the overall stick gradient accordingly (see figure 5.15).
4. The overall stick mapping shall be continuous and continuously differentiable, i.e. the stick deflection to command gradient shall not exhibit discrete jumps in the output value or gradient.

In accordance with the requirements stated above, the generalized stick mapping is defined in the following. Without loss of generality and due to symmetry, only one half of the stick range is considered. The mapping for the other half of the stick range follows analogously.

Within a fraction  $\alpha$  of the stick range, the command output  $y$  shall follow a linear mapping  $y_{\text{lin}}(d)$  based on the stick deflection  $d$ . The linear mapping is thereby given by

$$y = y_{\text{lin}}(d) = d \cdot \min(y_{\text{lin,max}}, y_{\text{abs,max}}) \quad \text{for } 0 \leq d \leq \alpha, \quad (5.54)$$

where  $y$  denotes the command output,  $0 \leq d \leq 1$  denotes the normalized unidirectional stick deflection,  $y_{\text{lin,max}}$  denotes the maximum command output of the linear mapping, and  $y_{\text{abs,max}}$  defines the limit command output according to requirement 2.

The min operation in (5.54) enforces requirement 3 and hence prevents a reversal of the stick gradient in case of excessive degradation of the performance in the respective command channel. However, in nominal conditions the linear limit  $y_{\text{lin,max}}$  is by design smaller than the absolute limit  $y_{\text{abs,max}}$ , which renders a constant mapping in accordance with requirement 1. Furthermore, the absolute command limit  $y_{\text{abs,max}}$  is dynamically calculated based on model assumptions and measurements and is discussed for each channel individually in subsection 5.3.3.4 and subsection 5.3.3.5.

For large stick deflections  $\alpha < d \leq 1$ , the mapping follows a quadratic relationship

$$y = y_{\text{qdr}}(d) = c_1 d^2 + c_2 d + c_3 \quad \text{for } \alpha < d \leq 1, \quad (5.55)$$

where the constants  $c_1$ ,  $c_2$ , and  $c_3$  follow from requirements 2 and 4 listed earlier, which enforce the continuity, continuous differentiability, and the maximum command output for a full stick deflection. This translates to the following constraints

$$y_{\text{qdr}}(d = \alpha) \stackrel{!}{=} y_{\text{lin}}(d = \alpha) = \alpha \cdot \min(y_{\text{lin,max}}, y_{\text{abs,max}}), \quad (5.56)$$

$$\left. \frac{\partial y_{\text{qdr}}}{\partial d} \right|_{d=\alpha} \stackrel{!}{=} \left. \frac{\partial y_{\text{lin}}}{\partial d} \right|_{d=\alpha} = \min(y_{\text{lin,max}}, y_{\text{abs,max}}), \quad (5.57)$$

$$y_{\text{qdr}}(d = 1) \stackrel{!}{=} y_{\text{abs,max}}. \quad (5.58)$$

Inserting (5.55) into the constraints (5.57) to (5.58) leads to the solution of the constants  $c_1$ ,  $c_2$ , and  $c_3$ :

$$c_1 = -\frac{\min(y_{\text{lin,max}}, y_{\text{abs,max}}) - y_{\text{abs,max}}}{(\alpha - 1)^2}, \quad (5.59)$$

$$c_2 = \min(y_{\text{lin,max}}, y_{\text{abs,max}}) - 2\alpha c_1, \quad (5.60)$$

$$c_3 = y_{\text{abs,max}} - c_1 - c_2. \quad (5.61)$$

In the following sections the sub-functions of the command scaling and transformation block are presented. Furthermore, the CMA-based stick mapping is applied to the vertical and turn channel for which the detailed derivations are worked out in subsection 5.3.3.4 and subsection 5.3.3.5.



### 5.3.3.2 Airspeed Limits

The *Airspeed Limits* block includes the logic for the calculation of the upper airspeed limit  $V_{CAS,lim,hi}$  and lower airspeed limit  $V_{CAS,lim,lo}$ . The airspeed limits are used within the command scaling and transformation for the longitudinal channel as well as the airspeed protection function that is located in the *Vertical Channel* command scaling block. An overview of the *Airspeed Limits* block and its internal structure is shown in figure 5.16.

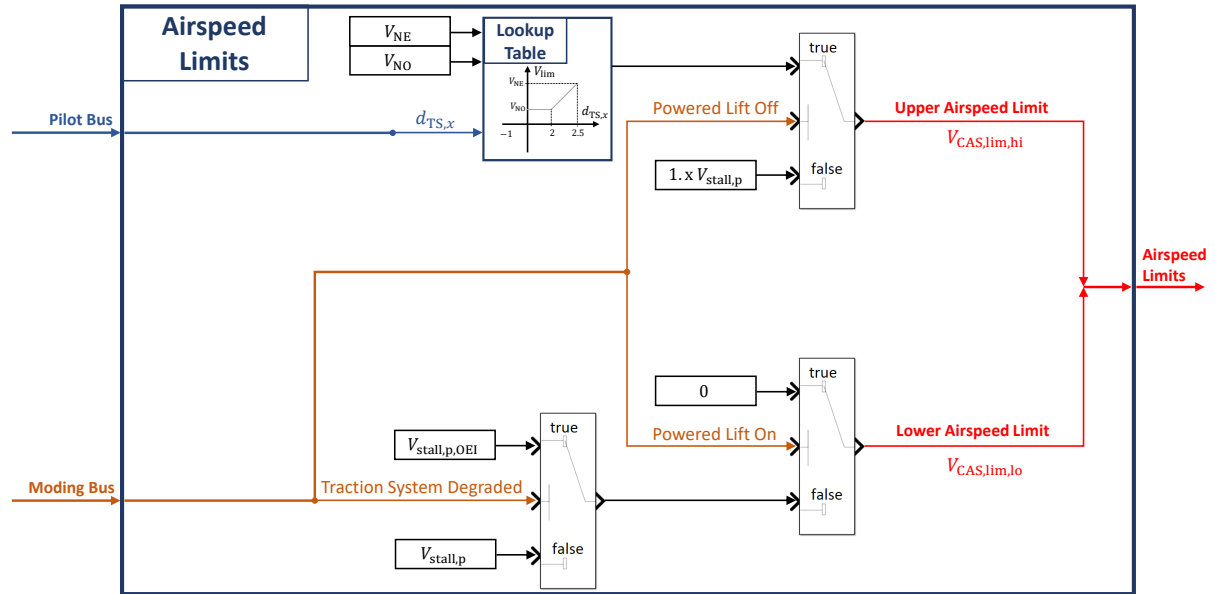


Figure 5.16: *Airspeed Limits* Block

Truth table 5.2 below summarizes the logic for the lower airspeed limit  $V_{CAS,lim,lo}$ :

Table 5.2: *Truth Table for Lower Airspeed Limit*

Powered Lift Mode	Degradation Mode	Lower Airspeed Limit
Powered Lift On == true	Traction System Degraded == false	0
	Traction System Degraded == true	
Powered Lift On == false	Traction System Degraded == false	$V_{stall,p}$
	Traction System Degraded == true	$V_{stall,p,OEI}$

While the powered lift system is engaged (according to subsection 5.3.2.3), the lower airspeed limit  $V_{CAS,lim,lo}$  is set to 0 (i.e. no lower limit) independent of the failure status of the traction system, since the lifting force can be provided regardless of the airspeed.

When the powered lift system is not engaged (i.e. it is turned off, turning off, or turning on according to subsection 5.3.2.3), the lower airspeed limit is motivated by sufficient margin towards the stall speed and providing optimum climb gradients. To this end,  $V_{CAS,lim,lo}$  is set to  $V_{stall,p}$  from (4.16) in the nominal case (i.e. when the traction system is fully functional) as was discussed in subsection 4.2.2.

In case of a traction system failure the controller degrades to *Traction System Degraded* mode and the lower airspeed limit  $V_{CAS,lim,lo}$  is set to  $V_{stall,p,OEI}$ , which accounts for the additional asymmetrical drag and guarantees optimum climb performance analogously to the take-off safety speed  $V_2$  [119].

The logic for the upper airspeed limit  $V_{CAS,lim,hi}$  is summarized in truth table 5.3:

**Table 5.3:** *Truth Table for Upper Airspeed Limit*

Powered Lift Mode	Degradation Mode	Upper Airspeed Limit
Powered Lift Off == false	Traction System Degraded == false	$1.x V_{stall,p}$
	Traction System Degraded == true	
Powered Lift Off == true	Traction System Degraded == false	$V_{NO} \dots V_{NE}$
	Traction System Degraded == true	

While the powered lift system is not completely off (i.e. it is turned on, turning on, or turning off according to subsection 5.3.2.3), the upper airspeed limit  $V_{CAS,lim,hi}$  is set to  $1.x V_{stall,p}$  in order to prevent excessive loads on the powered lift system as was discussed in subsection 4.2.2. Thereby, the notation  $1.x V_{stall,p}$  shall emphasize that this limit has to be greater than the lower airspeed limit  $V_{stall,p}$  in order to be able to perform a transition into pure fixed-wing flight.

When the powered lift system is off (according to subsection 5.3.2.3), the upper airspeed limit  $V_{CAS,lim,hi}$  is set to an airspeed between the maximum structural cruising speed  $V_{NO}$  [119] and the never-exceed speed  $V_{NE}$  [119]. Thereby, the airspeed limit is obtained by a linear look-up table dependent on the longitudinal deflection of the thrust stick  $d_{TS,x}$ .

To this end, the maximum allowed airspeed is set to the maximum structural cruising speed  $V_{NO}$  for stick deflections  $d_{TS,x} \leq 2$  according to figure 3.11. Furthermore, between the Maximum Continuous Thrust (MCT) stick position at  $d_{TS,x} = 2$  and the Maximum Peak Thrust (MPT) or take-off/go-around thrust (TOGA) stick position at  $d_{TS,x} = 2.5$  the upper airspeed limit  $V_{CAS,lim,hi}$  is linearly blended between  $V_{NO}$  and  $V_{NE}$ .

The upper and lower airspeed limits are furthermore summarized and provided as an output of the *Airspeed Limits* block. Note that the calculation of the airspeed limits can optionally be extended to account for the extension and retraction of a high-lift system.

### 5.3.3.3 Forward and Lateral Channel Command

The *Forward and Lateral Channel Command* block is aimed at generating the outer-loop commands for the forward and lateral channel. These include

- the desired horizontal kinematic velocity components in along-heading and across-heading direction  $V_{Cx,d}$  and  $V_{Cy,d}$  respectively, which are tracked during *Hover (Ground)* and *Hover (Air)* mode,
- the desired kinematic angle of attack  $\alpha_{kin,d}$  demand, which is tracked during *Transition* mode,
- and the desired airspeed  $V_{CAS,d}$ , lateral kinematic velocity  $V_{By,d}$ , and lateral specific force demand  $f_{By,d}$ , which are tracked during the highspeed phase in *Transition* and *Wingborne* mode.

The high-level structure of the *Forward and Lateral Channel* command scaling and transformation block is illustrated in figure 5.17.

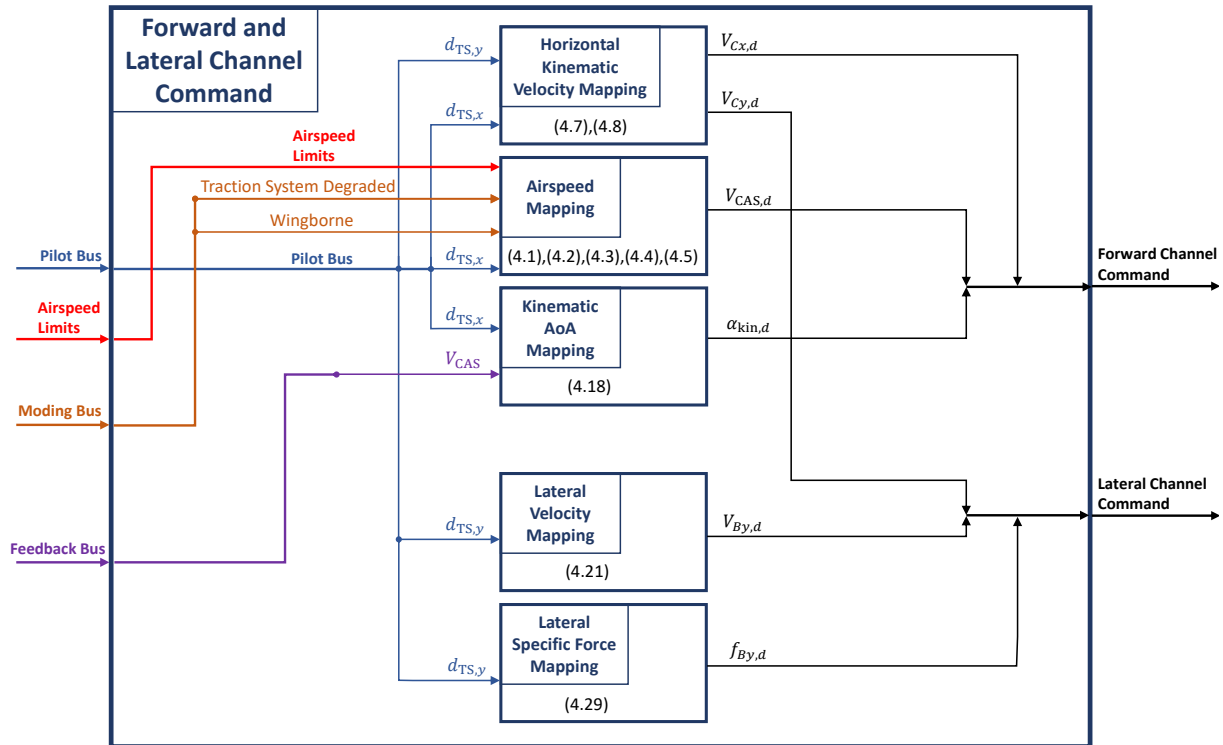


**Figure 5.17:** *Forward and Lateral Channel Command Block*

A brief summary of the individual mapping strategies is given in the following, which for the most part have been introduced in section 4.2 and are further detailed in the next paragraphs.

**Horizontal Kinematic Velocity Mapping** The desired horizontal kinematic velocity components  $V_{Cx,d}$  and  $V_{Cy,d}$  follow from the polar stick mapping in (4.7) and (4.8), which was introduced in subsection 4.2.1.1. Thereby, the longitudinal thrust stick deflection  $d_{TS,x}$  and the lateral thrust stick deflection  $d_{TS,y}$  (refer to figure 3.11) are mapped onto a horizontal kinematic velocity vector  $\begin{bmatrix} V_{Cx,d} & V_{Cy,d} \end{bmatrix}_C^T$ , such that

- the direction of the stick deflection in stick coordinates  $S$  is equivalent to the direction of the velocity in the control frame  $C$ , as is illustrated in figure 4.5 and
- the stick force to translational rate relationship yields Level 1 handling qualities according to the ADS-33E-PRF [12] requirements depicted in figure 4.6.

**Airspeed Mapping** The *Airspeed Mapping* block maps the longitudinal thrust stick deflection  $d_{TS,y}$  to the desired airspeed demand  $V_{CAS,d}$  according to figure 4.8. In order to prevent discontinuous variations in the airspeed command output upon mode switches between *Transition* and *Wingborne* mode, the continuity-based input-output mapping from section 4.1 is applied.

To this end, the desired airspeed demand  $V_{CAS,d}$  follows from equations (4.1), (4.2), (4.3), (4.4) and (4.5). Furthermore, the upper and lower airspeed limits are chosen according to  $V_{CAS,lim,lo}$  and  $V_{CAS,lim,hi}$  from table 5.2 and 5.3 respectively, which were introduced in subsection 5.3.3.2.

**Kinematic Angle of Attack Mapping** The *Kinematic Angle of Attack Mapping* block provides the desired kinematic angle of attack  $\alpha_{kin,d}$  during *Transition* mode based on the longitudinal thrust stick deflection  $d_{TS,x}$ . Thereby, the mapping follows equation (4.18) and is visualized in figure 4.7.

Note that in the beginning of the transition phase, the command output is interpreted as desired pitch angle and slowly blended over airspeed into a desired angle of attack in order to reduce the pitching sensitivity with respect to vertical path changes at low speeds.

**Lateral Velocity and Lateral Specific Force Mapping** In the *Lateral Velocity Mapping* and *Lateral Specific Force Mapping* blocks the relationships in (4.21) and (4.29) are used in order to convert a desired kinematic sideslip angle  $\beta_{kin}$ , aerodynamic sideslip angle  $\beta_{aer}$ , and lateral loadfactor  $n_{By}$  into the desired lateral velocity  $V_{By,d}$  and specific force  $f_{By,d}$  of the aircraft.

As was already mentioned in subsection 4.2.2.2 and subsection 4.2.3.2, the thrust stick's lateral degree of freedom is restricted within the thrust-lever region for  $d_{TS,x} > 1$ . Therefore, the zero-output in the command channel leads to an automatic lateral coordination during turns. However, as was also mentioned in subsection 3.2.2, the use of pedals for non-zero commands of sideslip angles or loadfactors can in general be considered.

### 5.3.3.4 Vertical Channel Command

The *Vertical Channel Command* block generates the desired climb and sink rate command  $\dot{h}_d$  for the VTOL transition aircraft based on the longitudinal climb stick deflection  $d_{CS,x}$  according to figure 3.11. Changes in the aircraft's vertical path are closely related to its performance capabilities. Therefore, the stick mapping has to account for the physically motivated absolute command limits of the aircraft, which was discussed in subsection 5.3.3.1 in the context of Control Margin Awareness (CMA).

An overview of the *Vertical Channel Command* block is given in figure 5.18 below.

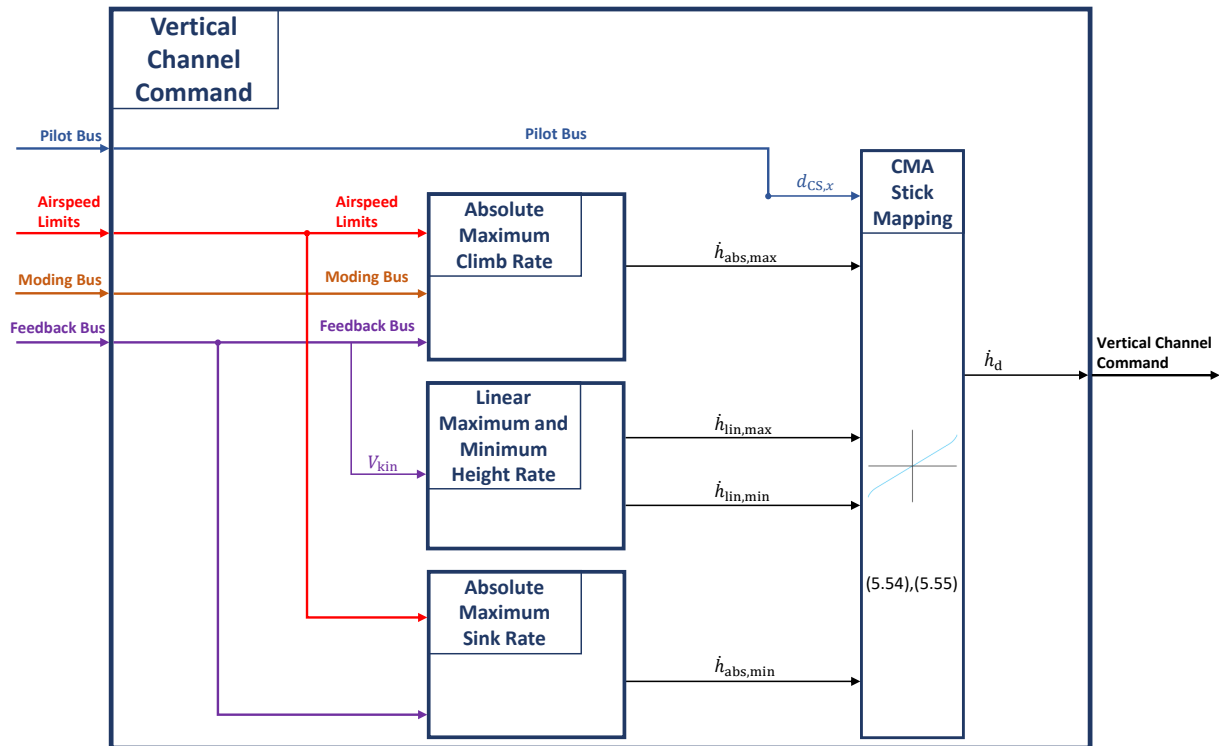


**Figure 5.18:** *Vertical Channel Command Block*

The *Vertical Channel Command* block consists of the following main functions:

- The generalized CMA-based stick mapping from subsection 5.3.3.1 is used in the *CMA Stick Mapping* block in order to calculate the desired height rate demand  $\dot{h}_d$  based on the longitudinal climb stick deflection  $d_{CS,x}$ , the absolute climb and sink rate limits  $\dot{h}_{abs,max}$  and  $\dot{h}_{abs,min}$ , and the linear climb and sink rate limits  $\dot{h}_{lin,max}$  and  $\dot{h}_{lin,min}$  respectively.
- The absolute climb rate limit  $\dot{h}_{abs,max}$  is dynamically calculated in the *Absolute Maximum Climb Rate* block.

- The absolute sink rate limit  $\dot{h}_{\text{abs,min}}$  is dynamically calculated in the *Absolute Maximum Sink Rate* block.
- The linear climb and sink rate limits  $\dot{h}_{\text{lin,max}}$  and  $\dot{h}_{\text{lin,min}}$  are dynamically calculated in the *Linear Maximum and Minimum Height Rate* block.

Since the Control-Margin-Awareness-based stick mapping was introduced in subsection 5.3.3.1, only the climb and sink rate limit calculations are discussed in detail in the following.

**Absolute Maximum Climb Rate** The high-level functional structure of the *Absolute Maximum Climb Rate* block is illustrated in figure 5.19 below.

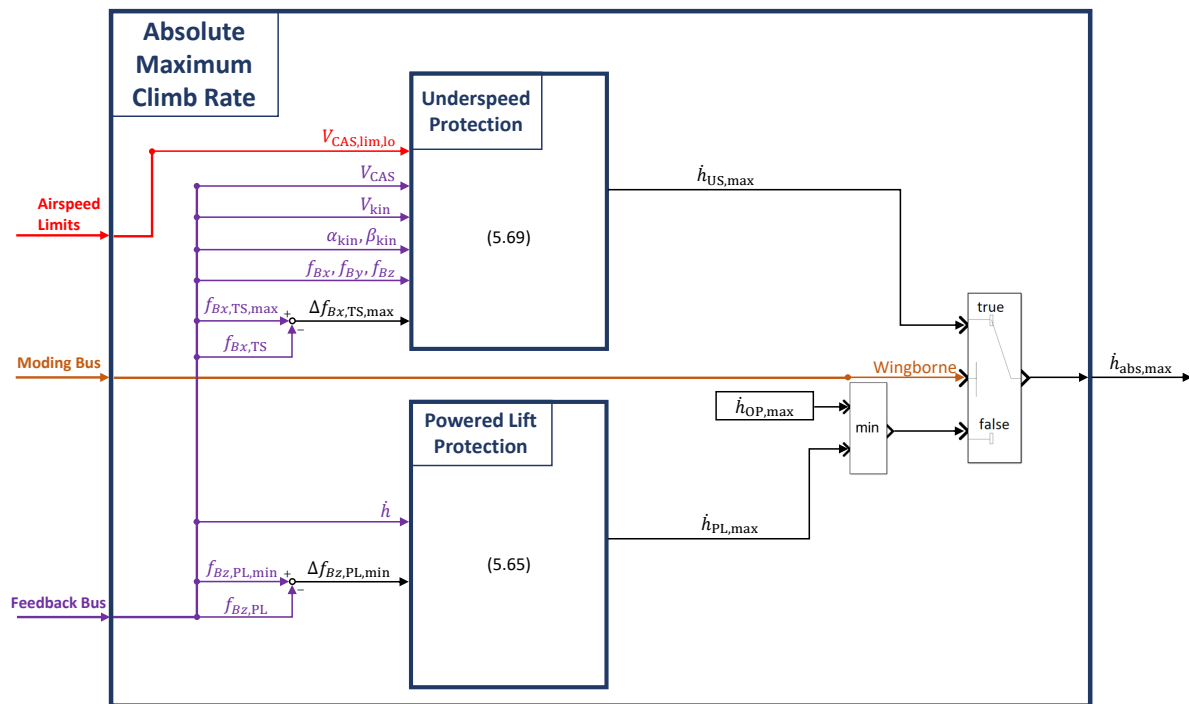


**Figure 5.19:** *Absolute Maximum Climb Rate Block*

The general objective of the block is to calculate the maximum admissible climb rate for which the system reaches one of the following limits:

- The specific powered lift force  $f_{Bz,PL}$  reaches the admissible limit value  $f_{Bz,PL,lim}$  in *Hover* and *Transition* mode. This protection aims to avoid excessive demands to the powered lift system that can reduce the remaining control authority in the rotational channel or lead to excessive loads on the lifting motors at higher speeds.
- The calibrated airspeed  $V_{CAS}$  reaches the lower airspeed limit  $V_{CAS,lim,lo}$  during *Wingborne* mode. This protection aims to avoid dangerous underspeed conditions and guarantees optimum climb performance during fixed-wing flight, as was discussed in subsection 4.2.3.3.

- The climb rate reaches the operational maximum climb rate  $\dot{h}_{\text{OP,max}}$ . This limit provides a constant absolute limit for the climb rate, which can account for operational limitations or handling qualities. In particular, limiting the admissible climb rate demand in hover might be necessary in order to yield the equivalent first-order response (4.146) in the vertical rate with the parameters from table 4.3. Latter represent the parameters for which Level 1 handling qualities are achieved in the vertical channel according to ADS-33E-PRF [12].

For the powered lift protection function, it is required that a maximum pull on the climb stick  $d_{\text{CS},x}$  yields the absolute maximum climb rate  $\dot{h}_{\text{abs,max}} = \dot{h}_{\text{PL,max}}$  for which the estimated powered lift reaches a limit value  $f_{Bz,\text{PL,lim}} = f_{Bz,\text{PL,min}}$ . To this end, the desired powered lift limit dynamics are stated as

$$\dot{f}_{Bz,\text{PL}} = K_{\text{PL,lim}} (f_{Bz,\text{PL,min}} - f_{Bz,\text{PL}}) , \quad (5.62)$$

where  $K_{\text{PL,lim}}$  denotes the desired bandwidth with which the estimated powered lift  $f_{Bz,\text{PL}}$  approaches the limit  $f_{Bz,\text{PL,min}}$ . Thereby, the limit value is either chosen as a constant maximum proportion of the available powered lift capability or dynamically adapted based on the current airspeed in order to account for aerodynamic loads.

Furthermore, the following simplified assumptions are made:

- A change in the VTOL's powered lift output is proportional to a change in the stationary climb rate

$$\Delta f_{Bz,\text{PL}} = K_{\dot{h} \rightarrow \text{PL}} \frac{1}{\cos(\phi) \cos(\theta)} \Delta \dot{h} , \quad (5.63)$$

where  $\frac{1}{\cos(\phi) \cos(\theta)}$  accounts for the attitude of the system. The parameter  $K_{\dot{h} \rightarrow \text{PL}}$  in (5.63) summarizes the effects of additional aerodynamic drag as a consequence of the increased climb rate.

- The resulting climb rate dynamics as a response to the absolute maximum climb rate demand  $\dot{h}_d = \dot{h}_{\text{PL,max}}$  are approximated by an equivalent first-order system and yield

$$\ddot{h} \approx K_{\dot{h}_{\text{ref}}} (\dot{h}_{\text{PL,max}} - \dot{h}) , \quad (5.64)$$

where  $K_{\dot{h}_{\text{ref}}}$  denotes the reference bandwidth of the height rate dynamics, which is discussed in further detail in subsection 5.3.4.1.

Considering the increments in (5.63) during a time increment  $\Delta t$  and inserting both (5.62) and (5.64) yields the maximum admissible climb rate

$$\dot{h}_{\text{PL,max}} = \dot{h} + \frac{K_{\text{PL,lim}}}{K_{\dot{h}_{\text{ref}}} K_{\dot{h} \rightarrow \text{PL}}} \cos(\phi) \cos(\theta) (f_{Bz,\text{PL,min}} - f_{Bz,\text{PL}}) , \quad (5.65)$$

which yields the desired powered lift dynamics in (5.62) and for which the model-based estimation of the powered lift  $f_{Bz,\text{PL}}$  is discussed in subsection 5.3.5.

The underspeed protection is active during fixed-wing flight and ensures that a maximum pull on the climb stick  $d_{CS,x}$  yields the absolute maximum climb rate  $\dot{h}_{\text{abs,max}} = \dot{h}_{\text{US,max}}$  for which the calibrated airspeed  $V_{\text{CAS}}$  reaches the lower airspeed limit  $V_{\text{CAS,lim,lo}}$ , which originates from the *Airspeed Limits* block in figure 5.16. To this end, the desired airspeed limit dynamics from (4.32) are recalled:

$$\dot{V} = \dot{V}_{\text{CAS,lim}} = \max\left(\dot{V}_{\text{CAS,min}}, K_{V,\text{lim}}(V_{\text{CAS,lim,lo}} - V_{\text{CAS}})\right), \quad (5.66)$$

where  $\dot{V}_{\text{CAS,min}}$  is the maximum admissible deceleration and  $K_{V,\text{lim}}$  denotes the desired bandwidth for the convergence of the airspeed  $V_{\text{CAS}}$  towards the lower airspeed limit  $V_{\text{CAS,lim,lo}}$  from table 5.2 in subsection 5.3.3.2.

The relationship between the maximum admissible climb rate  $\dot{h}_{\text{US,max}}$  and the resulting deceleration dynamics from (5.66) follows from the power balance equation (4.30) in subsection 4.2.3.3. To this end, it is assumed that the aircraft operates at the maximum admissible thrust setting yielding its *specific excess thrust* (SET).

The energy dynamics for the limit case are then given by

$$\dot{E} = mV\dot{V}_{\text{CAS,lim}} + mg\dot{h}_{\text{US,max}} = mV \cdot (\text{SET})_{Kx}, \quad (5.67)$$

where  $m$  denotes the aircraft's mass,  $g$  is the gravitational constant, and  $V$  is the kinematic speed of the aircraft. Furthermore, the influence of wind is neglected and  $(\text{SET})_{Kx}$  denotes the portion of SET in the longitudinal axis of the kinematic frame, i.e. in the direction of flight.

The specific excess thrust in forward direction of the K frame is furthermore approximated by transforming the body-fixed specific force and remaining thrust margin using (4.92) and considering the x-direction:

$$(\text{SET})_{Kx} = \begin{bmatrix} 1 & 0 & 0 \end{bmatrix}_K \mathbf{M}_{KB} \left[ (\mathbf{f})_B + \begin{bmatrix} \Delta f_{Bx,\text{TS,max}} \\ 0 \\ 0 \end{bmatrix}_B \right]. \quad (5.68)$$

Thereby,  $\mathbf{M}_{KB}$  denotes the rotation matrix between body and kinematic frame from (4.92),  $(\mathbf{f})_B$  denotes the specific force in the body frame, and  $\Delta f_{Bx,\text{TS,max}} = f_{Bx,\text{TS,max}} - f_{Bx,\text{TS}}$  is the remaining specific thrust margin of the traction system.

Note that (5.68) provides the specific excess thrust by adding the remaining margin towards the traction system's maximum thrust capability  $\Delta f_{Bx,\text{TS,max}}$  to a measurement of the specific force  $(\mathbf{f})_B$ , which incorporates the net effect of the current thrust and drag forces. In doing so, the model dependency regarding the maximum thrust of the aircraft is minimized through the use of a measurement. In particular, when the system is operating at the maximum thrust setting, the calculation of SET reduces to merely measuring the specific force  $(\mathbf{f})_B$  acting on the system.

The calculation of the traction system's specific thrust margin  $\Delta f_{Bx,\text{TS,max}} = f_{Bx,\text{TS,max}} - f_{Bx,\text{TS}}$  is discussed in further detail in subsection 5.3.5 and is assumed to be available as a feedback, as is illustrated in figure 5.19.



Furthermore, solving (5.67) for  $\dot{h}_{US,max}$  and considering (5.68), (5.66), and (4.92) yields the maximum admissible climb rate

$$\dot{h}_{US,max} = \frac{V}{g} \left[ (\text{SET})_{Kx} - \max \left( \dot{V}_{CAS,min}, K_{V,lim} (V_{CAS,lim,lo} - V_{CAS}) \right) \right] \quad (5.69)$$

with

$$(\text{SET})_{Kx} = \cos(\alpha_{kin}) \cos(\beta_{kin}) (f_{Bx} + \Delta f_{Bx,TS,max}) + \sin(\beta_{kin}) f_{By} + \sin(\alpha_{kin}) \cos(\beta_{kin}) f_{Bz}$$

for which the aircraft decelerates to the lower airspeed limit  $V_{CAS,lim,lo}$  according to (5.66).

**Absolute Maximum Sink Rate** The high-level functional structure of the *Absolute Maximum Sink Rate* block is illustrated in figure 5.20 below.

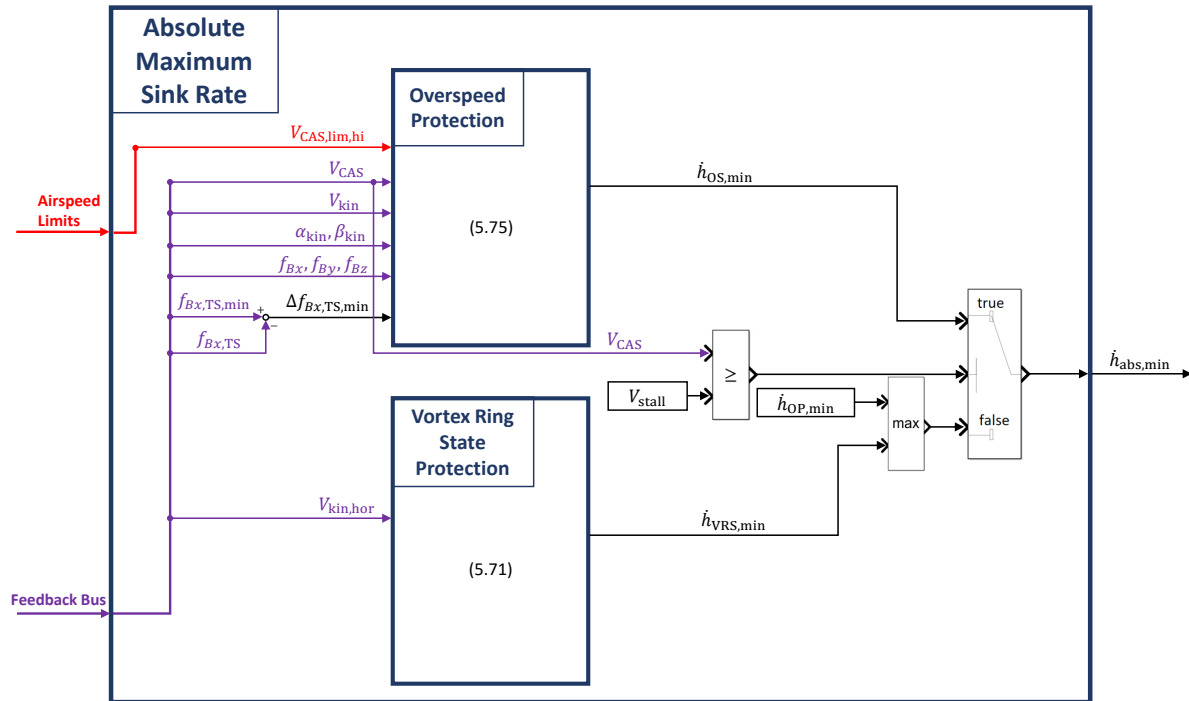


**Figure 5.20:** *Absolute Maximum Sink Rate Block*

The general objective of the block is to calculate the maximum admissible sink rate for which the system reaches one of the following limits:

- The system is about to enter the *vortex ring state* [14] [120]. Limiting the sink rate is aimed at protecting against dangerous aerodynamic conditions in which the VTOL aircraft descends into its own induced downwash, which can cause severe loss of powered lift [121] and uncontrolled pitch and roll oscillations [14].
- The calibrated airspeed  $V_{CAS}$  reaches the upper airspeed limit  $V_{CAS,lim,hi}$ . This protection aims to avoid dangerous overspeed conditions and hence excessive loads on the powered lift system and airframe, as was discussed in subsection 5.3.3.2.

- The sink rate reaches the operational maximum sink rate  $\dot{h}_{OP,\min}$ . Analogously to the operational maximum climb rate  $\dot{h}_{OP,\max}$ , this limit provides a constant absolute limit for the sink rate, which accounts for operational limitations or handling qualities.

The *Vortex Ring State Protection* block in figure 5.20 implements the functionality that yields the minimum admissible height rate  $\dot{h}_{VRS,\min}$  (i.e. the maximum admissible sink rate) for which the VTOL aircraft is about to enter vortex ring state (VRS) condition.

To this end, a stability region similar to figure 5.21 is used, which determines the stability boundary for the VRS. Thereby, the VRS boundary is defined in terms of the normalized horizontal and vertical velocity of the VTOL aircraft and yields the well-known [121] [120] [14] knee-shaped region in figure 5.21, which is determined based on experimental data and analytical derivation from [122] and [123].

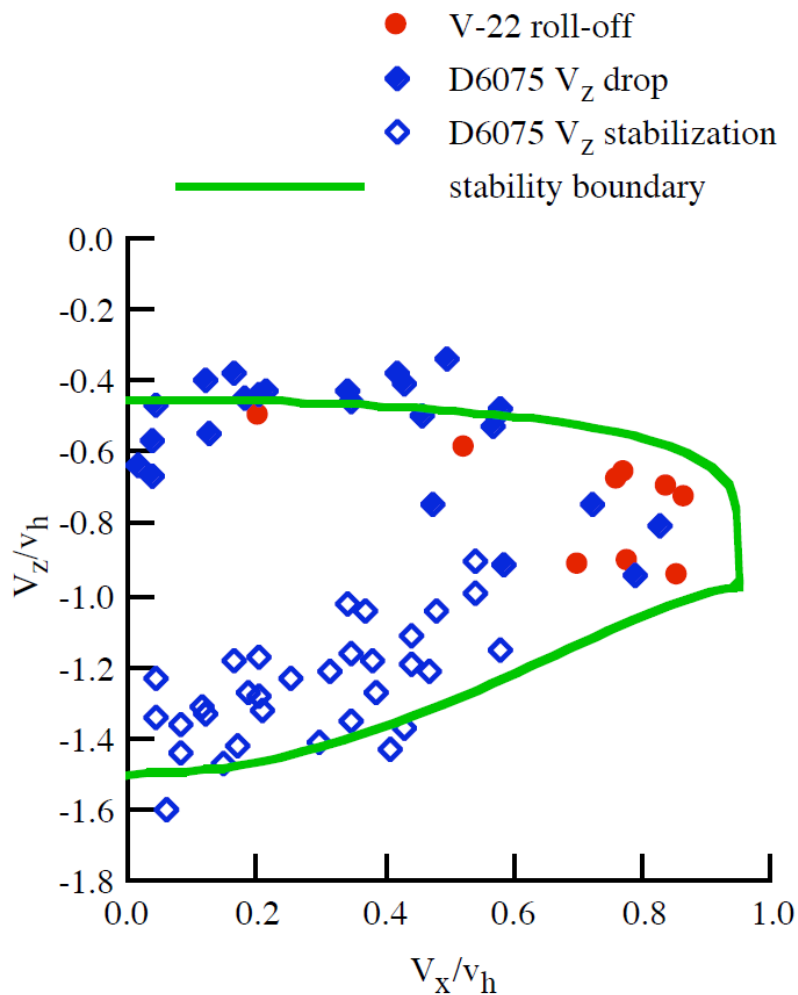


**Figure 5.21:** *Stability Boundary of VRS Model [14]*

The dimensionless velocities  $V_x/v_h$  and  $V_z/v_h$  in figure 5.21 are normalized with respect to the ideal hover induced velocity [14]

$$v_h = \sqrt{\frac{T}{2\rho A}}, \quad (5.70)$$

where  $T$  is the total powered lift force,  $\rho$  is the air density, and  $A$  is the total rotor disk area of the VTOL aircraft. Assuming a stationary hover state, the total rotor thrust equals the aircraft's weight and hence the induced velocity of the airflow is approximated by  $v_h = \sqrt{\frac{mg}{2\rho A}}$ .

The admissible vertical velocity is steadily decreasing as a function of increasing horizontal velocity, thereby avoiding the induced rotor downwash. Note that VRS does not occur when the horizontal velocity exceeds about  $1.0 \cdot v_h$ , which corresponds to a  $45^\circ$  deflected induced airflow from the horizontal plane.

Therefore, the maximum admissible sink rate  $\dot{h}_{\text{VRS,min}}$  is chosen as

$$\dot{h}_{\text{VRS,min}} = \begin{cases} c_1 V_{\text{kin,hor}}^2 + c_2, & \text{for } V_{\text{kin,hor}} \leq 1.0 \cdot v_h \\ \dot{h}_{\text{OP,min}}, & \text{for } V_{\text{kin,hor}} > 1.0 \cdot v_h \end{cases}, \quad (5.71)$$

where  $c_1 = -0.1852 \cdot \frac{1}{v_h}$  and  $c_2 = -0.45 \cdot v_h$  denote the parameters for a quadratic approximation of the upper stability boundary in figure 5.21.

Once the aircraft exceeds the stall speed  $V_{\text{stall}}$ , the overspeed protection is engaged and prevents the aircraft from exceeding the upper airspeed limit  $V_{\text{CAS,lim,hi}}$ , which is determined in the *Airspeed Limits* block from figure 5.16. To this end, an analogous approach is implemented as for the underspeed protection.

Upon completely pushing the climb stick  $d_{\text{CS},x}$ , the maximum admissible sink rate  $\dot{h}_{\text{abs,min}} = \dot{h}_{\text{OS,min}}$  is demanded, which shall lead to the desired airspeed dynamics

$$\dot{V} = \dot{V}_{\text{CAS,lim}} = \min \left( \dot{V}_{\text{CAS,max}}, K_{V,\text{lim}} (V_{\text{CAS,lim,hi}} - V_{\text{CAS}}) \right), \quad (5.72)$$

where  $\dot{V}_{\text{CAS,max}}$  is the maximum admissible acceleration and  $K_{V,\text{lim}}$  denotes the desired bandwidth for the convergence of the airspeed  $V_{\text{CAS}}$  towards the upper airspeed limit  $V_{\text{CAS,lim,hi}}$  from table 5.3 in subsection 5.3.3.2.

The relationship between the maximum admissible sink rate  $\dot{h}_{\text{OS,min}}$  and the resulting acceleration dynamics follow once again from a power balance equation as in (5.67). However, instead of considering the specific excess thrust (SET), the margin towards the minimum thrust setting is assumed and denoted as *specific thrust deficiency* (STD). Thereby, STD describes the expected amount of resulting drag-induced deceleration upon reducing the thrust to its minimum value.

The power balance equation in the limit case hence yields

$$\dot{E} = mV\dot{V}_{\text{CAS,lim}} + mg\dot{h}_{\text{OS,min}} = mV \cdot (\text{STD})_{K_x}, \quad (5.73)$$

where  $m$  denotes the aircraft's mass,  $g$  is the gravitational constant, and  $V$  is the kinematic speed of the aircraft. Once more the influence of wind is neglected.

The term  $(\text{STD})_{Kx}$  in (5.73) denotes the portion of STD in the direction of flight and is approximated analogously to (5.68):

$$(\text{STD})_{Kx} = \begin{bmatrix} 1 & 0 & 0 \end{bmatrix}_K \mathbf{M}_{KB} \begin{bmatrix} (\mathbf{f})_B + \begin{bmatrix} \Delta f_{Bx,TS,\min} \\ 0 \\ 0 \end{bmatrix}_B \end{bmatrix}, \quad (5.74)$$

with  $\mathbf{M}_{KB}$  from (4.92) and  $(\mathbf{f})_B$  denoting the specific force in the body frame. Furthermore,  $\Delta f_{Bx,TS,\min} = f_{Bx,TS,\min} - f_{Bx,TS}$  denotes the remaining specific thrust margin of the traction system towards the minimum thrust value. If the minimum specific thrust force  $f_{Bx,TS,\min}$  is assumed to be 0, the remaining margin towards the minimum thrust is just equal to the negative of the current estimated specific thrust force  $-f_{Bx,TS}$ .

Analogously to the estimation of the SET, when the system is operating at the minimum thrust setting, it follows that  $\Delta f_{Bx,TS,\min} = 0$  and the STD is obtained by merely measuring the specific force  $(\mathbf{f})_B$  acting on the system.

Furthermore, solving (5.73) for  $\dot{h}_{OS,\min}$  while considering (5.74), (5.72), and (4.92) yields the maximum admissible sink rate

$$\dot{h}_{OS,\min} = \frac{V}{g} \left[ (\text{STD})_{Kx} - \min \left( \dot{V}_{CAS,\max}, K_{V,\lim} (V_{CAS,\lim,\text{hi}} - V_{CAS}) \right) \right] \quad (5.75)$$

with

$$(\text{STD})_{Kx} = \cos(\alpha_{\text{kin}}) \cos(\beta_{\text{kin}}) (f_{Bx} + \Delta f_{Bx,TS,\min}) + \sin(\beta_{\text{kin}}) f_{By} + \sin(\alpha_{\text{kin}}) \cos(\beta_{\text{kin}}) f_{Bz}$$

for which the aircraft accelerates to the upper airspeed limit  $V_{CAS,\lim,\text{hi}}$  according to (5.72).

**Linear Maximum and Minimum Height Rate** In figure 5.22 the high-level functional structure of the *Linear Maximum and Minimum Height Rate* block is illustrated.

The linear limits serve the purpose of providing reference values for the linear portion of the mapping in figure 5.15. In contrast to the absolute limits, which are physically motivated by the overall performance capabilities of the aircraft, the linear limits are mainly motivated by operational requirements.

To this end, the maximum and minimum values of the linear limits  $\dot{h}_{\text{lin},\text{HV},\max}$  and  $\dot{h}_{\text{lin},\text{HV},\min}$  provide constant climb and sink rates at low kinematic velocities  $V_{\text{kin}}$  for constant stick deflections  $d_{\text{CS},x}$ . At higher speeds the maximum and minimum height rate values  $\dot{h}_{\text{lin},\gamma,\max}$  and  $\dot{h}_{\text{lin},\gamma,\min}$  ensure that the climb and sink gradients are kept constant for constant stick deflections  $d_{\text{CS},x}$ .

The constant limits  $\dot{h}_{\text{lin},\text{HV},\max}$  and  $\dot{h}_{\text{lin},\text{HV},\min}$  are chosen symmetrically and correspond to the admissible height rates for which VRS does not occur at vanishing horizontal velocities, hence the subscript HV for *Hover*. According to (5.71), the values are hence chosen as  $\dot{h}_{\text{lin},\text{HV},\max} = -c_2$  and  $\dot{h}_{\text{lin},\text{HV},\min} = c_2$ , where  $c_2 = -0.45 \cdot v_h$  denotes the vertex value of the VRS parabola approximation of the green boundary in figure 5.21.

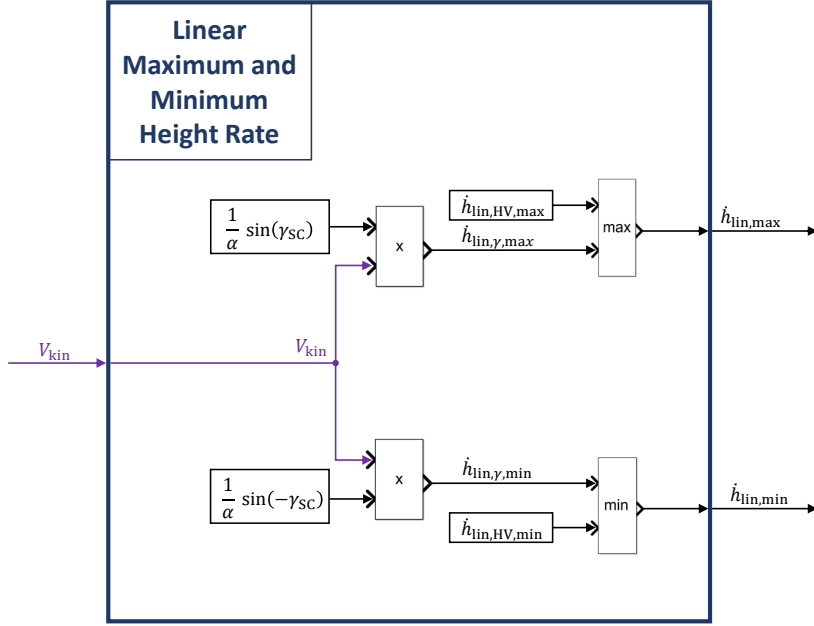


**Figure 5.22:** *Linear Maximum and Minimum Height Rate Block*

The ideal induced hover velocity  $v_h$  from (5.70) is thereby evaluated for stationary hover conditions and yields  $v_h = \sqrt{\frac{mg}{2\rho A}}$ , where  $mg$  is the weight of the VTOL aircraft,  $A$  is the total disk area, and  $\rho$  denotes the air density.

For higher velocities, the linear limits  $\dot{h}_{\text{lin},\gamma,\text{max}}$  and  $\dot{h}_{\text{lin},\gamma,\text{min}}$  shall provide consistent climb and sink gradients respectively. For stick deflections  $d_{\text{CS},x} = \pm\alpha$ , which correspond to the end of the linear region according to figure 5.15, the climb and sink gradients are motivated by the Special Condition VTOL requirements in MOC - Subpart B [6], which were presented in subsection 3.1.2. To this end, the resulting vertical path angle  $\gamma$  for a climb stick deflection  $d_{\text{CS},x} = \pm\alpha$  shall yield

$$\gamma(d_{\text{CS},x} = \pm\alpha) = \sin^{-1}\left(\frac{\dot{h}(d_{\text{CS},x} = \pm\alpha)}{V_{\text{kin}}}\right) \stackrel{!}{=} \pm\gamma_{\text{SC}}, \quad (5.76)$$

where  $\gamma_{\text{SC}}$  denotes the required climb gradient of 12.5% during departure and landing illustrated in figure 3.2, i.e

$$\pm\gamma_{\text{SC}} = \tan^{-1}\left(\pm\frac{12.5}{100}\right) = \pm 7.125^\circ. \quad (5.77)$$

Furthermore, using the linear portion of the generalized stick mapping (5.54) and inserting it in (5.76), it follows for the linear limits:

$$\dot{h}_{\text{lin},\gamma,\text{max}} = \frac{1}{\alpha} \sin(\gamma_{\text{SC}}) V_{\text{kin}} \quad (5.78)$$

and

$$\dot{h}_{\text{lin},\gamma,\text{min}} = \frac{1}{\alpha} \sin(-\gamma_{\text{SC}}) V_{\text{kin}}. \quad (5.79)$$

### 5.3.3.5 Turn Channel Command

The *Turn Channel Command* block generates the outer-loop commands that result in turn and yaw maneuvers of the VTOL aircraft. To this end, the desired heading rate  $\dot{\psi}_d$  and the desired roll angle  $\phi_d$  are calculated such that a consistent aircraft response throughout the entire flight envelope is provided, which was discussed in detail in section 4.2.

Figure 5.23 shows the high-level structure of the *Turn Channel Command* block.

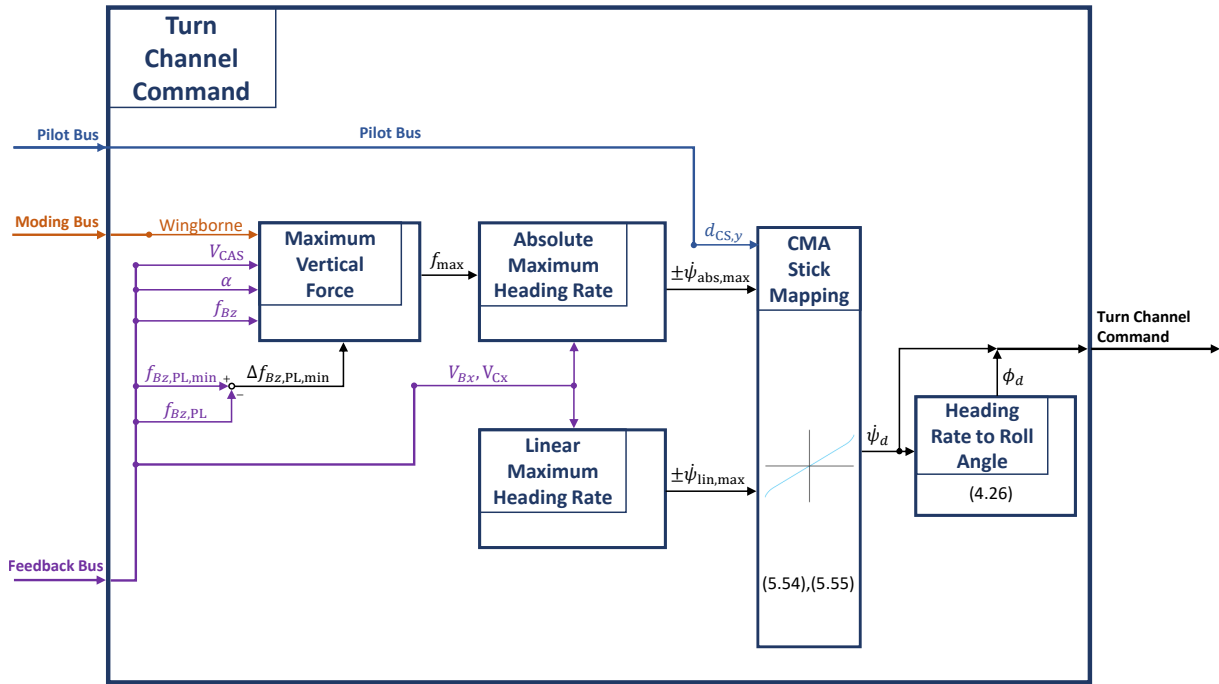


Figure 5.23: *Turn Channel Command* Block

Similarly to the *Vertical Channel Command* block, the *Turn Channel Command* block uses the Control-Margin-Awareness-based stick mapping from subsection 5.3.3.1, since the maximum turn performance is closely related to the physical capabilities of the VTOL aircraft. In particular, the turn performance is limited by the maximum vertical force that the aircraft can generate, which is accounted for in the calculation of the maximum command values for the turn channel.

The *Turn Channel Command* block consists of the following main functions:

- The generalized CMA-based stick mapping from subsection 5.3.3.1 is used in the *CMA Stick Mapping* block in order to calculate the desired heading rate demand  $\dot{\psi}_d$  based on the lateral climb stick deflection  $d_{CS,y}$ , the absolute heading rate limits  $\pm\dot{\psi}_{abs,max}$ , and the linear heading rate limits  $\pm\dot{\psi}_{lin,max}$ .
- The *Heading Rate to Roll Angle* block converts the desired heading rate into the desired roll angle according to (4.26) under the coordination constraint (4.22).

- The absolute heading rate limits  $\pm\dot{\psi}_{\text{abs,max}}$  are dynamically calculated in the *Absolute Maximum Heading Rate* block using the maximum available specific vertical force  $f_{\text{max}}$ .
- The linear heading rate limits  $\pm\dot{\psi}_{\text{lin,max}}$  are dynamically calculated in the *Linear Maximum Heading Rate* block.
- The *Maximum Vertical Force* block provides the maximum specific lifting net force that the VTOL aircraft can produce.

The CMA-based stick mapping was discussed in subsection 5.3.3.1 and the *Heading Rate to Roll Angle* block merely implements equation (4.26), which was derived in subsection 4.2.2.4. The remaining functional elements of the *Turn Channel Command* block are discussed in detail in the following.

**Maximum Vertical Force** In order to calculate the maximum admissible commands for the heading rate (and given the coordination condition hence for the turn rate), the control law has to account for the maximum body-vertical net force that the aircraft can generate. To this end, the *Maximum Vertical Force* block is utilized, which is illustrated in figure 5.24 below.

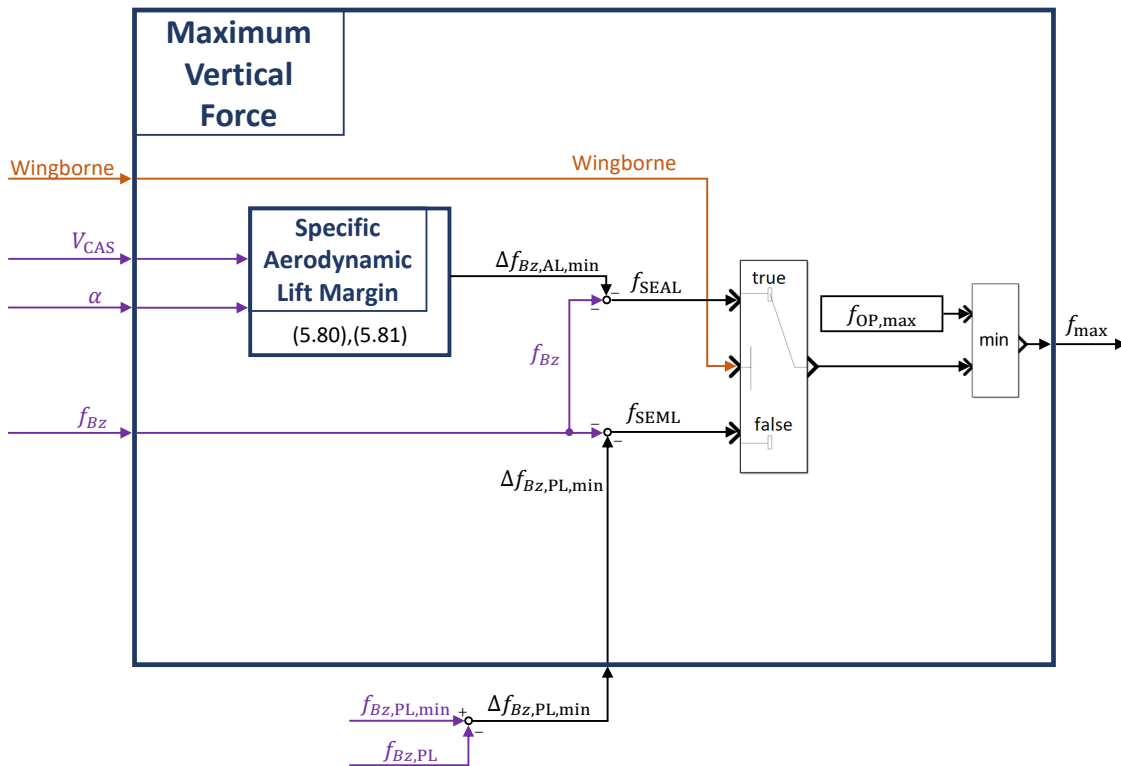


Figure 5.24: *Maximum Vertical Force Block*

During the *Wingborne* flight control mode, the maximum achievable body-vertical net force due to aerodynamic lift is estimated and denoted as *specific excess aerodynamic lift* (SEAL)  $f_{\text{SEAL}}$ . Similarly to the calculation of the specific excess thrust (SET) in (5.70) or the specific thrust deficiency (STD) in (5.76) for which the remaining margin towards the maximum or minimum thrust was considered, the calculation of SEAL is based on the margin in the achievable aerodynamic lift based on the proximity to stall.

To this end, the *specific aerodynamic lift margin* (SALM) is introduced, which follows from linearization of (4.99), (4.100), and (4.101) around the current angle of attack  $\alpha$  and yields

$$\text{SALM} = -\Delta f_{Bz, \text{AL}, \text{min}} = \frac{1}{m} \frac{1}{2} \rho_0 V_{\text{CAS}}^2 S C_{L\alpha} \Delta \alpha_{\text{max}}, \quad (5.80)$$

where  $m$  denotes the aircraft's mass,  $\rho_0$  is the reference air density on mean sea level,  $V_{\text{CAS}}$  is the calibrated airspeed,  $S$  is the reference wing area,  $C_{L\alpha}$  denotes the lift coefficient slope, and

$$\Delta \alpha_{\text{max}} = \alpha_{\text{stall}} - \alpha \quad (5.81)$$

denotes the margin of the angle of attack  $\alpha$  towards the stall angle of attack  $\alpha_{\text{stall}}$ .

Furthermore, using (5.80) and (5.81) the specific excess aerodynamic lift in body-vertical direction simply follows from

$$\begin{aligned} \underbrace{f_{\text{SEAL}}}_{\text{Specific Excess Aerodynamic Lift}} &= \underbrace{(-f_{Bz})}_{\text{Specific Aerodynamic Net Lift}} + \underbrace{(-\Delta f_{Bz, \text{AL}, \text{min}})}_{\text{Specific Aerodynamic Lift Margin}} \\ &= -f_{Bz} + \frac{1}{m} \frac{1}{2} \rho_0 V_{\text{CAS}}^2 S C_{L\alpha} (\alpha_{\text{stall}} - \alpha), \end{aligned} \quad (5.82)$$

where small angle of attacks are assumed and hence the equivalence of vertical direction in the body frame and in the aerodynamic frame.

Similarly, when the control law is not in *Wingborne* mode and the powered lift system is used for tracking the vertical channel, the maximum achievable body-vertical net force is estimated and denoted as *specific excess mixed lift* (SEML)  $f_{\text{SEML}}$ . Note that during transition flight, the SEML is the result of both aerodynamic lift due to the angle of attack regime in (4.18) and powered lift generated by the lifting motors.

Analogously to the SEAL, the SEML is calculated according to

$$\underbrace{f_{\text{SEML}}}_{\text{Specific Excess Mixed Lift}} = \underbrace{(-f_{Bz})}_{\text{Specific Mixed Net Lift}} + \underbrace{(-\Delta f_{Bz, \text{PL}, \text{min}})}_{\text{Specific Powered Lift Margin}}, \quad (5.83)$$

where  $\Delta f_{Bz, \text{PL}, \text{min}} = f_{Bz, \text{PL}, \text{min}} - f_{Bz, \text{PL}}$  denotes the margin of the current powered lift  $f_{Bz, \text{PL}}$  to the maximum powered lift value  $f_{Bz, \text{PL}, \text{min}}$  (in body-down direction), which was also used in (5.65) in the context of the maximum admissible climb rate.

Finally, the output of the *Maximum Vertical Force* block  $f_{\text{max}}$  is given by

$$f_{\text{max}} = \begin{cases} \min(f_{\text{SEAL}}, f_{\text{OP}, \text{max}}), & \text{for } \textit{Wingborne} == \textit{true} \\ \min(f_{\text{SEML}}, f_{\text{OP}, \text{max}}), & \text{for } \textit{Wingborne} == \textit{false} \end{cases}, \quad (5.84)$$

where  $f_{\text{OP}, \text{max}}$  denotes the maximum admissible specific vertical net force for the turn maneuver based on operational constraints (e.g. due to maximum load conditions).



**Absolute Maximum Heading Rate** Based on the maximum vertical specific net force  $f_{\max}$ , which is calculated in the *Maximum Vertical Force* block, the maximum and minimum admissible heading rate commands  $\pm\dot{\psi}_{\text{abs,max}}$  are calculated in the *Absolute Maximum Heading Rate* block, which is depicted in figure 5.25 below.

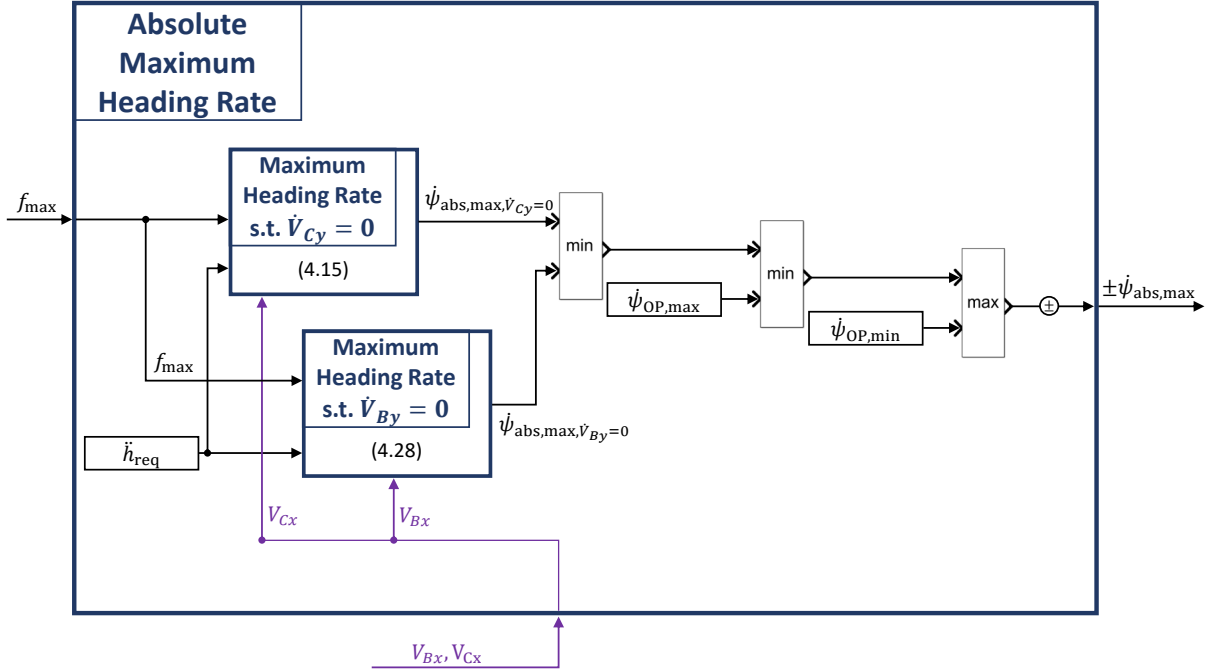


**Figure 5.25:** *Absolute Maximum Heading Rate Block*

To this end, the relationships in (4.15) and (4.28) are used, which yield the maximum admissible heading rates for which the coordination constraints  $\dot{V}_{Cy} = 0$  from (4.14) and  $\dot{V}_{By} = 0$  from (4.22) are met while reserving enough margin in the vertical force to achieve a minimum required vertical acceleration of  $\ddot{h}_{\text{req}}$ .

The maximum operational heading rate limit  $\dot{\psi}_{\text{OP,max}}$  is mainly relevant in the hover phase for which the heading rate is not limited by the coordination constraints (4.14) and (4.22) but rather by limitations of the lifting motors to generate yaw moments and the attainable handling qualities in the yaw channel. Thereby, handling quality requirements for the yaw channel can be found in subsection 3.3.6 of ADS-33E-PRF [12], which were also discussed in subsection 4.4.1.2 of this thesis.

The minimum operational heading rate limit  $\dot{\psi}_{\text{OP,min}}$  is driven by the performance requirements published by EASA in their publications of proposed means of compliance with the special condition VTOL [6] [41], which were discussed in detail in subsection 3.1.2. To this end, EASA states that the VTOL aircraft “should provide (...) a manoeuvring capability of not less than  $3^\circ/\text{s}$  of turn rate while not descending” [6, p. 9].

Furthermore, in subsection 4.2.3.4 it was shown that in case of insufficient vertical lift capability, the vertical acceleration margin  $\ddot{h}_{\text{req}}$  is traded in to allow for horizontal path changes by means of turning.

However, by design the lower airspeed limit  $V_{CAS,lim,lo}$  from table 5.2 provided by the *Airspeed Limits* block in figure 5.16 guarantees enough lifting capability during fixed-wing flight to enable not less than  $3^\circ/s$  of turn rate while not descending.

**Linear Maximum Heading Rate** Figure 5.26 below shows the high-level structure of the *Linear Maximum Heading Rate* block, which calculates the linear heading rate limits  $\pm\dot{\psi}_{lin,max}$ . Furthermore, the linear limits are used for the CMA-based stick mapping (5.54) and (5.55) from subsection 5.3.3.1, as is shown in figure 5.23.

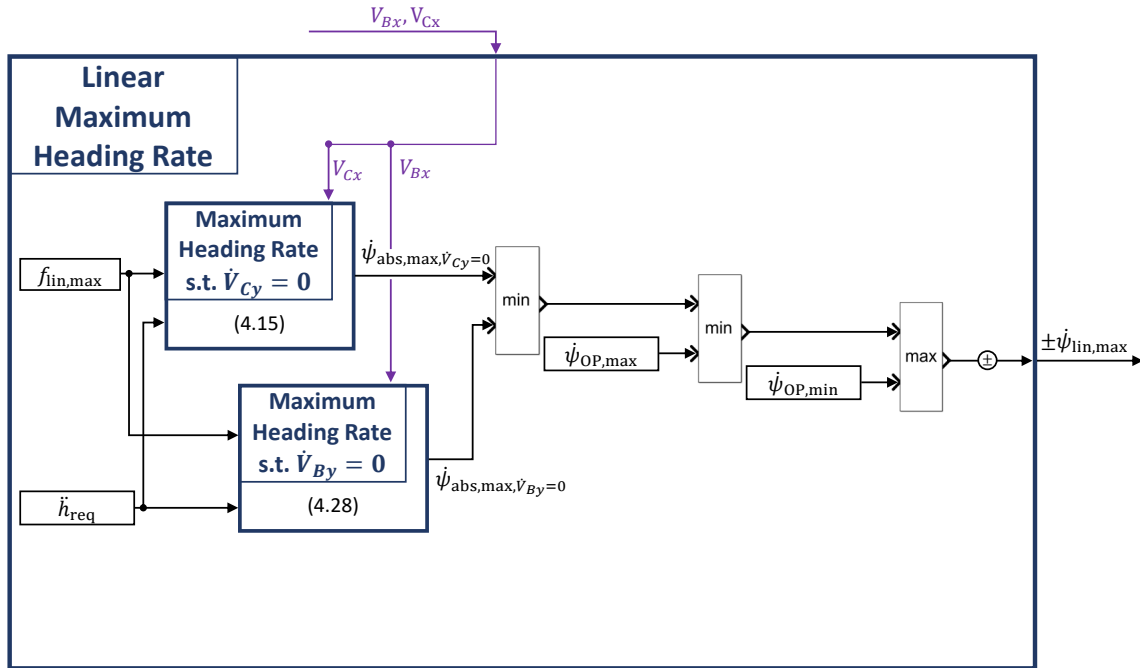


Figure 5.26: *Linear Maximum Heading Rate Block*

In contrast to the *Absolute Maximum Heading Rate* block, which uses the maximum body-vertical specific net force  $f_{max}$  that the aircraft can produce, the *Linear Maximum Heading Rate* block uses a constant specific force limit  $f_{lin,max}$  for the calculation of the linear heading rate limits  $\pm\dot{\psi}_{lin,max}$ .

Using a constant value for the maximum admissible vertical force yields a consistent turn response throughout the entire flight envelope for the  $\alpha$ -fraction of the climb stick's lateral axis  $d_{CS,y}$  (recall figure 3.11). In particular, deflecting the climb stick by an amount of  $|d_{CS,y}| \leq \alpha$ , the resulting heading rate demand  $\dot{\psi}_d$  corresponds to the  $d_{CS,y}$ -fraction of the heading rate  $\dot{\psi}_{lin,max}$  that results in a turn with a body-vertical load factor of  $\frac{f_{lin,max}}{g}$  (provided no acceleration demand in the height channel is present).

Analogously to the *Absolute Maximum Heading Rate* block, the resulting heading rate command is limited by the operational heading rate limit  $\dot{\psi}_{OP,max}$  at lower forward speeds, since the resulting yaw and turn rate for a given vertical load factor tends to infinity as the forward speed approaches zero, as can be seen from equations (4.15) and (4.28).

### 5.3.4 Outer Loop

The *Outer Loop* block represents the outer control loop, which takes the high-level commands from the *Command Scaling and Transformation* block and generates the necessary commands for the *Inner Loop* block. Figure 5.27 below shows a schematic overview of the outer loop in terms of a functional block diagram.

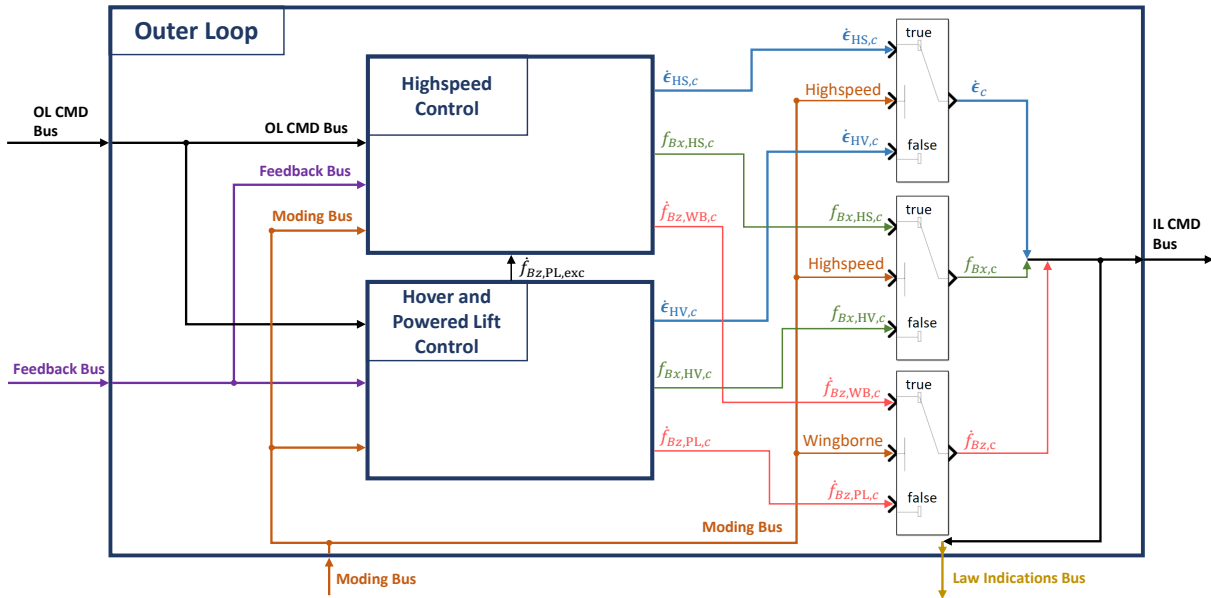


**Figure 5.27:** *Outer Loop Block*

The functionality of the outer loop is divided into two main blocks, both of which provide a complete set of inner loop commands, and a signal routing layer:

- The *Highspeed Control* block yields the control law for the *Transition* and *Wingborne* phase and implements the functions for
  - airspeed control, roll angle control, and lateral specific force or lateral velocity control during *Transition* and *Wingborne* mode (i.e. during *Highspeed* mode),
  - pitch angle and kinematic angle of attack control during *Transition* mode, and
  - vertical translational rate control using aerodynamic lift, turning off, and turning on the powered lift system during *Wingborne* mode.

Additionally, the attitude protection functionality ensures that no excessive roll and pitch angles occur during the *Transition* and *Wingborne* phase. The *Highspeed Control* block outputs the inner-loop commands consisting of the euler angle rate command  $\dot{\epsilon}_{HS,c}$  and the forward specific force command  $f_{Bx,HS,c}$  in the *Highspeed* mode as well as the specific powered lift rate command  $\dot{f}_{Bz,WB,c}$  in the *Wingborne* mode.

- The *Hover and Powered Lift Control* block yields the control law for the *Hover* phase as well as the powered lift system and implements the functions for
  - horizontal kinematic velocity control and heading rate control during *Hover* mode and
  - vertical translational rate control using the powered lift system during *Hover* and *Transition* Mode (i.e. in *Powered Lift On* mode when the powered lift system is engaged according to subsection 5.3.2.3).

The attitude protection functionality during *Hover* mode prevents excessive pitch and roll angles in the hover phase and incorporates the height above ground in order to prevent abnormal ground contact of the aircraft’s wings, lifting bars, or traction motors.

Despite similar implementation of the attitude protection function, two separate instances are deployed in the *Highspeed Control* block and the *Hover and Powered Lift Control* block in order to increase independence and decentralization of the control architecture and hence to comply with the design guidelines for good system architectures [3]. A more detailed rationalization is given in chapter 6.

The *Hover and Powered Lift Control* block outputs the inner-loop commands consisting of the euler angle rate command  $\dot{\epsilon}_{HV,c}$  and the forward specific force command  $f_{Bx,HV,c}$  in the *Hover* mode as well as the specific powered lift rate command  $\dot{f}_{Bz,PL,c}$  during *Powered Lift On* mode.

- The signal routing layer on the right of figure 5.27 assembles the inner-loop commands from the *Highspeed Control* block and the *Hover and Powered Lift Control* block into the *Inner-Loop Command Bus (IL CMD Bus)* and implements the necessary switching logics based on the *Highspeed* and *Wingborne* flags in the *Moding Bus* (recall the equivalence of *Wingborne* mode and  $\neg$  *Powered Lift On* mode from subsection 5.3.2 and figure 5.12).

In the following, a functional breakdown of the *Hover and Powered Lift Control* block and the *Highspeed Control* block are presented. Thereby, the basic control principles are similar to the ones presented in subsection 4.3.1. However, in the context of a complete control architecture specification, the emphasis is put on the concrete and exhaustive functional allocation and information flow within the control law.

Furthermore, additional functional elements are considered in the final control architecture, which are the result of the limited amount of available signals and their inherent characteristics (such as noise and delay) and which aim to increase the overall performance and robustness of the controller. To this end, reference models and feedback filters are discussed in the context of the outer and inner loop. Additionally, degradation strategies for the *Radar Altimeter Degraded* mode and *Traction System Degraded* mode are considered.

### 5.3.4.1 Hover and Powered Lift Control

Figure 5.28 below shows the functional structure of the *Hover and Powered Lift Control* block. This block implements the functions of horizontal kinematic velocity control during *Hover* mode as well as the powered lift based vertical translational rate control, which is active during the *Hover* and *Transition* phase.

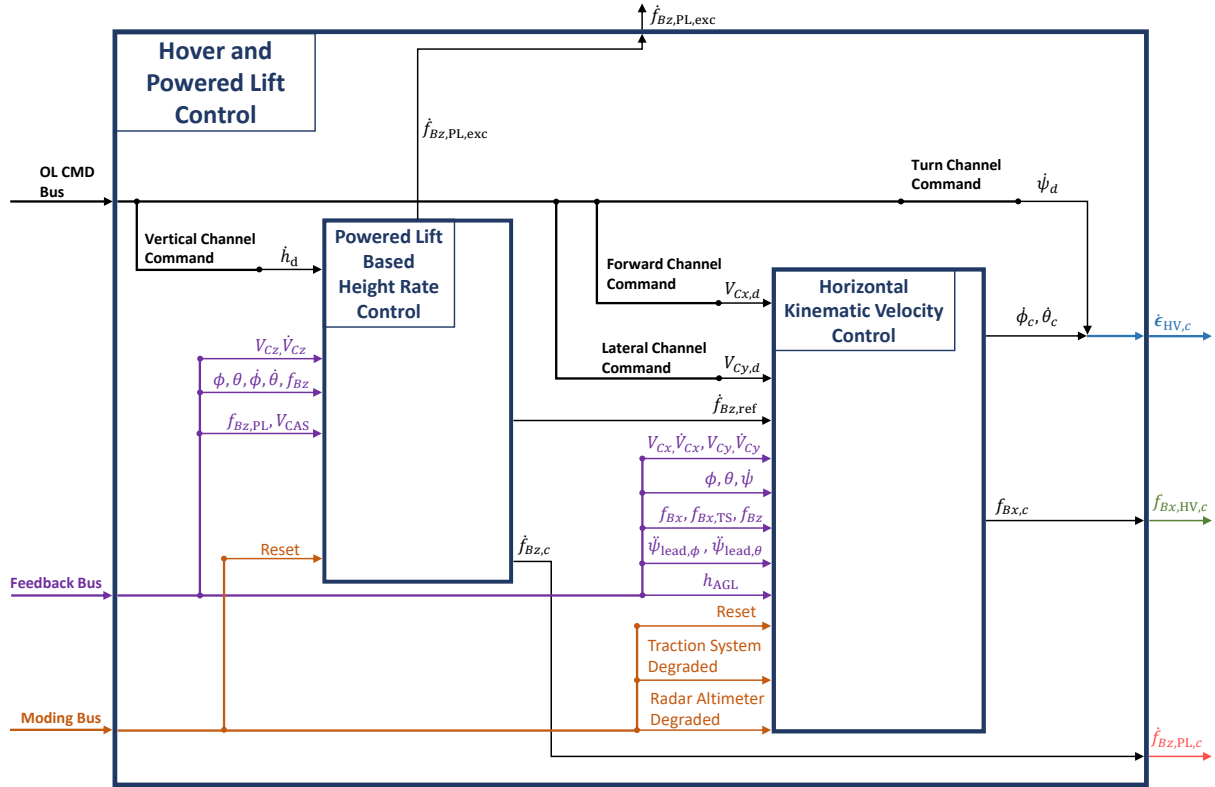


Figure 5.28: *Hover and Powered Lift Control Block*

In order to achieve functional independence of the low- and highspeed flight phase, the *Hover and Powered Lift Control* block is separated from the *Highspeed Control* block. As can be seen in figure 5.27, merely the specific excess powered lift rate  $\dot{f}_{Bz,PL,exc}$  is cross-fed. Latter represents the amount of demanded vertical jerk  $\dot{f}_{Bz,d}$  by the *Powered Lift Based Height Rate Control* block that exceeds the limit dynamics of the powered lift towards its lower limit  $f_{Bz,PL,max}$ . This term was introduced in the angle of attack rate limit (4.87) in subsection 4.3.2.3 and will be revisited in subsection 5.3.4.2 within the *Highspeed Control* block.

In the following, a functional decomposition of the *Powered Lift Based Height Rate Control* block and the *Horizontal Kinematic Velocity Control* block is conducted, which yields the commanded powered lift rate  $\dot{f}_{Bz,PL,c}$  on the one hand and the commanded forward specific force  $f_{Bx,c}$ , pitch angle rate  $\dot{\theta}_c$ , and roll angle rate  $\dot{\phi}_c$  on the other hand. Together with the heading rate demand  $\dot{\psi}_d$  from the outer-loop command bus, they represent the output of the *Hover and Powered Lift Control* block.

**Powered Lift Based Height Rate Control** The *Powered Lift Based Height Rate Control* block shall yield the necessary powered lift rate command  $\dot{f}_{Bz,c}$  in order to track a reference vertical velocity. To this end, it implements the following functional blocks, which are depicted in figure 5.29 and discussed in the remainder of this section:

- The *Height Rate Reference Model* block
- The *Height Rate Error Controller* block
- The *Dynamic Inversion* block
- The *Powered Lift Rate Command Saturation* block.

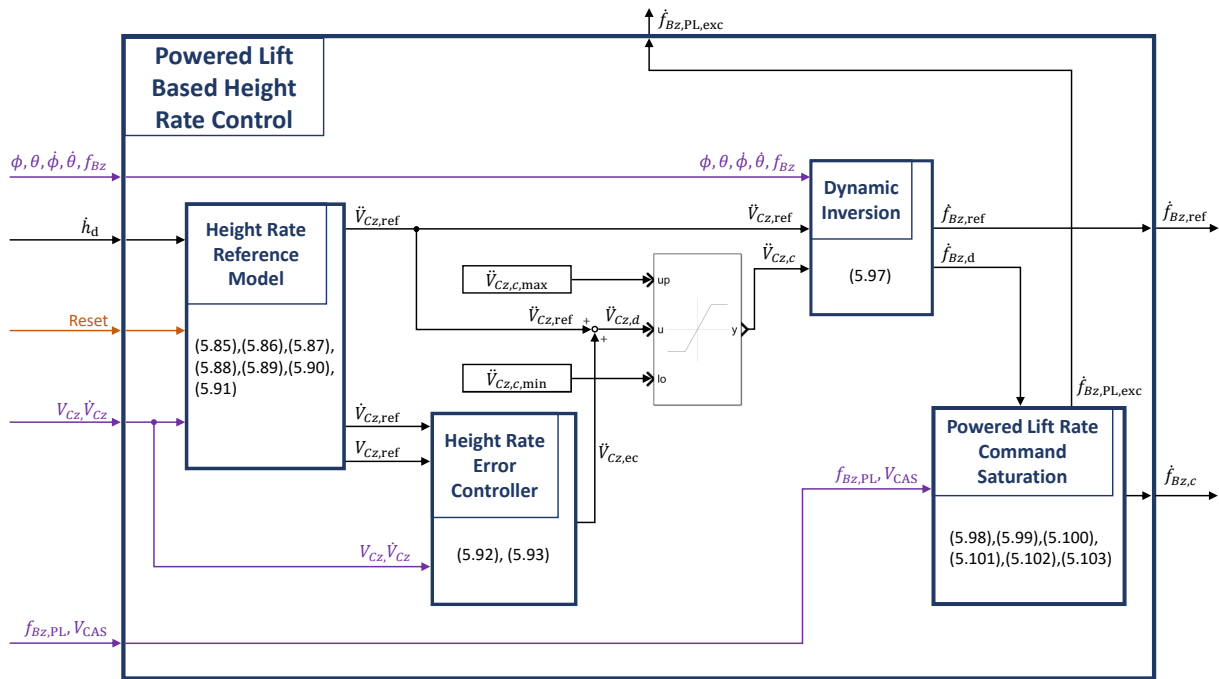


**Figure 5.29:** *Powered Lift Based Height Rate Control Block*

The *Height Rate Reference Model* provides a reference trajectory for the vertical velocity based on the height rate demand  $\dot{h}_d$ , which originates from the vertical command channel of the *Outer-Loop Command Bus (OL CMD Bus)*. To this end, it yields the reference earth-vertical jerk  $\ddot{V}_{Cz,ref} = -\ddot{h}$ , earth-vertical acceleration  $\dot{V}_{Cz,ref} = -\dot{h}$ , and earth-vertical velocity  $V_{Cz,ref} = -\dot{h}$ , which are denoted in the down direction of the control frame  $C$  from figure 4.4.

A second-order reference model for the vertical translational rate is chosen in order to account for the powered lift motor dynamics, which are approximated as first-order systems in the context of the control architecture. Hence, the highest derivative of the reference dynamics yields a direct feed-through to the desired motor rate commands, which is discussed in further detail in the *Inner Loop* block in subsection 5.3.5.

The following requirements are imposed on the reference dynamics:

1. The reference height rate  $\dot{h}_{\text{ref}} = -V_{Cz,\text{ref}}$  shall converge to the desired height rate  $\dot{h}_d$ .
2. The reference vertical rate dynamics shall comply with subsection 3.3.10 in ADS-33E-PRF [12], which states that the response characteristics of the height rate shall resemble an equivalent first-order transfer function with the parameters from table 4.3.
3. The reference vertical acceleration and jerk limits shall not exceed the physical capabilities or operational constraints of the VTOL aircraft, but they shall be sufficiently large such as to comply with requirement 2.
4. Upon initializing the reference dynamics, the reference states shall be sufficiently close to the true aircraft states in order to avoid transients.

In order to comply with the stated requirements, the reference vertical jerk is given by

$$\ddot{V}_{Cz,\text{ref}} = \min \left( \ddot{V}_{Cz,\text{ref,max}}, \max \left( \ddot{V}_{Cz,\text{ref,min}}, K_{\dot{V}_{Cz,\text{ref}}} \left( \dot{V}_{Cz,\text{ref,c}} - \dot{V}_{Cz,\text{ref}} \right) \right) \right), \quad (5.85)$$

with the reference vertical acceleration command

$$\dot{V}_{Cz,\text{ref,c}} = K_{V_{Cz,\text{ref}}} (V_{Cz,\text{ref,c}} - V_{Cz,\text{ref}}), \quad (5.86)$$

where the reference vertical velocity command  $V_{Cz,\text{ref,c}}$  is chosen as  $V_{Cz,\text{ref,c}} = -\dot{h}_d$  in order to comply with requirement 1.

Furthermore, the maximum and minimum reference vertical jerk limits are chosen as

$$\begin{aligned} \ddot{V}_{Cz,\text{ref,max}} &= \min \left( \ddot{V}_{Cz,\text{ref,OP,max}}, \ddot{V}_{Cz,\dot{V}_{\text{lim,max}}} \right), \\ \ddot{V}_{Cz,\text{ref,min}} &= \max \left( \ddot{V}_{Cz,\text{ref,OP,min}}, \ddot{V}_{Cz,\dot{V}_{\text{lim,min}}} \right), \end{aligned} \quad (5.87)$$

with the vertical jerks leading to the limit vertical reference accelerations

$$\begin{aligned} \ddot{V}_{Cz,\dot{V}_{\text{lim,max}}} &= K_{\dot{V}_{Cz,\text{lim}}} \left( \dot{V}_{Cz,\text{ref,max}} - \dot{V}_{Cz,\text{ref}} \right), \\ \ddot{V}_{Cz,\dot{V}_{\text{lim,min}}} &= K_{\dot{V}_{Cz,\text{lim}}} \left( \dot{V}_{Cz,\text{ref,min}} - \dot{V}_{Cz,\text{ref}} \right), \end{aligned} \quad (5.88)$$

the limit vertical reference accelerations given by

$$\begin{aligned} \dot{V}_{Cz,\text{ref,max}} &= \min \left( \dot{V}_{Cz,\text{ref,OP,max}}, \dot{V}_{Cz,V_{\text{lim,max}}} \right), \\ \dot{V}_{Cz,\text{ref,min}} &= \max \left( \dot{V}_{Cz,\text{ref,OP,min}}, \dot{V}_{Cz,V_{\text{lim,min}}} \right), \end{aligned} \quad (5.89)$$

and the vertical accelerations leading to the limit vertical velocities

$$\begin{aligned} \dot{V}_{Cz,V_{\text{lim,max}}} &= K_{V_{Cz,\text{lim}}} (V_{Cz,\text{ref,OP,max}} - V_{Cz,\text{ref}}), \\ \dot{V}_{Cz,V_{\text{lim,min}}} &= K_{V_{Cz,\text{lim}}} (V_{Cz,\text{ref,OP,min}} - V_{Cz,\text{ref}}). \end{aligned} \quad (5.90)$$

Thereby,  $\ddot{V}_{Cz,\text{ref},\text{OP,max}}$  and  $\ddot{V}_{Cz,\text{ref},\text{OP,min}}$  denote the maximum and minimum operational reference jerk limits,  $\dot{V}_{Cz,\text{ref},\text{OP,max}}$  and  $\dot{V}_{Cz,\text{ref},\text{OP,min}}$  denote the maximum and minimum operational reference acceleration limits, and  $V_{Cz,\text{ref},\text{OP,max}}$  and  $V_{Cz,\text{ref},\text{OP,min}}$  are the maximum and minimum operational reference velocity limits. These limits are chosen based on the physical capabilities of the VTOL aircraft according to requirement 3.

The gains  $K_{\dot{V}_{Cz,\text{ref}}}$  and  $K_{V_{Cz,\text{ref}}}$  define the frequency and damping characteristics of the unsaturated response of the height rate reference dynamics. Thereby, the resulting natural frequency and damping follow from  $\omega_0 = \sqrt{K_{\dot{V}_{Cz,\text{ref}}} K_{V_{Cz,\text{ref}}}}$  and  $d = \frac{1}{2} \sqrt{\frac{K_{\dot{V}_{Cz,\text{ref}}}}{K_{V_{Cz,\text{ref}}}}}$  respectively and shall yield corresponding handling qualities according to requirement 2.

Furthermore, the gains  $K_{\dot{V}_{Cz,\text{lim}}}$  and  $K_{V_{Cz,\text{lim}}}$  define the frequency and damping characteristics of the height rate's limit dynamics when approaching the maximum or minimum acceleration and velocity limit. Analogously, the resulting natural frequency and damping follow from  $\omega_0 = \sqrt{K_{\dot{V}_{Cz,\text{lim}}} K_{V_{Cz,\text{lim}}}}$  and  $d = \frac{1}{2} \sqrt{\frac{K_{\dot{V}_{Cz,\text{lim}}}}{K_{V_{Cz,\text{lim}}}}}$  respectively.

Note that the frequency and damping of the unsaturated dynamics can in general be different from the saturated dynamics in the limit case. In particular, one might chose to have critically damped (i.e. with a relative damping of  $d = 1$ ) convergence towards the acceleration and velocity limits in order to avoid overshoots, while the unsaturated response (e.g. for small amplitudes) can be designed with a relative damping of  $d = \frac{1}{\sqrt{2}}$  such as to minimize the ITAE (Integral Time Absolute Error) criterion [94].

Finally, the reference vertical acceleration  $\dot{V}_{Cz,\text{ref}}$  and velocity  $V_{Cz,\text{ref}}$  are obtained by integrating the vertical jerk from (5.85) with the initial conditions

$$\dot{V}_{Cz,\text{ref},0} = \dot{V}_{Cz} \quad V_{Cz,\text{ref},0} = V_{Cz}, \quad (5.91)$$

where  $\dot{V}_{Cz,\text{ref},0}$  and  $V_{Cz,\text{ref},0}$  denote the vertical reference acceleration and velocity during *Reset* mode, which are set to the corresponding aircraft states  $\dot{V}_{Cz}$  and  $V_{Cz}$  from the *Feedback Bus*. Setting the reference model states according to (5.91) ensures a transient-free initialization as was mentioned in requirement 4.

The *Height Rate Error Controller* yields the necessary control action that stabilizes the vertical dynamics around the reference trajectory provided by the *Height Rate Reference Model*. To this end, the control action is provided in terms of the error-control vertical jerk  $\ddot{V}_{Cz,\text{ec}}$ . Thereby, the error signals for the vertical velocity are defined as

$$e_{V_{Cz}} = V_{Cz,\text{ref}} - V_{Cz} \quad \dot{e}_{V_{Cz}} = \dot{V}_{Cz,\text{ref}} - \dot{V}_{Cz}, \quad (5.92)$$

with the reference states  $V_{Cz,\text{ref}}$  and  $\dot{V}_{Cz,\text{ref}}$  and the measured or estimated feedback signals  $V_{Cz}$  and  $\dot{V}_{Cz}$ .

The resulting error-control vertical jerk then follows from

$$\ddot{V}_{Cz,\text{ec}} = K_{\dot{V}_{Cz,\text{err}}} \left( \dot{e}_{V_{Cz}} + K_{V_{Cz,\text{err}}} e_{V_{Cz}} \right) = K_{\dot{V}_{Cz,\text{err}}} \dot{e}_{V_{Cz}} + K_{\dot{V}_{Cz,\text{err}}} K_{V_{Cz,\text{err}}} e_{V_{Cz}}, \quad (5.93)$$

where  $K_{\dot{V}_{Cz,\text{err}}}$  and  $K_{V_{Cz,\text{err}}}$  define the error controller gains.



Similarly to the reference dynamics gains, the error controller gains yield the natural frequency and damping characteristics of the height rate error dynamics, i.e.  $\omega_0 = \sqrt{K_{\dot{V}_{Cz,err}} K_{V_{Cz,err}}}$  and  $d = \frac{1}{2} \sqrt{\frac{K_{\dot{V}_{Cz,err}}}{K_{V_{Cz,err}}}}$  respectively.

As can be seen from figure 5.29, the resulting desired vertical jerk  $\ddot{V}_{Cz,d}$  follows from combining the feedforward and feedback terms into

$$\ddot{V}_{Cz,d} = \ddot{V}_{Cz,ref} + \ddot{V}_{Cz,ec}, \quad (5.94)$$

which yields the desired error dynamics

$$\ddot{e}_{V_{Cz}} \stackrel{!}{=} \ddot{V}_{Cz,ref} - \ddot{V}_{Cz,d} = -K_{\dot{V}_{Cz,err}} K_{V_{Cz,err}} e_{V_{Cz}} - K_{\dot{V}_{Cz,err}} \dot{e}_{V_{Cz}}. \quad (5.95)$$

Furthermore, the vertical jerk command  $\ddot{V}_{Cz,c}$  follows from subsequent saturation of (5.94) and yields

$$\ddot{V}_{Cz,c} = \min \left( \ddot{V}_{Cz,c,max}, \max \left( \ddot{V}_{Cz,c,min}, \ddot{V}_{Cz,d} \right) \right), \quad (5.96)$$

where  $\ddot{V}_{Cz,c,max}$  and  $\ddot{V}_{Cz,c,min}$  denote the maximum and minimum vertical jerk command limits.

The *Dynamic Inversion* block transforms the earth-vertical jerk  $\ddot{V}_{Cz}$  into body-vertical specific force rates  $\dot{f}_{Bz}$ . Thereby, the relationships in (4.41) and (4.44) are inverted and yield

$$\dot{f}_{Bz} = \underbrace{\tan(\phi) \dot{f}_{Bz} \dot{\phi} + \tan(\theta) \dot{f}_{Bz} \dot{\theta}}_{\text{Attitude Rate Compensation}} + \frac{\ddot{V}_{Cz}}{\cos(\phi) \cos(\theta)}. \quad (5.97)$$

Using the inversion from (5.97), the vertical jerk command  $\ddot{V}_{Cz,c}$  gets transformed into the desired specific powered lift rate  $\dot{f}_{Bz,d}$  and the reference vertical jerk  $\ddot{V}_{Cz,ref}$  gets transformed into the reference specific force rate  $\dot{f}_{Bz,ref}$ . Latter is used as a feedforward term in the *Horizontal Kinematic Velocity Control* block, which is discussed later in this section.

Finally, the desired specific powered lift rate  $\dot{f}_{Bz,d}$  is fed into the *Powered Lift Rate Command Saturation* block in order to provide the specific powered lift rate command  $\dot{f}_{Bz,c}$  and the specific excess powered lift rate  $\dot{f}_{Bz,PL,exc}$ . To this end, the maximum and minimum specific powered lift rates are defined as

$$\begin{aligned} \dot{f}_{Bz,c,max} &= \min \left( \dot{f}_{Bz,OP,max}, \dot{f}_{Bz,f_{lim},max} \right), \\ \dot{f}_{Bz,c,min} &= \max \left( \dot{f}_{Bz,OP,min}, \dot{f}_{Bz,f_{lim},min} \right), \end{aligned} \quad (5.98)$$

where  $\dot{f}_{Bz,OP,max}$  and  $\dot{f}_{Bz,OP,min}$  denote the maximum and minimum operational specific powered lift rates based on operational and physical limitations of the VTOL aircraft. Furthermore,  $\dot{f}_{Bz,f_{lim},max}$  and  $\dot{f}_{Bz,f_{lim},min}$  denote the specific powered lift rates leading to

the convergence of the applied powered lift to the maximum and minimum limit respectively and yield

$$\begin{aligned} \dot{f}_{Bz,PL,\max} &= K_{f_{Bz,PL,\lim}} (f_{Bz,PL,\max} - f_{Bz,PL}) , \\ \dot{f}_{Bz,PL,\min} &= K_{f_{Bz,PL,\lim}} (f_{Bz,PL,\min} - f_{Bz,PL}) , \end{aligned} \quad (5.99)$$

where  $K_{f_{Bz,PL,\lim}}^{-1}$  denotes the time constant for the convergence of the estimated powered lift  $f_{Bz,PL}$  to its respective limit.

Thereby,  $f_{Bz,PL,\max}$  denotes the maximum specific powered lift in body-down direction (i.e. the minimum admissible powered lift, see figure 5.30) and is without loss of generality chosen to be equal to the estimated powered lift for idle RPMs of the powered lift motors. Furthermore,  $f_{Bz,PL,\min}$  denotes the minimum specific powered lift in body-down direction and hence specifies the maximum admissible powered lift that can be allocated by the *Powered Lift Based Height Rate Control* block.

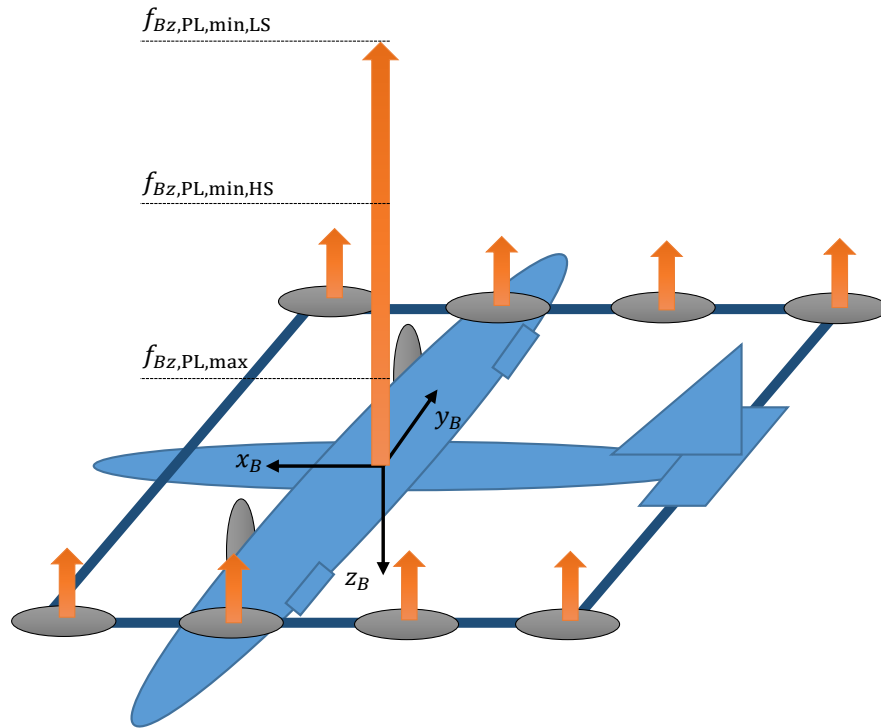


**Figure 5.30:** *Powered Lift Command Saturation*

Note that  $f_{Bz,PL,\min}$  is quadratically scheduled over the calibrated airspeed  $V_{CAS}$  in order to account for increasing dynamic pressure and hence mitigate excessive loads on the powered lift motors. It follows that

$$f_{Bz,PL,\min} = \min \left( f_{Bz,PL,\min,HS}, \max \left( f_{Bz,PL,\min,LS}, c_1 (V_{CAS} - V_{\text{hover}})^2 + c_2 \right) \right) , \quad (5.100)$$

with

$$c_1 = \frac{f_{Bz,PL,\min,HS} - f_{Bz,PL,\min,LS}}{V_{\text{stall,p}} - V_{\text{hover}}} \quad c_2 = f_{Bz,PL,\min,LS} , \quad (5.101)$$

where  $f_{Bz,PL,min,LS}$  and  $f_{Bz,PL,min,HS}$  denote the lowspeed (LS) and highspeed (HS) powered lift limits respectively and (5.101) yields the parameters for the quadratic scheduling in (5.100). Latter blends the powered lift limits between the maximum hover speed  $V_{hover}$  (see subsection 4.2.1), which is defined to be equal to  $V_{TOSS}$  (see subsection 3.1.2), and  $V_{stall,p}$  from (4.16), which denotes the target airspeed for transitioning into the fixed-wing flight and provides optimum climb gradients, as was pointed out in subsubsection 5.3.3.2. A schematic illustration of the specific powered lift limits is shown in figure 5.30.

Finally, the specific powered lift rate command  $\dot{f}_{Bz,c}$  follows from subsequent saturation of  $\dot{f}_{Bz,d}$  and yields

$$\dot{f}_{Bz,c} = \min \left( \dot{f}_{Bz,c,max}, \max \left( \dot{f}_{Bz,c,min}, \dot{f}_{Bz,d} \right) \right), \quad (5.102)$$

with the limits  $\dot{f}_{Bz,c,max}$  and  $\dot{f}_{Bz,c,min}$  from (5.98).

Besides the specific powered lift rate command  $\dot{f}_{Bz,c}$  from (5.102), the *Powered Lift Rate Command Saturation* block additionally outputs the specific excess powered lift rate  $\dot{f}_{Bz,PL,exc}$ , which denotes the amount of the desired vertical jerk  $\dot{f}_{Bz,d}$  that exceeds the limit dynamics of the powered lift towards its lower limit  $f_{Bz,PL,max}$ . In particular, the specific excess powered lift rate follows from

$$\dot{f}_{Bz,PL,exc} = \dot{f}_{Bz,d} - \dot{f}_{Bz,fim,max}, \quad (5.103)$$

with  $\dot{f}_{Bz,fim,max}$  from (5.99).

Note that the specific excess powered lift rate from (5.103) is used in the angle of attack loop of the *Highspeed Control* block in order to calculate the limit angle of attack rate  $\dot{\alpha}_{fim}$  yielding the limit dynamics from (5.99), analogously to (4.87) in subsubsection 4.3.2.3.

**Horizontal Kinematic Velocity Control** The *Horizontal Kinematic Velocity Control* block yields the commands for the forward specific force  $f_{Bx,c}$ , the pitch angle rate  $\dot{\theta}_c$ , and the roll angle rate  $\dot{\phi}_c$ , which together enable control of the horizontal kinematic velocity with respect to ground. To this end, it implements the following functional blocks, which are depicted in figure 5.31 and discussed in the remainder of this section:

- The *Forward Velocity Control* block
- The *Lateral Velocity Control* block
- The *Hover Attitude Protection* block.

As can be seen from figure 5.31, the *Horizontal Kinematic Velocity Control* block implements degradation strategies for *Traction System Degraded* mode and *Radar Altimeter Degraded* mode. Thereby, the *Traction System Degraded* mode is processed within the *Forward Velocity Control* block and alters the control strategies for the longitudinal channel between pitch- and traction-based velocity tracking.

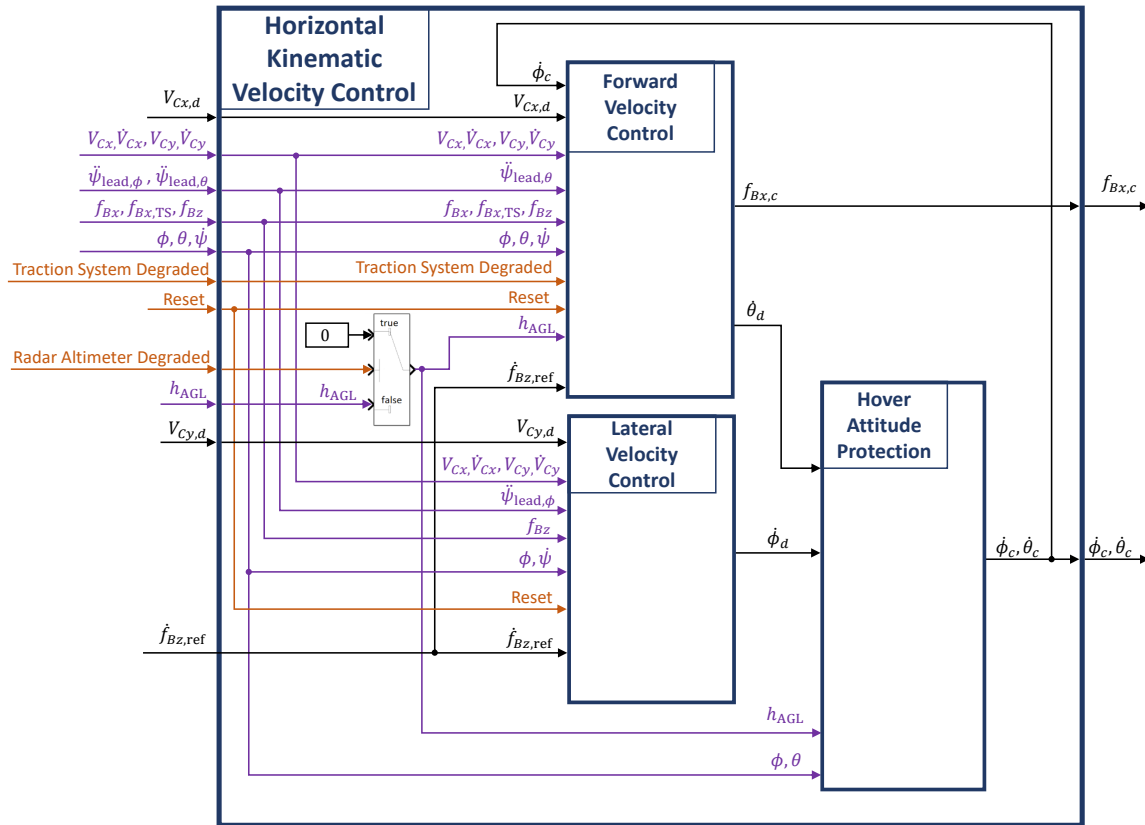


**Figure 5.31:** *Horizontal Kinematic Velocity Control block*

Furthermore, the *Radar Altimeter Degraded* mode leads to overriding the radar altimeter height measurement  $h_{AGL}$  with a constant value of 0. Upon losing the information about the VTOL aircraft's height above ground level, proximity to ground is assumed for the attitude protection and the equilibrium pitch angle within the traction-based forward control, which was already pointed out in subsection 5.3.2.4. This represents a conservative fallback strategy and enables fail-passive operation of the *Horizontal Kinematic Velocity Control* block.

In general, the *Horizontal Kinematic Velocity Control* block aims to track the along-heading kinematic velocity  $V_{Cx}$  and the across-heading kinematic velocity  $V_{Cy}$  while satisfying attitude limit constraints and providing fail-operational control upon partial or complete failure of the traction system. Furthermore, the functions of horizontal kinematic velocity control are merely used in the *Hover* mode, as is illustrated in figure 5.27 (recall the equivalence of *Hover* mode and  $\neg$  *Highspeed* mode from subsection 5.3.2 and figure 5.12).

In the following, a complete functional breakdown of the *Forward Velocity Control* block, the *Lateral Velocity Control* block, and the *Hover Attitude Protection* block is given. Thereby, the basic control principles were derived in subsection 4.3.1.2, subsection 4.3.1.3, and subsection 4.3.1.4 and are augmented as well as decomposed into a detailed control architecture in the following paragraphs.

**Forward Velocity Control** The *Forward Velocity Control* block implements the functions that provide nominal and degraded control of the desired along-heading kinematic velocity  $V_{Cx,d}$ , which is calculated in the *Command Scaling and Transformation* block from subsection 5.3.3 and fed into the *Horizontal Kinematic Velocity Control* block via the forward channel of the *Outer-Loop Command Bus (OL CMD Bus)*. The high-level structure of the *Forward Velocity Control* block is depicted in figure 5.32 and is comprised of the following functional elements:

- The *Forward Velocity Reference Model* block
- The *Traction-Variant Forward Velocity Error Controller* block
- The *Traction-Variant Dynamic Inversion* block
- The *Pitch-Variant Forward Velocity Error Controller* block
- The *Pitch-Variant Dynamic Inversion* block.

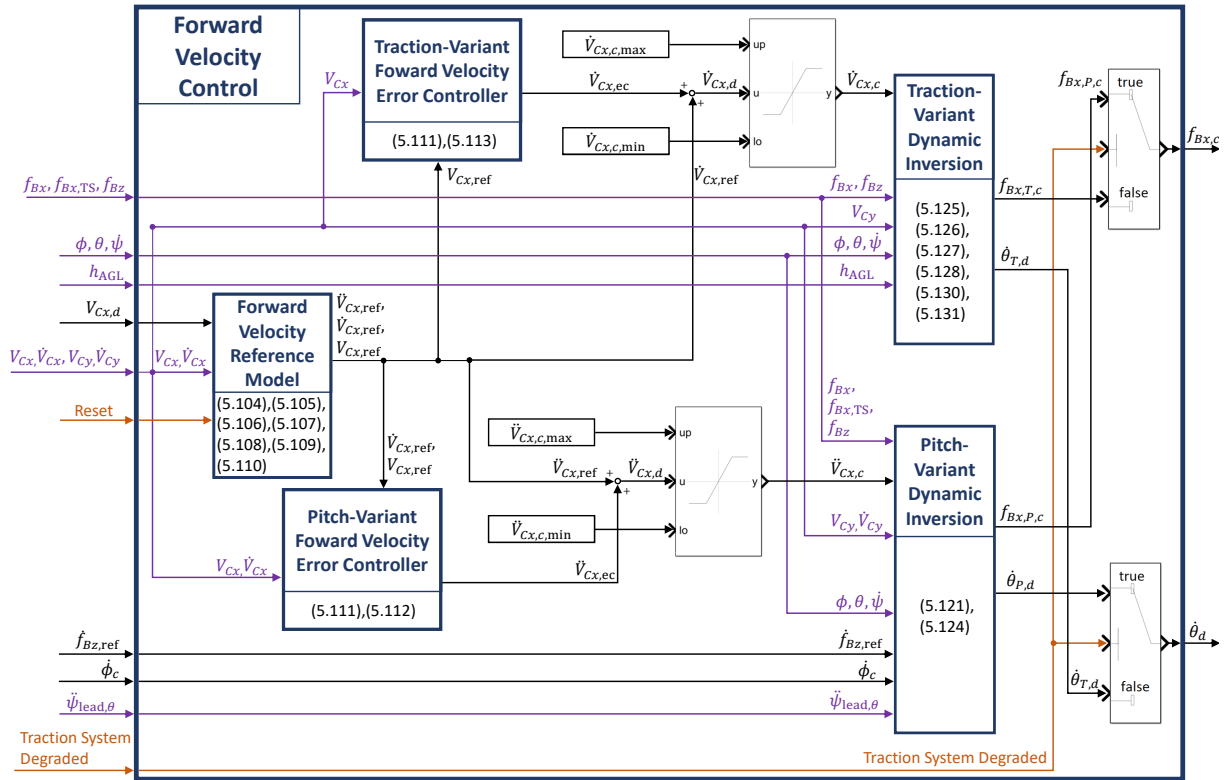


**Figure 5.32:** *Forward Velocity Control block*

Similarly to the vertical channel, the *Forward Velocity Reference Model* block provides the reference trajectory for the longitudinal motion of the VTOL aircraft. Thereby, the block yields the reference along-heading jerk  $\ddot{V}_{Cx,ref}$ , along-heading acceleration  $\dot{V}_{Cx,ref}$ , and along-heading velocity  $V_{Cx,ref}$ , which are denoted in the forward direction of the C-frame depicted in figure 4.4.

Note that the relative degree (i.e. the amount of output differentiations until reaching the final command input [47] [44]) of the forward velocity channel differs dependent on the control variant. Assuming first-order response characteristics for the powered lift and traction motors, the use of the traction system for generating forward forces yields a relative degree of 2, while changing the pitch attitude of the whole VTOL aircraft in order to tilt the powered lift direction yields a relative degree of 4. Nevertheless, a single reference model is used during both control variants and is for simplicity chosen to be of second order, which has proven to yield good handling qualities [74] [1].

Analogously to the vertical channel, the requirements for the *Forward Velocity Reference Model* block are as follows:

1. The reference along-heading velocity  $V_{C_{x,\text{ref}}}$  shall converge to the desired forward velocity  $V_{C_{x,d}}$ .
2. The translational rate dynamics in the longitudinal channel shall comply with subsection 3.3.12 in ADS-33E-PRF [12], which states that the translational rate response types shall have a first order appearance with an equivalent rise time between 2.5 s and 5 s. Refer to figure 4.17 for a definition of the equivalent rise time according to [12].
3. The reference longitudinal acceleration and jerk limits shall not exceed the physical capabilities or operational constraints of the VTOL aircraft, but they shall be sufficiently large such as to comply with requirement 2.
- 4 Upon initializing the reference dynamics, the reference states shall be sufficiently close to the true aircraft states in order to avoid transients.

From the requirements stated above it follows the definition of the forward velocity reference dynamics. To this end, the reference forward jerk is given by

$$\ddot{V}_{C_{x,\text{ref}}} = \min \left( \ddot{V}_{C_{x,\text{ref},\text{max}}}, \max \left( \ddot{V}_{C_{x,\text{ref},\text{min}}}, K_{\dot{V}_{C_{x,\text{ref}}}} \left( \dot{V}_{C_{x,\text{ref},c}} - \dot{V}_{C_{x,\text{ref}}} \right) \right) \right), \quad (5.104)$$

with the reference forward acceleration command

$$\dot{V}_{C_{x,\text{ref},c}} = K_{V_{C_{x,\text{ref}}}} (V_{C_{x,\text{ref},c}} - V_{C_{x,\text{ref}}}), \quad (5.105)$$

where the reference forward velocity command  $V_{C_{x,\text{ref},c}}$  is chosen as  $V_{C_{x,\text{ref},c}} = V_{C_{x,d}}$  in order to comply with requirement 1.

Furthermore, the maximum and minimum reference forward jerk limits are chosen as

$$\begin{aligned} \ddot{V}_{C_{x,\text{ref},\text{max}}} &= \min \left( \ddot{V}_{C_{x,\text{ref},\text{OP},\text{max}}}, \ddot{V}_{C_{x,\dot{V}_{\text{lim},\text{max}}}} \right), \\ \ddot{V}_{C_{x,\text{ref},\text{min}}} &= \max \left( \ddot{V}_{C_{x,\text{ref},\text{OP},\text{min}}}, \ddot{V}_{C_{x,\dot{V}_{\text{lim},\text{min}}}} \right), \end{aligned} \quad (5.106)$$

with the forward jerks leading to the limit forward reference accelerations

$$\begin{aligned}\ddot{V}_{C_x, \dot{V}_{\text{lim}, \text{max}}} &= K_{\dot{V}_{C_x, \text{lim}}} \left( \dot{V}_{C_x, \text{ref}, \text{max}} - \dot{V}_{C_x, \text{ref}} \right), \\ \ddot{V}_{C_x, \dot{V}_{\text{lim}, \text{min}}} &= K_{\dot{V}_{C_x, \text{lim}}} \left( \dot{V}_{C_x, \text{ref}, \text{min}} - \dot{V}_{C_x, \text{ref}} \right),\end{aligned}\quad (5.107)$$

the limit forward reference accelerations given by

$$\begin{aligned}\dot{V}_{C_x, \text{ref}, \text{max}} &= \min \left( \dot{V}_{C_x, \text{ref}, \text{OP}, \text{max}}, \dot{V}_{C_x, V_{\text{lim}, \text{max}}} \right), \\ \dot{V}_{C_x, \text{ref}, \text{min}} &= \max \left( \dot{V}_{C_x, \text{ref}, \text{OP}, \text{min}}, \dot{V}_{C_x, V_{\text{lim}, \text{min}}} \right),\end{aligned}\quad (5.108)$$

and the forward accelerations leading to the limit forward velocities

$$\begin{aligned}\dot{V}_{C_x, V_{\text{lim}, \text{max}}} &= K_{V_{C_x, \text{lim}}} (V_{C_x, \text{ref}, \text{OP}, \text{max}} - V_{C_x, \text{ref}}), \\ \dot{V}_{C_x, V_{\text{lim}, \text{min}}} &= K_{V_{C_x, \text{lim}}} (V_{C_x, \text{ref}, \text{OP}, \text{min}} - V_{C_x, \text{ref}}).\end{aligned}\quad (5.109)$$

Furthermore, the reference forward acceleration  $\dot{V}_{C_x, \text{ref}}$  and velocity  $V_{C_x, \text{ref}}$  are obtained by integrating the forward jerk from (5.104) with the initial conditions

$$\dot{V}_{C_x, \text{ref}, 0} = \dot{V}_{C_x} \qquad V_{C_x, \text{ref}, 0} = V_{C_x}, \quad (5.110)$$

where  $\dot{V}_{C_x, \text{ref}, 0}$  and  $V_{C_x, \text{ref}, 0}$  denote the forward reference acceleration and velocity during *Reset* mode, which are set to the corresponding aircraft states  $\dot{V}_{C_x}$  and  $V_{C_x}$  from the *Feedback Bus*. A transient-free initialization is thereby enforced, which complies with requirement 4.

The explanation of the respective limits and gains follows analogously to the vertical reference dynamics and is not repeated at this point. Note, however, that in contrast to the vertical dynamics, which are directly influenced by the powered lift motors and for which the relative degree is hence lower than for the horizontal dynamics, both the longitudinal and lateral reference dynamics have to account for the bandwidth and rate limitations of the system's attitude response.

Therefore, special attention is needed when choosing the parameters for the reference dynamics in (5.104), (5.105), (5.106), (5.107), (5.108), and (5.109), as they are dependent on the rotational dynamics, which are designed in the context of the *Inner Loop*. In particular, the concepts presented in section 5.2 yield guidelines as to how to find the optimum gain and saturation values for the outer-loop reference dynamics, given the bandwidth and rate limits of the inner-loop dynamics.

Both the traction- and the pitch-based error controller blocks differ in the type of pseudo-control output they provide. While the traction-based error controller provides outputs on the level of forward acceleration  $\dot{V}_{C_x}$ , the pitch variant provides outputs on the level of forward jerk  $\ddot{V}_{C_x}$ . This is because the pseudo controls after the dynamic inversion of both variants act on different dynamic levels. The pitch angle rate  $\dot{\theta}_d$  acts on the level of forward jerk, which can be seen from (4.41) and (4.44), while the forward

specific force  $f_{Bx}$  acts on the level of forward acceleration, which is shown in (4.62) and (4.63).

Defining the error signals for the forward velocity as

$$e_{V_{Cx}} = V_{Cx,\text{ref}} - V_{Cx} \quad \dot{e}_{V_{Cx}} = \dot{V}_{Cx,\text{ref}} - \dot{V}_{Cx}, \quad (5.111)$$

with the reference states  $V_{Cx,\text{ref}}$  and  $\dot{V}_{Cx,\text{ref}}$  and the measured or estimated feedback signals  $V_{Cx}$  and  $\dot{V}_{Cx}$ , it follows for the resulting error-control forward jerk  $\ddot{V}_{Cx,\text{ec}}$  of the *Pitch-Variant Forward Velocity Error Controller*

$$\ddot{V}_{Cx,\text{ec}} = K_{P,\dot{V}_{Cx,\text{err}}} \left( \dot{e}_{V_{Cx}} + K_{P,V_{Cx,\text{err}}} e_{V_{Cx}} \right) = K_{P,\dot{V}_{Cx,\text{err}}} \dot{e}_{V_{Cx}} + K_{P,\dot{V}_{Cx,\text{err}}} K_{P,V_{Cx,\text{err}}} e_{V_{Cx}}, \quad (5.112)$$

where  $K_{P,\dot{V}_{Cx,\text{err}}}$  and  $K_{P,V_{Cx,\text{err}}}$  define the error controller gains for the pitch variant.

Similarly, the resulting error-control forward acceleration  $\dot{V}_{Cx,\text{ec}}$  of the *Traction-Variant Forward Velocity Error Controller* yields

$$\dot{V}_{Cx,\text{ec}} = K_{T,V_{Cx,\text{err}}} e_{V_{Cx}}, \quad (5.113)$$

where  $K_{T,V_{Cx,\text{err}}}$  defines the error controller gain for the traction variant.

Furthermore, the overall desired forward jerk and acceleration demand for the pitch and traction variant respectively follow by adding up the feedforward signals from the reference model with the feedback signals of the error controller:

$$\ddot{V}_{Cx,d} = \ddot{V}_{Cx,\text{ref}} + \ddot{V}_{Cx,\text{ec}} \quad (5.114)$$

and

$$\dot{V}_{Cx,d} = \dot{V}_{Cx,\text{ref}} + \dot{V}_{Cx,\text{ec}}. \quad (5.115)$$

In order to obtain the final pseudo control command signals, (5.114) and (5.115) are furthermore limited, i.e.

$$\ddot{V}_{Cx,c} = \min \left( \ddot{V}_{Cx,c,\text{max}}, \max \left( \ddot{V}_{Cx,c,\text{min}}, \ddot{V}_{Cx,d} \right) \right) \quad (5.116)$$

respectively

$$\dot{V}_{Cx,c} = \min \left( \dot{V}_{Cx,c,\text{max}}, \max \left( \dot{V}_{Cx,c,\text{min}}, \dot{V}_{Cx,d} \right) \right), \quad (5.117)$$

where  $\ddot{V}_{Cx,c,\text{max}}$ ,  $\ddot{V}_{Cx,c,\text{min}}$ ,  $\dot{V}_{Cx,c,\text{max}}$ , and  $\dot{V}_{Cx,c,\text{min}}$  denote the upper and lower jerk respectively acceleration command limits.

The *Pitch-Variant Dynamic Inversion* block provides the necessary pitch angle rate  $\dot{\theta}_{P,d}$  that results in the commanded forward jerk from (5.116). To this end, the relationships from (4.44) and (4.41) are inverted and yield

$$\dot{\theta} = \underbrace{-\frac{\tan(\theta)}{f_{Bz}} \dot{f}_{Bz} + \tan(\phi) \tan(\theta) \dot{\phi}}_{\text{Climb and Turn Compensation}} - \frac{\ddot{\psi} V_{Cy} + \dot{\psi} \dot{V}_{Cy}}{\cos(\phi) \cos(\theta) f_{Bz}} + \frac{\ddot{V}_{Cx}}{\cos(\phi) \cos(\theta) f_{Bz}}. \quad (5.118)$$



As was already pointed out in subsection 4.3.1.3, the resulting pitch angle rate demand  $\dot{\theta}_{P,d}$  has to account for the slower response characteristics of the attitude rate loop. Additionally, the resulting pseudo control signal has to account for noise in the feedback signals. Therefore, the following adaptations are proposed for the dynamic inversion in (5.118):

- The heading acceleration  $\ddot{\psi}$  is replaced by the lead-filtered term  $\ddot{\psi}_{\text{lead},\theta}$ , which takes into account the pitch angle rate dynamics of the inner loop. It follows analogously to (4.53) by considering the equivalent first-order time constant of the pitch angle rate dynamics and is given by

$$\ddot{\psi}_{\text{lead},\theta} = K_{\dot{\theta}_{\text{ref}}}^{-1} \ddot{\psi}_{\text{ref}} + \dot{\psi}_{\text{ref}}, \quad (5.119)$$

where  $K_{\dot{\theta}_{\text{ref}}}$  denotes the gain for the reference pitch angle rate loop and  $\ddot{\psi}_{\text{ref}}$  and  $\dot{\psi}_{\text{ref}}$  are the reference heading jerk and acceleration respectively. Using the reference signals from the inner loop's *Attitude Rate Control* block instead of relying on external feedback signals (as it was done e.g. for the DRM) prevents excessive noise in the command channel.

- Similarly, the roll angle rate  $\dot{\phi}$  is replaced by the roll angle rate command  $\dot{\phi}_c$  from the *Attitude Protection* block in figure 5.31 in order to provide the necessary lead for the pitch angle rate command. Thereby, it is assumed for simplicity that both the roll angle rate and pitch angle rate dynamics are sufficiently similar. Alternatively, the lead characteristics could be achieved analogously to (5.119) by using

$$\dot{\phi}_{\text{lead},\theta} = K_{\dot{\theta}_{\text{ref}}}^{-1} \ddot{\phi}_{\text{ref}} + \dot{\phi}_{\text{ref}}. \quad (5.120)$$

- The body-vertical specific force rate  $\dot{f}_{Bz}$  is not directly measured and obtaining it from filtering would induce a lot of noise. Therefore, the reference body-vertical specific force rate  $\dot{f}_{Bz,\text{ref}}$  is used instead, which was obtained from dynamic inversion of the reference vertical jerk  $\ddot{V}_{Cz,\text{ref}}$ , as can be seen in figure 5.29. By only using reference states for generating the signal, excessive noise in the command channel is prevented.

The resulting pitch angle rate demand  $\dot{\theta}_{P,d}$  for the pitch-based forward control hence follows from

$$\dot{\theta}_{P,d} = \underbrace{-\frac{\tan(\theta)}{f_{Bz}} \dot{f}_{Bz,\text{ref}} + \tan(\phi) \tan(\theta) \dot{\phi}_c}_{\text{Climb and Turn Compensation}} - \frac{\ddot{\psi}_{\text{lead},\theta} V_{Cy} + \dot{\psi} \dot{V}_{Cy}}{\cos(\phi) \cos(\theta) f_{Bz}} + \frac{\ddot{V}_{Cx,c}}{\cos(\phi) \cos(\theta) f_{Bz}}, \quad (5.121)$$

with the forward jerk command  $\ddot{V}_{Cx,c}$  from (5.116).

Furthermore, since the traction system shall not be used during pitch-based control, the command for the forward specific force  $f_{Bx,c}$  is chosen such as to bring the traction

system specific force  $f_{Bx,TS}$  to its minimum value  $f_{Bx,TS,min}$ . To this end, the knowledge about the demanded forward specific force rate  $\dot{f}_{Bx,d}$  is used, which will be discussed in the context of the inner loop. Latter is given by

$$\dot{f}_{Bx,d} = K_{f_{Bx}} (f_{Bx,c} - f_{Bx}) , \quad (5.122)$$

where  $K_{f_{Bx}}$  denotes the design bandwidth of the forward specific force dynamics.

In order for the traction system specific force  $f_{Bx,TS}$  to converge to its minimum value  $f_{Bx,TS,min}$ , the following dynamics are specified:

$$\dot{f}_{Bx,TS} \stackrel{!}{=} K_{f_{Bx}} (f_{Bx,TS,min} - f_{Bx,TS}) . \quad (5.123)$$

As will be pointed out in the inner loop section, the allocated traction system specific force rate  $\dot{f}_{Bx,TS}$  follows directly from the commanded forward specific force rate  $\dot{f}_{Bx,c}$ , i.e.  $\dot{f}_{Bx,TS} = \dot{f}_{Bx,c}$ . If command saturations are neglected, it furthermore follows that  $\dot{f}_{Bx,c} = \dot{f}_{Bx,d}$ . Finally, setting equal (5.122) and (5.123) directly yields the necessary forward specific force command for the pitch-based velocity control

$$f_{Bx,P,c} = f_{Bx} + f_{Bx,TS,min} - f_{Bx,TS} , \quad (5.124)$$

which results in the desired dynamics (5.123) and hence lets the traction system converge to its minimum RPM value.

The *Traction-Variant Dynamic Inversion Block* provides the necessary forward specific force command  $f_{Bx,T,c}$  and pitch angle rate demand  $\dot{\theta}_{T,d}$  that shall lead to the commanded forward acceleration  $\dot{V}_{Cx,c}$  from (5.117). To this end, the concepts from subsection 4.3.1.4 are recalled and extended such as to yield the final functional breakdown of the traction-based forward control.

The desired forward specific force  $f_{Bx,d}$  follows from inverting (4.62) and (4.63) and is repeated here for convenience:

$$f_{Bx,d} = -\cos(\phi) \tan(\theta) f_{Bz} - \frac{\dot{\psi} V_{Cy}}{\cos(\theta)} + \frac{\dot{V}_{Cx,c}}{\cos(\theta)} , \quad (5.125)$$

with the commanded forward acceleration  $\dot{V}_{Cx,c}$  from (5.117).

In (5.125) it is assumed that the specific force dynamics are much faster than the pitch dynamics, thereby following the concepts of time-scale separation. Furthermore, the final forward specific force command for the traction-based forward control follows after limiting (5.125) and yields

$$f_{Bx,T,c} = \min (f_{Bx,c,max}, \max (f_{Bx,c,min}, f_{Bx,d})) , \quad (5.126)$$

where  $f_{Bx,c,max}$  and  $f_{Bx,c,min}$  denote the maximum and minimum admissible specific force commands.

The desired pitch angle rate dynamics from (4.66) are extended by a height-dependent equilibrium pitch angle  $\theta_{0,T}(h_{AGL})$  and yield

$$\dot{\theta}_d = K_{T,\theta} (\theta_{0,T} - \theta) , \quad (5.127)$$

where  $K_{T,\theta}$  denotes the desired exponential convergence rate of the pitch angle  $\theta$  towards the equilibrium pitch angle

$$\theta_{0,T}(h_{AGL}) = \min \left( \theta_{0,T,hi}, \max \left( \theta_{0,T,lo}, \frac{h_{AGL} - h_{AGL,T,lo}}{h_{AGL,T,hi} - h_{AGL,T,lo}} (\theta_{0,T,hi} - \theta_{0,T,lo}) + \theta_{0,T,lo} \right) \right) , \quad (5.128)$$

with  $\theta_{0,T,hi}$  and  $\theta_{0,T,lo} = 0$  denoting the equilibrium pitch angles at the border of the linear blending (5.128) at  $h_{AGL} = h_{AGL,T,hi}$  and  $h_{AGL} = h_{AGL,T,lo}$  respectively.

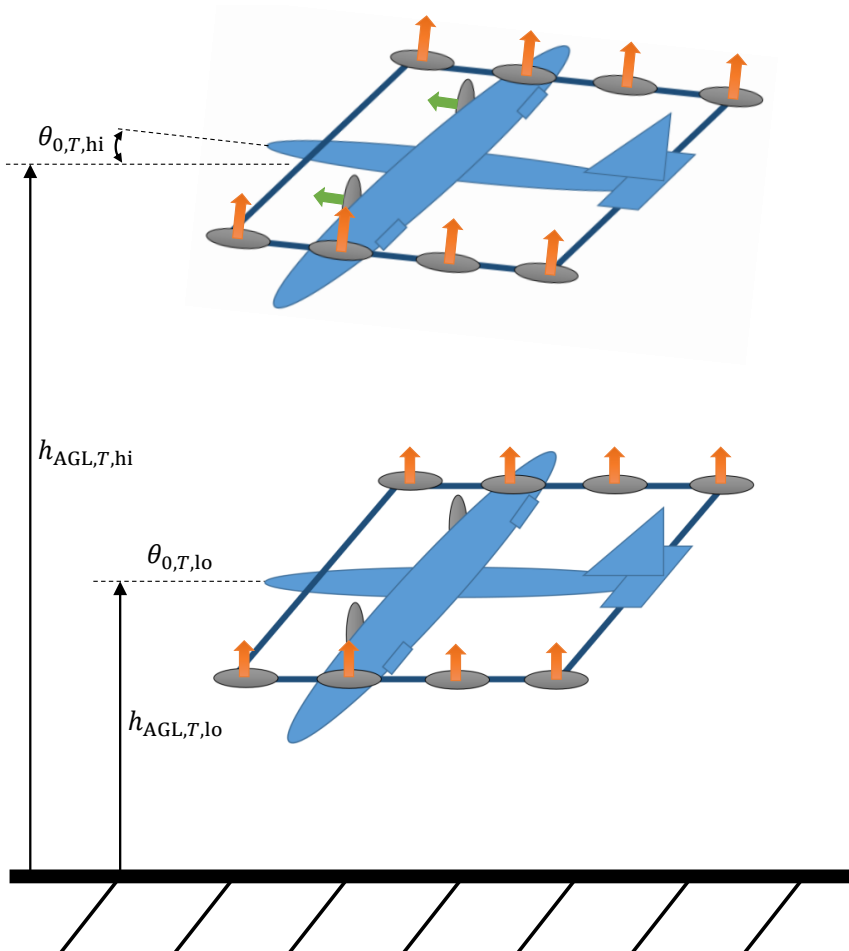


**Figure 5.33:** *Equilibrium Pitch Angle During Traction-Based Forward Control*

As is illustrated in figure 5.33, the linear blending regime from (5.128) reduces the equilibrium pitch angle to  $\theta_{0,T,lo} = 0$  upon approaching the ground in order to enable horizontal landing of the VTOL aircraft. When operating above  $h_{AGL} = h_{AGL,T,hi}$ , the resulting equilibrium pitch angle  $\theta_{0,T,hi} > 0$  enables a faster translational rate response in the backwards direction, which was pointed out in subsection 4.3.1.4 and was illustrated in figure 4.16.

Furthermore, the pitch angle rate from (5.127) is limited, such as to not induce a change in the along-heading specific force  $f_{Cx}$  when approaching the lower traction force limit  $f_{Bx,TS,min}$ . To this end, recall the linearization of (4.63) around the desired specific force demand in the forward direction of the control frame  $C$

$$\Delta f_{Cx,d} = (\cos(\phi) \cos(\theta) f_{Bz} - \sin(\theta) f_{Bx}) \Delta \theta + \cos(\theta) \Delta f_{Bx,d} \stackrel{!}{=} 0, \quad (5.129)$$

which relates the change of pitch angle  $\Delta \theta$  to a change in the demanded forward specific force  $\Delta f_{Bx,d}$ .

From (5.129) directly follows the limit pitch angle rate

$$\dot{\theta}_{f_{TS,lim}} = K_{f_{TS,lim}} \Delta \theta_{f_{TS,lim}} = \frac{-\cos(\theta) K_{f_{TS,lim}} \Delta f_{Bx,d,lim}}{\cos(\phi) \cos(\theta) f_{Bz} - \sin(\theta) f_{Bx}}, \quad (5.130)$$

which brings the traction system specific force to its minimum value  $f_{Bx,TS,min}$  with the exponential rate  $K_{f_{TS,lim}}$ . Thereby,  $\Delta f_{Bx,d,lim} = f_{Bx,TS,min} - f_{Bx,d}$  denotes the distance of demanded forward specific force to the minimum admissible traction system specific force.

The final pitch angle rate demand for the traction-based forward control hence follows from

$$\dot{\theta}_{T,d} = \max(\dot{\theta}_d, \dot{\theta}_{f_{TS,lim}}), \quad (5.131)$$

with  $\dot{\theta}_d$  from (5.127) and  $\dot{\theta}_{f_{TS,lim}}$  from (5.130).

The control law in (5.131) ensures that deceleration demand exceeding the lower limit of the traction system is still met, since the pitch angle rate is bounded by the limit  $\dot{\theta}_{f_{TS,lim}}$ , which leads to a positive pitch rate response and hence deceleration due to the powered lift being tilted backwards. For more details on the control law, the reader may refer to subsection 4.3.1.4.

Finally, the outputs of the *Forward Velocity Control* block  $f_{Bx,c}$  and  $\dot{\theta}_d$  are switched between the corresponding pseudo control signals of the traction-variant and pitch-variant forward control based on the *Traction System Degraded* mode:

$$f_{Bx,c} = \begin{cases} f_{Bx,P,c} \text{ from (5.124),} & \text{for } \textit{Traction System Degraded} == \textit{true} \\ f_{Bx,T,c} \text{ from (5.126),} & \text{for } \textit{Traction System Degraded} == \textit{false} \end{cases} \quad (5.132)$$

and

$$\dot{\theta}_d = \begin{cases} \dot{\theta}_{P,d} \text{ from (5.121),} & \text{for } \textit{Traction System Degraded} == \textit{true} \\ \dot{\theta}_{T,d} \text{ from (5.131),} & \text{for } \textit{Traction System Degraded} == \textit{false} \end{cases}. \quad (5.133)$$

Hence, the presented functions allow for seamlessly accounting for failures of the traction system by switching to the pitch-based forward control in case of degradation. Furthermore, it might be desired to manually switch between both variants, if the use of the traction system during hover turns out to be disadvantageous from an operational or safety point of view.

**Lateral Velocity Control** The *Lateral Velocity Control* block implements the functions for tracking the desired across-heading kinematic velocity  $V_{Cy,d}$ , which is provided by the *Command Scaling and Transformation* block from subsection 5.3.3 via the lateral channel of the *Outer-Loop Command Bus (OL CMD Bus)*. The high-level structure of the *Lateral Velocity Control* block is depicted in figure 5.34 and is comprised of the following functional elements:

- The *Lateral Velocity Reference Model* block
- The *Lateral Velocity Error Controller* block
- The *Dynamic Inversion* block.

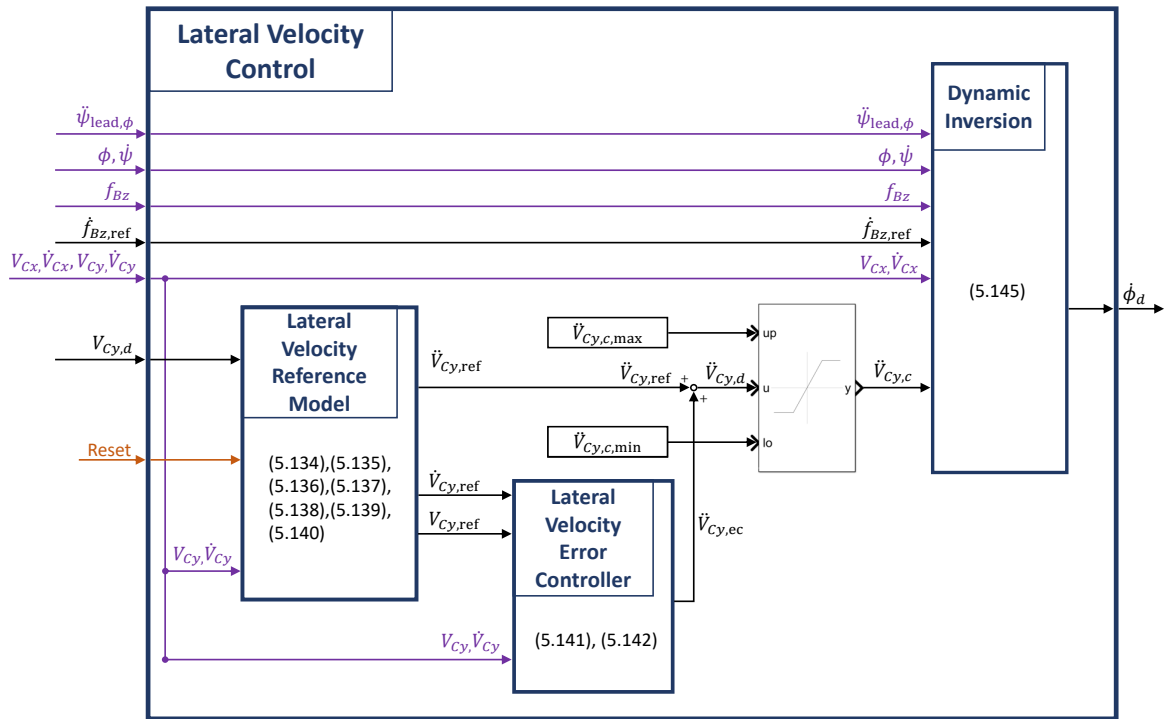


**Figure 5.34:** Forward Velocity Control block

Analogously to the *Forward Velocity Reference Model* block, the *Lateral Velocity Reference Model* block provides the reference trajectory for the across-heading kinematic velocity  $V_{Cy}$  in terms of a second-order nonlinear (due to saturation) dynamical model. Due to lacking capabilities for sideforce generation, lateral motion during hover is initiated through a roll response, which yields a relative degree for the lateral velocity of 4 (assuming first-order characteristics of the powered lift motors). Nevertheless, the choice of a second-order reference model for the lateral channel has proven to yield good handling qualities [74] [1].

To this end, the *Lateral Velocity Reference Model* block yields the reference across-heading jerk  $\ddot{V}_{Cy,ref}$ , across-heading acceleration  $\dot{V}_{Cy,ref}$ , and across-heading velocity  $V_{Cy,ref}$ , which are denoted in the lateral direction of the control frame  $C$  depicted in figure 4.4. Furthermore, the requirements for the *Lateral Velocity Reference Model* block follow analogously to the forward channel:

1. The reference across-heading velocity  $V_{Cy,ref}$  shall converge to the desired lateral velocity  $V_{Cy,d}$ .
2. The translational rate dynamics in the lateral channel shall comply with subsection 3.3.12 in ADS-33E-PRF [12], which states that the translational rate response types shall have a first order appearance with an equivalent rise time between 2.5 s and 5 s. Refer to figure 4.17 for a definition of the equivalent rise time according to [12].
3. The reference lateral acceleration and jerk limits shall not exceed the physical capabilities or operational constraints of the VTOL aircraft, but they shall be sufficiently large such as to comply with requirement 2.
4. Upon initializing the reference dynamics, the reference states shall be sufficiently close to the true aircraft states in order to avoid transients.

The definition of the reference lateral jerk dynamics is hence given as

$$\ddot{V}_{Cy,ref} = \min \left( \ddot{V}_{Cy,ref,max}, \max \left( \ddot{V}_{Cy,ref,min}, K_{\dot{V}_{Cy,ref}} \left( \dot{V}_{Cy,ref,c} - \dot{V}_{Cy,ref} \right) \right) \right), \quad (5.134)$$

with the reference lateral acceleration command

$$\dot{V}_{Cy,ref,c} = K_{V_{Cy,ref}} (V_{Cy,ref,c} - V_{Cy,ref}), \quad (5.135)$$

where the reference lateral velocity command  $V_{Cy,ref,c}$  is chosen as  $V_{Cy,ref,c} = V_{Cy,d}$  in order to comply with requirement 1.

Furthermore, the maximum and minimum reference lateral jerk limits are chosen as

$$\begin{aligned} \ddot{V}_{Cy,ref,max} &= \min \left( \ddot{V}_{Cy,ref,OP,max}, \ddot{V}_{Cy,\dot{V}_{lim,max}} \right), \\ \ddot{V}_{Cy,ref,min} &= \max \left( \ddot{V}_{Cy,ref,OP,min}, \ddot{V}_{Cy,\dot{V}_{lim,min}} \right), \end{aligned} \quad (5.136)$$

with the lateral jerks leading to the limit lateral reference accelerations

$$\begin{aligned} \ddot{V}_{Cy,\dot{V}_{lim,max}} &= K_{\dot{V}_{Cy,lim}} \left( \dot{V}_{Cy,ref,max} - \dot{V}_{Cy,ref} \right), \\ \ddot{V}_{Cy,\dot{V}_{lim,min}} &= K_{\dot{V}_{Cy,lim}} \left( \dot{V}_{Cy,ref,min} - \dot{V}_{Cy,ref} \right), \end{aligned} \quad (5.137)$$

the limit lateral reference accelerations given by

$$\begin{aligned} \dot{V}_{Cy,ref,max} &= \min \left( \dot{V}_{Cy,ref,OP,max}, \dot{V}_{Cy,V_{lim,max}} \right), \\ \dot{V}_{Cy,ref,min} &= \max \left( \dot{V}_{Cy,ref,OP,min}, \dot{V}_{Cy,V_{lim,min}} \right), \end{aligned} \quad (5.138)$$

and the lateral accelerations leading to the limit lateral velocities

$$\begin{aligned}\dot{V}_{C_y, V_{\text{lim}}, \text{max}} &= K_{V_{C_y, \text{lim}}} (V_{C_y, \text{ref}, \text{OP}, \text{max}} - V_{C_y, \text{ref}}) , \\ \dot{V}_{C_y, V_{\text{lim}}, \text{min}} &= K_{V_{C_y, \text{lim}}} (V_{C_y, \text{ref}, \text{OP}, \text{min}} - V_{C_y, \text{ref}}) .\end{aligned}\quad (5.139)$$

The discussion about the respective limits and gains follows analogously to the vertical and forward velocity reference dynamics. Additionally, the lateral reference dynamics have to account for the bandwidth and rate limitations of the system's attitude response, which was pointed out in translational forward control section. Again, the concepts from section 5.2 can be used in order to find optimum gain and saturation parameters for the lateral reference dynamics based on the characteristics of the aircraft's roll rate response.

The reference lateral acceleration  $\dot{V}_{C_y, \text{ref}}$  and velocity  $V_{C_y, \text{ref}}$  are furthermore obtained by integrating the lateral jerk from (5.134) with the initial conditions

$$\dot{V}_{C_y, \text{ref}, 0} = \dot{V}_{C_y} \qquad V_{C_y, \text{ref}, 0} = V_{C_y} , \quad (5.140)$$

where  $\dot{V}_{C_y, \text{ref}, 0}$  and  $V_{C_y, \text{ref}, 0}$  denote the lateral reference acceleration and velocity during *Reset* mode, which are set to the corresponding aircraft states  $\dot{V}_{C_y}$  and  $V_{C_y}$  from the *Feedback Bus*. A transient-free initialization is thereby enforced, which complies with requirement 4.

Furthermore, the error signals for the lateral velocity are

$$e_{V_{C_y}} = V_{C_y, \text{ref}} - V_{C_y} \qquad \dot{e}_{V_{C_y}} = \dot{V}_{C_y, \text{ref}} - \dot{V}_{C_y} , \quad (5.141)$$

with the reference states  $V_{C_y, \text{ref}}$  and  $\dot{V}_{C_y, \text{ref}}$  and the measured or estimated feedback signals  $V_{C_y}$  and  $\dot{V}_{C_y}$ .

The resulting error-control lateral jerk  $\ddot{V}_{C_y, \text{ec}}$  is given by

$$\ddot{V}_{C_y, \text{ec}} = K_{\dot{V}_{C_y, \text{err}}} \left( \dot{e}_{V_{C_y}} + K_{V_{C_y, \text{err}}} e_{V_{C_y}} \right) = K_{\dot{V}_{C_y, \text{err}}} \dot{e}_{V_{C_y}} + K_{\dot{V}_{C_y, \text{err}}} K_{V_{C_y, \text{err}}} e_{V_{C_y}} , \quad (5.142)$$

where  $K_{\dot{V}_{C_y, \text{err}}}$  and  $K_{V_{C_y, \text{err}}}$  define the error controller gains.

Finally, the desired lateral jerk demand, which enforces the lateral error dynamics defined by the gains  $K_{\dot{V}_{C_y, \text{err}}}$  and  $K_{V_{C_y, \text{err}}}$ , is given by

$$\ddot{V}_{C_y, d} = \ddot{V}_{C_y, \text{ref}} + \ddot{V}_{C_y, \text{ec}} , \quad (5.143)$$

where  $\ddot{V}_{C_y, \text{ref}}$  denotes the feedforward lateral reference jerk from (5.134) and  $\ddot{V}_{C_y, \text{ec}}$  is the feedback error-control lateral jerk from (5.142).

The final pseudo control command is obtained after limiting (5.143):

$$\ddot{V}_{C_y, c} = \min \left( \ddot{V}_{C_y, c, \text{max}} , \max \left( \ddot{V}_{C_y, c, \text{min}} , \ddot{V}_{C_y, d} \right) \right) , \quad (5.144)$$

with the upper and lower lateral jerk command limits  $\ddot{V}_{C_y, c, \text{max}}$  and  $\ddot{V}_{C_y, c, \text{min}}$  respectively, which are related to the admissible roll rates of the systems.

The *Dynamic Inversion* block furthermore yields the necessary roll rate  $\dot{\phi}_d$  that leads to the commanded across-heading jerk from (5.144). Similarly to the inversion of the forward channel, the dynamic relationships from (4.44) and (4.41) are inverted and solved for the roll angle rate

$$\dot{\phi}_d = \underbrace{-\frac{\tan(\phi)}{f_{Bz}} \dot{f}_{Bz,\text{ref}} - \frac{\ddot{\psi}_{\text{lead},\phi} V_{Cx} + \dot{\psi} \dot{V}_{Cx}}{\cos(\phi) f_{Bz}}}_{\text{Climb and Turn Compensation}} - \frac{\ddot{V}_{Cy,c}}{\cos(\phi) f_{Bz}}, \quad (5.145)$$

with the lead-filtered heading acceleration signal

$$\ddot{\psi}_{\text{lead},\phi} = K_{\dot{\phi}_{\text{ref}}}^{-1} \ddot{\psi}_{\text{ref}} + \dot{\psi}_{\text{ref}}, \quad (5.146)$$

where  $K_{\dot{\phi}_{\text{ref}}}$  denotes the gain for the reference roll angle rate loop and  $\ddot{\psi}_{\text{ref}}$  and  $\dot{\psi}_{\text{ref}}$  are the reference heading jerk and acceleration respectively.

As was also pointed out in the forward control section, (5.146) accounts for the delayed response in the roll channel by approximating the roll angle rate loop as a first-order system with a bandwidth of  $K_{\dot{\phi}_{\text{ref}}}$ . This considerably improves the coordination during turn maneuvers. Additionally, the reference body-vertical specific force rate  $\dot{f}_{Bz,\text{ref}}$  is used instead of a measurement or estimation for the sake of noise suppression during vertical maneuvers in the presence of roll angles.

**Hover Attitude Protection** The *Hover Attitude Protection* block limits the admissible attitude of the VTOL aircraft during the *Hover* mode. To this end, the desired pitch angle rate  $\dot{\theta}_d$  and roll angle rate  $\dot{\phi}_d$ , which are the output of the forward and lateral velocity control blocks respectively, are dynamically saturated. The functional structure of the *Hover Attitude Protection* block is illustrated in figure 5.35.

Both the pitch angle rate and the roll angle rate are limited by their respective maximum and minimum admissible values

$$\dot{\theta}_{c,\text{max}} = \min(\dot{\theta}_{\text{OP,max}}, \dot{\theta}_{\theta_{\text{lim,max}}}) \quad \dot{\phi}_{c,\text{max}} = \min(\dot{\phi}_{\text{OP,max}}, \dot{\phi}_{\phi_{\text{lim,max}}}) \quad (5.147)$$

and

$$\dot{\theta}_{c,\text{min}} = \max(\dot{\theta}_{\text{OP,min}}, \dot{\theta}_{\theta_{\text{lim,min}}}) \quad \dot{\phi}_{c,\text{min}} = \max(\dot{\phi}_{\text{OP,min}}, \dot{\phi}_{\phi_{\text{lim,min}}}), \quad (5.148)$$

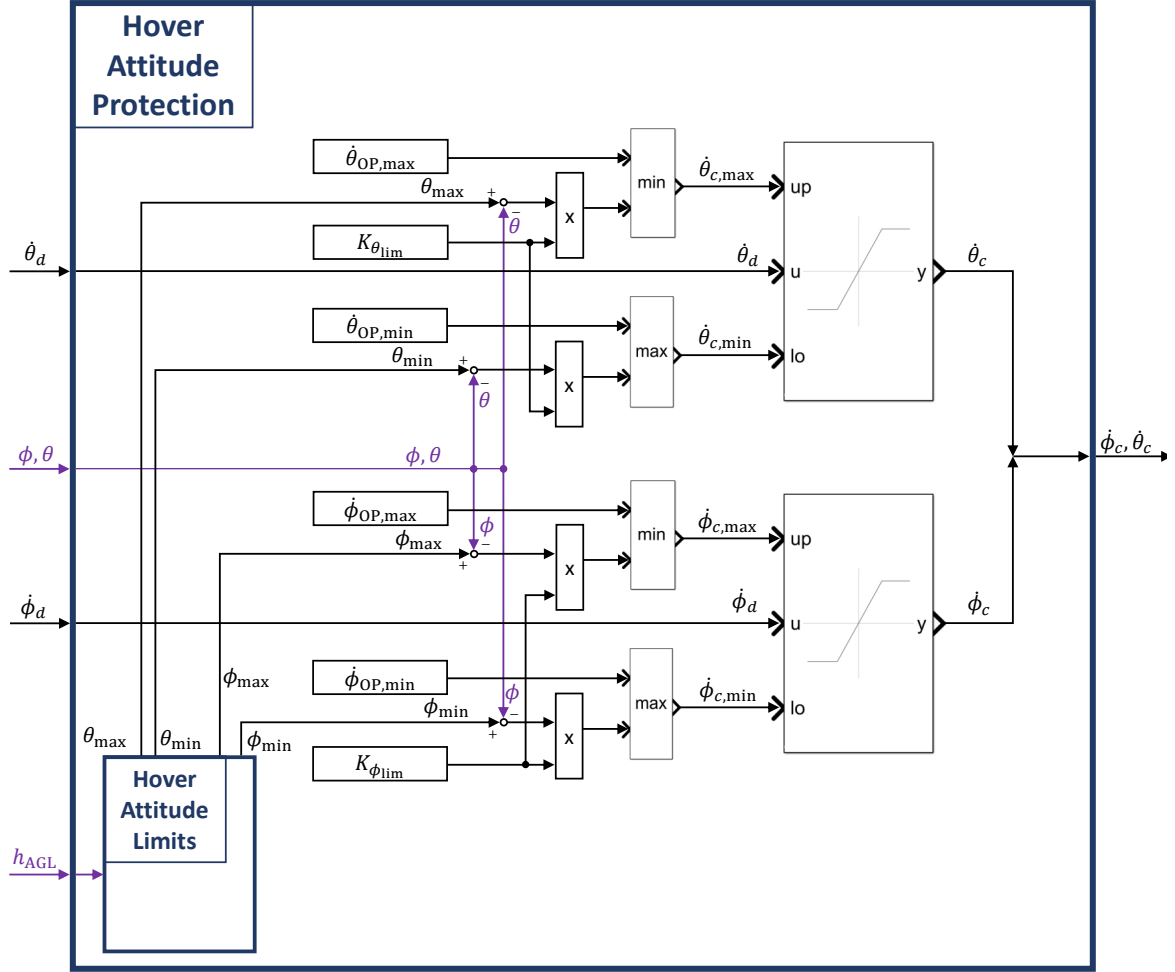
where  $\dot{\theta}_{\text{OP,max}}$  and  $\dot{\phi}_{\text{OP,max}}$  denote the operational maximum pitch and roll angle rates and  $\dot{\theta}_{\text{OP,min}}$  and  $\dot{\phi}_{\text{OP,min}}$  denote the operational minimum pitch and roll angle rates respectively. The pitch and roll angle rates that lead to the limit attitudes are furthermore denoted as

$$\dot{\theta}_{\theta_{\text{lim,max}}} = K_{\theta_{\text{lim}}} (\theta_{\text{max}} - \theta) \quad \dot{\phi}_{\phi_{\text{lim,max}}} = K_{\phi_{\text{lim}}} (\phi_{\text{max}} - \phi) \quad (5.149)$$

and

$$\dot{\theta}_{\theta_{\text{lim,min}}} = K_{\theta_{\text{lim}}} (\theta_{\text{min}} - \theta) \quad \dot{\phi}_{\phi_{\text{lim,min}}} = K_{\phi_{\text{lim}}} (\phi_{\text{min}} - \phi), \quad (5.150)$$




 Figure 5.35: *Hover Attitude Protection block*

where  $K_{\theta_{lim}}$  and  $K_{\phi_{lim}}$  denote the convergence rates towards the maximum pitch angle  $\theta_{max}$  and roll angle  $\phi_{max}$  as well as the minimum pitch angle  $\theta_{min}$  and roll angle  $\phi_{min}$  respectively.

Furthermore, the *Hover Attitude Protection* function incorporates the height above ground  $h_{AGL}$  in order to render the attitude limits  $\theta_{max}$ ,  $\phi_{max}$ ,  $\theta_{min}$ , and  $\phi_{min}$  height dependent. Thereby, the admissible attitude is limited based on the proximity to ground such as to avoid abnormal ground contact, which is illustrated in figure 5.36.

To this end, the maximum admissible pitch and roll angle are given by

$$\theta_{max}(h_{AGL}) = \min \left( \theta_{max,hi}, \max \left( \theta_{max,lo}, \frac{h_{AGL} - h_{AGL,A,lo}}{h_{AGL,A,hi} - h_{AGL,A,lo}} (\theta_{max,hi} - \theta_{max,lo}) + \theta_{max,lo} \right) \right) \quad (5.151)$$

and

$$\phi_{max}(h_{AGL}) = \min \left( \phi_{max,hi}, \max \left( \phi_{max,lo}, \frac{h_{AGL} - h_{AGL,A,lo}}{h_{AGL,A,hi} - h_{AGL,A,lo}} (\phi_{max,hi} - \phi_{max,lo}) + \phi_{max,lo} \right) \right), \quad (5.152)$$

where (5.151) and (5.152) yield a linear blending between the low attitude maximum

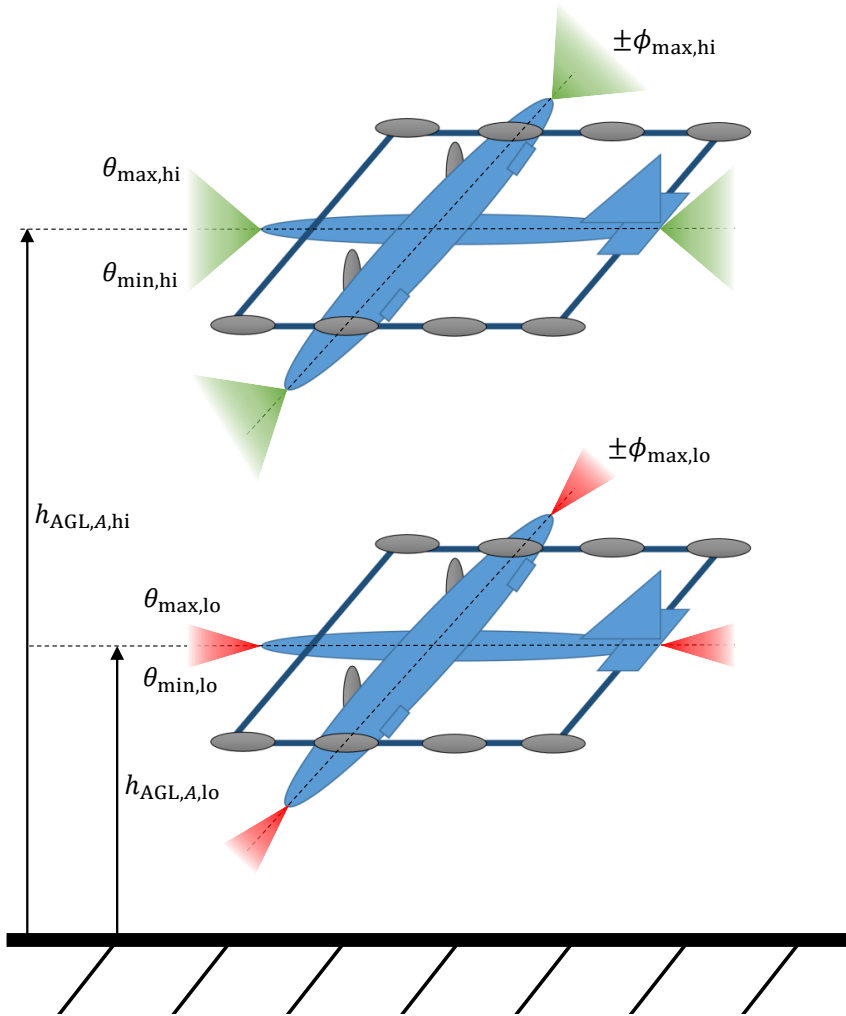


**Figure 5.36:** *Attitude Limits in Different Heights*

pitch and roll angles  $\theta_{\max,lo}$ ,  $\phi_{\max,lo}$  and the high attitude maximum pitch and roll angles  $\theta_{\max,hi}$ ,  $\phi_{\max,hi}$  respectively. The blending is performed between the lower attitude limit  $h_{AGL,A,lo}$  and the higher attitude limit  $h_{AGL,A,hi}$ .

Analogously, the minimum admissible pitch and roll angle are given by

$$\theta_{\min}(h_{AGL}) = \max \left( \theta_{\min,hi}, \min \left( \theta_{\min,lo}, \frac{h_{AGL} - h_{AGL,A,lo}}{h_{AGL,A,hi} - h_{AGL,A,lo}} (\theta_{\min,hi} - \theta_{\min,lo}) + \theta_{\min,lo} \right) \right) \quad (5.153)$$

and

$$\phi_{\min}(h_{AGL}) = \max \left( \phi_{\min,hi}, \min \left( \phi_{\min,lo}, \frac{h_{AGL} - h_{AGL,A,lo}}{h_{AGL,A,hi} - h_{AGL,A,lo}} (\phi_{\min,hi} - \phi_{\min,lo}) + \phi_{\min,lo} \right) \right), \quad (5.154)$$

where  $\phi_{\min,lo} = -\phi_{\max,lo}$  and  $\phi_{\min,hi} = -\phi_{\max,hi}$  due to symmetry.

### 5.3.4.2 Highspeed Control

Figure 5.37 below shows the functional structure of the *Highspeed Control* block. As the name suggests, this block implements functions that are relevant in the *Highspeed* flight phase, which comprises the *Transition* and *Wingborne* mode according to figure 5.12.

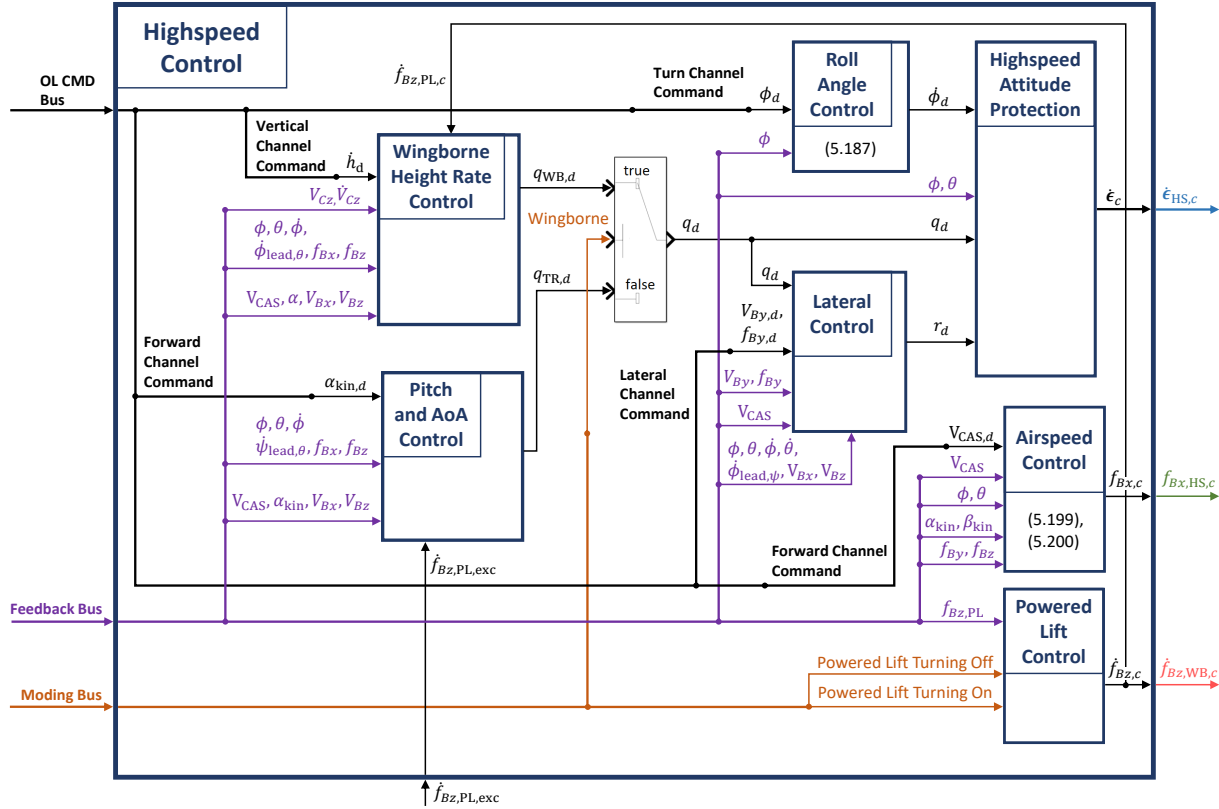


Figure 5.37: *Highspeed Control Block*

The following functions are realized within the *Highspeed Control* block:

- Control of the vertical channel during the fixed-wing flight phase is provided by the *Wingborne Height Rate Control* block.
- During the *Transition* mode, control of the kinematic angle of attack and pitch attitude of the VTOL aircraft is realized in the *Pitch and AoA Control* block.
- Turn maneuvers follow from banking, which is realized via the *Roll Angle Control* block.
- Coordination and lateral stabilization of sideslip conditions is performed in the *Lateral Control* block.
- The *Airspeed Control* block provides airspeed tracking and autothrottle functionality.

- Disengagement and Engagement of the powered lift system is realized in the *Powered Lift Control* block.
- Attitude protection during the *Highspeed* phase is provided in the *Highspeed Attitude Protection* block.

A detailed functional specification of the *Highspeed Control* subsystems is provided in the following subsections.

**Wingborne Height Rate Control** A functional breakdown of the *Wingborne Height Rate Control* block is given below in figure 5.38.

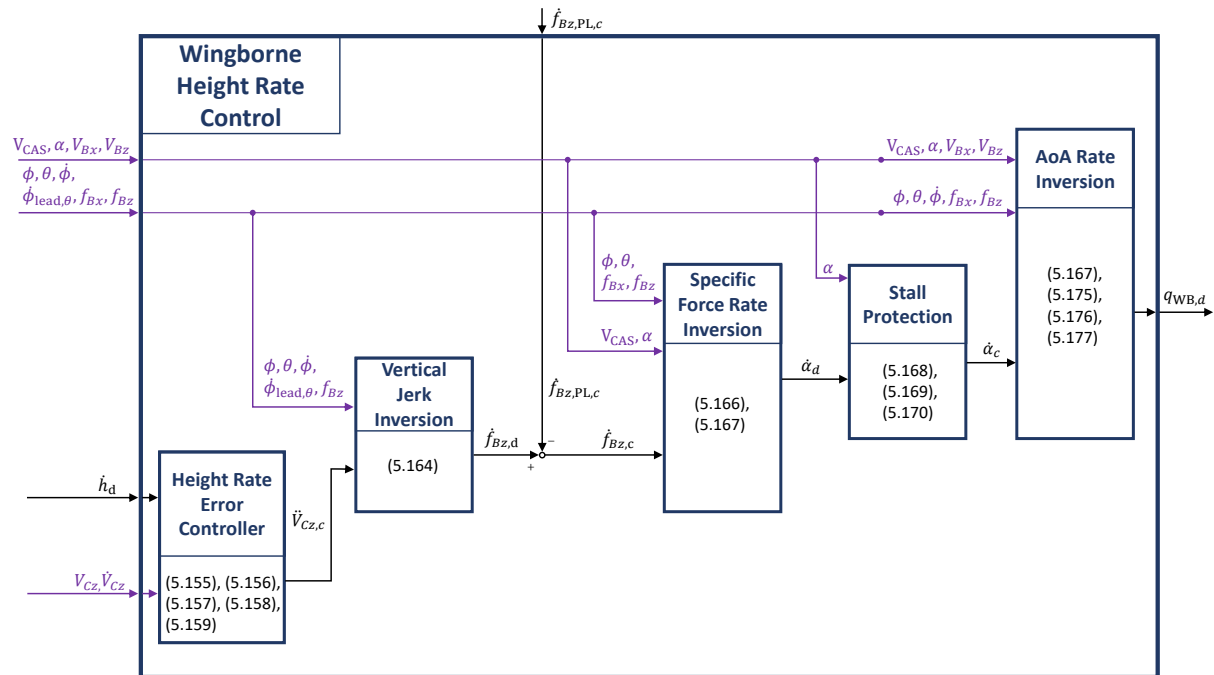


**Figure 5.38:** *Wingborne Height Rate Control Block*

The overall objectives for the vertical control channel during the fixed-wing flight phase are

1. to control a given desired height rate demand  $\dot{h}_d$ , which is provided by the vertical command channel of the *Outer-Loop Command Bus (OL CMD Bus)*, by means of a necessary pitch rate demand  $q_{WB,d}$  that results in sufficient aerodynamic lift by altering the angle of attack,
2. to provide sufficient roll compensation by adjusting the generated aerodynamic lift through an additional pitch rate demand upon performing turn maneuvers, and
3. to provide protection functions against entering dangerous stall conditions by limiting the resulting pitch rate demand upon approaching the stall angle  $\alpha_{stall}$ .

Note that the requirements for underspeed and overspeed protection are considered in the *Vertical Channel Command* block by adjusting the maximum and minimum admissible height rate demand  $\dot{h}_d$  accordingly. Additionally, the maximum (and minimum) vertical jerks and accelerations are also protected within the *Height Rate Error Controller* block.

To this end, the desired height rate dynamics are given by the vertical jerk

$$\ddot{V}_{Cz} \stackrel{!}{=} \ddot{V}_{Cz,d} = K_{\dot{V}_{Cz,err}} (\dot{V}_{Cz,c} - \dot{V}_{Cz}) , \quad (5.155)$$

with the commanded vertical acceleration

$$\dot{V}_{Cz,c} = K_{V_{Cz,err}} (V_{Cz,c} - V_{Cz}) , \quad (5.156)$$

where the vertical velocity command is chosen to be  $V_{Cz,c} = -\dot{h}_d$ . The error gains  $K_{\dot{V}_{Cz,err}}$  and  $K_{V_{Cz,err}}$  thereby influence the overall bandwidth and damping characteristics of the height rate response in the *Wingborne* mode.

Analogously to the *Powered Lift Based Height Rate Control* block, a vertical rate reference model could be used in order to generate feedforward signals and the reference states for the error controller. However, for the sake of simplicity the use of a reference model for the vertical channel is omitted in the *Wingborne Height Rate Control* block, as the degree of command channel coupling is less than in the hover phase in which the reference specific force rate  $\dot{f}_{Bz,ref}$  is accounted for in the horizontal velocity channel.

Nevertheless, the integration of a reference model would be straightforward and can increase the overall performance in the vertical channel during fixed-wing flight. The resulting control structure would then follow analogously to the *Powered Lift Based Height Rate Control* block depicted in figure 5.29.

In order to generate the final vertical jerk command  $\ddot{V}_{Cz,c}$ , the demand in (5.155) is furthermore limited by

$$\ddot{V}_{Cz,c} = \min \left( \ddot{V}_{Cz,c,max}, \max \left( \ddot{V}_{Cz,c,min}, \ddot{V}_{Cz,d} \right) \right) , \quad (5.157)$$

with the maximum and minimum vertical jerk command limits

$$\begin{aligned} \ddot{V}_{Cz,c,max} &= \min \left( \ddot{V}_{Cz,OP,max}, \ddot{V}_{Cz,\dot{V}_{lim,max}} \right) , \\ \ddot{V}_{Cz,c,min} &= \max \left( \ddot{V}_{Cz,OP,min}, \ddot{V}_{Cz,\dot{V}_{lim,min}} \right) , \end{aligned} \quad (5.158)$$

and the vertical jerks leading to the limit vertical accelerations

$$\begin{aligned} \ddot{V}_{Cz,\dot{V}_{lim,max}} &= K_{\dot{V}_{Cz,lim}} \left( \dot{V}_{Cz,OP,max} - \dot{V}_{Cz} \right) , \\ \ddot{V}_{Cz,\dot{V}_{lim,min}} &= K_{\dot{V}_{Cz,lim}} \left( \dot{V}_{Cz,OP,min} - \dot{V}_{Cz} \right) , \end{aligned} \quad (5.159)$$

where  $\ddot{V}_{Cz,OP,max}$ ,  $\ddot{V}_{Cz,OP,min}$ ,  $\dot{V}_{Cz,OP,max}$  and  $\dot{V}_{Cz,OP,min}$  denote the maximum and minimum operational jerk and acceleration limits in the down direction respectively and  $K_{\dot{V}_{Cz,lim}}$  denotes the convergence rate towards the acceleration limits.

As was already pointed out in the *Powered Lift Based Height Rate Control* section, distinguishing between  $K_{\dot{V}_{Cz, \text{err}}}$  from (5.155) and  $K_{\dot{V}_{Cz, \text{lim}}}$  from (5.159) allows for choosing different convergence characteristics for small- and large-amplitude vertical acceleration commands respectively. Furthermore, the convergence towards the maximum and minimum admissible vertical velocity can be dealt with in a similar manner, but is left out in this context for the sake of simplicity.

Next, the *Vertical Jerk Inversion* block provides the necessary body-vertical specific force rate demand  $\dot{f}_{Bz,d}$  that leads to the commanded earth-vertical jerk command  $\ddot{V}_{Cz,c}$  from (5.157). To this end, equations (4.41) and (4.44) are inverted in order to yield

$$\dot{f}_{Bz} = \tan(\phi)f_{Bz}\dot{\phi} + \tan(\theta)f_{Bz}\dot{\theta} + \frac{\ddot{V}_{Cz}}{\cos(\phi)\cos(\theta)}. \quad (5.160)$$

Furthermore, for the turn compensation term  $\dot{f}_{Bz,TC} = \tan(\phi)f_{Bz}\dot{\phi} = \frac{\sin(\phi)}{\cos^2(\phi)}\cos(\phi)f_{Bz}\dot{\phi}$  in (5.160) the lead-filtered signal

$$\dot{f}_{Bz,TC, \text{lead}, \theta} = \tan(\phi)f_{Bz}\dot{\phi}_{\text{lead}, \theta} + K_{\dot{\theta}_{\text{ref}}}^{-1} \left( 1 + 2 \tan^2(\phi) \right) f_{Bz}\dot{\phi}^2, \quad (5.161)$$

with

$$\dot{\phi}_{\text{lead}, \theta} = K_{\dot{\theta}_{\text{ref}}}^{-1} \ddot{\phi}_{\text{ref}} + \dot{\phi}_{\text{ref}} \quad (5.162)$$

is used, which was introduced in subsection 4.3.3.1. Thereby,  $K_{\dot{\theta}_{\text{ref}}}$  denotes the reference bandwidth of the pitch angle rate's equivalent first-order dynamics and  $\ddot{\phi}_{\text{ref}}$  and  $\dot{\phi}_{\text{ref}}$  are the reference roll angle acceleration and rate respectively.

In (5.161) it is assumed that the turn compensation term  $\dot{f}_{Bz,TC}$  builds up according to the pitch channel's equivalent first-order response

$$\ddot{f}_{Bz,TC} = K_{\dot{\theta}_{\text{ref}}} \left( \dot{f}_{Bz,TC, \text{lead}, \theta} - \dot{f}_{Bz,TC} \right) \quad (5.163)$$

and that the force in the earth-vertical direction remains constant, i.e.  $\frac{d}{dt}(\cos(\phi)f_{Bz}) = 0$ .

Furthermore, the effect of tilting the lift direction due to changes in the pitch angle is typically much smaller than due to changes in the roll angle and therefore  $\tan(\theta)f_{Bz}\dot{\theta} \approx 0$  is assumed, which was pointed out in subsection 4.3.3.1. It follows the final inversion law for the specific force rate demand:

$$\dot{f}_{Bz,d} = \underbrace{\tan(\phi)f_{Bz}\dot{\phi}_{\text{lead}, \theta} + K_{\dot{\theta}_{\text{ref}}}^{-1} \left( 1 + 2 \tan^2(\phi) \right) f_{Bz}\dot{\phi}^2}_{\text{Turn Compensation}} + \frac{\ddot{V}_{Cz,c}}{\cos(\phi)\cos(\theta)}, \quad (5.164)$$

with  $\dot{\phi}_{\text{lead}, \theta}$  from (5.162) and  $\ddot{V}_{Cz,c}$  from (5.157).

The *Specific Force Rate Inversion* block further provides the desired angle of attack rate demand  $\dot{\alpha}_d$  that yields the commanded specific force rate

$$\dot{f}_{Bz,c} = \dot{f}_{Bz,d} - \dot{f}_{Bz,PL,c}, \quad (5.165)$$

where the portion from shutting down (or turning on) the powered lift system  $\dot{f}_{Bz,PL,c}$  is subtracted in order to yield the desired specific force rate  $\dot{f}_{Bz,d}$  from (5.164).

To this end, the relationship from (4.102) is inverted, which follows from differentiation of (4.99) while considering (4.100) and (4.101), and yields

$$\dot{\alpha}_d = -\frac{2(C_{L0} + C_{L\alpha}\alpha)\dot{V}_{CAS}}{C_{L\alpha}V_{CAS}} - \frac{\dot{f}_{Bz,c}}{\frac{1}{m}\frac{1}{2}\rho_0V_{CAS}^2SC_{L\alpha}}, \quad (5.166)$$

where  $C_{L0}$  and  $C_{L\alpha}$  are the aircraft's zero lift coefficient and lift slope coefficient respectively,  $\alpha$  is the angle of attack,  $m$  and  $S$  denote the VTOL's mass and reference wing area,  $\rho_0$  is the reference air density on mean sea level,  $\dot{f}_{Bz,c}$  is the specific force rate command from (5.165), and  $V_{CAS}$  and  $\dot{V}_{CAS}$  denote the calibrated airspeed and its derivative.

Furthermore,  $\dot{V}_{CAS}$  is given by

$$\dot{V}_{CAS} = (\sin(\alpha)\cos(\phi)\cos(\theta) - \cos(\alpha)\sin(\theta))g + \cos(\alpha)f_{Bx} + \sin(\alpha)f_{Bz}, \quad (5.167)$$

which follows from (4.90) while considering (4.91) and (4.92) and neglecting the influence of changing wind direction and magnitude.

In order to avoid undesired stall conditions, the angle of attack rate demand  $\dot{\alpha}_d$  from (5.166) is dynamically saturated in the *Stall Protection* block, which yields the final angle of attack rate command

$$\dot{\alpha}_c = \min(\dot{\alpha}_{c,\max}, \max(\dot{\alpha}_{c,\min}, \dot{\alpha}_d)), \quad (5.168)$$

with the maximum and minimum angle of attack rate command limits

$$\begin{aligned} \dot{\alpha}_{c,\max} &= \min(\dot{\alpha}_{OP,\max}, \dot{\alpha}_{\alpha_{lim},\max}), \\ \dot{\alpha}_{c,\min} &= \max(\dot{\alpha}_{OP,\min}, \dot{\alpha}_{\alpha_{lim},\min}), \end{aligned} \quad (5.169)$$

where the angle of attack rates leading to the limit angle of attack values are given by

$$\begin{aligned} \dot{\alpha}_{\alpha_{lim},\max} &= K_{\alpha_{lim}}(\alpha_{\max} - \alpha), \\ \dot{\alpha}_{\alpha_{lim},\min} &= K_{\alpha_{lim}}(\alpha_{\min} - \alpha). \end{aligned} \quad (5.170)$$

Thereby,  $\dot{\alpha}_{OP,\max}$  and  $\dot{\alpha}_{OP,\min}$  denote the maximum and minimum operational angle of attack rate limits,  $K_{\alpha_{lim}}$  denotes the convergence rate towards the angle of attack limits, and  $\alpha_{\max}$  and  $\alpha_{\min}$  denote the angle of attack limits, which provide sufficient margin towards aerodynamic stall.

Finally, the *AoA Rate Inversion* block provides the necessary pitch rate demand  $q_{WB,d}$  leading to the commanded angle of attack rate  $\dot{\alpha}_c$  from (5.168). Thereby, the subscript WB helps to distinguish from the pitch rate demand  $q_{TR,d}$ , which is used during the *Transition* mode in order to track the desired kinematic angle of attack  $\alpha_{kin,d}$  provided by the forward command channel of the *Outer-Loop Command Bus (OL CMD Bus)* and is derived in the context of the *Pitch and AoA Control* block.

To this end, recall the relationship from (4.79)

$$q = \dot{\alpha} - \frac{V_{Bx} (f_{Bz} + \cos(\phi) \cos(\theta)g) - V_{Bz} (f_{Bx} - \sin(\theta)g)}{V_{Bx}^2 + V_{Bz}^2}, \quad (5.171)$$

which is derived from differentiation of (4.75) and yields the pitch rate  $q$  that results in a given angle of attack rate  $\dot{\alpha}$ . Note that in (5.171) it is assumed that the body-lateral velocity  $V_{By}$  is much smaller than the body-longitudinal velocity  $V_{Bx}$  and hence changes in angle of attack are mainly influenced by pitch motion. Furthermore, the effects of changing wind direction and magnitude are neglected.

The term

$$q_{\text{path}} = -\frac{V_{Bx} (f_{Bz} + \cos(\phi) \cos(\theta)g)}{V_{Bx}^2 + V_{Bz}^2} \quad (5.172)$$

is the dominating part in (5.171) due to  $V_{Bx} \gg V_{Bz}$  and accounts for the additional pitch rate demand that compensates the flight path curvature resulting from body-vertical inertial acceleration. In order to increase the performance of the angle of attack inversion law, the path curvature term (5.172) is considered by using the first-order approximation

$$\dot{q}_{\text{path}} = K_{\dot{\theta}_{\text{ref}}} (q_{\text{path},d} - q_{\text{path}}), \quad (5.173)$$

where  $K_{\dot{\theta}_{\text{ref}}}$  denotes the reference bandwidth of the pitch angle rate reference dynamics. Note that the equivalence of pitch rate  $q$  and pitch angle rate  $\dot{\theta}$  is only valid for small roll angles  $\phi$ . However, due to similar bandwidth of all attitude rate channels the assumption in (5.173) is justified.

Furthermore, setting (5.173) equal to the derivative of (5.172) yields

$$\dot{q}_{\text{path}} = K_{\dot{\theta}_{\text{ref}}} (q_{\text{path},d} - q_{\text{path}}) \stackrel{!}{=} -\frac{V_{Bx} (\dot{f}_{Bz} - \sin(\phi) \cos(\theta)g\dot{\phi})}{V_{Bx}^2 + V_{Bz}^2}, \quad (5.174)$$

where the influence of changing body-vertical specific force and gravity coupling due to rolling are considered for the path curvature.

Solving (5.174) for  $q_c$  yields the lead-filtered pitch rate demand for the path curvature compensation

$$q_{\text{path},d} = -\frac{V_{Bx} (f_{Bz} + \cos(\phi) \cos(\theta)g)}{V_{Bx}^2 + V_{Bz}^2} - K_{\dot{\theta}_{\text{ref}}}^{-1} \frac{V_{Bx} (\dot{f}_{Bz,\text{res}} - \sin(\phi) \cos(\theta)g\dot{\phi})}{V_{Bx}^2 + V_{Bz}^2}, \quad (5.175)$$

where the resulting body-vertical specific force rate  $\dot{f}_{Bz,\text{res}}$  in (5.175) is estimated using the commanded angle of attack rate  $\dot{\alpha}_c$  from (5.168) and the relationship from (4.102):

$$\dot{f}_{Bz,\text{res}} = -\frac{1}{m} \frac{1}{2} \rho_0 S (C_{L0} + C_{L\alpha}\alpha) 2V_{\text{CAS}} \dot{V}_{\text{CAS}} - \frac{1}{m} \frac{1}{2} \rho_0 V_{\text{CAS}}^2 S C_{L\alpha} \dot{\alpha}_c, \quad (5.176)$$

with  $\dot{V}_{\text{CAS}}$  from (5.167).

The final pitch rate demand hence is given by

$$q_{\text{WB},d} = \dot{\alpha}_c + q_{\text{path},d} + \frac{V_{Bz} (f_{Bx} - \sin(\theta)g)}{V_{Bx}^2 + V_{Bz}^2}, \quad (5.177)$$

with  $\dot{\alpha}_c$  from (5.168) and  $q_{\text{path},d}$  from (5.175).



**Pitch and Angle of Attack Control** The *Pitch and Angle of Attack Control* block provides stabilization and control of the the pitch channel during the *Transition* mode. The high-level functional structure is shown in figure 5.39.

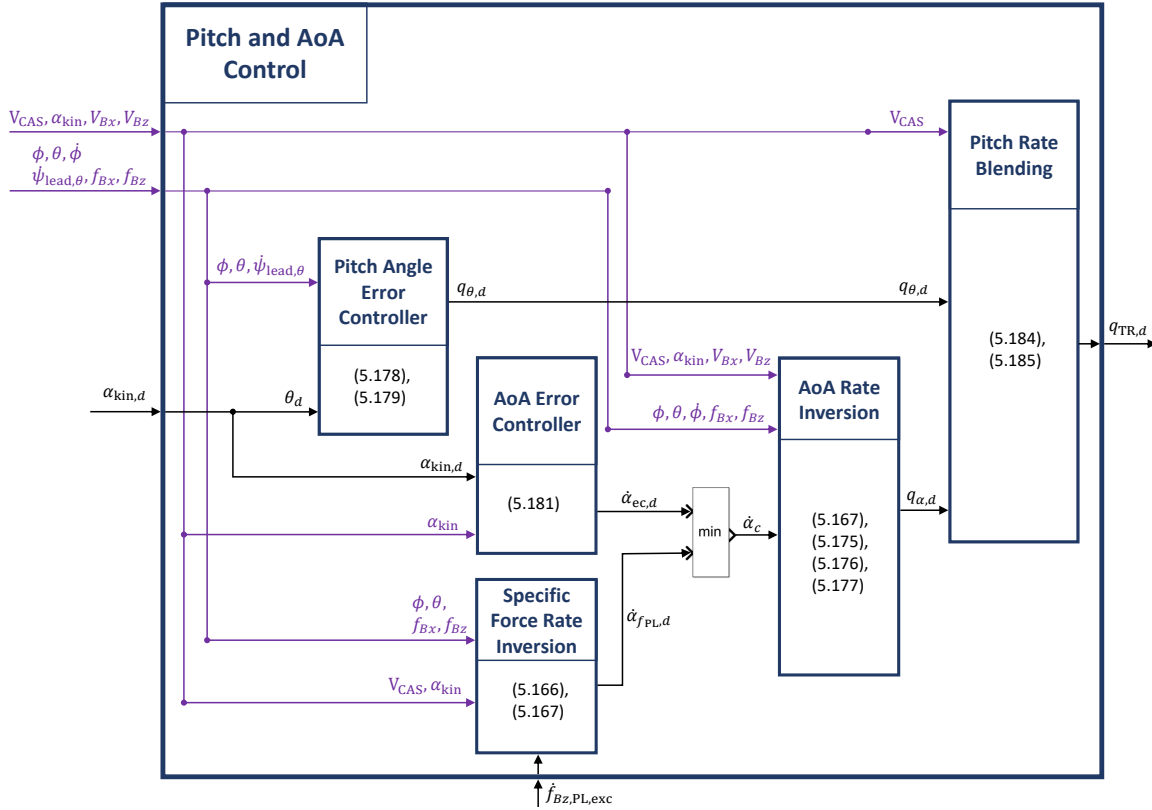


**Figure 5.39:** *Pitch and Angle of Attack Control Block*

The output of the *Pitch and Angle of Attack Control* block is the desired pitch rate  $q_{TR,d}$  in the transition phase, which is blended over the calibrated airspeed  $V_{CAS}$  in the *Pitch Rate Blending* block. Hence, it is distinguished between the low- and high-velocity pitch rate demand, which is motivated by the increasing significance of the angle of attack at higher airspeeds and its sensitivity with respect to body-vertical velocity changes at lower airspeeds.

In particular, tracking the desired kinematic angle of attack  $\alpha_{kin,d}$  results in an increased pitch angle upon initiating climb maneuvers. As was already pointed out in subsection 4.2.2.3, this behavior can support deceleration at medium airspeeds. However, in order to avoid excessive pitch motion upon vertical maneuvers, the pitch angle  $\theta$  is tracked instead of the kinematic angle of attack  $\alpha_{kin}$  at lower velocities during the transition phase.

To this end, the *Pitch Angle Error Controller* yields the necessary pitch angle rate command

$$\dot{\theta}_c = \min \left( \dot{\theta}_{OP,max}, \max \left( \dot{\theta}_{OP,min}, K_\theta (\theta_d - \theta) \right) \right), \quad (5.178)$$

which stabilizes the pitch angle  $\theta$  around the setpoint  $\theta_d = \alpha_{kin,d}$ .

Thereby,  $\alpha_{\text{kin},d}$  represents the desired kinematic angle of attack demand, which is provided by the forward command channel in the *Outer-Loop Command Bus (OL CMD Bus)* and is reinterpreted as desired pitch angle at low airspeeds. The operational pitch angle rate limits are furthermore denoted as  $\dot{\theta}_{\text{OP,max}}$  and  $\dot{\theta}_{\text{OP,min}}$ .

Using the inverse strapdown equation (4.121), the corresponding pitch rate demand  $q_{\theta,d}$  is given by

$$q_{\theta,d} = \cos(\phi)\dot{\theta}_c + \sin(\phi)\cos(\theta)\dot{\psi}_{\text{lead},\theta}, \quad (5.179)$$

with  $\dot{\theta}_c$  from (5.178) and the lead-filtered heading rate signal

$$\dot{\psi}_{\text{lead},\theta} = K_{\dot{\theta}_{\text{ref}}}^{-1}\ddot{\psi}_{\text{ref}} + \dot{\psi}_{\text{ref}}, \quad (5.180)$$

which accounts for the delayed pitch response of the aircraft.

At higher airspeeds, the kinematic angle of attack is tracked using the saturated desired angle of attack rate signal from (4.74) with  $\alpha_{\text{kin},c} = \alpha_{\text{kin},d}$ , i.e.

$$\dot{\alpha}_{\text{ec},d} = \min(\dot{\alpha}_{\text{OP,max}}, \max(\dot{\alpha}_{\text{OP,min}}, K_{\alpha}(\alpha_{\text{kin},d} - \alpha_{\text{kin}}))) , \quad (5.181)$$

where  $K_{\alpha}$  denotes the desired bandwidth of the angle of attack loop and  $\dot{\alpha}_{\text{OP,max}}$  and  $\dot{\alpha}_{\text{OP,min}}$  are the operational limits for the angle of attack rate.

In order to avoid uncontrolled climbing, the specific excess powered lift rate  $\dot{f}_{Bz,PL,exc}$  from (5.103) is considered in the calculation of the limit angle of attack rate  $\dot{\alpha}_{f_{PL},d}$  for which the powered lift would reach its minimum value according to the specified dynamics in (5.99). This concept was introduced in subsection 4.3.2.3 and is reused in the context of the control architecture specification.

To this end, figure 5.40 illustrates the idea and shows the VTOL aircraft in three identical states during the transition phase for decreasing desired total lift demands. The light blue portion thereby denotes the excess powered lift and represents the amount of lifting force that could be allocated into a change in angle of attack  $\Delta\alpha$ , which would result in a minimum (idle) powered lift setting while reaching the desired total lift.

For the conversion of the specific excess powered lift rate  $\dot{f}_{Bz,PL,exc}$  into the corresponding limit angle of attack rate  $\dot{\alpha}_{f_{PL},d}$ , the same *Specific Force Rate Inversion* function is used as in the *Wingborne Height Rate Control* block. However, instead of using a measurement of the aerodynamic angle of attack  $\alpha$  in (5.166) and (5.167), the kinematic angle of attack  $\alpha_{\text{kin}}$  is used for the transformation.

Despite a less accurate inversion in the presence of wind and gusts, using the kinematic angle of attack  $\alpha_{\text{kin}}$  instead of the aerodynamic angle of attack  $\alpha$  protects against signal distortion due to adverse effects of the powered lift motors' induced velocity when measuring aerodynamic flow angles. Hence, only the kinematic angle of attack estimation

$$\alpha_{\text{kin}} = \tan^{-1}\left(\frac{V_{Bz}}{V_{Bx}}\right) \quad (5.182)$$

is used within the *Pitch and AoA Control* block, which results from the ratio of the kinematic vertical and forward velocity in the body frame according to (5.182). Figure 4.12 in subsection 4.3.2.2 thereby illustrates the geometric relationships.

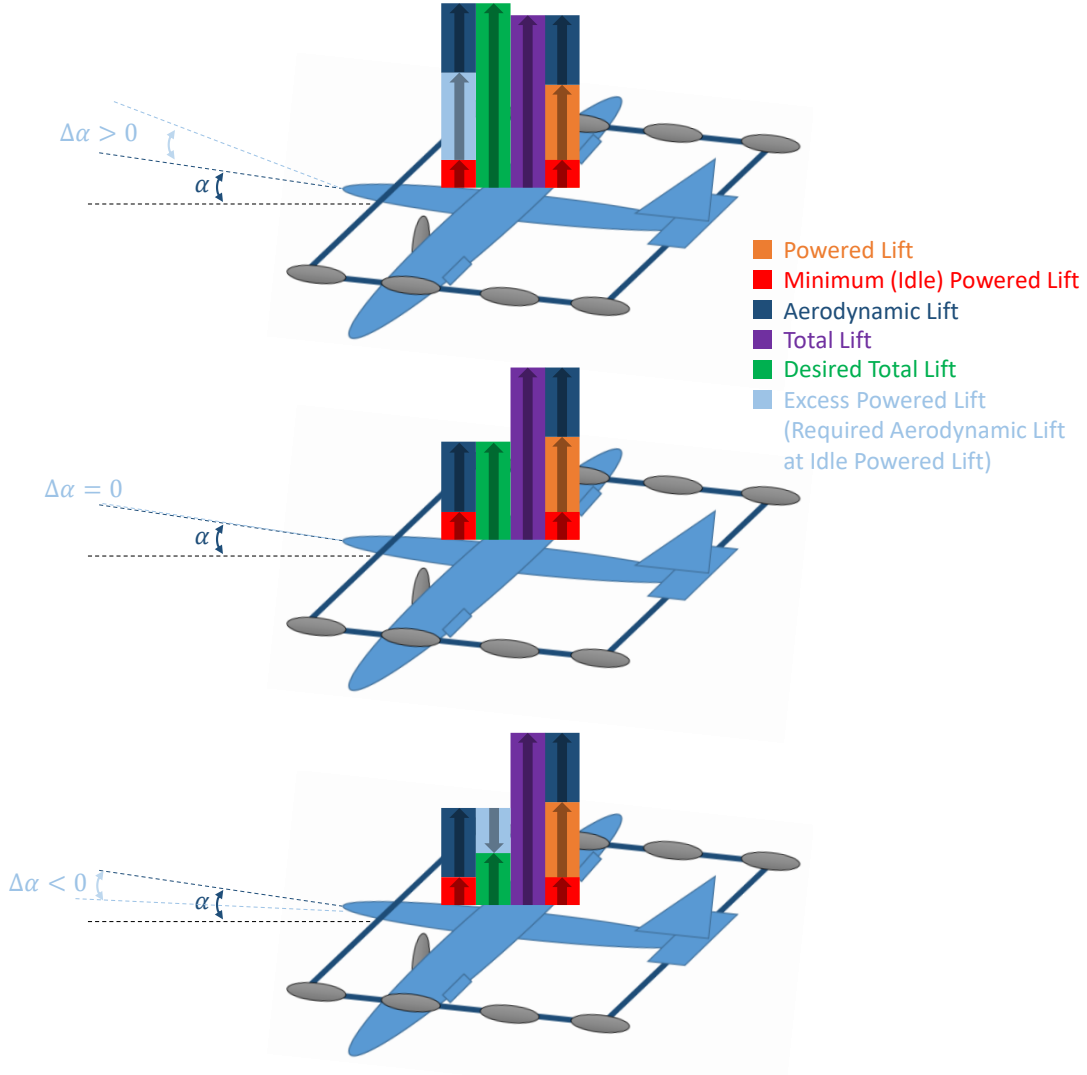


**Figure 5.40:** *Excess Powered Lift for Different Total Lift Demands*

The final angle of attack rate command  $\dot{\alpha}_c$  follows from taking the smaller value of both  $\dot{\alpha}_{ec,d}$  and  $\dot{\alpha}_{f_{PL},d}$ , i.e.

$$\dot{\alpha}_c = \min(\dot{\alpha}_{ec,d}, \dot{\alpha}_{f_{PL},d}), \quad (5.183)$$

which ensures that the angle of attack never exceeds the value for which the powered lift system would undershoot its idle state.

The subsequent inversion of the commanded angle of attack rate  $\dot{\alpha}_c$  into the corresponding pitch rate demand  $q_{\alpha,d}$  is performed using the *AoA Rate Inversion* block. Similarly to the *Specific Force Rate Inversion*, the kinematic angle of attack  $\alpha_{kin}$  is used instead of the aerodynamic angle of attack  $\alpha$  in (5.167), (5.175), (5.176), and (5.177).

Finally, the *Pitch Rate Blending* block blends the resulting pitch rate demand  $q_{TR,d}$  according to

$$q_{TR,d} = (1 - \lambda_q) q_{\theta,d} + \lambda_q q_{\alpha,d}, \quad (5.184)$$

with the blending parameter

$$\lambda_q(V_{CAS}) = \min \left( 1, \max \left( 0, \frac{V_{CAS} - V_{CAS,lo}}{V_{CAS,hi} - V_{CAS,lo}} \right) \right). \quad (5.185)$$

The relationship described in (5.184) and (5.185) linearly blends the pitch rate demand over the airspeed  $V_{CAS}$  from  $q_{\theta,d}$  for  $V_{CAS} \leq V_{CAS,lo}$  to  $q_{\alpha,d}$  for  $V_{CAS} \geq V_{CAS,hi}$ .

As is illustrated in figure 5.37, the final pitch rate demand  $q_d$  follows from switching between the pitch rate demand provided by the *Wingborne Height Rate Control* block  $q_{WB,d}$  from (5.177) and the pitch rate demand provided by the *Pitch and AoA Control* block  $q_{TR,d}$  from (5.184):

$$q_d = \begin{cases} q_{WB,d} \text{ from (5.177),} & \text{for } Wingborne == \text{true} \\ q_{TR,d} \text{ from (5.184),} & \text{for } Wingborne == \text{false} \end{cases}. \quad (5.186)$$

**Roll Angle Control** The *Roll Angle Control* block stabilizes the roll angle  $\phi$  around the desired roll angle  $\phi_d$ , which is provided by the turn command channel of the *Outer-Loop Command Bus (OL CMD Bus)*. The desired roll angle rate  $\dot{\phi}_d$  is recalled from subsection 4.3.2.1 and yields

$$\dot{\phi}_d = K_\phi (\phi_d - \phi), \quad (5.187)$$

where  $K_\phi$  denotes the design bandwidth of the roll angle loop, which can also be chosen to adapt to the current dynamic pressure, such as to account for the increased roll authority at increasing airspeeds.

Note that additional roll angle and roll angle rate protection is realized in the *Highspeed Attitude Protection* block. Furthermore, since the maximum admissible loadfactor of the aircraft is considered within the *Maximum Vertical Force* block from figure 5.24, the generation of the desired roll angle  $\phi_d$  in the *Turn Channel Command Block* shown in figure 5.23 accounts for the overall lift capabilities of the system and hence indirectly includes a command limitation for the roll channel.

**Lateral Control** The coordination and lateral stabilization of sideslip conditions is performed in the *Lateral Control* block during the *Highspeed* phase. Thereby, the lateral velocity  $V_{By}$  and specific force  $f_{By}$  are controlled in a blended scheme using the body-relative lateral acceleration  $\dot{V}_{By,d}$  as a pseudo control, which is converted into a desired yaw rate demand  $r_d$ . The functional structure of the *Lateral Control* block is depicted in figure 5.41.

The basis for the control law is given by the relationship between body-relative lateral acceleration  $\dot{V}_{By}$  and yaw rate  $r$ , which is revisited from (4.82):

$$r = \frac{f_{By} + \sin(\phi) \cos(\theta) g + \dot{\phi} V_{Bz} - \sin(\phi) \tan(\theta) V_{Bz} q - \dot{V}_{By}}{V_{Bx} + \cos(\phi) \tan(\theta) V_{Bz}}, \quad (5.188)$$

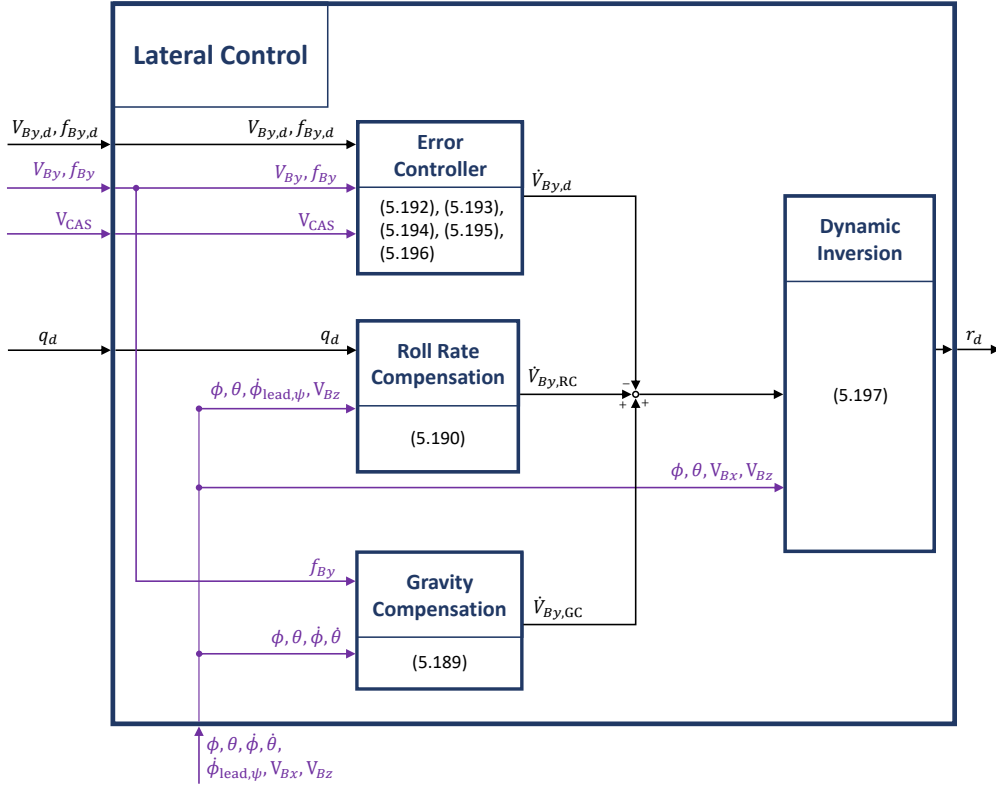


**Figure 5.41:** *Lateral Control Block*

which follows from (4.22) while substituting the roll rate  $p$  using the inverse strapdown equation (4.119).

The following three main components are identified within (5.188):

- The gravity-induced term  $f_{By} + \sin(\phi) \cos(\theta)g$  accounts for the inertial lateral acceleration of the aircraft and is calculated in the *Gravity Compensation* block. As was presented in subsection 4.3.2.2, the delayed yaw response of the system can be anticipated in terms of the linear first-order dynamics of the reference heading rate, which yields the final compensation term

$$\dot{V}_{By,GC} = f_{By} + \underbrace{\sin(\phi) \cos(\theta) \dot{\phi} - \sin(\phi) \sin(\theta) \dot{\theta}}_{\text{Lead Portion}} g, \quad (5.189)$$

where  $K_{\dot{\psi}_{ref}}$  denotes the reference bandwidth of the heading rate loop.

- The roll rate induced term  $\dot{\phi}V_{Bz} - \sin(\phi) \tan(\theta)V_{Bz}q$  in (5.188) results from kinematic coupling of the roll rate  $p = \dot{\phi} - \sin(\phi) \tan(\theta)q - \cos(\phi) \tan(\theta)r$  into the lateral channel according to (4.22). Again, the delayed yaw response of the system is accounted for in terms of the linear first-order approximation of the reference heading rate and hence the *Roll Compensation* term yields

$$\dot{V}_{By,RC} = \dot{\phi}_{lead, \psi} V_{Bz} - \sin(\phi) \tan(\theta) V_{Bz} q_d, \quad (5.190)$$

with the lead-filtered roll angle rate

$$\dot{\phi}_{\text{lead},\psi} = K_{\psi_{\text{ref}}}^{-1} \ddot{\phi}_{\text{ref}} + \dot{\phi}_{\text{ref}} \quad (5.191)$$

and the pitch rate demand  $q_d$  from (5.186).

- The *Error Controller* block in figure 5.41 provides the necessary pseudo control output  $\dot{V}_{By,d}$  that stabilizes the body-lateral velocity  $V_{By}$  and specific force  $f_{By}$  around the respective set points  $V_{By,d}$  and  $f_{By,d}$ , which originate from the lateral command channel of the *Outer-loop Command Bus (OL CMD Bus)*.

To this end, the desired body-lateral acceleration demand is given according to

$$\dot{V}_{By,d} = \left(1 - \lambda_{\dot{V}_{By}}\right) \underbrace{\dot{V}_{By,V_{By,d}}}_{(5.194)} + \lambda_{\dot{V}_{By}} \underbrace{\dot{V}_{By,f_{By,d}}}_{(5.196)}, \quad (5.192)$$

with the blending parameter

$$\lambda_{\dot{V}_{By}}(V_{\text{CAS}}) = \min\left(1, \max\left(0, \frac{V_{\text{CAS}} - V_{\text{CAS,lo}}}{V_{\text{CAS,hi}} - V_{\text{CAS,lo}}}\right)\right), \quad (5.193)$$

which blends the lateral acceleration demand over the airspeed  $V_{\text{CAS}}$  from  $\dot{V}_{By,V_{By,d}}$  for  $V_{\text{CAS}} \leq V_{\text{CAS,lo}}$  to  $\dot{V}_{By,f_{By,d}}$  for  $V_{\text{CAS}} \geq V_{\text{CAS,hi}}$ .

Thereby,  $\dot{V}_{By,V_{By,d}}$  denotes the pseudo control law that stabilizes the lateral kinematic velocity  $V_{By}$  around the desired value  $V_{By,d}$  and is given by

$$\dot{V}_{By,V_{By,d}} = K_{V_{By}}(V_{By,d} - V_{By}), \quad (5.194)$$

where  $K_{V_{By}}$  denotes the desired bandwidth for the lateral velocity control loop.

Furthermore, the desired body-lateral specific force rate

$$\dot{f}_{By,d} = K_{f_{By}}(f_{By,d} - f_{By}), \quad (5.195)$$

which stabilizes the lateral specific force  $f_{By}$  around the desired value  $f_{By,d}$ , is converted into the corresponding body-lateral acceleration signal  $\dot{V}_{By,f_{By,d}}$  using the relationships in (4.111), (4.112), and (4.113):

$$\dot{V}_{By,f_{By,d}} = \frac{2m}{\rho_0 V_{\text{CAS}} S C_{Q\beta}} \dot{f}_{By,d}, \quad (5.196)$$

where  $m$  denotes the aircraft's mass,  $\rho_0$  is the reference air density on mean sea level,  $V_{\text{CAS}}$  is the calibrated airspeed,  $S$  denotes the reference wing area of the aircraft,  $C_{Q\beta}$  is the gradient of the lateral force coefficient, and  $\dot{f}_{By,d}$  is the desired specific force rate from (5.195). The relevant geometric and aerodynamic relationships were furthermore illustrated in figure 4.13.

Adding up the three terms from (5.189), (5.190), and (5.192) and applying (5.188) yields the final yaw rate demand

$$r_d = \frac{\dot{V}_{By,\text{GC}} + \dot{V}_{By,\text{RC}} - \dot{V}_{By,d}}{V_{Bx} + \cos(\phi) \tan(\theta) V_{Bz}}. \quad (5.197)$$

**Airspeed Control** The *Airspeed Control* block tracks the desired airspeed demand  $V_{CAS,d}$  provided by the forward command channel of the *Outer-Loop Command Bus (OL CMD Bus)*. Thereby, the function is active during the *Transition* and *Wingborne* mode, i.e. during the *Highspeed* phase of the flight.

The overall control concept is adapted from subsection 4.3.2.4 and recalled here for completeness. Additional modifications are applied, in order to improve the airspeed tracking in the presence of (kinematic) sideslip angles  $\beta_{kin}$ . To this end, the airspeed derivative from (4.90) is extended by the terms containing the sideslip angle  $\beta$

$$\begin{aligned} \dot{V}_{CAS} = & (\sin(\alpha) \cos(\beta) \cos(\phi) \cos(\theta) + \sin(\beta) \sin(\phi) \cos(\theta) - \cos(\alpha) \cos(\beta) \sin(\theta)) g \\ & + \cos(\alpha) \cos(\beta) f_{Bx} + \sin(\beta) f_{By} + \sin(\alpha) \cos(\beta) f_{Bz} \end{aligned} \quad (5.198)$$

for which the rotation matrices  $\mathbf{M}_{CB}$  from (4.43) and  $\mathbf{M}_{KB}$  from (4.92) are used to yield the portions of forward specific force and gravity in the direction of flight. Again, the influence of changing wind direction and magnitude is neglected for simplicity.

Furthermore, the acceleration command is given by

$$\dot{V}_{CAS,c} = \min(\dot{V}_{CAS,OP,max}, \max(\dot{V}_{CAS,OP,min}, K_{V_{CAS}} (V_{CAS,d} - V_{CAS}))), \quad (5.199)$$

where  $K_{V_{CAS}}^{-1}$  denotes the time constant of the airspeed control loop and  $\dot{V}_{CAS,OP,max}$  and  $\dot{V}_{CAS,OP,min}$  are the maximum and minimum operational acceleration limits respectively.

The required forward specific force is finally obtained by inverting (5.198) and applying (5.199):

$$\begin{aligned} f_{Bx,c} = & \frac{\dot{V}_{CAS,c}}{\cos(\alpha_{kin}) \cos(\beta_{kin})} - \frac{\tan(\beta_{kin})}{\cos(\alpha_{kin})} f_{By} - \tan(\alpha_{kin}) f_{Bz} \\ & - \underbrace{\left( \tan(\alpha_{kin}) \cos(\phi) \cos(\theta) + \frac{\tan(\beta_{kin})}{\cos(\alpha_{kin})} \sin(\phi) \cos(\theta) - \sin(\theta) \right)}_{\text{Gravity Compensation}} g, \end{aligned} \quad (5.200)$$

with  $\dot{V}_{CAS,c}$  from (5.199). Note that instead of the aerodynamic angle of attack  $\alpha$  and sideslip  $\beta$  the kinematic angles are used. This is because of the assumed absence of angle of sideslip measurements as well as the adverse effects of the powered lift system on aerodynamic flow angles, which was discussed in the course of the *Pitch and AoA Control* function.

**Highspeed Attitude Protection** The *Highspeed Attitude Protection* block limits the admissible attitude of the VTOL aircraft during the *Transition* and *Wingborne* mode (i.e. during *Highspeed* mode) and converts the pitch and yaw rate signals  $q_d$  from (5.186) and  $r_d$  from (5.197) into the corresponding pitch angle and heading rate commands  $\dot{\theta}_c$  and  $\dot{\psi}_c$  respectively. Furthermore, the desired roll angle rate  $\dot{\phi}_d$ , pitch angle rate  $\dot{\theta}_d$ , and heading rate  $\dot{\psi}_d$  are dynamically saturated. The functional structure of the *Highspeed Attitude Protection* block is illustrated in figure 5.42.

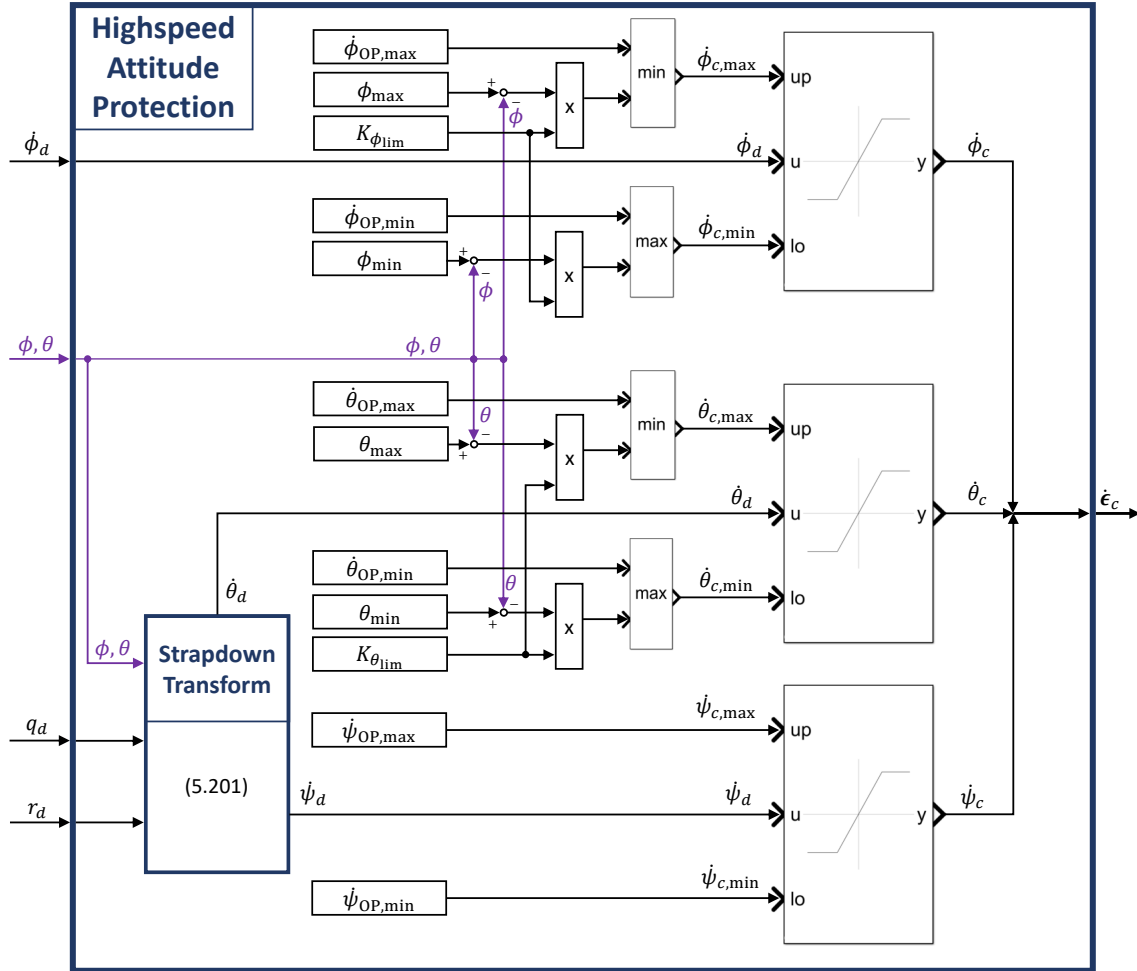


Figure 5.42: Highspeed Attitude Protection block

As was illustrated in subsection 4.3.2.2, the pitch rate demand  $q_d$  and yaw rate demand  $r_d$  are converted using the strapdown differential equation

$$\begin{bmatrix} \dot{\theta}_d \\ \dot{\psi}_d \end{bmatrix} = \begin{bmatrix} \cos(\phi) & -\sin(\phi) \\ \frac{\sin(\phi)}{\cos(\theta)} & \frac{\cos(\phi)}{\cos(\theta)} \end{bmatrix} \begin{bmatrix} q_d \\ r_d \end{bmatrix}. \quad (5.201)$$

Hence, the *Strapdown Transform* block outputs the desired pitch angle rate  $\dot{\theta}_d$  and heading rate  $\dot{\psi}_d$ .

Similarly to the *Hover Attitude Protection* function, the roll angle rate, pitch angle rate, and heading rate are limited by their respective maximum and minimum admissible values

$$\dot{\phi}_{c,max} = \min(\dot{\phi}_{OP,max}, \dot{\phi}_{\phi_{lim},max}) \quad \dot{\theta}_{c,max} = \min(\dot{\theta}_{OP,max}, \dot{\theta}_{\theta_{lim},max}) \quad \dot{\psi}_{c,max} = \dot{\psi}_{OP,max} \quad (5.202)$$

and

$$\dot{\phi}_{c,min} = \max(\dot{\phi}_{OP,min}, \dot{\phi}_{\phi_{lim},min}) \quad \dot{\theta}_{c,min} = \max(\dot{\theta}_{OP,min}, \dot{\theta}_{\theta_{lim},min}) \quad \dot{\psi}_{c,min} = \dot{\psi}_{OP,min}, \quad (5.203)$$



where  $\dot{\phi}_{OP,max}$ ,  $\dot{\theta}_{OP,max}$ , and  $\dot{\psi}_{OP,max}$  denote the operational maximum roll, pitch, and heading angle rates and  $\dot{\phi}_{OP,min}$ ,  $\dot{\theta}_{OP,min}$ , and  $\dot{\psi}_{OP,min}$  denote the operational minimum roll, pitch, and heading angle rates respectively.

Furthermore, the pitch and roll angle rates that lead to the limit attitudes are denoted as

$$\dot{\theta}_{lim,max} = K_{\theta_{lim}} (\theta_{max} - \theta) \quad \dot{\phi}_{lim,max} = K_{\phi_{lim}} (\phi_{max} - \phi) \quad (5.204)$$

and

$$\dot{\theta}_{lim,min} = K_{\theta_{lim}} (\theta_{min} - \theta) \quad \dot{\phi}_{lim,min} = K_{\phi_{lim}} (\phi_{min} - \phi) , \quad (5.205)$$

where  $K_{\theta_{lim}}$  and  $K_{\phi_{lim}}$  denote the convergence rates towards the maximum pitch angle  $\theta_{max}$  and roll angle  $\phi_{max}$  as well as the minimum pitch angle  $\theta_{min}$  and roll angle  $\phi_{min}$  respectively.

The commanded roll, pitch, and heading angle rates are then summarized and output as attitude rate command  $\dot{\epsilon}_c$  from the *Hover Attitude Protection* block. Note that by converting the desired body-fixed rotational rates into euler angle rate commands, an unified interface to the inner loop is facilitated, which increases the modularity of the overall control architecture.

**Powered Lift Control** The *Powered Lift Control* block manages the activation and deactivation of the powered lift system during the fixed-wing flight phase. Its functional structure is illustrated in figure 5.43.

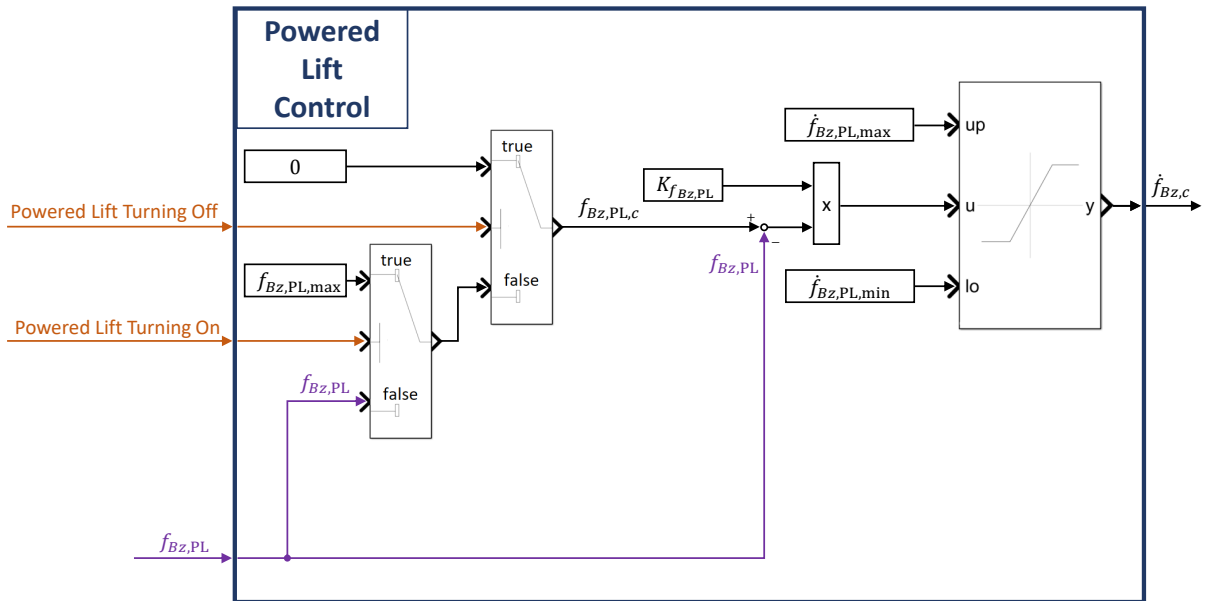


Figure 5.43: *Powered Lift Control Block*

The *Powered Lift Control* block is active during the *Wingborne* mode and implements the following functions:

- During *Powered Lift Turning Off* mode, the *Powered Lift Control* block yields the command to the inner loop that shuts down the powered lift motors by controlling the estimated powered lift value to 0.
- During *Powered Lift Turning On* mode, the *Powered Lift Control* block yields the command to the inner loop that turns on the powered lift motors and adjusts the RPMs such that the resulting estimated powered lift corresponds to the idle powered lift value  $f_{Bz,PL,max}$ .
- In any other case, the *Powered Lift Control* block yields a zero powered lift rate command, which keeps the lifting motors at the current RPM.

To this end, the body-vertical specific force rate command  $\dot{f}_{Bz,c}$  is determined as follows:

$$\dot{f}_{Bz,c} = \min(\dot{f}_{Bz,PL,max}, \max(\dot{f}_{Bz,PL,min}, K_{f_{Bz,PL}} (f_{Bz,PL,c} - f_{Bz,PL}))), \quad (5.206)$$

where  $\dot{f}_{Bz,PL,max}$  and  $\dot{f}_{Bz,PL,min}$  denote the maximum and minimum specific powered lift rate limits and  $K_{f_{Bz,PL}}^{-1}$  denotes the time constant for the convergence of the estimated specific powered lift  $f_{Bz,PL}$  towards the command  $f_{Bz,PL,c}$ .

Furthermore, the specific powered lift command  $f_{Bz,PL,c}$  is chosen according to

$$f_{Bz,PL,c} = \begin{cases} 0, & \text{for } \textit{Powered Lift Turning Off} == \textit{true} \\ f_{Bz,PL,max}, & \text{for } \textit{Powered Lift Turning On} == \textit{true} \\ f_{Bz,PL}, & \text{else} \end{cases} . \quad (5.207)$$

Note that when both *Powered Lift Turning Off* and *Powered Lift Turning On* are *false* (i.e. the third case), (5.206) yields a zero specific powered lift rate command and hence the lifting motors remain at the current RPM value. The case that both modes *Powered Lift Turning Off* and *Powered Lift Turning On* are *true* is excluded by design.

### 5.3.5 Inner Loop

The *Inner Loop* block represents the inner control loop, which yields the final commands to all available control effectors and motors such that the tracking demands from the *Outer Loop* are met. Thereby, it represents the final functional stage of the control architecture and exhibits explicit dependency on the specific topology of available force and moments producers on the lower specification level (especially for the *Control Allocation*). However, the presented high-level architecture of the inner loop is compatible with different types of configurations. Figure 5.44 below shows a schematic overview of the inner loop in terms of a functional block diagram.

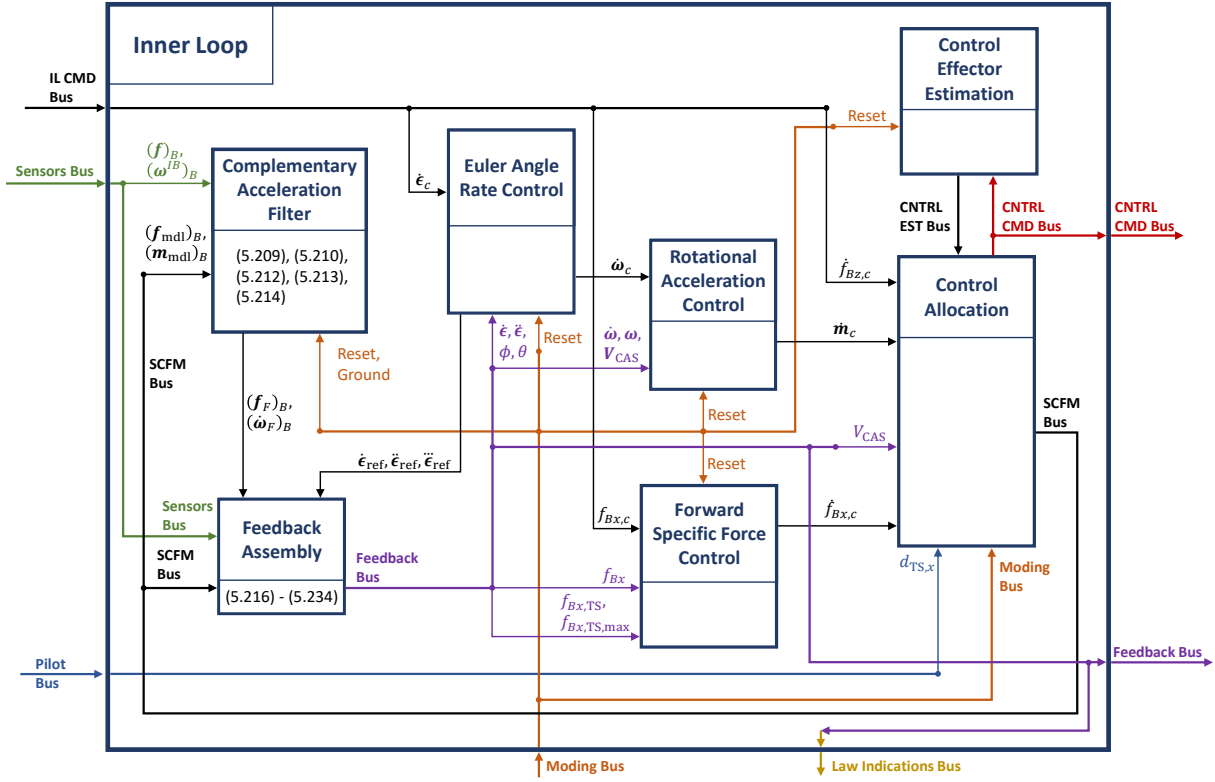


Figure 5.44: Inner Loop Block

The *Inner Loop* consists of the following functional blocks that are presented in the following sections:

- The *Complementary Acceleration Filter* provides a filtered estimation of the rotational acceleration  $(\dot{\omega}_F^{IB})_B^B$  and specific force  $(\mathbf{f}_F)_B$  denoted in body-fixed coordinates by fusing the information from the *Sensors Bus* and the *Specific Control Forces and Moments Bus (SCFM Bus)*.
- The *Feedback Assembly* block outputs the *Feedback Bus*, which contains the necessary feedback signals that are used in the various functional subsystems of the controller. It thereby assembles and transforms signals from different sources and provides additional signals based on kinematic calculations.
- The *Euler Angle Rate Control* block contains the control law for tracking the euler angle rate command  $\dot{\epsilon}_c$  and outputs the therefor required rotational acceleration command  $(\dot{\omega}_c^{IB})_B^B$  (which is denoted as  $\dot{\omega}_c$  from here on for better readability).
- The *Rotational Acceleration Control* yields the commanded specific moment rate  $(\dot{\mathbf{m}}_c)_B^B$  in the body frame (which was first introduced in subsection 4.3.4 and is from here on denoted as  $\dot{\mathbf{m}}_c$  for better readability). Latter is aimed at tracking the rotational acceleration command  $\dot{\omega}_c$  and is fed into the *Control Allocation* block.

- The *Forward Specific Force* block provides the required specific force rate command in body-forward direction  $\dot{f}_{Bx,c}$  to the *Control Allocation*. Thereby, it is aimed at tracking the commanded forward specific force  $f_{Bx,c}$  from the *Inner-Loop Command Bus (IL CMD Bus)*.
- The *Control Effector Estimation* block yields the *Control Effector Estimation Bus (CNTRL EST Bus)*, which contains estimations about the deflections and rotational rates of the available control surfaces and motors respectively based on the *Control Effector Command Bus (CNTRL CMD Bus)*.
- The *Control Allocation* block outputs the *Control Effector Command Bus (CNTRL CMD Bus)*, which contains the required deflection and rotational rate commands to the available aerodynamic control surfaces, traction motors, and lifting motors such as to yield the required specific force and moment rates in the context of the incremental control strategy. It furthermore provides the *Specific Control Forces and Moments Bus (SCFM Bus)*, which contains information about the model-based estimation of specific forces and moments that are generated by the control effectors as well as the (remaining margin to the) maximum achievable specific forces, which are e.g. used in the context of the envelope protections discussed in subsection 5.3.3.4 and subsection 5.3.3.5.

#### 5.3.5.1 Complementary Acceleration Filter

The complementary filter is a data fusion algorithm that uses information from different sources in order to obtain a filtered estimate of a particular signal of interest. It is a well-studied approach and due to its simplicity widely adopted in the aerospace industry, e.g. for attitude estimation [124] [125] [126]. In contrast to the well-known Kalman filter [127], which is derived from a probabilistic and statistical background, the complementary filter is motivated by frequency domain analysis. The interested reader may refer to an exhaustive comparison between the complementary filter and the Kalman filter in [128].

The presented incremental control approach ultimately relies on the use of acceleration feedback in the form of rotational accelerations and specific forces. As was already mentioned in section 5.1, the high-bandwidth nature of INDI control renders the control strategy highly sensitive to sensor delays. Therefore, prediction or filtering of accelerations is a useful means of providing high-bandwidth feedback information to the controller [43] [129].

To this end, the objective of the filter is to yield estimates of the specific force  $(\mathbf{f}_F)_B$  and rotational acceleration  $(\dot{\boldsymbol{\omega}}_F^{IB})_B^B$  denoted in body-fixed coordinates, which are denoted as  $\mathbf{f}_F$  and  $\dot{\boldsymbol{\omega}}_F$  for better readability. Thereby, the filter process shall reject noise and vibrations while not introducing excessive delay into the measurements, which yields conflicting requirements.

In general, the presented strategy makes use of available measurements and model-based estimations of the specific forces and moments resulting from the control effectors. Due to the different nature of available measurements, the filter algorithms for the specific forces and rotational accelerations are derived separately and presented in the following.

**Specific Force Complementary Filtering** In order to obtain a filtered estimate of the specific force  $\mathbf{f}_F$ , the information from two sources are fused:

- the measurement of the specific force  $\mathbf{f}_{\text{msr}}$ , which is provided by the inertial measurement unit (IMU), and
- the model-based estimation  $\mathbf{f}_{\text{mdl}}$ , which is provided by the *Control Allocation* block.

The general idea of the filtering process is to write the filtered signal  $y_F$  in the frequency domain as

$$y_F = \frac{K_F}{s + K_F} y_{\text{LF}} + \frac{s}{s + K_F} y_{\text{HF}}, \quad (5.208)$$

where (5.208) denotes the so-called Laplace transform [130] with the complex variable  $s$ . Thereby, the subscripts  $\text{LF}$  and  $\text{HF}$  shall indicate that from the respective signal either the low-frequency or high-frequency portion is passed through, which is governed by the first-order transfer characteristics with the bandwidth  $K_F$ .

Furthermore, rewriting (5.208) in pure-integrator form yields

$$y_F = y_{\text{HF}} + \frac{1}{s} K_F (y_{\text{LF}} - y_F), \quad (5.209)$$

which is illustrated as a block diagram in figure 5.45 and referred to as *First Order Complementary Filter Type I*.

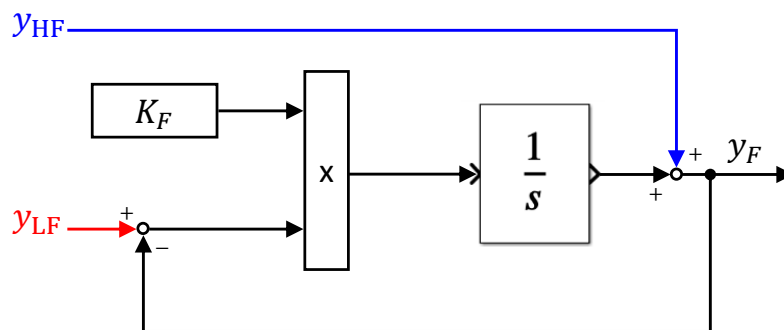


**Figure 5.45:** *First Order Complementary Filter Type I*

The  $\frac{1}{s}$ -block in figure 5.45 indicates a pure integration and facilitates the representation of differential equations in a compact way. Note that for a specific implementation of this function, chapter 6 discusses the underlying numerical methods. However, in the context of merely providing a functional specification, the notation in (5.209) and figure 5.45 are sufficient.

In order to apply the presented filter to the problem of filtering specific forces, the following relations are introduced:

$$y_F = \mathbf{f}_F \quad y_{LF} = \mathbf{f}_{\text{msr}} \quad y_{\text{HF}} = \mathbf{f}_{\text{mdl}}. \quad (5.210)$$

Hence, the filter combines the low-frequency information of the inertial measurements with the high-frequency information of the model-based estimation, thereby suppressing measurement noise and vibrations while not introducing inadvertent delays through the filtering process.

**Rotational Acceleration Complementary Filtering** The filtering process for the rotational acceleration  $\dot{\boldsymbol{\omega}}_F$  follows in a similar way as for the specific forces. To this end, the information from the following sources are fused:

- the measurement of the rotational rate  $\boldsymbol{\omega}_{\text{msr}}$ , which is provided by the inertial measurement unit (IMU), and
- the model-based estimation  $\dot{\boldsymbol{\omega}}_{\text{mdl}}$ , which is obtained by considering the estimated specific control moments from the *Control Allocation* block.

In contrast to the specific forces, the rotational accelerations  $\dot{\boldsymbol{\omega}}$  are not measured directly, but instead the rotational rates  $\boldsymbol{\omega}$  are measured. This assumption was made in the beginning of section 5.3, since sensors that directly measure the rotational acceleration are less common than conventional inertial measurement units (IMU), which measure rotational rates and specific forces. In case of direct rotational acceleration measurements, the same filtering approach can be used as for the specific forces.

However, due to using rotational rates as the measurement, the Laplace transform for the filtered signal  $y_F$  is chosen as

$$y_F = \frac{K_F}{s + K_F} s y_{\text{LF},f} + \frac{s}{s + K_F} y_{\text{HF}}, \quad (5.211)$$

where  $s$  is the complex Laplace variable and  $y_{\text{LF},f} = \frac{1}{s} y_{\text{LF}}$  denotes the integrated low-frequency signal. Furthermore,  $K_F$  denotes the bandwidth of the first-order filter.

Analogously to (5.209), the relationship in (5.211) can be expressed in pure-integrator form and yields

$$y_F = y_{\text{HF}} + K_F \left( y_{\text{LF},f} - \frac{1}{s} y_F \right), \quad (5.212)$$

which is illustrated as a block diagram in figure 5.46 and referred to as *First Order Complementary Filter Type II*.

Note that in contrast to the *First Order Complementary Filter Type I*, the low-frequency portion (red signal in figure 5.45 and figure 5.46) has a direct feed-through into the filtered output for the *First Order Complementary Filter Type II*. This is due to the differentiating behavior of the second filter type with respect to the low-frequency signal, which results from estimating a signal  $y_F$  that represents the derivative of the

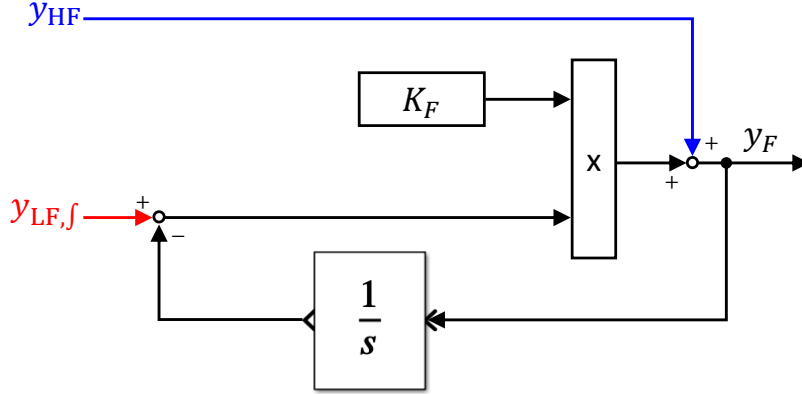


**Figure 5.46:** *First Order Complementary Filter Type II*

signal  $y_{LF,f}$ . However, in case of insufficient noise and vibration attenuation, the filter for the rotational accelerations can also be chosen to be of second order without loss of generality.

Furthermore, the following relations are introduced in order to apply the presented filter to the problem of filtering rotational accelerations:

$$y_F = \dot{\omega}_F \quad y_{LF,f} = \omega_{msr} \quad y_{HF} = \dot{\omega}_{mdl} . \quad (5.213)$$

Thereby, the model-based estimation for the rotational acceleration  $\dot{\omega}_{mdl}$  is obtained by using (4.123), i.e.

$$\dot{\omega}_{mdl} = \mathbf{m}_{mdl} - \mathbf{I}^{-1} (\omega_{msr} \times \mathbf{I} \omega_{msr}) , \quad (5.214)$$

where

$$\mathbf{m}_{mdl} = \mathbf{I}^{-1} \mathbf{M}_{mdl} \quad (5.215)$$

denotes the specific control moments around the center of gravity, which are estimated in the *Control Allocation* block by means of the control effector induced moments around the center of gravity  $\mathbf{M}_{mdl}$ . Furthermore,  $\mathbf{I}$  denotes the moment of inertia around the center of gravity. Indices and superscripts are dropped for better readability, however, for a comprehensive formulation of the equations refer to e.g. subsection 4.3.4.

In order to avoid the wind-up phenomena on ground inherent in incremental control, the *Ground* flag from the *Moding Bus* (see subsection 5.3.2.2) is used to switch the filtered estimations of the specific force  $\mathbf{f}_F$  and rotational acceleration  $\dot{\omega}_F$  with the pure model-based estimations  $\mathbf{f}_{mdl}$  and  $\dot{\omega}_{mdl}$  respectively.

In doing so, the control loops that are actively controlling system accelerations by providing pseudo control outputs on the level of specific force and moment rates will not wind-up the commands against e.g. reaction forces on ground. Instead, the demand to the control effectors will converge such that the model-based accelerations are tracked, thereby rendering the innermost control law open-loop.

### 5.3.5.2 Feedback Assembly

The *Feedback Assembly* block is aimed at assembling and transforming signals from different sources and generating additional signals based on kinematic calculations. In the following, all feedback signals that are used within the controller subsystems are derived and summarized based on the following incoming signals of the *Feedback Assembly* block:

- The *Sensors Bus* consisting of
  - the measured specific forces  $(\mathbf{f}_{\text{msr}})_B = [f_{Bx,\text{msr}} \ f_{By,\text{msr}} \ f_{Bz,\text{msr}}]^T$  in body-fixed coordinates,
  - the measured rotational rates  $(\boldsymbol{\omega}_{\text{msr}})_B = [p_{\text{msr}} \ q_{\text{msr}} \ r_{\text{msr}}]^T$  in body-fixed coordinates,
  - the euler angles  $\boldsymbol{\epsilon} = [\phi \ \theta \ \psi]^T$ ,
  - the kinematic GPS-based velocity  $(\mathbf{V})_O = [V_{Ox} \ V_{Oy} \ V_{Oz}]^T$  in north-east-down coordinates,
  - the calibrated airspeed  $V_{\text{CAS}}$ , and
  - the aerodynamic angle of attack  $\alpha_{\text{aer}}$ .
- The *Specific Control Forces and Moments Bus* consisting of
  - the estimated specific control forces  $(\mathbf{f}_{\text{mdl}})_B = [f_{Bx,\text{mdl}} \ f_{By,\text{mdl}} \ f_{Bz,\text{mdl}}]^T$  in body-fixed coordinates,
  - the estimated specific traction force  $f_{Bx,\text{TS}}$  and maximum admissible specific traction force  $f_{Bx,\text{TS,max}}$  in body-forward direction,
  - the estimated specific powered lift force  $f_{Bz,\text{PL}}$  and minimum admissible specific powered lift force  $f_{Bz,\text{PL,min}}$  in body-down direction, and
  - the estimated specific control moments around the center of gravity  $(\mathbf{m}_{\text{mdl}})_B = [m_{Bx,\text{mdl}} \ m_{By,\text{mdl}} \ m_{Bz,\text{mdl}}]^T$  in body-fixed coordinates.
- The complementary filtered specific forces  $(\mathbf{f}_F)_B$  and rotational accelerations  $(\dot{\boldsymbol{\omega}}_F)_B$  from the *Complementary Acceleration Filter* block denoted in the body frame  $B$ .
- The reference attitude rate signals  $\dot{\boldsymbol{\epsilon}}_{\text{ref}} = [\dot{\phi}_{\text{ref}} \ \dot{\theta}_{\text{ref}} \ \dot{\psi}_{\text{ref}}]^T$ , reference attitude acceleration signals  $\ddot{\boldsymbol{\epsilon}}_{\text{ref}} = [\ddot{\phi}_{\text{ref}} \ \ddot{\theta}_{\text{ref}} \ \ddot{\psi}_{\text{ref}}]^T$ , and reference attitude jerk signals  $\dddot{\boldsymbol{\epsilon}}_{\text{ref}} = [\dddot{\phi}_{\text{ref}} \ \dddot{\theta}_{\text{ref}} \ \dddot{\psi}_{\text{ref}}]^T$ .

Additionally to assembling all incoming buses and signals into the *Feedback Bus*, the following coordinate transformations and kinematic calculations are performed:



## Euler Angle Rates and Accelerations

- The euler angle rates  $\dot{\epsilon}$  follow from the strapdown equation

$$\dot{\epsilon} = \begin{bmatrix} \dot{\phi} \\ \dot{\theta} \\ \dot{\psi} \end{bmatrix} = \mathbf{S}(\boldsymbol{\omega}_{\text{msr}})_B, \quad (5.216)$$

with the strapdown matrix

$$\mathbf{S} = \begin{bmatrix} 1 & \sin(\phi) \tan(\theta) & \cos(\phi) \tan(\theta) \\ 0 & \cos(\phi) & -\sin(\phi) \\ 0 & \frac{\sin(\phi)}{\cos(\theta)} & \frac{\cos(\phi)}{\cos(\theta)} \end{bmatrix}. \quad (5.217)$$

- The euler angle accelerations  $\ddot{\epsilon}$  follow from the derivative of the strapdown equation

$$\ddot{\epsilon} = \begin{bmatrix} \ddot{\phi} \\ \ddot{\theta} \\ \ddot{\psi} \end{bmatrix} = \dot{\mathbf{S}}(\boldsymbol{\omega}_{\text{msr}})_B + \mathbf{S}(\dot{\boldsymbol{\omega}}_F)_B, \quad (5.218)$$

with the derivative of the strapdown matrix

$$\dot{\mathbf{S}} = \begin{bmatrix} 0 & \cos(\phi) \tan(\theta) \dot{\phi} + \frac{\sin(\phi)}{\cos(\theta)^2} \dot{\theta} & -\sin(\phi) \tan(\theta) \dot{\phi} + \frac{\cos(\phi)}{\cos(\theta)^2} \dot{\theta} \\ 0 & -\sin(\phi) \dot{\phi} & -\cos(\phi) \dot{\phi} \\ 0 & \frac{\cos(\phi) \cos(\theta) \dot{\phi} + \sin(\phi) \sin(\theta) \dot{\theta}}{\cos(\theta)^2} & \frac{-\sin(\phi) \cos(\theta) \dot{\phi} + \cos(\phi) \sin(\theta) \dot{\theta}}{\cos(\theta)^2} \end{bmatrix}. \quad (5.219)$$

- The lead-filtered heading acceleration  $\ddot{\psi}_{\text{lead},\phi}$  with respect to the roll dynamics:

$$\ddot{\psi}_{\text{lead},\phi} = K_{\dot{\phi}_{\text{ref}}}^{-1} \ddot{\psi}_{\text{ref}} + \ddot{\psi}_{\text{ref}}. \quad (5.220)$$

- The lead-filtered heading acceleration  $\ddot{\psi}_{\text{lead},\theta}$  with respect to the pitch dynamics:

$$\ddot{\psi}_{\text{lead},\theta} = K_{\dot{\theta}_{\text{ref}}}^{-1} \ddot{\psi}_{\text{ref}} + \ddot{\psi}_{\text{ref}}. \quad (5.221)$$

- The lead-filtered heading rate  $\dot{\psi}_{\text{lead},\theta}$  with respect to the pitch dynamics:

$$\dot{\psi}_{\text{lead},\theta} = K_{\dot{\theta}_{\text{ref}}}^{-1} \dot{\psi}_{\text{ref}} + \dot{\psi}_{\text{ref}}. \quad (5.222)$$

- The lead-filtered roll angle rate  $\dot{\phi}_{\text{lead},\theta}$  with respect to the pitch dynamics:

$$\dot{\phi}_{\text{lead},\theta} = K_{\dot{\theta}_{\text{ref}}}^{-1} \dot{\phi}_{\text{ref}} + \dot{\phi}_{\text{ref}}. \quad (5.223)$$

- The lead-filtered roll angle rate  $\dot{\phi}_{\text{lead},\psi}$  with respect to the heading dynamics:

$$\dot{\phi}_{\text{lead},\psi} = K_{\dot{\psi}_{\text{ref}}}^{-1} \dot{\phi}_{\text{ref}} + \dot{\phi}_{\text{ref}}. \quad (5.224)$$

### Translational Rates and Accelerations

- The overall kinematic velocity  $V_{\text{kin}}$  follows from taking the Euclidean norm of the kinematic GPS-based velocity vector  $(\mathbf{V})_O$ :

$$V_{\text{kin}} = \sqrt{V_{O_x}^2 + V_{O_y}^2 + V_{O_z}^2}. \quad (5.225)$$

- The horizontal kinematic velocity  $V_{\text{kin,hor}}$  follows from:

$$V_{\text{kin,hor}} = \sqrt{V_{O_x}^2 + V_{O_y}^2}. \quad (5.226)$$

- The height rate  $\dot{h}$  follows from:

$$\dot{h} = -V_{O_z}. \quad (5.227)$$

- The kinematic velocity  $(\mathbf{V})_C$  denoted in the control frame  $C$  (see figure 4.4) follows from coordinate transformation:

$$(\mathbf{V})_C = \begin{bmatrix} V_{C_x} \\ V_{C_y} \\ V_{C_z} \end{bmatrix}_C = \mathbf{M}_{CO}(\mathbf{V})_O, \quad (5.228)$$

where indices and superscripts are dropped for better readability and with the rotation matrix between the north-east-down frame  $O$  and the control frame  $C$

$$\mathbf{M}_{CO} = \begin{bmatrix} \cos(\psi) & \sin(\psi) & 0 \\ -\sin(\psi) & \cos(\psi) & 0 \\ 0 & 0 & 1 \end{bmatrix}. \quad (5.229)$$

- The kinematic velocity  $(\mathbf{V})_B$  denoted in the body frame  $B$  (see figure 4.4) follows from coordinate transformation:

$$(\mathbf{V})_B = \begin{bmatrix} V_{B_x} \\ V_{B_y} \\ V_{B_z} \end{bmatrix}_B = \mathbf{M}_{BC}(\mathbf{V})_C, \quad (5.230)$$

where indices and superscripts are dropped for better readability and with the rotation matrix between the control frame  $C$  and the body frame  $B$

$$\mathbf{M}_{BC} = \begin{bmatrix} \cos(\theta) & 0 & -\sin(\theta) \\ \sin(\phi) \sin(\theta) & \cos(\phi) & \sin(\phi) \cos(\theta) \\ \cos(\phi) \sin(\theta) & -\sin(\phi) & \cos(\phi) \cos(\theta) \end{bmatrix}. \quad (5.231)$$

- The acceleration  $(\dot{\mathbf{V}})_C^C$  with respect to the control frame  $C$  denoted in the control frame  $C$ , which follows from (4.40):

$$(\dot{\mathbf{V}})_C^C = \begin{bmatrix} \dot{V}_{C_x} \\ \dot{V}_{C_y} \\ \dot{V}_{C_z} \end{bmatrix}_C = \mathbf{M}_{BC}^T(\mathbf{f}_F)_B + \begin{bmatrix} 0 \\ 0 \\ g \end{bmatrix}_C - \begin{bmatrix} 0 \\ 0 \\ \dot{\psi} \end{bmatrix}_C \times (\mathbf{V})_C. \quad (5.232)$$

### Kinematic Flow Angles

- The kinematic angle of attack  $\alpha_{\text{kin}}$ :

$$\alpha_{\text{kin}} = \tan^{-1} \left( \frac{V_{Bz}}{V_{Bx}} \right). \quad (5.233)$$

- The kinematic angle of sideslip  $\beta_{\text{kin}}$ :

$$\beta_{\text{kin}} = \tan^{-1} \left( \frac{V_{By}}{\sqrt{V_{Bx}^2 + V_{Bz}^2}} \right). \quad (5.234)$$

The presented signals are added into the *Feedback Bus*, which is used in the respective controller subsystems. The centralized structure, which is obtained by assembling all signals in one block and distributing them via a single (virtual) bus, helps minimizing the number of interfaces between the controller subsystems. Due to the linear and serial structure of the *Feedback Assembly* block, the centralization of its functionality is not in direct conflict with the *decentralization* principle for good system architectures [3].

However, as will be discussed in chapter 6, the need for testability of individual controller blocks and consecutive development through piecemeal engineering might require posing additional requirements on the allocation of functions and interfaces for the final implementation. Nevertheless, in the scope of defining the functional specification of the controller, implementation-related aspects can be neglected as long as the overall architecture is in principle realizable.

#### 5.3.5.3 Euler Angle Rate Control

The *Euler Angle Rate Control* block takes the commanded euler angle rates  $\dot{\epsilon}_c$  as an input and provides the necessary rotational acceleration vector  $\dot{\omega}_c$  as an output. It thereby makes use of the feedforward/feedback control strategy that is used within most of the outer loop control blocks. Figure 5.47 shows a functional block diagram of the *Euler Angle Rate Control* block.

Due to the identical structure of each channel's reference model, the underlying dynamics are explained using index notation. Thereby, the symbols  $\epsilon_i$ ,  $\dot{\epsilon}_i$ , etc. shall denote the roll, pitch, or heading channel respectively.

To this end, the reference euler angle jerk dynamics follow analogously to the outer-loop reference models and are given by

$$\ddot{\epsilon}_{\text{ref},i} = \min \left( \ddot{\epsilon}_{\text{ref,max},i}, \max \left( \ddot{\epsilon}_{\text{ref,min},i}, K_{\dot{\epsilon}_{\text{ref},i}} (\ddot{\epsilon}_{\text{ref},c,i} - \ddot{\epsilon}_{\text{ref},i}) \right) \right), \quad (5.235)$$

with the reference euler angle acceleration command

$$\ddot{\epsilon}_{\text{ref},c,i} = K_{\dot{\epsilon}_{\text{ref},i}} (\dot{\epsilon}_{\text{ref},c,i} - \dot{\epsilon}_{\text{ref},i}), \quad (5.236)$$

where the reference euler angle rate command  $\dot{\epsilon}_{\text{ref},c,i}$  is chosen as  $\dot{\epsilon}_{\text{ref},c,i} = \dot{\epsilon}_{c,i}$ , i.e. as  $\dot{\phi}_c$ ,  $\dot{\theta}_c$ , or  $\dot{\psi}_c$  and  $K_{\ddot{\epsilon}_{\text{ref},i}}$  and  $K_{\dot{\epsilon}_{\text{ref},i}}$  denote the reference angular acceleration and angular rate bandwidth respectively.

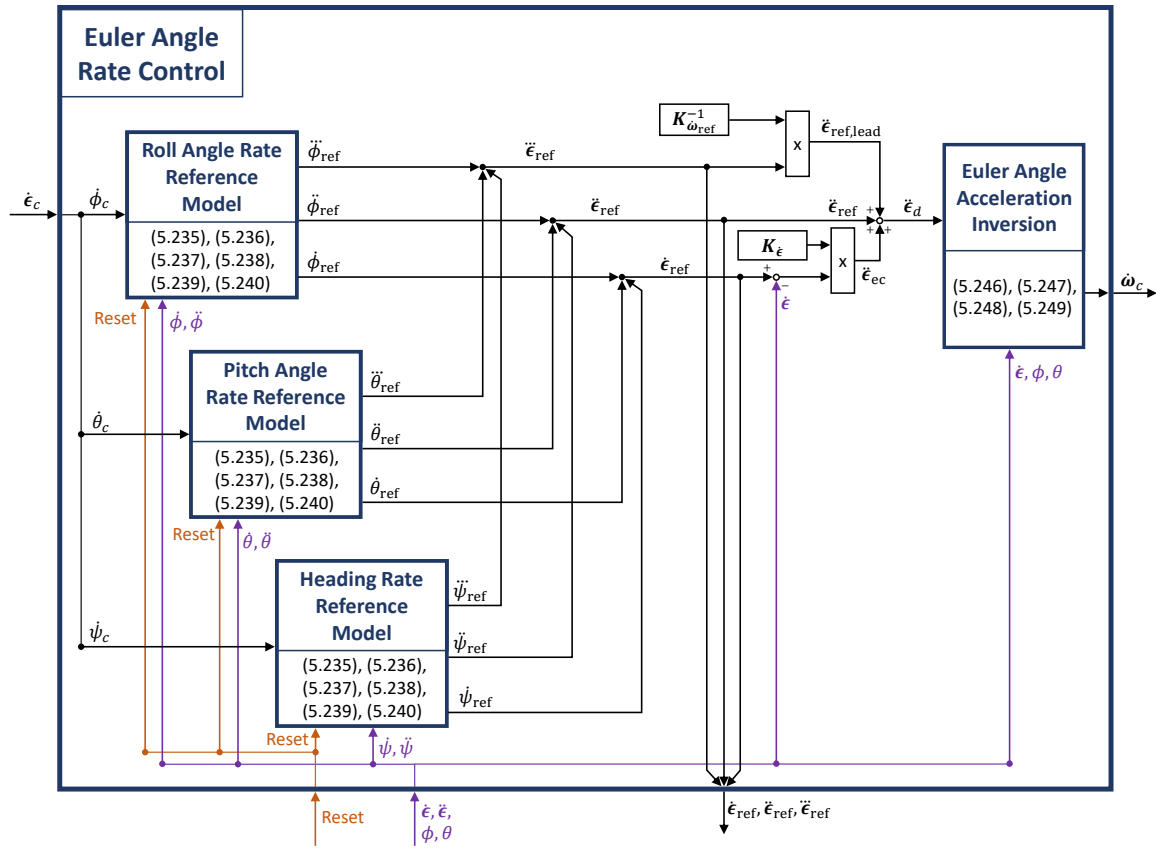


Figure 5.47: Euler Angle Rate Control Block

Furthermore, the maximum and minimum euler angle jerk limits are chosen as

$$\begin{aligned}\ddot{\epsilon}_{\text{ref,max},i} &= \min \left( \ddot{\epsilon}_{\text{ref,OP,max},i}, \ddot{\epsilon}_{\dot{\epsilon}_{\text{lim,max},i}} \right), \\ \ddot{\epsilon}_{\text{ref,min},i} &= \max \left( \ddot{\epsilon}_{\text{ref,OP,min},i}, \ddot{\epsilon}_{\dot{\epsilon}_{\text{lim,min},i}} \right),\end{aligned}\quad (5.237)$$

with the angular jerks leading to the limit reference angular accelerations

$$\begin{aligned}\ddot{\epsilon}_{\dot{\epsilon}_{\text{lim,max},i}} &= K_{\dot{\epsilon}_{\text{lim},i}} \left( \ddot{\epsilon}_{\text{ref,max},i} - \ddot{\epsilon}_{\text{ref},i} \right), \\ \ddot{\epsilon}_{\dot{\epsilon}_{\text{lim,min},i}} &= K_{\dot{\epsilon}_{\text{lim},i}} \left( \ddot{\epsilon}_{\text{ref,min},i} - \ddot{\epsilon}_{\text{ref},i} \right),\end{aligned}\quad (5.238)$$

the limit reference angular accelerations given by

$$\begin{aligned}\ddot{\epsilon}_{\text{ref,max},i} &= \min \left( \ddot{\epsilon}_{\text{ref,OP,max},i}, \ddot{\epsilon}_{\dot{\epsilon}_{\text{lim,max},i}} \right), \\ \ddot{\epsilon}_{\text{ref,min},i} &= \max \left( \ddot{\epsilon}_{\text{ref,OP,min},i}, \ddot{\epsilon}_{\dot{\epsilon}_{\text{lim,min},i}} \right),\end{aligned}\quad (5.239)$$

and the angular accelerations leading to the limit angular rates

$$\begin{aligned}\dot{\epsilon}_{\dot{\epsilon}_{\text{lim,max},i}} &= K_{\dot{\epsilon}_{\text{lim},i}} \left( \dot{\epsilon}_{\text{ref,OP,max},i} - \dot{\epsilon}_{\text{ref},i} \right), \\ \dot{\epsilon}_{\dot{\epsilon}_{\text{lim,min},i}} &= K_{\dot{\epsilon}_{\text{lim},i}} \left( \dot{\epsilon}_{\text{ref,OP,min},i} - \dot{\epsilon}_{\text{ref},i} \right).\end{aligned}\quad (5.240)$$

Note that the angular jerk and acceleration limits are directly influenced by the system's ability to produce moment rates and moments respectively. Furthermore, the choice of respective saturation limits and gains follows by applying the concepts introduced in section 5.2. Additionally, operational limits can be imposed in order to enforce safety or handling quality requirements.

The reference signals for the angular accelerations and angular rates follow from successive integration of the angular jerk signals. Furthermore, the generated euler angle jerks, euler angle accelerations, and euler angle rates are output separately from the *Euler Angle Rate Control* block and forwarded to the *Feedback Assembly* block from which they are distributed to the outer-loop subsystems as the lead-filtered signals derived in (5.220), (5.221), (5.222), (5.223), and (5.224).

Additionally, the reference signals are used in order to yield the overall desired euler angle acceleration vector  $\ddot{\epsilon}_d = [\ddot{\phi}_d \ \ddot{\theta}_d \ \ddot{\psi}_d]^T$ . To this end, it is assumed that the angular acceleration  $\ddot{\epsilon}$  of the aircraft builds up according to the rotational acceleration dynamics governed by the *Rotational Acceleration Control* block:

$$\ddot{\epsilon} = \mathbf{K}_{\dot{\omega}_{\text{ref}}} (\ddot{\epsilon}_d - \ddot{\epsilon}) , \quad (5.241)$$

where  $\mathbf{K}_{\dot{\omega}_{\text{ref}}}$  denotes the reference bandwidth matrix of the rotational acceleration dynamics, which will be discussed in the context of the *Rotational Acceleration Control*.

Note that the desired pseudo control for the euler rate control strategy is chosen to be the euler angle acceleration  $\ddot{\epsilon}_d$  rather than the euler angle jerk  $\ddot{\epsilon}_d$ . This is because the inversion of the euler angle jerk would require taking the derivative of (5.218) and (5.219) respectively, which leads to overly complicated terms due to the trigonometric relationships of the strapdown equation.

Instead, the inversion is performed on the level of euler angle accelerations and (5.241) is used to yield the lead characteristics for the feedforward command, which takes into account the delayed response of the rotational acceleration dynamics. To this end, the desired euler angle acceleration vector  $\ddot{\epsilon}_d$  is composed of the lead-filtered feedforward command  $\ddot{\epsilon}_{\text{ff,lead}}$  and the feedback command from the error control law  $\ddot{\epsilon}_{\text{ec}}$ :

$$\ddot{\epsilon}_d = \ddot{\epsilon}_{\text{ff,lead}} + \ddot{\epsilon}_{\text{ec}} . \quad (5.242)$$

Thereby, the lead-filtered feedforward angular acceleration command  $\ddot{\epsilon}_{\text{ff,lead}}$  follows from using the reference signals and the relationship in (5.241) and yields

$$\ddot{\epsilon}_{\text{ff,lead}} = \mathbf{K}_{\dot{\omega}_{\text{ref}}}^{-1} \ddot{\epsilon}_{\text{ref}} + \ddot{\epsilon}_{\text{ref}} . \quad (5.243)$$

Furthermore, the feedback control signal of the error controller follows from

$$\ddot{\epsilon}_{\text{ec}} = \mathbf{K}_{\dot{\epsilon}} (\dot{\epsilon}_{\text{ref}} - \dot{\epsilon}) , \quad (5.244)$$

with the desired error bandwidth diagonal matrix  $\mathbf{K}_{\dot{\epsilon}}$  and the feedback signal of the euler angle rates  $\dot{\epsilon}$ .

The resulting angular acceleration demand from (5.242) is subsequently inverted and saturated in order to yield the commanded rotational acceleration vector  $\dot{\boldsymbol{\omega}}_c$ . To this end, the inverse strapdown equation from (4.120) is recalled

$$\dot{\boldsymbol{\omega}} = \dot{\boldsymbol{S}}^{-1} \dot{\boldsymbol{\epsilon}} + \boldsymbol{S}^{-1} \ddot{\boldsymbol{\epsilon}}, \quad (5.245)$$

with the inverse strapdown matrix

$$\boldsymbol{S}^{-1} = \begin{bmatrix} 1 & 0 & -\sin(\theta) \\ 0 & \cos(\phi) & \sin(\phi) \cos(\theta) \\ 0 & -\sin(\phi) & \cos(\phi) \cos(\theta) \end{bmatrix} \quad (5.246)$$

and its derivative

$$\dot{\boldsymbol{S}}^{-1} = \begin{bmatrix} 0 & 0 & -\cos(\theta)\dot{\theta} \\ 0 & -\sin(\phi)\dot{\phi} & \cos(\phi) \cos(\theta)\dot{\phi} - \sin(\phi) \sin(\theta)\dot{\theta} \\ 0 & -\cos(\phi)\dot{\phi} & -\sin(\phi) \cos(\theta)\dot{\phi} - \cos(\phi) \sin(\theta)\dot{\theta} \end{bmatrix}. \quad (5.247)$$

Hence, the final rotational acceleration command is given by

$$\dot{\boldsymbol{\omega}}_c = \min(\dot{\boldsymbol{\omega}}_{\text{OP,max}}, \max(\dot{\boldsymbol{\omega}}_{\text{OP,min}}, \dot{\boldsymbol{\omega}}_d)), \quad (5.248)$$

with

$$\dot{\boldsymbol{\omega}}_d = \dot{\boldsymbol{S}}^{-1} \dot{\boldsymbol{\epsilon}} + \boldsymbol{S}^{-1} \ddot{\boldsymbol{\epsilon}}_d \quad (5.249)$$

and the desired angular acceleration  $\ddot{\boldsymbol{\epsilon}}_d$  from (5.242).

#### 5.3.5.4 Rotational Acceleration Control

Figure 5.48 shows the functional structure of the *Rotational Acceleration Control* block and represents the inner-most rotational control loop of the proposed INDI architecture. Using the commanded rotational acceleration vector  $\dot{\boldsymbol{\omega}}_c$  as an input, the *Rotational Acceleration Control* block yields the necessary specific moment rate vector  $\dot{\boldsymbol{m}}_c$ , which is then forwarded to the *Control Allocation* as the final rotational pseudo control in order to be allocated into the available control effectors.

The presented control strategy is thereby adopted from subsection 4.3.4 and complemented by feedforward control through the use of reference models. Additionally, the influence of aerodynamic damping moments is explicitly accounted for in the *Rotational Jerk Inversion* block.

Due to the first-order approximation of the control effector dynamics, the relative degree (i.e. the necessary differentiations until reaching the final command input [47] [44]) of the aircraft's rotational acceleration is 1. Hence, using first-order dynamics for the rotational acceleration reference models is sufficient to yield a direct feedthrough of the generated reference rotational jerks into the control effector command channels via the commanded specific moment rates.

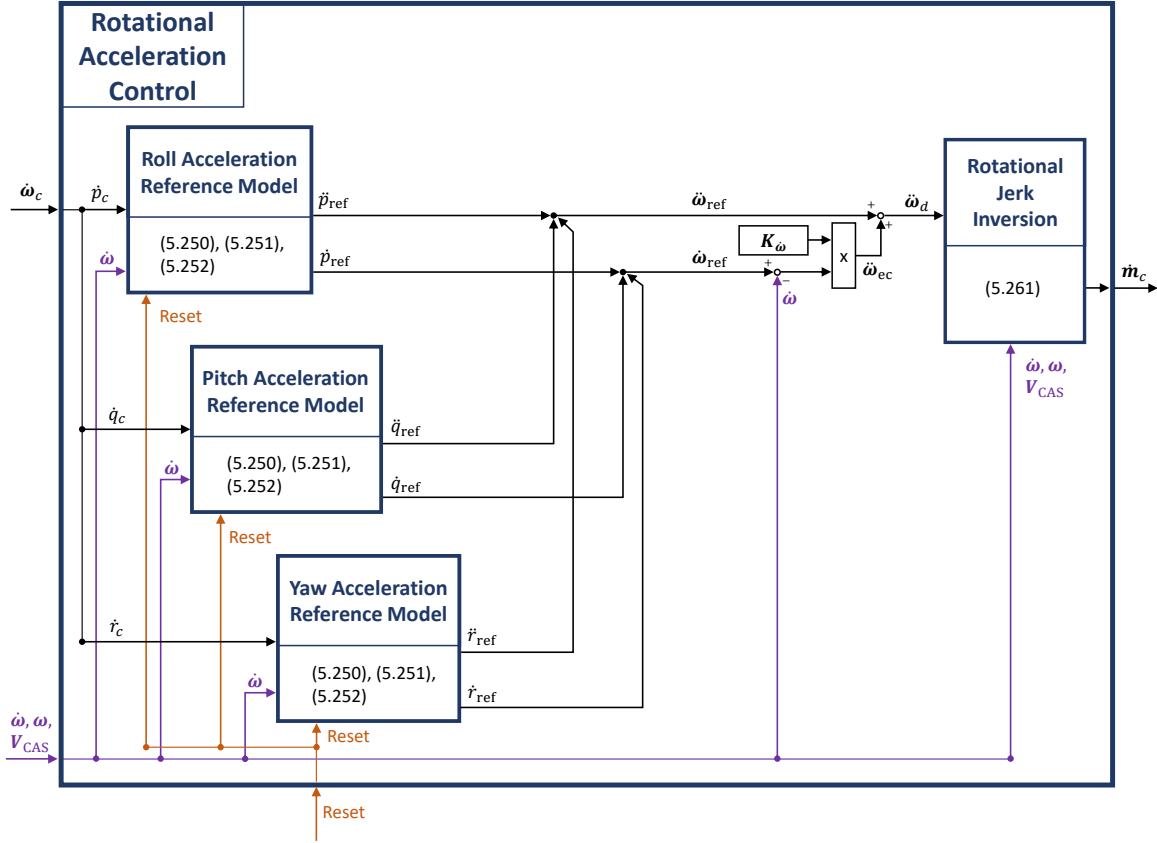


**Figure 5.48:** *Rotational Acceleration Control Block*

Analogously to the *Euler Angle Rate Control*, the underlying rotational acceleration dynamics are explained using index notation. Thereby, the symbols  $\dot{\omega}_i$  and  $\ddot{\omega}_i$  shall denote the rotational acceleration and rotational jerk of the roll, pitch, or yaw channel respectively.

The reference rotational jerk is given by

$$\ddot{\omega}_{\text{ref},i} = \min \left( \ddot{\omega}_{\text{ref,max},i}, \max \left( \ddot{\omega}_{\text{ref,min},i}, K_{\dot{\omega}_{\text{ref},i}} (\dot{\omega}_{\text{ref},c,i} - \dot{\omega}_{\text{ref},i}) \right) \right), \quad (5.250)$$

where the reference rotational acceleration command  $\dot{\omega}_{\text{ref},c,i}$  is chosen as  $\dot{\omega}_{\text{ref},c,i} = \dot{\omega}_{c,i}$ , i.e. as  $\dot{p}_c$ ,  $\dot{q}_c$ , or  $\dot{r}_c$ . Furthermore,  $K_{\dot{\omega}_{\text{ref},i}}$  denotes the reference rotational acceleration bandwidth of each channel.

The limit reference rotational jerks are given by

$$\begin{aligned} \ddot{\omega}_{\text{ref,max},i} &= \min \left( \ddot{\omega}_{\text{ref,OP,max},i}, \ddot{\omega}_{\dot{\omega}_{\text{lim,max},i}} \right), \\ \ddot{\omega}_{\text{ref,min},i} &= \max \left( \ddot{\omega}_{\text{ref,OP,min},i}, \ddot{\omega}_{\dot{\omega}_{\text{lim,min},i}} \right), \end{aligned} \quad (5.251)$$

with the rotational jerks leading to the limit rotational accelerations

$$\begin{aligned} \ddot{\omega}_{\dot{\omega}_{\text{lim,max},i}} &= K_{\dot{\omega}_{\text{lim},i}} (\dot{\omega}_{\text{ref,OP,max},i} - \dot{\omega}_{\text{ref},i}), \\ \ddot{\omega}_{\dot{\omega}_{\text{lim,min},i}} &= K_{\dot{\omega}_{\text{lim},i}} (\dot{\omega}_{\text{ref,OP,min},i} - \dot{\omega}_{\text{ref},i}). \end{aligned} \quad (5.252)$$

The maximum and minimum admissible rotational jerks are directly related to the ability of the system to change the control effector induced moments acting on it. Latter is thereby dependent on the rate at which the powered lift motors can change their rotational speed (i.e. maximum motor acceleration) and the rate at which the aerodynamic control surfaces can change their deflection angle (i.e. maximum control surface deflection rate). As was already pointed out in section 5.2, the control effector rate limitations primarily stem from existing electric current saturations and gain in significance as the size of the controlled aerial system increases. Furthermore, subsection 5.2.5 utilizes the concepts derived in subsection 5.2.2, subsection 5.2.3, and subsection 5.2.4 in order to find optimum control parameters for the roll stabilization task of a simplified 2D example with current-limited control effectors.

Using the reference rotational jerk from (5.250) and the reference rotational acceleration, which follows from integration of (5.250), the desired rotational jerk vector is given by

$$\ddot{\boldsymbol{\omega}}_d = \ddot{\boldsymbol{\omega}}_{\text{ref}} + \underbrace{\mathbf{K}_{\dot{\boldsymbol{\omega}}}}_{\ddot{\boldsymbol{\omega}}_{\text{ec}}} (\dot{\boldsymbol{\omega}}_{\text{ref}} - \dot{\boldsymbol{\omega}}), \quad (5.253)$$

where  $\dot{\boldsymbol{\omega}}$  denotes the complementary filtered rotational acceleration estimate and  $\mathbf{K}_{\dot{\boldsymbol{\omega}}}$  represents the error bandwidth matrix.

The *Rotational Jerk Inversion* block shall output the necessary specific moment rate vector  $\dot{\mathbf{m}}_e$ , which yields the desired rotational jerk from (5.253). To this end, the rotational equation of motion is recalled from (4.123):

$$\dot{\boldsymbol{\omega}} = \mathbf{I}^{-1} \mathbf{M}_{\text{tot}} - \mathbf{I}^{-1} (\boldsymbol{\omega} \times \mathbf{I} \boldsymbol{\omega}), \quad (5.254)$$

where superscripts and indices are left out for better readability. Thereby,  $\mathbf{I}$  denotes the moment of inertia with respect to the center of gravity and  $\mathbf{M}_{\text{tot}}$  represents the total moments acting on the system.

Furthermore, the total moments are assumed to be composed of control moments  $\mathbf{M}_{\text{ctr}}$ , which are induced by the control effectors, and the aerodynamic moments  $\mathbf{M}_{\text{aer}}$ , which summarize the airframe-induced aerodynamic effects acting on the system:

$$\mathbf{M}_{\text{tot}} = \mathbf{M}_{\text{ctr}} + \mathbf{M}_{\text{aer}}. \quad (5.255)$$

Thereby, the aerodynamic moments denoted in the body frame can be written as [77]:

$$\mathbf{M}_{\text{aer}} = \bar{q} S \begin{bmatrix} b C_l \\ \bar{c} C_m \\ b C_n \end{bmatrix}_B, \quad (5.256)$$

where  $\bar{q} = \frac{1}{2} \rho_0 V_{\text{CAS}}^2$  denotes the dynamic pressure,  $S$  is the reference wing area,  $\bar{c}$  denotes the mean aerodynamic chord,  $b$  denotes the wing span, and  $C_l$ ,  $C_m$ , and  $C_n$  denote the aerodynamic moment coefficients around the pitch, roll, and yaw axis respectively.



Within the *Rotational Jerk Inversion* block, the aerodynamic damping moments shall be canceled out. In order to derive the underlying relationships, the effect of body rotation  $\boldsymbol{\omega}$  on the aerodynamic moments in (5.256) is of interest. Neglecting the influence of inter-axis coupling of the rotational rates on the damping moments, a small change in aerodynamic moments  $\Delta \mathbf{M}_{\text{aer}}$  as a consequence of a small change in rotational rate  $\Delta \boldsymbol{\omega} = [\Delta p \ \Delta q \ \Delta r]^T_B$  can be written as

$$\Delta \mathbf{M}_{\text{aer}} = \bar{q} S \begin{bmatrix} b \frac{\partial C_l}{\partial p} \Delta p \\ \bar{c} \frac{\partial C_m}{\partial q} \Delta q \\ b \frac{\partial C_n}{\partial r} \Delta r \end{bmatrix}_B. \quad (5.257)$$

Thereby,  $\frac{\partial C_l}{\partial p}$ ,  $\frac{\partial C_m}{\partial q}$ , and  $\frac{\partial C_n}{\partial r}$  denote the derivatives of each aerodynamic moment coefficient with respect to the rotational rate of that channel. Since the rotational rates influence the local aerodynamic flow angles as shown in figure 5.49, the partial derivatives are approximated by

$$\frac{\partial C_i}{\partial \omega_i} = C_{i\alpha} \frac{\partial \alpha}{\partial \omega_i} \propto \frac{1}{V}, \quad (5.258)$$

which shows an inverse proportionality of each moment coefficient  $C_i$  with respect to the velocity  $V$ .

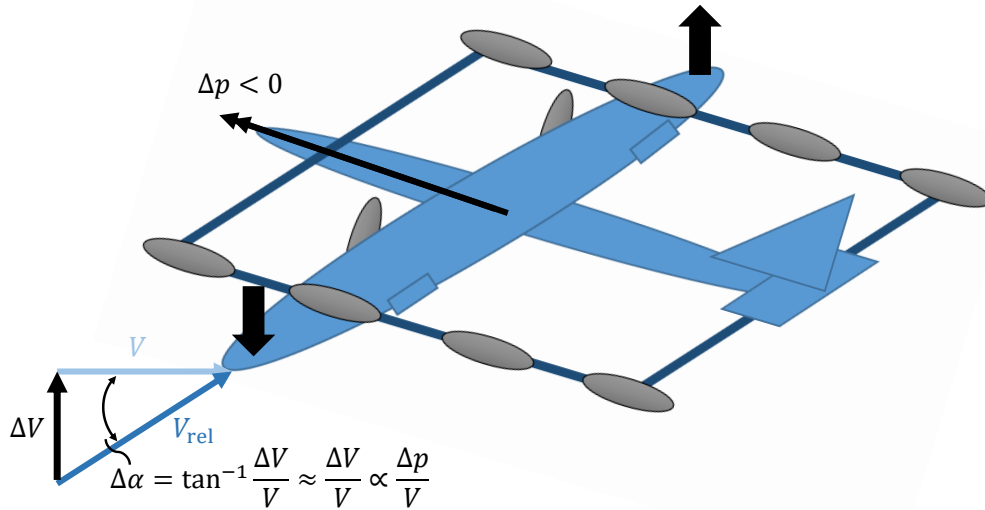


**Figure 5.49:** Roll Rate Induced Local Angle of Attack Change

Following the results from (5.257) and (5.258), the Jacobian matrix of the aerodynamic moments with respect to the rotational rates is given by

$$\frac{\partial \mathbf{M}_{\text{aer}}}{\partial \boldsymbol{\omega}} = \mathbf{C}_{\text{damp}} V_{\text{CAS}}, \quad (5.259)$$

where the constant matrix  $\mathbf{C}_{\text{damp}}$  summarizes the parameters regarding the reference air density on mean sea level, aircraft wing span and mean aerodynamic chord, and other geometric properties of the aircraft including the relevant lever arms and surface areas.

Although (5.259) includes several simplifying assumptions, it yields the general trend of linearly increasing damping moments with increasing airspeed. The linear trend thereby follows from combining the effects of the airspeed's quadratic influence on the dynamic pressure and its reciprocal relationship with respect to the aerodynamic flow angles and hence moment coefficients shown in (5.258) and figure 5.49.

In order to derive the relationship between the rotational jerk  $\dot{\boldsymbol{\omega}}$  and the necessary specific control moment rate  $\dot{\mathbf{m}}_c$ , the time derivative of (5.254) is obtained while considering (5.255) and (5.259):

$$\begin{aligned}\dot{\boldsymbol{\omega}} &= \underbrace{\mathbf{I}^{-1}\dot{\mathbf{M}}_{\text{ctr}}}_{\dot{\mathbf{m}}_c} + \mathbf{I}^{-1} \underbrace{\dot{\mathbf{M}}_{\text{aer}}}_{\frac{\partial \mathbf{M}_{\text{aer}}}{\partial \boldsymbol{\omega}} \dot{\boldsymbol{\omega}}} - \mathbf{I}^{-1} (\dot{\boldsymbol{\omega}} \times \mathbf{I} \boldsymbol{\omega} + \boldsymbol{\omega} \times \mathbf{I} \dot{\boldsymbol{\omega}}) \\ &= \dot{\mathbf{m}}_c + \mathbf{I}^{-1} (\mathbf{C}_{\text{damp}} V_{\text{CAS}} \dot{\boldsymbol{\omega}} - \dot{\boldsymbol{\omega}} \times \mathbf{I} \boldsymbol{\omega} - \boldsymbol{\omega} \times \mathbf{I} \dot{\boldsymbol{\omega}}),\end{aligned}\quad (5.260)$$

where  $\dot{\mathbf{M}}_{\text{aer}} = \frac{\partial \mathbf{M}_{\text{aer}}}{\partial \boldsymbol{\omega}} \dot{\boldsymbol{\omega}}$  is used with  $\frac{\partial \mathbf{M}_{\text{aer}}}{\partial \boldsymbol{\omega}} = \mathbf{C}_{\text{damp}} V_{\text{CAS}}$  from (5.259).

Finally, the commanded specific moment rate vector is calculated by inverting and saturating the relationship in (5.260) and yields

$$\dot{\mathbf{m}}_c = \min \left( \dot{\mathbf{m}}_{c,\text{max}}, \max \left( \dot{\mathbf{m}}_{c,\text{min}}, \dot{\boldsymbol{\omega}}_d - \mathbf{I}^{-1} (\mathbf{C}_{\text{damp}} V_{\text{CAS}} \dot{\boldsymbol{\omega}} - \dot{\boldsymbol{\omega}} \times \mathbf{I} \boldsymbol{\omega} - \boldsymbol{\omega} \times \mathbf{I} \dot{\boldsymbol{\omega}}) \right) \right), \quad (5.261)$$

with the maximum and minimum specific moment rate command  $\dot{\mathbf{m}}_{c,\text{max}}$  and  $\dot{\mathbf{m}}_{c,\text{min}}$  respectively and the desired rotational jerk  $\dot{\boldsymbol{\omega}}_d$  from (5.253).

### 5.3.5.5 Forward Specific Force Control

The *Forward Specific Force Control* block contains the control law for tracking the commanded forward specific force  $f_{Bx,c}$ , which is provided by the *Inner-Loop Command Bus (IL CMD Bus)*. To this end, the forward specific force rate command  $\dot{f}_{Bx,c}$  is output as the inner-most pseudo control of the longitudinal channel and forwarded to the *Control Allocation*. The functional architecture of the *Forward Specific Force Control* block is depicted in figure 5.50.

Similarly to the rotational acceleration, the relative degree of the forward specific force channel is 1 (assuming first order response types for the traction motor RPM and blade pitch angle). Hence, the reference dynamics for the forward specific force follow analogously to the rotational acceleration reference signals. It follows for the reference forward specific force rate

$$\dot{f}_{Bx,\text{ref}} = \min \left( \dot{f}_{Bx,\text{ref,max}}, \max \left( \dot{f}_{Bx,\text{ref,min}}, K_{f_{Bx,\text{ref}}} (f_{Bx,\text{ref},c} - f_{Bx,\text{ref}}) \right) \right), \quad (5.262)$$

where the reference forward specific force command  $f_{Bx,\text{ref},c}$  is chosen as  $f_{Bx,\text{ref},c} = f_{Bx,c}$  and  $K_{f_{Bx,\text{ref}}}$  denotes the reference bandwidth of the forward specific force dynamics.

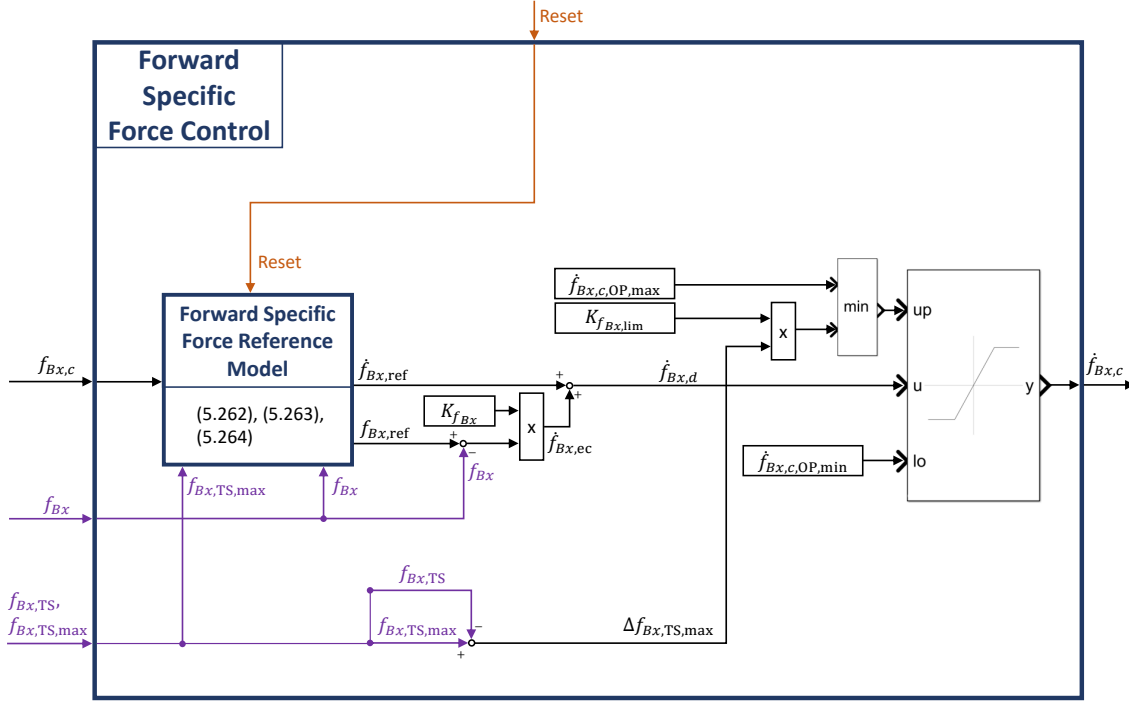


Figure 5.50: Forward Specific Force Control Block

Furthermore, the limits for the reference forward specific force rate are given by

$$\begin{aligned}\dot{f}_{Bx,ref,max} &= \min \left( \dot{f}_{Bx,ref,OP,max}, \dot{f}_{Bx,f_{lim},max} \right), \\ \dot{f}_{Bx,ref,min} &= \max \left( \dot{f}_{Bx,ref,OP,min}, \dot{f}_{Bx,f_{lim},min} \right),\end{aligned}\quad (5.263)$$

with the forward specific force rates leading to the limit specific forces

$$\begin{aligned}\dot{f}_{Bx,f_{lim},max} &= K_{f_{Bx,lim}} (f_{Bx,ref,OP,max} - f_{Bx,ref}), \\ \dot{f}_{Bx,f_{lim},min} &= K_{f_{Bx,lim}} (f_{Bx,ref,OP,min} - f_{Bx,ref}),\end{aligned}\quad (5.264)$$

where  $K_{f_{Bx,lim}}$  denotes the convergence rate towards the operational forward specific force limits  $f_{Bx,ref,OP,max}$  and  $f_{Bx,ref,OP,min}$ . As was also pointed out for the *Rotational Acceleration Control*, the choice of respective force and force rate limits is directly related to the capability of the traction system to generate forward thrust and its capability to change the forward thrust.

The resulting forward specific force rate demand  $\dot{f}_{Bx,d}$  follows from combining the reference specific force rate signal  $\dot{f}_{Bx,ref}$  from (5.262) as the feedforward command and the specific force rate error control signal  $\dot{f}_{Bx,ec}$  as the feedback command:

$$\dot{f}_{Bx,d} = \dot{f}_{Bx,ref} + \underbrace{K_{f_{Bx}} (f_{Bx,ref} - f_{Bx})}_{\dot{f}_{Bx,ec}},\quad (5.265)$$

where  $K_{f_{Bx}}$  denotes the error bandwidth and  $f_{Bx,ref}$  is the reference forward specific force, which follows from integration of (5.262).

Finally, the forward specific force rate command  $\dot{f}_{Bx,c}$  follows from saturating (5.265) according to

$$\dot{f}_{Bx,c} = \min \left( \dot{f}_{Bx,c,\max}, \max \left( \dot{f}_{Bx,c,\min}, \dot{f}_{Bx,d} \right) \right), \quad (5.266)$$

with the specific force rate command limits

$$\begin{aligned} \dot{f}_{Bx,c,\max} &= \min \left( \dot{f}_{Bx,c,OP,\max}, \dot{f}_{Bx,c,f_{lim},\max} \right), \\ \dot{f}_{Bx,c,\min} &= \dot{f}_{Bx,c,OP,\min}. \end{aligned} \quad (5.267)$$

Thereby, the maximum specific force rate command that yields the maximum admissible specific traction force  $f_{Bx,TS,\max}$  is given by

$$\dot{f}_{Bx,c,f_{lim},\max} = K_{f_{Bx,lim}} (f_{Bx,TS,\max} - f_{Bx,TS}), \quad (5.268)$$

where  $f_{Bx,TS,\max}$  and  $f_{Bx,TS}$  denote the maximum admissible and estimated specific traction force respectively, which are provided by the *Specific Control Forces and Moments Bus* via the *Feedback Bus* and are calculated in the *Control Allocation* block. Thereby, the calculation of the maximum admissible specific traction force  $f_{Bx,TS,\max}$  incorporates the longitudinal stick deflection of the thrust stick  $d_{TS,x}$  in order to distinguish between Maximum Continuous Thrust (MCT) or Maximum Peak Thrust (MPT). Hence, (5.267) ensures that the specific force rate command to the *Control Allocation* does not exceed the maximum admissible traction force for a given flight condition.

### 5.3.5.6 Control Effector Estimation

The *Control Effector Estimation* block contains models that aim to estimate the current states of the available control effectors. To this end, it includes the *Powered Lift Motor Estimation*, *Traction Motor Estimation*, *Traction Blade Pitch Estimation*, and *Aerodynamic Surface Estimation*. Figure 5.51 shows the structure of the *Control Effector Estimation* block.

The estimated rotational rates and deflection angles of the VTOL aircraft's control effectors are used within the *Control Allocation* block for:

- the inversion of the control effector dynamics, which yields the well-known incremental form in the scope of INDI control, and
- the estimation of the control effector induced specific forces and moments, which are output via the *Specific Control Forces and Moments Bus*.

To this end, the control effector dynamics are approximated using nonlinear differential equations that incorporate the saturation effects on the acceleration and rate level. Additionally, the limited deflection and rotational rate capabilities of aerodynamic control surfaces and electric motors respectively are also included within the control effector models.

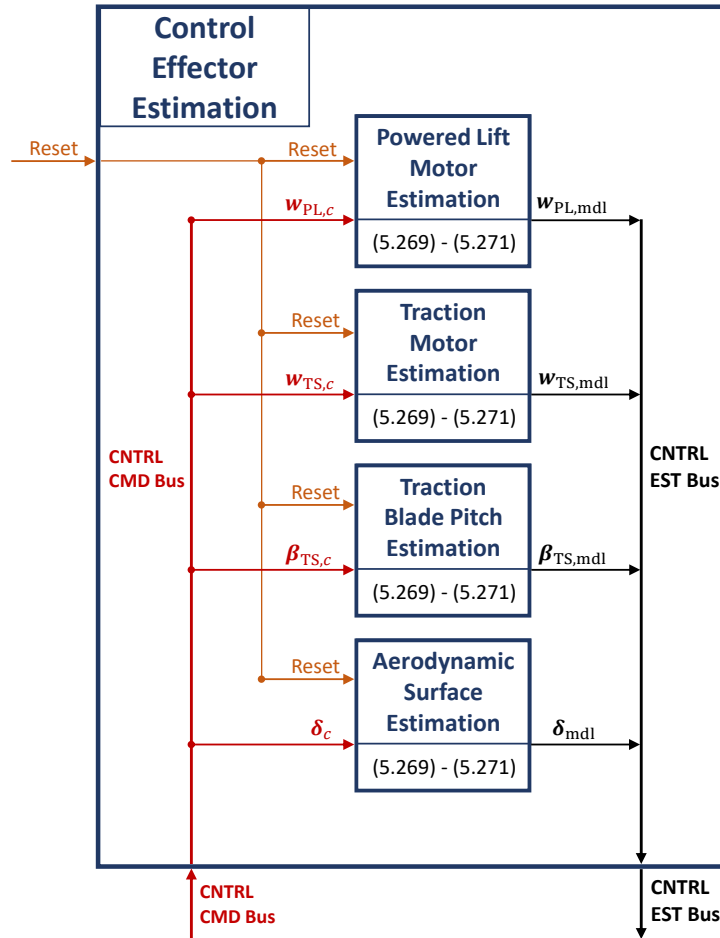


**Figure 5.51:** *Control Effector Estimation Block*

When neglecting the fast dynamics of electric current, electromechanical actuators (EMA) can in general be modeled as second-order systems [131], whereas electric motors can be well approximated by first-order systems [132]. This follows from the assumption that the electric torque of the actuator and motor follows directly as a consequence of the applied electric current and that the deflection angle of the EMA results after two integrations, while the rotational rate of the motor results after one integration according to Euler's equation of motion.

However, for the sake of simplicity it is sufficient to model each control effector as an equivalent first-order system that captures its bandwidth, rate saturations, and absolute limits. As will be shown in the scope of the control architecture validation and verification in section 5.4, these simplifications are justified in the context of incremental control and yield a well-performing control law. Note that in contrast to the effector models within the controller, the functional control effector models of the simulated plant can and should be modeled as higher-order nonlinear systems that reflect the real dynamics of the actuators and motors as closely as possible.

The controller-internal estimation for each control effector's output  $C_{\text{mdl},i}$  follows from the saturated first-order differential equation

$$\dot{C}_{\text{mdl},i} = \min \left( \dot{C}_{\text{max},i} \max \left( \dot{C}_{\text{min},i}, K_{C_i} (C_{c,i} - C_{\text{mdl},i}) \right) \right), \quad (5.269)$$

where  $C_{c,i}$  denotes the command to the control effector,  $K_{C_i}$  denotes its bandwidth for small command amplitudes, and  $\dot{C}_{\text{max},i}$  and  $\dot{C}_{\text{min},i}$  denote the maximum and minimum control effector rate limits that follow from

$$\begin{aligned} \dot{C}_{\text{max},i} &= \min \left( \dot{C}_{\text{abs,max},i}, \dot{C}_{C_{\text{lim,max},i}} \right), \\ \dot{C}_{\text{min},i} &= \max \left( \dot{C}_{\text{abs,min},i}, \dot{C}_{C_{\text{lim,min},i}} \right), \end{aligned} \quad (5.270)$$

where  $\dot{C}_{\text{abs,max},i}$  and  $\dot{C}_{\text{abs,min},i}$  denote the upper and lower absolute control effector rate limits. Furthermore, the control effector rates leading to the absolute control effector limits are given by

$$\begin{aligned} \dot{C}_{C_{\text{lim,max},i}} &= K_{C_{\text{lim},i}} (C_{\text{max},i} - C_{\text{mdl},i}), \\ \dot{C}_{C_{\text{lim,min},i}} &= K_{C_{\text{lim},i}} (C_{\text{min},i} - C_{\text{mdl},i}), \end{aligned} \quad (5.271)$$

where  $C_{\text{max},i}$  and  $C_{\text{min},i}$  represent the upper and lower absolute control effector limits.

For control effectors that yield second-order characteristics rather than first-order, the dynamics (for small amplitudes) can be represented as

$$\ddot{C}_{\text{mdl},i} = -2d_i\omega_{0,i}\dot{C}_{\text{mdl},i} + \omega_{0,i}^2 (C_{c,i} - C_{\text{mdl},i}), \quad (5.272)$$

where  $\omega_{0,i}$  denotes the natural frequency and  $d_i$  denotes the relative damping of the control effector.

Furthermore, rewriting (5.272) into a cascaded form consisting of the inner loop

$$\ddot{C}_{\text{mdl},i} = K_{\dot{C}_i} \left( \dot{C}_{c,i} - \dot{C}_{\text{mdl},i} \right) \quad (5.273)$$

and the outer loop

$$\dot{C}_{c,i} = K_{C_i} (C_{c,i} - C_{\text{mdl},i}) \quad (5.274)$$

allows to identify the outer-loop gain  $K_{C_i}$  and inner-loop gain  $K_{\dot{C}_i}$  through termwise comparison between (5.272), (5.273), and (5.274):

$$K_{C_i} = \frac{\omega_{0,i}}{2d_i} \quad K_{\dot{C}_i} = 2d_i\omega_{0,i}. \quad (5.275)$$

Note that the ratio of inner-loop gain to outer-loop gain  $\frac{K_{\dot{C}_i}}{K_{C_i}} = 4d_i^2$  determines the applicability of time-scale separation and hence the quality of the first-order approximation of (5.272). The time-scale separation between inner and outer loop thereby increases with increasing relative damping  $d_i$ . As a consequence, the inner-loop dynamics (5.273) can be neglected for higher damping values and treated as a quasi-stationary system.

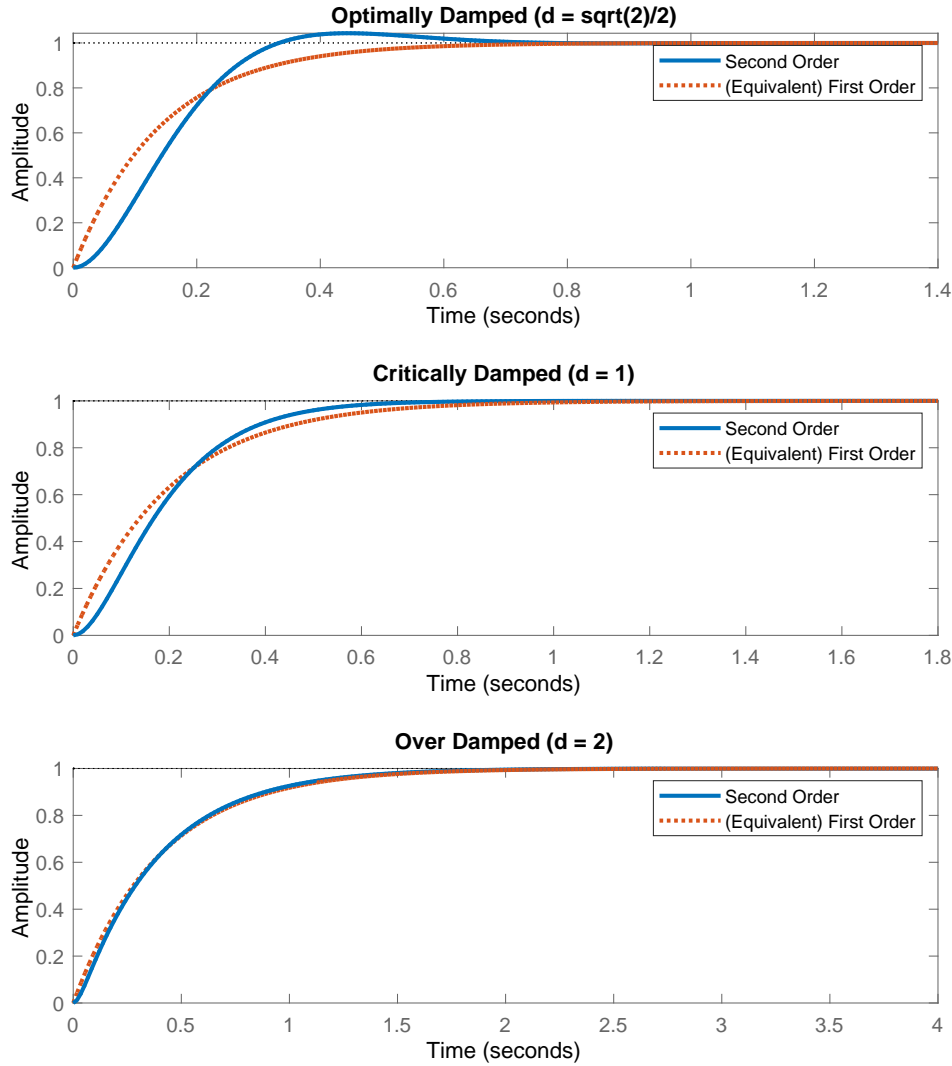


**Figure 5.52:** Comparison of Second-Order Dynamics and Equivalent First-Order Dynamics for Different Relative Dampings

In particular, for  $K_{\dot{C}_i} \gg K_{C_i}$  it follows from (5.273) and (5.274):

$$\dot{C}_{\text{mdl},i} \approx \dot{C}_{c,i} = K_{C_i} (C_{c,i} - C_{\text{mdl},i}) , \quad (5.276)$$

with  $K_{C_i}$  from (5.275), which has the same form as the first-order dynamics in (5.269) (neglecting the saturations).

Figure 5.52 illustrates three step responses of a second-order system with increasing relative damping and the corresponding equivalent first-order responses. Table 5.4 below summarizes the parameters for each case. Note that for increasing damping values the first-order step response matches the second-order step response better.

The applicability of equivalent first-order dynamics for estimating the control effector states has to be considered on an individual basis and shall be validated in the context of a closed-loop simulation of the control architecture together with a functional simulation

**Table 5.4:** *Parameters of Second-Order and Equivalent First-Order System for Different Dampings*

Damping	2nd Order System	Equivalent 1st Order System
Optimally Damped	$\omega_0 = 10$	$K_C = \frac{10}{\sqrt{2}} \approx 7.07$
	$d = \frac{\sqrt{2}}{2}$	
Critically Damped	$\omega_0 = 10$	$K_C = \frac{10}{2} = 5$
	$d = 1$	
Over Damped	$\omega_0 = 10$	$K_C = \frac{10}{4} = 2.5$
	$d = 2$	

model of the plant. Note that the presented control structure does not explicitly rule out the use of second-order (or even higher-order) control effector models. However, in the scope of the control effector inversion within the *Control Allocation* block, first-order dynamics are assumed in order to yield the final commands to the motors and actuators.

The explicit use of control effector measurements is not applied in the context of the given control effector estimation. However, measurements of the current motor RPMs and actuator deflection angles can in general be incorporated into the estimation process by means of complementary filtering, as it was shown in subsection 5.3.5.1 for the specific forces. Instead of using the modeled and measured specific forces, the filter architecture of figure 5.45 would then be applied to the modeled and measured control effector outputs.

### 5.3.5.7 Control Allocation

The *Control Allocation* represents the final block in the functional flow of the presented control strategy. Thereby, the following high- and low-level requirements are identified:

- The *Control Allocation* block shall yield the rotational speed commands to the powered lift motors  $\mathbf{w}_{\text{PL},c}$ , deflection commands to the aerodynamic control surfaces  $\boldsymbol{\delta}_c$ , as well as rotational speed commands  $\mathbf{w}_{\text{TS},c}$  and blade pitch commands  $\boldsymbol{\beta}_{\text{TS},c}$  to the traction system, which together yield the required specific force and moment rates  $\dot{f}_{Bz,c}$ ,  $\dot{f}_{Bx,c}$ , and  $\dot{\mathbf{m}}_c$ .

This problem statement is usually referred to as *Control Allocation* in the common literature and has been addressed using various methods. In [133] the most common approaches are listed and briefly introduced.

- The commands to the control effectors shall not exceed the limits imposed by their inherent rate saturations and absolute RPM or deflection saturations. This requirement holds regardless of whether or not the commanded motors and actuators can handle commands that exceed their physical limits.



- The commands to the control effectors shall account for saturated or failed control effectors and compensate the allocated deficit by redistributing it to other available control effectors. Sufficient redundancy is assumed among the control effectors and only single failures are treated within this scope.
- The allocation between the different control effector groups shall account for the physical characteristics and limitations inherent to the type of control effector. In particular, aerodynamic surfaces shall be used primarily at higher dynamic pressures, while powered lift motors shall be used primarily at low dynamic pressures.
- The remaining degrees of freedom after allocating the required specific force and moment rates shall be used for optimizing secondary objectives. In particular, the control effector commands shall not lead to excessive loads on the airframe (force fighting) or shall not yield unnecessarily high power consumption (high RPMs).
- The *Control Allocation* block shall yield model-based estimations of the control effector induced specific forces and moments and distribute them via the *Specific Control Forces and Moments Bus (SCFM Bus)*, which shall contain:
  - the model-based estimation of the generated specific powered lift  $f_{Bz,PL}$ ,
  - the model-based estimation of the generated specific traction force  $f_{Bx,TS}$  and the maximum admissible specific traction force  $f_{Bx,TS,max}$ , which is based on power limitations governed by the deflection of the thrust stick  $d_{TS,x}$ ,
  - the model-based estimations of the generated specific moments denoted in the body frame of both the powered lift motors  $(\mathbf{m}_{PL})_B$  and of the aerodynamic surfaces  $(\mathbf{m}_{AS})_B$ , and
  - the model-based estimation of the total control effector induced specific forces  $(\mathbf{f}_{mdl})_B$  and moments  $(\mathbf{m}_{mdl})_B$  denoted in the body frame.

The high-level structure of the *Control Allocation* block is depicted in figure 5.53. It contains the following subsystems:

- The model-based estimation of the specific control forces and moments (SCFM) is located in the *SCFM Estimation* block.
- The *Specific Moment Rate Blending* block determines the contribution of powered lift motors and aerodynamic control surfaces to the generation of the required specific moment rate demand based on the dynamic pressure.
- The *Powered Lift Allocation* block, *Aerodynamic Surface Allocation* block, and *Traction System Allocation* block incorporate the necessary inversion and redundancy management and provide the final commands to the control effectors.

In the following paragraphs, the individual subsystems are further decomposed and described on a functional level. Note that, in general, the realization of the *Control Allocation* functionality requires an extensive amount of computations due to the complicated nature of the inversion problem. Thereby, the complexity is mainly driven by the system's over-actuation and the requirements to incorporate rate-limited control effectors, failure mitigation capabilities, and different control effector characteristics throughout the entire flight envelope.

In particular, the iterative nature of the *Redistributed Scaled Pseudo-Inverse* (RSPI) algorithm [134] [135] [136] [137] [138] [8], which is used in the scope of the specific force and moment rate inversion, and the therein used inverted matrices might require special caution as to minimizing the required computational effort. A segmentation of the involved matrices, the extraction of constant components, and the subsequent precomputation and storage of their *Singular Value Decomposition* (SVD) [139] is one possible way to reduce the computational cost of the involved algorithms.

However, the optimization of computational effort with respect to a specific implementation of the functionality is not in the scope of this section, which is only concerned with providing a functional specification. Implementation-related aspects are discussed in more detail in chapter 6.

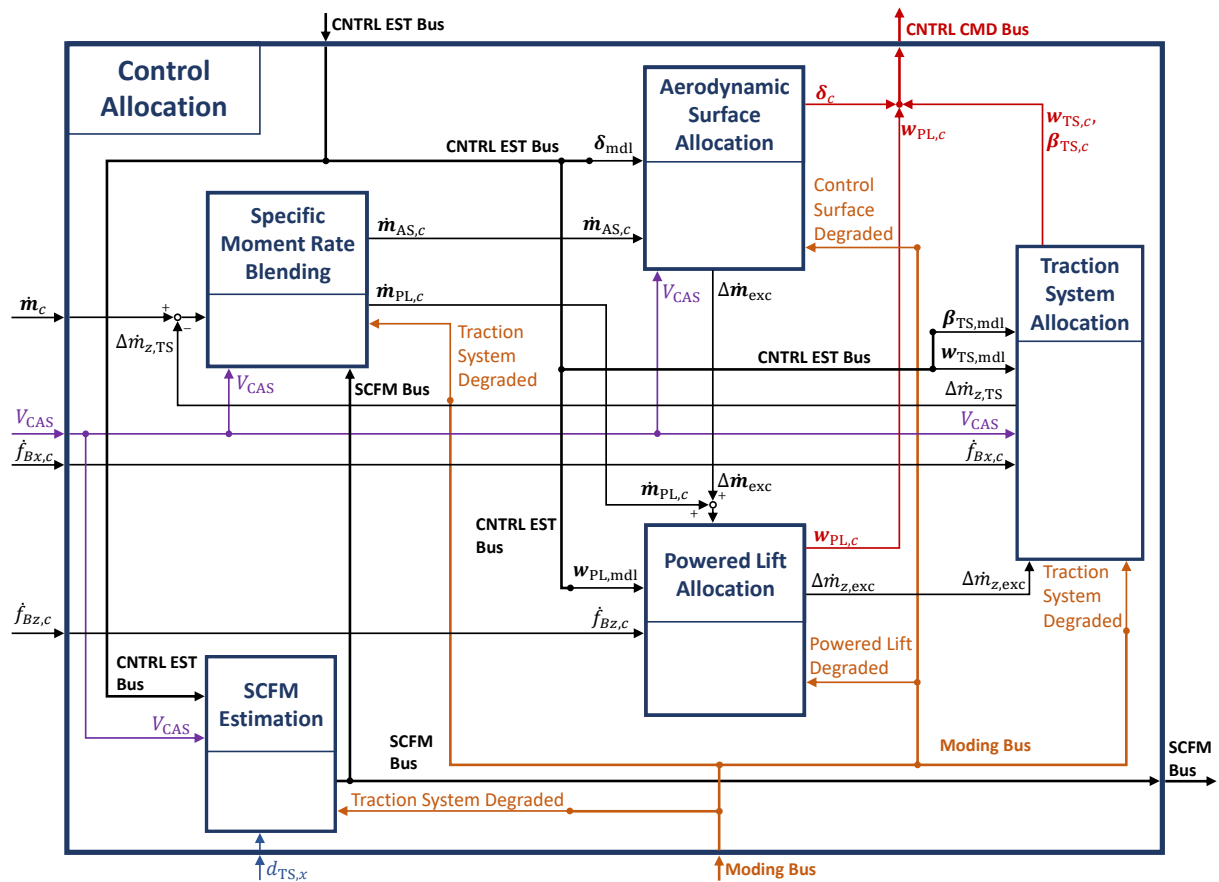


Figure 5.53: Control Allocation Block

**SCFM Estimation** The *SCFM Estimation* block estimates the specific forces and moments that are generated by the control effectors. To this end, the control effector groups are considered separately and the individual contributions are summed up.

The estimation of the vertical specific control force  $f_{Bz,PL}$  and specific control moments  $\mathbf{m}_{PL}$  in body-fixed coordinates, which are generated by the powered lift motors, follows from

$$\begin{bmatrix} f_{Bz,PL} \\ \mathbf{m}_{PL} \end{bmatrix} = \underbrace{\begin{bmatrix} \mathbf{B}_{f_{Bz} \leftarrow \mathbf{u}_{PL}} \\ \mathbf{B}_{\mathbf{m} \leftarrow \mathbf{u}_{PL}} \end{bmatrix}}_{\mathbf{B}_{\nu_{PL} \leftarrow \mathbf{u}_{PL}}} \mathbf{u}_{PL,mdl}, \quad (5.277)$$

where  $\mathbf{B}_{\nu_{PL} \leftarrow \mathbf{u}_{PL}}$  is the powered lift control effectiveness matrix, which includes relevant propeller parameters, lever arms, aircraft mass, and aircraft inertia. Furthermore,

$$\mathbf{u}_{PL,mdl} = \begin{bmatrix} w_{PL,mdl,1}^2 \\ \vdots \\ w_{PL,mdl,m_{PL}}^2 \end{bmatrix} \quad (5.278)$$

denotes the vector of the squared rotational rate estimations of the powered lift motors. Thereby, the number of powered lift motors is denoted as  $m_{PL}$  and is assumed to be high enough such as to provide a sufficient degree of redundancy. As was pointed out in section 5.1, the control forces generated by the propellers are approximately proportional to the squared rotor speeds and hence the resulting dynamic pressure at the rotor blade [83] [84], which enables the input-affine structure in (5.277).

Similarly, the estimation of the specific control moments produced by the aerodynamic surfaces  $\mathbf{m}_{AS}$  follows from

$$\mathbf{m}_{AS} = \mathbf{B}_{\mathbf{m} \leftarrow \mathbf{u}_{AS}} \mathbf{u}_{AS,mdl}, \quad (5.279)$$

where  $\mathbf{B}_{\mathbf{m} \leftarrow \mathbf{u}_{AS}}(V_{CAS})$  is the aerodynamic surface control effectiveness matrix, which includes relevant control surface parameters, lever arms, the reference wing area, aircraft inertia, and the dynamic pressure. Furthermore,

$$\mathbf{u}_{AS,mdl} = \begin{bmatrix} \delta_{mdl,1} \\ \vdots \\ \delta_{mdl,m_{AS}} \end{bmatrix} \quad (5.280)$$

denotes the vector of estimated aerodynamic surface deflections. The total number of control surfaces is furthermore given by  $m_{AS}$ . Similarly to the powered lift motors, a sufficient degree of redundancy is presupposed.

The specific force in forward direction  $f_{Bx,TS}$  and specific yaw moment  $m_{Bz,TS}$  generated by the traction system follows a similar formula as for the powered lift motors:

$$\begin{bmatrix} f_{Bx,TS} \\ m_{Bz,TS} \end{bmatrix} = \underbrace{\begin{bmatrix} \mathbf{B}_{f_{Bx} \leftarrow \mathbf{u}_{TS}} \\ \mathbf{B}_{m_{Bz} \leftarrow \mathbf{u}_{TS}} \end{bmatrix}}_{\mathbf{B}_{\nu_{TS} \leftarrow \mathbf{u}_{TS}}} \mathbf{u}_{TS,mdl}, \quad (5.281)$$

where  $\mathbf{B}_{\nu_{\text{TS}} \leftarrow \mathbf{u}_{\text{TS}}}(V_{\text{CAS}}, \boldsymbol{\beta}_{\text{TS,mdl}})$  is the traction system control effectiveness matrix, which includes relevant propeller parameters, lever arms, aircraft mass and inertia, the airspeed and the estimated blade pitch angle of the traction propellers.

Furthermore,

$$\mathbf{u}_{\text{TS,mdl}} = \begin{bmatrix} w_{\text{TS,mdl},1}^2 \\ \vdots \\ w_{\text{TS,mdl},m_{\text{TS}}}^2 \end{bmatrix} \quad (5.282)$$

denotes the vector of the squared rotational rate estimations of the traction motors.

The maximum admissible forward specific force that can be generated by the traction motors is needed for the underspeed protection functionality shown in figure 5.19, which is located in the *Vertical Channel Command* block of the outer loop . To this end, the maximum specific traction force is estimated by

$$f_{Bx,\text{TS,max}} = \mathbf{B}_{f_{Bx} \leftarrow \mathbf{u}_{\text{TS}}} \mathbf{u}_{\text{TS,max}} , \quad (5.283)$$

where

$$\mathbf{u}_{\text{TS,max}} = \begin{bmatrix} w_{\text{TS,max},1}^2 \\ \vdots \\ w_{\text{TS,max},m_{\text{TS}}}^2 \end{bmatrix} \quad (5.284)$$

denotes the vector of the squared estimated maximum rotational rates that the traction system can yield in a given flight setting. Thereby, each individual maximum rotational rate  $w_{\text{TS,max},i}$  is a function of:

- the current airspeed  $V_{\text{CAS}}$  and estimated blade pitch angle  $\boldsymbol{\beta}_{\text{TS,mdl}}$ ,
- the maximum admissible power to the traction system based on the thrust stick position  $d_{\text{TS},x}$ , and
- the failure status of each motor provided by the *Traction System Degraded* signal.

Finally, the individual force and moment contributions of each control effector group are summed up in order to yield the overall control effector induced specific forces and moments denoted in the body frame:

$$(\mathbf{f}_{\text{mdl}})_B = \begin{bmatrix} f_{Bx,\text{TS}} \\ 0 \\ f_{Bz,\text{PL}} \end{bmatrix}_B \quad (\mathbf{m}_{\text{mdl}})_B = \mathbf{m}_{\text{PL}} + \mathbf{m}_{\text{AS}} + \begin{bmatrix} 0 \\ 0 \\ m_{Bz,\text{TS}} \end{bmatrix}_B . \quad (5.285)$$

The total control forces and moments from (5.285) are assembled with the individual contributions from (5.277), (5.279), and (5.281) and are output via the *Specific Control Forces and Moments Bus (SCFM Bus)*.

**Specific Moment Rate Blending** The *Specific Moment Rate Blending* block distributes the required specific moment rate command  $\dot{\mathbf{m}}_c$  among the powered lift motors and the aerodynamic surfaces by using a blending scheme. Thereby, the blending is driven by the dynamic pressure

$$\bar{q} = \frac{1}{2} \rho_0 V_{\text{CAS}}^2, \quad (5.286)$$

which is calculated using the calibrated airspeed  $V_{\text{CAS}}$  and the reference air density on mean sea level  $\rho_0$ .

The general ideal behind the blending is to gradually shift the control authority for the moment creation from the powered lift motors at low dynamic pressures to the aerodynamic control surfaces at high dynamic pressures. To this end, the total specific moment rate command  $\dot{\mathbf{m}}_c$  is divided into two parts:

$$\dot{\mathbf{m}}_c = \dot{\mathbf{m}}_{\text{PL},c} + \dot{\mathbf{m}}_{\text{AS},c}, \quad (5.287)$$

where  $\dot{\mathbf{m}}_{\text{PL},c}$  and  $\dot{\mathbf{m}}_{\text{AS},c}$  denote the specific moment rates that shall be allocated into the powered lift motors and aerodynamic control surfaces respectively.

Furthermore, the individual specific moment rate contributions are given by

$$\dot{\mathbf{m}}_{\text{PL},c} = (1 - \lambda_{\dot{\mathbf{m}}}) \dot{\mathbf{m}}_c + \lambda_{\dot{\mathbf{m}}} \dot{\mathbf{m}}_{\text{PL},0} - (1 - \lambda_{\dot{\mathbf{m}}}) \dot{\mathbf{m}}_{\text{AS},0} \quad (5.288)$$

and

$$\dot{\mathbf{m}}_{\text{AS},c} = \lambda_{\dot{\mathbf{m}}} \dot{\mathbf{m}}_c + (1 - \lambda_{\dot{\mathbf{m}}}) \dot{\mathbf{m}}_{\text{AS},0} - \lambda_{\dot{\mathbf{m}}} \dot{\mathbf{m}}_{\text{PL},0}, \quad (5.289)$$

where  $\lambda_{\dot{\mathbf{m}}}$  denotes the blending parameter, which is a function of the dynamic pressure and follows from

$$\lambda_{\dot{\mathbf{m}}}(\bar{q}) = \min \left( 1, \max \left( 0, \frac{\bar{q} - \bar{q}_{\text{lo}}}{\bar{q}_{\text{hi}} - \bar{q}_{\text{lo}}} \right) \right), \quad (5.290)$$

with  $\bar{q}$  from (5.286). Thereby,  $\bar{q}_{\text{lo}}$  and  $\bar{q}_{\text{hi}}$  denote the lower and higher dynamic pressure threshold of the linear blending respectively.

Furthermore, the terms  $\dot{\mathbf{m}}_{\text{PL},0}$  and  $\dot{\mathbf{m}}_{\text{AS},0}$  serve the purpose of preventing force fighting between both control effector groups by gradually allocating the stabilizing moment rates, which let the specific moments from (5.277) and (5.279) converge to predefined values. In particular,

$$\dot{\mathbf{m}}_{\text{PL},0} = \mathbf{K}_{\mathbf{m}_{\text{PL}}} (\mathbf{m}_{\text{PL},0} - \mathbf{m}_{\text{PL}}) \quad (5.291)$$

is aimed at setting the estimated powered lift induced specific moment  $\mathbf{m}_{\text{PL}}$  from (5.277) to  $\mathbf{m}_{\text{PL},0}$  with the dynamics governed by the matrix  $\mathbf{K}_{\mathbf{m}_{\text{PL}}}$ , while

$$\dot{\mathbf{m}}_{\text{AS},0} = \mathbf{K}_{\mathbf{m}_{\text{AS}}} (\mathbf{m}_{\text{AS},0} - \mathbf{m}_{\text{AS}}) \quad (5.292)$$

is aimed at setting the estimated specific moment induced by the aerodynamic surfaces  $\mathbf{m}_{\text{AS}}$  from (5.279) to  $\mathbf{m}_{\text{AS},0}$  with the dynamics governed by the matrix  $\mathbf{K}_{\mathbf{m}_{\text{AS}}}$ .

Thereby, the equilibrium specific moments  $\mathbf{m}_{\text{PL},0}$  and  $\mathbf{m}_{\text{AS},0}$  are chosen to be zero in the nominal case. In case of an asymmetric failure condition of the traction system, the equilibrium specific moments can be used to pre-allocate a yaw moment, which helps to compensate the yawing tendency due to the unilateral forward propulsion.

**Specific Control Force and Moment Rate Inversion** This paragraph is aimed to introduce the strategy for the inversion of the specific control force and moment rates into the required control input rates. Due to the similar application across all control effector groups, the derivation of the inversion functionality and the used notation is generalized in the following.

Furthermore, it is assumed that each control effector group provides sufficient redundancy to yield a well-posed inversion problem both for nominal and failure conditions. The case of rank deficiency in the forward and yaw channel upon one-sided traction system failures is accounted for separately in the *Traction System Allocation*.

Due to the differentiating characteristics of INDI on the level of the force and moment producers, the incremental control strategy renders the inversion problem linear. In particular, for a given commanded pseudo control rate vector  $\dot{\boldsymbol{\nu}}_c$ , the inversion problem is concerned with finding a suitable control input rate vector  $\dot{\boldsymbol{u}}_c$  such that

$$\dot{\boldsymbol{\nu}}_c = \mathbf{B}\dot{\boldsymbol{u}}_c, \quad (5.293)$$

where  $\mathbf{B}$  is the control effectiveness matrix and  $\dot{\boldsymbol{u}}_c \in \dot{\mathcal{U}}$  is a feasible solution for the control input rate vector.

Note that the presence of control effector (rate) saturations renders the admissible solution set  $\dot{\mathcal{U}}$  finite and hence a more suitable objective can be formulated in terms of the constrained optimization problem [133]

$$\begin{aligned} & \max_{\alpha \leq 1} \alpha, \\ & \text{subject to: } \alpha \dot{\boldsymbol{\nu}}_c = \mathbf{B}\dot{\boldsymbol{u}}_c, \text{ with } \dot{\boldsymbol{u}}_c \in \dot{\mathcal{U}}, \end{aligned} \quad (5.294)$$

which is referred to as the direct allocation problem [140].

Thereby, (5.294) is aimed at either yielding a feasible solution that satisfies (5.293), or at least maximizing the generated pseudo control rate in the direction of the target vector  $\dot{\boldsymbol{\nu}}_c$ . This reformulation of the inversion problem helps to account for the typically limited set of attainable forces and moments (respectively force and moment rates), which is referred to as *Attainable Moment Set* (AMS) in aerospace applications [133].

Within the scope of the allocation function for each control effector group, the pseudo controls are given by the specific forces and moments, which can be formulated according to (5.277), (5.279), and (5.281). Furthermore, due to the incremental nature of the control law, the allocated vector corresponds to the time derivative of the pseudo controls (i.e. specific force and moment rates), hence yielding the problem description in (5.294).

As a consequence of allocating pseudo control rates  $\dot{\boldsymbol{\nu}}_c$  into control input rates  $\dot{\boldsymbol{u}}_c$  (rather than allocating absolute pseudo controls  $\boldsymbol{\nu}_c$  into absolute control inputs  $\boldsymbol{u}_c$ ), special attention needs to be paid as to accounting for the redundancy in the control inputs. In particular, the wide-spread application of the Moore-Penrose Pseudo-Inverse [139] to the control allocation problem for over-actuated systems yields a solution that minimizes the norm of the control input rate vector.

However, when allocating control input rates rather than absolute control inputs for over-actuated systems, minimizing the norm of the solution does not uniquely determine the stationary distribution of the control inputs for a given pseudo control demand, which can lead to adverse command constellations among the control effectors. Therefore, the *Incremental Nullspace Optimization* (INO) is introduced in the remainder of this paragraph. Latter yields an additional control input rate demand, which is aimed at redistributing the control effort among the motors and actuators in order to satisfy secondary objectives such as minimizing the overall norm of the control input.

The problem of specific control force and moment rate inversion is hence addressed in two separate steps, which are described in the following:

1. The nominal allocation for solving (5.294) using the *Redistributed Scaled Pseudo-Inverse* (RSPI) algorithm and
2. The control input redistribution using *Incremental Nullspace Optimization* (INO).

**Redistributed Scaled Pseudo-Inverse** The *Redistributed Scaled Pseudo-Inverse* (RSPI) [134] [135] [136] [137] [138] [8] is an iterative algorithm, which is used in the context of the presented control architecture in order to allocate a commanded pseudo control rate vector  $\dot{\boldsymbol{\nu}}_c$  into a feasible control input rate vector  $\dot{\boldsymbol{u}}_c$ . Thereby,  $\dot{\boldsymbol{\nu}}_c$  and  $\dot{\boldsymbol{u}}_c$  represent:

- the commanded specific powered lift induced force and moment rates as well as the commanded rate of squared powered lift motor rotational speeds

$$\dot{\boldsymbol{\nu}}_c = \dot{\boldsymbol{\nu}}_{\text{PL},c} = \begin{bmatrix} \dot{f}_{Bz,c} \\ \dot{\boldsymbol{m}}_{\text{PL},c} \end{bmatrix} \quad \dot{\boldsymbol{u}}_c = \dot{\boldsymbol{u}}_{\text{PL},c} = \begin{bmatrix} 2w_{\text{PL},\text{mdl},1} \dot{w}_{\text{PL},c,1} \\ \vdots \\ 2w_{\text{PL},\text{mdl},m_{\text{PL}}} \dot{w}_{\text{PL},c,m_{\text{PL}}} \end{bmatrix} \quad (5.295)$$

in the context of the *Powered Lift Allocation*,

- the commanded aerodynamic specific moment rates as well as the commanded rate of aerodynamic surface deflections

$$\dot{\boldsymbol{\nu}}_c = \dot{\boldsymbol{\nu}}_{\text{AS},c} = \dot{\boldsymbol{m}}_{\text{AS},c} \quad \dot{\boldsymbol{u}}_c = \dot{\boldsymbol{u}}_{\text{AS},c} = \begin{bmatrix} \dot{\delta}_{c,1} \\ \vdots \\ \dot{\delta}_{c,m_{\text{AS}}} \end{bmatrix} \quad (5.296)$$

in the context of the *Aerodynamic Surface Allocation*, and

- the commanded traction system induced specific force and yaw moment rate as well as the commanded rate of squared traction motor rotational speeds

$$\dot{\boldsymbol{\nu}}_c = \dot{\boldsymbol{\nu}}_{\text{TS},c} = \begin{bmatrix} \dot{f}_{Bx,c} \\ \Delta \dot{m}_{Bz,\text{exc}} \end{bmatrix} \quad \dot{\boldsymbol{u}}_c = \dot{\boldsymbol{u}}_{\text{TS},c} = \begin{bmatrix} 2w_{\text{TS},\text{mdl},1} \dot{w}_{\text{TS},c,1} \\ \vdots \\ 2w_{\text{TS},\text{mdl},m_{\text{TS}}} \dot{w}_{\text{TS},c,m_{\text{TS}}} \end{bmatrix} \quad (5.297)$$

in the context of the *Traction System Allocation*.

Furthermore, the corresponding control effectiveness matrix  $\mathbf{B}$  follows analogously to (5.277), (5.279), and (5.281).

The set of admissible control input rates  $\dot{\mathcal{U}}$  is defined by an  $m$ -dimensional hypercube:

$$\dot{\mathcal{U}} = \{ \dot{\mathbf{u}} \in \mathbb{R}^m \mid \dot{u}_{\min,i} \leq \dot{u}_i \leq \dot{u}_{\max,i}, \forall i = 1 \dots m \}, \quad (5.298)$$

where  $m$  is the number of control inputs and  $\dot{u}_{\min,i}$  and  $\dot{u}_{\max,i}$  denote the lower and upper rate limits for the  $i$ -th control input respectively, which are given by

$$\begin{aligned} \dot{u}_{\min,i} &= \max(\dot{u}_{\text{abs,min},i}, \dot{u}_{u_{\text{lim},\min},i}), \\ \dot{u}_{\max,i} &= \min(\dot{u}_{\text{abs,max},i}, \dot{u}_{u_{\text{lim},\max},i}). \end{aligned} \quad (5.299)$$

Thereby,  $\dot{u}_{\text{abs,min},i}$  and  $\dot{u}_{\text{abs,max},i}$  denote the absolute minimum and maximum rate limits of the  $i$ -th control input respectively and

$$\begin{aligned} \dot{u}_{u_{\text{lim},\min},i} &= K_{u_{\text{lim},i}}(u_{\min,i} - u_i), \\ \dot{u}_{u_{\text{lim},\max},i} &= K_{u_{\text{lim},i}}(u_{\max,i} - u_i) \end{aligned} \quad (5.300)$$

denote the rates for which the control input converges to its absolute lower or upper limit  $u_{\min,i}$ ,  $u_{\max,i}$  respectively with the convergence rate  $K_{u_{\text{lim},i}}$ . Note that (5.299) and (5.300) ensure that admissible solutions for the control input rates not only adhere to the rate limits, but also to the absolute control input limits.

The RSPI algorithm is presented briefly in the following:

1. **Initialization.** The parameters are initialized at the beginning of the iteration:

$$\Delta \dot{\nu}_{c,0} = \dot{\nu}_c \quad \mathbf{B}_0 = \mathbf{B} \quad \Delta \dot{\mathbf{u}}_{\min,0} = \dot{\mathbf{u}}_{\min} \quad \Delta \dot{\mathbf{u}}_{\max,0} = \dot{\mathbf{u}}_{\max} \quad \dot{\mathbf{u}}_{c,0} = \mathbf{0} \quad k = 0. \quad (5.301)$$

2. **Unconstrained Solution.** The unconstrained solution is calculated by inversion:

- Set  $k = k + 1$ .
- Calculate the unconstrained solution candidate  $\Delta \dot{\mathbf{u}}_{\text{cand},k} = \mathbf{B}_{k-1}^\dagger \Delta \dot{\nu}_{c,k-1}$ , where  $\mathbf{B}_{k-1}^\dagger = \mathbf{B}_{k-1}^T (\mathbf{B}_{k-1} \mathbf{B}_{k-1}^T)^{-1}$  denotes the Moore-Penrose Pseudo-Inverse [139] of the control effectiveness matrix.

3. **Scaling.** The unconstrained solution candidate  $\Delta \dot{\mathbf{u}}_{\text{cand},k}$  is scaled down with a scalar  $\alpha$  such as to not violate the control input rate constraints while preserving the direction of the allocated pseudo control rate:

- For each candidate control input rate  $\Delta \dot{u}_{\text{cand},k,i}$ , determine the scalar factor  $s_i$  that scales the input rate to its corresponding limit:

$$s_i = \begin{cases} \frac{\Delta \dot{u}_{\min,k-1,i}}{\Delta \dot{u}_{\text{cand},k,i}}, & \text{for } \Delta \dot{u}_{\text{cand},k,i} < 0 \\ \frac{\Delta \dot{u}_{\max,k-1,i}}{\Delta \dot{u}_{\text{cand},k,i}}, & \text{for } \Delta \dot{u}_{\text{cand},k,i} > 0 \\ 1, & \text{for } \Delta \dot{u}_{\text{cand},k,i} = 0 \end{cases} \quad (5.302)$$



- Set the scaling parameter to the most conservative value:  $\alpha = \min(1, s_1, \dots, s_m)$ .
- Calculate the resulting control input rate contribution of the current iteration by scaling the solution candidate from step 2:  $\Delta \dot{\mathbf{u}}_{c,k} = \alpha \Delta \dot{\mathbf{u}}_{\text{cand},k}$ .
- Add the contribution to the control input rate solution:  $\dot{\mathbf{u}}_{c,k} = \dot{\mathbf{u}}_{c,k-1} + \Delta \dot{\mathbf{u}}_{c,k}$ .  
If  $\alpha = 1$ , the algorithm terminates, since the original solution candidate already satisfies the limit constraints.  
If  $\alpha < 1$ , identify the index  $i_{\text{sat}}$  of the control input rate that yields the most conservative (i.e. smallest) scaling. If more than one control input rate yield the same conservative scaling, the first one is considered.

4. **Pseudo Control Rate Deficit.** The pseudo control rate deficit is determined by subtracting the allocated pseudo control rate of the current iteration from the target pseudo control rate:

- Calculate the pseudo control rate contribution that was achieved in this iteration:  $\Delta \dot{\boldsymbol{\nu}}_k = \mathbf{B}_{k-1} \Delta \dot{\mathbf{u}}_{c,k}$ .
- Determine the deficit between the target and the achieved pseudo control rate and set it as the next iteration's target:  $\Delta \dot{\boldsymbol{\nu}}_{c,k} = \Delta \dot{\boldsymbol{\nu}}_{c,k-1} - \Delta \dot{\boldsymbol{\nu}}_k$ .

5. **Control Input Rate Limit Update.** The upper and lower control input rate limits are updated in order to account for the pre-allocated control input rate contribution  $\Delta \dot{\mathbf{u}}_{c,k}$ :

- The lower limit is updated according to  $\Delta \dot{\mathbf{u}}_{\text{min},k} = \Delta \dot{\mathbf{u}}_{\text{min},k-1} - \Delta \dot{\mathbf{u}}_{c,k}$ .
- The upper limit is updated according to  $\Delta \dot{\mathbf{u}}_{\text{max},k} = \Delta \dot{\mathbf{u}}_{\text{max},k-1} - \Delta \dot{\mathbf{u}}_{c,k}$ .

6. **Control Effectiveness Update.** The saturated control input rates are removed from the further allocation process by setting the  $i_{\text{sat}}$ -th column of the control effectiveness matrix to  $\mathbf{0}$ :

$$\mathbf{B}_k = \mathbf{B}_{k-1} \mathbf{M}_{\text{sat}}, \quad (5.303)$$

with

$$\mathbf{M}_{\text{sat}} = \text{diag} \left( \left[ \begin{array}{ccccccc} 1 & \cdots & 1 & \underbrace{0}_{i_{\text{sat}}\text{-th column}} & 1 & \cdots & 1 \end{array} \right] \right). \quad (5.304)$$

Steps 2 to 6 are furthermore repeated until either:

- the unconstrained solution from step 2 yields a scaling of  $\alpha = 1$  in step 3, thereby indicating the successful allocation of the (remaining) pseudo control rate vector,
- the column rank of  $\mathbf{B}_{k-1}$  degrades, yielding an ill-posed inversion problem in step 2, or
- some predefined number of maximum iterations  $k_{\text{max}}$  is reached.

In contrast to just clipping the saturated control inputs, which is done for the conventional *Redistributed Pseudo-Inverse* (RPI) algorithm, RSPI scales down the individual control input rate contributions of each iteration in order to meet the limit constraints. Hence, the direction of the allocated pseudo control rate is preserved due to the linear nature of the problem and therefore RSPI guarantees that the solution further improves for each completed iteration.

Note that control effector failures can easily be integrated into the algorithm by preconditioning the control effectiveness matrix  $\mathbf{B}_0$  from step 1 analogously to step 6. However, instead of setting the column of the saturated input to  $\mathbf{0}$ , the column of the failed control effector is set to  $\mathbf{0}$  instead.

**Incremental Nullspace Optimization** The *Incremental Nullspace Optimization* (INO) is aimed at redistributing the control inputs within the (right) nullspace of  $\mathbf{B}$  such as to not violate the allocated pseudo control rate from the RSPI step. To this end, the *Singular Value Decomposition* (SVD) [139] of the control effectiveness matrix  $\mathbf{B} \in \mathbb{R}^{n \times m}$  is utilized:

$$\mathbf{B} = \mathbf{U}\mathbf{\Sigma}\mathbf{V}^T, \quad (5.305)$$

where  $\mathbf{U} \in \mathbb{R}^{n \times n}$  and  $\mathbf{V} \in \mathbb{R}^{m \times m}$  denote unitary matrices for which  $\mathbf{U}\mathbf{U}^T = \mathbf{U}^T\mathbf{U} = \mathbf{I}_{n \times n}$  respectively  $\mathbf{V}\mathbf{V}^T = \mathbf{V}^T\mathbf{V} = \mathbf{I}_{m \times m}$  holds. Furthermore,  $\mathbf{\Sigma} \in \mathbb{R}^{n \times m}$  represents a rectangular diagonal matrix containing the singular values  $\sigma_i \geq 0$  on the diagonal, which are typically ordered in descending order.

Note that for the allocation problem at hand,  $n$  corresponds to the dimension of the commanded pseudo control rate vector  $\dot{\mathbf{v}}_c$  and  $m$  denotes the dimension of the commanded control input rate vector  $\dot{\mathbf{u}}_c$ . Due to the assumed redundancy among the control inputs, it holds that  $n < m$  and hence the control effectiveness matrix yields a short and fat matrix. As a consequence, the rectangular matrix  $\mathbf{\Sigma}$  is a short and fat matrix as well and contains a block of zeros in the last  $m - n$  columns (assuming that the available control inputs span the whole output space, i.e. when  $\text{rank}(\mathbf{B}) = n$ ). Hence, the last  $m - n$  rows of  $\mathbf{V}^T$  (respectively last  $m - n$  columns of  $\mathbf{V}$ ) denote the directions within the input space that are mapped onto zero and are therefore referred to as the (right) *Nullspace* of  $\mathbf{B}$ .

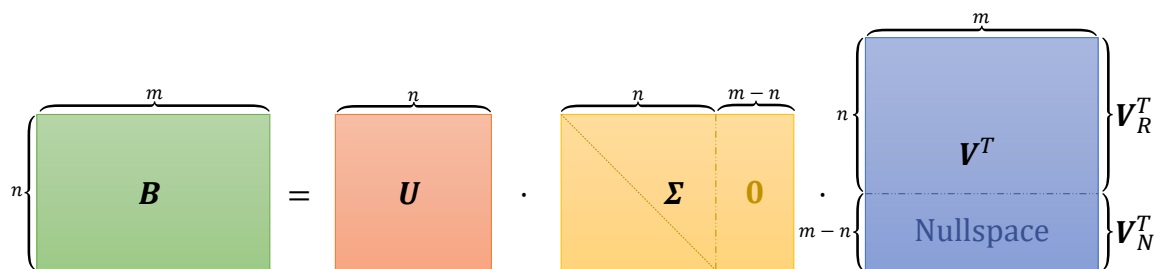


**Figure 5.54:** *Singular Value Decomposition (SVD)*

Figure 5.54 visualizes the *Singular Value Decomposition* for a short and fat control effectiveness matrix  $\mathbf{B}$ . Thereby, the last  $m - n$  rows of  $\mathbf{V}^T$  are denoted as  $\mathbf{V}_N^T$  and represent the orthonormal basis vectors of the nullspace, whereas the first  $n$  rows span the row space of  $\mathbf{B}$  and are denoted as  $\mathbf{V}_R^T$ .

Note that as a consequence, the product of the control effectiveness matrix  $\mathbf{B}$  into the nullspace matrix  $\mathbf{V}_N$

$$\mathbf{B}\mathbf{V}_N = \mathbf{0}_{n \times (m-n)} \quad (5.306)$$

yields the zero matrix, since the column vectors of  $\mathbf{V}_N$  span an orthonormal basis of the nullspace.

The general idea of the *Incremental Nullspace Optimization* is to minimize the distance of the (estimated) control input  $\mathbf{u}_{\text{mdl}}$  towards a predefined trim command  $\mathbf{u}_0$  within the nullspace of the control effectiveness matrix. This objective is aimed at both resolving the ambiguity of the stationary command distribution for a given pseudo control vector and harmonizing the overall control effort in order to yield optimal command constellations.

To this end, the distance vector between the modeled control input  $\mathbf{u}_{\text{mdl}}$  and the trim command value  $\mathbf{u}_0$  projected into the nullspace is denoted as the error signal

$$\mathbf{e}_N = \mathbf{V}_N^T (\mathbf{u}_{\text{mdl}} - \mathbf{u}_0) , \quad (5.307)$$

with  $\mathbf{V}_N$  representing the nullspace matrix, which follows from the SVD in (5.305) and figure 5.54. The objective function is furthermore given by the squared Euclidean norm of the error signal

$$J = \mathbf{e}_N^T \mathbf{e}_N . \quad (5.308)$$

The goal of the nullspace optimization is to yield an additional control input rate command in the nullspace

$$\dot{\mathbf{u}}_N = \mathbf{V}_N \mathbf{k}_N , \quad (5.309)$$

which:

1. does not violate the pseudo control rate allocation from the RSPI step and
2. minimizes the error norm in (5.308).

Both the control input rate from the RSPI algorithm  $\dot{\mathbf{u}}_{\text{RSPI}}$  and the contribution from the nullspace optimization  $\dot{\mathbf{u}}_N$  together make up the final control input rate command of the control allocation

$$\dot{\mathbf{u}}_c = \dot{\mathbf{u}}_{\text{RSPI}} + \dot{\mathbf{u}}_N . \quad (5.310)$$

Note that due to (5.306), the allocated pseudo control rate  $\dot{\boldsymbol{\nu}}_N$  resulting from  $\dot{\mathbf{u}}_N$  is given by

$$\dot{\boldsymbol{\nu}}_N = \mathbf{B}\dot{\mathbf{u}}_N = \underbrace{\mathbf{B}\mathbf{V}_N}_{\mathbf{0}_{n \times (m-n)}} \mathbf{k}_N = \mathbf{0} , \quad (5.311)$$

which by definition yields no contribution to the overall pseudo control objective, thereby satisfying the first requirement.

In order to address the second requirement, the time derivative of the objective function shall yield

$$\dot{J} = 2\mathbf{e}_N^T \dot{\mathbf{e}}_N = 2\mathbf{e}_N^T \mathbf{V}_N^T \dot{\mathbf{u}}_{\text{mdl}} \stackrel{!}{=} -\gamma J, \quad (5.312)$$

which leads to an exponential decay of the objective in (5.308) governed by the constant factor  $\gamma$ .

The final conversion of the control input rate command  $\dot{\mathbf{u}}_c$  into the individual control effector commands, which is discussed in the scope of the *Powered Lift Allocation*, *Aerodynamic Surface Allocation*, and *Traction System Allocation*, is realized by inverting the same relationships that are used to yield the model-based estimation of the control input rate vector  $\dot{\mathbf{u}}_{\text{mdl}}$  based on the control effector commands. Hence, it follows that  $\dot{\mathbf{u}}_c = \dot{\mathbf{u}}_{\text{mdl}}$ . Furthermore, Inserting (5.308), (5.310), and (5.309) into (5.312) yields

$$2\mathbf{e}_N^T \mathbf{V}_N^T \dot{\mathbf{u}}_{\text{RSPI}} + 2\mathbf{e}_N^T \underbrace{\mathbf{V}_N^T \mathbf{V}_N}_{\mathbf{I}} \mathbf{k}_N \stackrel{!}{=} -\gamma \mathbf{e}_N^T \mathbf{e}_N, \quad (5.313)$$

where  $\mathbf{V}_N^T \mathbf{V}_N = \mathbf{I}_{(m-n) \times (m-n)}$  yields the identity matrix, which follows from the orthonormality of the columns in the nullspace matrix  $\mathbf{V}_N$ .

Furthermore, it follows from termwise comparison in (5.313) that the solution vector in nullspace coordinates yields

$$\mathbf{k}_N = -\mathbf{V}_N^T \dot{\mathbf{u}}_{\text{RSPI}} - \frac{\gamma}{2} \mathbf{e}_N \quad (5.314)$$

and hence the overall control input rate contribution from the nullspace optimization follows from (5.309) and is given by

$$\begin{aligned} \dot{\mathbf{u}}_N &= \mathbf{V}_N \mathbf{k}_N = -\mathbf{V}_N \mathbf{V}_N^T \dot{\mathbf{u}}_{\text{RSPI}} - \frac{\gamma}{2} \mathbf{V}_N \mathbf{e}_N \\ &= -\mathbf{V}_N \mathbf{V}_N^T \dot{\mathbf{u}}_{\text{RSPI}} - \frac{\gamma}{2} \mathbf{V}_N \mathbf{V}_N^T (\mathbf{u}_{\text{mdl}} - \mathbf{u}_0), \end{aligned} \quad (5.315)$$

which mathematically corresponds to a projection of both the error signal  $(\mathbf{u}_{\text{mdl}} - \mathbf{u}_0)$  and the nominal RSPI solution  $\dot{\mathbf{u}}_{\text{RSPI}}$  into the nullspace of  $\mathbf{B}$ .

Note that for RSPI solutions that terminate after the first iteration (i.e. without yielding a saturated control input), it follows that  $\dot{\mathbf{u}}_{\text{RSPI}} = \mathbf{B}^\dagger \dot{\mathbf{v}}_c = \mathbf{B}^T (\mathbf{B}\mathbf{B}^T)^{-1} \dot{\mathbf{v}}_c$  and hence the solution for  $\dot{\mathbf{u}}_N$  simplifies to

$$\begin{aligned} \dot{\mathbf{u}}_N &= -\mathbf{V}_N \underbrace{\mathbf{V}_N^T \mathbf{B}^T}_{\mathbf{0}} (\mathbf{B}\mathbf{B}^T)^{-1} \dot{\mathbf{v}}_c - \frac{\gamma}{2} \mathbf{V}_N \mathbf{V}_N^T (\mathbf{u}_{\text{mdl}} - \mathbf{u}_0) \\ &= -\frac{\gamma}{2} \mathbf{V}_N \mathbf{V}_N^T (\mathbf{u}_{\text{mdl}} - \mathbf{u}_0), \end{aligned} \quad (5.316)$$

where  $\mathbf{V}_N^T \mathbf{B}^T = \mathbf{0}_{(m-n) \times n}$  follows from (5.306). For the unsaturated case, the RSPI algorithm yields the minimum-norm solution for  $\dot{\mathbf{u}}_{\text{RSPI}}$  by using the Moore-Penrose Pseudo-Inverse, which does not contain any contribution within the nullspace and hence vanishes upon the projection operation in (5.316).

The resulting solution for  $\dot{\mathbf{u}}_N$  is furthermore scaled according to step 3 from the RSPI algorithm in order to adhere to the control input rate limitations while preserving the direction within the nullspace. To this end, the upper and lower control input rate limits for the scaling of the nullspace solution follow from

$$\begin{aligned}\dot{\mathbf{u}}_{N,\min} &= \dot{\mathbf{u}}_{\min} - \dot{\mathbf{u}}_{\text{RSPI}} \\ \dot{\mathbf{u}}_{N,\max} &= \dot{\mathbf{u}}_{\max} - \dot{\mathbf{u}}_{\text{RSPI}},\end{aligned}\tag{5.317}$$

where  $\dot{\mathbf{u}}_{\text{RSPI}}$  is the nominal solution from the RSPI algorithm and  $\dot{\mathbf{u}}_{\min}$  and  $\dot{\mathbf{u}}_{\max}$  denote the total control input rate limits from (5.299) and (5.300) respectively. Hence, the limits in (5.317) ensure that the control input rate contribution in the nullspace is scaled according to the remaining rate limit constraints after the nominal allocation via RSPI.

**Aerodynamic Surface Allocation** Based on the generalized concepts derived in the context of the *Specific Control Force and Moment Rate Inversion*, the allocation strategy for the aerodynamic surfaces is presented in the following, which yields the final commands to the aerodynamic control effectors. To this end, the pseudo control rate  $\dot{\mathbf{v}}_{\text{AS},c} = \dot{\mathbf{m}}_{\text{AS},c}$  is given according to (5.296), where  $\dot{\mathbf{m}}_{\text{AS},c}$  follows from (5.289). Furthermore, the aerodynamic surface control effectiveness matrix  $\mathbf{B} = \mathbf{B}_{m \leftarrow u_{\text{AS}}}(V_{\text{CAS}})$  from (5.279) is used in the RSPI and INO algorithm.

Based on the definition of the control input rate vector for the aerodynamic surfaces

$$\dot{\mathbf{u}}_{\text{AS}} = \begin{bmatrix} \dot{\delta}_1 \\ \vdots \\ \dot{\delta}_{m_{\text{AS}}} \end{bmatrix},\tag{5.318}$$

it follows for the upper and lower control input rate limit according to (5.299) and (5.300):

$$\begin{aligned}\dot{u}_{\text{AS},\min,i} &= \max(\dot{u}_{\text{AS},\text{abs},\min,i}, \dot{u}_{\text{AS},u_{\text{lim}},\min,i}), \\ \dot{u}_{\text{AS},\max,i} &= \min(\dot{u}_{\text{AS},\text{abs},\max,i}, \dot{u}_{\text{AS},u_{\text{lim}},\max,i}),\end{aligned}\tag{5.319}$$

where  $\dot{u}_{\text{AS},\text{abs},\min,i} = \dot{\delta}_{\text{abs},\min,i}$  and  $\dot{u}_{\text{AS},\text{abs},\max,i} = \dot{\delta}_{\text{abs},\max,i}$  denote the absolute minimum and maximum rate limits of the  $i$ -th control input respectively, which correspond to the minimum and maximum rate limit of the  $i$ -th aerodynamic control surface.

Furthermore,

$$\begin{aligned}\dot{u}_{\text{AS},u_{\text{lim}},\min,i} &= K_{\delta_{\text{lim},i}} (\delta_{\min,i} - \delta_{\text{mdl},i}), \\ \dot{u}_{\text{AS},u_{\text{lim}},\max,i} &= K_{\delta_{\text{lim},i}} (\delta_{\max,i} - \delta_{\text{mdl},i})\end{aligned}\tag{5.320}$$

denote the control input rates for which the modeled aerodynamic surface deflection  $\delta_{\text{mdl},i}$  converges to its absolute lower or upper limit  $\delta_{\min,i}$ ,  $\delta_{\max,i}$  respectively with the convergence rate  $K_{\delta_{\text{lim},i}}$ .

After applying the RSPI and INO algorithm, it follows the control input rate command for the aerodynamic surfaces  $\dot{\mathbf{u}}_{AS,c} = [\dot{\delta}_{c,1} \ \cdots \ \dot{\delta}_{c,m_{AS}}]^T$ . Furthermore, using the generalized control effector dynamics equation from (5.269), it follows for each aerodynamic surface deflection rate that

$$\dot{\delta}_i = \min \left( \dot{\delta}_{\max,i} \max \left( \dot{\delta}_{\min,i}, K_{\delta_i} (\delta_{c,i} - \delta_{mdl,i}) \right) \right) \stackrel{!}{=} \dot{\delta}_{c,i}. \quad (5.321)$$

Note that since RSPI and INO necessarily provide solutions that lie within the set of admissible control input rates, the min and max operations in (5.321) can be omitted for the inversion and it follows for each control effector command:

$$\delta_{c,i} = \delta_{mdl,i} + \underbrace{K_{\delta_i}^{-1} \dot{\delta}_{c,i}}_{\Delta \delta_{c,i}}, \quad (5.322)$$

where  $K_{\delta_i}$  denotes the aerodynamic surface's bandwidth and  $\dot{\delta}_{c,i} = \dot{u}_{AS,c,i}$  follows from the control input rate solution  $\dot{\mathbf{u}}_{AS,c}$  from the RSPI and INO algorithm.

Despite the preceding distribution of the required specific moment rate between the powered lift motors and the aerodynamic surfaces based on the dynamic pressure, uncertainties or failures among the aerodynamic control surfaces can lead to failed allocation of the complete specific moment rate demand. Therefore, the portion of the specific moment rate  $\Delta \dot{\mathbf{m}}_{exc}$ , which cannot be allocated due to saturation of aerodynamic control surfaces, is added to the specific moment rate target of the powered lift motors, which is similar to the *Daisy Chaining* [133] method.

To this end, the specific moment rate deficit follows from the difference of the commanded and the allocated specific moment rate:

$$\Delta \dot{\mathbf{m}}_{exc} = \dot{\mathbf{m}}_{AS,c} - \mathbf{B}_{m \leftarrow u_{AS}} \dot{\mathbf{u}}_{AS,c} \quad (5.323)$$

and is used in the next allocation step.

**Powered Lift Allocation** The *Powered Lift Allocation* yields the final commands to the powered lift motors, which shall lead to the required control input rate vector  $\dot{\mathbf{u}}_{PL,c}$  resulting from the RSPI and INO step. To this end, the commanded pseudo control rate

$$\dot{\mathbf{v}}_{PL,c} = \begin{bmatrix} \dot{f}_{Bz,c} \\ \dot{\mathbf{m}}_{PL,c} + \Delta \dot{\mathbf{m}}_{exc} \end{bmatrix} \quad (5.324)$$

follows from augmenting (5.295) with the excess specific moment rate  $\Delta \dot{\mathbf{m}}_{exc}$  from (5.323) and using  $\dot{\mathbf{m}}_{PL,c}$  from (5.288). Furthermore, the powered lift control effectiveness matrix  $\mathbf{B} = \mathbf{B}_{\nu_{PL} \leftarrow u_{PL}}$  from (5.277) is used for the inversion and nullspace optimization.

Based on the definition of the control input rate vector for the powered lift motors

$$\dot{\mathbf{u}}_{PL} = \frac{d}{dt} \begin{bmatrix} w_{PL,1}^2 \\ \vdots \\ w_{PL,m_{PL}}^2 \end{bmatrix} = \begin{bmatrix} 2w_{PL,1} \dot{w}_{PL,1} \\ \vdots \\ 2w_{PL,m_{PL}} \dot{w}_{PL,m_{PL}} \end{bmatrix}, \quad (5.325)$$

it follows for the upper and lower control input rate limit according to (5.299) and (5.300):

$$\begin{aligned}\dot{u}_{\text{PL},\text{min},i} &= \max(\dot{u}_{\text{PL},\text{abs},\text{min},i}, \dot{u}_{\text{PL},u_{\text{lim}},\text{min},i}), \\ \dot{u}_{\text{PL},\text{max},i} &= \min(\dot{u}_{\text{PL},\text{abs},\text{max},i}, \dot{u}_{\text{PL},u_{\text{lim}},\text{max},i}),\end{aligned}\quad (5.326)$$

where  $\dot{u}_{\text{PL},\text{abs},\text{min},i} = 2w_{\text{PL},\text{mdl},i}\dot{w}_{\text{PL},\text{abs},\text{min},i}$  and  $\dot{u}_{\text{PL},\text{abs},\text{max},i} = 2w_{\text{PL},\text{mdl},i}\dot{w}_{\text{PL},\text{abs},\text{max},i}$  denote the absolute minimum and maximum rate limits of the  $i$ -th control input, which are a function of the minimum and maximum rotational acceleration limit of the  $i$ -th powered lift motor  $\dot{w}_{\text{PL},\text{abs},\text{min},i}$  and  $\dot{w}_{\text{PL},\text{abs},\text{max},i}$  respectively.

Furthermore,

$$\begin{aligned}\dot{u}_{\text{PL},u_{\text{lim}},\text{min},i} &= 2w_{\text{PL},\text{mdl},i}K_{w_{\text{PL},\text{lim},i}}(w_{\text{PL},\text{min},i} - w_{\text{PL},\text{mdl},i}), \\ \dot{u}_{\text{PL},u_{\text{lim}},\text{max},i} &= 2w_{\text{PL},\text{mdl},i}K_{w_{\text{PL},\text{lim},i}}(w_{\text{PL},\text{max},i} - w_{\text{PL},\text{mdl},i})\end{aligned}\quad (5.327)$$

denote the control input rates for which the modeled powered lift motor rotational rate  $w_{\text{PL},\text{mdl},i}$  converges to its absolute lower or upper limit  $w_{\text{PL},\text{min},i}$ ,  $w_{\text{PL},\text{max},i}$  respectively with the convergence rate  $K_{w_{\text{PL},\text{lim},i}}$ .

Analogously to the *Aerodynamic Surface Allocation*, the generalized control effector dynamics from (5.269) are used to yield the final powered lift motor command

$$w_{\text{PL},c,i} = w_{\text{PL},\text{mdl},i} + \underbrace{K_{w_{\text{PL},i}}^{-1}}_{\Delta w_{\text{PL},c,i}} \dot{w}_{\text{PL},c,i}, \quad (5.328)$$

where  $K_{w_{\text{PL},i}}$  denotes the powered lift motor's bandwidth. The powered lift motor rotational acceleration command  $\dot{w}_{\text{PL},c,i}$  follows via (5.325) and yields

$$\dot{w}_{\text{PL},c,i} = \frac{\dot{u}_{\text{PL},c,i}}{2w_{\text{PL},\text{mdl},i}}, \quad (5.329)$$

with the  $i$ -th control input rate command  $\dot{u}_{\text{PL},c,i}$  resulting from the RSPI and INO step. As was mentioned in section 5.1, the denominator in (5.329) needs to be protected due to the singularity for  $w_{\text{PL},\text{mdl},i} = 0$ , which originates from the quadratic relationship between the motor speed and the generated pseudo control [83] [84] and the resulting vanishing gradients at zero rotational motor rates.

Note that due to the *Specific Moment Rate Mixing*, the assigned specific moment rate to the powered lift motors  $\dot{\mathbf{m}}_{\text{PL},c}$  leads to the allocation of a stationary specific moment  $\mathbf{m}_{\text{PL},0} = \mathbf{0}$  at high dynamic pressures according to (5.291). This renders the powered lift system a pure lift producer at higher velocities, which allows for a seamless deactivation upon entering the wingborne phase. Additionally, the allocation of the excess specific moment rate  $\Delta \dot{\mathbf{m}}_{\text{exc}}$  from (5.323) is omitted upon entering the wingborne phase.

Similar to the deficit in the allocated aerodynamic specific moment rates from (5.323), the traction system can be used to support the powered lift system in generating yaw moments. As was pointed out in section 4.2 and section 4.3, the capability of conventional multi-rotor systems to produce yaw moments is limited in comparison to traditional helicopters equipped with a tail rotor.

Therefore, the deficit in the allocated specific yaw moment rate by the powered lift system

$$\Delta\dot{m}_{Bz,exc} = \begin{bmatrix} 0 & 0 & 0 & 1 \end{bmatrix} (\dot{\boldsymbol{\nu}}_{PL,c} - \mathbf{B}_{\boldsymbol{\nu}_{PL} \leftarrow \mathbf{u}_{PL}} \dot{\mathbf{u}}_{PL,c}) \quad (5.330)$$

is obtained by subtracting the allocated powered lift pseudo control rate  $\mathbf{B}_{\boldsymbol{\nu}_{PL} \leftarrow \mathbf{u}_{PL}} \dot{\mathbf{u}}_{PL,c}$  from the commanded one  $\dot{\boldsymbol{\nu}}_{PL,c}$  and considering the fourth entry corresponding to the yaw channel. The excess specific yaw moment rate  $\Delta\dot{m}_{Bz,exc}$  is furthermore used in the *Traction System Allocation*.

**Traction System Allocation** The *Traction System Allocation* follows analogously to the *Powered Lift Allocation* and yields the final commands to the traction motors, which shall lead to the required control input rate vector  $\dot{\mathbf{u}}_{TS,c}$  resulting from the RSPI and INO step. Note that the failure condition for the traction system is treated separately to the failure of a powered lift motor or an aerodynamic control surface, since the loss of a traction motor is assumed to yield a rank deficient mapping with respect to the forward force and yaw moment channel.

In particular, it is assumed in this context that the failure of a traction motor leads to an unilateral thrust condition thereby coupling the generation of thrust and yaw moments. When considering VTOL configurations for which the traction motors are aligned along the longitudinal axis of the aircraft (e.g. as a pusher and puller configuration), the presented approach for commanding the traction system simplifies to a pure forward thrust allocation.

However, within the scope of the presented control architecture, it is assumed that the traction motors have a lever arm in body-lateral direction, which enables the generation of yaw moments using differential thrust. To this end, the allocation is conditioned on the failure case of the traction system:

- In the nominal case (i.e. if *Traction System Degraded* == false), the allocated pseudo control rate vector is given by

$$\dot{\boldsymbol{\nu}}_{TS,c} = \begin{bmatrix} \dot{f}_{Bx,c} \\ \Delta\dot{m}_{Bz,exc} \end{bmatrix} \quad (5.331)$$

according to (5.297), where  $\Delta\dot{m}_{Bz,exc}$  follows from (5.330). Furthermore, the traction system control effectiveness matrix  $\mathbf{B}_{\boldsymbol{\nu}_{TS} \leftarrow \mathbf{u}_{TS}}(V_{CAS}, \boldsymbol{\beta}_{TS,mdl})$  from (5.281) is used for the inversion within the RSPI algorithm.

However, for the nullspace optimization within the INO step, the reduced traction system control effectiveness matrix  $\mathbf{B}_{f_{Bx} \leftarrow \mathbf{u}_{TS}}$  from (5.281) is used, which only accounts for the generation of forward specific force rates. As a consequence, the *Incremental Nullspace Optimization* distributes and equalizes the traction motor rotational rates within the nullspace of the forward force only, thereby generating a specific yaw moment rate  $\Delta\dot{m}_{Bz,TS} = \mathbf{B}_{m_{Bz} \leftarrow \mathbf{u}_{TS}} \dot{\mathbf{u}}_{N,TS}$ .



Thereby,  $\dot{\mathbf{u}}_{N,TS}$  represents the nullspace solution from (5.315). In order to compensate the uncommanded yaw moment rate,  $\Delta\dot{m}_{Bz,TS}$  is subtracted from the total specific moment rate demand  $\dot{\mathbf{m}}_c$ . In doing so, the traction motors slowly converge to a symmetrical constellation without changing the forward thrust, while the thereby induced change in yaw moment is canceled out by the aerodynamic surfaces and powered lift motors. Note that in case the induced specific yaw moment rate due to the nullspace optimization cannot be compensated, the deficit is fed back via (5.330) and cancels out the INO portion of the command in the RSPI step.

- In the failure case (i.e. if *Traction System Degraded* == true), the allocated pseudo control rate vector reduces to merely the forward specific force and is given by

$$\dot{\mathbf{v}}_{TS,fail,c} = \dot{f}_{Bx,c}, \quad (5.332)$$

where the reduced traction system control effectiveness matrix  $\mathbf{B}_{f_{Bx} \leftarrow \mathbf{u}_{TS}}(V_{CAS}, \boldsymbol{\beta}_{TS,mdl})$  from (5.281) is used for the inversion within the RSPI algorithm. Similarly to the nominal case, the same reduced traction system control effectiveness matrix  $\mathbf{B}_{f_{Bx} \leftarrow \mathbf{u}_{TS}}$  is used within the nullspace optimization in the failure case. This time, the optimization is concerned with equalizing the remaining traction motor RPMs on either side of the transition aircraft. Note that in case of only two traction motors, the INO step is omitted upon a traction motor failure, as there is no nullspace to perform the optimization in.

In either case, the resulting total control input rate command  $\dot{\mathbf{u}}_{TS,c}$  yields a specific yaw moment rate  $\Delta\dot{m}_{Bz,TS,fail} = \mathbf{B}_{m_{Bz} \leftarrow \mathbf{u}_{TS}} \dot{\mathbf{u}}_{TS,c}$ , which is compensated by subtracting it from the total specific moment rate demand  $\dot{\mathbf{m}}_c$ . In case the traction system induced yaw moment cannot be compensated by the aerodynamic control surfaces and powered lift motors, the forward thrust is limited such as to not yield excessive sideslip angles.

Furthermore, based on the definition of the control input rate vector for the traction motors

$$\dot{\mathbf{u}}_{TS} = \frac{d}{dt} \begin{bmatrix} w_{TS,1}^2 \\ \vdots \\ w_{TS,m_{TS}}^2 \end{bmatrix} = \begin{bmatrix} 2w_{TS,1}\dot{w}_{TS,1} \\ \vdots \\ 2w_{TS,m_{TS}}\dot{w}_{TS,m_{TS}} \end{bmatrix}, \quad (5.333)$$

it follows for the upper and lower control input rate limit according to (5.299) and (5.300):

$$\begin{aligned} \dot{u}_{TS,min,i} &= \max(\dot{u}_{TS,abs,min,i}, \dot{u}_{TS,u_{lim},min,i}), \\ \dot{u}_{TS,max,i} &= \min(\dot{u}_{TS,abs,max,i}, \dot{u}_{TS,u_{lim},max,i}), \end{aligned} \quad (5.334)$$

where  $\dot{u}_{TS,abs,min,i} = 2w_{TS,mdl,i}\dot{w}_{TS,abs,min,i}$  and  $\dot{u}_{TS,abs,max,i} = 2w_{TS,mdl,i}\dot{w}_{TS,abs,max,i}$  denote the absolute minimum and maximum rate limits of the  $i$ -th control input, which are a function of the minimum and maximum rotational acceleration limit of the  $i$ -th traction motor  $\dot{w}_{TS,abs,min,i}$  and  $\dot{w}_{TS,abs,max,i}$  respectively.

Furthermore,

$$\begin{aligned}\dot{w}_{\text{TS},u_{\text{lim},\text{min},i}} &= 2w_{\text{TS},\text{mdl},i}K_{w_{\text{TS},\text{lim},i}}(w_{\text{TS},\text{min},i} - w_{\text{TS},\text{mdl},i}), \\ \dot{w}_{\text{TS},u_{\text{lim},\text{max},i}} &= 2w_{\text{TS},\text{mdl},i}K_{w_{\text{TS},\text{lim},i}}(w_{\text{TS},\text{max},i} - w_{\text{TS},\text{mdl},i})\end{aligned}\quad (5.335)$$

denote the control input rates for which the modeled traction motor rotational rate  $w_{\text{TS},\text{mdl},i}$  converges to its absolute lower or upper limit  $w_{\text{TS},\text{min},i}$ ,  $w_{\text{TS},\text{max},i}$  from (5.284) respectively with the convergence rate  $K_{w_{\text{TS},\text{lim},i}}$ .

Again, each traction motor rotational rate command follows from inverting the generalized control effector dynamics from (5.269) and is given by

$$w_{\text{TS},c,i} = w_{\text{TS},\text{mdl},i} + \underbrace{K_{w_{\text{TS},i}}^{-1}\dot{w}_{\text{TS},c,i}}_{\Delta w_{\text{TS},c,i}}, \quad (5.336)$$

where  $K_{w_{\text{TS},i}}$  denotes the traction motor's bandwidth. The traction motor rotational acceleration command  $\dot{w}_{\text{TS},c,i}$  is derived from (5.333) and yields

$$\dot{w}_{\text{TS},c,i} = \frac{\dot{w}_{\text{TS},c,i}}{2w_{\text{TS},\text{mdl},i}}. \quad (5.337)$$

Thereby, the  $i$ -th control input rate command  $\dot{w}_{\text{TS},c,i}$  results from the RSPI and INO step. Analogously to the *Powered Lift Allocation*, the denominator in (5.337) shall be protected due to the singularity for  $w_{\text{TS},\text{mdl},i} = 0$ .

Furthermore, each traction motor blade pitch command  $\beta_{\text{TS},c,i} = f(V_{\text{CAS}})$  follows from a lookup table over the calibrated airspeed  $V_{\text{CAS}}$ , which optimizes the inflow angle of the propeller for a given airspeed and thrust value based on trim calculations. However, a detailed derivation is not in the scope of this thesis. By passing the blade pitch commands through the controller-intern effector models, the estimated blade pitch angles  $\beta_{\text{TS},\text{mdl}}$  are furthermore used in order to generate the required traction system control effector matrix  $B_{\nu_{\text{TS}} \leftarrow u_{\text{TS}}}(V_{\text{CAS}}, \beta_{\text{TS},\text{mdl}})$  from (5.281).

## 5.4 Verification and Validation of Control Architecture

After having derived the functional specification of the controller in section 5.3, the resulting Control Architecture Specification Model (CASM) is used for verification and validation of the proposed controller requirements. To this end, the CASM is simulated together with a functional model of the VTOL transition aircraft, which is referred to as *plant* from here on.

Note that the plant's interfaces shall be consistent with the presupposed input and output signals of the CASM, which were summarized in the beginning of section 5.3. In particular, the topology of available force and moment producers as well as sensor signals

shall be compatible with the assumptions made in the scope of the control architecture development. Furthermore, the simulated sensor signals are augmented by dirt effects such as vibrations, delays, and sensor noise.

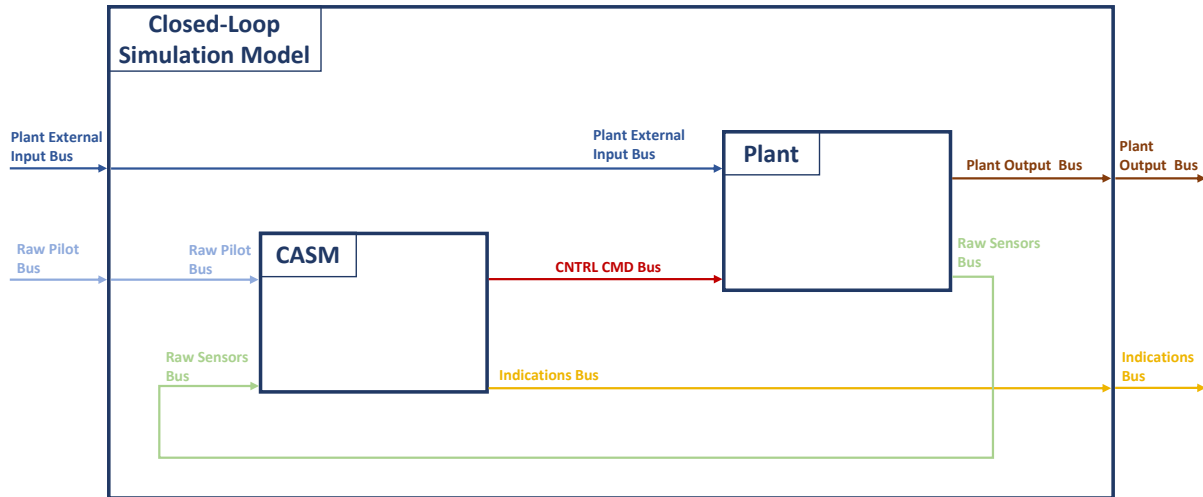


**Figure 5.55:** *Closed-Loop Model with CASM and Plant*

Figure 5.55 shows the general structure of the closed-loop simulation model, which is used for both automatic requirement assessment as well as manual pilot-in-the-loop tests in a simulator mockup such as shown in figure 3.10 and 4.21. The inputs to the *Closed-Loop Simulation Model* consist of the *Raw Pilot Bus*, which contains all pilot inputs such as control inceptor deflections and button presses, and the *Plant External Input Bus*, which contains additional external input signals to the plant model regarding failures, atmospheric disturbances, uncertainties, configuration management, and initial conditions.

The outputs are given by the *Plant Output Bus*, which contains all relevant signals of the VTOL transition aircraft and its subsystems including kinematic states (such as accelerations, velocities, rotational rates, and attitude), control effector states (such as deflections, rotational rates, loads, currents), and additional signals that are needed to verify and validate the interaction of CASM and plant. Furthermore, the *Indications Bus* from the CASM is output as well such as to integrate relevant controller indications into a pilot-in-the-loop simulation environment.

Since the overall interaction between pilot, CASM, and plant has to be assessed as a whole, pilot indications are an important factor that influence the emergent behavior of the overall system and are hence crucial for the validation process. However, a detailed break-down of which information is displayed to the pilot in what manner falls under the focus of human-machine interface (HMI) design and is therefore not in the scope of this thesis.

The development of the CASM and the decomposition into its functional subsystems is aimed at meeting the high-level requirements imposed by the behavioral specification from section 4.2 as well as additional safety requirements regarding failure mitigation in the context of the plant's functional topology. To this end, the control architecture was successively broken down into functional blocks throughout section 5.3. Thereby, the individual blocks as well as the aggregation and interaction of multiple blocks represent the functional low-level requirements of the controller, which can be further decomposed into derived functional elements and requirements on the lower levels.

Within the scope of the verification and validation of the CASM, the following questions are of particular interest:

- Does a given functional element on the lowest level of the controller specification correctly implement the requirement that it represents (horizontal verification)?
- Does a given controller subsystem and the decomposition into its functional elements meet the low-level requirements that drove the design of the controller subsystem (local vertical verification)?
- Does the overall control architecture and the decomposition into the individual controller subsystems meet the high-level requirements that drove the design of the controller (global vertical verification)?
- Does the proposed control architecture represent a valid design solution, which satisfies all stakeholder and user needs, goals, and objectives (validation)?

As can be seen, the questions are ordered from the particular to the general and thereby resemble the rising right branch of the presented 'V'-shaped process model from subsection 2.2.2, which was concerned with the integration, verification, and validation of the final controller. However, in this context the same process is applied to the CASM only, thereby yielding a virtual 'V'-model approach that is nested within the descending left branch of the global 'V'-shaped process model.

Additionally, the terms *local vertical verification* and *global vertical verification* are used in order to differentiate between the verification of a given controller subsystem or the overall architecture against low-level or high-level requirements respectively. The different types of verification are furthermore illustrated in figure 5.56.

The *horizontal verification* step is in general concerned with verifying if elementary building blocks of the CASM such as sums, products, switching blocks, min and max operations, singular value decompositions, inversions, or integrators behave according to their specifications and hence are correctly implemented. By using a high-fidelity modeling environment such as Matlab Simulink [78], the *horizontal verification* step is omitted, because it is assumed that the provided elementary blocks yield the correct functional behavior.

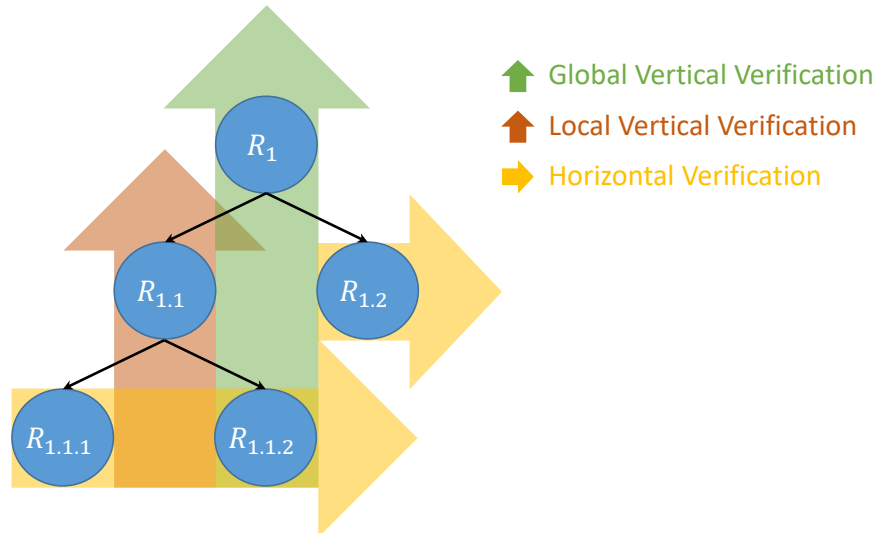


**Figure 5.56:** *Types of Verification for Requirements on Different Levels*

Note that the decision of what falls under the category of *horizontal verification* is mainly driven by the choice of abstraction level for a given element in the architecture. Only those elements that are not further decomposed vertically are verified in a horizontal manner, which is illustrated in figure 5.56. The underlying assumption is that although an elementary building block of the architecture could always be further broken down into smaller parts (such as a sum block that is decomposed into individual bit operations in the context of the simulation program running on an operating system installed on a computing platform made of individual transistors, etc.), it is represented as a black box, whose emergent property is a placeholder for the underlying structure that creates its behavior.

In the scope of the *local vertical verification*, the functionality of e.g. the *Control Effector Estimation*, *Complementary Filter*, *Control Allocation*, *Rotational Acceleration Control*, and *Euler Angle Rate Control* are assessed. Thereby, the various controller subsystems and the corresponding low-level requirements are verified bottom-up, which facilitates a systematic assessment of the controller. In particular, this means that e.g. the function of the *Complementary Filter* is verified before the *Rotational Acceleration* block, since latter is dependent on the acceleration feedback of the former.

As part of the *global vertical verification*, the overall control architecture and the interaction of all its subsystems is verified against e.g. the high-level objectives for height rate tracking during low- and high-speed operation as well as the tracking requirements for side-step maneuvers during hover flight. Note that the exemplary simulation tests in the following subsections are non-exhaustive and shall only give a general idea of the model-based verification and validation activity during the flight control architecture development.

### 5.4.1 Bottom-Up Verification of Side-Step Maneuver

This subsection is aimed to give insight into an exemplary bottom-up verification process of a lateral velocity maneuver by means of model-based simulation. The implementation of the CASM and the plant model were performed in Matlab Simulink [78] at the Institute of Flight System Dynamics (FSD) of the Technical University of Munich (TUM).

#### 5.4.1.1 Plant Description

The plant is implemented as a multi-component 6-DOF rigid-body simulation model including high-fidelity aerodynamics and higher-order nonlinear control effector models, which reflect the physical characteristics through explicit consideration of electric current limitations. Additionally, atmospheric models such as the International Standard Atmosphere (ISA) for static effects as well as gust and turbulence models for dynamic effects are used in order to increase the fidelity of the simulation.

The simulated sensor signals, which were summarized in the beginning of section 5.3, are furthermore corrupted by vibration and noise effects. Hence, the attenuation of undesired signal noise by the overall control architecture can be evaluated in a closed-loop manner as well.

The overall VTOL transition aircraft yields a lift-to-cruise configuration and is similar to the concept depicted in e.g. figure 5.33. In particular, it is equipped with 8 powered lift motors, 2 traction motors, 4 elevators, 4 ailerons, and 2 rudders. The overall dimensions correspond to an optionally person-carrying aircraft configuration.

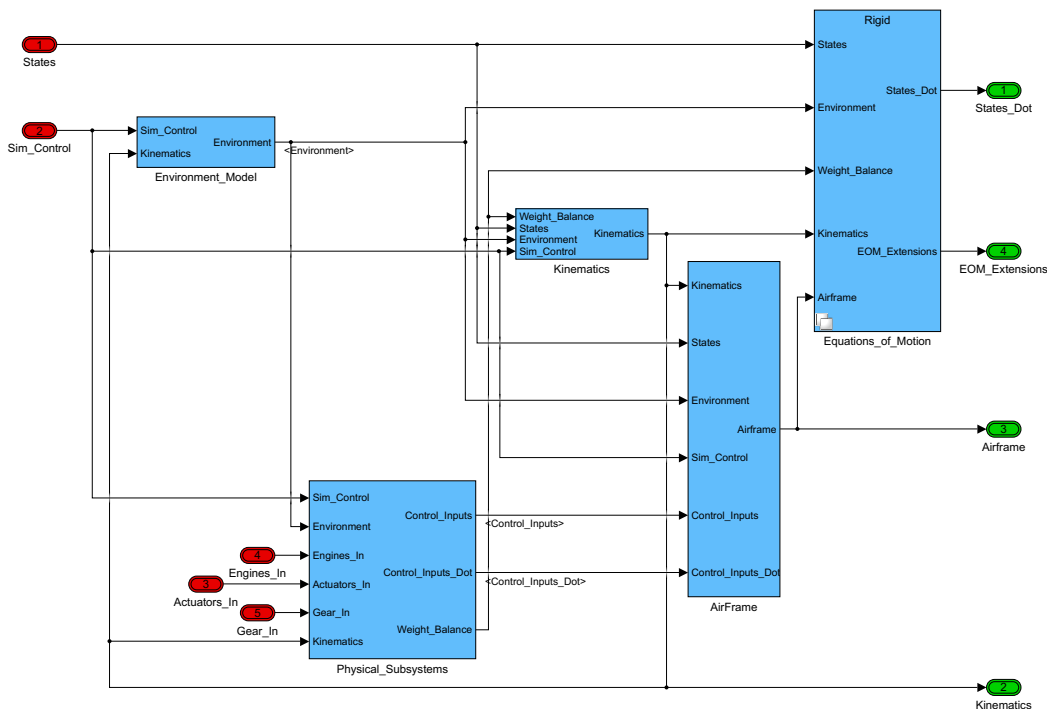
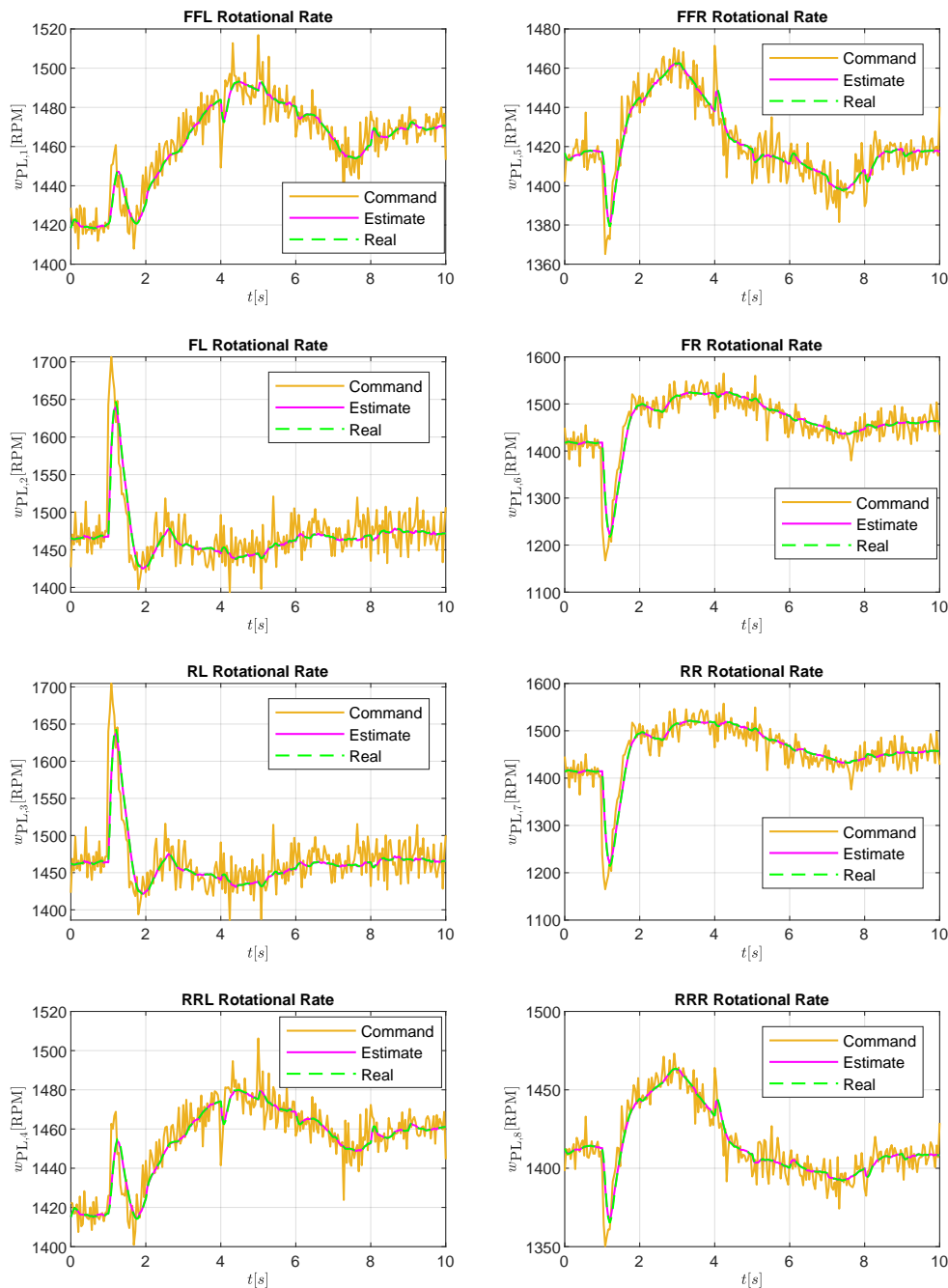


Figure 5.57: Core of Plant Simulation Model in Matlab Simulink

### 5.4.1.2 Simulation Results

After an initial stabilization phase, the aircraft starts from a hovering state at rest and a side-step maneuver is initiated by injecting an unit step into the lateral channel of the thrust stick  $d_{TS,y}$  at time  $t = 1$  s. Figure 5.58 shows the resulting command, estimation, and real RPM values of the 8 powered lift motors, which are named according to their relative positions on the lifting bars: Front-Front-Left (FFL), Front-Front-Right (FFR), Front-Left (FL), Front-Right (FR), Rear-Left (RL), Rear-Right (RR), Rear-Rear-Left (RRL), and Rear-Rear-Right (RRR).



**Figure 5.58:** Powered Lift Motor RPMs During Side-Step Maneuver

The evaluation of the powered lift motor estimation models from figure 5.51, which are located within the inner loop of the CASM, enables:

- the verification of the proposed design of the control effector models implementing the dynamics from (5.269), (5.270), and (5.271), as well as
- the verification of the specified control effector parameters within the controller regarding rate limits and bandwidth.

Thereby, the correct choice of rate limits and bandwidth for the motors and actuators is crucial not only for the accurate estimation of RPMs and surface deflections, but also for the (incremental) allocation of pseudo control rates within the *Control Allocation* block from figure 5.53. In particular, the control effector rate (and absolute) limits are used to constrain the admissible set of control input rate solutions, and the control effector bandwidth is used within the control effector inversion in (5.322), (5.328), and (5.336).

Note that despite the noisy powered lift command signals in figure 5.58, which are the result of vibrations and sensor noise, the estimated and real RPM values are smooth, because the plant motor models and controller motor models act as a filter.

Since the lateral side-step maneuver yields a roll response of the VTOL aircraft, the allocation of the commanded specific roll moment rate  $\dot{m}_{x,c}$  is verified next. To this end, figure 5.59 shows the commanded specific control roll moment rate  $\dot{m}_{x,c}$  (yellow solid line) and the resulting real specific control roll moment rate  $\dot{m}_x$  (green dashed line).

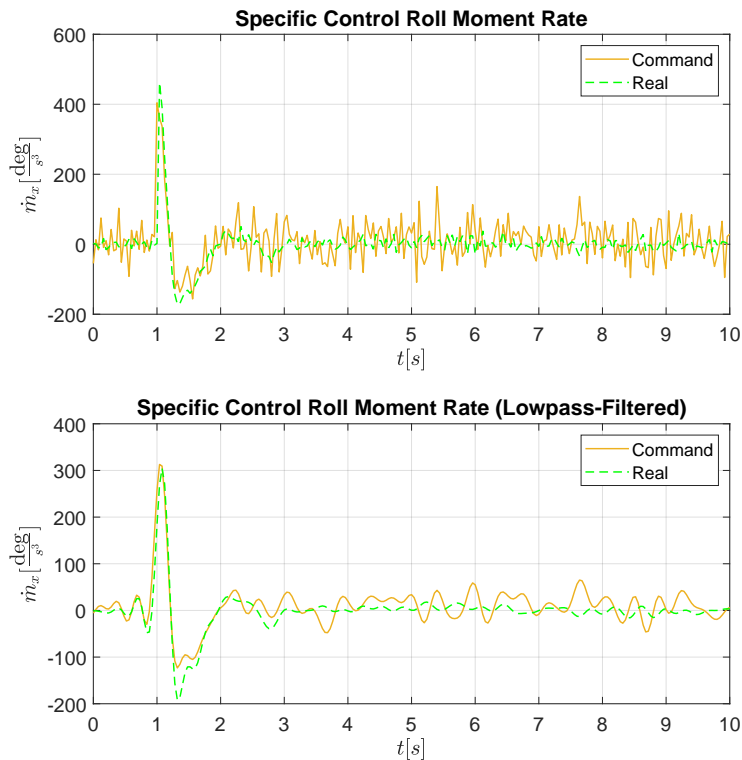


**Figure 5.59:** *Specific Control Roll Moment Rate*



The lowpass-filtered signals in the lower half of figure 5.59 thereby enable a comparison between commanded and real value. Furthermore, assessing the allocation of the commanded pseudo control rate enables:

- the verification of the designed control allocation algorithm, in particular the verification of the pseudo control rate inversion into control input rates and the subsequent inversion into the final control effector commands, and
- the verification of the specified control effectiveness parameters, which are embodied in the control effectiveness matrices  $\mathbf{B}$ .

Additionally to calculating the control effector commands, the *Control Allocation* also yields the model-based estimations of the control effector induced specific moments and forces, which are used in the *Complementary Filter* in order to calculate the model-based estimation of e.g. the roll acceleration  $\dot{p}_{\text{mdl}}$  according to (5.214). Latter is fused together with the measurement of the roll rate  $p_{\text{msr}}$  according to the complementary filter architecture depicted in figure 5.46.

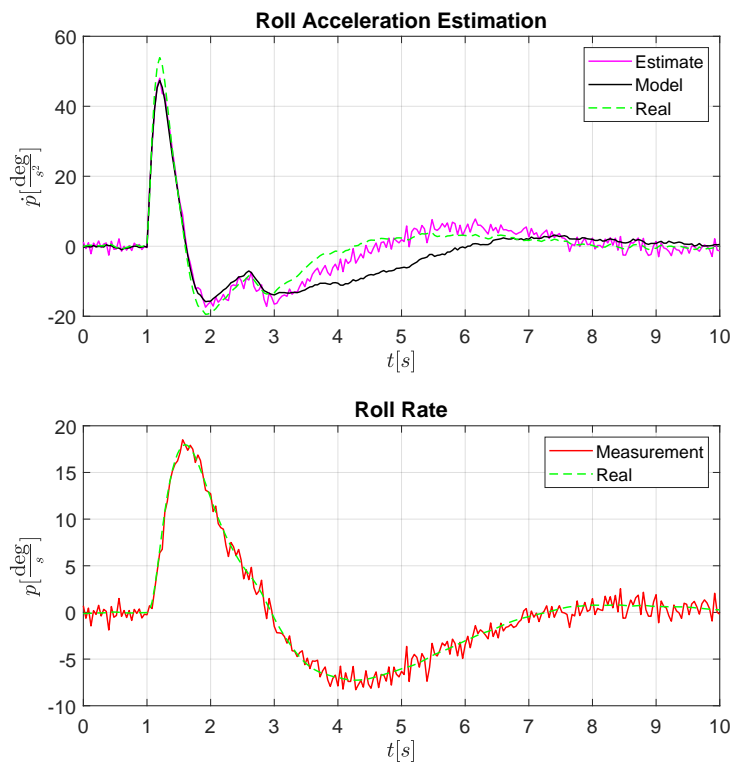


**Figure 5.60:** *Roll Acceleration Estimation*

The upper plot in figure 5.60 thereby shows the complementary filtered roll acceleration signal  $\dot{p}_F$  according to (5.211) (magenta solid line), the model-based roll acceleration  $\dot{p}_{\text{mdl}}$  according to (5.214) (black solid line), and the real roll acceleration  $\dot{p}$  (green dashed line). The lower plot in figure 5.60 shows the real roll rate  $p$  (green dashed line) and the measured roll rate  $p_{\text{msr}}$  (red solid line), which is corrupted by vibrations and noise.

Despite the differentiating characteristics of the roll acceleration filter with respect to the noisy roll rate measurement, complementing the estimation with the model-based smooth roll acceleration signal results in a significantly improved signal-to-noise ratio. Note that the model-based roll acceleration  $\dot{p}_{\text{mdl}}$  significantly diverges from the real roll acceleration  $\dot{p}$  in the time window  $3\text{ s} \leq t \leq 7\text{ s}$ , which leads to a deviation in the roll acceleration estimation. However, since the complementary filter architecture only considers the high-frequency portion of the model-based estimation, the deviation is gradually washed out over time according to the bandwidth of the filter.

The divergence of the model-based roll acceleration signal is furthermore rooted in the presence of an additional aerodynamic roll moment due to the lateral airflow during the side-step maneuver, which is not considered in the calculation of the induced control moments. The roll angle and lateral velocity during the maneuver are depicted in the first plot of figure 5.61 and show that the deviation in estimated roll acceleration correlates with the simultaneous presence of both an increased roll angle and lateral velocity value, which lead to a vertical airflow on the wing and hence induce a roll moment.

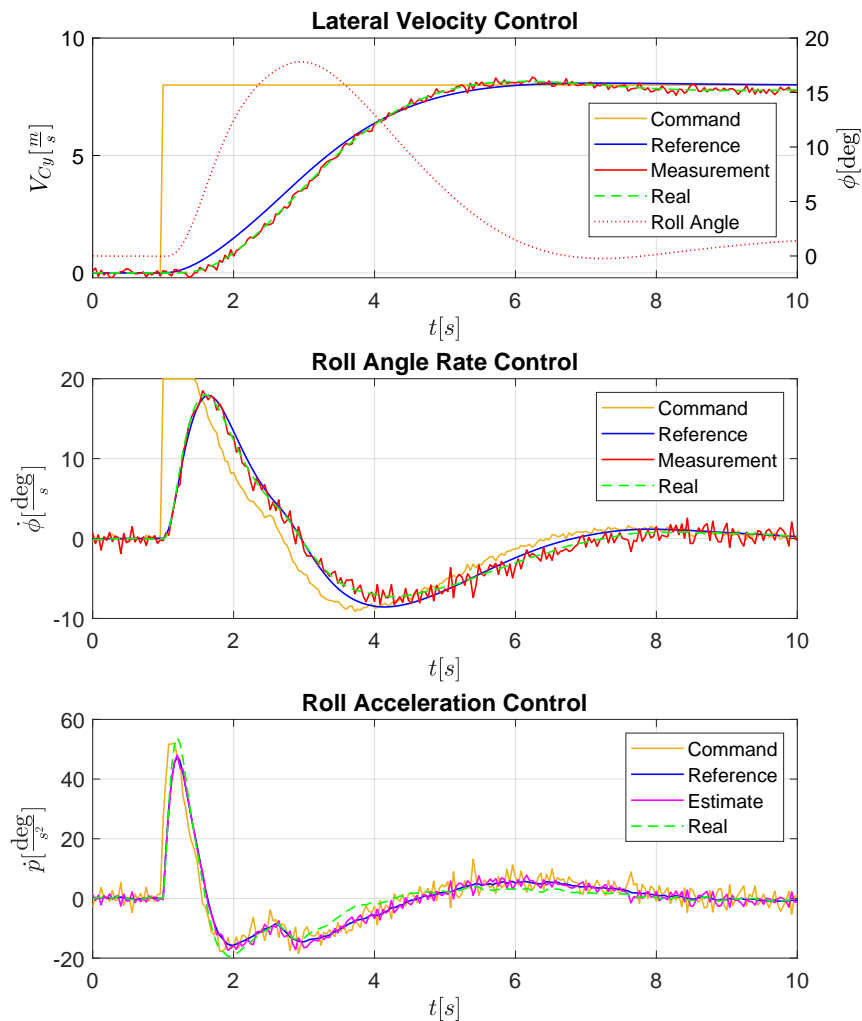


**Figure 5.61:** *Tracking Performance During Side-Step Maneuver*

The three plots in figure 5.61 furthermore illustrate the causal chain of the nested control loops for the lateral channel. The unit step in the lateral command channel (yellow solid line) leads to the generation of the reference trajectory of the lateral velocity (blue solid line), which is illustrated in the first plot of figure 5.61.

According to the control law in the *Lateral Velocity Control* block from figure 5.34, the desired roll angle rate  $\dot{\phi}_d$  is forwarded to the *Euler Angle Rate Control* block from figure 5.47, which generates the reference trajectory for the roll angle (blue solid line) based on the commanded value (yellow solid line). The corresponding signals are shown in the second plot of figure 5.61, which illustrates the tracking performance for the roll angle rate.

The commanded roll acceleration follows according to the control law in the *Euler Angle Rate Control* block and is forwarded to the *Rotational Acceleration Control* block from figure 5.48. Latter is aimed to track the generated reference signal for the roll acceleration (blue solid line) based on the estimated roll acceleration signal (magenta solid line), which is illustrated in the third plot of figure figure 5.61.

The presented tracking performance yields sufficient evidence for the general functionality of the proposed control architecture even in the presence of uncertainties, noise, and vibrations. Note that despite sufficient tracking in the roll channel, the lateral velocity initially lags behind its reference value, which is explained by the low-order approximation of the reference dynamics for the lateral channel. However, as was also investigated in [74] and [1], the overall response characteristics of the lateral channel as judged by the pilot nevertheless yield excellent handling qualities.

## 5.4.2 Validation by Full Flight Mission Simulation

In order to obtain insights into the feasibility of the control architecture with respect to an explicit use case, a full flight mission is simulated as part of the validation process. Figure 5.62 shows the simulated flight path of the mission divided into separate phases, which are analyzed with regard to EASA's special condition VTOL [6] in the following.

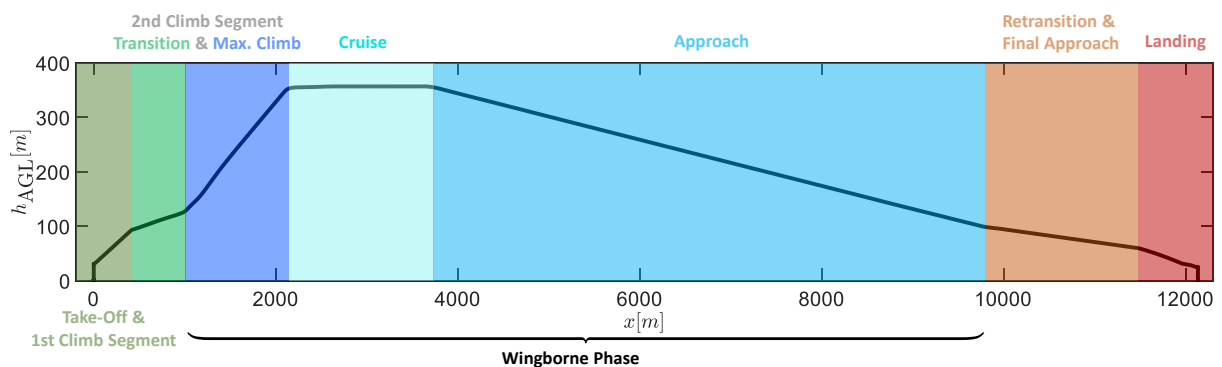
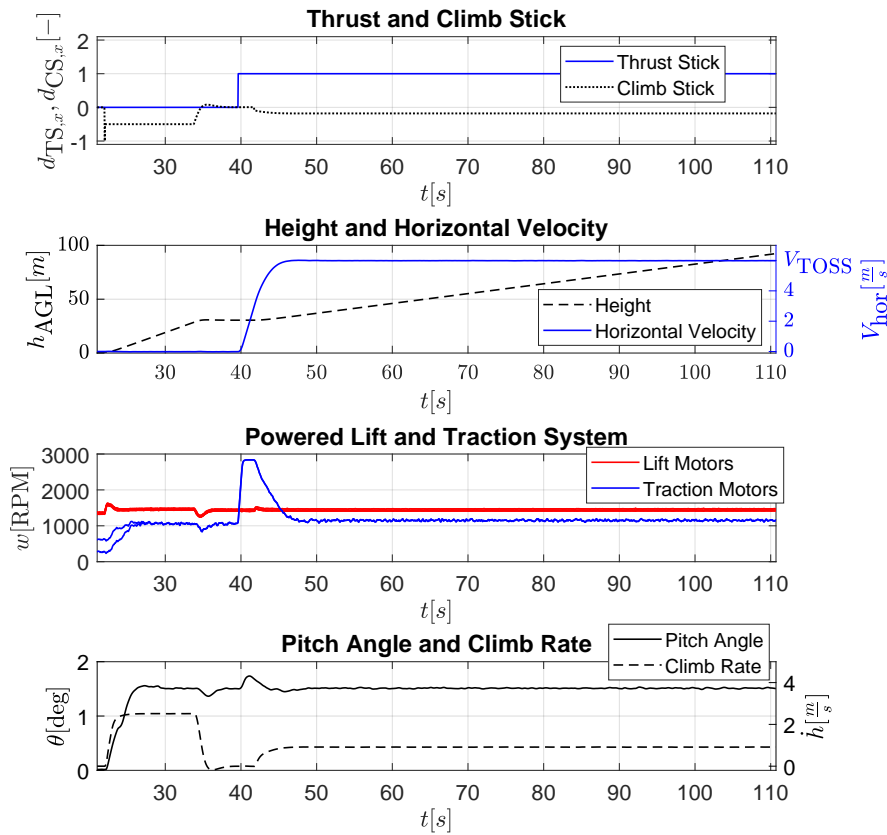


Figure 5.62: *Flight Mission Simulation*

### 5.4.2.1 Take-Off and First Climb Segment

The first phase of the proposed flight mission consists of a vertical take-off from ground and the subsequent first climb segment according to EASA's special condition VTOL [6], which was illustrated in figure 3.1 in subsection 3.1.2.1.

Figure 5.63 depicts the time history of stick deflections and several aircraft states for the first phase of the flight mission. It thereby shows the thrust and climb stick deflections in the first plot, aircraft height and horizontal velocity in the second plot, the RPM values of the powered lift and traction motors in the third plot, as well as the pitch angle and climb rate in the fourth plot.



**Figure 5.63:** *Take-Off and First Climb Segment*

In the context of the vertical take-off and landing procedures for VTOL aircraft, EASA introduced the standardized reference volume from figure 3.2, which was discussed in subsection 3.1.2.1. Thereby, the virtual surface at 30.5 m (100 ft) is referred to as the virtual elevated vertiport.

The initial vertical climb is aimed at reaching the height of the virtual elevated vertiport and takes place in the time window  $0 \text{ s} \leq t \leq 35 \text{ s}$ . Within this time period, the pitch angle increases from a horizontal attitude on ground to the equilibrium pitch angle  $\theta_{0,T}(h_{AGL} \geq 5 \text{ m}) \approx 1.5^\circ$  from (5.128). Furthermore, the traction motors' RPM ramp up in order to balance the resulting backwards force induced by the powered lift system.

Upon reaching a height of 30.5 m (100 ft), the first climb segment is initiated and takes place in the time window  $35 \text{ s} \leq t \leq 110 \text{ s}$ . To this end, the VTOL aircraft accelerates to and stays at the Take-off Safety Speed ( $V_{\text{TOSS}}$ , see table 3.1) while maintaining a climb gradient of 15%, thereby adhering to the reference volume from figure 3.2 for which a gradient of at least 12.5% is required for obstacle clearance. The first climb segment ends as soon as the aircraft reaches a height of 61 m (200 ft) above the virtual elevated vertiport, which corresponds to a total height of 91.5 m (300 ft) [6].

#### 5.4.2.2 Transition and Second Climb Segment

The next phase of the flight mission corresponds to the second climb segment [6] according to figure 3.1 in subsection 3.1.2.1. This phase is divided into two parts: the transition into the fixed-wing flight regime in the time window  $110 \text{ s} \leq t \leq 135 \text{ s}$  (figure 5.64) and a maximum climb maneuver in the time window  $135 \text{ s} \leq t \leq 165 \text{ s}$  (figure 5.65) at the optimum climb speed  $V_{\text{stall,p}}$ .

Figure 5.64 shows the transition into the wingborne phase and depicts the stick deflections in the first plot, aircraft height and calibrated airspeed in the second plot, the RPM values of the powered lift and traction motors and the deflection angles of the elevators in the third plot, as well as the pitch angle and angle of attack in the fourth plot.

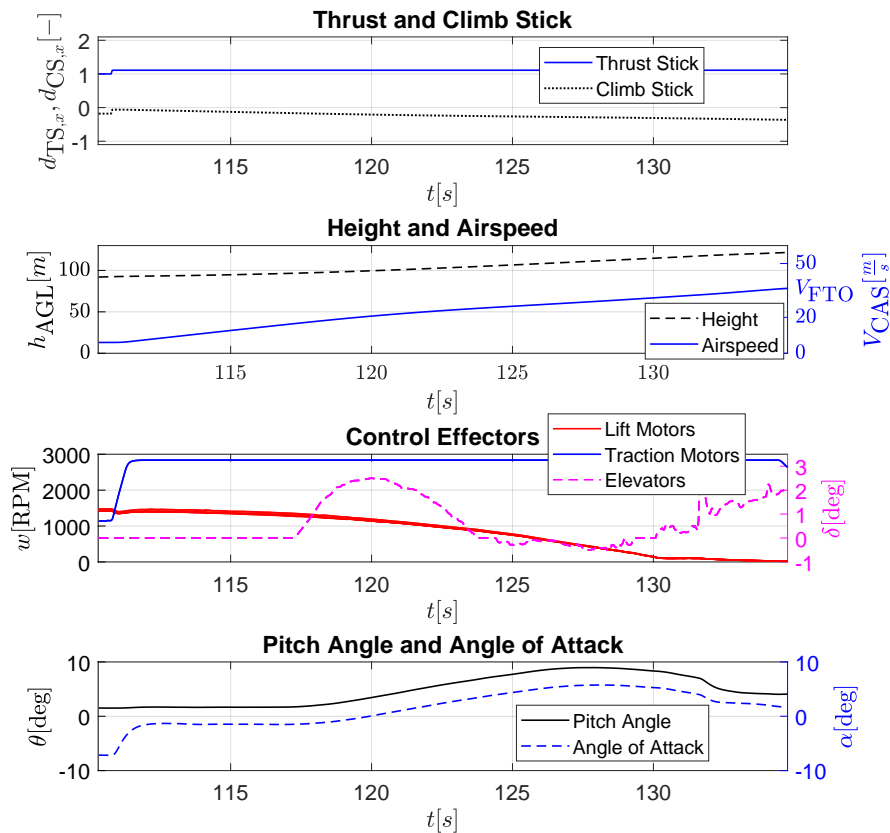


**Figure 5.64:** *Transition to the Fixed-Wing Flight Regime*

The transition is initiated by pushing the thrust stick  $d_{TS,x}$  above the detent notch. While the VTOL aircraft is accelerating towards the Final Take-off Speed ( $V_{FTO}$ , see table 3.1) and for the subsequent climb at or above  $V_{FTO}$ , a minimum climb gradient of 2.5% is required according to [6]. Note that in the context of the developed control architecture  $V_{FTO}$  is equal to both the target velocity for the transition into the wingborne phase  $V_{stall,p}$  and the speed for which optimum climb performance can be achieved.

Due to the increasing airspeed and angle of attack during the transition phase, the powered lift motors' RPM values are steadily decreasing to account for the rising aerodynamic lift, which is depicted in the third plot of figure 5.64. Furthermore, the elevators start replacing the lifting motors with regards to generating the necessary pitch moments during flight.

The fourth plot of figure 5.64 shows how the pitch attitude of the VTOL aircraft is increasing during the transition in order to adhere to the angle of attack regime from (4.18), which was visualized in figure 4.7. Note, however, that in the time window  $128\text{ s} \leq t \leq 135\text{ s}$  the angle of attack is decreased according to the protected angle of attack rate law from (5.183), which accounts for the specific excess powered lift rate and ensures that the angle of attack never exceeds the value for which the powered lift system would undershoot its idle state (recall figure 5.40).

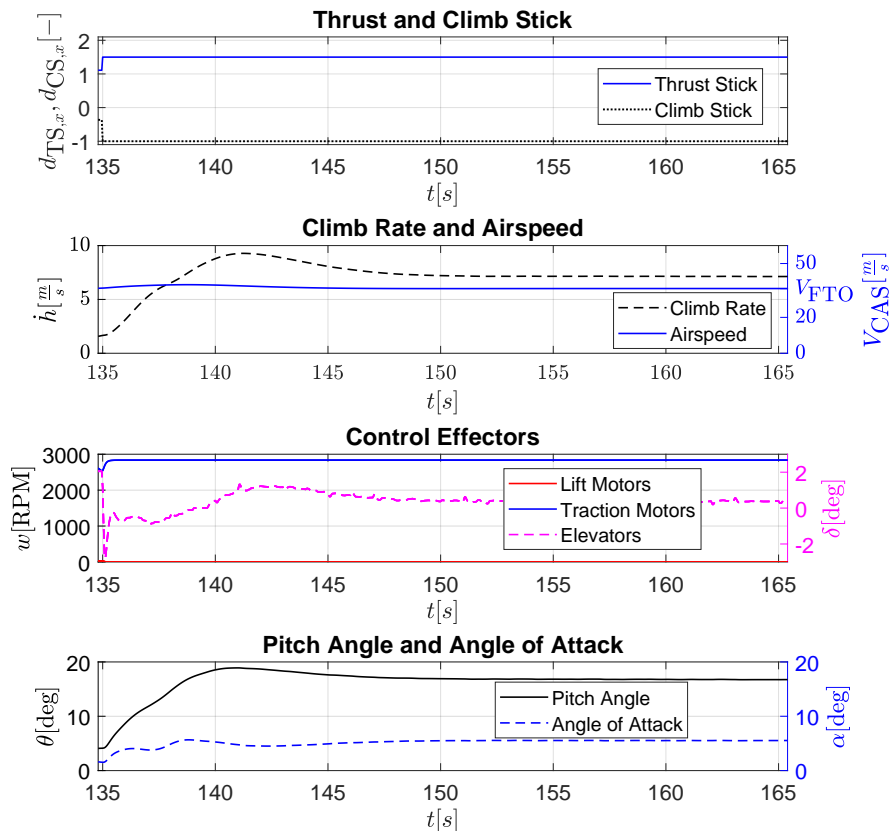


**Figure 5.65:** *Maximum Climb During Second Climb Segment*

After successful transition into the wingborne phase, a maximum climb maneuver is initiated in the time window  $135\text{ s} \leq t \leq 165\text{ s}$  in order to reach the required height of 305 m (1000 ft) above the virtual elevated vertiport and complete the second segment of the take-off path [6].

To this end, the maximum climb rate follows from the relationship in (5.69) and ensures that the airspeed converges to and does not fall below the Final Take-off Speed (i.e. below  $V_{\text{stall,p}}$ ), which also represents the minimum airspeed limit for the wingborne phase according to table 5.2 in subsection 5.3.3.2. Hence, the climb rate peaks at around  $t = 141\text{ s}$  until the airspeed drops back to the optimum climb speed  $V_{\text{stall,p}}$  upon which the climb rate converges to the stationary maximum value for the remainder of the second climb segment. The first plot in figure 5.65 illustrates the height and height rate during the maneuver, which is completed upon reaching the final altitude of 305 m (1000 ft) above the virtual elevated vertiport, i.e. a total height of 335.5 m (1100 ft) [6].

### 5.4.2.3 Cruise Flight

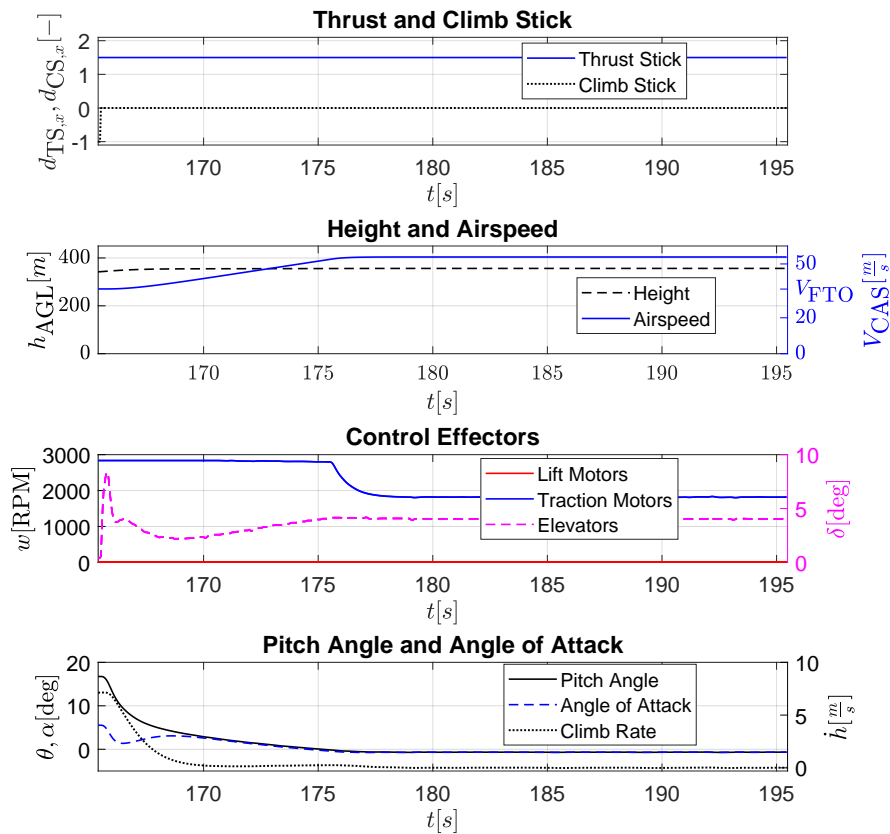


**Figure 5.66:** *Cruise Flight*

Figure 5.66 shows the cruise phase of the flight mission, which for demonstration purposes is condensed to 30 s in the time window  $165\text{ s} \leq t \leq 195\text{ s}$ . In the beginning of the presented flight phase the VTOL aircraft accelerates to the target cruise speed while

reducing the height rate from the previous climb segment until reaching horizontal flight in order to maintain the altitude for the remainder of the cruise flight.

The third plot in figure 5.66 thereby shows the rotational speed of the traction motors, which reduce their RPM values from the maximum setting to cruise RPM upon reaching the target airspeed. Furthermore, the positive deflection of the elevator is depicted, which initiates a pitch down maneuver in the beginning of the flight segment in order to decrease the climb rate and reach a horizontal flight state. The resulting climb rate is shown in the fourth plot of figure 5.66 along side with the pitch angle and angle of attack.

#### 5.4.2.4 Approach

The next segment within the presented flight mission is the approach phase, which serves two main purposes:

- to reduce the altitude of the aircraft to a value of 100.5 m (330 ft) above ground level and
- to reduce its airspeed to the Final Take-off Speed  $V_{\text{FTO}} = V_{\text{stall,p}}$  in order to prepare for the retransition.

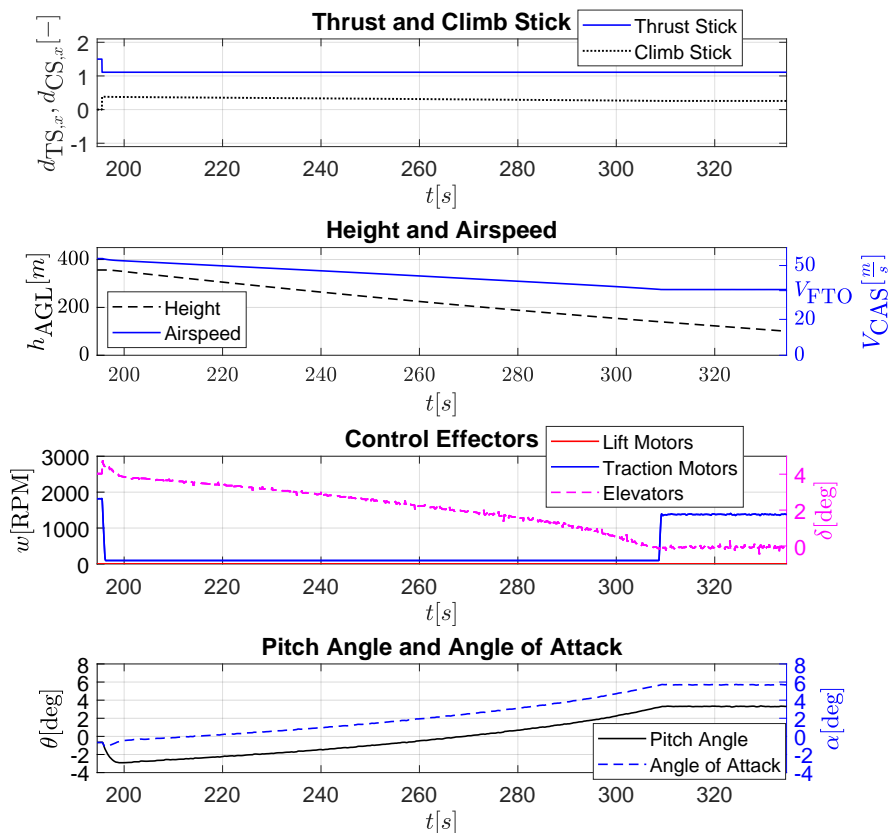


Figure 5.67: Approach

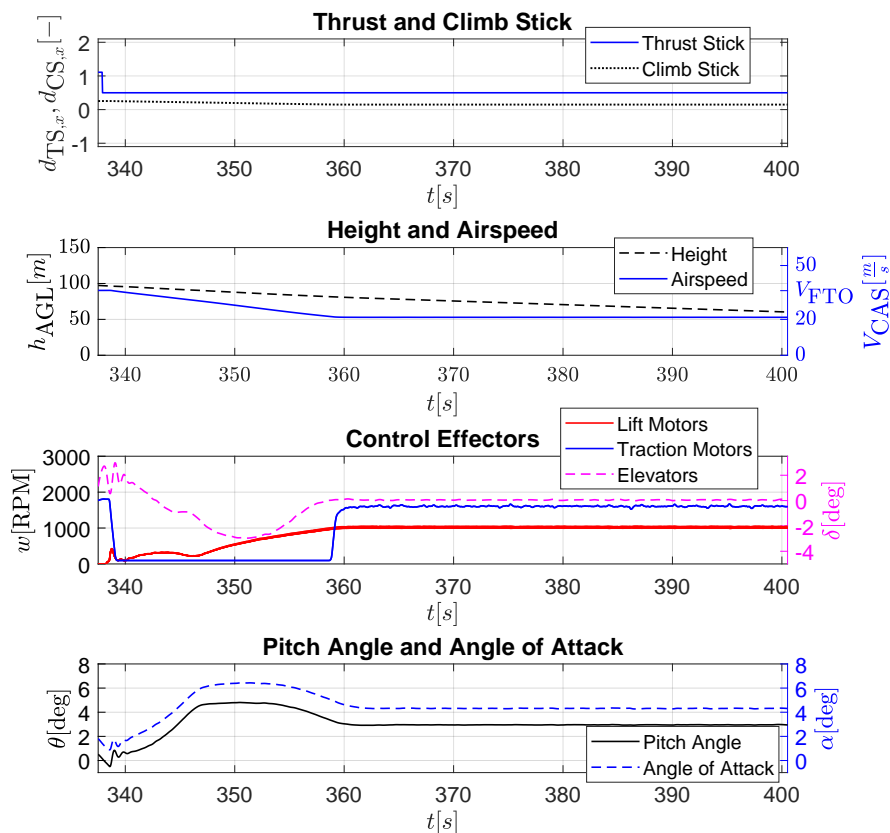


Figure 5.67 shows the approach phase in the time window  $195\text{ s} \leq t \leq 330\text{ s}$ . Thereby, the traction motors are commanded at their idle RPM values throughout the entire deceleration phase at  $197\text{ s} \leq t \leq 307\text{ s}$ , which is shown in the third plot of figure 5.67. Upon decelerating to the target airspeed for the retransition, the descent is continued until a height of  $100.5\text{ m}$  ( $330\text{ ft}$ ) above ground level is reached.

#### 5.4.2.5 Retransition and Final Approach

The next mission segment consist of the retransition phase and the final approach towards the landing site. During the entire segment the aircraft is further descending in order to prepare for the vertical landing phase. Figure 5.68 depicts the stick deflections as well as corresponding aircraft and control effector states in the time window  $330\text{ s} \leq t \leq 400\text{ s}$ .

The retransition is initiated by pulling the thrust stick  $d_{TS,x}$  below the detent notch. After the successful activation of the powered lift motors and the subsequent confirmation via RPM feedback, the control of the vertical channel is taken over by the powered lift system, which was illustrated in the schematic overview of the outer control loop in figure 5.27. Hence, the VTOL transition aircraft can further decelerate below the minimum wingborne speed  $V_{\text{stall,p}}$  (i.e. the Final Take-Off Speed) until it reaches the final approach speed, which is shown in the time window  $339\text{ s} \leq t \leq 359\text{ s}$  in figure 5.68.



**Figure 5.68:** *Retransition and Final Approach*

During the retransition phase the aircraft keeps descending with idle traction motors at a rate that allows for sufficient deceleration. Due to the resulting decrease in aerodynamic lift, the powered lift motor RPM values further increase until the aircraft has decelerated to the final approach speed, which is illustrated in the third plot of figure 5.68. The final approach ends when the aircraft reaches a height of 61 m (200 ft) above ground.

#### 5.4.2.6 Landing

The final segment of the presented flight mission includes the deceleration of the VTOL aircraft into the pure hover state and the subsequent vertical landing on ground. Figure 5.69 shows the corresponding maneuver in the time window  $400 \text{ s} \leq t \leq 445 \text{ s}$ .

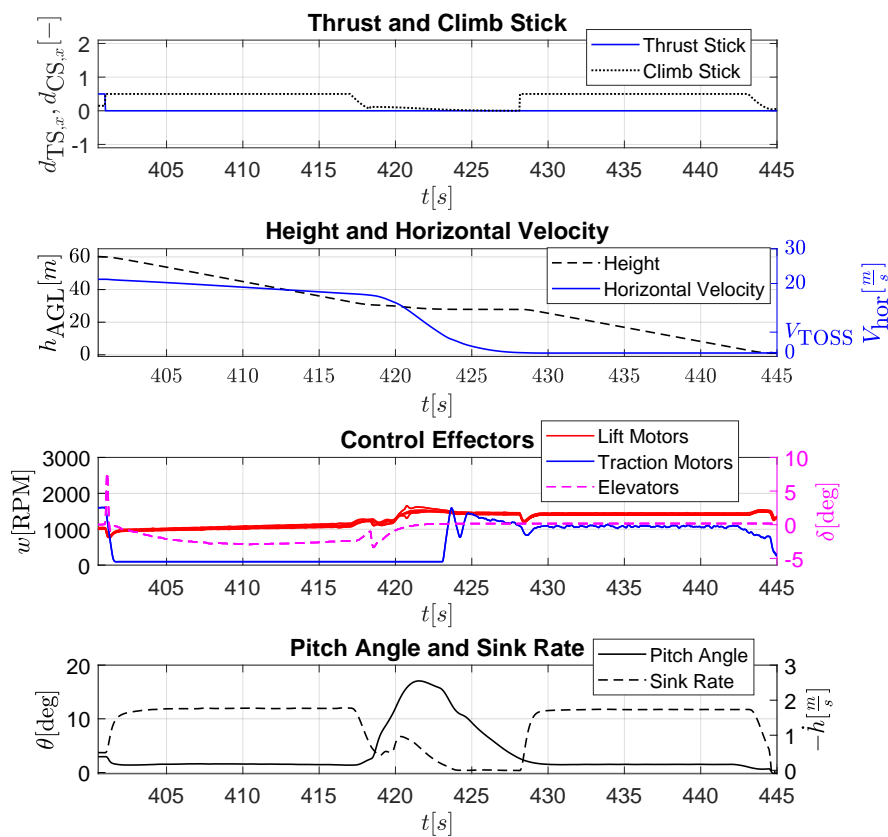


**Figure 5.69:** *Vertical Landing*

The first part of the landing phase consists of the descent to the virtual elevated vertiport's height of 30.5 m (100 ft) [6] in the time window  $400 \text{ s} \leq t \leq 425 \text{ s}$ . The aircraft keeps decelerating with idle traction motors and constant pitch angle during the descent until it is slow enough to enter the *Hover* phase upon which it completes the deceleration maneuver by increasing the pitch angle according to the control law from (5.131).

Once the aircraft has come to a halt at  $t = 428 \text{ s}$ , the vertical landing is initiated in the time window  $428 \text{ s} \leq t \leq 445 \text{ s}$ . Finally, the landing is completed once the VTOL aircraft touches the ground.

# 6

## Control Algorithm Design and Implementation

After the specification of the control architecture in chapter 5, this chapter is aimed to discuss the final steps in the controller development, which deal with the design and implementation of the control algorithms on the lowest abstraction level. The final result of the flight control systems engineering process thereby yields the actual source code, which can be compiled and deployed on a target computing platform and can then be embedded into the overall system architecture of the VTOL transition aircraft.

This stage of the development process is thereby highly dependent on the specific realization of the individual aircraft components and the context in which the controller is operating, since the design of the flight control algorithms has to explicitly take into account the existing system architecture and its physical manifestation. More specifically, the clear delimitation of the flight controller in the context of the overall avionics system and the resulting unambiguous and complete definition of interfaces on the lowest implementation level becomes a crucial step in this phase of the development. Since no specific aircraft is assumed throughout this thesis, the presented chapter is aimed at merely introducing a general approach for the control algorithm design and implementation, but does not provide an exhaustive breakdown of the flight control algorithms.

The flight control functionality is realized on a computer platform, which is referred to as *Flight Control Computer* (FCC) throughout the remainder of this chapter. Hence, the concept of discretization becomes a crucial method for realizing the proposed control algorithms in a clocked environment. To this end, section 6.1 introduces the general idea of discretization, which is then applied to the complementary filter from subsection 5.3.5.1 in order to yield an algorithmic realization of its proposed functionality.

In accordance to the model-based development process, section 6.2 furthermore introduces the *Control Design Model* (CDM), which represents the specification of the flight control algorithms on the highest concretization level in terms of an executable and code-generateable model. By adhering to strict modeling guidelines during the development, a high functional integrity of the CDM is realized.

Furthermore, the CDM is developed in view of automatically generating platform-specific source code, which can then be compiled and deployed on a FCC. By complying with modeling guidelines and software development standards such as *MISRA C* [141], which is developed by the *MISRA* (Motor Industry Software Reliability Association) consortium, or the aerospace software certification standard DO-178C [18], the integrity and reliability of the generated source code can be ensured.

Finally, section 6.3 discusses various strategies regarding the verification and validation of the CDM and the resulting generated code for the flight controller. By using a wide variety of tools such as *Markov Chain Monte Carlo* (MCMC) [142] simulation for Bayesian inference of failure probabilities, counter optimization for analysis of worst-case inputs, or dynamic and static program analysis such as unit tests and code coverage tests, the verification against low-level and high-level requirements can be performed in an extensive manner. Furthermore, using hardware-in-the-loop simulation or iron-bird testing allows for comprehensive evaluation and validation of the proposed control algorithms in applicable use case scenarios.

## 6.1 Controller Discretization

This section is aimed at deriving the necessary theoretical background for discretizing the control laws from section 5.3. In particular, the presented methods are used to realize the filter components of the controller in the clocked environment of a computer platform in terms of discretized algorithms.

To this end, subsection 6.1.1 introduces the z-transformation [143], which is the discrete-time domain counterpart of the Laplace transform [130] for continuous systems. The z-transformation is thereby used to convert a discrete-time signal into a complex-valued function, which provides insights into its frequency characteristics and is thereby closely related to the discrete Fourier transform (DFT) [144] of a signal.

In subsection 6.1.2 the bilinear transformation [145] is introduced, which is an approximate method for obtaining the z-transform of a continuous-time transfer function  $G(s)$ . It is derived from approximating the integration of a signal between two sample time steps using the trapezoidal rule [145] and is also referred to as Tustin's method.

Due to the approximate nature of the bilinear transformation, frequency characteristics of the transformed continuous-time system (such as the target bandwidth of the complementary filter) are not preserved throughout the mapping into the z-domain. Therefore, subsection 6.1.3 derives the concept of frequency prewarping, which is used to adjust the bilinear transformation such that the resulting frequency characteristics of the discretized system match with the continuous system at a predefined design point.

Finally, subsection 6.1.4 applies the discretization concepts of this section to the rotational acceleration complementary filter. As a result, the difference equation of the filter is obtained, which can be used for implementation on a computer platform.

### 6.1.1 Derivation of the Z-Transformation

Given a continuous-time signal  $x(t)$ , the Laplace transform is defined [130] as

$$\mathcal{L}\{x(t)\} = X(s) = \int_{t=0}^{\infty} x(t)e^{-st}dt, \quad (6.1)$$

where  $s = \sigma + j\omega$  denotes a complex-valued variable and  $\sigma$  and  $\omega$  represent the damping and frequency value respectively. The resulting transformed function in the frequency domain is denoted with a capital letter  $X(s)$  in order to distinguish it from the time domain representation  $x(t)$ . Note that (6.1) can also be interpreted as a generalization of the Fourier transform, which results from setting the damping value to  $\sigma = 0$  and optionally normalizing the integration result (dependent on which definition of the Fourier transformation is used).

In order to obtain a continuous-time representation of the signal  $x(t)$  being sampled equidistantly with a sample time of  $T$ , the pulsed signal

$$x_p(t) = x(t) \sum_{k=0}^{\infty} \delta(t - kT) = \sum_{k=0}^{\infty} x(kT)\delta(t - kT) \quad (6.2)$$

is defined, where  $\delta(t - kT)$  denotes the Dirac delta function [143]. Latter represents an infinite pulse at time  $t = kT$  with an unit area for which the following relationship holds:

$$\int_{t=0}^{\infty} \delta(t - c)f(t)dt = f(c), \quad c \geq 0. \quad (6.3)$$

The pulsed signal  $x_p(t)$  in (6.2) results from multiplying the original signal  $x(t)$  with a pulse train  $\sum_{k=0}^{\infty} \delta(t - kT)$ , which is also referred to as *dirac comb* and is schematically illustrated in figure 6.1.

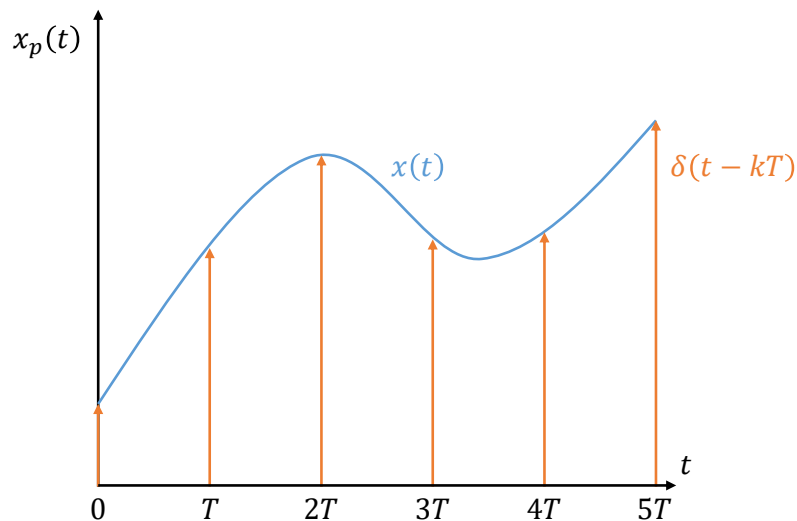


**Figure 6.1:** *Discretizing a Signal With the Dirac Comb*

Using the relationship in (6.1) and (6.3), the Laplace transform of the pulsed signal  $x_p(t)$  from (6.2) yields

$$\begin{aligned}
\mathcal{L}\{x_p(t)\} = X_p(s) &= \int_{t=0}^{\infty} x_p(t)e^{-st} dt = \int_{t=0}^{\infty} \sum_{k=0}^{\infty} x(kT)\delta(t - kT)e^{-st} dt \\
&= \sum_{k=0}^{\infty} x(kT) \underbrace{\int_{t=0}^{\infty} \delta(t - kT)e^{-st} dt}_{=e^{-skT} \text{ according to (6.3)}} \\
&= \sum_{k=0}^{\infty} x(kT)e^{-skT} \\
&= \sum_{k=0}^{\infty} x(kT)(e^{sT})^{-k}. \tag{6.4}
\end{aligned}$$

Finally, after introducing the definitions  $x(kT) := x[k]$  and

$$z = e^{sT}, \tag{6.5}$$

the z-transformation of the discrete signal  $x[k]$  is defined as follows:

$$\mathcal{Z}\{x[k]\} = X(z) = \sum_{k=0}^{\infty} x[k]z^{-k}, \tag{6.6}$$

where  $z = re^{j\phi}$  denotes a complex-valued variable with the magnitude  $r$  and the angle  $\phi$ . Similarly to the Laplace transform, the z-transform provides information about the frequency content of the discrete signal  $x[k]$ . Furthermore, the discrete Fourier transform (DFT) directly follows from the z-transform when enforcing  $z$  to be on the complex unit circle, i.e. for  $r = 1$ .

An important property of the z-transform follows from deriving the transformation of a signal that is delayed by one sample time step  $T$ :

$$\begin{aligned}
\mathcal{Z}\{x[k-1]\} &= \sum_{k=0}^{\infty} x[k-1]z^{-k} \stackrel{(\tilde{k}:=k-1)}{=} \sum_{\tilde{k}=-1}^{\infty} x[\tilde{k}]z^{-(\tilde{k}+1)} \\
&= \sum_{\tilde{k}=0}^{\infty} x[\tilde{k}]z^{-\tilde{k}}z^{-1} = X(z)z^{-1}, \tag{6.7}
\end{aligned}$$

where  $x[-1] = 0$  is used due to the assumption of causal signals in the scope of the unilateral z-transform.

Hence, it follows from (6.7) that the z-transform of a signal delayed by one sample time step  $T$  is the z-transform of the undelayed signal multiplied by  $z^{-1}$ . This property makes the application of the z-transform especially useful for obtaining difference equations, which can be seamlessly integrated on a clocked computer platform.

In general, the use of the z-transform is widely adopted in the area of signal processing and digital control system [143]. Together with the Laplace transform it makes up the basis of modern control theory and allows for analytical studies of a (closed-loop) system's stability margins and frequency characteristics.

### 6.1.2 Bilinear Transformation

Following the derivation of the z-transform in subsection 6.1.1, this subsection is aimed at deriving the bilinear transformation, which is used to convert an existing transfer function in the continuous time-domain  $G(s)$  into a discrete-time transfer function  $G(z)$ . Latter can then be used to obtain the difference equation for the input and output signal, which yields the underlying dynamics of  $G(s)$  in a discretized manner.

One might be inclined to use the exact relationship  $z = e^{sT}$  from (6.5) with the sampling time  $T$  in order to obtain the discretized form of a continuous transfer function, i.e.  $G(z) = G(s)|_{s=T^{-1}\ln(z)}$ , where  $s = T^{-1}\ln(z)$  follows from inverting (6.5). However, the resulting z-transform would contain nonlinear logarithmic terms, which omit the application of the relationship in (6.7) and hence prevent a simple synthesis of the transferred signal in the discrete-time domain using difference equations.

Instead, the bilinear transformation is aimed at yielding an approximate relationship between the s- and z-domain. To this end, the Laplace transform of a signal's time derivative is recalled [130]:

$$\mathcal{L}\{\dot{x}(t)\} = \dot{X}(s) = sX(s) \Leftrightarrow X(s) = \frac{1}{s}\dot{X}(s), \quad (6.8)$$

where  $x(0) = 0$  is assumed without loss of generality. Similarly, the right side of (6.8) relates the Laplace transform of an integrated signal to its integrand via multiplication with  $\frac{1}{s}$ .

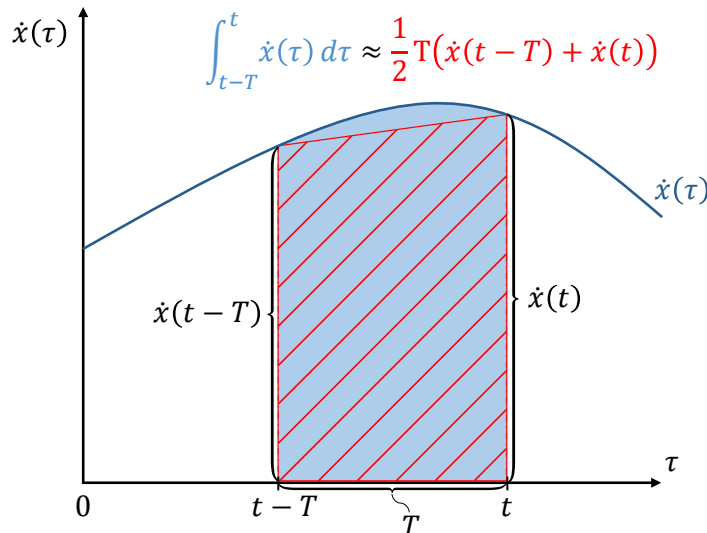


**Figure 6.2:** *Approximating an Integral with Trapezoidal Integration*

Furthermore, in order to derive the bilinear transformation, the time-domain solution of (6.8) for a single time step of length  $T$  is considered:

$$x(t) = x(t - T) + \int_{t-T}^t \dot{x}(\tau) d\tau. \quad (6.9)$$

Figure 6.2 thereby shows how the exact integral of  $\dot{x}(\tau)$  between  $\tau = t - T$  and  $\tau = t$  can be approximated by the trapezoidal area given by the time step length  $T$  and the function values of the integrand  $\dot{x}(t - T)$  and  $\dot{x}(t)$ . Hence, it follows that

$$x(t) = x(t - T) + \int_{t-T}^t \dot{x}(\tau) d\tau \approx x(t - T) + \frac{1}{2}T (\dot{x}(t - T) + \dot{x}(t)) . \quad (6.10)$$

Furthermore, assuming the time step  $T$  to be equal to the sample time, the z-transform of (6.10) is given by

$$\begin{aligned} \mathcal{Z}\{x(t)\} = X(z) &= X(z)z^{-1} + \frac{1}{2}T (\dot{X}(z)z^{-1} + \dot{X}(z)) \\ \Rightarrow X(z) &= \frac{T}{2} \frac{z+1}{z-1} \dot{X}(z), \end{aligned} \quad (6.11)$$

where the property from (6.7) was used to yield the z-transform of the delayed signals.

Finally, when equating the Laplace transform from (6.8) to the z-transform from (6.11), the relationship between the s- and z-domain directly follows from

$$s = \frac{2}{T} \frac{z-1}{z+1} \Leftrightarrow z = \frac{1 + \frac{T}{2}s}{1 - \frac{T}{2}s} . \quad (6.12)$$

Note that the resulting transformation from the Laplace domain to the z-domain is realized by a rational function. As a consequence, the corresponding z-transform of the continuous transfer function can be expressed as a rational function as well, which facilitates the straight-forward synthesis of the transferred signal in terms of a difference equation.

Surprisingly, one could have arrived at the same result as in (6.12) by considering the exact relationship  $z = e^{sT}$  from (6.5) and approximating it as the ratio of two first order Taylor polynomials:

$$z = e^{sT} = \frac{e^{\frac{1}{2}sT}}{e^{-\frac{1}{2}sT}} \approx \frac{1 + \frac{T}{2}s}{1 - \frac{T}{2}s} . \quad (6.13)$$

This kind of approximation in terms of a rational function is also referred to as Padé approximation [146]. Furthermore, approximating the exact relationship  $z = e^{sT}$  in terms of  $z = e^{sT} \approx 1 + Ts$  or  $z = e^{sT} = \frac{1}{e^{-sT}} \approx \frac{1}{1-Ts}$  yields the transformations, which are referred to as forward and backward Euler method respectively [147].

The forward and backward Euler methods thereby approximate the integral from 6.2 by a rectangle of width  $T$  and of height  $\dot{x}(t - T)$  or  $\dot{x}(t)$  respectively. However, it can be shown [145] that the bilinear transformation, which can be seen as a combination of both forward and backward Euler method, preserves the stability characteristics of the original continuous-time transfer function and provides a more precise mapping between the s- and z-domain compared to the Euler methods.



### 6.1.3 Frequency Prewarping

As was clarified in subsection 6.1.2, the bilinear transformation has the advantage of yielding a rational function in the  $z$ -domain when transforming a continuous-time transfer function. The bilinear property results in the presence of polynomials in the nominator and denominator of the discrete transfer function, which yields a linear combination of the values within the discrete input and output signal history and hence results in a linear difference equation.

However, due to the approximate nature of the transformation, frequency characteristics of a continuous-time transfer function get distorted and warped through the bilinear mapping. Thereby, the extent to which the frequency characteristics are distorted increases with higher frequencies and larger sampling times, which can also be explained by the increasing distance of the argument  $sT = j\omega T$  (the damping  $\sigma$  is omitted) in the context of the Padé approximation of  $z = e^{sT}$ .

In order to mitigate the distorting effects of the bilinear transformation, the concept of *frequency prewarping* [145] can be applied. Thereby, the bilinear transformation is adapted such that a specific frequency of interest yields identical representations in the  $s$ - and  $z$ - domain. Specifically, considering a design frequency  $\omega_c$ , which is derived in the context of a continuous-time analysis, the prewarped discrete-time frequency  $\omega_d$  shall yield the same output under the bilinear transformation as the original continuous-time frequency under the exact transformation  $z = e^{sT}$  from (6.5):

$$z = e^{j\omega_c T} \stackrel{!}{=} \frac{1 + \frac{T}{2}j\omega_d}{1 - \frac{T}{2}j\omega_d}$$

$$\Rightarrow \omega_d = \frac{2j}{T} \frac{1 - e^{j\omega_c T}}{1 + e^{j\omega_c T}} = \frac{2j}{T} \frac{e^{-j\frac{1}{2}\omega_c T} 1 - e^{j\omega_c T}}{e^{-j\frac{1}{2}\omega_c T} 1 + e^{j\omega_c T}} = \frac{2j}{T} \frac{e^{-j\frac{1}{2}\omega_c T} - e^{j\frac{1}{2}\omega_c T}}{e^{-j\frac{1}{2}\omega_c T} + e^{j\frac{1}{2}\omega_c T}}. \quad (6.14)$$

Furthermore, using Euler's identity for complex numbers

$$e^{j\alpha} = \cos(\alpha) + j \sin(\alpha), \quad (6.15)$$

it follows for the prewarped discrete-time frequency  $\omega_d$ :

$$\omega_d = \frac{2j}{T} \frac{e^{-j\frac{1}{2}\omega_c T} - e^{j\frac{1}{2}\omega_c T}}{e^{-j\frac{1}{2}\omega_c T} + e^{j\frac{1}{2}\omega_c T}} = \frac{2j}{T} \frac{-2j \sin\left(\frac{1}{2}\omega_c T\right)}{2 \cos\left(\frac{1}{2}\omega_c T\right)} = \frac{2}{T} \tan\left(\frac{1}{2}\omega_c T\right). \quad (6.16)$$

Note that the discrete-time frequency  $\omega_d$  from (6.16) yields a singularity and tends to infinity for a continuous-time (angular) frequency of  $\omega_c = \frac{\pi}{T}$ , which happens to be the Nyquist frequency [148]  $f_N = \frac{1}{2T} = \frac{1}{2}f_S$  with  $f_S = \frac{1}{T}$  denoting the sampling rate in Hertz. According to the Nyquist-Shannon sampling theorem [148], the Nyquist frequency thereby corresponds to the highest frequency which can be represented in the discrete-time domain for a given sample rate without the occurrence of aliasing.

An alternative way to perform the prewarping is to directly use the modified bilinear transformation [145]

$$s = \frac{\omega_c}{\tan\left(\frac{1}{2}\omega_c T\right)} \frac{z-1}{z+1} \Leftrightarrow z = \frac{1 + \frac{\tan\left(\frac{1}{2}\omega_c T\right)}{\omega_c} s}{1 - \frac{\tan\left(\frac{1}{2}\omega_c T\right)}{\omega_c} s}, \quad (6.17)$$

which can be analogously derived by imposing the requirement of preserving a given design frequency  $\omega_c$  throughout the mapping.

### 6.1.4 Implementation of the Difference Equation

Applying the concepts presented in the previous subsections, the difference equation of the rotational acceleration complementary filter from subsection 5.3.5.1 is derived in the following. For the sake of simplicity, only one channel of the rotational acceleration is considered. However, the concepts can be extended to the remaining channels analogously.

To this end, the filter equation from (5.211) in the Laplace domain is recalled:

$$\dot{\Omega}_F(s) = \frac{K_F}{s + K_F} s \Omega_{\text{msr}}(s) + \frac{s}{s + K_F} \dot{\Omega}_{\text{mdl}}(s), \quad (6.18)$$

where  $\dot{\Omega}_F(s) = \mathcal{L}\{\dot{\omega}_F(t)\}$ ,  $\Omega_{\text{msr}}(s) = \mathcal{L}\{\omega_{\text{msr}}(t)\}$ , and  $\dot{\Omega}_{\text{mdl}}(s) = \mathcal{L}\{\dot{\omega}_{\text{mdl}}(t)\}$  represent the Laplace transforms of the filtered rotational acceleration, measured rotational rate, and model-based rotational acceleration respectively. Furthermore,  $K_F$  denotes the target bandwidth of the filter, which is presented in a continuous-time context and yields an attenuation of 3 dB  $\left(\frac{\sqrt{2}}{2}\right)$  for frequencies equal to the bandwidth  $\omega = K_F$ .

In order to preserve the cutoff frequency for the discrete filter, the target bandwidth  $K_F$  is prewarped according to the concepts from subsection 6.1.3. To this end, the prewarped bandwidth parameter  $K_{F,d}$  of the discrete filter follows according to (6.16) and is given by

$$K_{F,d} = \frac{2}{T} \tan\left(\frac{1}{2} K_F T\right), \quad (6.19)$$

where  $T$  denotes the target sample time of the algorithm.

Furthermore, the  $z$ -transform of the filter in (6.18) is obtained by substituting the Laplace variable  $s$  using the bilinear transformation from (6.12) and replacing the continuous-time bandwidth parameter  $K_F$  with the prewarped frequency from (6.19):

$$\dot{\Omega}_F(z) = \frac{K_{F,d}}{\frac{2}{T} \frac{z-1}{z+1} + K_{F,d}} \frac{2}{T} \frac{z-1}{z+1} \Omega_{\text{msr}}(z) + \frac{\frac{2}{T} \frac{z-1}{z+1}}{\frac{2}{T} \frac{z-1}{z+1} + K_{F,d}} \dot{\Omega}_{\text{mdl}}(z). \quad (6.20)$$

Rearranging the terms in (6.20) yields

$$\begin{aligned} \dot{\Omega}_F(z) = & \frac{1 - \frac{K_{F,d} T}{2}}{1 + \frac{K_{F,d} T}{2}} \dot{\Omega}_F(z) z^{-1} + \frac{K_{F,d}}{1 + \frac{K_{F,d} T}{2}} \Omega_{\text{msr}}(z) (1 - z^{-1}) \\ & + \frac{1}{1 + \frac{K_{F,d} T}{2}} \dot{\Omega}_{\text{mdl}}(z) (1 - z^{-1}), \end{aligned} \quad (6.21)$$

which can then be transformed back into the discrete-time domain using the relationship from (6.7):

$$\begin{aligned} \dot{\omega}_F[k] = & \frac{1 - \frac{K_{F,d}T}{2}}{1 + \frac{K_{F,d}T}{2}} \dot{\omega}_F[k-1] + \frac{K_{F,d}}{1 + \frac{K_{F,d}T}{2}} (\omega_{\text{msr}}[k] - \omega_{\text{msr}}[k-1]) \\ & + \frac{1}{1 + \frac{K_{F,d}T}{2}} (\dot{\omega}_{\text{mdl}}[k] - \dot{\omega}_{\text{mdl}}[k-1]), \end{aligned} \quad (6.22)$$

with the sampling time  $T$  and the parameter  $K_{F,d}$  from (6.19).

The difference equation in (6.22) can directly be used for the implementation in a clocked environment. Furthermore, every other transfer function defined in the context of the control architecture can be transformed analogously. However, functions that specify signals according to nonlinear differential equations (such as the rate and acceleration limited reference and control effector models) cannot be converted into linear transfer functions in the Laplace domain.

Hence, manual numerical integration of the underlying differential equations becomes necessary in order to realize the specified dynamics in the discrete-time domain. To this end, consider the nonlinear differential equation (5.269) from subsection 5.3.5.6, which describes the first-order dynamics of the control effector model:

$$\dot{C}_{\text{mdl},i} = \min \left( \dot{C}_{\text{max},i} \max \left( \dot{C}_{\text{min},i}, K_{C_i} (C_{c,i} - C_{\text{mdl},i}) \right) \right) = f(C_{c,i}, C_{\text{mdl},i}), \quad (6.23)$$

where  $f$  is representative of a nonlinear function, which in case of the control effector differential equation yields its nonlinear characteristics due to the saturation by the min and max operation.

Similarly to the derivation of the bilinear transformation in subsection 6.1.2, the goal of the numerical integration method is to yield the solution of the nonlinear differential equation in (6.23). Several methods of numerical integration are described in the literature [149], which can in general be grouped as one-step or multi-step and explicit or implicit algorithms.

The presented forward Euler method from subsection 6.1.2 is considered an explicit one-step method, while the backward Euler method is categorized as an implicit one-step method. Implicit methods thereby have the disadvantage that in case of nonlinear differential equations they can often only be solved iteratively in the scope of an optimization problem or using root finding algorithms such as the Newton–Raphson method [150].

The presented trapezoidal integration method, which serves as the basis of the bilinear Tustin transformation, represents an implicit multi-step method, which approximates the integration by considering the value of the integrand at multiple time steps. Similarly to the backward Euler method, it represents an implicit algorithm, since it incorporates the solution of the differential equation at the next time step into the equation for finding this same solution in the first place. While the resulting implicit equation can be solved in the linear case (which yielded the bilinear transformation from (6.12)), finding the analytical solution in the nonlinear case can be intractable.

The well-known Runge-Kutta methods [149] thereby represent multi-step algorithms that resolve the implicit character by approximating the solution of the differential equation at the next time step using an explicit method (such as forward Euler) and incorporating it in a multi-step process to yield the final integration result. These methods provide excellent results for solving differential equations and are commonly used in the numerical solver of commercial simulation software such as Matlab Simulink [78].

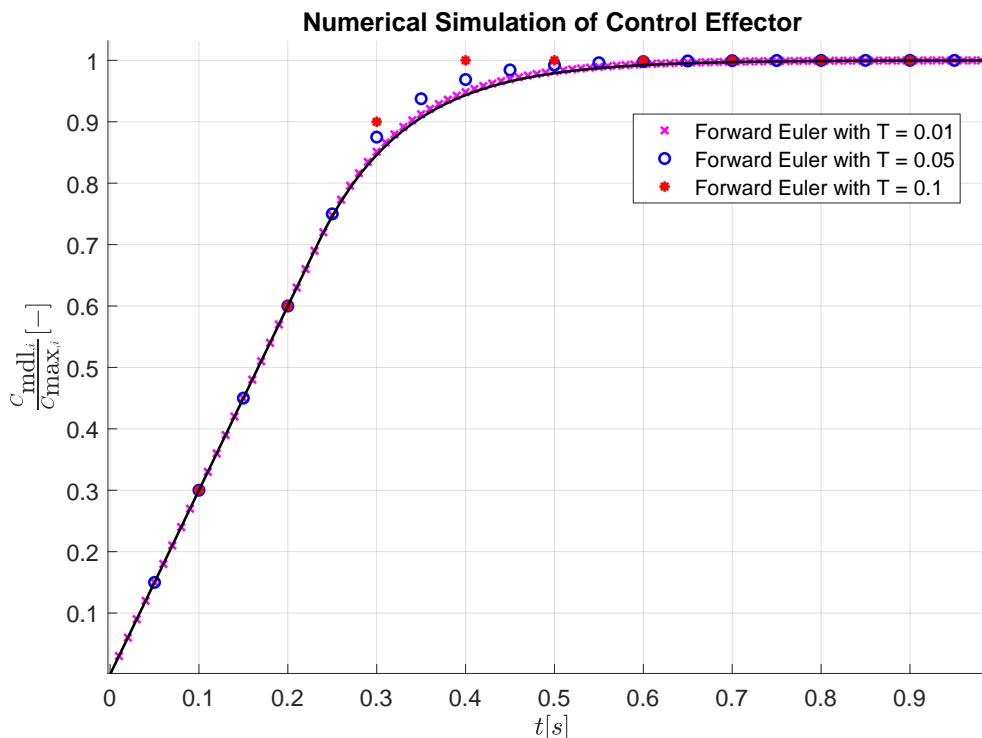


**Figure 6.3:** *Forward Euler Integration of Control Effector Step Response for Different Sample Times*

However, depending on the step length of the numerical integration in relation to the dynamics that are simulated, the precision of the result can differ. Figure 6.3 shows the simulated step response of (6.23) for a control effector bandwidth of  $K_{C,i} = 10$  and rate limit of  $\dot{C}_{max,i} = 3$  using forward Euler integration with different step lengths. It can be observed that with increasing sample times  $T$  (i.e. with increasing step lengths), the solution to the differential equation starts to deviate more from the exact solution (black solid line).

Hence the consideration of which integration method shall be used is ultimately driven by the sample time and the specified dynamics within the functional blocks of the control architecture. However, due to the comparatively slow time constants in the context of larger VTOL transition aircraft, the forward Euler method seems a reasonable choice for the implementation of reference models and control effector models, which are governed by nonlinear differential equations.

## 6.2 Control Design Model

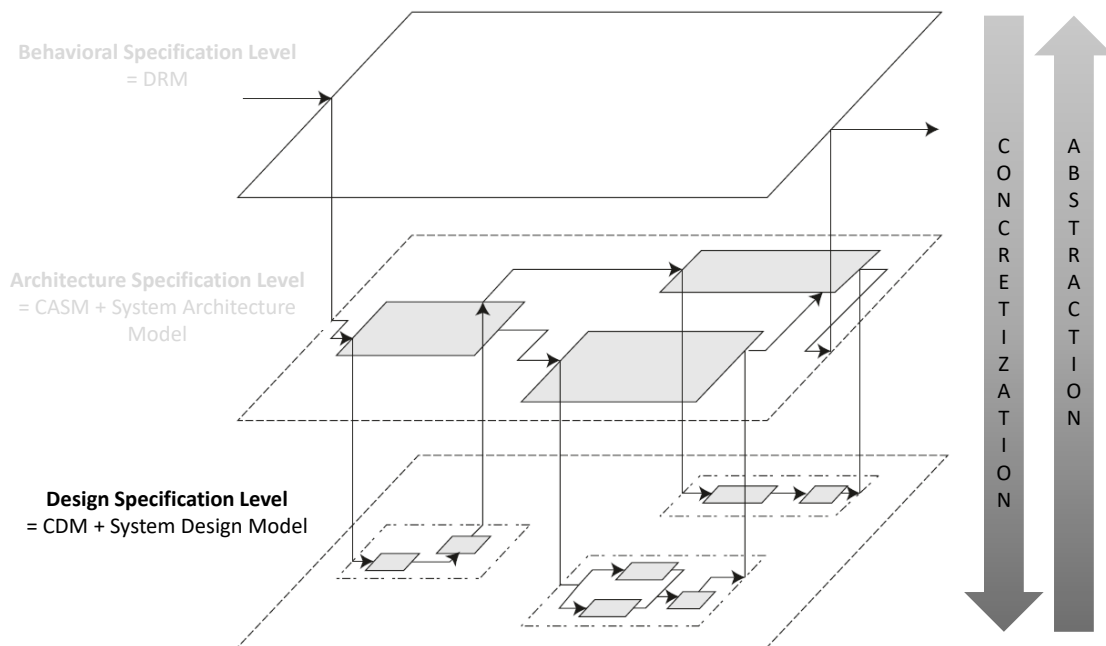


**Figure 6.4:** *Control Design Model (CDM) on the Design Specification Level (figure adapted from [3])*

The *Control Design Model* (CDM) specifies the final design of the flight control algorithms on the highest concretization level (i.e. the lowest abstraction level). It thereby represents the implementation-specific realization of the functional specification, which is embodied by the CASM, in terms of an executable and code-generable model. Due to the automatic code generation and compilation, the specification and implementation of the flight control source code are condensed into one seamless process step.

In order to yield a high degree of modularity, the CDM is composed of individual *Component Design Models*, which represent the algorithmic implementations of the functional controller subsystems discussed in section 5.3. Decomposition of the implementation into multiple components thereby supports their verification with respect to the low-level controller requirements by the comprehensive application of unit tests. Additionally, the possibility to code-freeze individual controller components facilitates adhering to the concepts of consecutive development and piecemeal engineering [3].

The stepwise design, implementation, verification, and integration of the individual Component Design Models into the CDM thereby follows the systems engineering process model. Furthermore, being part of the final stage within the overall flight control development, the design of the CDM yields the most granular work flow and requires the most specific considerations during the modeling process.

In contrast to the CASM, which represents the functional controller requirements in terms of an executable specification model, the CDM yields the concretized algorithmic realization of the controller functions in the context of the physical implementation of the system. Therefore, the design of the CDM has to account for implementation-related constraints such as:

- interfaces to other avionics components in terms of signal name, unit, data type, and sample rate,
- characteristics of the target flight control computer platform in terms of its software and hardware architecture as well as its computational performance, and
- development environment and application of toolchains, which enable the automatic model-based generation of the flight control source code by using the CDM as specification.

The development of the CDM thereby represents the final step in the context of the proposed model-based systems engineering process and yields the full specification of the flight control code. By the subsequent use of automatic code generation [151], the algorithm design specification represented by the CDM is converted into platform-specific source code. However, in order to ensure the functional integrity of the code, the CDM has to adhere to strict modeling standards.

To this end, subsection 6.2.1 introduces the concept of modeling guidelines, which are used for the development of models and the generation of code for high-integrity systems [152] using Matlab Simulink [78]. These guidelines are based on several software safety standards such as DO-178C [18] and are targeted at ensuring that the implemented models and generated source code are complete, robust, and maintain a high functional integrity [152].

Furthermore, subsection 6.2.2 shows the exemplary implementation of the Component Design Model for the rotational acceleration complementary filter using the difference equation from (6.22), which was derived in subsection 6.1.4. Thereby, the application of modeling guidelines from subsection 6.2.1 is demonstrated.

Finally, subsection 6.2.3 presents the code generation for the component design model from subsection 6.2.2 as the final step of the implementation. The model as well as the therefrom generated source code can subsequently be used in the verification and validation process, which is further discussed in section 6.3.

Due to the extended degree of specificity, the development of the CDM is not presented in an exhaustive manner. However, despite not yielding the complete implementation, the given process demonstrates the general work flow for the overall development of the flight controller.

### 6.2.1 Modeling Guidelines

The presented modeling guidelines in this subsection provide an example of rules and recommendations for designing and creating Simulink [78] models for subsequent code generation and integration into high-integrity systems. Especially for the development of safety-critical software, the strict application of standards and processes is needed in order to ensure the overall quality of the final outcome [153].

According to Mathworks, “[t]he guidelines provide model setting, block usage, and block parameter considerations for creating models that are complete, unambiguous, statically deterministic, robust, and verifiable” [152]. The rationale behind these modeling standards is to:

- increase the functional integrity of the generated code through compiler and programming language considerations,
- adhere to the constraints of the applied toolchain including the code generator, the compiler, and the target platform,
- facilitate the traceability of model and generated code with respect to the underlying requirements, and
- improve the testability and maintainability of the generated artifacts.

Table 6.1 shows an example of modeling guidelines as they are proposed in [17]:

**Table 6.1:** *Example of Modeling Guidelines [17]*

<b>Name</b>	<i>Model File Names and Model Object Names</i>
<b>Description</b>	<p>For model file names and model object names:</p> <ul style="list-style-type: none"> <li>• Only use characters a-z, A-Z, 0-9, and underscore (<code>_</code>).</li> <li>• Strings shall be more than 2 and less than 64 characters for file names and less than 32 characters for object names.</li> <li>• Do not start the name with a number or underscore, use more than one consecutive underscore, or end the name with an underscore.</li> </ul>
<b>Rational</b>	<p>Due to the code generation of the individual model files and the included objects, their names are propagated into the final source code as function and variable names. Typically, compilers have strict limitations regarding the usage of symbols in function and variable names in order to reduce ambiguity. Furthermore, the proposed rules increase the readability of the model files and objects as well as the resulting program code and facilitate the traceability between them.</p>

<b>Name</b>	<i>Protection Against Division by Zero</i>
<b>Description</b>	When performing division operations, protect the divisor from going to zero.
<b>Rational</b>	Division by zero can lead to undefined behavior dependent on the programming language, compiler setting, and data type of the dividend and divisor.
<b>Name</b>	<i>Protection Against Recursive Function Calls</i>
<b>Description</b>	Recursion occurs, when a function calls itself directly or indirectly through another function call.
<b>Rational</b>	Recursive function calls cannot always be proven to yield a finite execution time. In order to promote a bounded function call behavior, recursion shall be avoided.
<b>Name</b>	<i>Usage of Gain Blocks</i>
<b>Description</b>	Values of gain blocks must not resolve to 1.
<b>Rational</b>	Gain operations that resolve to the unity gain can be removed during the code generation due to optimization. This results in missing traceability between certain model elements and the generated code.
<b>Name</b>	<i>Avoidance of Implicit Data Type Casts</i>
<b>Description</b>	When using relational operators, the same data type shall be used for each operand.
<b>Rational</b>	Relational Operators (such as $<$ , $>$ , $!=$ , etc.) relate two operands with each other. If the operands yield different data types, implicit casting is performed during the code generation or compilation stage, which can lead to unexpected results.
<b>Name</b>	<i>Avoidance of Dead Code</i>
<b>Description</b>	According to DO-178C, dead code is “executable object code (or data) which exists as a result of a software development error but cannot be executed (code) or used (data) in any operational configuration of the target computer environment. It is not traceable to a system or software requirement” [18].
<b>Rational</b>	Dead code by definition is not executable during run time in any operational setting of the program. As a result, it is not covered by requirements-based testing and can produce unexpected results upon inadvertent activation.

The presented modeling guidelines are merely a subset of all available rules and standards and are aimed to provide a general idea of the concepts. An exhaustive treatment of all modeling guidelines is not in the scope of this thesis. However, the interested reader may refer to [152], [17], [154], and [153].



## 6.2.2 Implementation of Component Design Model for Complementary Filter

The following subsection presents the implementation of the Component Design Model for the rotational acceleration complementary filter algorithm from (6.22), which was derived in subsection 6.1.4. Figure 6.5 below shows the code-compliant design model implemented in Matlab Simulink [78].

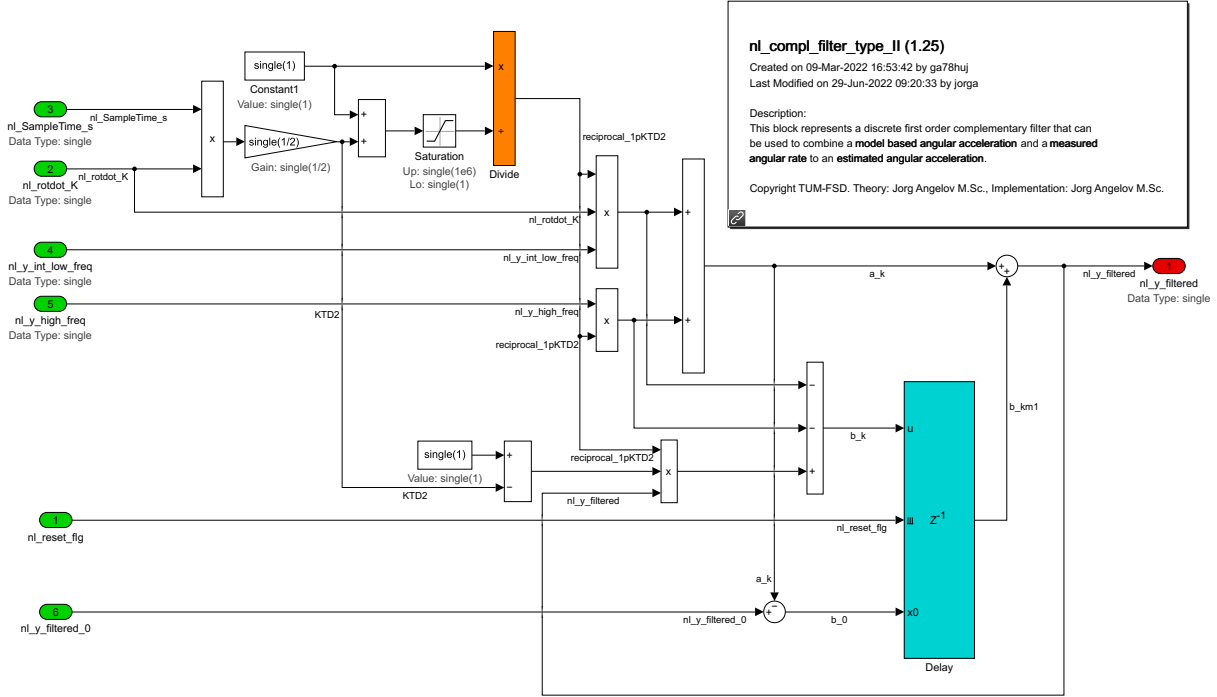


**Figure 6.5:** *Component Design Model of Complementary Filter*

To this end, recall the difference equation from (6.22):

$$\begin{aligned} \dot{\omega}_F[k] = & \frac{1 - \frac{K_{F,d}T}{2}}{1 + \frac{K_{F,d}T}{2}} \dot{\omega}_F[k-1] + \frac{K_{F,d}}{1 + \frac{K_{F,d}T}{2}} (\omega_{\text{msr}}[k] - \omega_{\text{msr}}[k-1]) \\ & + \frac{1}{1 + \frac{K_{F,d}T}{2}} (\dot{\omega}_{\text{mdl}}[k] - \dot{\omega}_{\text{mdl}}[k-1]), \end{aligned} \quad (6.24)$$

which summarizes the algorithm for the complementary filter. Note that the structure of (6.24) requires storing three individual states (i.e. the delayed signals  $\dot{\omega}_F[k-1]$ ,  $\omega_{\text{msr}}[k-1]$ , and  $\dot{\omega}_{\text{mdl}}[k-1]$ ) in order to calculate the filtered output at the current time step  $\dot{\omega}_F[k]$ .

However, since the design of the CDM takes into account implementation-specific constraints such as the limited amount of storage on the target computer platform, the filter equation can be rearranged into

$$\dot{\omega}_F[k] = a[k] + b[k-1], \quad (6.25)$$

with the terms

$$a = \frac{K_{F,d}}{1 + \frac{K_{F,d}T}{2}}\omega_{\text{msr}} + \frac{1}{1 + \frac{K_{F,d}T}{2}}\dot{\omega}_{\text{mdl}} \quad (6.26)$$

and

$$b = \frac{1 - \frac{K_{F,d}T}{2}}{1 + \frac{K_{F,d}T}{2}}\dot{\omega}_F - \frac{K_{F,d}}{1 + \frac{K_{F,d}T}{2}}\omega_{\text{msr}} - \frac{1}{1 + \frac{K_{F,d}T}{2}}\dot{\omega}_{\text{mdl}}. \quad (6.27)$$

In contrast to (6.24), the filter equation in (6.25) requires storing only one single state corresponding to the value of  $b$  in (6.27) from the previous computation step.

The utilized block performing the delay operation is depicted in figure 6.5 in cyan. It is additionally marked with the  $z^{-1}$  symbol, thereby referencing the corresponding delay operation in the discrete-time domain. The delay block has three inputs:

- The first input corresponds to the signal that is to be delayed. It is denoted as `b_k` in figure 6.5 and calculated according to (6.27) using the signals from the current time step.
- The second input denotes the reset signal, which initializes the internal state of the delay block to the initial condition. Thereby, the specific implementation of the reset operation can be adjusted such as to trigger upon a rising or falling (or both) edge of the reset signal as well as during the application of a nonzero reset signal.
- The third input denotes the initial condition, which is applied to the internal state of the delay block during the reset.

Furthermore, the initial condition `b_0` of the delay block is calculated according to

$$b_0 = \text{nl\_y\_filtered\_0} - a_k, \quad (6.28)$$

where `nl_y_filtered_0` denotes the desired initial condition of the filter and `a_k` is calculated according to (6.26). Note that during the reset of the filter, its output is rendered equal to `nl_y_filtered_0`, which follows from inserting (6.28) into (6.25).

All input ports to the Component Design Model from figure 6.5 are colored in green:

- `nl_SampleTime_s` denotes the sampling time  $T$  in seconds.
- `nl_rotdot_K` denotes the prewarped filter bandwidth  $K_{F,d}$  from (6.19).
- `nl_y_int_low_freq` denotes the rotational rate measurement  $\omega_{\text{msr}}$ .
- `nl_y_high_freq` denotes the model-based rotational acceleration estimation  $\dot{\omega}_{\text{mdl}}$ .
- `nl_reset_flag` denotes the reset signal.
- `nl_y_filtered_0` denotes the desired initial condition of the filter output  $\dot{\omega}_F$ .

Furthermore, the orange block in figure 6.5 performs the division operation specified by the denominator in (6.24) by outputting the signal `reciprocal_1pKTD2`, which corresponds to  $\frac{1}{1 + \frac{K_{F,d}T}{2}}$ . According to the modeling guideline *Protection Against Division by Zero* from table 6.1, the divisor shall be protected from going to zero in order to avoid unexpected results during the division.

To this end, a saturation block is implemented before the divisor signal is entering the division block at the second input, which provides a lower limit of 1 for the denominator  $1 + \frac{K_{F,d}T}{2}$ . Note that although the sample time  $T$  and the prewarped bandwidth  $K_{F,d}$  by definition are both guaranteed to be greater than zero, the implementation of the saturation block provides an additional layer of protection against design errors.

The output of the Component Design Model is shown as a red port in figure 6.5 and yields the filtered signal at the current time step  $\hat{\omega}_F[k]$ . In general, all parameters used during the calculation are chosen to have the data type *single*. This reduces the amount of storage for the saved parameters and – depending on the target hardware architecture – accelerates the operations for addition, subtraction, multiplication, and division. In general, however, the choice of the used data types is highly dependent on the specific application and has to be considered based on the required precision of the results.

### 6.2.3 Code Generation and Software-in-the-Loop Simulation of Complementary Filter

After having designed the Component Design Model for the rotational acceleration complementary filter, the next step is concerned with the code generation. To this end, the embedded toolchain from Matlab Simulink [78] is used, which converts the model from figure 6.5 into C code.

Matlab provides an interface through the model configuration file, which “includes parameters for defining the code generation process including target selection (...) [and] also (...) for inserting comments and pragmas into the generated code for data and functions” [155]. Thereby, the configuration of the model with respect to the code generation has to be adapted to the specific hardware requirements of the target platform.

The generated code is subsequently compiled into a binary executable file, which embodies the specified functional algorithm of the complementary filter in the form of machine code. Latter represents the set of instructions that are directly interpreted by the central processing unit (CPU) of the target computer. For demonstration purposes, the generated code is adapted for the operation on a desktop PC rather than a specific embedded platform representing the flight control computer.

The compiled executable can furthermore be tested in the context of a software-in-the-loop (SIL) simulation. In particular, comparing the input-output relationship of both the compiled source code and the corresponding design model that served as the specification, allows for gaining confidence in the correct conversion of the model into code.

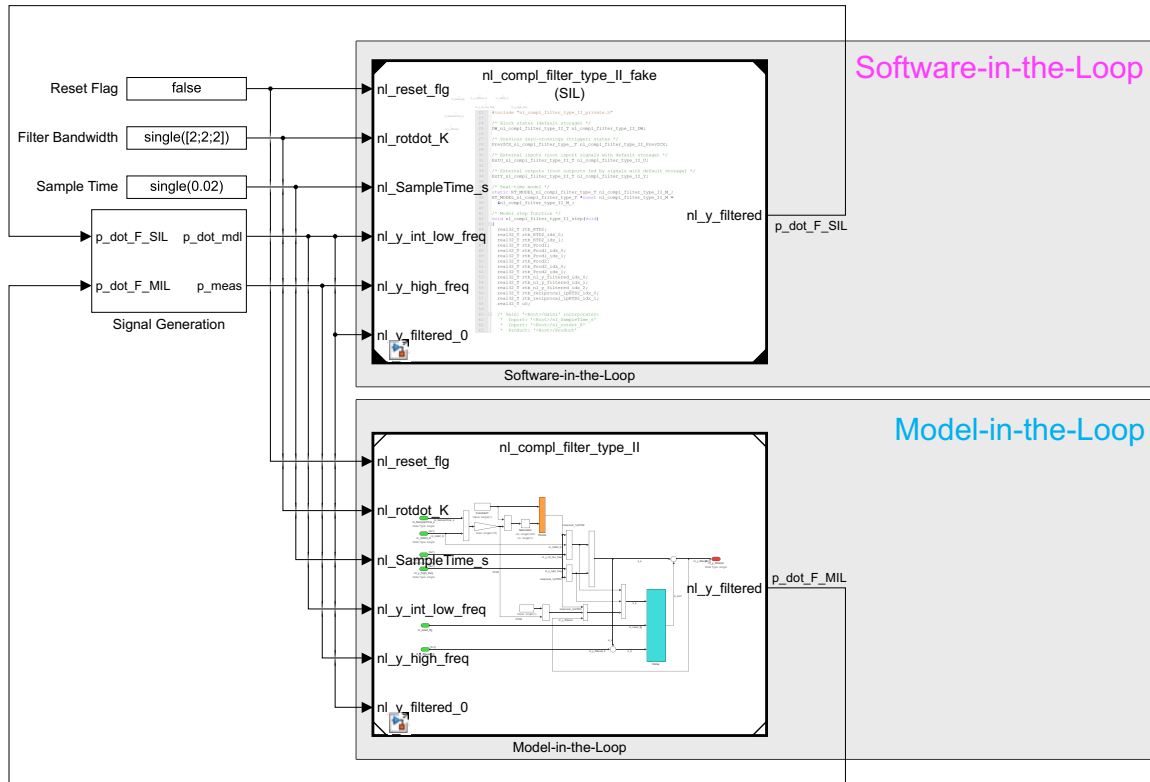


**Figure 6.6:** *Software- vs. Model-in-the-Loop Simulation of Complementary Filter*

To this end, figure 6.6 illustrates a setup in which the Component Design Model from figure 6.5 (bottom) is simulated in parallel with the compiled executable code (top) generated from it. Thereby, the executable binary at the top is embedded into the same model wrapper as the design model on the bottom and hence provides an identical interface.

However, the execution of the algorithm is performed externally and decoupled from the simulation environment by calling the executable as a separate process. Furthermore, Mathworks states that “[b]y comparing normal and SIL simulation results, you can test the numerical equivalence of your model and the generated code. During a SIL simulation, you can collect code coverage and execution-time metrics for the generated code” [156].

In order to test the equivalence of the design model and the executable binary in terms of their simulation results, the same input signals are used for both entities. To this end, the signal generation block in figure 6.6 provides an exemplary set of two time series for the measured roll rate and the model-based roll acceleration.

Thereby, the real roll rate signal is obtained by integration of a smooth reference roll acceleration signal. The roll rate measurement is additionally corrupted by sensor noise, which is modeled as a zero-mean Gaussian distribution and added to the clean roll rate signal. The model-based roll acceleration signal is obtained from the clean roll acceleration signal through addition of a constant bias, which shall account for an unmodeled external roll moment (similar to subsection 5.4.1.2).

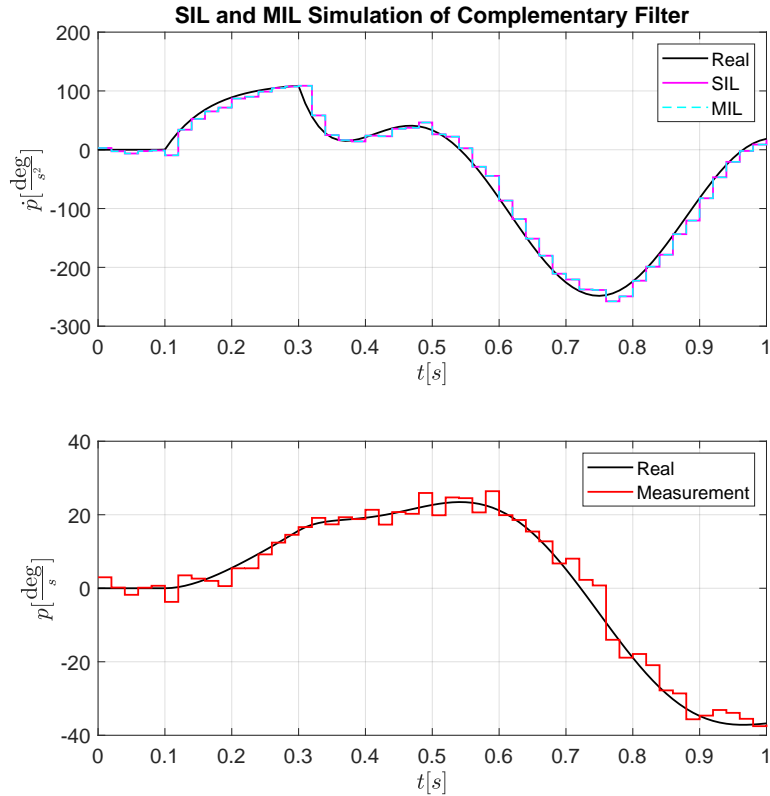


**Figure 6.7:** *Simulation Results of Software- vs. Model-in-the-Loop Simulation of Complementary Filter*

Furthermore, both the Component Design Model and the compiled binary are operated at a sampling rate of 50 Hz (i.e. a sample time of 0.02 s) and are configured with a prewarped filter bandwidth of  $2 \frac{\text{rad}}{\text{s}}$  without loss of generality. Figure 6.7 shows the simulation results of the software- and model-in-the-loop test. The lower plot shows the real roll rate in black and the measured roll rate in red, which is illustrated as a zero-order-hold signal by applying the *stairs* function [157] on the discretized measurement.

The upper plot in figure 6.7 shows the real roll acceleration in black as well as the two filtered signals generated by the Component Design Model (cyan) and the executable binary (magenta). Similar to the sampled roll rate, the filtered roll acceleration signals are plotted using the *stairs* function [157], which holds the discrete values during the length of one sample time for each step.

The comparison between both simulation outputs shows the numerical equivalence of the model-based algorithm and its concretization in terms of the executable machine code file. Hence, it is verified that the functional integrity is preserved under the code generation and compilation process. In addition to testing the equivalence of both filter outputs, the functional requirements of the complementary filter algorithm itself can also be assessed by comparing the real roll acceleration signal with the filtered output. However, the comprehensive verification and validation of the control algorithm and the resulting source code is discussed in section 6.3.

## 6.3 Verification and Validation of Control Algorithms and Source Code

The preceding sections yielded the final artifact of the model-based systems engineering process for the flight control development of a VTOL transition aircraft: the source code of the overall control-related functionality, which is automatically generated from its specification embodied by the Control Design Model.

This section shall give an overview over the possible verification and validation activities, which can be used to thoroughly test and assess the correctness and feasibility of the proposed control algorithm design and the resulting manifestation in terms of compilable source code and executable machine code. This final testing phase is crucial in order to ensure the quality and integrity of the developed flight controller.

Especially in the context of person-carrying VTOL aircraft, the flight control functionality represents a safety-critical element for which a design error or implementation error can lead to severe material damage, injuries, or catastrophic events including fatalities. Therefore, the verification and validation activities proposed in the following are aimed at yielding confidence in the correct implementation and satisfactory emergent behavior of the flight controller to the highest degree possible.

### 6.3.1 Static Code Analysis

Static code analysis represents an important concept for finding vulnerabilities and defects in a given program without having to compile and execute the underlying source code [158] [15]. Thereby, it complements the dynamic code analysis, which treats the compiled and executable program as a black box and performs the tests based on the emergent functionality of the program.

By systematically analyzing the structure of the source code as well as the underlying data and control flow through the program, “[s]tatic analyzers have the potential to find rare occurrences or hidden back doors” [158, p. 3]. Furthermore, [158, p. 3] adds that since “[s]tatic checkers consider code independently of any particular execution (...) [and] analyz[e] the code without compiling it[,] (...) [they] can enumerate all possible interactions between the different modules and components of the analyzed code”.

One particular type of static code analysis is referred to as modified condition/decision coverage (MC/DC) [15] and is required for the development of safety-critical software with Design Assurance Level A (DAL-A) according to the *Software Considerations in Airborne Systems and Equipment Certification* document DO-178C [18]. Thereby, the Design Assurance Level relates to the rigorosity and amount of requirements (objectives) that have to be satisfied by the software based on the potential effects of a failure condition involving the developed item.

To this end, [18] classifies the failure conditions and assigns the Design Assurance Levels (DAL) according to table 6.2, which lists the amount of applicable objectives for each case. Thereby, independent objectives refer to those software requirements that have to be tested by a different person or team than the one implementing it.

**Table 6.2:** *Design Assurance Levels and Applicable Process Objectives in DO-178C [18]*

<b>Failure Condition Classification</b>	<b>Failure Condition Description</b>	<b>Design Assurance Level</b>	<b>Number of Objectives</b>
Catastrophic	Failure that prevents continued safe flight and landing and can result in loss of aircraft and multiple fatalities.	A	71 (30 independent)
Hazardous	Failure that results in excessive crew workload and severe or fatal injuries.	B	69 (18 independent)
Major	Failure that leads to significant reduction of safety margins and presence of physical discomfort and increased crew workload.	C	62 (5 independent)
Minor	Failure that leads to slight increase in crew workload.	D	26 (2 independent)
No Safety Effect	Failure that has no effect on safety.	E	0 (0 independent)

The modified condition/decision coverage (MC/DC) testing thereby represents one of the 71 objectives prescribed by the DAL-A classification of a software item and is part of a process that is referred to as structural coverage analysis [15]. Together with the requirement coverage analysis, both methods are concerned with yielding “the extent to which a given verification activity has satisfied its objectives” [15, p. 10].

In the case of requirement coverage, the term refers to how well the testing strategy covers the list of existing software requirements by verification of their corresponding implementation. The maximum degree of coverage thereby refers to verifying the implemented software items against every single software requirement by means of a test case and providing the corresponding traceability between both.

However, requirement coverage alone does not guarantee the functional integrity of the software, since [15]:

- the list of software requirements is not guaranteed to be complete,
- not every test case necessarily tests the corresponding requirement in an exhaustive manner, and
- the presence of unintended functionality cannot be excluded even for full requirement coverage.

Therefore, the software assessment process is complemented by the method of structural coverage analysis, which is concerned with confirming that “the requirements-based test procedures exercised the code structure” [18] sufficiently. Furthermore, [15, p. 9] states that “typical statistical approaches to quality assurance, which work well for physical devices, do not apply to software (...) [and] [c]onsequently, drawing conclusions about software quality short of testing every possible input to the program is fraught with danger” [15, p. 9].

Coverage Criteria	Statement Coverage	Decision Coverage	Condition Coverage	Condition/Decision Coverage	MC/DC	Multiple Condition Coverage
Every point of entry and exit in the program has been invoked at least once		•	•	•	•	•
Every statement in the program has been invoked at least once	•					
Every decision in the program has taken all possible outcomes at least once		•		•	•	•
Every condition in a decision in the program has taken all possible outcomes at least once			•	•	•	•
Every condition in a decision has been shown to independently affect that decision's outcome					•	•
Every combination of condition outcomes within a decision has been invoked at least once						•

**Figure 6.8:** *Types of Structural Coverage [15]*

To this end, MC/DC testing represents one of many types of structural coverage analysis, which are summarized in figure 6.8 in increasing order of rigorosity. Only *Multiple Condition Coverage* would provide a more comprehensive measure, however proves to be impractical for complex software with a large number of conditions [15]. Thereby, the terms *condition* and *decision* refer to specific semantic constructs in the source code that often entail a branching point in the control flow of the program.



Within DO-178C [18] the following definitions are provided:

*Condition* – A Boolean expression containing no Boolean operators.

*Decision* – A Boolean expression composed of conditions and zero or more Boolean operators. A decision without a Boolean operator is a condition. If a condition appears more than once in a decision, each occurrence is a distinct condition.

*Modified Condition/Decision Coverage* – Every point of entry and exit in the program has been invoked at least once, every condition in a decision in the program has taken all possible outcomes at least once, every decision in the program has taken all possible outcomes at least once, and each condition in a decision has been shown to independently affect that decision’s outcome. A condition is shown to independently affect a decision’s outcome by varying just that condition while holding fixed all other possible conditions.

In the scope of the MC/DC analysis it is hence assessed, how much of the source code – including different outcomes for conditions and decisions – is covered by the requirements-based testing routine. High coverage thereby is a good indicator that the developed source code was tested thoroughly against the requirements and that the presence of unintended functionality is minimized.

### 6.3.2 Unit and Integration Tests

While the static code analysis discussed in subsection 6.3.1 is concerned with assessing the structural coverage of the flight control source code, the unit and integration tests represent the underlying process to exercise the code structure in terms of requirements-based testing. Hence, these tests fall under the category of dynamic code analysis and are targeted at analyzing the emergent behavior of the compiled source code.

To this end, unit tests are used in order to verify the algorithm design and implementation of individual controller subsystems with respect to applicable low-level requirements by simulation of the corresponding Component Design Model or the therefrom generated executable binary file. One example of a possible unit test setup is given in subsection 6.2.3, where the equivalence between the Component Design Model and the generated and compiled source code of the complementary filter was assessed in the scope of a model- and software-in-the-loop simulation.

While the simulation setup from figure 6.7 was primarily targeted at verifying the correct conversion of the executable algorithm specification (embodied by the Component Design Model) into the algorithm implementation (represented by the generated and compiled code), no explicit assessment of their functionality with respect to requirements was performed.

Thereby, possible test cases for the complementary filter could include verifying if the algorithm:

- yields the same functionality as the corresponding functional specification model from figure 5.46 (which is part of the CASM),
- is compatible with the target computer platform (e.g. in terms of data types and computational effort),
- yields a good estimation of the real roll acceleration signal, and
- has the desired frequency characteristics and provides sufficient noise attenuation.

Additionally to verifying individual components of the controller by performing unit tests, the complete control algorithm is verified by execution and evaluation of comprehensive integration tests. The controller can thereby be represented in terms of its design model (CDM), its compiled binary file, or its physical manifestation in terms of the FCC, which yields a model-, software-, or hardware-in-the-loop simulation setup respectively.

To this end, the controller interacts with a system design model, which provides the correct and concretized interfaces on the implementation level and reflects the overall system behavior. Thereby, the system design model does not necessarily have to represent the complete aircraft architecture on the lowest level, but merely needs to embed the interfaces to all peripherals of the flight controller such as the inertial measurement unit (IMU), air data system (ADS), electronic speed controllers (ESC), and battery management system (BMS). The model fidelity of the flight controller peripherals and the remaining aircraft components can thereby be adjusted based on the specific requirements and derived functionality of the control algorithms.

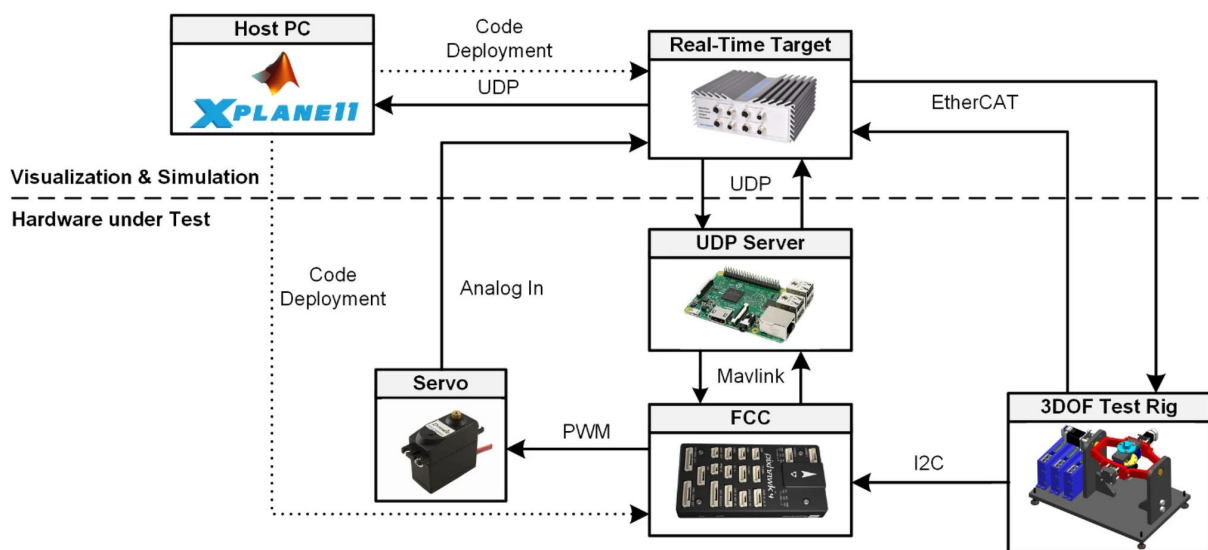


**Figure 6.9:** Exemplary Hardware-in-the-Loop Setup for a Flight Control Computer [16]

For hardware-in-the-loop (HIL) simulation setups, some of the aircraft component models can be replaced with their physical representations, i.e. the actual component. Figure 6.9 shows an exemplary setup of a HIL simulation for a flight control computer (FCC) that interacts with a servo motor via pulse-width modulation (PWM) and receives data from an IMU.

The IMU is thereby excited by a 3DOF motorized rotation stage, which converts the simulated rotational body rates of the system into the corresponding motion of the inertial sensors by actuating the rotary frame [16]. The target rotational rates thereby result from the rigid-body simulation model running on the host PC, which simulates the system response by incorporating the physical deflection angle of the servo motor. Latter is fed back into the simulation loop via analog-to-digital conversion.

By conducting model-, software-, or hardware-in-the-loop integration tests, the final controller implementation can be verified against existing high-level requirements. Thereby, the emergent functionality of the control algorithms can be assessed with respect to:

- tracking performance,
- handling qualities,
- stability characteristics, and
- failure mitigation capabilities.

Furthermore, by conducting pilot-in-the-loop simulation tests that require performing a full flight mission or Mission Task Elements [12], the implementation of the flight controller can be validated with respect to explicit use case scenarios. Additionally, integrating the controller into an iron bird setup allows for comprehensive evaluation of the FCC's interaction with peripheral avionic components.

### **6.3.3 Subset Simulation and Counter Optimization for Finding Rare Failure Events**

Unit and integration tests discussed in subsection 6.3.2 represent an effective way to conduct comprehensive verification and validation of the developed flight control algorithms. However, conventional testing methods usually do not exhaust the whole set of possible outcomes and rare failure events might not be encountered during the testing phase [159] [160].

During the assessment of the controller, the requirements-based test scenarios are usually performed with fixed parameter settings or predetermined parameter ranges or distributions. Thereby, parameters yield the possibility to introduce variability into the individual test scenarios by altering specific characteristics of:

- the aircraft (such as mass, center of gravity, inertia, or aerodynamic properties),

- the control effectors (such as power output, bandwidth, and effectiveness),
- the sensors (such as bias, scale factor, misalignment, and noise level), and
- the environment (such as air temperature, density, wind/gust direction, speed, and duration).

Note that in practice, however, the high-dimensional parameter space prohibits exhaustive testing of all possible parameter combinations (curse of dimensionality). To this end, the well-known method of Monte Carlo Sampling (MCS) [161], which is widely adopted in the industry, yields an effective method to assess the probability distribution of any variable of interest or the probabilities of specific outcomes such as the violation or fulfillment of requirements.

In particular, each parameter  $\theta_i$  is modeled as a random variable following a predefined probability distribution. Thereby, the specific shape of the probability density function (PDF) depends on the characteristics of each parameter, but can often be approximated by a Gaussian (i.e. normal), Binomial, or Poisson distribution [161]. The general idea of MCS is to perform a large number of simulations  $N$  for which each parameter is sampled according to its inherent probability density at the beginning of every simulation run. Subsequently, specific variables of interest are analyzed and their resulting probability distributions are inferred numerically based on the large amount of simulation data.

Monte Carlo simulation represents a very naive and straight-forward approach to Bayesian inference and provides an effective way to estimate the probabilities or probability distributions of specific outcomes and variables of interest. However, the number of required simulations and the achieved precision in estimating the probabilities of certain events highly depends on their nature of occurrence. It is generally desired that the probability of requirement violations should be as low as possible. Hence, the events characterizing the failure of requirements are rare by design.

In particular, if a given failure event  $F$  occurs with a probability of  $P(F)$  in each simulation run, the required average number of simulations to observe the failure event once is given by  $N = \frac{1}{P(F)}$ . As a rule of thumb [159], at least 10 samples should be generated in order to obtain reliable statistics about the probability of a given failure event using statistical averaging of the form

$$P(F) = \frac{1}{N} \sum_{k=1}^N I(\boldsymbol{\theta}_k \in \mathcal{F}), \quad (6.29)$$

where  $P(F)$  is the probability of the failure  $F$  occurring,  $N$  is the number of samples (i.e. simulation runs),  $\boldsymbol{\theta}_k = [\theta_{1,k} \ \theta_{2,k} \ \cdots \ \theta_{n,k}]$  is the vector of  $n$  parameters for the  $k$ -th simulation run, and

$$I(\boldsymbol{\theta}_k \in \mathcal{F}) = \begin{cases} 1, & \text{if } \boldsymbol{\theta}_k \in \mathcal{F} \\ 0, & \text{otherwise} \end{cases} \quad (6.30)$$

denotes the indicator function, which yields a value of 1 only if the parameters  $\theta_k$  are within the failure domain  $\mathcal{F}$ , i.e. if a failure event has occurred. Thereby, the value of the indicator function  $I$  for each individual parameter vector  $\theta_k$  is obtained by simulating the test scenario for each sample and evaluating if the requirement of interest is violated ( $I = 1$ ) or not ( $I = 0$ ).

For a failure event probability of e.g.  $P(F) = 10^{-9}$  it would hence require around 10 billion (i.e.  $10^{10}$ ) simulation runs on average to obtain reasonable statistical information (i.e. with low coefficient of variation). For large and complex simulation models, however, each test run requires a substantial amount of computational effort and time. Therefore, the conventional Monte Carlo method yields an effective but inefficient approach to estimate the probabilities of rare events, such as the occurrence of failures expressed as requirement violations.

A substantially more efficient method for yielding simulation samples from the failure domain is referred to as *Subset Simulation* (SS) [159] [160] [162] [163] [164] [165] [166], which was originally developed “for estimation of structural reliability of complex civil engineering systems such as tall buildings and bridges at risk from earthquakes” [164, p. 1]. Furthermore, [164, p. 1] elaborates that “[t]he method turned out to be so powerful and general that over the last decade, SS has been successfully applied to reliability problems in geotechnical, aerospace, fire, and nuclear engineering”.

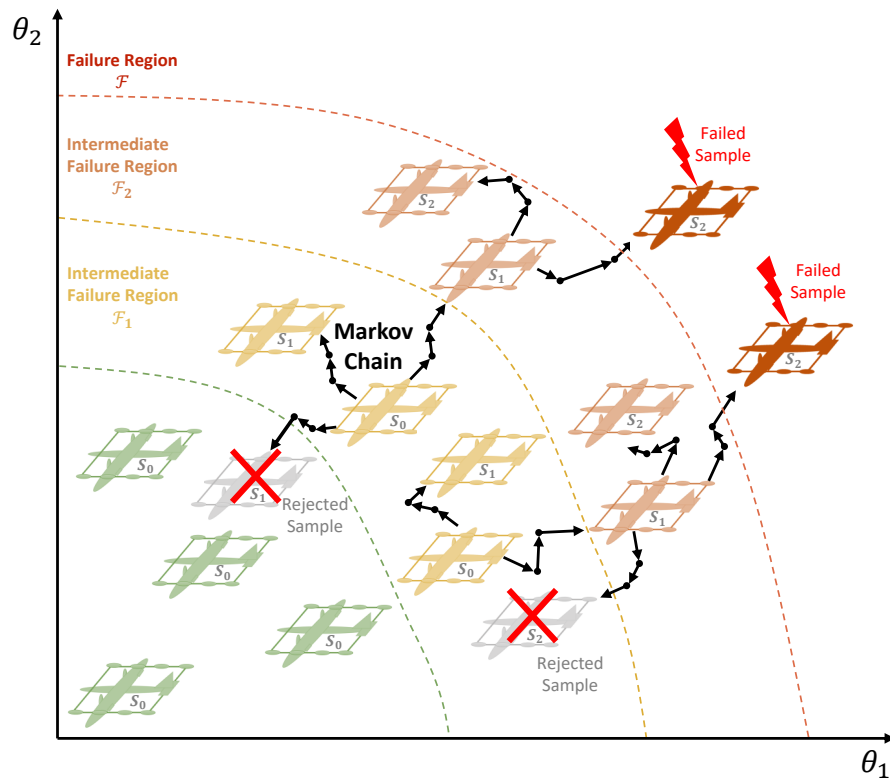


**Figure 6.10:** Finding Rare Failure Events With Subset Simulation Using Markov Chain Monte Carlo Sampling

The main idea of SS is to successively approach the process of sampling from the failure domain by sampling from intermediate failure distributions first. Thereby, the overall goals of SS in this context are:

- to efficiently yield parameter samples  $\theta_k \in \mathcal{F}$ , which lie in the failure domain  $\mathcal{F}$ . Consequently, the corresponding simulated test scenarios violate the requirement of interest.

According to the concepts of conditional probability, the sampling process hence yields parameter distributions that correspond to the probability density function  $P(\theta|F)$  conditioned on the failure event  $F$ , which represents the likelihood of a given parameter combination  $\theta$  given that the failure event  $F$  has occurred. A subsequent sensitivity analysis can yield insights into how individual parameters or parameter combinations manifest themselves in a failure scenario.

- to yield the overall probability  $P(F)$  of a failure event  $F$ . Being able to efficiently assess the probability of a requirement violation allows for verification of the controller against probabilistic requirements. Rather than just stating if a particular requirement is violated, the probability of violation is additionally obtained.

Furthermore, by conducting sensitivity analysis on the failure probabilities  $P(F|\theta_i)$  conditioned on a specific parameter  $\theta_i$  allows for identifying those parameters or parameter combinations that are critical with respect to the failure event.

A schematic representation of the sampling process is illustrated in figure 6.10. The interested reader is referred to [160], [162], and [164] for a detailed discussion and derivation of Subset Simulation. The resulting sampling process in the context of SS exhibits similarities to gradient-free optimization approaches such as evolutionary algorithms [167]. Furthermore, using so-called Counter Optimization (CO) methods [168] [169] [170] allows for finding worst-case inputs during a test scenario such that requirements of interest are purposely violated.

To this end, [168] uses deep Q-learning based worst-case analysis of a nonlinear flight control law for a fixed-wing aircraft. Thereby, a virtual agent is trained to violate a given requirement by means of Reinforcement Learning (RL). Similarly to SS, the performance objective  $Y$  can be used as a reward signal and the underlying neural networks are fit in order to approximate an optimal strategy for yielding a failure event.

The concepts introduced in this subsection can be used for both unit and integration tests and considerably increase the confidence in the functional integrity of the developed algorithms.

# 7

## Conclusion and Outlook

This final chapter is aimed to provide a brief summary of the presented work with an emphasis on the proposed contributions of this thesis, which were listed in section 1.4. To this end, section 7.1 addresses the individual contributions and reviews them critically. Thereby, practical experience from the flight control development of an existing VTOL transition aircraft is applied, which was gathered by the author at the Institute of Flight System Dynamics (FSD) throughout the creation of this thesis. In section 7.2 further outlook and perspectives in the context of VTOL transition aircraft are presented and possible future research topics are mentioned.

### 7.1 Summary and Conclusion

The contributions of this thesis were targeted at providing a model-based systems engineering approach to developing flight control functionality for VTOL transition aircraft. Since person-carrying capabilities pose additional requirements on the rigorosity of the development process and on the safety aspects of aircraft operation and control, the presented contents were focused on maximizing the quality of the developed behavioral concepts and control algorithms through consecutive model-based validation. The individual contributions of this thesis are listed and discussed in the following.

#### **Contribution 1: Unified Command Concept for Simplified Vehicle Operations of Onboard Piloted VTOL Transition Aircraft**

In the context of the behavioral specification of the system discussed in chapter 4, a unified command concept for VTOL transition aircraft was proposed, which is aimed at providing an intuitive and consistent aircraft response throughout the whole flight envelope under consideration of control margins and flight envelope protections. In combination with a comprehensive system automation concept, which was not in the focus of this work, the developed behavioral strategy enables Simplified Vehicle Operations (SVO) of a person-carrying VTOL transition aircraft.

In contrast to existing SVO concepts such as 'Unified' [75] and 'E-Z-Fly' [76], the presented operational concept is adapted to the novel control inceptor design presented in subsection 3.2.2, which is illustrated in figures 3.10 and 3.11. The extended stick concept allows for excellent flight state awareness through absolute kinematic and aerodynamic speed control of the aircraft based on the position of the novel control inceptor.

The adaptive scaling of high-level command variables upon approaching full stick deflections, which was discussed in subsection 5.3.3, as well as the comprehensive consideration of flight envelope protections throughout every phase of a flight mission allows for carefree operation of the VTOL transition aircraft. By additionally automating various aspects of the flight operation such as the reconfiguration activities during the (re)transition phase, the qualification requirements of the pilot are considerably reduced and the workload during the flight mission is kept at a minimum.

The presented command concept was extensively tested throughout its development at FSD. In the scope of simulated flight test campaigns conducted in [74] and [1], the concept yielded excellent handling qualities as evaluated on the Cooper-Harper Handling Quality Rating Scale (HQRS) by both pilots and subjects with no flight experience.

In particular, the polar stick mapping for direction preserving control, which is covered by **contribution C.1.1** in section 1.4 and was derived in subsection 4.2.1, proved to be essential for performing the Hover Mission Task Element (MTE) for diagonal repositioning presented in [171]. Furthermore, **contribution C.1.2** covers the forward translational rate concept for lift-plus-cruise configurations discussed in subsection 4.3.1.4 and subsection 5.3.4.1, which was consistently favored by the test subjects over the conventional pitch-based control during virtual flight tests.

The presented SVO concept was additionally assessed by professional test pilots with a lot of experience in rotorcraft and fixed-wing flight. Especially for pilots of rotary-wing aircraft the proposed layout of the control inceptors in figure 3.11 turned out to be quite counterintuitive. In particular, since rotorcraft pilots use the collective and cyclic stick to control the vertical and horizontal channel with their left and right hand respectively, the proposed control inceptor layout in this thesis of having the climb stick on the right side and the thrust stick on the left side led to confusion especially for experienced pilots. However, switching the position of both control inceptors resolved the initial confusion.

### **Contribution 2: Methodology to Implement and Validate Desired System Behavior by Executable Specification Model**

Early validation of novel system concepts is a crucial step to reduce development cost and increase the quality of the final outcome. In the systems engineering context of flight control for VTOL transition aircraft, the specification and validation of the behavioral concept is conducted in the beginning of the development. To this end, section 4.3 introduced the Design Reference Model (DRM), which represents an executable specification model of the closed-loop system behavior.



Since the DRM represents the aircraft behavior in terms of a system-architecture-agnostic rigid-body simulation model, it is developed independent of any assumptions regarding specific control effectors, sensors, and other elements of the overall aircraft architecture. However, by considering the kinetic characteristics and constraints of the system, such as the maximum amount of forces and moments that can be produced, the rate with which they build up, the mass and inertia of the aircraft as well as preliminary aerodynamic properties of the air frame, the DRM can yield a realistic motion response of the aircraft to pilot inputs and disturbances.

Consequently, the overall behavioral specification of the system based on the SVO concept can be validated in a virtual simulation environment by using pilot-in-the-loop flight tests such as in [74] and [1]. Furthermore, the behavioral concept can be verified quantitatively against existing handling quality requirements, which was demonstrated in section 4.4. Additionally, by yielding the specified system behavior with fixed kinetic constraints regarding the generation of forces and moments, the DRM can also be used to derive the specification for the required performance characteristics of motors, propellers, actuators, and control surfaces.

While the high abstraction level of the DRM enables modeling and validation of system requirements very early in the development, attention should be paid to those system aspects that are not sufficiently represented at this stage of the development process. Hence, the application of development iterations between different levels of the systems engineering process flow might sometimes be inevitable, however, can be considerably reduced by thorough model-based validation.

**Contribution 3: Incremental Strategy for Consecutive Executable Requirements Capture and Validation to Facilitate Process Frontloading** The present thesis proposed a model-based development process for yielding the flight control functionality of a person-carrying VTOL transition aircraft. Thereby, the concepts of systems engineering are applied, which were discussed in section 2.1.

The resulting strategy is based on the well-known ‘V’-model based development process and tightly integrates the consecutive creation of and validation through system models of increasing concretization that serve as executable requirement specification. To this end, the overall process flow in this thesis was structured into three phases:

- the specification and validation of the desired *closed-loop system behavior*, which was discussed in chapter 4,
- the specification and validation of the *control architecture*, which was discussed in chapter 5, and
- the specification and validation of the *control algorithm implementation*, which was discussed in chapter 6.

Each individual phase was thereby concerned with the specification of requirements on that particular level through stepwise decomposition of the high-level objectives from the preceding step and with the subsequent design and implementation of a requirement specification model. The resulting executable model was then extensively tested and analyzed, thereby following the concepts of model-based verification and validation introduced in subsection 2.2.2.

As was already clarified for **contribution C.2**, section 4.3 introduced the *Design Reference Model*, which enabled early validation of the behavioral specification and kinetic design of the aircraft. The DRM can hence be interpreted as the manifestation of the operational and performance requirements provided in section 1.3 into an executable behavioral specification model, which embodies the high-level control concept of the VTOL transition aircraft.

Furthermore, section 5.3 introduced the *Control Architecture Specification Model (CASM)*, which specifies the target behavior of the flight control components as well as their interfaces and interactions in terms of executable functional representations. The control architecture and the individual components thereby follow from functional requirement decomposition of the behavioral specification from the preceding step and are aimed to realize the behavior represented by the DRM.

Since the CASM specifies the desired control algorithm topology in terms of functional representations of all control components, it yields an implementation-agnostic representation of the controller and is hence independent of the specific realization of individual systems and components as well as implementation-related aspects such as computing platforms and interfaces to peripherals. The subsequent testing by simulation in the loop with a functional representation of the overall VTOL aircraft facilitates the validation of the proposed control architecture as well as the functional aircraft architecture in terms of the assumed control effectors and sensors, which was demonstrated in section 5.4.

Finally, section 6.2 discussed the *Control Design Model (CDM)*, which specifies the flight control algorithm design on the highest concretization level and thereby represents the implementation-specific realization of the functional controller specification given by the CASM in terms of an executable and code-generateable model. By adhering to strict modeling guidelines, which were introduced in subsection 6.2.1, the functional integrity of the resulting auto-generated source code is preserved, which can be verified by simulating the CDM and the resulting compiled binary in parallel. An example for comparing the model-in-the-loop and software-in-the-loop simulation results of an implemented control component was given in subsection 6.2.3.

Furthermore, section 6.3 presented different methods for the verification and validation of the developed control algorithms. To this end, subsection 6.3.1 briefly covered the concept of static code analysis. In particular, structural coverage analysis enables the assessment of how much of the code structure has been covered by requirements-based testing and hence supports uncovering program defects and vulnerabilities.

In subsection 6.3.2, conventional unit and integration tests were covered, which represent the main activity during the verification and validation of the developed control algorithms. Finally, subsection 6.3.3 discussed the concept of Subset Simulation (SS) for finding rare failure events by using Markov Chain Monte Carlo (MCMC) sampling and briefly introduced Counter Optimization for yielding worst-case input sequences.

The proposed strategy was applied in practice by the author during the flight control development of a VTOL transition aircraft prototype. Thereby, the thorough model-based validation activities in each development phase proved to be essential for ensuring correct requirements and considerably reduced the amount of development iterations. Furthermore, the resulting flight control software has been shown to yield excellent handling qualities and robustness against uncertainties and disturbances in the scope of pilot-in-the-loop simulation tests.

**Contribution 4: Continuity-Based Input-Output Mapping** A novel input-output mapping concept was introduced in section 4.1, which enables transition-free control authority transfer between different modes of operation while maintaining maximum authority and continuity of each mode. The developed concept was published by the author in [2] and was originally derived in the scope of developing a fly-by-wire direct law approach for a tandem-seat aircraft. The requirement of ensuring the continuity of the output and maintaining full authority over the command upon priority transfer between pilots was the driving motivation behind the algorithm development.

In the context of the present flight control development for VTOL transition aircraft, the continuity-based input-output algorithm was applied to the command mapping of the forward speed based on the stick deflection of the novel control inceptor from figure 4.3. Since the individual flight modes of the VTOL are subject to distinct speed envelopes, the mapping was aimed at avoiding discrete jumps in the command channel when transitioning from one flight regime to the other. The general concept was shown by an example in figure 4.1.

It was pointed out in subsection 4.2.3.1 that the continuity-based input-output mapping has the disadvantage of not providing consistent outputs given the same input in contrast to a constant stick mapping. For a high-level command variable such as the airspeed, a fixed mapping between control inceptor deflection and absolute speed demand might be desired in order to increase the pilot's awareness with respect to the flight state. Furthermore, recent adaptations of the proposed thrust stick yielded an extended stick range, which enabled the mapping of the transition aircraft's complete speed envelope onto the trust stick's longitudinal channel and hence rendered the proposed continuity-based mapping redundant for this application. However, for low-level control applications such as commanding control surface deflections in the context of a fly-by-wire direct law, the proposed mapping strategy can considerably improve the handling upon mode switches such as the priority transfer between pilots, which was pointed out in [2].

**Contribution 5: Design Guidelines for Controllers to Accommodate Control Effector Limitations** With increasing size of electric VTOL aircraft, the inertia of lifting propellers scales at least quadratically with the overall vehicle mass, which leads to an over-proportional increase of the required electric current to accelerate the powered lift motors of a larger system. Due to electric current limits in the motors and power electronics, the resulting saturation of the propeller’s rotational acceleration represents a strong nonlinearity in the control loop and can lead to performance degradation if not properly accounted for.

To this end, section 5.2 introduced guidelines to accommodate control effector limitations in the controller design. By introducing the concept of an equivalent inner-loop bandwidth in subsection 5.2.3, the necessary relationships were derived in subsection 5.2.4 that enable the optimum choice of outer loop gains and saturation values such as to maximize the resulting equivalent outer-loop bandwidth (i.e. minimizing the step time for a given command amplitude).

The derived concepts were validated in subsection 5.2.5 by means of simulating a simplified 2D example for roll rate stabilization and yielded good results, which was shown in figure 5.8. Furthermore, the same concepts were applied for designing the gain and saturation values of the reference models in section 5.3, which was mentioned in e.g. subsection 5.3.4.1 and subsection 5.3.5.3.

## 7.2 Outlook and Perspectives

With the steadily increasing presence of safety-critical software in modern systems, the role of proper verification becomes indispensable. As is pointed out by [31], emerging properties of software-intensive systems such as handling qualities or safety have to be addressed with the concepts of systems thinking.

Due to continuous improvements in computational capabilities, the application of statistical testing methods have gained in popularity [172]. Exploring the vast amount of possible emerging behaviors for complex software-driven systems is hard if not impossible to do in an analytical way. Hence, the systematic exploitation of the high-dimensional space of possible outcomes by means of simulation represents an effective approach to address these challenges. Furthermore, these concepts are well suited for the verification and validation of VTOL transition aircraft functions, which rely on and are highly augmented by complex software solutions.

At the time of writing this thesis, several companies are developing electric VTOL aircraft. However, none have completed the certification process yet and hence the practical experience with respect to regular application scenarios for this new type of aircraft is still pending up to this point. In the upcoming years, operation of VTOL aircraft will increase in frequency and the proposed control strategies and concept of operations will be validated in real world scenarios.

Currently, there are no mandatory requirements with regard to the built-in control inceptors or concept of operations for VTOL aircraft. Hence, companies are developing their own strategies for operation and control. However, standardizing interface, control, and operation concepts could increase the compatibility between different aircraft models in the future. Depending on upcoming application scenarios, the seamless transition of the pilot or operator from one aircraft model to another might enable additional use cases for the operation of these vehicles.

Furthermore, with increasing reliability of electric motors, batteries, sensors, and computing platforms as well as high levels of functional integrity for safety-critical software, the complete autonomy of electric VTOL (transition) aircraft represents the next logical step in the revolution of air mobility. Thereby, the automotive industry leads the way with the development of self-driving cars, which are typically classified according to five levels of autonomy [173].

The requirements regarding reliability and availability of the underlying functions for self driving (or self flying) vehicles get more rigorous with increasing level of autonomy. Although the present technological maturity would allow for completely automated transportation in nominal, *sunny-day* conditions, feasible solutions have to account for off-nominal, *rainy-day* scenarios as well, which considerably increases the complexity and cost of such systems.

The inherent as well as perceived safety of novel transportation concepts plays a significant role in the public acceptance of these vehicles. Especially for person-carrying systems that are integrated into urban mobility and are highly augmented by software, the damage potential is high and the assignment of responsibility becomes increasingly more difficult. Besides the technical challenges that are faced by the engineer, ethical aspects come into focus as well, which are often referred to as the trolley problem [174].

The upcoming trends and developments in the area of electric aerial vehicles yield exciting opportunities and VTOL aircraft will become an integral part of transportation in the near future. Equipped with the knowledge and insights acquired in the scope of writing this thesis, the author is looking forward to contribute his part to the future of air mobility.



# Bibliography

- [1] J. Angelov and F. Holzapfel, “A novel command concept for simplified vehicle operations of onboard piloted VTOL transition aircraft,” in *Deutsche Gesellschaft für Luft- und Raumfahrt 2021*.
- [2] J. Angelov and F. Holzapfel, “A continuity-based command mapping approach applied to airspeed control of VTOL transition aircraft in the context of simplified vehicle operations,” in *AIAA SCITECH 2022 Forum*, (Reston, Virginia), American Institute of Aeronautics and Astronautics, 01032022.
- [3] R. Haberfellner, P. Nagel, M. Becker, A. Büchel, and H. von Massow, *Systems engineering*. Springer, 2019.
- [4] W. Stallings, “Gerald m. weinberg. an introduction to general systems thinking. new york: Wiley, 1975, 279 pp,” *Behavioral Science*, vol. 21, no. 4, pp. 289–290, 1976.
- [5] H. Hick, M. Bajzek, and C. Faustmann, “Definition of a system model for model-based development,” *SN Applied Sciences*, vol. 1, no. 9, 2019.
- [6] European Union Aviation Safety Agency, “Second publication of proposed means of compliance with the special condition VTOL.” <https://www.easa.europa.eu/downloads/128938/en>, 2021.
- [7] W. Johnson, C. Silva, and E. Solis, “Concept vehicles for VTOL air taxi operations,” 2018.
- [8] C. Silva, W. R. Johnson, E. Solis, M. D. Patterson, and K. R. Antcliff, “VTOL urban air mobility concept vehicles for technology development,” in *2018 Aviation Technology, Integration, and Operations Conference*, (Reston, Virginia), American Institute of Aeronautics and Astronautics, 06252018.
- [9] T. Lombaerts, J. Kaneshige, and M. Feary, “Control concepts for simplified vehicle operations of a quadrotor eVTOL vehicle,” in *AIAA AVIATION 2020 FORUM*, (Reston, Virginia), American Institute of Aeronautics and Astronautics, 06152020.
- [10] B. English and J. Bevirt, “Aircraft control system and method,” Pub. No.: US 2020/0333805 A1. Joby Aero, Inc., Santa Cruz, CA (US), 2020.

- [11] D. Dollinger, P. Reiss, J. Angelov, D. Löbl, and F. Holzapfel, “Control inceptor design for onboard piloted transition VTOL aircraft considering simplified vehicle operation,” in *AIAA Scitech 2021 Forum*, 2021.
- [12] United States Army Aviation and Missile Command Aviation Engineering Directorate, “Aeronautical design standard, performance specification, handling qualities requirements for military rotorcraft.”
- [13] J. McGough, K. Moses, W. Platt, G. Reynolds, and J. Strole, “Integrity in electronic flight control systems.” North Atlantic Treaty Organization Advisory Group for Aerospace Research and Development, 1977.
- [14] W. Johnson, “Model for Vortex Ring State Influence on Rotorcraft Flight Dynamics.” NASA Ames Research Center. <https://ntrs.nasa.gov/api/citations/20060024029/downloads/20060024029.pdf>, December, 2005. Accessed on: March 09, 2022. [Online].
- [15] K. J. Hayhurst and D. S. Veerhusen, “A practical approach to modified condition/decision coverage,” in *20th DASC. 20th Digital Avionics Systems Conference (Cat. No.01CH37219)*, pp. 1B2/1–1B2/10, IEEE, 2001.
- [16] F. Prochazka, S. Krüger, G. Stomberg, and M. Bauer, “Development of a hardware-in-the-loop demonstrator for the validation of fault-tolerant control methods for a hybrid uav,” *CEAS Aeronautical Journal*, vol. 12, no. 3, pp. 549–558, 2021.
- [17] MathWorks, “Model configuration parameters: Code generation.” <https://de.mathworks.com/help/rtw/ref/code-generation-pane-general.html>. Accessed on: June 30, 2022. [Online].
- [18] RTCA, “DO-178C/EUROCAE ED-12,” *Software Considerations in Airborne Systems and Equipment Certification*, 2011.
- [19] A. Pukhova, C. Llorca, A. Moreno, Q. Zhang, and R. Moeckel, “Urban air mobility: another disruptive technology or just an insignificant addition,” in *European Transport Conference. Dublin, Ireland*, 2019.
- [20] Osborne Clarke, “Battery technology advances are powering the rapid rise of electric vehicles.” <https://www.osborneclarke.com/insights/battery-technology-advances-powering-rapid-rise-electric-vehicles>, March 26, 2021. Accessed on: July 03, 2021. [Online].
- [21] A. W. Wymore, *Model-based systems engineering*, vol. 3. CRC press, 2018.
- [22] A. Vogelsang, *Model-Based Requirements Engineering for Multifunctional Systems*. Dissertation, Technical University of Munich, Munich, 15.12.2014.



- 
- [23] H. Andersson, *Model Based Systems Engineering in Avionics Design and Aircraft Simulation*. Dissertation, Linköpings universitet, Linköping, Sweden, 2009.
- [24] J. M. Borcky and T. H. Bradley, *Effective Model-Based Systems Engineering*. Cham: Springer International Publishing, 2019.
- [25] NASA, “Urban air mobility (uam) market study.” <https://ntrs.nasa.gov/api/citations/20190026762/downloads/20190026762.pdf>, November 2018. Accessed on: August 02, 2021. [Online].
- [26] Uber, “Redefining the future of safe on-demand air travel and transportation.” <https://uberpubpolicy.medium.com/fast-forwarding-to-a-future-of-on-demand-urban-air-transportation-f6ad36950ffa>, October 27, 2016. Accessed on: June 05, 2021. [Online].
- [27] Airbus, “Rethinking urban air mobility.” <https://www.airbus.com/newsroom/stories/rethinking-urban-air-mobility.html>, 2017. Accessed on: June 13, 2021. [Online].
- [28] Aurora, “Passenger air vehicle: Redefining the future of safe on-demand air travel and transportation.” <https://www.aurora.aero/pav-evtol-passenger-air-vehicle>. Accessed on: June 05, 2021. [Online].
- [29] Volocopter, “Urban air mobility: Innovation for a better city.” <https://www.volocopter.com/urban-air-mobility>. Accessed on: July 03, 2021. [Online].
- [30] Lilium, “Architectural performance assessment of an electric vertical take-off and landing (e-VTOL) aircraft based on a ducted vectored thrust concept.” [https://lilium.com/files/redaktion/refresh\\_feb2021/investors/Lilium\\_7-Seater\\_Paper.pdf](https://lilium.com/files/redaktion/refresh_feb2021/investors/Lilium_7-Seater_Paper.pdf), April 07, 2021. Accessed on: June 05, 2021. [Online].
- [31] N. G. Leveson, *Engineering a safer world: Systems thinking applied to safety*. The MIT Press, 2016.
- [32] R. Shishko and R. Aster, “Nasa systems engineering handbook,” *NASA Special Publication*, vol. 6105, 1995.
- [33] European Union Aviation Safety Agency, “Proposed means of compliance with the special condition VTOL.” [https://www.easa.europa.eu/sites/default/files/dfu/proposed\\_moc\\_sc\\_vtol\\_issue\\_1.pdf](https://www.easa.europa.eu/sites/default/files/dfu/proposed_moc_sc_vtol_issue_1.pdf), 2020.
- [34] Z. Zaludin and A. S. M. Harituddin, “Challenges and trends of changing from hover to forward flight for a converted hybrid fixed wing VTOL UAS from automatic flight control system perspective,” in *2019 IEEE 9th International Conference on System Engineering and Technology (ICSET)*, pp. 247–252, IEEE, 102019.

- [35] D. R. Vieira, D. Silva, and A. Bravo, “Electric VTOL aircraft: the future of urban air mobility (background, advantages and challenges),” *International Journal of Sustainable Aviation*, vol. 5, no. 2, p. 101, 2019.
- [36] V. A. Marvakov and F. Holzapfel, “Defining robust transition and re-transition procedures for unmanned fixed-wing VTOL aircraft,” in *AIAA Scitech 2021 Forum*, (Reston, Virginia), American Institute of Aeronautics and Astronautics, 01112021.
- [37] A. D. Hall, *A Methodology for Systems Engineering*. Princeton, NJ: van Nostrand, 1962.
- [38] M. Rabe, S. Spieckermann, and S. Wenzel, “Verification and validation activities within a new procedure model for v&v in production and logistics simulation,” 2009.
- [39] United States Department of Defense, “MIL-F-83300: Flying qualities of piloted v/stol aircraft.”
- [40] United States Department of Defense, “MIL-F-8785C: Flying qualities of piloted airplanes: Military specification.”
- [41] European Union Aviation Safety Agency, “Special condition for small-category VTOL aircraft.” <https://www.easa.europa.eu/sites/default/files/dfu/SC-VTOL-01%20proposed.pdf>, 2020.
- [42] F. Allgöwer, “Approximate input-output linearization of nonminimum phase nonlinear systems,” in *1997 European Control Conference (ECC)*, pp. 2359–2364, 1997.
- [43] S. Sieberling, Q. P. Chu, and J. A. Mulder, “Robust flight control using incremental nonlinear dynamic inversion and angular acceleration prediction,” *Journal of Guidance, Control, and Dynamics*, vol. 33, no. 6, pp. 1732–1742, 2010.
- [44] F. Holzapfel, *Nichtlineare adaptive Regelung eines unbemannten Fluggerätes*. Zugl.: München, techn. univ., diss., 2004, Verl. Dr. Hut, München, 2004.
- [45] S. A. Raab, J. Zhang, P. Bhardwaj, and F. Holzapfel, “Proposal of a unified control strategy for vertical take-off and landing transition aircraft configurations,” in *2018 Applied Aerodynamics Conference*, 2018.
- [46] S. A. Raab, J. Zhang, P. Bhardwaj, and F. Holzapfel, “Consideration of control effector dynamics and saturations in an extended indi approach,” in *AIAA Aviation 2019 Forum*, p. 3267, 2019.
- [47] D. ENNS, D. A. BUGAJSKI, R. HENDRICK, and G. STEIN, “Dynamic inversion: an evolving methodology for flight control design,” *International Journal of Control*, vol. 59, no. 1, pp. 71–91, 1994.

- 
- [48] J. H. Rountree, “Systems thinking—some fundamental aspects,” *Agricultural Systems*, vol. 2, no. 4, pp. 247–254, 1977.
- [49] International Council on Systems Engineering, “System and systems engineering definition.” <https://www.incose.org/about-systems-engineering/system-and-se-definition>. Accessed on: August 27, 2021. [Online].
- [50] L. Fortuna, G. Rizzotto, M. Lavorgna, G. Nunnari, M. G. Xibilia, and R. Caponetto, “Evolutionary optimization algorithms,” in *Soft Computing* (M. J. Grimble, M. A. Johnson, L. Fortuna, G. Rizzotto, M. Lavorgna, G. Nunnari, M. G. Xibilia, and R. Caponetto, eds.), Advanced Textbooks in Control and Signal Processing, pp. 97–116, London: Springer London, 2001.
- [51] A. B. Moniruzzaman and S. A. Hossain, “Comparative study on agile software development methodologies,” *arXiv preprint arXiv:1307.3356*, 2013.
- [52] S. P. M. Smith, K. Hargroves, and C. Desha, “Whole system design textbook - chapter 2 - the fundamentals of systems engineering to inform a whole system approach,” 2009.
- [53] E. McFadzean, “The creativity continuum: Towards a classification of creative problem solving techniques,” *Creativity and Innovation Management*, vol. 7, no. 3, pp. 131–139, 1998.
- [54] C. Zangemeister, *Nutzwertanalyse in der Systemtechnik: Eine Methodik zur multidimensionalen Bewertung und Auswahl von Projekialternativen: Teilw. zugl.: Berlin, Univ., Diss., 1970*. Norderstedt: Books on Demand, 5., erw. Aufl. ed., 2014.
- [55] SAE International, “ARP4754A (guidelines for development of civil aircraft and systems),” December 2010.
- [56] S. D. Junqueira Barbosa, P. Chen, A. Cuzzocrea, X. Du, J. Filipe, O. Kara, I. Kotenko, K. M. Sivalingam, D. Ślęzak, T. Washio, X. Yang, D. Zowghi, and Z. Jin, *Requirements Engineering*, vol. 432. Berlin, Heidelberg: Springer Berlin Heidelberg, 2014.
- [57] Inflectra, “Principles of requirements engineering.” <https://www.inflectra.com/ideas/whitepaper/principles-of-requirements-engineering.aspx>, February 13, 2020. Accessed on: September 24, 2021. [Online].
- [58] L. S. Wheatcraft, “Thinking ahead to verification and validation,” *Requirements Experts*, 2012.
- [59] O. Larses, *Architecting and modeling automotive embedded systems*. PhD thesis, Royal Institute of Technology, Stockholm, Sweden, 2005.

- [60] S. Friedenthal, A. Moore, and R. Steiner, *A practical guide to SysML: The systems modeling language*. The MK/OMG Press, Waltham, MA: Elsevier/Morgan Kaufmann, third edition ed., 2015.
- [61] A. Bacchini and E. Cestino, “Electric VTOL configurations comparison,” *Aerospace*, vol. 6, no. 3, p. 26, 2019.
- [62] W. Johnson and C. Silva, “Observations from exploration of VTOL urban air mobility designs,” 2018.
- [63] A. Z. Ibsen, “The politics of airplane production: The emergence of two technological frames in the competition between boeing and airbus,” *Technology in Society*, vol. 31, no. 4, pp. 342–349, 2009.
- [64] Y. C. Yeh, “Design considerations in boeing 777 fly-by-wire computers,” in *Proceedings Third IEEE International High-Assurance Systems Engineering Symposium (Cat. No.98EX231)*, pp. 64–72, IEEE Comput. Soc, 1998.
- [65] C. Favre, “Fly-by-wire for commercial aircraft: the airbus experience,” *International Journal of Control*, vol. 59, no. 1, pp. 139–157, 1994.
- [66] N. Oliver, T. Calvard, and K. Potočník, “Cognition, technology, and organizational limits: Lessons from the air france 447 disaster,” *Organization Science*, vol. 28, no. 4, pp. 729–743, 2017.
- [67] R. Hosman, B. Benard, and H. Fourquet, “Active and passive side stick controllers in manual aircraft control,” in *1990 IEEE International Conference on Systems, Man, and Cybernetics Conference Proceedings*, pp. 527–529, IEEE, 1990.
- [68] Bureau d’Enquêtes et d’Analyses pour la sécurité de l’aviation civile, “Final report on the accident on 1st June 2009 to the Airbus A330-203 registered F-GZCP operated by Air France flight AF 447 Rio de Janeiro - Paris.” <https://www.bea.aero/docspa/2009/f-cp090601.en/pdf/f-cp090601.en.pdf>, July, 2019. Accessed on: February 21, 2022. [Online].
- [69] Electric VTOL News by the Vertical Flight Society, “eVTOL Aircraft Directory.” <https://https://evtol.news/aircraft>. Accessed on: January 12, 2022. [Online].
- [70] R. SIRACUSE and K. GOVINDARAJ, “The VISTA/F-16 programmable feel system,” in *Flight Simulation Technologies Conference*, (Reston, Virigina), American Institute of Aeronautics and Astronautics, 08241992.
- [71] R. BAILEY, B. POWERS, and M. SHAFER, “Interaction of feel system and flight control system dynamics on lateral flying qualities,” in *15th Atmospheric Flight Mechanics Conference*, (Reston, Virigina), American Institute of Aeronautics and Astronautics, 08151988.

- [72] E. AMMONS, “F-16 flight control system redundancy concepts,” in *Guidance and Control Conference*, (Reston, Virginia), American Institute of Aeronautics and Astronautics, 08061979.
- [73] D. JOHNSTON and D. MCRUER, “Investigation of limb-sidestick dynamic interaction with roll control,” in *Guidance, Navigation and Control Conference*, (Reston, Virginia), American Institute of Aeronautics and Astronautics, 08191985.
- [74] G. Diaz Garcia, D. Seiferth, V. Meidinger, D. Dollinger, P. Nagarajan, and F. Holzapfel, “Conduction of mission task elements within simulator flight tests for handling quality evaluation of an eVTOL aircraft,” in *AIAA Scitech 2021 Forum*, p. 1897, 2021.
- [75] Nicholas, O. P., and Bennett, P. J., “Proposed wide envelope unified control concept for vectored thrust vstol aircraft.” Technical Memorandum FS312, Royal Aircraft Establishment RAE, 1980.
- [76] G. Meyer and L. S. Cicolani, “A formal structure for advanced automatic flight-control systems,” 1975.
- [77] D. A. Caughey, “Introduction to aircraft stability and control course notes for M&AE 5070,” *Sibley School of Mechanical & Aerospace Engineering Cornell University*, 2011.
- [78] MATLAB, *version 7.10.0 (R2010a)*. Natick, Massachusetts: The MathWorks Inc, 2010.
- [79] P. Bhardwaj, S. A. Raab, J. Zhang, and F. Holzapfel, “Thrust command based Integrated Reference Model with Envelope Protections for Tilt-rotor VTOL Transition UAV,” in *AIAA Aviation 2019 Forum*, (Reston, Virginia), American Institute of Aeronautics and Astronautics, 06172019.
- [80] P. Bhardwaj, S. A. Raab, and F. Holzapfel, “Higher order reference model for continuous dynamic inversion control,” in *AIAA Scitech 2021 Forum*, (Reston, Virginia), American Institute of Aeronautics and Astronautics, 01112021.
- [81] G. P. Falconi, J. Angelov, and F. Holzapfel, “Adaptive Fault-Tolerant Position Control of a Hexacopter Subject to an Unknown Motor Failure,” *International Journal of Applied Mathematics and Computer Science*, vol. 28, no. 2, pp. 309–321, 2018.
- [82] G. P. Falconi, J. Angelov, and F. Holzapfel, “Hexacopter outdoor flight test results using adaptive control allocation subject to an unknown complete loss of one propeller,” in *2016 3rd Conference on Control and Fault-Tolerant Systems (SysTol)*, pp. 373–380, IEEE, 92016.

- [83] R. Martinez-Alvarado, F. J. Ruiz-Sanchez, A. Sanchez-Orta, and O. Garcia-Salazar, "Dynamic response of bldc-thruster for small scale quadrotors under aerodynamic load torque," in *2014 IEEE International Autumn Meeting on Power, Electronics and Computing (ROPEC)*, pp. 1–6, IEEE, 112014.
- [84] P. Burgers, "A thrust equation treats propellers and rotors as aerodynamic cycles and calculates their thrust without resorting to the blade element method," *International Journal of Aviation, Aeronautics, and Aerospace*, 2019.
- [85] V. S. Akkinapalli and F. Holzapfel, "Incremental dynamic inversion based velocity tracking controller for a multicopter system," in *2018 AIAA Guidance, Navigation, and Control Conference*, (Reston, Virginia), American Institute of Aeronautics and Astronautics, 01082018.
- [86] P. Acquatella, W. Falkena, E.-J. van Kampen, and Q. P. Chu, "Robust nonlinear spacecraft attitude control using incremental nonlinear dynamic inversion," in *AIAA Guidance, Navigation, and Control Conference*, (Reston, Virginia), p. 813, American Institute of Aeronautics and Astronautics, 08132012.
- [87] J. Koschorke, W. Falkena, E.-J. van Kampen, and Q. P. Chu, "Time delayed incremental nonlinear control," in *AIAA Guidance, Navigation, and Control (GNC) Conference*, (Reston, Virginia), American Institute of Aeronautics and Astronautics, 08192013.
- [88] R. E. Neapolitan and K. Hee Nam, *AC Motor Control and Electrical Vehicle Applications*. CRC press, 2018.
- [89] Y. Wei, Y. Xu, J. Zou, and Y. Li, "Current Limit Strategy for BLDC Motor Drive With Minimized DC-Link Capacitor," *IEEE Transactions on Industry Applications*, vol. 51, no. 5, pp. 3907–3913, 2015.
- [90] R. Rabinoff, "Moments of inertia by scaling arguments: How to avoid messy integrals," *American Journal of Physics*, vol. 53, no. 5, pp. 501–502, 1985.
- [91] D. Thompson, *Envelope Analysis of Speed-Controlled eVTOL Urban Air Mobility Vehicles*. Master's thesis, Embry-Riddle Aeronautical University, 2021.
- [92] M. Duffy, A. E. Sevier, R. Hupp, E. Perdomo, and S. Wakayama, "Propulsion scaling methods in the era of electric flight," in *2018 AIAA/IEEE Electric Aircraft Technologies Symposium*, (Reston, Virginia), American Institute of Aeronautics and Astronautics, 07092018.
- [93] V. H. Alulema, E. A. Valencia, E. Cando, and D. Rodriguez, "Preliminary sizing correlations for UAVs' propulsion system," in *AIAA Propulsion and Energy 2019*

- Forum*, (Reston, Virginia), American Institute of Aeronautics and Astronautics, 08192019.
- [94] C. S. Rao, S. Santosh, and D. R. V, “Tuning optimal PID controllers for open loop unstable first order plus time delay systems by minimizing ITAE criterion,” *IFAC-PapersOnLine*, vol. 53, no. 1, pp. 123–128, 2020.
- [95] Z.-Q. Lang and S. A. Billings, “Output frequency characteristics of nonlinear systems,” *International Journal of Control*, vol. 64, no. 6, pp. 1049–1067, 1996.
- [96] N. Noiray, D. Durox, T. Schuller, and S. Candel, “A unified framework for nonlinear combustion instability analysis based on the flame describing function,” *Journal of Fluid Mechanics*, vol. 615, pp. 139–167, 2008.
- [97] J. Angelov, Y. E. Yoon, E. N. Johnson, and F. Holzapfel, “Analytical derivation of the sinusoidal input describing function for adaptive augmenting control algorithms,” in *2018 AIAA Guidance, Navigation, and Control Conference*, (Reston, Virginia), American Institute of Aeronautics and Astronautics, 01082018.
- [98] N. Ahmad, R. A. R. Ghazilla, N. M. Khairi, and V. Kasi, “Reviews on Various Inertial Measurement Unit (IMU) Sensor Applications,” *International Journal of Signal Processing Systems*, pp. 256–262, 2013.
- [99] J.-H. Kim, S. Sukkarieh, and S. Wishart, “Real-Time Navigation, Guidance, and Control of a UAV Using Low-Cost Sensors,” in *Field and Service Robotics* (S. Yuta, H. Asama, E. Prassler, T. Tsubouchi, and S. Thrun, eds.), vol. 24 of *Springer Tracts in Advanced Robotics*, pp. 299–309, Berlin/Heidelberg: Springer-Verlag, 2006.
- [100] J. Gregory and T. Liu, eds., *Introduction to Flight Testing*. Wiley, 2021.
- [101] O. I. Iloputaife, “Design of Deep Stall Protection for the C-17A,” *Journal of Guidance, Control, and Dynamics*, vol. 20, no. 4, pp. 760–767, 1997.
- [102] R. K. Raney, “The delay/doppler radar altimeter,” *IEEE Transactions on Geoscience and Remote Sensing*, vol. 36, no. 5, pp. 1578–1588, 1998.
- [103] D. Moormann, U. Korte, B. Fischer, and M. Kurze, “The baracuda autoflight module for autonomous flight,” *IFAC Proceedings Volumes*, vol. 40, no. 7, pp. 846–851, 2007.
- [104] W. Tang, G. Howell, and Y.-H. Tsai, “Barometric altimeter short-term accuracy analysis,” *IEEE Aerospace and Electronic Systems Magazine*, vol. 20, no. 12, pp. 24–26, 2005.

- [105] G. Di Francesco and M. Mattei, “Modeling and incremental nonlinear dynamic inversion control of a novel unmanned tiltrotor,” *Journal of Aircraft*, vol. 53, no. 1, pp. 73–86, 2016.
- [106] L.N.C. Sikkel, E.J.J. Smeur, G.C.H.E de Croon, B.D.W. Remes, and Q.P. Chu, “Robust rotorcraft control using an incremental sliding mode controller,”
- [107] A. Tomczyk, “Experimental fly-by-wire control system for general aviation aircraft,” in *AIAA Guidance, Navigation, and Control Conference and Exhibit*, (Reston, Virginia), American Institute of Aeronautics and Astronautics, 08112003.
- [108] C. Slivinsky and J. Givens, “Monitoring and Voting in Asynchronous Sampling,” *IEEE Transactions on Aerospace and Electronic Systems*, vol. AES-21, no. 1, pp. 92–99, 1985.
- [109] C. Liu, X. Wang, and X. Liu, “Research on Hybrid Redundancy Voting Algorithm Based on Fuzzy Theory,” *Journal of Physics: Conference Series*, vol. 2035, no. 1, p. 012016, 2021.
- [110] R. R. Wilcox, *Introduction to robust estimation and hypothesis testing*. Statistical modeling and decision science, Amsterdam: Academic Press, fourth edition ed., 2017.
- [111] M. P. Herlihy and J. M. Wing, “Specifying graceful degradation,” *IEEE Transactions on Parallel and Distributed Systems*, vol. 2, no. 1, pp. 93–104, 1991.
- [112] V. Marvakov, *Automating the Transition of Lift-to-Cruise eVTOL Aircraft*. Dissertation, Technische Universität München, München, 2023 (not yet submitted).
- [113] K. J. Astrom and L. Rundqwist, “Integrator windup and how to avoid it,” in *1989 American Control Conference*, pp. 1693–1698, IEEE, 61989.
- [114] J. G. Grabowski, S. P. Baker, and G. Li, “Ground crew injuries and fatalities in U.S. commercial aviation, 1983-2004,” *Aviation, space, and environmental medicine*, vol. 76, no. 11, pp. 1007–1011, 2005.
- [115] I. E. Garrick and W. H. Reed, “Historical development of aircraft flutter,” *Journal of Aircraft*, vol. 18, no. 11, pp. 897–912, 1981.
- [116] R. Steffensen, A. Steinert, and F. Holzapfel, “Longitudinal incremental reference model for fly-by-wire control law using incremental non-linear dynamic inversion,” in *AIAA SCITECH 2022 Forum*, (Reston, Virginia), American Institute of Aeronautics and Astronautics, 01032022.



- 
- [117] V. Stepanyan, K. Krishnakumar, G. Dorais, S. Reardon, J. Barlow, A. Lampton, and G. Hardy, “Loss-of-control mitigation via predictive cuing,” *Journal of Guidance, Control, and Dynamics*, vol. 40, no. 4, pp. 831–846, 2017.
- [118] I. Yavrucuk and J. V. R. Prasad, “Online dynamic trim and control limit estimation,” *Journal of Guidance, Control, and Dynamics*, vol. 35, no. 5, pp. 1647–1656, 2012.
- [119] National Archives and Records Administration (NARA), “Code of Federal Regulations.” <https://www.ecfr.gov/current/title-14/chapter-I/subchapter-A/part-1/section-1.2>, February 25, 2022. Accessed on: March 01, 2022. [Online].
- [120] C. Chen and J. Prasad, “Theoretical investigations of a helicopter rotor in steep descent,” in *AIAA Modeling and Simulation Technologies Conference and Exhibit*, (Reston, Virginia), American Institute of Aeronautics and Astronautics, 08152005.
- [121] B. Dang-Vu, “Vortex ring state protection flight control law,” in *39th European Rotorcraft Forum*, (MOSCOU, Russia), 2013.
- [122] Taghizad, Armin, Jimenez, Jeremy, Binet, Laurent, Heuzé, and Daniel, “Experimental and theoretical investigations to develop a model of rotor aerodynamics adapted to steep descents,” in *American Helicopter Society 58th Annual Forum*, (Montreal, Canada), 2002.
- [123] Javier Jiménez, André Desopper, Armin Taghizad, and Laurent Binet, “Induced velocity model in steep descent and vortex-ring state prediction,” in *27th European Rotorcraft Forum*, (Moscow, Russia), 2001.
- [124] M. Euston, P. Coote, R. Mahony, J. Kim, and T. Hamel, “A complementary filter for attitude estimation of a fixed-wing uav,” in *2008 IEEE/RSJ International Conference on Intelligent Robots and Systems*, pp. 340–345, IEEE, 092008.
- [125] T. S. Yoo, S. K. Hong, H. M. Yoon, and S. Park, “Gain-scheduled complementary filter design for a mems based attitude and heading reference system,” *Sensors (Basel, Switzerland)*, vol. 11, no. 4, pp. 3816–3830, 2011.
- [126] J. Wu, Z. Zhou, J. Chen, H. Fourati, and R. Li, “Fast complementary filter for attitude estimation using low-cost mag sensors,” *IEEE Sensors Journal*, vol. 16, no. 18, pp. 6997–7007, 2016.
- [127] M. S. Grewal, “Kalman filtering,” in *International Encyclopedia of Statistical Science* (M. Lovric, ed.), pp. 705–708, Berlin, Heidelberg: Springer Berlin Heidelberg, 2011.
- [128] W. Higgins, “A comparison of complementary and kalman filtering,” *IEEE Transactions on Aerospace and Electronic Systems*, vol. AES-11, no. 3, pp. 321–325, 1975.

- [129] Y. Li, X. Liu, P. Lu, Q. He, R. Ming, and W. Zhang, “Angular acceleration estimation-based incremental nonlinear dynamic inversion for robust flight control,” *Control Engineering Practice*, vol. 117, p. 104938, 2021.
- [130] D. V. Widder, “What is the laplace transform?,” *The American Mathematical Monthly*, vol. 52, no. 8, pp. 419–425, 1945.
- [131] T. Wu, S. Bozhko, G. Asher, P. Wheeler, and D. Thomas, “Fast reduced functional models of electromechanical actuators for more-electric aircraft power system study,” in *SAE Technical Paper Series*, SAE Technical Paper Series, SAE International400 Commonwealth Drive, Warrendale, PA, United States, 2008.
- [132] B. Bilgin, J. Liang, M. V. Terzic, J. Dong, R. Rodriguez, E. Trickett, and A. Emadi, “Modeling and analysis of electric motors: State-of-the-art review,” *IEEE Transactions on Transportation Electrification*, vol. 5, no. 3, pp. 602–617, 2019.
- [133] T. A. Johansen and T. I. Fossen, “Control allocation—a survey,” *Automatica*, vol. 49, no. 5, pp. 1087–1103, 2013.
- [134] J. Virnig and D. Bodden, “Multivariable control allocation and control law conditioning when control effectors limit,” in *Guidance, Navigation, and Control Conference*, (Reston, Virginia), American Institute of Aeronautics and Astronautics, 08011994.
- [135] R. Eberhardt and D. Ward, “Indirect adaptive flight control of a tailless fighter aircraft,” in *Guidance, Navigation, and Control Conference and Exhibit*, (Reston, Virginia), American Institute of Aeronautics and Astronautics, 08091999.
- [136] G. Di Francesco, M. Mattei, and E. D’Amato, “Incremental nonlinear dynamic inversion and control allocation for a tilt rotor uav,” in *AIAA Guidance, Navigation, and Control Conference*, (Reston, Virginia), p. r2006, American Institute of Aeronautics and Astronautics, 01132014.
- [137] M. Bodson, “Evaluation of optimization methods for control allocation,” in *AIAA Guidance, Navigation, and Control Conference and Exhibit*, (Reston, Virginia), American Institute of Aeronautics and Astronautics, 08062001.
- [138] J. Zhang, J. Wang, F. Zhang, and F. Holzapfel, “Modeling and incremental nonlinear dynamic inversion control for a highly redundant flight system,” in *AIAA Scitech 2019 Forum*, (Reston, Virginia), American Institute of Aeronautics and Astronautics, 01072019.
- [139] R. A. Horn and C. R. Johnson, *Matrix analysis*. New York, NY: Cambridge University Press, second edition, corrected reprint ed., 2017.

- [140] W. C. Durham, “Constrained control allocation,” *Journal of Guidance, Control, and Dynamics*, vol. 16, no. 4, pp. 717–725, 1993.
- [141] R. Bagnara, A. Bagnara, and P. M. Hill, “The misra c coding standard and its role in the development and analysis of safety- and security-critical embedded software.”
- [142] S. Chib, “Markov chain monte carlo methods: Computation and inference,” vol. 5 of *Handbook of Econometrics*, pp. 3569–3649, Elsevier, 2001.
- [143] U. Graf, “z-transformation,” in *Applied Laplace Transforms and z-Transforms for Scientists and Engineers* (U. Graf, ed.), pp. 77–113, Basel: Birkhäuser Basel, 2004.
- [144] S. Winograd, “On computing the discrete fourier transform,” *Mathematics of Computation*, vol. 32, no. 141, pp. 175–199, 1978.
- [145] S. A. Dyer and J. S. Dyer, “The bilinear transformation,” *IEEE Instrumentation & Measurement Magazine*, vol. 3, no. 1, pp. 30–34, 2000.
- [146] J. L. Basdevant, “The padé approximation and its physical applications,” *Fortschritte der Physik*, vol. 20, no. 5, pp. 283–331, 1972.
- [147] D. F. Griffiths and D. J. Higham, “Euler’s method,” in *Numerical Methods for Ordinary Differential Equations* (D. F. Griffiths and D. J. Higham, eds.), Springer Undergraduate Mathematics Series, pp. 19–31, London: Springer London, 2010.
- [148] H. J. Landau, “Sampling, data transmission, and the nyquist rate,” *Proceedings of the IEEE*, vol. 55, no. 10, pp. 1701–1706, 1967.
- [149] P. J. Davis, *Methods of Numerical Integration*. Burlington: Elsevier Science, 2nd ed. ed., 2014.
- [150] T. J. Ypma, “Historical development of the newton–raphson method,” *SIAM Review*, vol. 37, no. 4, pp. 531–551, 1995.
- [151] J. Krizan, L. Ertl, M. Bradac, M. Jasansky, and A. Andreev, “Automatic code generation from matlab/simulink for critical applications,” in *2014 IEEE 27th Canadian Conference on Electrical and Computer Engineering (CCECE)*, pp. 1–6, IEEE, 52014.
- [152] MathWorks, “stairs: Stairstep graph.” <https://de.mathworks.com/help/matlab/ref/stairs.html>. Accessed on: June 30, 2022. [Online].
- [153] T. Erkkinen and M. Conrad, “Safety-critical software development using automatic production code generation,” in *SAE Technical Paper Series*, SAE Technical Paper Series, SAE International400 Commonwealth Drive, Warrendale, PA, United States, 2007.

- [154] M. Hochstrasser, *Modular model-based development of safety-critical flight control software*. Dissertation, Technische Universität München, München, 2020.
- [155] MathWorks, “Model advisor checks for high-integrity modeling guidelines.” [https://de.mathworks.com/help/simulink/mdl\\_gd/hi/model-advisor-checks-for-high-integrity-modeling-guidelines.html](https://de.mathworks.com/help/simulink/mdl_gd/hi/model-advisor-checks-for-high-integrity-modeling-guidelines.html). Accessed on: June 27, 2022. [Online].
- [156] MathWorks, “High-integrity system modeling: Modeling guidelines for high-integrity systems.” <https://de.mathworks.com/help/simulink/high-integrity-systems.html>. Accessed on: June 27, 2022. [Online].
- [157] MathWorks, “Software-in-the-loop simulation: Test generated code on development computer.” <https://de.mathworks.com/help/ecoder/software-in-the-loop-simulation.html>. Accessed on: June 30, 2022. [Online].
- [158] Alexandru G. Bardas, “Static code analysis,” *Romanian Economic Business Review*, vol. 4, no. 2, pp. 99–107, 2010.
- [159] S. K. Au, J. Ching, and J. L. Beck, “Application of subset simulation methods to reliability benchmark problems,” *Structural Safety*, vol. 29, no. 3, pp. 183–193, 2007.
- [160] S.-K. Au and Y. Wang, *Engineering Risk Assessment with Subset Simulation*. Wiley, 2014.
- [161] A. Shapiro, “Monte carlo sampling methods,” in *Stochastic Programming*, vol. 10 of *Handbooks in Operations Research and Management Science*, pp. 353–425, Elsevier, 2003.
- [162] D. Löbl, *A Total Capability Approach for the Development of Safety-Critical Functions*. Dissertation, Technische Universität München, München, 2018.
- [163] D. Löbl and F. Holzapfel, “Subset simulation for estimating small failure probabilities of an aerial system subject to atmospheric turbulences,” in *AIAA Atmospheric Flight Mechanics Conference*, (Reston, Virginia), American Institute of Aeronautics and Astronautics, 01052015.
- [164] K. M. Zuev, “Subset simulation method for rare event estimation: An introduction,” in *Encyclopedia of Earthquake Engineering* (M. Beer, I. A. Kougioumtzoglou, E. Patelli, and I. S.-K. Au, eds.), pp. 1–25, Berlin, Heidelberg: Springer Berlin Heidelberg, 2021.
- [165] S. Sun and X. Li, “Fast statistical analysis of rare failure events for memory circuits in high-dimensional variation space,” in *The 20th Asia and South Pacific Design Automation Conference*, pp. 302–307, IEEE, 12015.

- [166] C. Mishra, F. Schwaiger, N. M. Bähr, F. Sax, M. A. Kleser, P. Nagarajan, and F. Holzapfel, “Efficient verification and validation of performance-based safety requirements using subset simulation,” in *AIAA Scitech 2021 Forum*, (Reston, Virginia), American Institute of Aeronautics and Astronautics, 01112021.
- [167] D. Simon, *Evolutionary optimization algorithms: Biologically-inspired and population-based approaches to computer intelligence*. Hoboken, NJ: Wiley, 1. ed. ed., 2013.
- [168] D. Braun, R. Steffensen, A. Steinert, and F. Holzapfel, “Counter Optimization-Based Testing of Flight Envelope Protections in a Fly-By-Wire Control Law Using Deep Q-Learning,” in *CEAS EuroGNC 2022*.
- [169] J. Diepolder, J. Z. Ben-Asher, and F. Holzapfel, “Flight control law clearance using worst-case inputs under parameter uncertainty,” *Journal of Guidance, Control, and Dynamics*, vol. 43, no. 10, pp. 1967–1974, 2020.
- [170] A. A. Herrmann and J. Z. Ben-Asher, “Flight control law clearance using optimal control theory,” *Journal of Aircraft*, vol. 53, no. 2, pp. 515–529, 2016.
- [171] European Organisation for Civil Aviation Equipment (EUROCAE), “VTOL Flight Control Handling Qualities Verification,” 2021.
- [172] D. L. Parnas, A. J. van Schouwen, and S. P. Kwan, “Evaluation of safety-critical software,” *Communications of the ACM*, vol. 33, no. 6, pp. 636–648, 1990.
- [173] S. Liu, J. Tang, Z. Zhang, and J.-L. Gaudiot, “Computer architectures for autonomous driving,” *Computer*, vol. 50, no. 8, pp. 18–25, 2017.
- [174] T. Holstein, “The misconception of ethical dilemmas in self-driving cars,” in *Proceedings of the IS4SI 2017 Summit DIGITALISATION FOR A SUSTAINABLE SOCIETY, Gothenburg, Sweden, 12–16 June 2017*, (Basel Switzerland), p. 174, MDPI, 2017.